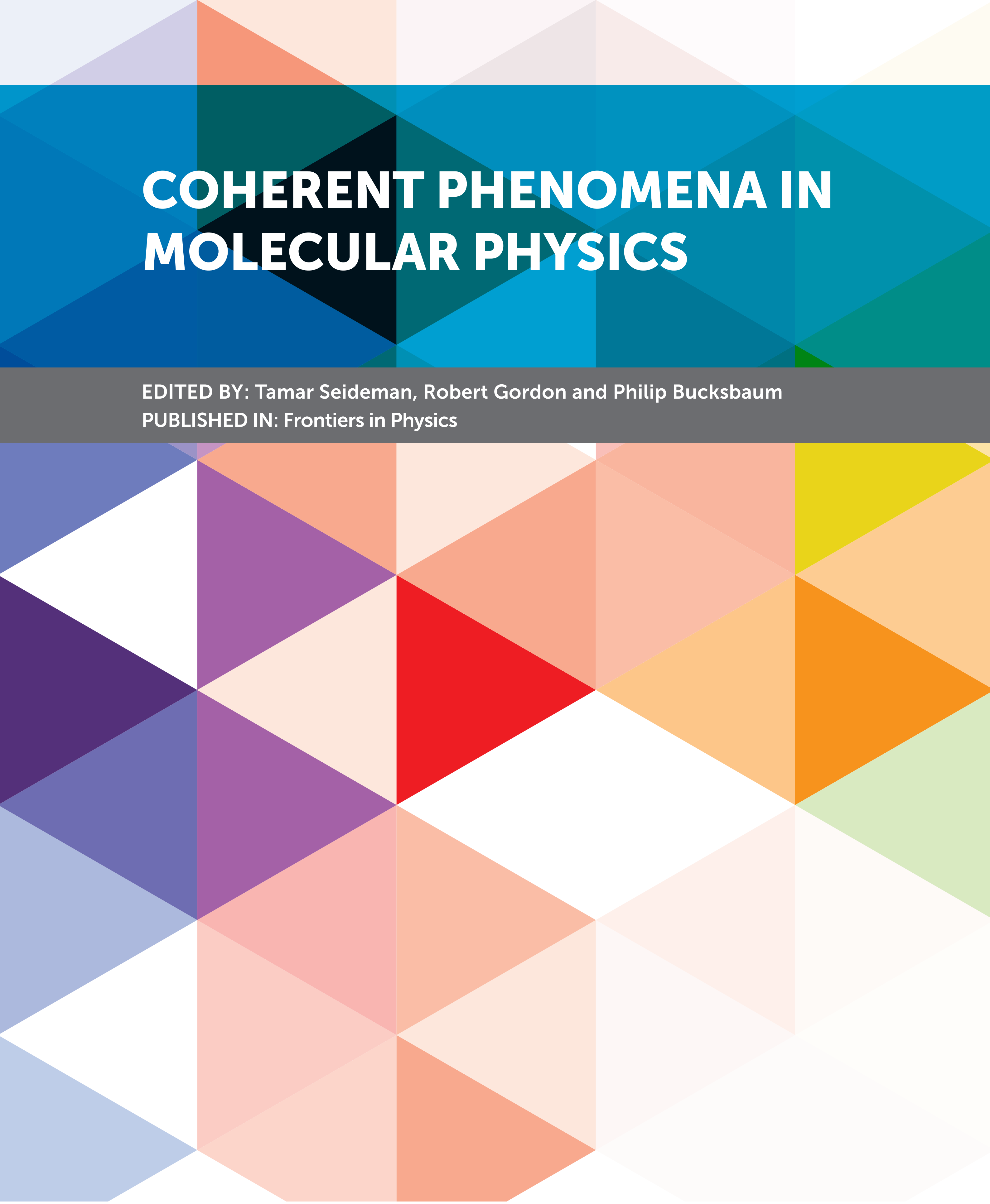

COHERENT PHENOMENA IN MOLECULAR PHYSICS

EDITED BY: Tamar Seideman, Robert Gordon and Philip Bucksbaum
PUBLISHED IN: Frontiers in Physics

frontiers Research Topics

ISSN 1664-8714
ISBN 978-2-88976-755-7
DOI 10.3389/978-2-88976-755-7

About Frontiers

Frontiers is more than just an open-access publisher of scholarly articles: it is a pioneering approach to the world of academia, radically improving the way scholarly research is managed. The grand vision of Frontiers is a world where all people have an equal opportunity to seek, share and generate knowledge. Frontiers provides immediate and permanent online open access to all its publications, but this alone is not enough to realize our grand goals.

Frontiers Journal Series

The Frontiers Journal Series is a multi-tier and interdisciplinary set of open-access, online journals, promising a paradigm shift from the current review, selection and dissemination processes in academic publishing. All Frontiers journals are driven by researchers for researchers; therefore, they constitute a service to the scholarly community. At the same time, the Frontiers Journal Series operates on a revolutionary invention, the tiered publishing system, initially addressing specific communities of scholars, and gradually climbing up to broader public understanding, thus serving the interests of the lay society, too.

Dedication to Quality

Each Frontiers article is a landmark of the highest quality, thanks to genuinely collaborative interactions between authors and review editors, who include some of the world's best academicians. Research must be certified by peers before entering a stream of knowledge that may eventually reach the public - and shape society; therefore, Frontiers only applies the most rigorous and unbiased reviews.
Frontiers revolutionizes research publishing by freely delivering the most outstanding research, evaluated with no bias from both the academic and social point of view. By applying the most advanced information technologies, Frontiers is catapulting scholarly publishing into a new generation.

What are Frontiers Research Topics?

Frontiers Research Topics are very popular trademarks of the Frontiers Journals Series: they are collections of at least ten articles, all centered on a particular subject. With their unique mix of varied contributions from Original Research to Review Articles, Frontiers Research Topics unify the most influential researchers, the latest key findings and historical advances in a hot research area! Find out more on how to host your own Frontiers Research Topic or contribute to one as an author by contacting the Frontiers Editorial Office: frontiersin.org/about/contact

COHERENT PHENOMENA IN MOLECULAR PHYSICS

Topic Editors:
Tamar Seideman, Northwestern University, United States
Robert Gordon, University of Illinois at Chicago, United States
Philip Bucksbaum, Stanford University, United States

Citation: Seideman, T., Gordon, R., Bucksbaum, P., eds (2022). Coherent Phenomena in Molecular Physics. Lausanne: Frontiers Media.
doi: 10.3389/978-2-88976-755-7

Table of Contents

frontiers in Physics

ORIGINAL RESEARCH
published: 21 April 2021
doi: 10.3389/fphy.2021.657333

High Order Coherence Functions and Spectral Distributions as Given by the Scully-Lamb Quantum Theory of the Laser

*Tao Peng[1], Xingchen Zhao[1], Yanhua Shih[2] and Marlan O. Scully[1,3,4]**

[1] Texas A&M University, College Station, TX, United States, [2] University of Maryland, Baltimore County, Baltimore, MD, United States, [3] Baylor University, Waco, TX, United States, [4] Princeton University, Princeton, NJ, United States

We propose and demonstrate a method for measuring the time evolution of the off-diagonal elements $\rho_{n,n+k}(t)$ of the reduced density matrix obtained from the quantum theory of the laser. The decay rates of the off-diagonal matrix element $\rho_{n,n+k}(t)$ (k = 2,3) are measured for the first time and compared with that of $\rho_{n,n+1}(t)$, which corresponds to the linewidth of the laser. The experimental results agree with the Scully-Lamb quantum theory of the laser.

Keywords: high order coherence, quantum theory of the laser, spectral line distribution, density matrix, heterodyne detection

Edited by:
Tamar Seideman,
Northwestern University, United States

Reviewed by:
Qing Ai,
Beijing Normal University, China
Andre Bandrauk,
Université de Sherbrooke, Canada

Correspondence:
Marlan O. Scully
scully@tamu.edu

Specialty section:
This article was submitted to Optics and Photonics, a section of the journal Frontiers in Physics

Received: *22 January 2021*
Accepted: *23 March 2021*
Published: *21 April 2021*

Citation:
Peng T, Zhao X, Shih Y and Scully MO (2021) High Order Coherence Functions and Spectral Distributions as Given by the Scully-Lamb Quantum Theory of the Laser. Front. Phys. 9:657333. doi: 10.3389/fphy.2021.657333

1. INTRODUCTION

Quantum coherence effects in molecular physics are largely based on the existence of the laser [1]. Indeed, in most of our experiments and calculations we take the laser to be an ideal monochromatic light source. If the laser linewidth is important then we usually just include a "phase diffusion" linewidth into the logic. But what if we are thinking about higher order correlation effects in an ensemble of coherently driven molecules. For example, photon correlation and light beating spectroscopy involving Glauber second order correlation functions [2, 3]. Furthermore, third and higher order photon correlations of the laser used to drive our molecular system can be important. The investigation of higher order quantum laser noise is the focus of the present paper.

Fifty years ago the Scully-Lamb (SL) quantum theory of the laser (QTL) was developed using a density matrix formalism [4]. In the interesting threshold region [5, 6] the steady state laser photon statistics is given by the diagonal elements of the laser density matrix as

$$\rho_{n,n} = \mathfrak{N} \prod_{m=0}^{n} [\alpha - \beta m]/\gamma, \tag{1}$$

where α is the linear gain, β is the non-linear saturation coefficient, γ is the cavity loss rate, and $\mathfrak{N}$ is the normalization constant:

$$\mathfrak{N}^{-1} = \sum_{n} \prod_{m=0}^{n} [\alpha - \beta m]/\gamma. \tag{2}$$

Equation (1) is plotted in **Figure 1** where it is compared with a coherent state.

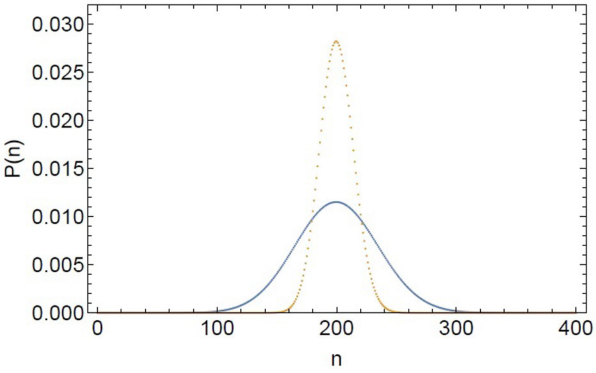

FIGURE 1 | Steady state photon distribution function for coherent (orange dashed line) and laser radiation (blue solid line). The laser is taken to be 20 percent above threshold, $\langle n \rangle = 200$.

TABLE 1 | Parameters in laser and BEC systems.

	Laser	BEC
α	Linear stimulated emission gain	Rate of cooling due to interaction with walls times the number of atom N
β	Non-linear saturation due to the reabsorption of photons generated by stimulated emission	Non-linearity parameter due to the constraint that there are N atoms in the BEC: numerically equal to α/N.
γ	Loss rate due to photons absorbed in cavity mirrors etc.	Loss rate due to photon absorption from the thermal bath (walls) equal to $\alpha(T/T_c)^3$.

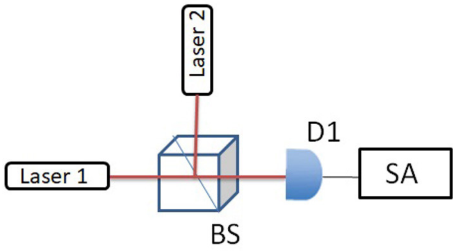

FIGURE 2 | Experimental setup used in measuring the spectrum of the beat note between lasers 1 and 2. The beat note signal is measured by the detector (*D*1) and analyzed by the spectrum analyzer(SA). BS, non-polarizing beamsplitter.

The formalism developed in the QTL density matrix analysis has since been successfully applied to many other physical systems such as the single-atom maser(aka the micromaser) [7], the Bose-Einstein condensate (aka the atom laser, see **Table 1**) [8], pion physics [9], etc. Other applications of the formalism have been developed recently and more will likely emerge. Thus, we are motivated to deeper our understanding of the QTL by further analyzing and experimentally verifying the time dependence of off-diagonal elements $\rho_{n,n+k}(t) \equiv \rho_n^{(k)}(t)$. The diagonal elements of the laser density matrix for which $k = 0$, have been well-studied. Not as for the off-diagonal elements. In particular $\rho_n^{(1)}(t)$ yields the Schawlow-Townes laser linewidth. But what about the higher order correlations $k = 2, 3\cdots$? That is the focus of the current paper.

2. THEORY AND EXPERIMENT

The off-diagonal elements vanish at steady state, regressing to zero as [4]

$$\rho_n^{(k)}(t) = \rho_n^{(k)}(0)\exp(-k^2Dt) \tag{3}$$

where $D = \gamma/\bar{n}$ is the Schawlow-Townes phase diffusion linewidth and $\bar{n} = (\alpha - \gamma)/\beta$. The expectation value of the laser amplitude operator is given by

$$\langle \hat{E}(z,t)\rangle = \mathscr{E}_0 e^{i\kappa z}\sum_n \rho_n^{(1)}(0)\sqrt{n+1}\,e^{-Dt}e^{-i\nu t}, \tag{4}$$

where ν is the center frequency of the laser field and the electric field per photon is given by $\mathscr{E}_0 = \sqrt{\hbar\nu/\epsilon_0 V}$, where ϵ_0 is the permittivity of free space and V is the laser cavity volume.

As is discussed in the following, the second order off-diagonal elements are given by the field operator averages

$$\langle \hat{E}(z,t)\hat{E}(z,t)\rangle = \mathscr{E}_0^2 e^{i2\kappa z}\sum_n \rho_n^{(2)}(0)\sqrt{(n+1)(n+2)}\,e^{-4Dt}e^{-i2\nu t}, \tag{5}$$

and the third order off-diagonal elements are given by

$$\begin{aligned}&\langle \hat{E}(z,t)\hat{E}(z,t)\hat{E}(z,t)\rangle\\ &= \mathscr{E}_0^3 e^{i3\kappa z}\sum_n \rho_n^{(3)}(0)\sqrt{(n+1)(n+2)(n+3)}\,e^{-9Dt}e^{-i3\nu t}.\end{aligned} \tag{6}$$

Equation (4) gives the time evolution associated with the first order off-diagonal elements $\rho_n^{(1)}$, yielding the spectral profile of the laser. The heterodyne method is usually adapted to measure the linewidth of the laser [10, 11], in which case the center frequency is shifted from optical frequency to the radio frequency range. A natural way to measure the laser linewidth is to beat two almost identical but uncorrelated lasers [12] such that the beat frequency between the lasers is in the MHz range. The result, as seen from Equation (10), is twice of the laser linewidth when the two independent lasers are nearly identical.

Many experiments have been carried out to determine the linewidth [10] and photon statistics [13] of the laser. Other experiments have measured the intensity correlation of the laser at threshold [14], revealing the influence of the intensity fluctuation on the laser spectrum. However, to the best of our knowledge, no measurements have been made of the higher order phase correlations ($k \geq 2$). Here we measure the second and third correlation of the heterodyne signals from two independent lasers, which yields the second and third order time evolution of a laser above threshold. Specifically, we performed the following

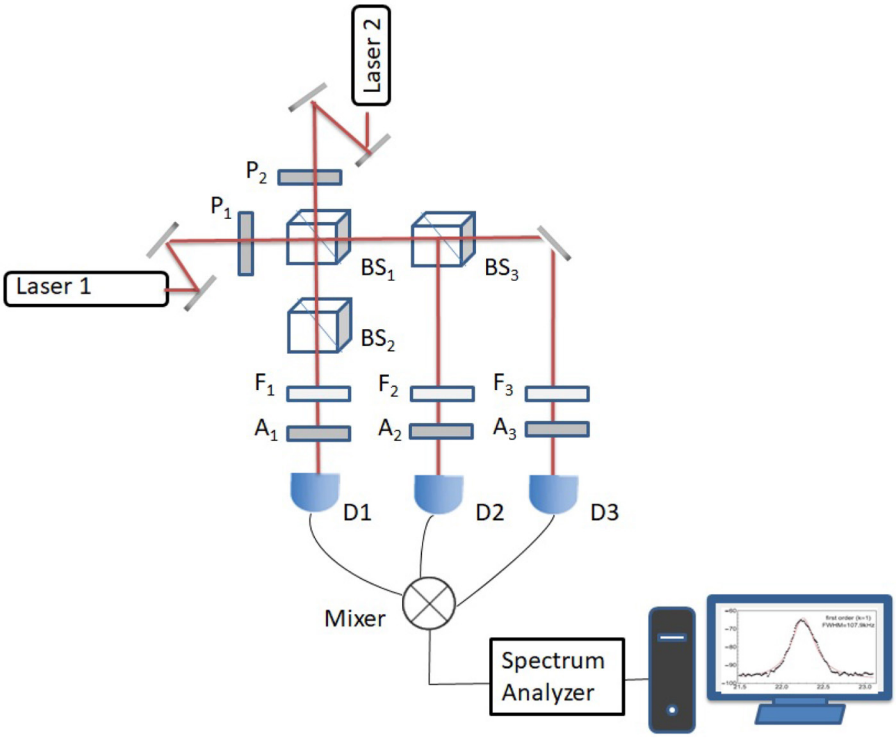

FIGURE 3 | Schematic setup for measuring higher order spectral line distribution up to 3rd order. Laser 1 and 2 : He-Ne lasers; P, polarizer; F, filter; A, analyzer; BS, non-polarizing beamsplitter; Mixer, frequency mixer; *D*1, *D*2, and *D*3, photodiode detectors.

experiments: the first set of experiments is to measure the spectral profile of the laser beat note, i.e., allows us to measure the decay rate as shown in Equation (4). The other two sets of experiments determine the spectral profile of the second and third order correlated beat notes, this allows us to measure the decay rate as shown in Equations (5) and (6).

Figure 2 illustrates the setup of the first set of experiments. This is a typical heterodyne detection setup, the center frequency between the two He-Ne lasers is in the MHz range. This difference allows us to analyze the beat signal around a non-zero value hence the full shape of the linewidth is obtained unambiguously. A non-polarizing beamsplitter (BS) is used to mix the two laser beams. The beat signal is then directed to the photodiode (*D*1) after the BS. A fast Fourier transform (FFT) of the signal is performed by the spectrum analyzer (SA) giving the frequency spectrum of the beat note.

For the first set of experiments, the first order coherence function [3, 4] is

$$\begin{aligned} G^{(1)}(t) &= \mathrm{Tr}\{\rho[(\hat{E}_1^\dagger(t)+\hat{E}_2^\dagger(t))(\hat{E}_1(t)+\hat{E}_2(t))]\} \\ &= \mathrm{Tr}\{(\rho_1\otimes\rho_2)[|\hat{E}_1(t)|^2+|\hat{E}_2(t)|^2+\hat{E}_1^\dagger(t)\hat{E}_2(t)+c.c.\} \\ &= \mathscr{E}_1^2\mathrm{Tr}[\rho_1\hat{a}_1^\dagger(t)\hat{a}_1(t)]+\mathscr{E}_2^2\mathrm{Tr}[\rho_2\hat{a}_2^\dagger(t)\hat{a}_2(t)] \\ &\quad+\mathscr{E}_1\mathscr{E}_2\{\mathrm{Tr}[(\rho_1\otimes\rho_2)\hat{a}_1^\dagger(t)\hat{a}_2(t)]e^{i(\nu_2-\nu_1)t}+c.c.]\}, \end{aligned} \tag{7}$$

where $\rho = \rho_1 \otimes \rho_2$ is the density operator of the system, ρ_1 and ρ_2 represent the density operators of laser 1 and 2, ν_1 and ν_2 represent the center frequencies of the lasers 1 and 2, respectively.

From the above equation, we can see the only terms that carry the beat note frequency are

$$\Gamma^{(1)}(t) = \mathscr{E}_1\mathscr{E}_2\mathrm{Tr}[(\rho_1\otimes\rho_2)\hat{a}_1^\dagger(t)\hat{a}_2(t)]e^{i\nu_0 t}, \tag{8}$$

with its complex conjugate which contributes to the $-\nu_0$ frequency component, where $\nu_0 \equiv \nu_2 - \nu_1$. Under the condition that the two lasers are independent, we can rewrite Equation (8) as

$$\begin{aligned} \Gamma^{(1)}(\nu_0,t) \;=\; & \mathscr{E}_1\sum_{n_1}\sqrt{n_1+1}\rho_{n_1}^{(1)}(0)e^{-D_1 t}e^{-i\nu_1 t} \\ & \times\mathscr{E}_2\sum_{n_2}\sqrt{n_2}\rho_{n_2}^{(-1)}(0)e^{-D_2 t}e^{i\nu_2 t}. \end{aligned} \tag{9}$$

Taking the Fourier transform, we have a Lorentzian spectrum centered at the beat frequency ν_0 with a width $D' = D_1 + D_2$, which is essentially twice the width of one laser

$$S_{\nu_0}(\omega) \propto \frac{D'}{(\omega-\nu_0)^2+(D')^2}. \tag{10}$$

The second and third experiments measure the spectral profile of the second and third order correlation of beat notes, the setup is

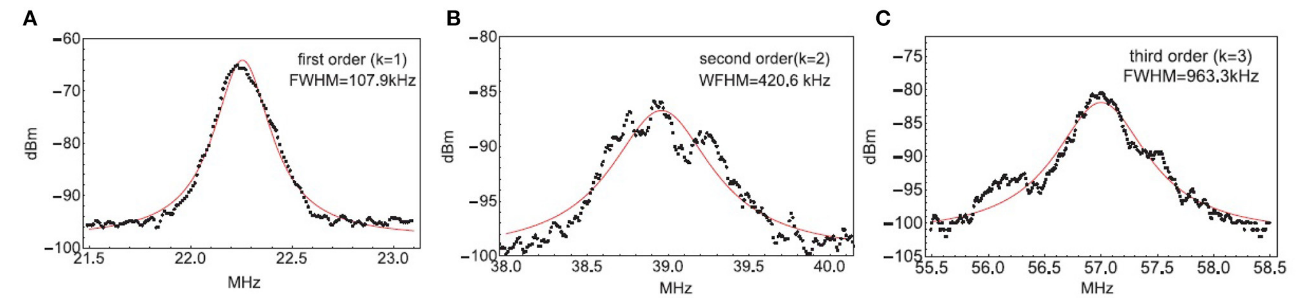

FIGURE 4 | Experimental results from the two sets of measurements. The bandwidths of the detectors are 50 MHz, the resolution bandwidth of the SA is 10 kHZ. The black dots are experimental data and the red curves are theory. **(A)** is the beat signals from $D1$, where the FWHM is 107.9 kHz with average 50 times. Theory is the Fourier transform of the laser fields time evolution ($e^{-D't}$) associated with frequency ν_0, as shown in Equation (10); **(B)** is correlated signal from $D1$ and $D2$, where the FWHM bandwidth is 420.6 kHz with average 50 times. Theory is the Fourier transform of the correlated laser fields time evolution ($e^{-4D't}$) associated with frequency $2\nu_0$, as shown in Equation (13). **(C)** is correlated signal from $D1$, $D2$, and $D3$, where the FWHM is 963.3 kHz with average 50 times. Theory is the Fourier transform of the correlated laser fields time evolution ($e^{-9D't}$) associated with frequency $3\nu_0$, as shown in Equation (16).

shown in **Figure 3**. We used the same two lasers to create the beat signal, where three detectors $Di(i = 1, 2, 3)$ are used. The outputs from the photodiodes are used as inputs for a frequency mixer. The output from the mixer is then sent to the spectrum analyzer and the frequency spectrum of the correlated signal is obtained after the FFT. As shown in **Figure 3**, this set of experiments measures the laser field correlation that is governed by the time evolution of the second and third order off-diagonal elements $\rho_n^{(2)}(t)$ and $\rho_n^{(3)}(t)$, respectively. The quantity we now measure is determined by the correlation of the heterodyne signals from detectors as in **Figure 3**. We have the signal of interest at frequency $2\nu_0$ from the second order coherence function is

$$\Gamma^{(2)}(t) = \mathscr{E}_1^2\mathscr{E}_2^2\mathrm{Tr}(\rho_1 \otimes \rho_2)\hat{a}_1^\dagger(t)\hat{a}_1^\dagger(t)\hat{a}_2(t)\hat{a}_2(t)e^{i2\nu_0 t}. \tag{11}$$

The correlated heterodyne signal is

$$\begin{aligned}\Gamma^{(2)}(2\nu_0, t) = {}& \mathscr{E}_1^2 \sum_{n_1} \rho_{n_1}^{(2)}(0)\sqrt{(n_1+2)(n_1+1)}e^{-4D_1 t}e^{-i2\nu_1 t} \\ & \times \mathscr{E}_2^2 \sum_{n_2} \rho_{n_2}^{(-2)}(0)\sqrt{(n_2-1)n_2}e^{-4D_2 t}e^{i2\nu_2 t}.\end{aligned} \tag{12}$$

Taking the Fourier transform, we get a Lorentzian spectral profile centered at $2\nu_0$ with a width of $4D'$

$$S_{2\nu_0}(\omega) \propto \frac{4D'}{(\omega - 2\nu_0)^2 + (4D')^2}. \tag{13}$$

similarly, the signal of interest at frequency $3\nu_0$ from the third order coherence function is

$$\Gamma^{(3)}(t) = \mathscr{E}_1^3\mathscr{E}_2^3\mathrm{Tr}(\rho_1 \otimes \rho_2)\hat{a}_1^\dagger(t)\hat{a}_1^\dagger(t)\hat{a}_1^\dagger(t)\hat{a}_2(t)\hat{a}_2(t)\hat{a}_2(t)e^{i3\nu_0 t}. \tag{14}$$

The correlated heterodyne signal is

$$\begin{aligned}\Gamma^{(3)}(3\nu_0, t) = {}& \mathscr{E}_1^3 \sum_{n_1} \rho_{n_1}^{(3)}(0)\sqrt{(n_1+3)(n_1+2)(n_1+1)}e^{-9D_1 t}e^{-i3\nu_1 t} \\ & \times \mathscr{E}_2^3 \sum_{n_2} \rho_{n_2}^{(-3)}(0)\sqrt{(n_2-2)(n_2-1)n_2}e^{-9D_2 t}e^{i3\nu_2 t}.\end{aligned} \tag{15}$$

We therefore get a Lorentzian spectral profile centered at $3\nu_0$ with a width of $9D'$

$$S_{3\nu_0}(\omega) \propto \frac{9D'}{(\omega - 3\nu_0)^2 + (9D')^2}. \tag{16}$$

The main experimental results are shown in **Figure 4**. All measurements were taken with the laser operating at the same average output power level. The resolution bandwidth (RBW) of the SA is 10 kHz, video bandwidth (VBW) is 30 kHz in all the measurements. For the sake of simplicity, the Full width at half maximum (FWHM) linewidth is taken at the -3 dB width of the measured spectrum by considering only the Lorentzian fitting [12]. **Figure 4A** represents the data of the first set of experiments with an average of 50 measurements of beat note signal from $D1$. The theoretical fitting in the red solid line is based on Equation (10), and the FWHM is 107.9 kHz. **Figure 4B** represents the data of the second set of experiments with 50 measurements of correlated beat note signals from $D1$ and $D2$. The theoretical fitting in the red solid line is based on Equation (13), and the FWHM is estimated to be 420.6 kHz. **Figure 4C** represents the data of the third order experiments with 50 measurements from all three detectors. The theoretical fitting in the red solid line is based on Equation (16), and the FWHM is estimated to be 963.3 kHz. First of all, we see that the obtained linewidth from the second order correlation spectrum is essentially 4 times wider than that of the single beat note linewidth, as well as the third order spectrum is 9 times wider than that of the single beat note linewidth, validating our theoretical expectation. Secondly, we see that the theoretical curves fit the data well in the center peak, but not as good at the tails. This is mainly due to the influences from other noises that also contribute to the spectral profile. For the same reason, we see that the single beat note signal can be better fitted than the second and third order correlation signals. There are some small peaks in the higher order measurements, due to our remeasured higher order spectral signal is close to the noise level of the detection system. Ideally, more averaging ($\gg$50) should be able to smooth out these peaks. However, we note here that, there is a trade-off between time averaging and the accurate measurement of the center beat note frequency, due to the drifting of center frequencies of the two lasers. Further using an intense local oscillator and sensitive detection system (detector and spectral analyzer) should be able to solve this issue. Nevertheless, our data confirms the Lorentizan spectral profile of the signal and the time evolution described by Equation (3), in the case of $k = 1$, $k = 2$, and $k = 3$.

3. CONCLUSION

In conclusion, we have studied the time evolution of the higher degrees of off-diagonality obtained SL theory of the laser. We particularly measured the bandwidth of the laser beat note and the bandwidth of the correlated laser beat note, which reveal the evolution of the first, second, and third order off-diagonal elements of the laser density operator. The higher order spectra reveal the influence of the randomness in the phase of the laser field due to quantum fluctuation. Experimental results agreed with the SL QTL showing that the bandwidth of the third order and second order spectral profile are nine times and four times wider than that of the first order spectral profile, respectively.

DATA AVAILABILITY STATEMENT

The raw data supporting the conclusions of this article will be made available by the authors, without undue reservation.

AUTHOR CONTRIBUTIONS

TP, YS, and MS discussed the design principle. TP and XZ performed the experiment and data analysis. TP and MS wrote the paper. All the authors polished the paper.

FUNDING

This study was funded by Air Force Office of Scientific Research (Award No. FA9550-20-1-0366 DEF), Office of Naval Research (Award No. N00014-20-1-2184), Robert A. Welch Foundation (Grant No. A-1261), National Science Foundation (Grant No. PHY-2013771), King Abdulaziz City for Science and Technology (KACST).

ACKNOWLEDGMENTS

We thank Z. H. Yi, R. Nessler, H. Cai, and J. Sprigg for helpful discussion.

REFERENCES

1. Pestov D, Murawski RK, Ariunbold GO, Wang X, Zhi M, Sokolov AV, et al. Optimizing the laser-pulse configuration for coherent Raman spectroscopy. *Science*. (2007) 316:265–8. doi: 10.1126/science.1139055
2. Cummins H. *Photon Correlation and Light Beating Spectroscopy. Vol. 3*. Springer Science & Business Media (2013).
3. Glauber RJ. The quantum theory of optical coherence. *Phys Rev*. (1963) 130:2529. doi: 10.1103/PhysRev.130.2529
4. Scully M, Lamb W Jr. Quantum theory of an optical maser. *Phys Rev Lett*. (1966) 16:853.
5. Haken H. Theory of intensity and phase fluctuations of a homogeneously broadened laser. *Z Phys*. (1966) 190:327–56. doi: 10.1007/BF01333598
6. DeGiorgio V, Scully MO. Analogy between the laser threshold region and a second-order phase transition. *Phys Rev A*. (1970) 2:1170. doi: 10.1103/PhysRevA.2.1170
7. Meschede D, Walther H, Müller G. One-atom maser. *Phys Rev Lett*. (1985) 54:551. doi: 10.1103/PhysRevLett.54.551
8. Scully MO. Condensation of N bosons and the laser phase transition analogy. *Phys Rev Lett*. (1999) 82:3927. doi: 10.1103/PhysRevLett.82.3927
9. Hoang T. Remarks on the charged multiplicity of hadronic Z 0 (91) decays. *Z Phys C Part Fields*. (1997) 73:149–52. doi: 10.1007/s002880050304
10. Okoshi T, Kikuchi K, Nakayama A. Novel method for high resolution measurement of laser output spectrum. *Electron Lett*. (1980) 16:630–1. doi: 10.1049/el:19800437
11. Richter L, Mandelberg H, Kruger M, McGrath P. Linewidth determination from self-heterodyne measurements with subcoherence delay times. *IEEE J Quant Electron*. (1986) 22:2070–4. doi: 10.1109/JQE.1986.1072909
12. Muanzuala L, Ravi H, Sylvan K, Natarajan V. Measuring the linewidth of a stabilized diode laser. *arXiv preprint* arXiv:151003683 (2015).
13. Arecchi FT. Measurement of the statistical distribution of Gaussian and laser sources. *Phys Rev Lett*. (1965) 15:912. doi: 10.1103/PhysRevLett.15.912
14. Corti M, Degiorgio V, Arecchi F. Measurements of the fine structure of laser intensity correlations near threshold. *Opt Commun*. (1973) 8:329–32. doi: 10.1016/0030-4018(73)90207-1

Conflict of Interest: The authors declare that the research was conducted in the absence of any commercial or financial relationships that could be construed as a potential conflict of interest.

frontiers
in Physics

ORIGINAL RESEARCH
published: 23 April 2021
doi: 10.3389/fphy.2021.615168

Direct Optimal Control Approach to Laser-Driven Quantum Particle Dynamics

*A. R. Ramos Ramos and O. Kühn**

Institut für Physik, Universität Rostock, Rostock, Germany

Optimal control theory is usually formulated as an indirect method requiring the solution of a two-point boundary value problem. Practically, the solution is obtained by iterative forward and backward propagation of quantum wavepackets. Here, we propose direct optimal control as a robust and flexible alternative. It is based on a discretization of the dynamical equations resulting in a nonlinear optimization problem. The method is illustrated for the case of laser-driven wavepacket dynamics in a bistable potential. The wavepacket is parameterized in terms of a single Gaussian function and field optimization is performed for a wide range of particle masses and lengths of the control interval. Using the optimized field in a full quantum propagation still yields reasonable control yields for most of the considered cases. Analysis of the deviations leads to conditions which have to be fulfilled to make the semiclassical single Gaussian approximation meaningful for field optimization.

Keywords: optimal control, quantum dynamics, semiclassical dynamics, Gaussian wavepackets, proton transfer

OPEN ACCESS

Edited by:
Tamar Seideman,
Northwestern University,
United States

Reviewed by:
Ilya Averbukh,
Weizmann Institute of Science, Israel
Ilia Tutunnikov,
Weizmann Institute of Science,
Rehovot, Israel, in collaboration with
reviewer [IA]
Regina De Vivie-Riedle,
Ludwig Maximilian University of
Munich, Germany

****Correspondence:***
O. Kühn
oliver.kuehn@uni-rostock.de

Specialty section:
This article was submitted to
Physical Chemistry and Chemical
Physics,
a section of the journal
Frontiers in Physics

Received: *08 October 2020*
Accepted: *09 February 2021*
Published: *23 April 2021*

Citation:
Ramos Ramos AR and Kühn O (2021)
Direct Optimal Control Approach to
Laser-Driven Quantum
Particle Dynamics.
Front. Phys. 9:615168.
doi: 10.3389/fphy.2021.615168

1 INTRODUCTION

“Teaching lasers to control molecules” has been a long-standing goal in molecular physics [1]. Among the various methods of the early days [1–5], optical control theory (OCT) emerged as a versatile tool. Originally developed by Rabitz et al. [6, 7] and Kosloff et al. [8], numerous methodological extensions have been developed over the years (for reviews, *see* e.g., [9–12]). In terms of practical realizations of chemical reaction control, the feedback strategy [1, 13, 14] as well as straightforward resonant excitation schemes [15–17] have been most successful.

In quantum optimal control theory the goal of optimizing the expectation value of a target operator such as a projector onto a certain state, is formulated as a variational problem for a cost functional subject to certain constraints. The latter includes, for instance, some penalty for high field intensities or that the wavepacket should fulfill the Schrödinger equation. This control problem is usually solved using an *indirect* approach, i.e., the cost functional is not minimized directly. Instead, the stationarity condition for the cost functional is converted to a two-point boundary problem for two coupled Schrödinger equations. A numerical solution is obtained by iterative forward and backward propagation of the actual wavepacket and an auxiliary wavepacket, respectively (e.g., [18]). This procedure is sometimes referred to as the optimize and then discretize paradigm [19]. Indirect methods for optimal control are in use in other areas of physics, e.g., stochastic control [20], but also in engineering and biology [21].

Direct optimal control, in contrast, follows the discretize and then optimize paradigm, i.e. the cost functional is minimized directly using methods from nonlinear optimization. Although being popular, for instance, in applied mathematics [22], engineering [23], and biology [21], there have been no applications to quantum molecular dynamics so far. The present paper is devoted to fill this gap.

Indirect optimal control requires to solve iteratively two time-dependent Schrödinger equations where the numerical effort scales exponentially with the number of degrees of freedom. To cope with this situation the Multi-Configurational Time-Dependent Hartree (MCTDH) approach is most suited [24, 25]. An OCT implementation has been reported in Ref. [26], for an application see also Ref. [27]. The solution of the time-dependent Schrödinger equation requires a priori knowledge of the potential energy surface. But, when driving the wavepacket into a particular region of configuration space using laser control, a global potential might not be needed. Thus on-the-fly approaches, e.g., in the context of MCTDH [28, 29] could be of advantage. On the other hand, semiclassical approximations in terms of Gaussian wavepackets play a prominent role in molecular quantum dynamics [30] and indeed there has been a semiclassical formulation of indirect OCT reported in Refs. [31, 32] (for related work using Wigner space sampling, *see* Ref. [33]).

In this paper we explore direct OCT using a representation of the wavepacket dynamics in terms of a single Gaussian function. Although this choice has been made for numerical convenience, it also facilitates exploration of its limitations by comparison with solutions of the time-dependent Schrödinger equation. Specifically, for the considered problem of quantum particle motion in a bistable potential we are able to identify conditions for which the single Gaussian approximation is adequate.

2 THEORETICAL METHODS

2.1 Equations of Motion

The equations for the time evolution of a quantum mechanical state can be obtained from the time-dependent variational principle starting with the stationarity condition for the action S, i.e. [34].

$$\delta \mathrm{S} = \delta \int_{\mathrm{t}_1}^{\mathrm{t}_2} \mathrm{L}(\Psi, \Psi^*)\mathrm{dt} = 0\,, \tag{1}$$

where the quantum Lagrangian is given by (Note that atomic units are used throughout)

$$L = \left\langle \Psi \middle| i\frac{\partial}{\partial t} - H(t) \middle| \Psi \right\rangle . \tag{2}$$

In the following we will focus on one-dimensional systems (coordinate x and momentum p) coupled to a radiation field, $E(\mathrm{t})$, in dipole approximation (dipole operator $\mu(x)$). Thus the Hamiltonian operator in the coordinate representation is given by

$$H(t) = H_0 + H_{\mathrm{f}}(t) = -\frac{1}{2m}\frac{d^2}{dx^2} + V(x) - \mu(x)E(t)\,. \tag{3}$$

Equation 1 yields the condition [34].

$$\mathrm{Re}\left[\left\langle \delta\Psi \middle| \mathrm{i}\frac{\partial}{\partial \mathrm{t}} - \mathrm{H}(\mathrm{t}) \middle| \Psi \right\rangle\right] = 0\,. \tag{4}$$

Assuming that the time-dependence of the wavepacket is implicitly parameterized by the set of time-dependent real parameters $\boldsymbol{a}(t) = \{a_1(t), \ldots, a_n(t)\}$, this yields

$$\delta\Psi = \sum_{\mathrm{j}=1}^{\mathrm{n}} \left(\frac{\partial \Psi}{\partial a_{\mathrm{j}}}\right)\delta a_{\mathrm{j}}\,. \tag{5}$$

Inserting **Eq. 5** into **Eq. 4** gives the equations of motion for the general set of parameters used to describe the wavepacket

$$\dot{a}_i = -\sum_{j=1}^{n} K_{ij}\, \mathrm{Re}\left\langle \frac{\partial \Psi}{\partial a_j} \middle| H\Psi \right\rangle \quad \forall i = 1, \ldots, n\,, \tag{6}$$

with K_{ij} being the elements of the inverse of the matrix formed by $\mathrm{Im}\langle \partial\Psi/\partial a_i | \partial\Psi/\partial a_j \rangle$.

In order to connect to on-the-fly approaches and to reduce the number of differential equations of motion (and thus the computational cost) we assume that the wavepacket has the following Gaussian form [30] at all times

$$\Psi(x, \alpha, \beta, x_0, p_0) = \left(\frac{2\alpha}{\pi}\right)^{1/4} \exp\left[-(\alpha + i\beta)(x - x_0)^2 + ip_0(x - x_0)\right] \tag{7}$$

where α and β describe the width and tilt of the phase space Gaussian. Further, x_0 and p_0 are the average position and momentum, respectively. Hence, we identify $\boldsymbol{a}(t) = \{\alpha(t), \beta(t), x_0(t), p_0(t)\}$ and using **Eq. 6** gives the following set of coupled differential equations

$$\dot{\alpha} = \frac{4\alpha\beta}{m}, \tag{8}$$

$$\dot{\beta} = -\frac{2(\alpha^2 - \beta^2)}{m} - 4\alpha^2\frac{\partial}{\partial \alpha}U(\mathrm{t})\,, \tag{9}$$

$$\dot{x}_0 = \frac{p_0}{m}, \tag{10}$$

$$\dot{p}_0 = -\frac{\partial}{\partial x_0}U(t) \tag{11}$$

subject to some initial conditions at time t_0. Here, we defined the time-dependent expectation value of the potential

$$U(\mathrm{t}) = \langle \Psi(\mathrm{t}) | V(x) - \mu(x)E(\mathrm{t}) | \Psi(\mathrm{t}) \rangle \tag{12}$$

In the next section we will focus on the control problem assuming that these equations of motion can be solved, which implies that the expectation value of the potential and its derivatives are available.

2.2 Statement of the Control Problem

Let us start with a brief summary of optimal control theory [9, 10, 35]. Given a functional of the form

$$\mathcal{J}[\boldsymbol{a}, \boldsymbol{u}, \boldsymbol{k}] = \mathcal{T}\left[\boldsymbol{a}(t_{\mathrm{f}}), \boldsymbol{k}, t_{\mathrm{f}}\right] + \int_{t_0}^{t_{\mathrm{f}}} \mathcal{R}[\boldsymbol{a}(\mathrm{t}), \boldsymbol{u}(\mathrm{t}), \boldsymbol{k}, \mathrm{t}]\, dt\,. \tag{13}$$

where $\mathcal{T}$ and $\mathcal{R}$ are the terminal and running cost, respectively, the task is to find the state trajectory $\boldsymbol{a}(t)$, external control $\boldsymbol{u}(t)$ (where the time $t \in [\mathrm{t}_0, \mathrm{t}_{\mathrm{f}}]$) and the set of static parameters $\boldsymbol{k}$ that minimize the functional $\mathcal{J}[\boldsymbol{a},\boldsymbol{u},\boldsymbol{k}]$. The minimization is performed subject to the following differential constraints

$$\dot{\boldsymbol{a}}(t) = f[\boldsymbol{a}(t),\boldsymbol{u}(t),\boldsymbol{k},t]\ , t \in \left[t_0, t_\mathrm{f}\right]. \tag{14}$$

Further, there can be path constraints

$$\boldsymbol{h}_\mathrm{L} \le \boldsymbol{h}[\boldsymbol{a}(t),\boldsymbol{u}(t),\boldsymbol{k},t] \le \boldsymbol{h}_\mathrm{U}\ , \tag{15}$$

and event constraints such as

$$\boldsymbol{e}_\mathrm{L} \le \boldsymbol{e}\left[\boldsymbol{F}[\boldsymbol{a}(t),\boldsymbol{u}(t)],\boldsymbol{k},t_0,t_\mathrm{f}\right] \le \boldsymbol{e}_\mathrm{U}\ . \tag{16}$$

Here, the subscript L and and U denotes the lower and upper boundary, respectively, defining the constraints. Notice that in contrast to path constraints, event constraints are not time-dependent, but could include a functional, $\boldsymbol{F}$, of, e.g., the state trajectory or the external control (*see* below).

Next, we specify this general control problem to the model introduced in **Section 2.1**. The state is characterized by the set $\boldsymbol{a}(t) = \{\alpha(t),\beta(t),x_0(t),p_0(t)\}$ and the external control is given by the laser field $\boldsymbol{u}(t) = E(t)$. Additional time-independent parameters, $\boldsymbol{k}$, will not be used. The differential constraints (14) are given by **Eqs. 8–11**.

The goal of the optimization can be stated as follows. Given some initial quantum state $|\Psi(t_0)\rangle$, parameterized by $\boldsymbol{a}^\mathrm{i} = \{\alpha^\mathrm{i},\beta^\mathrm{i},x_0^\mathrm{i},p_0^\mathrm{i}\}$, find a laser field $E(t)$ such that the overlap is maximized between the time-evolved final state at $t = t_\mathrm{f}$, $\left|\Psi(t_\mathrm{f})\right\rangle$, and some target state $\left|\Phi^\mathrm{t}\right\rangle$. Thus, the terminal cost in **Eq. 13** is given by (notice the minus sign because the terminal cost will be minimized and we want to maximize the overlap)

$$\mathcal{T}\left(\boldsymbol{a}\left(t_\mathrm{f}\right),t_\mathrm{f}\right) = -\left|\left\langle\Psi\left(t_\mathrm{f}\right)\middle|\Phi^\mathrm{t}\right\rangle\right|^2 \tag{17}$$

Here, for simplicity we will use the parametrization of **Eq. 7** for the target state as well, labeling the target parameters as $\boldsymbol{a}^\mathrm{t} = \{\alpha^\mathrm{t},\beta^\mathrm{t},x_0^\mathrm{t},p_0^\mathrm{t}\}$.

The running cost will be chosen as follows

$$\mathcal{R}[E(t),t] = \kappa\frac{[E(t)]^2}{s(t)},\quad s(t) = \sin^2\left(\frac{\pi}{t_\mathrm{f}}t\right) + \epsilon. \tag{18}$$

Besides the field intensity we have included a factor κ scaling the penalty for high field strengths as well as a shape function $s(t)$, which ensures that the field increases(decreases) slowly when turned on(off) [36]. Note that ϵ is a small parameter introduced to avoid division by zero and numerical problems at times $t = 0$ and $t = t_\mathrm{f}$. Throughout the text we have used $\epsilon = 0.005$.

For the application presented below we don't use any path constraints, but event constraints. Given the event

$$\boldsymbol{e}[F[E(t)],\boldsymbol{a}(t_0)] = \begin{pmatrix} \alpha(t_0) \\ \beta(t_0) \\ x_0(t_0) \\ p_0(t_0) \\ \int_{t_0}^{t_\mathrm{f}} E(t)dt \end{pmatrix}, \tag{19}$$

upper and lower bounds will be chosen equal as follows

$$\boldsymbol{e}_\mathrm{L} = \boldsymbol{e}_\mathrm{U} = \begin{pmatrix} \alpha^\mathrm{i} \\ \beta^\mathrm{i} \\ x_0^\mathrm{i} \\ p_0^\mathrm{i} \\ 0 \end{pmatrix}. \tag{20}$$

Hence, the parameters of the initial state are fixed and not subject to optimization. Further, we enforce the zero-net-force condition by demanding that $F[E(t)] = \int_{t_0}^{t_\mathrm{f}} E(t)dt = 0$ [37].

The optimization problem will be solved using a direct method, i.e. by means of discretization of the differential equations. Details will be specified in the next section.

2.3 Model System and Computational Details

The direct optimal control approach will be applied to the problem of particle dynamics in a bistable potential. This could represent, for instance, proton or hydrogen atom transfer in a tautomerization reaction [38, 39]. The following potential will be used

$$V(x) = V_\mathrm{B}\left(\left(\frac{x}{x_\mathrm{B}}\right)^2 - 1\right)^2. \tag{21}$$

Here, x_B is the distance between the minimum of the potential and the top of the barrier, and V_B is the barrier height.

The system-field interaction is treated in semiclassical approximation, taking the polarization of the field in the same direction as the dipole, and assuming a linear model for the latter (q is the charge)

$$\mu(x) = qx. \tag{22}$$

Specific parameters for the numerical simulations have been chosen to mimic typical situations in proton transfer reactions [38, 39], i.e. $x_\mathrm{B} = 2a_0$ (≈ 1.06 Å), $V_\mathrm{B} = 0.01E_\mathrm{h}$ (≈ 6.3 kcal/mol), and $q = 1$ (= 1e). The particle's mass, m, will be used to tune the 'quantumness' of the dynamics. Exemplary, we show potential and eigenstates for two choices of the masses in **Figure 1**. Comparing the two cases we note that in particular the number of eigenstates below the barrier is 8 and 16 for masses of 1 m_H and 5 m_H respectively (where m_H is the hydrogen mass).

Using **Eqs. 21, 22** together with **Eq. 7** one can calculate the time-dependent expectation value of the potential, **Eq. 12**, and its derivatives with respect to α and x_0 required for the equations of motion (**Eqs. 9**, **11**). Although in the present case the required expectation value could have been calculated analytically, we have used a more general prescription. To this end the potential is globally approximated by a sum of Gaussians of the form

$$V(x) \approx \sum_{p=1}^{g} g_p e^{-b_p\left(x-x_p\right)^2}. \tag{23}$$

We have used $g = 5$ which gives $g_p = \{31.000, -1.529, -1.529, 31.000, 1.348\}$ (in units of V_B), $b_p = \{1.397,\ 1.658,\ 1.658,\ 1.397, 0.\}$ (in units of x_B^{-2}), and $x_p = \{-2.981, -1.142, 1.142, 2.981, 0.\}$ (in units of x_B).

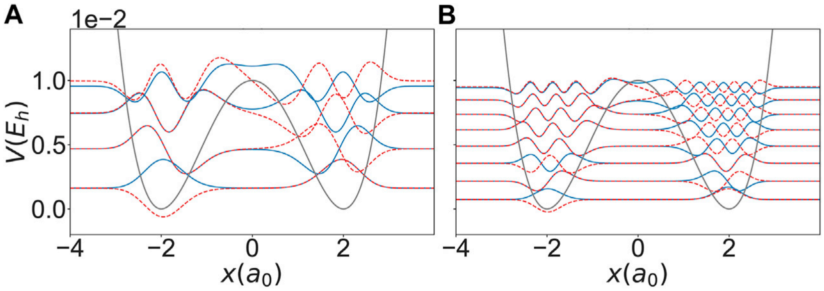

FIGURE 1 | Eigenstates for a particle of mass **(A)** 1 m_H and **(B)** 5 m_H in the potential given by **Eq. 21** with $x_B = 2a_0$ and $V_B = 0.01E_h$. Solid and dashed lines correspond to even and odd eigenstates, respectively.

Using **Eq. 23** one obtains for **Eq. 12**

$$U(t) = \sum_{p=1}^{5} g_p e^{-B_p} \left(\frac{2\alpha(t)}{2\alpha(t) + b_p} \right)^{1/2} - q x_0(t) E(t) , \tag{24}$$

$$\frac{\partial}{\partial \alpha} U(t) = \sum_{p=1}^{5} D_p \left(\frac{1}{4\alpha(t)^2} - \frac{b_p}{\alpha(t)\left(2\alpha(t) + b_p\right)} \left(x_0(t) - x_p\right)^2 \right) , \tag{25}$$

$$\frac{\partial}{\partial x_0} U(t) = -2 \sum_{p=1}^{5} D_p \left(x_0(t) - x_p\right) - qE(t) , \tag{26}$$

where

$$B_p = \frac{2\alpha(t) b_p}{2\alpha(t) + b_p} \left(x_0(t) - x_p\right)^2 \tag{27}$$

and

$$D_p = g_p b_p e^{-B_p} \left(\frac{2\alpha(t)}{2\alpha(t) + b_p} \right)^{3/2.} \tag{28}$$

For the solution of the control problem the software package PSOPT has been used [40]. This package employs an approximation for the state trajectory of the form

$$\boldsymbol{a}(t) \approx \boldsymbol{a}^N(t) = \sum_{k=0}^{N} \boldsymbol{a}(t_k) \mathcal{L}_k(t) , \tag{29}$$

where t_k are the Gauss-Lobatto quadrature nodes ($\boldsymbol{a}(t_k) = \boldsymbol{a}^N(t_k)$) and $\mathcal{L}_k$ are the Lagrange basis polynomials. This approximation allows to transform the performance functional (**Eq. 13**) into the performance function

$$G(\boldsymbol{y}) = \mathcal{T}\left[\boldsymbol{a}\left(t_f\right), \boldsymbol{k}, t_f\right] + \sum_{k=0}^{N} \mathcal{R}\left[\boldsymbol{a}^N(t_k), \boldsymbol{u}^N(t_k), \boldsymbol{k}, t_k\right] w_k , \tag{30}$$

and the differential constraints into a set of holonomic constraints for the decision vector $\boldsymbol{y} = (\boldsymbol{u}(t_0), \ldots, \boldsymbol{u}(t_N), \boldsymbol{a}(t_0), \ldots, \boldsymbol{a}(t_N), \boldsymbol{k}, t_0, t_f)$; w_k are the Gauss-Lobatto weights. For more details see Ref. [40]. The performance function (30) is optimized using nonlinear programming (NLP) algorithms, such as the ones implemented in IPOPT [41]. PSOPT provides different discretization schemes. The global pseudospectral Legendre and Chebyshev discretization yield very slow convergence for non-smooth functions [19], as it is the case for the solutions found for $\alpha(t)$ and $\beta(t)$ (see first and second row, (b) and (d) columns of **Figure 2** below). Increasing the number of nodes is not an option for these discretization schemes because of the non-sparsity of the Jacobian matrices which cannot be handled properly by the implemented IPOPT NLP solver. This issue translates into a disproportional increase of computational time. The local methods available are trapezoidal and Hermite-Simpson discretization. In order to check their performance we simulated the case of a particle of mass of 1 m_H and a final time of $t_f = 20{,}000$ au. In doing so the number of time discretization nodes has been scanned from 200 to 6,000. To evaluate the discretization error we use the maximum relative local error, $\varepsilon_{\text{disc}}$, defined in Ref. [40]. The results are shown in **Figure 3**. If the number of nodes is below 1,000 the trapezoidal method has a smaller error $\varepsilon_{\text{disc}}$ compared to Hermite-Simpson for the same number of nodes. Beyond 1,000 nodes, Hermite-Simpson outperforms the trapezoidal discretization. However, this comes at the expense of an increased computational time as can be seen in the lower panel of **Figure 3**. For the simulations reported below we have used Hermite-Simpson discretization with 2,000 nodes, which offers a good balance between accuracy and speed.

In order to quantify the importance of quantum effects beyond the simple Gaussian ansatz for the wavepacket, **Eq. 7**, MCTDH simulations have been performed using the optimized field. For this purpose the Heidelberg MCTDH package has been used [42].

3 RESULTS

3.1 Laser-Controlled Proton Transfer

In the following we present a proof-of-principle application of direct OCT using the example of proton transfer in a bistable potential. Specifically, the two cases (particle masses) given in **Figure 1** will be considered. For the initial state we choose the parameters of a Gaussian in the left well, and as the target state we choose a symmetrically located Gaussian in the right side well. The Gaussian parameters have been optimized to the ground state using a local harmonic approximation. Although direct

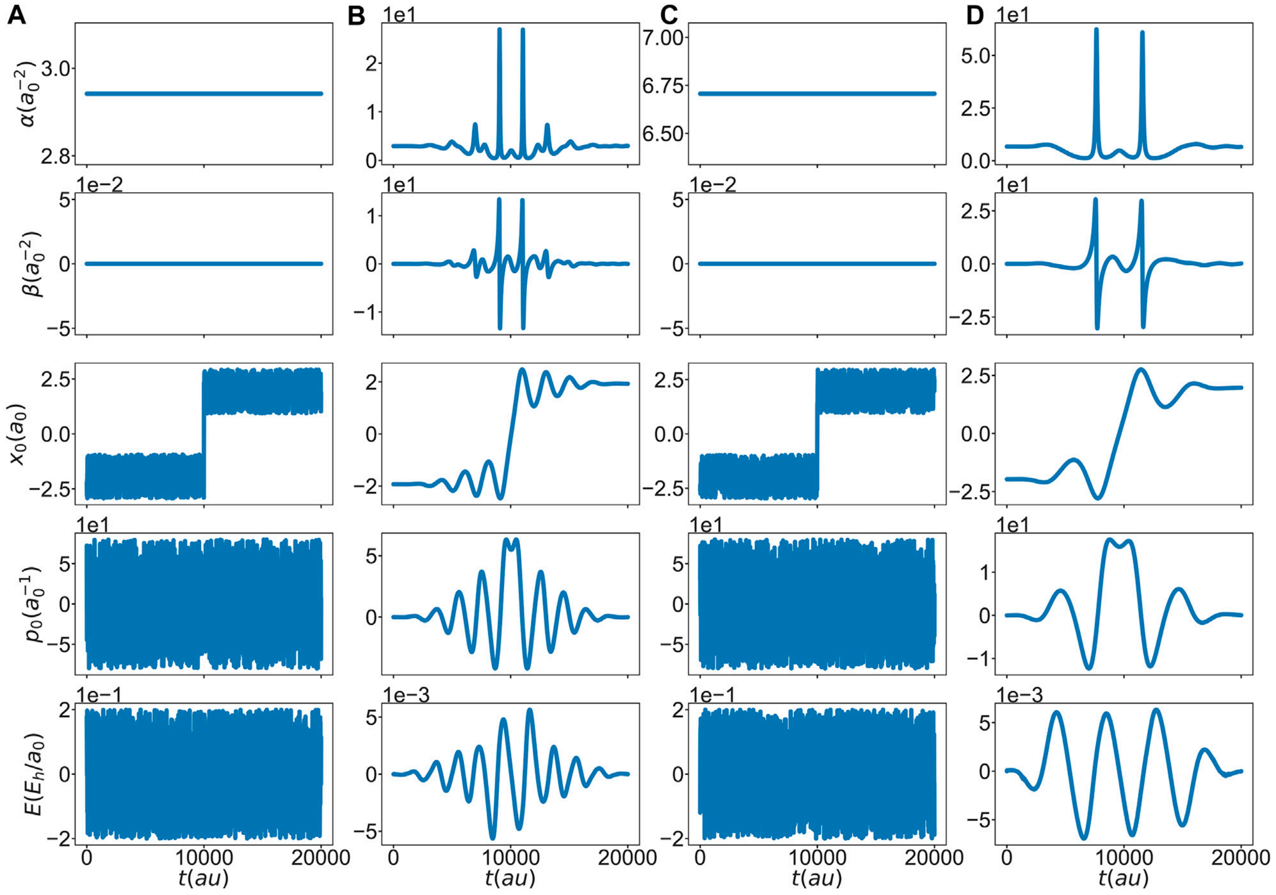

FIGURE 2 | Initial guess **(A)** and **(C)** and optimal solution **(B)** and **(D)** for state, ***a*** (t), and control field for two different particle masses (1 m_{H} – **(A)** and **(B)**, 5 m_{H} – **(C)** and **(D)**).

control in principle allows to vary the final time, in the present application the final time has been fixed to $t_{\mathrm{f}} = 20,000$ au. The penalty factor has been chosen as $\kappa = 0.3\ \mathrm{a}_0^2/\mathrm{E}_{\mathrm{h}}$ (cf. **Eq. 18**). To solve the problem we also have to provide an initial guess for states and control which is shown in **Figures 2A,C**. The rapid oscillations have been chosen randomly; there is no correlation between the different variables.

The optimal solutions for the two particle masses are given in **Figures 2B,D**. Apparently, the optimal field is able to drive the center of the wavepacket across the barrier into the right minimum at $t = t_{\mathrm{f}}$. In this respect one should note that the optimal fields have a relatively simple shape and little resemblance with the initial guess. This is one of the major advantages of the direct approach to optimal control problems, i.e. the convergence region of the initial guess is very broad. The dynamics is rather similar, i.e., in both cases the trajectory passes the barrier coming from the turning point at the left hand side. Just before and after the barrier the wavepacket gets localized in coordinate and delocalized in momentum space, whereas the position-momentum correlation (β) vanishes. The wavepacket passes the top of the barrier with large momentum.

The question now arises if the optimum field found for a single Gaussian wavepacket is able to trigger the same particle dynamics in the full quantum case. To this end the optimal field is used within a quantum dynamics simulation. The results are compared in **Figure 4** in terms of coordinate and momentum expectation values and the respective standard deviation. Until after the barrier crossing, Gaussian and full quantum results are rather similar. Indeed, if the goal would have been to trigger the localization of the wavepacket somewhere in the region of the right well at a particular time, the optimal field would still perform this task also in the quantum case. Of course, the agreement between classical and quantum propagation is better in case of the heavier mass even though there is considerable larger spread of the wavepacket in the quantum case after reflection at the right turning point. For the lighter mass the agreement after barrier crossing is less favorable due to the larger spread and the structured character of the quantum wavepacket which cannot be captured by a single Gaussian.

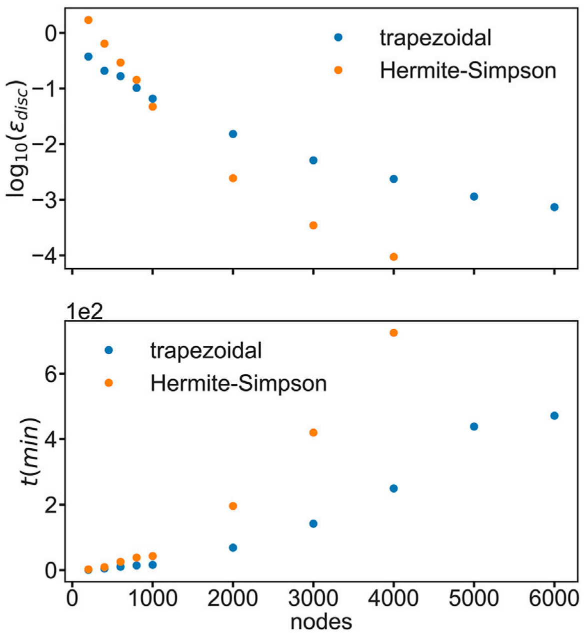

FIGURE 3 | Maximum relative local error **(upper panel)** and timing **(lower panel)** for trapezoidal (blue) and Hermite-Simpson (orange) as a function of the number of nodes.

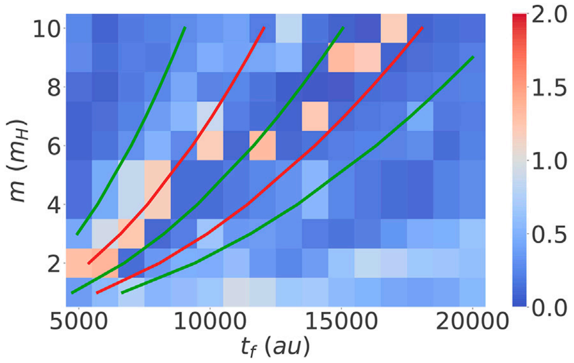

FIGURE 5 | Error according to **Eq. 31** as a function of different final times and masses. Green lines represent an odd number of half harmonic oscillation periods for the corresponding mass $(2n+1)T/2$ with $n = 1, 2, 3$ and red lines represent an integer number of periods nT with $n = 2, 3$.

3.2 Region of Validity of the Gaussian Wavepacket Approximation

Single Gaussians cannot capture the dynamics of structured wavepackets. Nevertheless, the agreement between Gaussian and full quantum results is at least qualitative, even for the lighter particle. This provides the motivation for the investigation of the validity of the Gaussian approximation over a wider range of parameters. Again the optimum field is obtained following the procedure described in **Section 3.1**, but now for different final times (ranging from 5,000 au to 20,000 au in steps of 1,000 au) and masses (ranging from 1 to 10 m_{H} in steps of 1 m_{H}). To evaluate the performance of the optimum field to drive the wavepacket to the right well in the full quantum case we choose the following error:

$$\mathrm{Err} = \frac{\left| x_0^{\mathrm{t}} - \langle \tilde{\Psi}(t_{\mathrm{f}}) | x | \tilde{\Psi}(t_{\mathrm{f}}) \rangle \right|}{x_{\mathrm{B}}}, \tag{31}$$

where $\tilde{\Psi}(t_f)$ is the exact quantum wavefunction at the final time. This error will be between 0 and 1 if the expectation value of the quantum wavepacket crossed the barrier and greater than 1 if it did not. Results are shown in **Figure 5**.

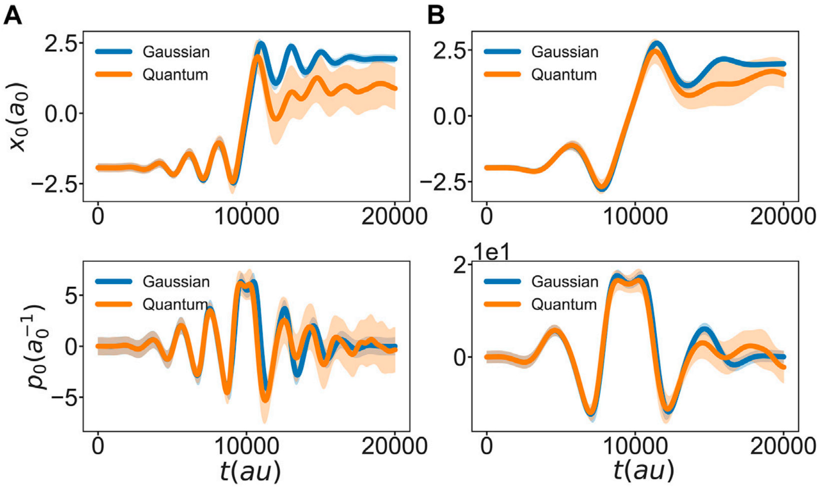

FIGURE 4 | Comparison of the coordinate **(top row)** and momentum **(bottom row)** expectation values and their respective standard deviation (shaded area), using the Gaussian approximation (blue) and the full quantum propagation (orange). Both trajectories are propagated under the influence of the optimal control field as obtained for the Gaussian **(A)** 1 m_{H} **(B)** 5 m_{H}).

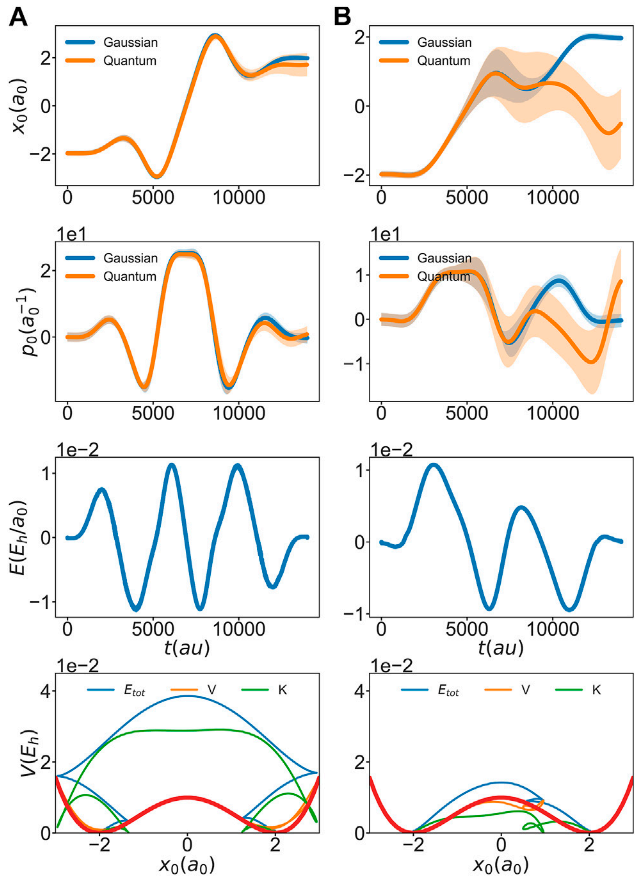

FIGURE 6 | Expectation values of coordinate and momentum (shaded areas indicate the standard deviation), optimal field, as well as total (E_{tot}), potential (V) and kinetic (K) energy of the moving wave packet **(rows from top to bottom)** for $t_f = 14,000$ au and **(A)** 6 m_H, **(B)** 7 m_H. In the bottom row the expectation values are plotted at the respective positions of the Gaussian wavepacket.

In general, we can see from **Figure 5** that the Gaussian optimal control fields are able to drive the particle reaction on a broad range of masses and final times. As expected the performance deteriorates for the lighter masses. There are some features which deserve closer attention. For example, there are regions where the Gaussian wavepacket approach works exceptionally well (characterized by stripes of intense blue color). In these regions the final time is matching a total integer number of well oscillations plus the barrier crossing time. Assuming that these oscillations are harmonic with period T and taking the barrier crossing time as being half of the harmonic period, these final times can be estimated. The middle green line in **Figure 5** corresponds to a final time of $5T/2$. It nicely matches with the dark blue region where the approach works well. Thus, in general one would expect regions with $(2n+1)T/2$ and nT where the approximation works well and not so well, respectively. This is roughly seen in **Figure 5**, although the deviation from the harmonic approximation causes some quantitative disagreement. This analysis points to the importance of the final time t_f for the effect of the quantumness of the dynamics on the overlap with the target. In passing we note that in principle direct optimal control offers the possibility to optimize the final time as well, e.g., to fulfill some constraints with respect to the spread of the wavepacket.

Another interesting feature apparent from **Figure 5** are the isolated "islands" of poor performance, e.g. at $t_f = 14,000$ au and $m = 7\,m_\mathrm{H}$. To rationalize this behavior **Figure 6** shows various expectation values for $t_f = 14,000$ au and $m = 6$ and $7\,m_\mathrm{H}$. The first and second row compares Gaussian and quantum results and we can notice that the corresponding trajectories diverge considerably more for $7\,m_\mathrm{H}$ (b) than for $6\,m_\mathrm{H}$ (a), even though a naive consideration would suggest that the performance of the single Gaussian approximation is better for the more massive particle. In general we observe that while in the good performing cases the wavepacket essentially stays localized, the opposite is true for the poor performing cases, which stands out as a likely reason for the discrepancy between Gaussian and quantum propagation in the later case. This holds irrespective of the actual mass of the particle. From the second and fourth rows of **Figure 6** we notice that the cases $m = 6$ and $7\,m_\mathrm{H}$ differ in the momentum and thus kinetic energy when crossing the barrier. While in the former case the momentum is maximum at the barrier top, in the latter the particle is slowed down when reaching the barrier. As a consequence it becomes rather delocalized in position space and thus the single Gaussian approximation fails.

In principle one could expect that decreasing the penalty factor κ would alleviate this problem, i.e. stronger fields would imply higher momentum. However, after inspecting **Figure 6**, it is apparent that for a given final time it depends on the initial direction of momentum whether the wavepacket will pass the barrier with high or low momentum. This idea supports the conclusion that not only the mass of the particle, but also the specific optimal path, are important for the validity of the single Gaussian approximation. Controlling the initial direction in a way which works in a black-box fashion for all cases covered in **Figure 5** has not been successfull. However, in contrast to indirect

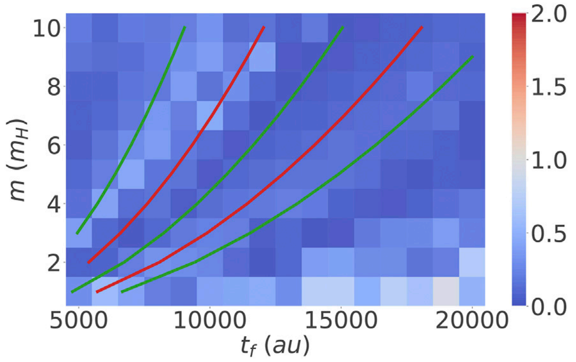

FIGURE 7 | Error according to **Eq. 31** as a function of different final times and masses. Running cost according to **Eq. 32** has been used together with **Eq. 18**. The penalty scaling factor was $\eta = 0.003$, except for a few cases where lower or higher values has been used, ranging from 0.001 to 0.015.

control, where one would have to compute running cost derivatives with respect to state variables to get coupling terms between forward and backward Schrödinger equation, including additional running costs is straightforward in direct control. To demonstrate this we have added a second term to the running costs of **Eq. 18**, which serves to maximize the kinetic energy, i.e.

$$\mathcal{R}'\left[p_0(t), t\right] = -\eta \frac{p_0^2(t)}{2m}. \qquad (32)$$

Here, η is a penalty scaling factor and the minus sign ensures that this term gets maximized. It is expected that this will lead to barrier crossing with high momentum and thus a reduced error, **Eq. 31**.

The results shown in **Figure 7** clearly support our hypothesis, i.e. adding the running cost functional **Eq. 32** leads to the elimination of the poor-performing islands. Hence, using the flexibility of the direct optimal control approach the region of validity of the single Gaussian approximation could be extended.

4 CONCLUSION

In this paper we have introduced a new tool for quantum optimal control. In contrast to indirect methods, which require the solution of a two-point boundary value problem, the present direct method builds on the first discretize and then optimize paradigm. Thus, by construction there is no need for explicit propagation of a wavepacket. So far direct methods have found application mostly in engineering [23, 40]. The performance and capabilities of the direct method have been demonstrated for the case of one-dimensional particle transfer in a bistable potential. For simplicity the wavepacket has been approximated by a single Gaussian function, but in principle other forms are possible, e.g., superposition of Gaussians [28] or even expansions in terms of an eigenstate basis. Of course, Gaussians have the potential advantage of being suited for on-the-fly simulations, which brings OCT into the realm of the dynamics of complex molecular systems, at least in principle. At this point it will be required to explore the scaling of the numerical effort associated with the direct method more thouroughly. Here, we merely explored the dependence on the number of nodes. But the number of parameters will be another limiting factor. Preliminary calculations performed on regular hardware showed that about 50 parameters and 500 nodes are feasible.

For a simple test system the question has been addressed whether the quantumness of the dynamics influences the final control yield, given a field which has been optimized for the single Gaussian approximation. Interestingly, it turned out that nearly complete particle transfer can be achieved for a wide range of masses and final times. Here, the important point is whether the wavepacket crosses the barrier with high or low momentum, which for the given model is decided by the sign of the momentum during the initial dynamics. As a consequence, even the optimization based on a simple Gaussian wavepacket, possibly using on-the-fly dynamics, may provide reasonable control fields.

DATA AVAILABILITY STATEMENT

The raw data supporting the conclusions of this article will be made available by the authors, without undue reservation.

AUTHOR CONTRIBUTIONS

ARR has performed the work and analyzed the results. OK has designed the project and supervised the scientific work. All authors have discussed and interpreted the results and contributed to writing the article.

FUNDING

This work has been funded by the grant Ku952/10–1 from the Deutsche Forschungsgemeinschaft (DFG).

REFERENCES

1. Judson RS, and Rabitz H. Teaching lasers to control molecules. *Phys Rev Lett* (1992) 68:1500. doi:10.1103/physrevlett.68.1500
2. Paramonov GK, and Savva VA. Resonance effects in molecule vibrational excitation by picosecond laser pulses. *Phys Lett A* (1983) 97:340–2. doi:10.1016/0375-9601(83)90658-8
3. Tannor DJ, and Rice SA. Control of selectivity of chemical reaction via control of wave packet evolution. *J Chem Phys* (1985) 83:5013–8. doi:10.1063/1.449767
4. Tannor DJ, Kosloff R, and Rice SA. Coherent pulse sequence induced control of selectivity of reactions: exact quantum mechanical calculations. *J Chem Phys* (1986) 85:5805. doi:10.1063/1.451542
5. Brumer P, and Shapiro M. Control of unimolecular reactions using coherent light. *Chem Phys Lett* (1986) 126:541–6. doi:10.1016/s0009-2614(86)80171-3
6. Shi S, Woody A, and Rabitz H. Optimal control of selective vibrational excitation in harmonic linear chain molecules. *J Chem Phys* (1988) 88:6870–83. doi:10.1063/1.454384
7. Shi S, and Rabitz H. Selective excitation in harmonic molecular systems by optimally designed fields. *Chem Phys* (1989) 139:185–99. doi:10.1016/0301-0104(89)90011-6
8. Kosloff R, Rice SA, Gaspard P, Tersigni S, and Tannor DJ. Wavepacket dancing: achieving chemical selectivity by shaping light pulses. *Chem Phys* (1989) 139:201–20. doi:10.1016/0301-0104(89)90012-8
9. Brif C, Chakrabarti R, and Rabitz H. Control of quantum phenomena: past, present and future. *New J Phys* (2010) 12:075008. doi:10.1088/1367-2630/12/7/075008
10. Werschnik J, and Gross EKU. Quantum optimal control theory. *J Phys B: Mol Opt Phys* (2007) 40:R175–211. doi:10.1088/0953-4075/40/18/r01
11. Worth GA, and Richings GW. Optimal control by computer. *Annu Rep Prog Chem Sect C: Phys Chem* (2013) 109:113. doi:10.1039/c3pc90003g
12. Keefer D, and de Vivie-Riedle R. Pathways to new applications for quantum control. *Acc Chem Res* (2018) 51:2279–86. doi:10.1021/acs.accounts.8b00244
13. Brixner T, and Gerber G. Quantum control of gas-phase and liquid-phase femtochemistry. *ChemPhysChem* (2003) 4:418. doi:10.1002/cphc.200200581
14. Prokhorenko VI, Nagy AM, Waschuk SA, Brown LS, Birge RR, and Miller RJD. Coherent control of retinal isomerization in bacteriorhodopsin. *Science* (2006) 313:1257–61. doi:10.1126/science.1130747

15. Stensitzki T, Yang Y, Kozich V, Ahmed AA, Kössl F, Kühn O, et al. Acceleration of a ground-state reaction by selective femtosecond-infrared-laser-pulse excitation. *Nat Chem* 10 (2018) 126–31. doi:10.1038/nchem.2909
16. Nunes CM, Pereira NAM, Reva I, Amado PSM, Cristiano MLS, and Fausto R. Bond-breaking/bond-forming reactions by vibrational excitation: infrared-induced bidirectional tautomerization of matrix-isolated thiotropolone. *J Phys Chem Lett* (2020) 11:8034–9. doi:10.1021/acs.jpclett.0c02272
17. Heyne K, and Kühn O. Infrared laser excitation controlled reaction acceleration in the electronic ground state. *J Am Chem Soc* (2019) 141: 11730–8. doi:10.1021/jacs.9b02600
18. Zhu W, and Rabitz H. A rapid monotonically convergent iteration algorithm for quantum optimal control over the expectation value of a positive definite operator. *J Chem Phys* (1998) 109:385–91. doi:10.1063/1.476575
19. Kelly M. An introduction to trajectory optimization: how to do your own direct collocation. *SIAM Rev* (2017) 59:849–904. doi:10.1137/16m1062569
20. Kappen HJ. An introduction to stochastic control theory, path integrals and reinforcement learning. *AIP Conf Proc* (2007) 887:149–81. doi:10.1063/1.2709596
21. Chen-Charpentier BM, and Jackson M. Direct and indirect optimal control applied to plant virus propagation with seasonality and delays. *J Comput Appl Math* (2020) 380:112983. doi:10.1016/j.cam.2020.112983
22. Betts JT. *Practical methods for optimal control and estimation using nonlinear programming*. Philadelphia, PA: Advances in design and control Society for Industrial and Applied Mathematics (2010).
23. Pardo D, Moller L, Neunert M, Winkler AW, and Buchli J. Evaluating direct transcription and nonlinear optimization methods for robot motion planning. *IEEE Robot Autom Lett* (2016) 1:946–53. doi:10.1109/lra.2016.2527062
24. Meyer H-D, Manthe U, and Cederbaum LS. The multi-configurational time-dependent Hartree approach. *Chem Phys Lett* (1990) 165:73–8. doi:10.1016/0009-2614(90)87014-i
25. Beck M, Jäckle A, Worth GA, and Meyer HD. The multiconfiguration time-dependent Hartree (MCTDH) method: a highly efficient algorithm for propagating wavepackets. *Phys Rep* (2000) 324:1–105. doi:10.1016/s0370-1573(99)00047-2
26. Schröder M, Carreón-Macedo J-L, and Brown A. Implementation of an iterative algorithm for optimal control of molecular dynamics into MCTDH. *Phys Chem Chem Phys* (2008) 10:850. doi:10.1039/b714821f
27. Accardi A, Borowski A, and Kühn O. Nonadiabatic quantum dynamics and laser control of Br2in solid argon†. *J Phys Chem A* (2009) 113:7491–8. doi:10.1021/jp900551n
28. Richings GW, Polyak I, Spinlove KE, Worth GA, Burghardt I, and Lasorne B. Quantum dynamics simulations using Gaussian wavepackets: the vMCG method. *Int Rev Phys Chem* (2015) 34:269–308. doi:10.1080/0144235x.2015.1051354
29. Richings GW, and Habershon S. MCTDH on-the-fly: efficient grid-based quantum dynamics without pre-computed potential energy surfaces. *J Chem Phys* (2018) 148:134116. doi:10.1063/1.5024869
30. Heller EJ. *The semiclassical way to dynamics and spectroscopy*. Princeton, NJ: Princeton University Press (2018).
31. Kondorskiy A, and Nakamura H. Semiclassical formulation of optimal control theory. *J Theor Comput Chem* (2005) 04:75–87. doi:10.1142/s0219633605001416
32. Kondorskiy A, Mil'nikov G, and Nakamura H. Semiclassical guided optimal control of molecular dynamics. *Phys Rev A* (2005) 72:041401. doi:10.1103/physreva.72.041401
33. Bonačić-Koutecký V, and Mitrić R. Theoretical exploration of ultrafast dynamics in atomic clusters: analysis and control. *Chem Rev* (2005) 105: 11–66. doi:10.1021/cr0206925
34. Broeckhove J, Lathouwers L, Kesteloot E, and Van Leuven P. On the equivalence of time-dependent variational principles. *Chem Phys Lett* (1988) 149:547–50. doi:10.1016/0009-2614(88)80380-4
35. Worth GA, and Sanz CS. Guiding the time-evolution of a molecule: optical control by computer. *Phys Chem Chem Phys* (2010) 12:15570. doi:10.1039/c0cp01740j
36. Sundermann K, and de Vivie-Riedle R. Extensions to quantum optimal control algorithms and applications to special problems in state selective molecular dynamics. *J Chem Phys* (2000) 110:1896. doi:10.1063/1.477856
37. Došlić N. Generalization of the Rabi population inversion dynamics in the sub-one-cycle pulse limit. *Phys Rev A* (2006) 74:013402. doi:10.1103/PhysRevA.74.013402
38. Došlić N, Kühn O, and Manz J. Infrared laser pulse controlled ultrafast H-atom switching in two-dimensional asymmetric double well potentials. *Ber Bunsen Ges Phys Chem* (1998) 102:292–7. doi:10.1002/bbpc.19981020303
39. Došlić N, Abdel-Latif MK, and Kühn O. Laser control of single and double proton transfer reactions. *Acta Chim Slov* (2011) 58:411–24.
40. Becerra VM. Solving complex optimal control problems at no cost with PSOPT. In: IEEE international symposium on computer-aided control system design; 2010 Sept 8–10; Yokohama, Japan. Piscataway, NJ: IEEE (2010). p. 1391–6.
41. Wächter A, and Biegler LT. On the implementation of an interior-point filter line-search algorithm for large-scale nonlinear programming. *Math Program* (2006) 106:25–57. doi:10.1007/s10107-004-0559-y
42. Worth GA, Beck MH, Jäckle A, Meyer HD, Meyer H-D, Vendrell O, et al. The MCTDH package version 8.2 (2000) Version 8.3 (2002) Version 8.4 (2007) Version 8.5 (2011), used Version 8.5.4 Available at: http://mctdh.uni-hd.de/. Tech. rep. (2000).

Conflict of Interest: The authors declare that the research was conducted in the absence of any commercial or financial relationships that could be construed as a potential conflict of interest.

frontiers in Physics

ORIGINAL RESEARCH
published: 11 May 2021
doi: 10.3389/fphy.2021.674794

Quantum Control Landscapes Beyond the Dipole Approximation: Controllability, Singular Controls, and Resources

Benjamin Russell [1], Re-Bing Wu [2] and Herschel Rabitz [1]*

[1] Frick Laboritory, Princeton University, Princeton, NJ, United States, [2] Department of Automation, Tsinghua University, Beijing, China

We investigate the control landscapes of closed *n*-level quantum systems beyond the dipole approximation by including a polarizability term in the Hamiltonian. The latter term is quadratic in the control field. Theoretical analysis of singular controls is presented, which are candidates for producing landscape traps. The results for considering the presence of singular controls are compared to their counterparts in the dipole approximation (i.e., without polarizability). A numerical analysis of the existence of traps in control landscapes for generating unitary transformations beyond the dipole approximation is made upon including the polarizability term. An extensive exploration of these control landscapes is achieved by creating many random Hamiltonians which include terms linear and quadratic in a single control field. The discovered singular controls are all found not to be local optima. This result extends a great body of recent work on typical landscapes of quantum systems where the dipole approximation is made. We further investigate the relationship between the magnitude of the polarizability and the fluence of the control resulting from optimization. It is also shown that including a polarizability term in an otherwise uncontrollable dipole coupled system removes traps from the corresponding control landscape by restoring controllability. We numerically assess the effect of a polarizability term on a known example of a particular three-level Λ-system with a second order trap in its control landscape. It is found that the addition of the polarizability removes the trap from the landscape. The general practical control implications of these simulations are discussed.

Keywords: quantum control, dipole approximation, polarizability, landscape topology, singular control

Edited by:
Robert Gordon,
University of Illinois at Chicago,
United States

Reviewed by:
Ignacio Sola,
Complutense University of Madrid,
Spain
Yuichi Fujimura,
Tohoku University, Japan

***Correspondence:**
Herschel Rabitz
hrabitz@princeton.edu

Specialty section:
This article was submitted to
Physical Chemistry and Chemical
Physics,
a section of the journal
Frontiers in Physics

Received: *02 March 2021*
Accepted: *06 April 2021*
Published: *11 May 2021*

Citation:
Russell B, Wu R-B and Rabitz H (2021) Quantum Control Landscapes Beyond the Dipole Approximation: Controllability, Singular Controls, and Resources. Front. Phys. 9:674794. doi: 10.3389/fphy.2021.674794

1. INTRODUCTION

There is extensive interest in quantum control, and in quantum control landscapes, which arises from the fundamental desire to manipulate quantum systems for both basic scientific reasons and for technological applications [1–13]. The field has been driven by many experimental and theoretical advances. Experimental domains extend from atoms and molecules including the control of chemical reactions [14, 15], out to manipulating biological systems [16]. One area of application for quantum control which has attracted interest is quantum information science [17–19] as optimal control offers the promise of discovering fields to implement quantum gates with high fidelity and to minimize errors introduced by decoherence and environmental noise. Typical desiderata in quantum control include driving a system to a desired density matrix ρ, maximizing the expectation value of an observable $\langle O\rangle$, and driving a unitary propagator $U(t)$ to a desired goal gate $W \in SU(n)$ (i.e., typical in quantum information science). In the latter case, one often seeks a minimum time control for maximizing the fidelity of the desired physical transformation W in order to better ensure that a gate is implemented with minimal decoherence induced by the environment. In some cases of minimum time optimal control, the associated control landscapes are known to have singular critical points [11, 20] resulting from singular controls. Accordingly, we focus on the unitary transformation fidelity landscape with a fixed end time T well above the minimal time.

In this work, we study the landscapes with numerical simulations, illustrated for the control of the quantum propagator of closed quantum systems having n levels with a single control field, thereby extending existing studies by moving beyond the typical dipole approximation through the inclusion of a polarizability term in the Hamiltonian [21, 22]. This extension is motivated by the fact that the polarizability term is inherently present in many physically realistic conditions, including the case of controlling molecules where the control field can result in a redistribution of charge. We specifically assess the potential for singular controls (i.e., see section 3 for basic definitions and relevant aspects of singular controls) to introduce traps into the landscapes of such systems in order to understand when gradient based (or any local) optimization algorithms should succeed in discovering high fidelity controls. Such findings aid in determining which algorithms are appropriate for use in simulations and in automated pulse discovery in the laboratory [2].

Given a prescribed final time $T \in \mathbb{R}$ and the desire to evolve the n-level quantum system to a specific *goal* gate $W \in \mathbf{U}(n)$ (i.e., the unitary Lie group), we specify the *fidelity* of evolution as:

$$J[U(T)] = \frac{1}{n^2}\left|Tr\left[W^\dagger U(T)\right]\right|^2, \tag{1}$$

whose maximum over all $U \in \mathbf{U}(n)$ is 1p. Supporting the landscape analysis of J as a functional of the control field are three assumptions (see section 2) whose satisfaction, at least in the dipole approximation, enables a theoretical analysis of the landscape topological features. The nature of such features are essential to understand in deciding the best algorithms to use for selecting an optimal control field, and even assessing if an optimal control exists. We note that the form of Equation (1) can be alternatively chosen as $\widetilde{J}(U(T)) = \Re\left(Tr(W^\dagger U(T))\right)$ in the case of $\mathbf{U}(n)$, but it is not recommended to use the latter form for $SU(n)$ (i.e., the special unitary group) as traps can arise in the landscape; the fidelity in Equation (1) should form a trap free landscape for $SU(n)$.

The critical point topology of the function J is discussed in detail in [23], where it is shown that it possess only global maxima, global minima and saddle points when considered as a function of U; that is, J possess no so-called *kinematic* landscape traps. We study the control landscape of the cost function: $F[E] = J[V_T[E]]$ where E is the control field, and V_T is the end-point map [see [11, 24] for a more detailed and general discussion of this map in control theory]. Thus, this work will distinguish between the kinematic landscape J and the dynamic analog F. V_T is a mapping from the space of controls to the corresponding final time solution $U(T)$ to the Schrödinger equation:

$$\dot{U}(t) = -iH(t)U(t). \tag{2}$$

Throughout this work $\hbar$ will be set to 1. The type of Hamiltonian we study has the following form:

$$H(t) = H_0 + E(t)H_1 + E^2(t)H_2, \tag{3}$$

where $iH_0, iH_1, iH_2 \in \mathfrak{u}(n)$. This is the first step toward including higher order terms beyond the dipole approximation (where only the first power of E is included) from the expansion:

$$H(t) = H_0 + \sum_{k=1}^{\infty} E^k(t)H_k, \tag{4}$$

wherein the sequence $\{H_k\}$ generally reduce in matrix norm with increasing k in keeping with diminishing higher order polarization effects. The terms H_k have a clear physical interpretation as the ability of the external field to redistribute the charge within a system so that an induced dipole is created. In a more physically complete model of a molecular system interacting with an external vector field, the term H_k would be replaced by a kth-order tensor. Some work on the control under these conditions can be found in [25–27]. For a physical discussion of this type of system and the interpretation of H_3 (i.e., the hyper-polarizability) and the terms beyond this see [28]. While the control landscapes of quantum systems have been studied intensively, landscape analysis of systems including the effect of polarizability, even at the level of H_2, has not yet been performed. The present work provides numerical evidence on the affect of H_2 in the presence of the H_1 term.

In this work we address the status of the assumptions of quantum control landscape analysis applied to systems which have a polarizability term H_2 present. In particular, we numerically investigate random quantum systems, with a polarizability term, for traps in their control landscapes. For a few dipole control system cases it has been shown that zero or some constant control is singular critical, and thus a potential trap. With a polarizability term present, we show numerically that no traps are present for initial controls near to the zero field for a specific example of such a system. We also assess the effect of the addition of a polarizability term on the controllability of systems which would not otherwise be controllable. In a large number of additional cases with $n = 4$ and random tuples (H_0, H_1, H_2, W) we find no numerical evidence of traps being present.

2. THE THREE ASSUMPTIONS OF LANDSCAPE ANALYSIS

Satisfaction of the following three assumptions imply a trap free landscape in the case $H = H_0 + E(t)H_1$. This scenario provides a backdrop to consider the roles of H_2 later in the paper. The three assumptions are:

1. The system is globally controllable. That is, beyond some critical time T^*, all $U \in \mathbf{U}(n)$ are reachable using some control, such that every unitary $U(T)$ can be implemented by some control E. Equivalently, the end-point map V_T is *globally surjective*.
2. The system is locally controllable. That is, V_T is *locally surjective*.
3. The controls are unconstrained, such that all control functions can be implemented without restriction.

Various studies [7, 8] as well as mathematical analysis [29–31] are consistent with the assumptions above ensuring that a given quantum control landscape should be trap free. However, the weakest sufficient conditions assuring a trap free landscape are not known. Consideration of the assumptions above are relevant to the paper, as we will numerically show that violation of either assumptions (1) or (2) can be lifted by the presence of a randomly chosen polarizability term H_2.

In the context of quantum control (for systems without the polarizability term), it has been shown [32] that assumption (1) regarding global controllability, generically holds when H_0, H_1 are chosen at random. More precisely, it is shown that controllability fails only for a null set of pairs $(iH_0, iH_1) \in \mathfrak{u}(n) \times \mathfrak{u}(n)$ [equivalent to full accessibility, such that every point on $\mathbf{U}(n)$ can be reached using some control at *some* final time T]. A controllability analysis of systems which include polarizability has been performed in [27] and controllability has been found to be similarly generic, but this advance has yet to be folded into a full landscape topology analysis (i.e., see remarks in section 5).

It has further been shown [6] that there exists a critical time T^* such that $\forall T \geq T^*$ the system is *fixed-time controllable* as long as it is controllable. If iH_0, iH_1 generate $\mathfrak{u}(n)$ and the final time T is large enough, one can always find a control E such that $U(T) = W$ for any goal operator W in $\mathbf{U}(n)$. In all simulations in this work a sufficiently large time has been chosen so that all systems are fully accessible whenever they are controllable. It is thus guaranteed that the first assumption will be satisfied for almost all systems with Hamiltonian terms H_0 and H_1 generated at random and controlled over sufficiently large intervals, as the set for which this fails is null. This circumstance does not imply that there are no uncontrollable systems in reality or that they cannot be deliberately mathematically constructed. Neither does it imply that the uncontrollable cases [6, 33], or additional cases, for examples, with insufficient resources [13] do not have interesting control landscape structure potentially including traps.

Assumption (2) has been shown to be violated for some specific systems [6] and potential effects on gradient based searches for optimal controls has been discussed in [11, 30]. See [31] for a refined discussion of assumption (2) in order to obtain a weaker sufficient condition for a trap free landscape based on the geometric notion of local *transversality* of the end point map from the level sets of fidelity rather than local surjectivity of this map [31]. It has been further shown that in two level systems, singular controls never represent traps [34, 35] on the landscape of ensemble average of observables. In randomly generated four level systems, singular controls are generally saddles within control space for the task of controlling the density matrix [11] for systems in the dipole approximation. It has not, however, been rigorously proven that *all* singular controls are always saddles to some order (i.e., where order refers to second or higher order derivatives of $F[E]$), despite mounting corroborating numerical evidence that this is the case.

Assumption (3) concerns resources, and is satisfied if no restriction is imposed on the control. Even in simulations resources have limits due to computational considerations, but this situation tends not to be a serious issue. However, in laboratory practice, there are always restrictions on the controls, although their influence is application specific. Control restrictions include the local peak amplitude of the fields, the total achievable field fluence, and also the ability to accurately implement and vary the control field. Typical scenarios are those of the control of molecules by electromagnetic fields. Importantly, access to control resources continues to increase. As such, this matter is a technological issue rather than a fundamental one. Noise is also always present in reality, and if the noise is weak it can be treated perturbatively; the present work will not treat the impact of noise and only considers closed systems.

In this work we will assess if systems violating assumptions (1) or (2) and exhibiting traps on the landscape created by H_0 and H_1 remain to have traps upon including the polarizabillity term. As it is known that the failure of either of these latter assumptions can indicate traps [6, 11, 33], we follow [11] attempting to understand the singular controls for systems beyond the dipole approximation.

3. SINGULAR CONTROLS AND SINGULAR CRITICAL POINTS

The work in [1] first discussed that singular controls could in principle introduce saddle type critical points, or even true local optima, into quantum control landscapes, but this was conjectured to be rare in practice. This conjecture has since been backed up with extensive simulations [11, 30]. Several studies [4–6, 11, 30] have discussed the potential effect of the existence of singular controls on the associated quantum landscapes and the significance of some of these findings has been debated [4, 5, 36, 37].

If the time-dependent Hamiltonian $H(t)$ of a (finite level) quantum system undergoes an arbitrary infinitesimal transformation $H(t) \mapsto H(t) + \delta H(t)$ then the end-point map $V_T[E] := U(T)$ varies according to:

$$U^\dagger(T)\delta U(T) = i\int_0^T U(t)\delta H(t)U^\dagger(t)dt \in \mathfrak{u}(n). \tag{5}$$

In the dipole approximation with a single control field, the Hamiltonian takes the form: $H(t) = H_0 + E(t)H_1$ and thus a variation $\delta E(t)$ of the control induces a corresponding variation $\delta H(t) = \delta E(t)H_1$. The latter formula put into in

Equation (5) yields:

$$U^{\dagger}(T)\delta U(T) = i\int_0^T \delta E(t)U^{\dagger}(t)H_1U(t)dt. \tag{6}$$

A control E is said to be *singular* if there exists at least one $B \in \mathfrak{su}(n)$ such that for all δE:

$$\left\langle U^{\dagger}(T)\delta U(T), B\right\rangle = 0, \tag{7}$$

where $\langle\cdot,\cdot\rangle$ is the trace inner product on $\mathfrak{su}(n)$. Applying the fundamental lemma of the calculus of variations [38] and then differentiating Equation (7) twice with respect to t yields an implicit formula for a singular E mathematically connecting it with a so called singular trajectory $U(t)$ in the case of a system in the dipole approximation [11]. Unfortunately, an explicit formula for the singular controls is not known and appears impossible to obtain by any method known to the authors. Intuitively, a singular control has the property that the corresponding end point $U(T)$ cannot be "steered" in at least one particular direction on $\mathbf{U}(n)$ by applying a small (infinitesimal) variation to the control field δE. It is noteworthy that, although a specific inner product is invoked here, the singularity of any given control does not depend on which inner product is chosen and any choice yields the same set of singular controls. Singularity of a given E is equivalent to the (Fréchet) derivative $\delta V_T/\delta E(t)$ being rank deficient for the field E in control space. By substituting Equation (6) into Equation (7) and applying the fundamental lemma of the calculus of variations, one sees that a singular control in the dipole approximation must satisfy:

$$\langle iU^{\dagger}(t)H_1U(t), B\rangle = 0, \quad \forall t \in [0, T]. \tag{8}$$

In the case of Equation (3), where the Hamiltonian contains the additional polarizability term $E^2(t)H_2$, the singular controls take a novel form. Equation (7) in this case implies:

$$\left\langle i\int_0^T \delta E(t)U^{\dagger}(t)\left[H_1 + 2E(t)H_2\right]U(t)dt, B\right\rangle = 0. \tag{9}$$

After again applying the fundamental lemma of calculus of variations and rearranging (assuming $\langle iU(t)^{\dagger}H_2U(t), B\rangle \neq 0$ $\forall t \in [0, T]$), we have:

$$E(t) = -\frac{1}{2}\frac{\langle iU^{\dagger}(t)H_1U(t), B\rangle}{\langle iU^{\dagger}(t)H_2U(t), B\rangle}, \tag{10}$$

which is in contrast to the results on controlling the density matrix in the dipole approximation found in [11]; in the latter case a second derivative with respect to t of the formula analogous to (8) was required to determine the corresponding form of the singular controls. However, a similar formula can be found in the case of controlling the propagator in the dipole approximation and it requires an identical differentiation procedure, which we do not include in this work. At points in time where the denominator in Equation (10) satisfies $\langle iU_tH_2U^{\dagger}(t), B\rangle = 0$ further differentiation (with respect to t) and rearrangement [i.e., analogous to the procedure found in [11] in a general form] results in a suitable formula for singular controls with the polarizability term present. The number of derivatives required to find a singular control is known as the *order* of a singular control and the quantity: $n^2 - \text{rank}(\delta V_T)$ is known as the co-rank of a singular control. The co-rank corresponds to the number of linearly independent dimensions of choices for B to which the image of δV_T is orthogonal. In contrast to the case without the polarizability term found in [11], a differential equation is now found as $\frac{dE}{dt}$ remains in the resulting equation. The full significance of this difference in form merits investigation and is left as a basis of further work.

A singular control may correspond to a *singular critical point* of the map F. That is, a singular control (satisfying Equation 7) E may have the property that:

$$\langle U^{\dagger}(T)\delta U(T), U^{\dagger}(T)\nabla J\big|_{U(T)}\rangle = 0, \ \ \forall\delta E. \tag{11}$$

These are candidates for traps (i.e., local optima) in the landscape F as they are controls for which $\nabla F\big|_E = 0$. These controls are critical points of F for which $V_T[E] = U(T)$ is not a critical point of J.

The analysis of which singular critical controls, if any, are true traps requires an assessment of the Hessian index of the end-point map evaluated at a singular critical point; such a task is computationally intensive. With or without polarizability, which controls are singular does not depend on the function J being optimized, but only on the form of the Hamiltonian. However, which controls are singular critical points does depend on J through ∇J. Insight into the issue can be gained by examining the derivative of F by applying the chain rule:

$$\frac{\delta F}{\delta E} = \frac{dJ}{dV_T[E]} \circ \frac{\delta V_T[E]}{\delta E}. \tag{12}$$

If a control E is singular then $\frac{\delta V_T[E]}{\delta E}$ fails to be full rank. One sees that a control being singular can, but does not always, introduce a critical point of F (i.e., a control E for which $\frac{\delta F}{\delta E} = 0$). In particular, only when $\delta U(T)$ cannot vary (when all δE are considered) in the direction of increasing J (i.e., in the direction of the gradient of ∇J) is there a critical point of F. However, such singular points may still not be traps if a pathway up the landscape is accessible via higher order derivatives in the Taylor expansion of the end-point map. Thus, generically, we expect that there is very little chance for a singular control to become a local trap along the search for global optimal controls. The remainder of the paper will expand upon this remark to consider the impact of a polarizability term being present in various scenarios, including the violation of assumptions (1) or (2).

4. NUMERICAL SIMULATIONS OF QUANTUM CONTROL LANDSCAPES INCLUDING POLARIZABILITY

In order to perform numerical optimization we approximate the smooth control field E by piecewise constant functions with M

pieces permitting significant freedom in E. This procedure is in keeping with a well-known theorem about approximating a general smooth function with a piecewise constant form [39].

The final time propagator, with the polarizability H_2 term, associated to the control E is

$$V_T : E \mapsto U(T) = \prod_{k=1}^{M} e^{-i(H_0 + E_k H_1 + E_k^2 H_2)\Delta T}, \tag{13}$$

where E_k is the amplitude of the kth piecewise-constant sub-pulse and $\Delta T = T/M$. The sequence in the product of Equation (13) is time ordered. The form in Equation (13) is used to optimize E with the gradient ascent algorithm (often known as GRAPE or gradient ascent pulse engineering in quantum control) [40].

In order to statistically assess for the existence of traps in the landscape associated with a given Hamiltonian, the algorithm must be repeated many times with different initial random fields E. If the algorithm consistently reaches the optimum, regardless of the starting point, this finding would indicate that the given Hamiltonian's landscape likely has no traps for generating a desired unitary transformation W. All calculations are performed with the system variables as dimensionless.

4.1. The Effect of Adding a Polarizability Term to a Globally Uncontrollable System With Traps

It is known that the landscapes of globally uncontrollable systems can contain traps [33]. Here we investigate whether or not including a polarizability term may eliminate the presence of such a trap. The system we study possess drift and control terms, respectively, given by:

$$H_0 = \begin{pmatrix} -2 & 0 & 0 & 0 & 0 \\ 0 & -1 & 0 & 0 & 0 \\ 0 & 0 & 0 & 0 & 0 \\ 0 & 0 & 0 & 1 & 0 \\ 0 & 0 & 0 & 0 & 2 \end{pmatrix}, \tag{14}$$

$$H_1 = \begin{pmatrix} 0 & 1 & 0 & 0 & 0 \\ 1 & 0 & 1.225 & 0 & 0 \\ 0 & 1.225 & 0 & 1.225 & 0 \\ 0 & 0 & 1.225 & 0 & 1 \\ 0 & 0 & 0 & 1 & 0 \end{pmatrix}. \tag{15}$$

The Lie algebra formed by H_0 and H_1 is rank deficient showing that this system is not globally controllable [i.e., violation of assumption (1) in section 2]. The target gate is chosen as $W = e^{-i\frac{\pi}{2}H_1}$. This globally uncontrollable system has traps [33], in particular at $J = 0.04$. We note that this system can be viewed as a controlled molecular rotor [33], but such character will not be exploited here, particularly in consideration of H_1 and H_2 both driven by the same scalar field $E(t)$ in keeping with the model in Equation (3) used throughout the paper.

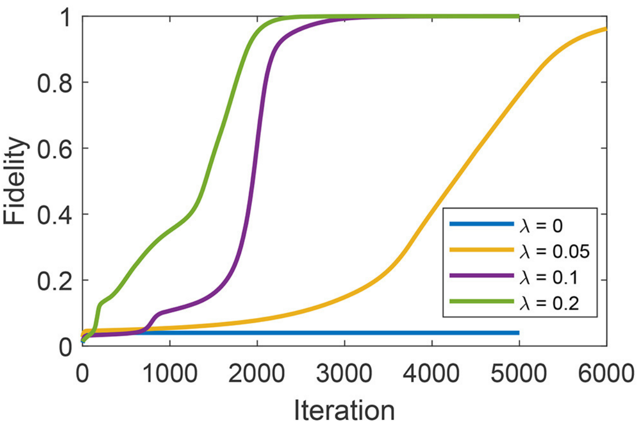

FIGURE 1 | The optimization from an initial control field that traps the system at $J = 0.04$ in the absence of polarizability ($\lambda = 0$). The presence of the random polarizability term (see the text for further details) steers the optimization away from the trap.

In order to assess the effect of adding a polarizability term, we first identify a sub-optimal field [33] corresponding to the trap $J = 0.04$. Then, we select the polarizability term H_2 randomly as a 5×5 complex Hermitian matrix with norm $\|H_2\| = \lambda$, and the optimization is started from the preselected field with $\lambda = 0, 0.05, 0.1, 0.2$, where $\lambda = 0$ corresponds to the case with only the dipole interaction H_1. It can be seen in **Figure 1** that the presence of polarizability steers the optimization away from the trap and on to full fidelity. section 4.4 returns to the globally uncontrollable Hamiltonian formed by Equations (14) and (15) for an examination of the landscape with random choices for W and H_2.

4.2. The Effect of Adding a Polarizability Term to a System With a Second-Order Trap

In this section we assess the potential for the addition of a polarizability term to remove a trap from the landscape of a system known to possess one due to the loss of local controllability [i.e., violation of assumption (2) in section 2]. This example can be found in [6] [i.e., and in [30] where it is referred to as "system E"]:

$$H_0 = \begin{bmatrix} 1 + \frac{\pi}{1000} & 0 & 0 \\ 0 & 1 & 0 \\ 0 & 0 & 2 \end{bmatrix}, \quad H_1 = \begin{bmatrix} -5\sqrt{\frac{2}{3}} & -1 & 0 \\ -1 & -4 & -1 \\ 0 & -1 & -1 \end{bmatrix}, \tag{16}$$

$$W = \begin{bmatrix} e^{i\frac{2\pi}{3}} & 0 & 0 \\ 0 & -ie^{i\frac{3\pi}{4}} & 0 \\ 0 & 0 & -ie^{i\phi} \end{bmatrix} \exp\left(-iH_0 \cdot 1000\right).$$

The field $E = 0$ is known to be a second order trap for this system.

We generated 1,000 random polarizability matrices $H_2 \in \mathfrak{u}(3)$ ($\frac{1}{10}$ of the norm of H_1), and for each case a random initial field was generated in the vicinity of the zero field. It was found that, for initial fields arbitrarily close to the zero field, all gradient ascent runs converged to full fidelity. As such, we can conclude that the dipole trapping effect due to Equation (16) observed in [30] can be counteracted by the addition of a polarizability term.

4.3. Observed Properties of Generic Systems With a Polarizability Term

In this section, we assess if the addition of a polarizability term can *introduce* traps into the landscapes of systems known to have none in practice without a polarizability term; that is, each of the cases utilizes randomly chosen H_0 and H_1, which are known [31] to almost always produce trap free landscapes for W. All the cases here and in section 4.4 have $n = 4$ levels, unless otherwise stated. We numerically analyze the landscape of general systems of the form in Equation (3), which include polarizability. One thousand random tuples $(H_0, H_1, H_2, W = e^{iA})$ were generated and their landscapes similarly analyzed with 100 runs, each with a random initial field $E(t)$. The real and imaginary elements of the complex Hermitian matrices H_0, H_1, H_2, and A were drawn separately from a uniform distribution over $[-1, 1]$. This procedure is used in the other studies below. The initial fields $E(t)$ were uniformly and randomly generated to have $E(t) \in [-1, 1]$ for all discretized components for $t \in [0, T]$, but the components were unrestricted in magnitude during the optimization. The resultant landscapes were found to be trap free, as all runs converged within practical computational timescales to fidelity above 0.99.

The term H_2 typically has a norm which is less than H_1 in physical applications. In situations where a control is exploiting the effect of H_2 to achieve the implementation of a desired gate W, one might reasonably conjecture that a small size polarizability H_2 requires a very strong field or very high total field fluence. The fidelity is plotted along with the field fluence of $E(t)$ in **Figure 2** vs. algorithm iteration for three cases of 100 randomly generated tuples (H_0, H_1, H_2, W). In all cases the fidelity reached at least 0.99. The fluence of a field E is defined as:

$$\|E\| = \frac{1}{T} \int_0^T E^2(t)dt.$$

All the simulations start from a small-fluence initial guess of the control field, and the fluence increases with iteration. When the polarization H_2 is weak (compared with the norm of H_1, as in **Figures 2A,B**, the fluence significantly increases with iteration, suggesting that the polarizability plays an important role requiring sufficient fluence. When H_1 and H_2 have the same norms (as in **Figure 2C**), the controls do not significantly increase in fluence with iteration. This case suggests that the effects of polarizability can be exploited for control without a significant rise in field amplitude over iteration. Moreover, in all cases and to some degree in **Figure 1** the inflection points in the fidelity vs. iteration curves likely indicate that the climbing trajectories come near saddles, which are known to exist in the case of $H = H_0 + E(t)H_1$ and are expected to be present when H_2 is included.

4.4. The Neighborhood of Singular Controls

In this section, we explore the neighborhood of singular controls to check for trapping behavior in several types of systems. It is not known generally what proportion of singular controls are singular critical controls, and what proportion of singular critical controls are traps. Here we assess if singular controls play a significant role in determining the topology of critical points on quantum control landscapes for systems with a polarizability term present. Following the work in [11], one can numerically solve the Schrödinger equation to obtain singular controls $E(t)$. This can be achieved by substituting Equation (10) into Equation (3) and then substituting the resulting Hamiltonian into Equation (2) to obtain the initial value problem (i.e., in Equation 17) it is understood that $E(t)$ is given by Equation (10), thereby making Equation (17) highly non-linear in $U(t)$:

$$\dot{U}(t) = -i\left[H_0 + E(t)H_1 + E^2(t)H_2\right]U(t), \quad U(0) = I. \quad (17)$$

A solution $U(t)$ to this system of equations is a singular trajectory emanating from the group identity at $t = 0$. Equation (10) shows that the set of all singular trajectories is parameterized by $B \in \mathfrak{su}(n)$. From a numerical solution of Equation (17), the corresponding singular control can be obtained by substituting the singular trajectory $U(t)$ into Equation (10).

In order to test if any given singular control E is a trap, it is possible to explore the neighborhood of E by evaluating $F[E+\delta E]$ for many small δE and assessing the sign of $\delta F = F[E+\delta E]-F[E]$. If two linearly independent δE can be found such that δF has different signs (i.e., one positive and one negative) then the point E must be a saddle in control space rather than a trap. Two types of systems were assessed in this respect.

In the first scenario 10,000 tuples (H_0, H_1, H_2, B, W) were uniformly and randomly generated, as previously described, and the corresponding singular control was found numerically by solving Equation (17) in order to obtain a singular trajectory and thus, in turn generate a singular control from Equation (10). In all cases, no traps were found, as an average of 3.23 variations δE of the control were required to identify two which resulted in fidelity variations of opposite sign. Furthermore, the highest number of trial variations required for any singular control was 70. This behavior indicates that all of the singular controls examined are saddles on the control landscape.

The second class of Hamiltonians assessed were those in Equations (14) and (15) with $n = 5$ for H_0 and H_1. Ten thousand tuples (H_2, B, W) were generated uniformly at random and the corresponding singular control was found numerically by solving Equation (17) in order to obtain a singular trajectory and thus a singular control, as before. In all cases, no trapping behavior was found, and the highest number of trial variations required for assessing the nature of any singular control was 200. This again indicates that all of the singular controls examined are saddles on the control landscape, even when the landscape derived from $H = H_0 + E(t)H_1$, which produces at least one trap (i.e., see the discussion in section 4.1).

From these cases upon visual examination of many singular controls, they can be seen to exhibit characteristic features. Most notably, there are two distinct classes. The dominant first class are all physically plausible fields as they are smooth and bounded. Controls in the second class all possess at least one blow-up point where the control becomes both unbounded and discontinuous (i.e., they possess infinite jump discontinuities, similar to the reciprocal function $f(x) = \frac{1}{x}$ at $x = 0$), as such, they are clearly excluded from physical consideration. This behavior arises from the denominator in Equation (10) passing through zero. The

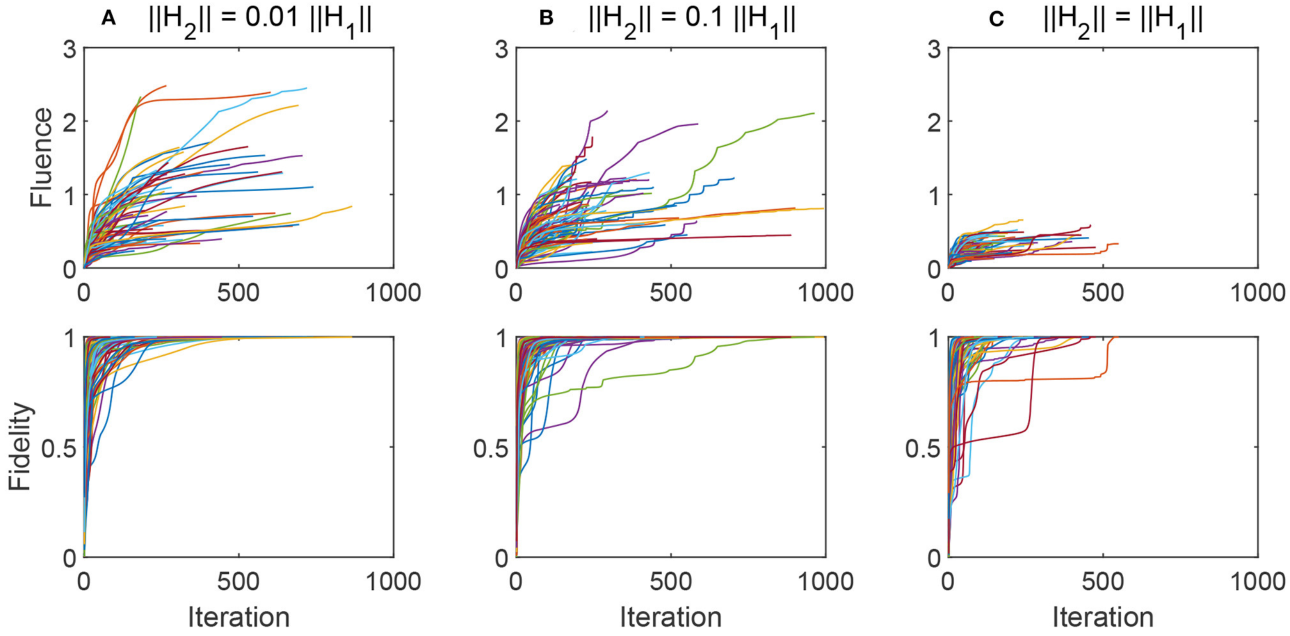

FIGURE 2 | Fidelity and fluence $\|E\|$ plotted verses algorithm iteration in three cases from weak to strong randomly chosen polarizability: **(A)** $\|H_2\| \sim 0.01\|H_1\|$, **(B)** $\|H_2\| \sim 0.1\|H_1\|$, and **(C)** $\|H_2\| \sim \|H_1\|$.

comments below Equation (10) explain how to deal with this behavior, but it was not explored in the simulations here.

For each matrix $B \in \mathfrak{su}(4)$, there is a singular control defined by Equations (17) and (10). Using randomized gradient decent for B, we can produce singular critical controls, rather than just singular ones. We thus optimize over B such that it is co-linear to $U^\dagger(T)\nabla J\big|_{U(T)}$ (to a numerical tolerance of 0.001 radians). For all cases, $U(T)$ was not found to be a kinematic critical point of $J(U(T))$. In the case of $\mathfrak{su}(4)$, this procedure consists of minimization over the 15 parameters of $\mathfrak{su}(4)$. One parameter can be discarded as the formula for a singular control in Equation (10) doesn't depend on the norm of B due to the linearity of the numerator and denominator in B. Thus, it is possible to restrict the search to the unit norm of B. We found that this search did not always succeed in finding a singular critical control; only about 5% of searches succeeded. This suggests that the set of singular critical controls is very small in the set of singular controls.

In order to explore the latter prospect, we studied the structure of the control landscape in systems with randomly generated tuples (H_0, H_1, H_2, B, W) as before. We analyzed the possibility of whether a singular critical control E is a trap on the control landscape of F by making many small variations $E' := E + \delta E$ around E. For each E' a randomized gradient ascent was initiated. If a singular critical E were a true trap, rather than a saddle, this would be identified by at least some gradient ascent runs returning back to E (or a control near to E of the same fidelity) when initiated from $E + \delta E$. If full fidelity was reached during the run, then E cannot be a trap. One hundred tuples (H_0, H_1, H_2, B, W) were generated and for each tuple 100 singular critical controls were created as described in the last paragraph. For each singular critical control E, 200 points E' in the neighborhood of E were generated and an associated gradient-ascent run was completed. The norm of δE was chosen to be random within $[0, 0.001]$ (which is typically very small compared to the norm of $E(t)$) so as to ensure exploring close to the candidate trap and the behavior around it. We found that all runs converged to $F[E] \simeq 1.0$ and displayed similar convergence rates as those cases seen when initial controls were chosen at random from the whole control space. Lastly, the singular critical controls generally exhibited no clear visually differentiating features when compared to the singular, non-critical controls. As such, no example is shown; also see the remarks earlier in this section regarding the denominator in Equation (10).

5. CONCLUSIONS, OUTLOOK, AND FURTHER STUDIES

We have shown that upon including a polarizability term in the Hamiltonian, and thus moving beyond the standard dipole approximation, a change in the character of quantum control landscapes is seen in some relevant $n = 3, 4$, and 5 level cases. We have also shown that there is a theoretical difference between the nature for the singular controls in the cases with and without the polarizability term.

There are two central conclusions from this work:

1. Including a polarizability term H_2 does not introduce traps into the landscape for typical tuples (H_0, H_1, H_2, W).
2. Including a random polarizability term can remove traps from the landscapes for a class of otherwise uncontrollable systems

based upon H_0 and H_1, including the situation of a trap at zero field.

It has been shown that almost all Hamiltonians based up on H_0 and H_1 do not correspond to traps in quantum control landscapes with the exceptions forming a null set of systems [31]. However, this result does not exclude exceptions to particularly violating assumptions (1) or (2) of section 2. Concerning satisfaction of global or local controllablity, this paper considered a few known exceptions and showed that the addition of a random H_2 term returned the augmented system to normal behavior [i.e., the original (H_0, H_1) driven traps were removed].

In this work for systems based on arbitrary (H_0, H_1, H_2, B, W), an algorithm was devised to search for singular critical controls and analyze if they are traps by examining F in a neighborhood of any discovered singular critical controls. Effectively, this process is exploring the nature of the eigenvalues of the Hessian of the end-point map (i.e., and possibly the impact of higher order derivatives of $F[E]$ playing a role) at the singular critical points. In [11] no trapping singular controls were found in the case of linear coupling H_1 and the control of the density matrix. Our work extends this finding in two respects. Firstly, we study the control of the full quantum propagator $U(t)$. Secondly, we study the role of non-linear polarizability coupling H_2 along with H_1. Future work should include repeating the numerical analysis of [11] in the case of the control of the density matrix and the observable maximization task for systems with a polarizability term and even higher order coupling terms in the Hamiltonian.

This work provides numerical evidence to bolster the claim that trap free landscapes are ubiquitous in the practice of quantum control. We conjecture that including more terms and their tensor character in the expansion in Equation (4) will have the general effect of removing traps from the landscape by adding novel dynamical mechanisms induced by the controls via couplings to an external field or fields (in the case of tensor H_k). This conjecture simply states that nominal system "complexity" aids in increasing the likelihood that assumptions (1) and (2) will hold, naturally assuming that adequate resources are available for this purpose [i.e., satisfaction of assumption (3)]. An assessment of this conjecture should form the basis for further analytical and numerical investigation. A possible path to proving this conjecture may lie in combining the proof of global controllability [27] with an extension of local controllability [41]. Importantly, in the laboratory with atoms and molecules additional terms beyond the dipole approximation will inherently be present, even if they are weak. In summary, this work goes beyond the majority of theoretical studies in quantum control and quantum control landscapes, which investigate systems restricted to the dipole approximation. The tantalizing numerical findings in the paper and the generic existence of molecular polarization warrants an assessment of the physical conjecture made above, which may be captured by the statement that system complexity appears to be a friend for finding favorable control landscape topology.

DATA AVAILABILITY STATEMENT

The original contributions presented in the study are included in the article, further inquiries can be directed to the corresponding author.

AUTHOR CONTRIBUTIONS

BR, R-BW, and HR contributed to conception and design of the study. BR performed the simulation, analysis, and composition. R-BW checked the simulation and help editing the paper. HR proposed the main idea and edit the paper. All authors contributed to the article and approved the submitted version.

FUNDING

HR acknowledges support from the US ARO (W911NF-19-1-0382) and BR acknowledges support from the US DOE (DE-FG02-02ER15344).

REFERENCES

1. Chakrabarti, Rabitz H. Quantum control landscapes. *Int Rev Phys Chem*. (2007) 26:671–735. doi: 10.1080/01442350701633300
2. Judson RS, Rabitz H. Teaching lasers to control molecules. *Phys Rev Lett*. (1992) 68:1500–3. doi: 10.1103/PhysRevLett.68.1500
3. Rabitz H, de Vivie-Riedle R, Motzkus M, Kompa K. Whither the future of controlling quantum phenomena? *Science*. (2000) 288:824–8. doi: 10.1126/science.288.5467.824
4. Pechen AN, Tannor DJ. Are there traps in quantum control landscapes? *Phys Rev Lett*. (2011) 106:120402. doi: 10.1103/PhysRevLett.106.120402
5. Rabitz H, Ho TS, Long R, Wu R, Brif C. Comment on "Are There Traps in Quantum Control Landscapes?". *Phys Rev Lett*. (2012) 108:198901. doi: 10.1103/PhysRevLett.108.198901
6. De Fouquieres P, Schirmer SG. A closer look at quantum control landscapes and their implication for control optimization. *Infinite Dimens Anal Quant Probabil Relat Top*. (2013) 16:1350021. doi: 10.1142/S0219025713500215
7. Roslund J, Rabitz H. Experimental quantum control landscapes: inherent monotonicity and artificial structure. *Phys Rev A*. (2009) 80:013408. doi: 10.1103/PhysRevA.80.013408
8. Roslund J, Rabitz H. Gradient algorithm applied to laboratory quantum control. *Phys Rev A*. (2009) 79:053417. doi: 10.1103/PhysRevA.79.053417
9. Palao JP, Kosloff R. Quantum computing by an optimal control algorithm for unitary transformations. *Phys Rev Lett*. (2002) 89:188301. doi: 10.1103/PhysRevLett.89.188301
10. Caneva T, Murphy M, Calarco T, Fazio R, Montangero S, Giovannetti V, et al. Optimal control at the quantum speed limit. *Phys Rev Lett*. (2009) 103:240501. doi: 10.1103/PhysRevLett.103.240501
11. Wu RB, Long R, Dominy J, Ho TS, Rabitz H. Singularities of quantum control landscapes. *Phys Rev A*. (2012) 86:013405. doi: 10.1103/PhysRevA.86.013405
12. Moore KW, Rabitz H. Exploring quantum control landscapes: topology, features, and optimization scaling. *Phys Rev A*. (2011) 84:012109. doi: 10.1103/PhysRevA.84.012109
13. Moore KW, Rabitz H. Exploring constrained quantum control landscapes. *J Chem Phys*. (2012) 137:134113. doi: 10.1063/1.4757133
14. Nuernberger P, Vogt G, Brixner T, Gerber G. Femtosecond quantum control of molecular dynamics in the condensed phase. *Phys Chem Chem Phys*. (2007) 9:2470–97. doi: 10.1039/b618760a

15. Levis RJ, Rabitz HA. Closing the loop on bond selective chemistry using tailored strong field laser pulses. *J Phys Chem A*. (2002) 106:6427–44. doi: 10.1021/jp0134906
16. Herek JL, Wohlleben W, Cogdell RJ, Zeidler D, Motzkus M. Quantum control of energy flow in light harvesting. *Nature*. (2002) 417:533–5. doi: 10.1038/417533a
17. Timoney N, Elman V, Glaser S, Weiss C, Johanning M, Neuhauser W, et al. Error-resistant single-qubit gates with trapped ions. *Phys Rev A*. (2008) 77:052334. doi: 10.1103/PhysRevA.77.052334
18. Lucero E, Kelly J, Bialczak RC, Lenander M, Mariantoni M, Neeley M, et al. Reduced phase error through optimized control of a superconducting qubit. *Phys Rev A*. (2010) 82:042339. doi: 10.1103/PhysRevA.82.042339
19. Arute F, Arya K, Babbush R, Bacon D, Bardin JC, Barends R, et al. Quantum supremacy using a programmable superconducting processor. *Nature*. (2019) 574:505–10. doi: 10.1038/s41586-019-1666-5
20. Lapert M, Zhang Y, Braun M, Glaser SJ, Sugny D. Singular extremals for the time-optimal control of dissipative spin $\frac{1}{2}$ particles. *Phys Rev Lett*. (2010) 104:083001. doi: 10.1103/PhysRevLett.104.083001
21. Applequist J, Carl JR, Fung KK. Atom dipole interaction model for molecular polarizability. Application to polyatomic molecules and determination of atom polarizabilities. *J Am Chem Soc*. (1972) 94:2952–60. doi: 10.1021/ja00764a010
22. Kaminski GA, Stern HA, Berne BJ, Friesner RA. Development of an accurate and robust polarizable molecular mechanics force field from *ab initio* quantum chemistry. *J Phys Chem A*. (2004) 108:621–7. doi: 10.1021/jp0301103
23. Fu H, Schirmer SG, Solomon AI. Complete controllability of finite-level quantum systems. *J Phys A Math Gen*. (2001) 34:1679. doi: 10.1088/0305-4470/34/8/313
24. Dominy J, Rabitz H. Dynamic homotopy and landscape dynamical set topology in quantum control. *J Math Phys*. (2012) 53:082201. doi: 10.1063/1.4742375
25. Grigoriu A. Stability analysis of discontinuous quantum control systems with dipole and polarizability coupling. *Automatica*. (2012) 48:2229–34. doi: 10.1016/j.automatica.2012.06.028
26. Coron JM, Grigoriu A, Lefter C, Turinici G. Quantum control design by Lyapunov trajectory tracking for dipole and polarizability coupling. *N J Phys*. (2009) 11:105034. doi: 10.1088/1367-2630/11/10/105034
27. Turinici G. Beyond bilinear controllability: applications to quantum control. In: Kunisch K, Sprekels J, Leugering G, Tröltzsch F, editors. *Control of Coupled Partial Differential Equations*. Basel: Birkhäuser Basel (2007). p. 293–309. doi: 10.1007/978-3-7643-7721-2_13
28. Verbiest T, Clays K, Samyn C, Wolff J, Reinhoudt D, Persoons A. Investigations of the hyperpolarizability in organic molecules from dipolar to octopolar systems. *J Am Chem Soc*. (1994) 116:9320–23. doi: 10.1021/ja00099a058
29. Long R, Riviello G, Rabitz H. The gradient flow for control of closed quantum systems. *IEEE Trans Automat Control*. (2013) 58:2665–9. doi: 10.1109/TAC.2013.2256677
30. Riviello G, Brif C, Long R, Wu RB, Tibbetts KM, Ho TS, et al. Searching for quantum optimal control fields in the presence of singular critical points. *Phys Rev A*. (2014) 90:013404. doi: 10.1103/PhysRevA.90.013404
31. Russell B, Rabitz H, Wu RB. Control landscapes are almost always trap free: a geometric assessment. *J Phys A Math Theoret*. (2017) 50:205302. doi: 10.1088/1751-8121/aa6b77
32. Altafini C. Controllability of quantum mechanical systems by root space decomposition of su(N). *J Math Phys*. (2002) 43:2051. doi: 10.1063/1.1467611
33. Wu RB, Hsieh MA, Rabitz H. Role of controllability in optimizing quantum dynamics. *Phys Rev A*. (2011) 83:062306. doi: 10.1103/PhysRevA.83.062306
34. Pechen A, Il'in N. Trap-free manipulation in the Landau-Zener system. *Phys Rev A*. (2012) 86:052117. doi: 10.1103/PhysRevA.86.052117
35. Pechen AN, Il'in NB. Coherent control of a qubit is trap-free. *Proc Steklov Instit Math*. (2014) 285:233–40. doi: 10.1134/S0081543814040166
36. Zhdanov DV. Comment on 'Control landscapes are almost always trap free: a geometric assessment'. *J Phys A Math Theoret*. (2018) 51:508001. doi: 10.1088/1751-8121/aaecf6
37. Russell B, Wu RB, Rabitz H. Reply to comment on 'control landscapes are almost always trap free: a geometric assessment'. *J Phys A Math Theoret*. (2018) 51:508002. doi: 10.1088/1751-8121/aaecf2
38. Jost J, Li-Jost X. *Calculus of Variations*. Cambridge, UK: Cambridge University Press (1998).
39. Sussmann HJ, editor. *Nonlinear Controllability and Optimal Control*. New York, NY: Chapman & Hall/CRC Pure and Applied Mathematics; Taylor & Francis; (1990).
40. Rowland B, Jones JA. Implementing quantum logic gates with gradient ascent pulse engineering: principles and practicalities. *Philos Trans R Soc A*. (2012). 370:4636–50. doi: 10.1098/rsta.2011.0361
41. Russell B, Vuglar S, Rabitz H. Control landscapes for a class of non-linear dynamical systems: sufficient conditions for the absence of traps. *J Phys A Math Theoret*. (2018) 51:335103. doi: 10.1088/1751-8121/aacc85

Conflict of Interest: The authors declare that the research was conducted in the absence of any commercial or financial relationships that could be construed as a potential conflict of interest.

frontiers in Physics

ORIGINAL RESEARCH
published: 20 May 2021
doi: 10.3389/fphy.2021.674573

Photo-Induced Coupled Nuclear and Electron Dynamics in the Nucleobase Uracil

Lena Bäuml[1†], *Thomas Schnappinger*[1†], *Matthias F. Kling*[2,3] *and Regina de Vivie-Riedle*[1*]

[1] *Department of Chemistry, Ludwig-Maximilians-University Munich, Munich, Germany,* [2] *Max Planck Institute of Quantum Optics, Garching, Germany,* [3] *Department of Physics, Ludwig-Maximilians-University Munich, Garching, Germany*

Photo-initiated processes in molecules often involve complex situations where the induced dynamics is characterized by the interplay of nuclear and electronic degrees of freedom. The interaction of the molecule with an ultrashort laser pulse or the coupling at a conical intersection (CoIn) induces coherent electron dynamics which is subsequently modified by the nuclear motion. The nuclear dynamics typically leads to a fast electronic decoherence but also, depending on the system, enables the reappearance of the coherent electron dynamics. We study this situation for the photo-induced nuclear and electron dynamics in the nucleobase uracil. The simulations are performed with our ansatz for the coupled description of the nuclear and electron dynamics in molecular systems (NEMol). After photo-excitation uracil exhibits an ultrafast relaxation mechanism mediated by CoIn's. Both processes, the excitation by a laser pulse and the non-adiabatic relaxation, are explicitly simulated and the coherent electron dynamics is monitored using our quantum mechanical NEMol approach. The electronic coherence induced by the CoIn is observable for a long time scale due to the delocalized nature of the nuclear wavepacket.

Keywords: quantum dynamics, coupled nuclear and electron dynamics, electronic coherence, conical intersection, photo-excitation, uracil

Edited by:
Tamar Seideman,
Northwestern University, United States

Reviewed by:
Burkhard Schmidt,
Freie Universität Berlin, Germany
Jiri Pittner,
J. Heyrovsky Institute of Physical Chemistry (ASCR), Czechia

Correspondence:
Regina de Vivie-Riedle
Regina.de_Vivie@cup.uni-muenchen.de

[†] *These authors have contributed equally to this work and share first authorship*

Specialty section:
This article was submitted to Physical Chemistry and Chemical Physics,
a section of the journal Frontiers in Physics

Received: *01 March 2021*
Accepted: *19 April 2021*
Published: *20 May 2021*

Citation:
Bäuml L, Schnappinger T, Kling MF and de Vivie-Riedle R (2021) Photo-Induced Coupled Nuclear and Electron Dynamics in the Nucleobase Uracil. Front. Phys. 9:674573. doi: 10.3389/fphy.2021.674573

1. INTRODUCTION

The interaction of molecular systems with light induces numerous chemical processes which can be natural, such as vision [1–3] and photosynthesis [4–7], or artificial like organic photovoltaics [8–12] and photocatalysis [13, 14]. In these processes a molecule often absorbs light with a wavelength in the visible or ultraviolet range where electrons are promoted from the molecular ground state to higher electronic states. The excited molecule can undergo radiative or non-radiative decay processes. Only the non-radiative processes can lead to photo-chemical reactions which are often mediated by non-adiabatic transitions [15]. The necessary non-adiabatic couplings (NACs) between the states involved are only present in the vicinity of a conical intersection (CoIn) [16–18] or an avoided crossing. Depending on the number of degrees of freedom these CoIn's are extraordinary points, seams or even higher dimensional crossing spaces. Besides the possibility of non-radiative relaxation they lead to the breakdown of the adiabatic separation between nuclear and electronic motion and equalize the time scales of their dynamics. Overall the excitation process and the non-adiabatic transitions are complex situation where both nuclear and electronic motion and their interaction play a key role. In order to simulate these situations a theoretical approach is needed that can describe the coupled nuclear and electron dynamics in a molecular system.

Most methods which can describe the electron dynamics are often modified versions of their well-known quantum-chemical counter parts and neglect the influence of the nuclear motion [19–23] or treat it classically [24–27]. One of the possibilities to treat both the nuclear and the electron dynamics in a molecular systems is the quantum-mechanical NEMol ansatz [28–32]. Within this ansatz the electronic wavefunctions are propagated in the eigenstate basis and coupled to the nuclear wavepacket propagated on coupled potential surfaces. Compared to similar but more expensive approaches based on the coupled propagation of the nuclear and electronic wavefunction on a single time-dependent potential energy surface [33–36], in NEMol the feedback of the electron motion to the nuclear dynamics is less directly included. In the beginning we give a brief introduction to the NEMol ansatz and how we determine the time-dependent electron density. This density is used to distinguish the Born-Oppenheimer part of the dynamics from the coherent electron dynamics. With the help of the NEMol ansatz the electron and nuclear dynamics along a photo-induced relaxation process in molecular systems can be simulated, including both interaction with a laser pulse and non-adiabatic events.

In the main part of this paper we apply NEMol to derive photo-induced dynamics in uracil which is one of the four nucleobases in RNA. Like all other nucleobases uracil absorbs mainly in the UV range due to an accessible $\pi \rightarrow \pi^*$ transition [37, 38]. After the excitation uracil can undergo harmful chemical modifications, such as methylation or base alteration [39–41]. The altered structures and the subsequent changed base pairings can lead to mutations, genomic instability and cancer [37, 40, 42]. To prevent potential mutations in advance, the inherent photostability of the nucleobases is a key factor, assuring that the vast majority of photoexcitations do not lead to harmful modifications [37]. The photostability of all nucleobases is due to the presence of fast relaxation mechanisms back to the ground state. Uracil exhibits an ultrafast relaxation mechanism with experimentally observed relaxation times between 50 fs and 2.4 ps [37, 43–46]. The relaxation is mediated via CoIn's between the first two excited states and has been well-studied using quantum-dynamics on two-dimensional surfaces [47, 48], as well as semi-classical approaches allowing for all degrees of freedom [38, 49–51]. As already demonstrated [52] the coherence induced by these CoIn's is long-lived since the non-adiabatic transition is rather a continuous process due to the delocalized nature of the nuclear wavepacket. We are following the photoinduced dynamics in uracil starting with the explicit simulation of the excitation processes via a laser pulse up to the relaxation via CoIn's. During the whole process NEMol is used to monitor the temporal evolution of the electron dynamics. The simulations demonstrate that the electron dynamics even in large molecular systems reflect coherence, decoherence, and reappearance due to nuclear motion. In previous work the effect of decoherence has been discussed from the nuclear dynamics side [53–55], and the reappearance has been reported for small molecular systems [56–58].

2. COUPLED NUCLEAR AND ELECTRON DYNAMICS IN MOLECULES (NEMol)

To describe the coupled nuclear and electron dynamics it is necessary to determine the temporal evolution of the total molecular wavefunction. This is realized with our NEMol ansatz [28–30]. In a system with multiple electronic states the total wavefunction $\Psi_{tot}(r, R, t)$ can be expressed as a sum over the products consisting of the electronic wavefunctions $\varphi(r, t; R)$ and the wavefunctions of the nuclei $\chi(R, t)$ (see Equation 1), with the nuclear and electronic coordinates R and r and the time t. In this ansatz both the electronic and the nuclear wavefunctions are explicitly time-dependent.

$$\Psi_{tot}(r, R, t) = \sum_i \chi_i(R, t) \cdot \varphi_i(r, t; R). \tag{1}$$

The electronic wavefunctions φ_i are parametrically depending on the nuclear coordinates R and define a multi-dimensional vector comprising the electronic states involved. Analogously, the total nuclear wavefunction χ_{tot} is given by a multi-dimensional vector composed of the nuclear wavefunctions χ_i residing in the i potential surfaces. Its temporal evolution is simulated on coupled potential energy surfaces (PES), for details see **Supplementary Section I**. Multiplying $\Psi_{tot}(r, R, t)$ from the left with χ_{tot} and the subsequent integration over the nuclear coordinates results in an expression of the coupled total electronic wavefunction [28–30].

$$\Phi_{tot}(r, t; \langle R\rangle(t)) = \int \chi^*_{tot}(R, t) \cdot \Psi_{tot}(r, R, t) dR \tag{2}$$

The individual components Φ_j of this vector are defined by the following equation:

$$\begin{aligned} \Phi_j(r, t; \langle R\rangle(t)) = {} & A_{jj}(t) \cdot \varphi_j(r, t; \langle R\rangle(t)) \\ & + \sum_{k \neq j} A_{jk}(t) \cdot \varphi_k(r, t; \langle R\rangle(t)), \end{aligned} \tag{3}$$

$$\text{with } A_{jk}(t) = \left\langle \chi_j(R, t) \middle| \chi_k(R, t) \right\rangle_R . \tag{4}$$

The time-dependent populations $A_{jj}(t)$ and the time-dependent nuclear overlap terms $A_{jk}(t)$ are determined by the nuclear quantum-dynamics simulation. The overlap terms specify the degree of coherence induced between two states j and k. If the coupling between the electronic states is weak, the nuclear wavefunctions propagate independently and the overlap term becomes zero. In this case, the coupled electronic wavefunctions Φ_j in Equation (3) become equivalent to the uncoupled electronic wavefunction φ_j. All electronic wavefunctions coupled and uncoupled are parametrically depending on the time-dependent expected value of the position $\langle R\rangle(t)$. This means that the coupled electronic wavefunctions are evaluated at one single nuclear geometry which changes with time. The time evolution of the $\varphi_j(r, t; \langle R\rangle(t))$ is determined by the deformation of the electronic structure induced by the nuclear motion and the propagation in the electronic phase space [28–30].

$$\varphi_j(r, t; \langle R\rangle(t)) = \varphi_j(r; \langle R\rangle(t)) \cdot e^{-i\xi_j(t)} \tag{5}$$

Here the $\varphi_j(r; \langle R\rangle(t))$ are the real-valued electronic wavefunctions of the relevant electronic states and $\xi_j(t)$ is the electronic phase factor computed by numerical integration of the electronic eigenenergies $E_j(\langle R\rangle(t))$ over time.

$$\xi_j(t) = \int_0^t E_j(\langle R\rangle(t))dt. \tag{6}$$

In practice the calculation of $\xi_j(t)$ has to be done recursively to retain the memory of the progressing electronic phase since $E_j(\langle R\rangle(t))$ changes with propagation time

$$\xi_j(t) = E_j(\langle R\rangle(t))\Delta t + \xi_j(t - \Delta t). \tag{7}$$

Thereby the propagation velocity of the phase in the complex plane changes smoothly in time while the nuclear wavepacket propagates. Within the original NEMol a much smaller time step must be used for the calculation of the phase term $\xi_j(t)$. The coupled total electronic wavefunction is used to determine the coupled one-electron density $\rho(r, t; \langle R\rangle(t))$ [28–30].

$$\begin{aligned}\rho(r, t; \langle R\rangle(t)) = &\sum_j A_{jj}(t)\rho_{jj}(r; \langle R\rangle(t)) \\ &+ \sum_{k>j} 2Re\{A_{jk}(t)\rho_{jk}(r; \langle R\rangle(t))e^{-i\xi_{jk}(t)}\},\end{aligned} \tag{8}$$

$$\text{with } \xi_{jk}(t) = \Delta E_{jk}(\langle R\rangle(t))\Delta t + \xi_{jk}(t - \Delta t). \tag{9}$$

The first summation consists of the state specific electronic density $\rho_{jj}(r; \langle R\rangle(t))$ weighted with the corresponding time-dependent population $A_{jj}(t)$. The second summation defines the coherent contribution to the coupled electron density and consists of the time-dependent overlap $A_{jk}(t)$, the one-electron transition density $\rho_{jk}(r; \langle R\rangle(t))$ and its pure electronic phase $\xi_{jk}(t)$ defined by the energy difference ΔE_{jk} between the electronic states involved. This coherent part of the density can be induced by an interaction with a laser pulse or by non-adiabatic coupling events. For non-dissociative molecular dynamics like in uracil the time-dependent overlap determines the disappearance and especially the potential reappearance of the coherent electron dynamics.

To go beyond this single geometry approximation we introduced the NEMol-grid [32] where the full nuclear coordinate space is split up into segments for which partial densities are calculated. In the limit the NEMol-grid is equal to the grid for the nuclear wavepacket propagation, but in practice we choose a coarser one. The partial densities $\rho_{ml}(r, t; R_{ml})$ are defined by:

$$\begin{aligned}\rho_{ml}(r, t; R_{ml}) = &\sum_j \alpha_{jj}^{ml}(t)\rho_{jj}(r; R_{ml}) \\ &+ \sum_{k>j} 2Re\{\alpha_{jk}^{ml}(t)\rho_{jk}(r; R_{ml})e^{-i\xi_{jk}^{ml}(t)}\},\end{aligned} \tag{10}$$

$$\text{with } \xi_{jk}^{ml}(t) = \Delta E_{jk}(R_{ml})\Delta t + \xi_{jk}^{ml}(t - \Delta t). \tag{11}$$

The population terms $\alpha_{jj}^{ml}(t)$ and the overlap terms $\alpha_{jk}^{ml}(t)$ are calculated by integration over the wavepackets within the boundaries of the segments. At the center R_{ml} of each segment the state specific electronic densities $\rho_{jj}(r; R_{ml})$, the one-electron transition densities $\rho_{jk}(r; R_{ml})$, and the pure electronic phase $\xi_{jk}^{ml}(t)$ are determined. Since the positions R_{ml} do not vary with time the time step for the calculation of the phase term can be chosen larger than for the original NEMol. In this work a time step of 1 a.u. is used. To obtain the total coupled electron density the individual contributions for each segment are summed up.

$$\rho(r, t; R) = \sum_{m=1}^{M}\sum_{l=1}^{L} \rho_{ml}(r, t; R_{ml}). \tag{12}$$

This total coupled one-electron density $\rho(r, t; R)$ (also called full electron density in the following) contains the information of all partial densities determined at multiple grid points weighted with the corresponding population and overlap terms. This is a significant difference from the original NEMol where the electronic structure was only considered at one geometry. To visualize the coupled one-electron density the weighted average R of all R_{ml} is formed. The NEMol-grid extension is used to sample the nuclear wavefunction to improve the resolution of the spatial dependence of the electronic phase term. This is crucial for situations where the nuclear wavepacket is delocalized and only parts of the wavepacket induce coherence in the system. As this is increasingly the case for two and more dimensional systems, the expected value of the position $\langle R\rangle(t)$ is no longer appropriate to capture the electron the electron dynamics. Since uracil is such case we apply the NEMol-grid for all calculations in this work. To study the electron dynamics the induced dipole moment vector $\vec{\mu}$ is calculated using the coupled one-electron density:

$$\vec{\mu}(t) = \int d\vec{r}\rho(r, t; R) \cdot \vec{r}. \tag{13}$$

If the entire dynamics or at least parts of it can be described by two coupled states, it is possible to obtain a simplified description of the electron density in the one-electron-two-orbital (1e-2o)

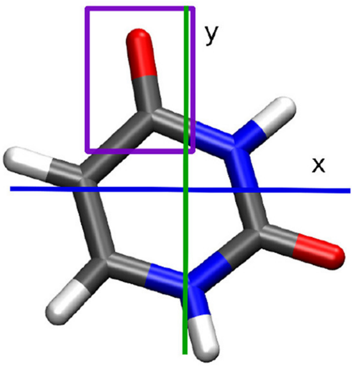

FIGURE 1 | Uracil molecule at the Franck-Condon point. The studied carbonyl group is indicated in purple. Carbon atoms are shown in gray, hydrogen in white, oxygen in red, and nitrogen in blue.

picture, which was derived and successfully applied in reference [32]. Based on the assumption that the two states are described by two Slater determinants, which only differ in the occupation of one spin orbital θ, it is possible to condense the coupled dynamics in a simple 1e-2o-density. The following Equation (14) is based on the original NEMol ansatz (see Equation 8), but the 1e-2o-density can also be determined in combination with the NEMol-grid.

$$\rho_{1e2o}(r,t;\langle R\rangle(t)) = A_{11}(t)|\theta_1(r;\langle R\rangle(t))|^2 + A_{22}(t)|\theta_2(r;\langle R\rangle(t))|^2 + 2Re\left\{A_{12}(t)\theta_1(r;\langle R\rangle(t))\theta_2(r;\langle R\rangle(t))e^{-i\xi_{12}(t)}\right\}. \tag{14}$$

Neglecting the contributions of the equally occupied orbitals, the first two terms represent the remaining two orbitals weighted with their respective population $A_{jj}(t)$. The third term denotes the coherence between the states characterized by the product of the two orbitals.

3. PHOTO-INDUCED DYNAMICS OF URACIL

In this work we investigate the photo-induced nuclear and electron dynamics of the nucleobase uracil with NEMol. The geometry of uracil at the Franck-Condon (FC) point is depicted in **Figure 1**. Uracil is characterized by an ultrafast photo-relaxation channel starting in the second excited state (S_2) which is mediated by CoIn's. As shown in previous studies [47, 48], the photo-excitation and the initial steps of the subsequent relaxation can be well-described on two-dimensional PES. We adopt these adiabatic PES, which were first reported by Keefer et al. [47] and later modified [52, 59]. The underlying two-dimensional coordinate space spanned by the vectors q_1 and q_2 includes all relevant structures, the FC point, the S_2 minimum, the optimized S_2/S_1 CoIn and also parts of the associated CoIn seam. Both vectors are depicted on the right side of **Figure 2**. The resulting PES for the bright S_2 state is shown on the left of **Figure 2**. The potential surface exhibits a double-well structure with a small barrier separating the S_2 minimum on the top left from the CoIn seam on the bottom right (black). Further information about the simulations can be found in the **Supplementary Section I**. The molecular orientation within the laboratory frame is chosen in such a way that the molecular plane is equal to the *xy*-plane at the FC point and the center of mass defines the origin of the laboratory frame (see **Figure 1**). To initiate the dynamics and promote the system from the electronic ground state to the S_2 state we use a Gaussian shaped pulse. Its parameters were adapted from a previous work [47]. The pulse has a central frequency ω_0 of 6.12 eV, a full width at half maximum (FWHM) of 30 fs and a maximum field strength of 0.036 GV cm^{-1}. This maximum is reached after 40 fs simulation time. The light-matter interaction is treated within the dipole approximation. We assume that the electric component of the pulse is optimally aligned with the transition dipole moment whose absolute value is used. The complete temporal evolution of the population of all three states is shown in **Figure 3**. The excitation pulse is active in the time period between 10 and 75 fs and leads to an S_2 population yield close to 90%. The motion of the wavepacket in the S_2 state is indicated in white in **Figure 2**. The wavepacket evolves from the FC point toward the S_2 minimum and oscillates back near the FC region. After this first oscillation period (about 80 fs) a part of the wavepacket splits and travels toward the CoIn seam. At around 100 fs the population of the S_2 state starts to decay. During the following oscillations this behavior continues leading to a rather continuous flow of population into the S_1 state.

The NEMol simulations are used to monitor the coupled nuclear and electron dynamics of uracil during the first 200 fs. We assume that the coherent part of the electron dynamics

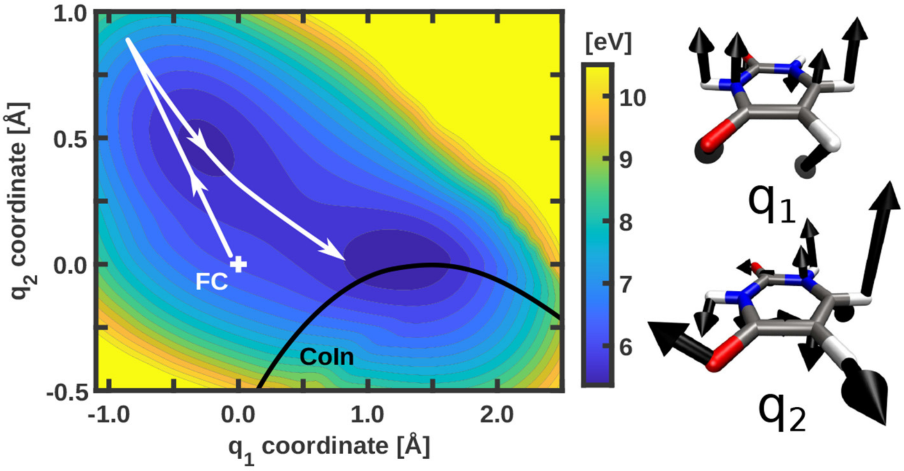

FIGURE 2 | Potential energy surface of the bright S_2 state of uracil with indicated CoIn seam (black) and a schematic representation of the path of the wavepacket (white). The energy scale is given with respect to the global minimum of the S_0 potential energy surface. The two coordinate vectors defining the two-dimensional coordinate space are shown on the right. Only contributions larger than 0.3 Å are depicted.

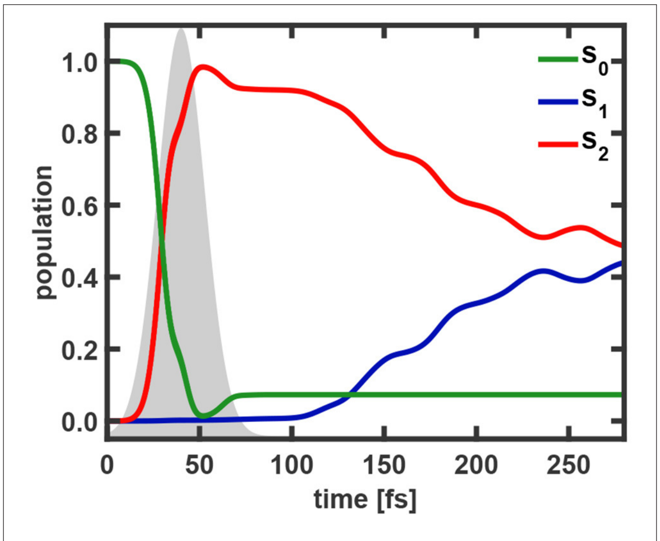

FIGURE 3 | Populations of the S_0, S_1, and S_2 state as a function of the simulation time. The envelope of the excitation pulse is indicated in gray.

is only active during the laser pulse excitation and when the wavepacket is interacting with the CoIn seam. Since these two events are spatially and temporally separated from each other we split our simulation into two parts. Within the interval of the excitation process (0–75 fs) we calculate the coupled electron density including only the properties (densities, population and overlap) of the S_0 and S_2 states. In the second part (75–200 fs), characterized by the relaxation via the CoIn seam, we include only the properties of the S_1 and S_2 states. For both cases we use a NEMol-grid of 14 × 10 segments equally distributed between −0.37 and 1.57 Å in the q_1 coordinate and from −0.57 to 0.86 Å in the q_2 coordinate, shown in **Supplementary Figure 1**. For each of these segments the population terms and the overlap terms of the involved states were determined. The population outside the NEMol-grid was added to the nearest segment on the edge of the grid. For the detailed analysis of the electron dynamics we focus on two quantities, the induced dipole moment and the temporal evolution of the local density at the upper carbonyl group (marked in purple in **Figure 1**). Both are observables, e.g., the fluctuations in the local density could be probed by transient X-ray absorption spectroscopy [60, 61]. Both observables show qualitatively very similar features. The results for the induced dipole moment are presented and discussed in the manuscript, while the ones for the local density are shown in the **Supplementary Material**. We should note that for the excitation dynamics it is important to ensure that the phase information of the laser pulse is solely imprinted on the electronic wavefunction and not also on the nuclear wavefunctions. In our previous work [62, 63], this was realized by calculating the dynamics in the rotating-wave-approximation to describe the laser-induced coupling between the molecular states. In this work we have chosen to remove the phase information of the laser pulse from the nuclear overlap terms.

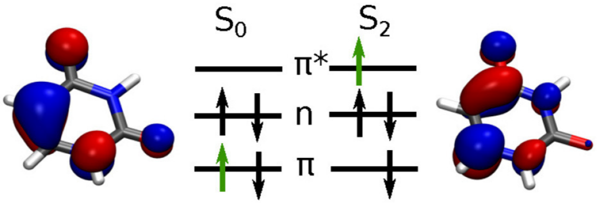

FIGURE 4 | Molecular orbital schemes for the $S_0 \rightarrow S_2$ excitation with the active electron indicated in green and corresponding orbitals at the Franck-Condon point. Orbitals are shown with an isovalue of 0.05.

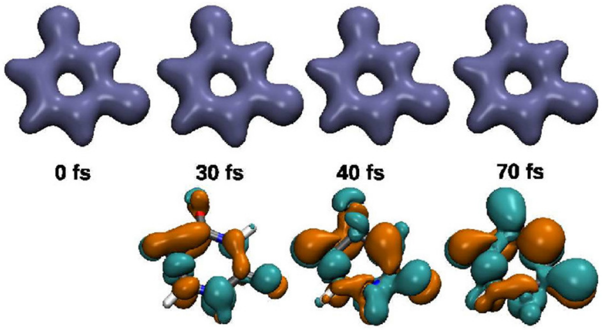

FIGURE 5 | Snapshots of the electron density and the difference in density relative to the density at $t = 0$ fs (green electron-loss, orange electron-gain) for the excitation-pulse induced dynamics between 0 and 75 fs. The isovalues used are 0.08, respectively ±0.003.

3.1. Excitation-Pulse Induced Dynamics

The dynamics induced by the laser pulse excitation is basically characterized by the excitation of one electron from a bonding π orbital into an anti-bonding π^* orbital. This process is illustrated in **Figure 4**. For the following analysis we calculate the full coupled electron density according to Equation (12).

Snapshots of the full coupled electron density are depicted in **Figure 5**. The excitation process follows with slight delay the profile of the resonant light pulse (**Figure 3**). Close to its maximum we observe a slight backtransfer from S_2 to S_0. Thereafter the S_2 population smoothly further increases up to nearly 100% reached at 52 fs. Toward the end of the pulse (at 60–70 fs) about 5% of the population is transferred back to the ground state. In total, 92% of the population was promoted into the S_2 state. With the naked eye nearly no variation is visible in the temporal evolution of the full electron density (top row **Figure 5**). However, studying the difference in density (bottom row) recorded with respect to the one at $t = 0$ fs the change in the bonding/anti-bonding pattern of the π-system becomes observable. In addition the deplanarization of the molecule leads to changes in the σ-system. The corresponding snapshots of the 1e-2o-density can be found in **Supplementary Figure 4**.

The temporal evolution of the induced dipole moment (DM) is determined with and without the coherent part of the coupled electron density included. The difference ΔDM is used to monitor the part of the dipole moment which is induced by the

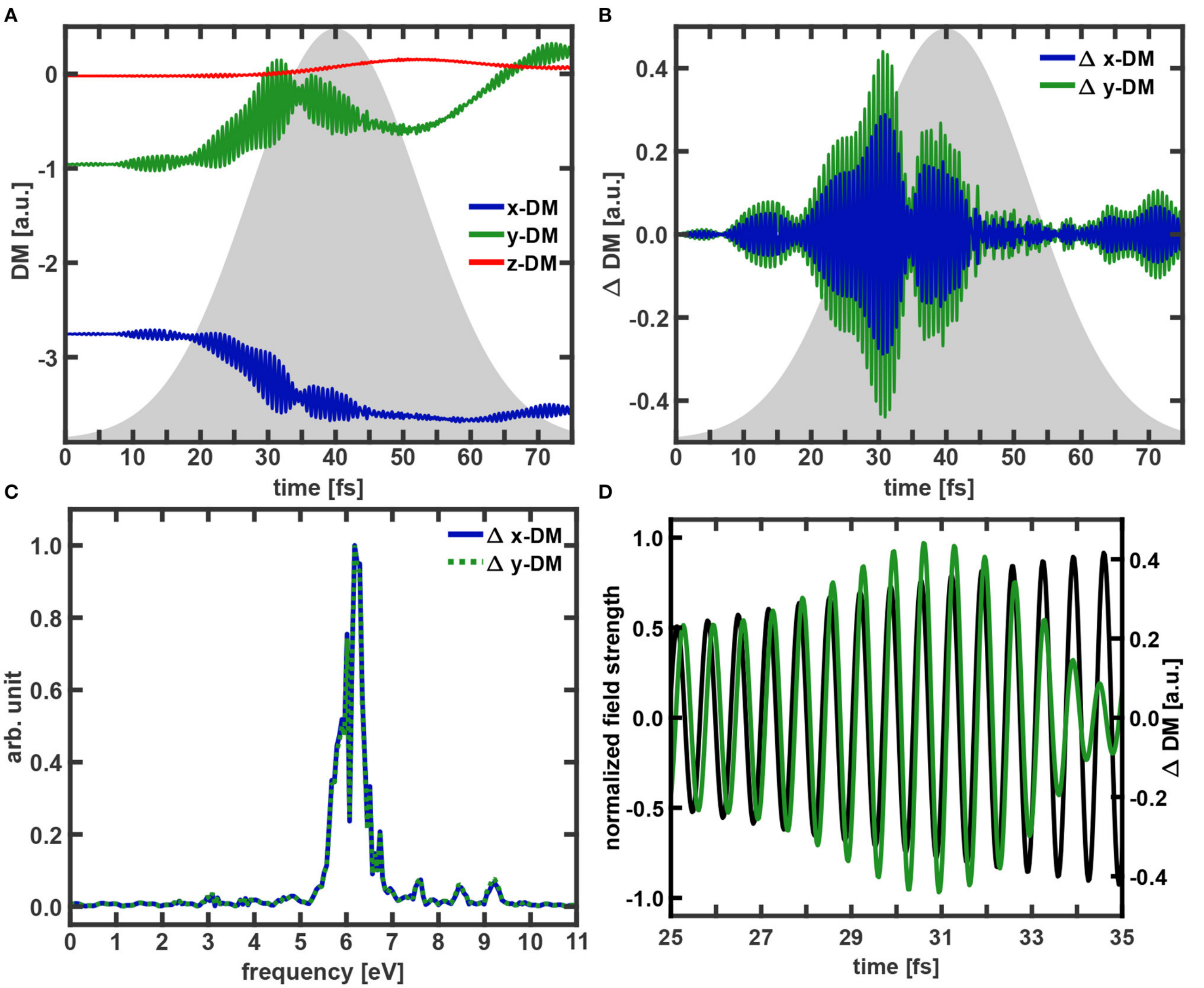

FIGURE 6 | Temporal evolution of the dipole moment components for **(A)** the calculation with the full density and **(B)** for the difference (Δ*DM*) between the dipole moment calculated with and without the coherence term included. The Δ*DM* are only shown for the for *x*- and *y*-components. The envelope of the excitation pulse is indicated in gray. **(C)** Fourier spectra of *x*-Δ*DM* and *y*–Δ*DM*. All spectra are normalized to one. **(D)** Comparison of *y*–Δ*DM* (green) and the electric field of the excitation pulse (black).

coherent electron dynamics. The *DM* components, the Δ*DM* along the *x*- and *y*-coordinate and their Fourier transforms are shown in **Figure 6**. In addition also the comparison of the *y*–Δ*DM* signal and the laser field is depicted. In the beginning of the excitation process the wavepacket mostly remains near the FC point and the molecular geometry stays planar in the *xy*-plane. Therefore, up to 30 fs the *z*-component of the induced dipole moment stays zero. After this period the wavepacket movement toward the S_2 minimum breaks up the planar structure and small modulations of the *z*-component are observed. Compared to the other two components it does not change significantly and is neglected for the further analysis. Regarding the *x*- and *y*-components of the *DM*, two main features are apparent. There is an overall increase (*y*-component), respectively decrease (*x*-component) in the *DM* which is modulated by a slow oscillation with a period of about 40 fs caused by the initial nuclear wavepacket motion around the S_2 minimum. The second feature is an extremely fast oscillation which is especially dominant in the range of 10–45 fs. With the help of the Δ*DM* components (**Figure 6B**) these fast oscillations can be attributed to the coherent electron dynamics. Close to the pulse maximum a pronounced destructive interference appears around 35 fs which coincides with the slight backtransfer of the population (**Figure 3**). The Fourier transforms (**Figure 6C**) of the two Δ*DM* signals clearly reveal that both components share the same main frequencies at 6.18 eV. These frequencies agree very well with the excitation frequency of 6.12 eV. A table of all observed frequencies with an intensity larger than 0.1 can be found in

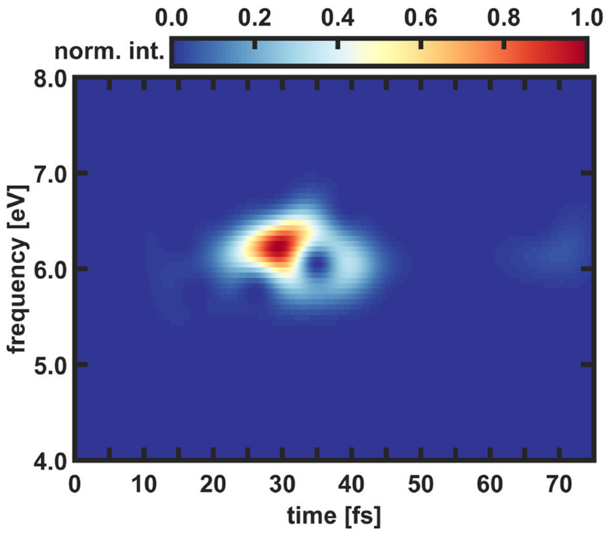

FIGURE 7 | Time-windowed Fourier transform of the y-component of ΔDM. The Fourier spectrogram is normalized and a Gaussian window function with a width of 120 data points corresponding to a time of 2.9 fs is used.

Supplementary Table 1. If we now compare the time evolution of the electric field of the pulse with the evolution of y–ΔDM (**Figure 6D**) this good agreement is confirmed and furthermore a maximum phase shift of about 0.5π between the field and the coherent part of the induced dipole moment can be recognized as expected [62, 63]. That means there is a briefly delayed response of the electron dynamics to the laser pulse. Also the beginning of the destructive interference of the electron wavefunctions at 33 fs is visible. In a final step of the analysis we have used a time-windowed Fourier transform of the y–ΔDM signal to determine the time at which the observed frequencies occur. In **Figure 7** the result of the time-windowed Fourier transform is shown applying a Gaussian window function with a width of 120 data points corresponding to a time of 2.9 fs.

In the spectrogram only frequencies in an energy window between 5.5 and 7 eV are visible. During the simulation these frequencies are occurring twice, once between 10 and 45 fs with the maximum being located between 25 and 35 fs, and a second time much weaker from 60 fs onward. The first one is directly induced by the laser pulse and the starting point of this signal matches with the beginning of the population transfer into S_2 state. The second occurrence takes place at the end of the excitation pulse. Until then parts of the wavepacket traveled back to the FC area and are again resonant with the excitation pulse. This enables backtransfer from the S_2 state to the ground state creating again non-zero nuclear overlap terms in Equation (10) and thus coherent electron dynamics. As described in the theory section instead of using the total coupled electron density it is also possible to perform the calculations in the 1e-2o picture (see Equation 14). Besides small deviations, the results in the 1e-2o picture are quite similar and can be found in the **Supplementary Material**. A complete summary of all performed analyses of the coupled electron density can be found in **Supplementary Section IIIA**. In summary, the laser pulse builds up electronic coherence in the molecule. The subsequent nuclear movement leads to decoherence within 10 fs, but about 40 fs later a weak reappearance of the signal due to laser coupling is observed.

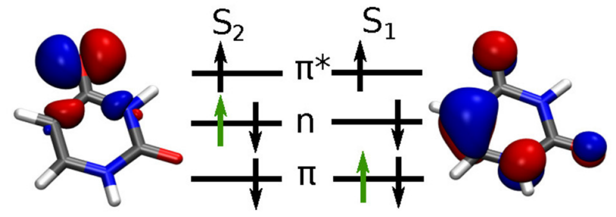

FIGURE 8 | Molecular orbital schemes for the $S_2 \rightarrow S_1$ relaxation with the active electron indicated in green and corresponding orbitals at the Franck-Condon point. Orbitals are shown with an isovalue of 0.05.

3.2. Conical Intersection Induced Dynamics

Since the coupled dynamics of the excitation process is well-described in the 1e-2o picture, we also performed the simulation for the conical intersection induced dynamics in this picture. The two active orbitals which are required to describe the NEMol-dynamics according to Equation (14) are shown in **Figure 8** at the FC point. In this simplified picture the CoIn dynamics is characterized by the transfer of one electron from a non-bonding orbital into a bonding π orbital.

The population dynamics in the time window from 75 to 200 fs and snapshots of the coupled electron density in the 1e-2o picture are depicted in **Figure 9**. The corresponding snapshots obtained with the full electron density are show in **Supplementary Figure 11**. A slow but steady decay of the S_2 population indicating two shallow steps (from 110 to 160 fs and from 170 to 200 fs) is visible. This rather continuous relaxation process is due to the delocalized nature of the nuclear wavepacket. In the 1e-2o picture the variation in the temporal evolution of the electron density is clearly visible (top row **Figure 9B**). For illustration also the difference in density with respect to the one at $t = 75$ fs is depicted. The snapshots reveal a transition from an exclusive non-bonding character at 75 fs to a mixed non-bonding and π character at 195 fs. Over the observed time the majority of the density is located at the upper oxygen atom, but the two left carbon atoms gain more and more density and a π-bond is formed.

For further analysis the temporal evolution of the induced dipole moment calculated with and without the coherent part of the electron density included was determined. The resulting DM components, the ΔDM of the x- and y-components and their Fourier transforms are shown in **Figure 10**. In addition the time-windowed Fourier transform of the y–ΔDM signal is depicted there, applying a Gaussian window function with a width of 2.9 fs. As for the excitation dynamics, the z-component of the induced dipole moment does not play a major role and is neglected also in the discussion of the CoIn induced dynamics.

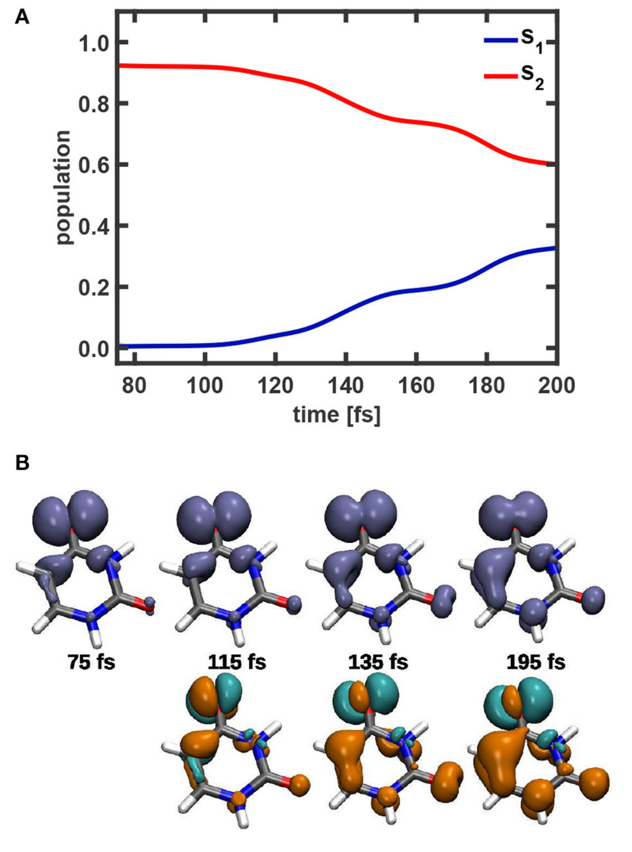

FIGURE 9 | (A) Temporal evolution of the population of the S_1 and S_2 state during the time period between 75 and 200 fs. **(B)** Snapshots of the 1e-2o electron density and the difference in density relative to the density at $t = 75$ fs (green electron-loss, orange electron-gain) in the 1e-2o picture.The isovalues used are 0.002, respectively ±0.0008.

In the overall picture the x-component exhibits a slow and rather small increase, only the y-component shows significant changes and decreases step-wise analogously to the population in S_2. Since the electron density moves mainly along the y-coordinate (see **Figure 9B**), it is logical that this component changes most. Superimposed weak and fast oscillations can be recognized for the y-DM signal and to some extent also for the x-DM signal. As in the previous analysis of the laser induced dynamics these oscillations can be assigned to the coherent electron dynamics. Using the ΔDM components (see **Figure 10B**), intervals with fast oscillations and with slow oscillations can be identified. For the y-component the fast ones appear in the range from 75 to 100 fs, around 120 and 180 fs while the slow ones have larger amplitudes and appear from 100 to 120 fs, 130 to 170 fs, and after 180 fs. Correspondingly two prominent frequency bands occur in the Fourier transforms (**Figure 10C**) of these two ΔDM signals. For the y-component, e.g., the stronger band is centered in a range from 0.25 to 0.75 eV and a weaker band is located between 0.9 and 1.25 eV. A table of all observed frequencies with an intensity larger than 0.1 can be found in **Supplementary Table 3**. Again, as final step of the analysis we performed a time-windowed Fourier transform of the y–ΔDM signal using a Gaussian window function with a width of 2.9 fs. Compared to the case of the laser induced ΔDM (see **Figure 7**) the spectrogram (**Figure 10D**) shows significantly more structured signals. We observe two main peaks in an energy range from 0 to 0.75 eV at 170 and 195 fs and additionally many weaker signals in the same energy region, as well as for higher frequencies (1.0–1.25 eV). The frequencies appearing at early times (75–100 fs) origin from the first parts of the nuclear wavepacket reaching the coupling region but not actually the CoIn seam. This explains the higher energy reflecting the actual energy gap ΔE. Later at 100 fs also lower frequencies appear as the wavepacket now hits the CoIn seam and the energy gap between the states closes. From now on parts of the moving nuclear wavepacket can be found close to the CoIn or in its environment. The intense signals at 170 and 195 fs correlate with the efficient transitions through the CoIn (see **Figure 9A**). The same simulations were also performed to obtain the total coupled electron density according to Equation (12). Comparing the results of the full and the 1e-2o density, the same frequencies and pattern are observed in the electron dynamics. However, the intensities for the higher frequencies are dominant for full density. The results for the full density can be found in the **Supplementary Material**. A complete summary of all performed analyses of the total coupled electron density can be found in **Supplementary Section IIIB**.

In summary, two observations can be made from our NEMol simulation of the conical intersection induced dynamics. The first one is, that the CoIn induces coherent electron dynamics which slows down the closer the system approaches the CoIn. This is expected since CoIn's equalize the time scales of the electron and nuclear dynamics [16, 17]. The second aspect is the longevity of the observed coherence. Due to the delocalized character of the nuclear wavepacket parts of it induce almost continuously coherence in the vicinity of the CoIn leading to a long lived observable signal. This is in good agreement with recently published simulations [52] of TRUECARS signals (transient redistribution of ultrafast electronic coherences in attosecond Raman signals) of the uracil S_2/S_1 CoIn. There, the long lived signal of coherence is also observed and the time-resolved vibronic frequency maps are in the same energy region.

4. CONCLUSION

In this paper, we applied our ansatz for the calculation of the coupled electron and nuclear dynamics in molecular systems (NEMol) [28–32] to the nucleobase uracil. We use the recently formulated extended version [32] operating on the NEMol-grid. As the interplay between nuclear and electron dynamics plays a crucial role in excitation processes as well as during non-adiabatic transitions both situations were studied. The NEMol ansatz treats the nuclear and the electron dynamics both quantum-mechanically. The electronic wavefunctions are propagated in the eigenstate bases and coupled to the nuclear dynamics simulated on coupled potential energy surfaces.

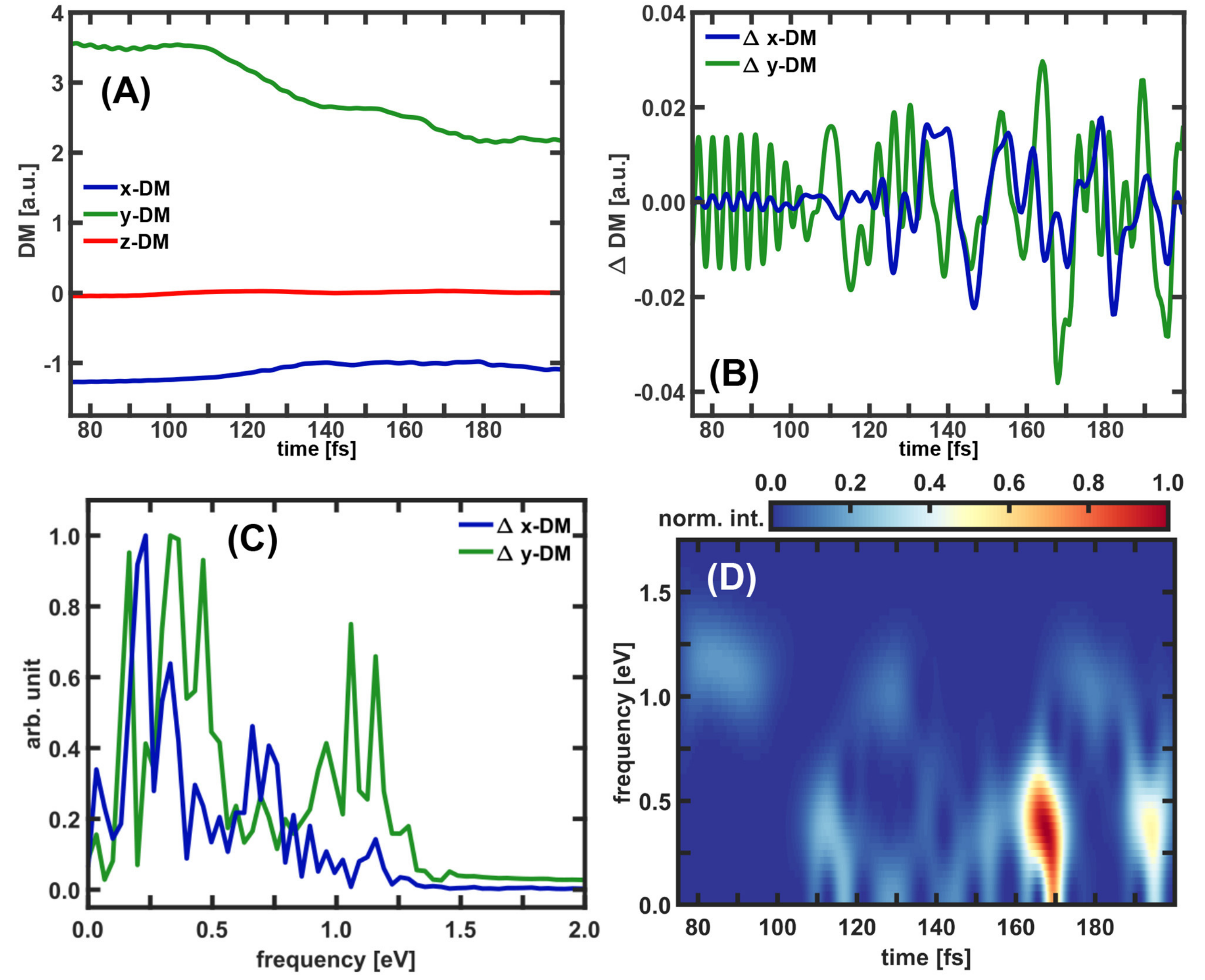

FIGURE 10 | Temporal evolution of the dipole moment for **(A)** the calculation with the 1e-2o picture density and **(B)** for the difference between the dipole moment calculated with and without the coherence term included. The ΔDM are only shown for the for x- and y-components. **(C)** Fourier spectra of x-ΔDM and y–ΔDM. All spectra are normalized to one. **(D)** Time-windowed Fourier transform of the y-component of ΔDM. The Fourier spectrogram is normalized and a Gaussian window function with a width of 120 data points corresponding to a time of 2.9 fs is used.

With a simple approximation it was possible to simplify the description of the excitation and relaxation processes by expressing the total electron density in the one-electron-two-orbital (1e-2o) picture [32]. In this work, both, the total coupled electron density and the simplified 1e-2o picture, were applied.

The NEMol simulations were used to study the photo-excitation and the CoIn mediated relaxation in uracil. By the choice of ultrashort light pulses these two processes are temporally and spatially separated and can be treated separately. During the excitation one electron is promoted from a bonding π orbital into an anti-bonding π^* orbital. This general change is clearly visible in the NEMol dynamics but it also enables us to analyze the excitation process in greater depth. As a possible observable in an experiment we choose to focus on the induced dipole moment. Studying its temporal evolution, fast oscillations are observed which could be directly attributed to the coherent electron dynamics. Their frequencies are close to the central frequency of the excitation pulse. The coherent dynamics is induced by the laser pulse and subsequent nuclear movement leads to decoherence. A partial reappearance is induced at the end of the laser pulse when the S_2 wavepacket has reentered the FC area. The good agreement between the results obtained with the total electron density and that of the 1e-2o picture supports that the simplified 1e-2o picture can be sufficient to describe the coupled electron dynamics. This 1e-2o picture was used to monitor the coupled electron dynamics induced by the S_2/S_1 conical intersection. The electronic coherence is induced by parts of the rather delocalized nuclear wavepacket and its recurrences at the CoIn and thus can be observed for long times. The frequencies in the induced dipole moment are now rather small, as expected since at the CoIn's the electron dynamics slows down [16–18]. A distinct modulation of these frequencies is observed in the time-windowed Fourier transform reflecting the movement of the nuclear wavepacket around the CoIn seam. Both the longevity and the modulation of the coherence by the nuclear motion is in good agreement with the recent simulation of the TRUECARS signal of the uracil S_2/S_1 CoIn [52]. Here, we demonstrated the capability of the NEMol ansatz to describe the coupled nuclear and electron dynamics in a complex molecular system like uracil. We were able to investigate the electronic coherence that is built up by the laser excitation and modulated by the subsequent nuclear motion. The following relaxation via a conical intersection induces again electronic coherence in the system, which is also treated within the NEMol approach. The verified 1e-2o picture will allow to simulate even larger system.

DATA AVAILABILITY STATEMENT

The raw data supporting the conclusions of this article are available from the corresponding author upon reasonable request.

AUTHOR CONTRIBUTIONS

TS, MK, and RV-R initiated the project. LB performed the calculations. LB, TS, and RV-R analyzed and interpreted the results. All authors contributed to the final version of the manuscript.

ACKNOWLEDGMENTS

The authors gratefully acknowledge the support by the German Research Foundation via VI 144/9-1 and KL-1439/11-1 and the center of excellence Munich Centre of Advanced Photonics (MAP).

SUPPLEMENTARY MATERIAL

The Supplementary Material for this article can be found online at: https://www.frontiersin.org/articles/10.3389/fphy.2021.674573/full#supplementary-material
See the **Supplementary Material** for the details of the wavepacket simulation setup and additional figures and tables for the analyses of the NEMol-dynamics. Animations of the coupled electron density in the 1e-2o picture and the ones using the full density for dynamics induced by the excitation pulse and the CoIn are also shown in the **Supplementary Material**.

Supplementary Data Sheet 1 | Movie_electron dynamics at CoIn.

Supplementary Data Sheet 2 | Movie of electron dynamics during excitation.

REFERENCES

1. Khorana HG. Rhodopsin, photoreceptor of the rod cell–an emerging pattern for structure and function. *J Biol Chem*. (1992) 267:1–4. doi: 10.1016/S0021-9258(18)48444-X
2. Send R, Sundholm D. Stairway to the conical intersection: a computational study of the retinal isomerization. *J Phys Chem A*. (2007) 111:8766–73. doi: 10.1021/jp073908l
3. Polli D, Altoè P, Weingart O, Spillane KM, Manzoni C, Brida D, et al. Conical intersection dynamics of the primary photoisomerization event in vision. *Nature*. (2010) 467:440–3. doi: 10.1038/nature09346
4. Webber AN, Lubitz W. P700: the primary electron donor of photosystem I. *Biochim Biophys Acta*. (2001) 1507:61–79. doi: 10.1016/S0005-2728(01)00198-0
5. Mirkovic T, Ostroumov EE, Anna JM, van Grondelle R, Govindjee, Scholes GD. Light absorption and energy transfer in the antenna complexes of photosynthetic organisms. *Chem Rev*. (2017) 117:249–93. doi: 10.1021/acs.chemrev.6b00002
6. Loll B, Kern J, Saenger W, Zouni A, Biesiadka J. Towards complete cofactor arrangement in the 3.0 angstrom resolution structure of photosystem II. *Nature*. (2005) 438:1040–4. doi: 10.1038/nature04224
7. Scholes GD, Fleming GR, Olaya-Castro A, van Grondelle R. Lessons from nature about solar light harvesting. *Nat Chem*. (2011) 3:763–74. doi: 10.1038/nchem.1145
8. Collings AF, Critchley C. *Artificial Photosynthesis: From Basic Biology to Industrial Application*. London: Wiley (2005). doi: 10.1002/3527606742
9. Andrea Rozzi C, Maria Falke S, Spallanzani N, Rubio A, Molinari E, Brida D, et al. Quantum coherence controls the charge separation in a prototypical artificial light-harvesting system. *Nat Commun*. (2013) 4:1602. doi: 10.1038/ncomms2603
10. Roncali J, Leriche P, Blanchard P. Molecular materials for organic photovoltaics: small is beautiful. *Adv Mater*. (2014) 26:3821–38. doi: 10.1002/adma.201305999
11. Mazzio KA, Luscombe CK. The future of organic photovoltaics. *Chem Soc Rev*. (2015) 44:78–90. doi: 10.1039/C4CS00227J
12. Pelzer KM, Darling SB. Charge generation in organic photovoltaics: a review of theory and computation. *Mol Syst Des Eng*. (2016) 1:10–24. doi: 10.1039/C6ME00005C
13. Ismail AA, Bahnemann DW. Photochemical splitting of water for hydrogen production by photocatalysis: a review. *Solar Energy Mater Solar Cells*. (2014) 128:85–101. doi: 10.1016/j.solmat.2014.04.037
14. Wenderich K, Mul G. Methods, mechanism, and applications of photodeposition in photocatalysis: a review. *Chem Rev*. (2016) 116:14587–619. doi: 10.1021/acs.chemrev.6b00327
15. Nelson TR, White AJ, Bjorgaard JA, Sifain AE, Zhang Y, Nebgen B, et al. Non-adiabatic excited-state molecular dynamics: theory and applications for modeling photophysics in extended molecular materials. *Chem Rev*. (2020) 120:2215–87. doi: 10.1021/acs.chemrev.9b00447
16. Yarkony DR. Diabolical conical intersections. *Rev Mod Phys*. (1996) 68:985–1013. doi: 10.1103/RevModPhys.68.985
17. Baer M. Introduction to the theory of electronic non-adiabatic coupling terms in molecular systems. *Phys Rep*. (2002) 358:75–142. doi: 10.1016/S0370-1573(01)00052-7
18. Domcke W, Yarkony D, Köppel H. *Conical Intersections: Electronic Structure, Dynamics and Spectroscopy*. Vol. 15. Singapore: World Scientific (2004). doi: 10.1142/5406
19. Runge E, Gross EKU. Density-functional theory for time-dependent systems. *Phys Rev Lett*. (1984) 52:997–1000. doi: 10.1103/PhysRevLett.52.997
20. Klamroth T. Laser-driven electron transfer through metal-insulator-metal contacts: time-dependent configuration interaction singles calculations for a Jellium model. *Phys Rev B*. (2003) 68:245421. doi: 10.1103/PhysRevB.68.245421

21. Rohringer N, Gordon A, Santra R. Configuration-interaction-based time-dependent orbital approach for ab initio treatment of electronic dynamics in a strong optical laser field. *Phys Rev A*. (2006) 74:043420. doi: 10.1103/PhysRevA.74.043420
22. Skeidsvoll AS, Balbi A, Koch H. Time-dependent coupled-cluster theory for ultrafast transient-absorption spectroscopy. *Phys Rev A*. (2020) 102:023115. doi: 10.1103/PhysRevA.102.023115
23. Vila FD, Rehr JJ, Kas JJ, Kowalski K, Peng B. Real-time coupled-cluster approach for the cumulant Green's function. *J Chem Theory Comput*. (2020) 16:6983–92. doi: 10.1021/acs.jctc.0c00639
24. Ojanperä A, Havu V, Lehtovaara L, Puska M. Nonadiabatic Ehrenfest molecular dynamics within the projector augmented-wave method. *J Chem Phys*. (2012) 136:144103. doi: 10.1063/1.3700800
25. Alonso JL, Castro A, Echenique P, Rubio A. In: Marques MAL, Maitra NT, Nogueira FMS, Gross EKU, Rubio A, editors. On the combination of TDDFT with molecular dynamics: new developments. In: *Fundamentals of Time-Dependent Density Functional Theory*. Berlin; Heidelberg: Springer Berlin Heidelberg (2012). p. 301–15. doi: 10.1007/978-3-642-23518-4_15
26. Takatsuka K. Theory of molecular nonadiabatic electron dynamics in condensed phases. *J Chem Phys*. (2017) 147:174102. doi: 10.1063/1.4993240
27. Takatsuka K. Nuclear wavepackets along quantum paths in nonadiabatic electron wavepacket dynamics. *Chem Phys*. (2018) 515:52–9. doi: 10.1016/j.chemphys.2018.07.006
28. Geppert D, von den Hoff P, de Vivie-Riedle R. Electron dynamics in molecules: a new combination of nuclear quantum dynamics and electronic structure theory. *J Phys B Atomic Mol Opt Phys*. (2008) 41:074006. doi: 10.1088/0953-4075/41/7/074006
29. von den Hoff P, Znakovskaya I, Kling MF, de Vivie-Riedle R. Attosecond control of the dissociative ionization via electron localization: a comparison between D2 and CO. *Chem Phys*. (2009) 366:139–47. doi: 10.1016/j.chemphys.2009.09.021
30. Znakovskaya I, von den Hoff P, Zherebtsov S, Wirth A, Herrwerth O, Vrakking MJJ, et al. Attosecond control of electron dynamics in carbon monoxide. *Phys Rev Lett*. (2009) 103:103002. doi: 10.1103/PhysRevLett.103.103002
31. Kling MF, von den Hoff P, Znakovskaya I, de Vivie-Riedle R. (Sub-)femtosecond control of molecular reactions via tailoring the electric field of light. *Phys Chem Chem Phys*. (2013) 15:9448–67. doi: 10.1039/c3cp50591j
32. Schnappinger T, de Vivie-Riedle R. Coupled nuclear and electron dynamics in the vicinity of a conical intersection. *J Chem Phys*. (2021) 154:134306. doi: 10.1063/5.0041365
33. Cederbaum LS. Born–Oppenheimer approximation and beyond for time-dependent electronic processes. *J Chem Phys*. (2008) 128:124101. doi: 10.1063/1.2895043
34. Abedi A, Maitra NT, Gross EKU. Exact factorization of the time-dependent electron-nuclear wave function. *Phys Rev Lett*. (2010) 105:123002. doi: 10.1103/PhysRevLett.105.123002
35. Abedi A, Maitra NT, Gross EKU. Correlated electron-nuclear dynamics: exact factorization of the molecular wavefunction. *J Chem Phys*. (2012) 137:22A530. doi: 10.1063/1.4745836
36. Chiang YC, Klaiman S, Otto F, Cederbaum LS. The exact wavefunction factorization of a vibronic coupling system. *J Chem Phys*. (2014) 140:054104. doi: 10.1063/1.4863315
37. Middleton CT, de La Harpe K, Su C, Law YK, Crespo-Hernández CE, Kohler B. DNA excited-state dynamics: from single bases to the double helix. *Annu Rev Phys Chem*. (2009) 60:217–39. doi: 10.1146/annurev.physchem.59.032607.093719
38. Barbatti M, Aquino AJA, Lischka H. The UV absorption of nucleobases: semi-classical ab initio spectra simulations. *Phys Chem Chem Phys*. (2010) 12:4959–67. doi: 10.1039/b924956g
39. Esposito L, Banyasz A, Douki T, Perron M, Markovitsi D, Improta R. Effect of C5-methylation of cytosine on the photoreactivity of DNA: a joint experimental and computational study of TCG trinucleotides. *J Am Chem Soc*. (2014) 136:10838–41. doi: 10.1021/ja5040478
40. Tommasi S, Denissenko MF, Pfeifer GP. Sunlight induces pyrimidine dimers preferentially at 5-methylcytosine bases. *Cancer Res*. (1997) 57:4727–30.
41. Pfeifer GP, You YH, Besaratinia A. Mutations induced by ultraviolet light. *Mutat Res Fundam Mol Mech Mutagen*. (2005) 571:19–31. doi: 10.1016/j.mrfmmm.2004.06.057
42. de Gruijl FR. Skin cancer and solar UV radiation. *Eur J Cancer*. (1999) 35:2003–9. doi: 10.1016/S0959-8049(99)00283-X
43. He YG, Wu CY, Kong W. Decay pathways of thymine and methyl-substituted uracil and thymine in the gas phase. *J Phys Chem A*. (2003) 107:5145–8. doi: 10.1021/jp034733s
44. Kang H, Lee KT, Jung B, Ko YJ, Kim SK. Intrinsic lifetimes of the excited state of DNA and RNA bases. *J Am Chem Soc*. (2002) 124:12958–9. doi: 10.1021/ja027627x
45. Crespo-Hernandez CE, Cohen B, Hare PM, Kohler B. Ultrafast excited-state dynamics in nucleic acids. *Chem Rev*. (2004) 104:1977–2019. doi: 10.1021/cr0206770
46. Ullrich S, Schultz T, Zgierski MZ, Stolow A. Electronic relaxation dynamics in DNA and RNA bases studied by time-resolved photoelectron spectroscopy. *Phys Chem Chem Phys*. (2004) 6:2796–801. doi: 10.1039/b316324e
47. Keefer D, Thallmair S, Matsika S, de Vivie-Riedle R. Controlling photorelaxation in uracil with shaped laser pulses: a theoretical assessment. *J Am Chem Soc*. (2017) 139:5061–6. doi: 10.1021/jacs.6b12033
48. Reiter S, Keefer D, de Vivie-Riedle R. RNA environment is responsible for decreased photostability of uracil. *J Am Chem Soc*. (2018) 140:8714–20. doi: 10.1021/jacs.8b02962
49. Hudock HR, Levine BG, Thompson AL, Satzger H, Townsend D, Gador N, et al. Ab initio molecular dynamics and time-resolved photoelectron spectroscopy of electronically excited uracil and thymine. *J Phys Chem A*. (2007) 111:8500–8. doi: 10.1021/jp0723665
50. Richter M, Mai S, Marquetand P, Leticia Gonzalez L. Ultrafast intersystem crossing dynamics in uracil unravelled by *ab initio* molecular dynamics. *Phys Chem Chem Phys*. (2014) 16:24423–36. doi: 10.1039/C4CP04158E
51. Fingerhut BP, Dorfman KE, Mukamel SJ. Probing the conical intersection dynamics of the RNA base uracil by UV-pump stimulated-Raman-probe signals; *ab initio* simulations. *J Chem Theory Comput*. (2014) 10:1172–88. doi: 10.1021/ct401012u
52. Keefer D, Schnappinger T, de Vivie-Riedle R, Mukamel S. Visualizing conical intersection passages via vibronic coherence maps generated by stimulated ultrafast X-ray Raman signals. *Proc Natl Acad Sci USA*. (2020) 117:24069–75. doi: 10.1073/pnas.2015988117
53. Vacher M, Mendive-Tapia D, Bearpark MJ, Robb MA. Electron dynamics upon ionization: control of the timescale through chemical substitution and effect of nuclear motion. *J Chem Phys*. (2015) 142:094105. doi: 10.1063/1.4913515
54. Jenkins AJ, Vacher M, Twidale RM, Bearpark MJ, Robb MA. Charge migration in polycyclic norbornadiene cations: winning the race against decoherence. *J Chem Phys*. (2016) 145:164103. doi: 10.1063/1.4965436
55. Arnold C, Vendrell O, Santra R. Electronic decoherence following photoionization: full quantum-dynamical treatment of the influence of nuclear motion. *Phys Rev A*. (2017) 95:033425. doi: 10.1103/PhysRevA.95.033425
56. von den Hoff P, Siemering R, Kowalewski M, de Vivie-Riedle R. Electron dynamics and its control in molecules: from diatomics to larger molecular systems. *IEEE J Select Top Quantum Electron*. (2012) 18:119–29. doi: 10.1109/JSTQE.2011.2107893
57. Nikodem A, Levine RD, Remacle F. Quantum nuclear dynamics pumped and probed by ultrafast polarization controlled steering of a coherent electronic state in LiH. *J Phys Chem A*. (2016) 120:3343–52. doi: 10.1021/acs.jpca.6b00140
58. Jia D, Manz J, Yang Y. Timing the recoherences of attosecond electronic charge migration by quantum control of femtosecond nuclear dynamics: a case study for HCCI+. *J Chem Phys*. (2019) 151:244306. doi: 10.1063/1.5134665
59. Schüppel F, Schnappinger T, Bäuml L, de Vivie-Riedle R. Waveform control of molecular dynamics close to a conical intersection. *J Chem Phys*. (2020) 153:224307. doi: 10.1063/5.0031398
60. Bhattacherjee A, Leone SR. Ultrafast X-ray transient absorption spectroscopy of gas-phase photochemical reactions: a new universal probe of photoinduced molecular dynamics. *Acc Chem Res*. (2018) 51:3203–11. doi: 10.1021/acs.accounts.8b00462

61. Zinchenko KS, Ardana-Lamas F, Seidu I, Neville SP, van der Veen J, Lanfaloni VU, et al. Sub-7-femtosecond conical-intersection dynamics probed at the carbon K-edge. *Science*. (2021) 371:489–94. doi: 10.1126/science.abf1656
62. Bayer T, Braun H, Sarpe C, Siemering R, von den Hoff P, de Vivie-Riedle R, et al. Charge oscillation controlled molecular excitation. *Phys Rev Lett*. (2013) 110:123003. doi: 10.1103/PhysRevLett.110.123003
63. Braun H, Bayer T, Sarpe C, Siemering R, de Vivie-Riedle R, Baumert T, et al. Coupled electron-nuclear wavepacket dynamics in potassium dimers. *J Phys B Atomic Mol Opt Phys*. (2014) 47:124015. doi: 10.1088/0953-4075/47/12/124015

Conflict of Interest: The authors declare that the research was conducted in the absence of any commercial or financial relationships that could be construed as a potential conflict of interest.

ORIGINAL RESEARCH
published: 28 May 2021
doi: 10.3389/fphy.2021.671997

A Bi-Axial Quantum State That Controls Molecular Collisions Like a Double-Slit Interferometer

William E. Perreault, Haowen Zhou, Nandini Mukherjee and Richard N. Zare**

Department of Chemistry, Stanford University, Stanford, CA, United States

To control molecular scattering, we consider hydrogen molecules prepared in a coherent superposition of m states within a single rovibrational (v, j) energy eigenstate using Stark-induced adiabatic Raman passage (SARP). Specifically, SARP can prepare a bi-axial state of the HD molecule in which the HD bond axis exists simultaneously in two possible alignments at right angles to one another with a well-defined relative phase. We show that scattering from this biaxial state will interfere, resulting in a φ -dependent scattering intensity distribution, where φ is the azimuthal angle about the collision velocity direction. Using the scattering matrix extracted from our experiments on the rotationally inelastic collisions of quantum state prepared HD at low temperatures, we calculate the differential scattering cross-section $d\sigma/d\Omega$, which shows an interference pattern as function of θ and φ in the image plane perpendicular to the collision velocity. The calculated scattering image shows that scattering from the bi-axial state directs molecules along well-defined angles, corresponding to interference maxima. Thus, the bi-axial state behaves like a double slit for molecular scattering. Moreover, by rotating the polarizations of the SARP preparation lasers, we can control the interference thereby altering the scattering angular distribution. This molecular interferometer, which experimentally measures the relative phases of the scattering matrix elements, allows a direct test of theoretical calculations on important, fundamental collision processes.

Keywords: interference, biaxial spatial distribution, angular distribution, molecular scattering, coherence

Edited by:
Tamar Seideman,
Northwestern University, United States

Reviewed by:
David Parker,
Radboud University
Nijmegen, Netherlands
Vitaly V. Kresin,
University of Southern California,
Los Angeles, United States

****Correspondence:***
Nandini Mukherjee
nmukherj@stanford.edu
Richard N. Zare
zare@stanford.edu

Specialty section:
This article was submitted to
Physical Chemistry and Chemical
Physics,
a section of the journal
Frontiers in Physics

Received: *24 February 2021*
Accepted: *15 April 2021*
Published: *28 May 2021*

Citation:
Perreault WE, Zhou H, Mukherjee N and Zare RN (2021) A Bi-Axial Quantum State That Controls Molecular Collisions Like a Double-Slit Interferometer. Front. Phys. 9:671997. doi: 10.3389/fphy.2021.671997

INTRODUCTION

Interference is a fundamental characteristic of the physical world that results from the intrinsic uncertainty in which multiple definite pathways connect the initial and final states of a system [1]. This uncertainty arises because, at the most fundamental level, a physical system is described by a quantum mechanical wavefunction that defines the state variables probabilistically. While interference plays an important role in controlling dynamics at the atomic scale, its effects are generally impossible to discern at the macroscopic level because the presence of many quantum states with randomly fluctuating phases either removes the interference or obscures its effects. Control over the quantum state of the system is therefore a necessary prerequisite for the interrogation of any interference effects in collision processes [2].

The progenitor of the quantum mechanical interference experiment is Young's double-slit experiment, where interference was observed as light passed through two different optical pathways. A long series of more modern experiments has successfully demonstrated interference of this type using collimated monoenergetic beams of electrons, atoms, and molecules [3–5]. In these experiments, constructive, and destructive interference of two coupled pathways connecting the impinging beam and the detector created positional maxima and minima of particle detection probability in much the same way as bright and dark optical fringes appeared in Young's experiment. Interference is only observed whenever the two slits are separated by nearly the De Broglie wavelength of the particles, meaning that finer and finer control is required as the mass of the system is increased.

Quantum interference that arises from the wave nature of matter contributes to the dynamics of many collision systems. Using advanced techniques to prepare the quantum states of isolated atomic and molecular systems, recent experiments have illustrated the effects of these interferences on the integral or differential cross section of the scattering process. In each of these instances the interference effects resulted because of the possibility of two or more pathways connecting the initial and final states of the matter system. One dramatic example exists in the photoionization of a diatomic molecule [6, 7]. Because the electron is delocalized over two atomic centers, the nuclei function analogously to a double slit in creating two distinct pathways for the excited electron to leave the molecule, thus generating an interference effect that has been measured in the angle-resolved double photoionization of H_2 molecules. In addition to the photoionization half-reaction, signatures of interference are also present in two-body collision processes when the transformation involved is mediated by two separate pathways [8–10]. Interference effects of this type have been measured in the rotationally inelastic scattering of optically excited states of small molecular systems including Na_2 and CO, where the interference occurred between the singlet and triplet pathways [11]. Similarly, such interferences have been observed in the reactive scattering of systems ranging from $H + H_2$ to $Li + NaLi$ [12–16]. However, in most of the prior experimental interrogations of scattering interferences, the multiple pathways were determined entirely by the material properties of the system, and therefore the interferences could not be controlled experimentally.

With even more precise ability to define the molecular quantum state, interference resulting from multiple quantum mechanical pathways can be exploited to control the outcome of a molecular collision [8, 10, 17–20]. This is achieved by preparing the atom-molecule collision system in a phase coherent superposition of quantum states. Because each state in the superposition provides a distinct pathway to the scattering output, control can be achieved by varying the amplitudes and phases of the superposed states. An experimental example can be found in the work of Nichols et al. who prepared NO in a coherent mixture of even and odd Λ-doublet states by the application of a DC field, to study how an inelastic scattering process is influenced by quantum interference between the coherently coupled initial states [8]. In this paper, we will consider the rotationally inelastic collision between a state-prepared H_2 molecule and a ground state He atom. Prior to the collision event, the H_2 has been placed in a specific target state that consists of a coherent superposition of m states belonging to a rovibrational (v, j) energy eigenstate. Here, the m quantum number defines the projection of the rotational angular momentum j on a suitable symmetry axis of the collision system. Following preparation, collision with the He atom will induce the Δj transition $(v, j, m \rightarrow v, j_f, m_f)$. The target state can be expressed as follows:

$$\psi_T = \exp(-iE_{v,j}t/\hbar) \sum_m C_m \left|v, j, m\right\rangle, \tag{1}$$

where the coefficients C_m are the complex numbers representing the time-independent amplitudes to find the target state in a specific m sublevel. When calculating the probability density of this state, $|C_m|^2$ gives the population of the various m sublevels, while the terms $C_m^* C_{m\prime}$ $(m \neq m\prime)$ are the off-diagonal elements of the density matrix $\hat{\rho}$ describing the coherences between different m sublevels. As opposed to a rotational wavepacket [21–23], the superposition in Equation (1) evolves with a single frequency $E_{v,j}/\hbar$, and so the superposition is a temporally stationary state, which is most desirable in a collision experiment. Optical excitation can be used to prepare a degenerate superposition of m states, thereby injecting optical coherence into the molecular system. To prepare large atomic and molecular ensembles in a coherent superposition of the m sublevels, many coherent optical methods including stimulated Raman adiabatic passage (STIRAP) [24–27], and Stark-induced adiabatic Raman passage (SARP) [28–30] have been developed.

The inelastically scattered quantum state of the H_2 molecule can be expressed as:

$$\psi_P(v, j_f, \theta, \varphi) = \sum_{m_f} A_{m_f}(v, j_f, \theta, \varphi) \left|v, j_f, m_f\right\rangle, \tag{2}$$

where $A_{m_f}(v, j_f, \theta, \varphi)$ is the probability amplitude to find the scattered product (H_2) in a rovibrational m eigenstate $|v, j_f, m_f\rangle$ within a unit solid angle along the direction $|v, j_f, m_f\rangle$. The polar angle (θ, φ) is defined in the center of mass coordinate system with the Z axis oriented along the relative velocity of the colliding partners. Equation (2) is fully general in that it can describe a pure scattered state as well as one that is coherently generated as a superposition of degenerate m states. In this case, the collision process, be it reactive, inelastic, or elastic, has transferred coherence (information) from the target state defined by Equation (1) to the product state defined by Equation (2). The product state coherence is determined by the off-diagonal density matrix elements $\rho_{m_f m_f\prime}$ proportional to $A_{m_f}(v, j_f, \theta, \varphi)^* A_{m_f\prime}(v, j_f, \theta, \varphi)$.

In this paper, we consider theoretically a state-resolved scattering experiment where the unpolarized differential scattering cross section is measured as a sum over all sublevels m_f:

$$\left.\frac{d\sigma}{d\Omega}\right|_{j\rightarrow j_f} = \sum_{m_f} |A_{m_f}(v, j_f, \theta, \varphi)|^2. \tag{3}$$

The scattering amplitude $A_{m_f}(v, j_f, \theta, \varphi)$ may be expressed as:

$$A_{m_f}(v, j_f, \theta, \varphi) = \sum_m C_m \, q(v, j, m, E_c \rightarrow v, j_f, m_f), \tag{4}$$

where $q(v, j, m, E_c \rightarrow v, j_f, m_f)$ is the state-to-state reaction amplitude within a unit solid angle defined by $\hat{r}(\theta, \varphi)$ in the center-of-mass frame. For scattering with well-defined initial momentum, the incoming orbital state is a plane wave described by a superposition of many partial waves. Each of these incoming orbitals is then scattered by the interaction potential to produce multiple orbitals in the outgoing channel. A scattering process can thus be regarded as the diffraction of the incoming matter wave by the colliding partner, where the diffraction efficiency is determined by the strength of the interaction forces. The scattering amplitudes $q(v, j, m, E_c \rightarrow v, j_f, m_f)$ are determined by the coherent sum over the contribution of all these outgoing waves. These individual contributions are given by the scattering matrix, which asymptotically connects the incoming and outgoing orbital states and contains information about the dynamics of the molecular interaction.

The measured state-resolved differential scattering cross-section (unpolarized) is given by

$$\begin{aligned} \left.\frac{d\sigma(\theta,\varphi)}{d\Omega}\right|_{j\to j_f} &= \sum_{m_f}\left|A_{m_f}(v,j_f,\theta,\varphi)\right|^2 \\ &= \sum_{m_f}\left|\sum_{m} C_m\, q(v,j,m,E_c\to v,j_f,m_f)\right|^2 \\ &= \left.\frac{d\sigma(\theta,\varphi)}{d\Omega}\right|_{\text{Pop.}} + \sum_{m\neq m'} C_m{}^{*} C_{m'}\, Q_{mm'}. \end{aligned} \tag{5}$$

Here, $Q_{mm'}$ contains the phase information of the state-to-state scattering amplitude q as follows:

$$Q_{mm'} = \sum_{m_f} q^{*}(v,j,m \to v,j_f,m_f)\, q(v,j,m' \to v,j_f,m_f)\,. \tag{6}$$

The population-driven term in Equation (5) is defined as follows:

$$\left.\frac{d\sigma}{d\Omega}\right|_{\text{Pop.}} = \sum_{m} |C_m|^2 \sum_{m_f} |q(v,j,m \to v,j_f,m_f)|^2. \tag{7}$$

Equation (7) shows that without m state coherence, the collision cross-section measured in a scattering experiment is determined solely by the m state population of the target state. This is because without coherence each m state contributes independently to the differential cross-section. As a result, no information about the phase of the state-to-state scattering amplitude q can be determined.

The second term on the right-hand side of Equation (5) contains $C_m^{*} C_{m'}$ terms, and thus gives rise to the interference effects in the scattering angular distribution. Specifically, the terms $Q_{mm'}$ defined in Equation (6) give the products of the state-to-state reaction amplitudes for two different initial target states and $|v, j, m'\rangle$ that scatter into the same final product state$|v, j_f, m_f\rangle$, thus describing interference between two coherently tied input channels. The interference thus results from the fact that each m state in the superposition provides a possible quantum mechanical pathway connecting an incoming orbital to an outgoing or scattered orbital. The m state superposition thus behaves much like a multi-slit interferometer where the number of slits, or the number of m states, and their separations, or their relative phase, can be varied experimentally. The maxima and minima of the resulting interference are determined by the amplitudes as well as the relative phases of the complex amplitudes C_m. However, if the molecules are not prepared in a phase coherent superposition of m states, the effect of these cross terms vanish, $\langle C_m C_{m'}{}^{*}\rangle = \rho_{mm'} \approx 0$ for $m \neq m'$, where the angular bracket represents the ensemble average.

We show in this paper that the outcome of a collision experiment can be directly controlled using modulation of the superposition of the target state. Further, we demonstrate that the interference in the state-resolved differential scattering cross-section for molecular targets prepared in addressable quantum states is a useful probe for both the magnitude and the phase of the state-to-state reaction amplitudes $q(v, j, m, E_c \rightarrow v, j_f, m_f)$. To illustrate these points, we consider the molecular interferometer created by preparing specific superpositions of m states, including an entangled biaxial state, of the HD molecule and show the interference effects in the rotational relaxation of these state-prepared HD by collision with a ground-state He atom. Our work here parallels a recent theoretical study that investigated coherent control using m state superposition in the $F + H_2$ reaction [31].

A MOLECULAR INTERFEROMETER ILLUSTRATED BY PREPARING HD MOLECULES IN A SUPERPOSITION STATE

The molecular interferometer discussed in this work has been previously prepared using SARP [28, 32]. SARP accomplishes population transfer by manipulating the crossings of the optically dressed adiabatic states using a pair of partially overlapping nanosecond laser pulses of unequal intensities. The dynamic Stark shift from the intense laser pulse controls the crossing of resonance. A large population is adiabatically transferred to the target state in the presence of a strong two-photon Rabi frequency as the Stark-shifted detuning slowly passes through the Raman resonance. The molecular axis orientation is controlled by the polarization of the two laser pulses. A comprehensive description of SARP can be found elsewhere [29, 30, 33, 34]. **Figure 1** describes the geometry of SARP excitation where the lasers propagate along the Y axis, while their polarizations are confined to the XZ plane. By rotating the pump and Stokes laser polarizations, various molecular axis orientations can be realized as shown in **Figure 1B**. Throughout this paper, we will consider the Z axis as the angular momentum quantization axis.

We consider three specific axis alignments, shown in **Figure 1B** as well as the top panel of **Figure 2** below. The simplest, called HSARP, is prepared when $\alpha = 0$ and $\beta = 0$ and consists of only $|m = 0\rangle$. Because HSARP is a pure uniaxial state preferentially polarized along the collision velocity axis, the density matrix has only one element $\rho_{mm} = 1$. Choosing both polarizations perpendicular to the Z axis ($\alpha = 0, \beta = \pi/2$) creates the superposition state $(-1/2)\,|m = 0\rangle + \sqrt{3/8}\,|m = \pm 2\rangle$ with non-zero off diagonal density matrix

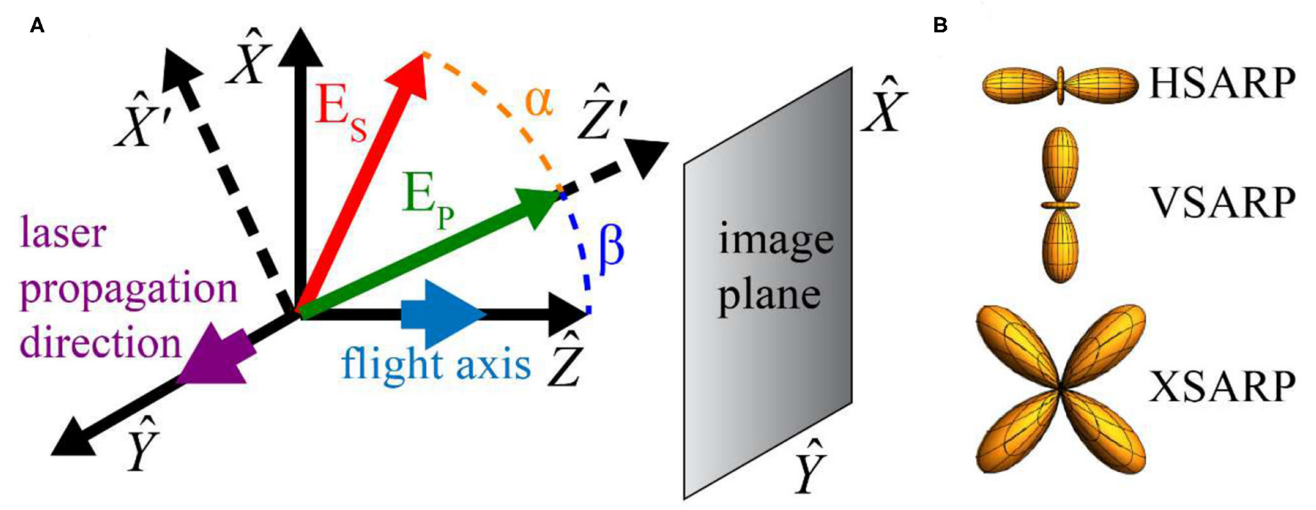

FIGURE 1 | (A) The coordinate system used in this paper. The Z axis is the direction of the molecular beam, which defines the collision velocity, while the laser propagates along the Y axis. The polarization of the pump and Stokes lasers are in the XZ plane, and their directions are given by the angles β and α. The scattered particles are imaged in the XY plane. **(B)** Axis distributions for the three specific alignment states discussed in the paper shown with the plane of the page as the XZ plane.

elements called VSARP. However, it is possible to diagonalize its density matrix by appropriate rotation of the coordinate system because VSARP is a uniaxial state preferentially polarized perpendicular to the collision velocity axis. Rotating only one polarization away from the Z axis ($\alpha = \pi/2, \beta = 0$) produces the state $|m = \pm 1\rangle / \sqrt{2}$ called XSARP. The off-diagonal elements are $\rho_{mm\prime} = -1/2$ for $m \neq m\prime, |m| = |m\prime| = 1$. The XSARP state is a biaxial, and so there is no coordinate rotation that transforms it to a pure state. The presence of two simultaneous axis alignments provides two possibilities for the rotationally inelastic scattering. The two distinct pathways connecting the initial and the final scattering states will interfere, making XSARP the molecular scattering analog of an optical double-slit experiment.

To show the interference effects in molecular collisions produced by a superposition of m quantum states, we consider the specific example of cold, rotationally inelastic hydrogen-helium scattering. We have previously studied cold HD ($v = 1, j = 2$) → ($v = 1, j_f = 0$) rotational relaxation via collision with a ground state He atom [35]. These collisions were confined within a single supersonic beam moving along the Z axis in **Figure 1**, thus precisely defining the collision geometry. **Figure 2** shows the calculated differential scattering cross-section $d\sigma(\theta, \varphi)/d\Omega$ given in Equation (5), which we also call the scattering image, in the X-Y plane. The scattering image is calculated using the experimentally determined scattering matrix from our earlier work. In this calculation, each of the scattering amplitudes $q(v, j, m, E_c \rightarrow v, j_f, m_f)$ is expanded in terms of the outgoing partial waves with complex amplitudes proportional to the scattering matrix element $S^J\left(j = 2, l; j_f l_f\right)$. Here, l and l_f give the orbital angular momentum of the incoming and outgoing orbitals, respectively, and J gives the total angular momentum, which is conserved in the collision process. A detailed description of the scattering calculation can be found in our publications [32, 35, 36] and is briefly reproduced in the **Supplementary Material**. Although we have considered here a specific example of $\Delta j = 2$ rotational relaxation with a single final state ($j_f = 0, m_f = 0$), our treatment will remain valid even if there are multiple final states. For example, in $\Delta j = 1$ transition with ($j_f = 1, m_f = 0, \pm 1$), the scattered intensity will be just the sum of the intensities for each individual m_f state shown in Equation (5).

The second panel in **Figure 2** shows the image of scattered HD ($v = 1, j_f = 0$) for the HSARP, XSARP, and VSARP axis orientations. The cylindrical symmetry of HSARP about the collision velocity is readily reflected in the scattering image shown in **Figure 2A**. The cylindrical symmetry about the Z-axis is broken for the VSARP orientation as seen in **Figure 2C**. The scattering image for the XSARP orientation in **Figure 2B** differs drastically from the HSARP and VSARP images. For the XSARP scattering not only is the azimuthal symmetry about the collision velocity broken, two bright interference fringes separated by a dark region in the center of the image are created. The dark center corresponds to a complete absence of the intense forward and backward scattering present for the HSARP and VSARP orientations. We note that the XSARP axis orientation scatters particles in well-defined directions in space much like a grating interferometer for optical waves. The third panel of **Figure 2** shows the φ dependence of the scattering images for the three axis distributions. The scattering intensity as a function of φ was calculated by integrating $d\sigma(\theta, \varphi)/d\Omega$ over all polar angles θ . The characteristic interference pattern for the XSARP makes it clear that the scattering of this state acts like a classic double-slit interferometer for molecular scattering. Because of the symmetry about the collision velocity, HASRP does not produce any φ dependency. The VSARP orientation breaks

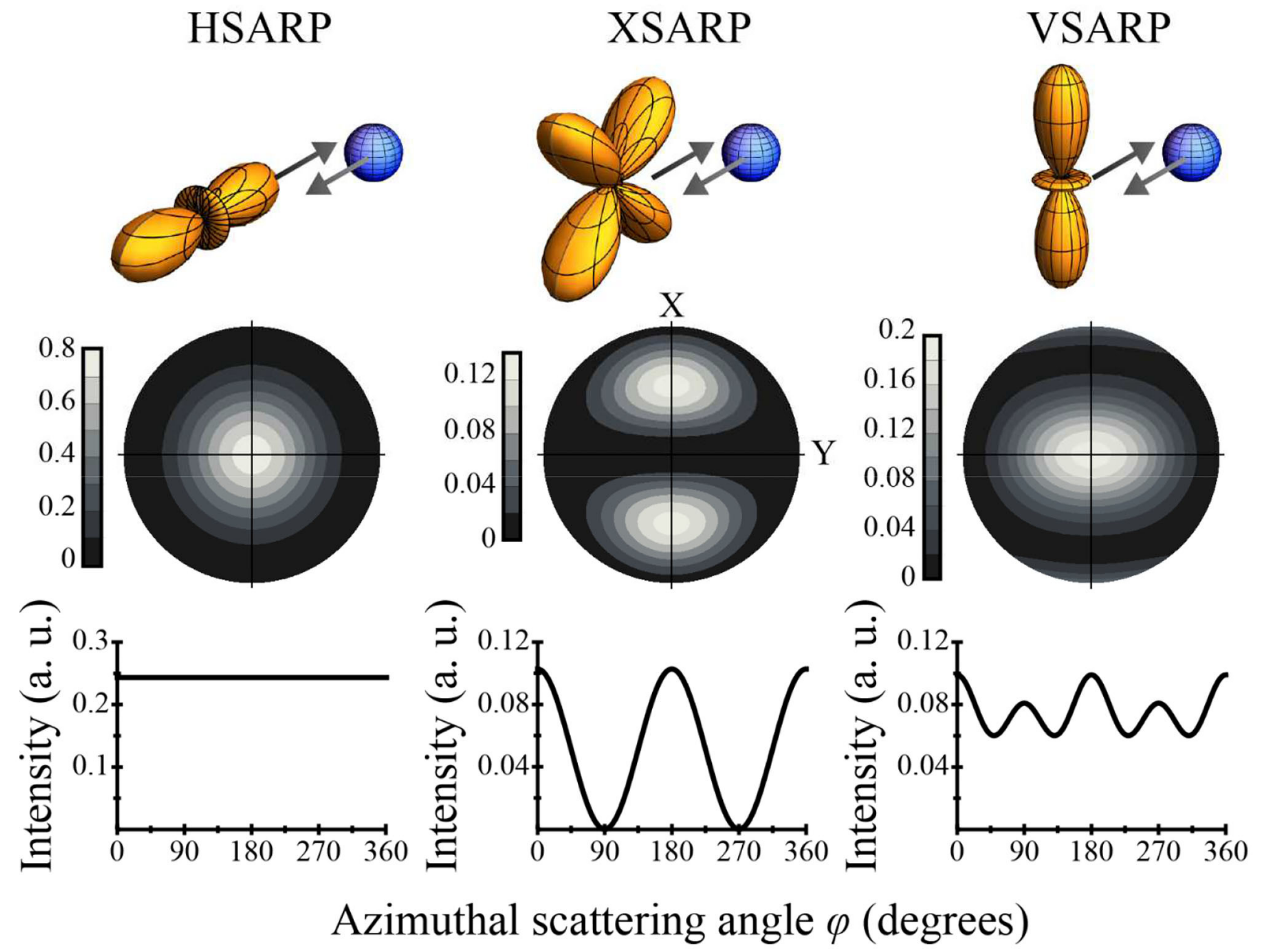

FIGURE 2 | Controlling molecular collision using m state superposition of three orientations: **(A)** HSARP $|m = 0\rangle$ obtained with pump and Stokes polarizations given by $\alpha = 0$, $\beta = 0$ in **Figure 1**. **(B)** XSARP: $|m = \pm 1\rangle / \sqrt{2}$ obtained with $\alpha = \pi/2$, $\beta = 0$. **(C)** VSARP: $(-1/2)\,|m = 0\rangle + \sqrt{3/8}\,|m = \pm 2\rangle$. Here the plane of the page is the XY image plane shown in **Figure 1A**, which is perpendicular to the collision velocity along Z. The top panel gives the axis distributions and the collision geometry. The second panel shows the scattered images of rotationally relaxed HD ($v = 1$, $j_f = 0$, $m_f = 0$). The third panel shows the φ dependence of the scattering images.

the cylindrical symmetry about the collision velocity axis and modulates the scattering intensity as a function of φ. However, compared to XSARP, the φ dependence is much weaker because VSARP is still a uniaxial state and therefore does not act as a double-slit interferometer.

Figure 3 compares the scattering images for the XSARP and VSARP orientations calculated with and without the coherence terms. For the right-hand images with coherence turned off, the calculation is performed by setting the off-diagonal density matrix elements $\rho_{mm'} = C_m C_{m'}$for $m \neq m'$ to zero. As described by Equation (7), in the absence of m state coherence the scattering angular distribution is determined by the m state populations. The cylindrically symmetric scattering angular distributions shown in **Figure 3** prove that the symmetry about the collision velocity can be broken only by introducing m sublevel or Zeeman coherence.

TESTING THE S-MATRIX USING THE MOLECULAR DOUBLE-SLIT INTERFEROMETER

An optical interferometer measures the phase shift between two optical waves. Given the direct parallel between the XSARP state and an optical double slit, this molecular interferometer ought to be able to measure phase shift of the scattered waves. The scattering image is generated as the coherent sum of the many partial waves, whose complex amplitudes are determined by the scattering matrix elements. To calculate the images shown in **Figure 4**, the phase of one of the scattering matrix elements was varied from 0 to π. As the phase of the chosen scattering matrix element is changed by relatively small increments from 0.6 to 0.8π, the calculated image changes dramatically, demonstrating the power of the molecular interferometer as an experimental

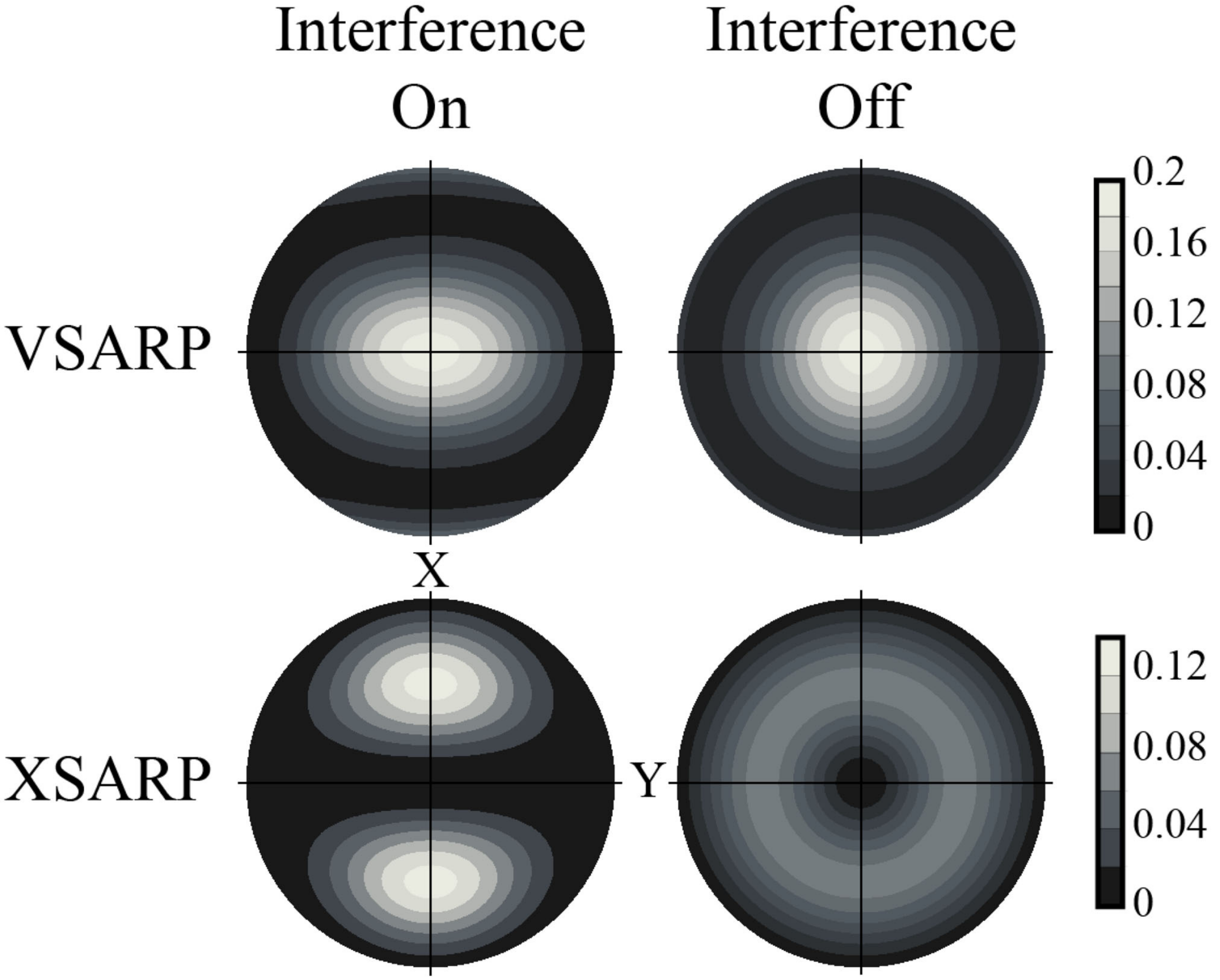

FIGURE 3 | The effect of the coherent interfering terms given in Equation (6) on the scattering images of rotationally relaxed HD ($v = 1, j_f = 0, m_f = 0$) for the VSARP and XSARP axis orientations. The scattering images including the coherence terms are given on the left side, while those without are given on the right side. Clearly, the m state superposition breaks the φ symmetry.

tool to interrogate the scattering matrix. This tool may be instrumental in resolving the many disagreements between experiment and theory that persist for even the simplest low temperature atom-diatom scattering. This is especially true for all-important scattering resonances, where the phase of the scattering matrix becomes more sensitive to the exact structure of the long-range potential.

CONTROL OF MOLECULAR DIFFRACTION BY ROTATING THE POLARIZATION OF THE PREPARATION LASER

Figure 5 shows how the diffraction by the molecular grating can be controlled simply by rotating the polarization of one of the preparation lasers. In these examples the different axis distributions are generated by rotating the Stokes laser polarization angle (α) in the XZ plane, while the pump laser polarization is kept fixed parallel to the X axis corresponding to $\beta = 90^\circ$ (see **Figure 1**). The oriented rovibrational ($v, j = 2$) state can be expressed as:

$$|\psi\rangle = \sum_{m'} \left[\cos\alpha \, d^{j=2}_{0m'}(\beta)|m=0\rangle + \frac{\sin\alpha}{\sqrt{2}} \left(d^{j=2}_{1m'}(\beta)|m=1\rangle \right.\right.$$
$$\left.\left. - d^{j=2}_{-1m'}(\beta)|m=-1\rangle \right) \right] \tag{8}$$

In Equation (8) $d^{j=2}_{mm'}(\beta)$ represents the Wigner rotation matrix for the $j = 2$ rotational state. **Figure 5** illustrates the control of scattering using four specific axis distributions obtained by varying the Stokes polarization according to (a) $\alpha = 0, \beta = 90^\circ$, (b) $\alpha = 30^\circ, \beta = 90^\circ$, (c) $\alpha = 60^\circ, \beta = 90^\circ$, (d) $\alpha = 90^\circ, \beta = 90^\circ$. **Figure 5** shows that the three-dimensional

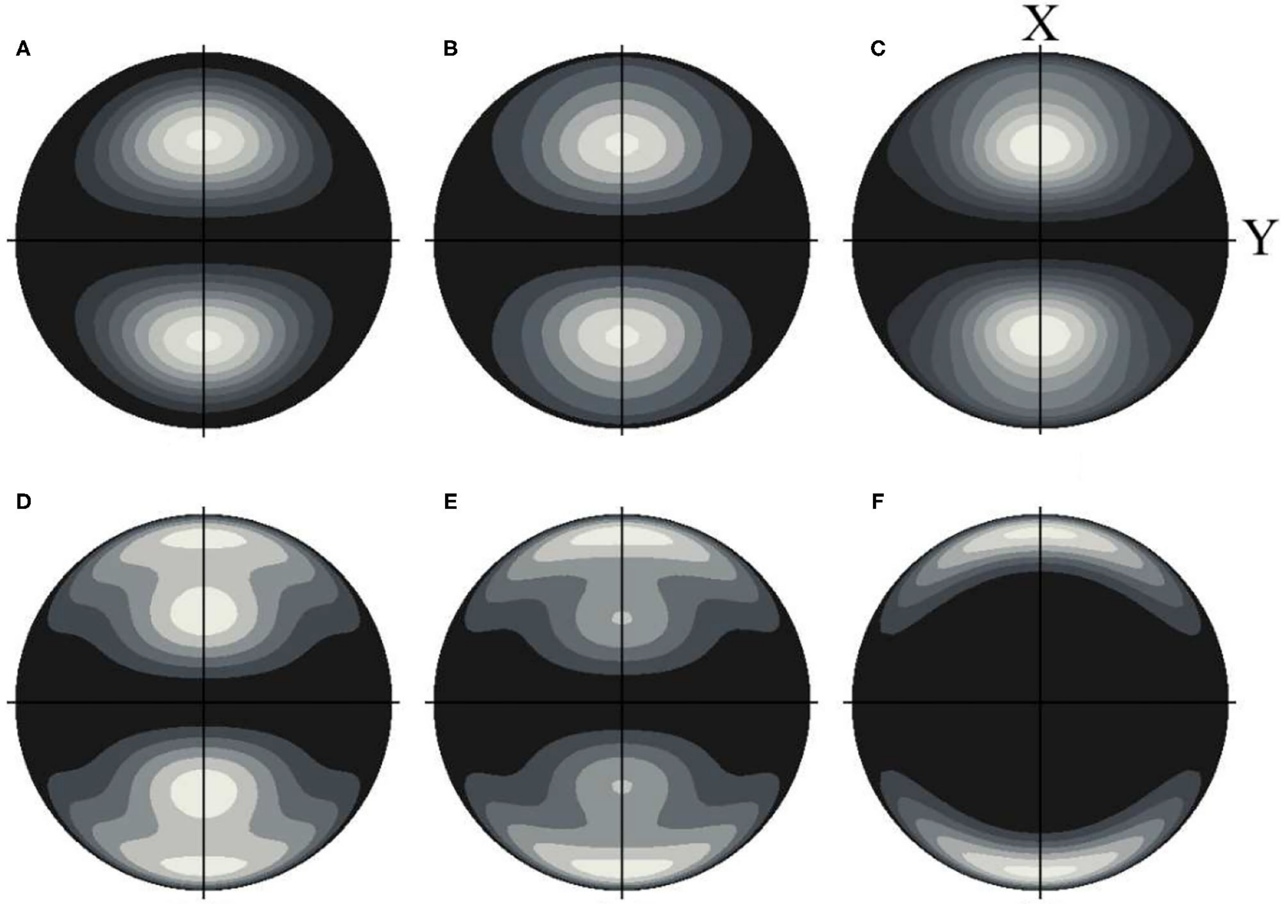

FIGURE 4 | Scattering images of rotationally relaxed HD ($v = 1, j_f = 0, m_f = 0$) calculated by varying the phase of one of the scattering matrix element $S^{J=2}$ ($j = 2, l = 2; j_f = 0, l_f = 2$) (see **Supplementary Material**). From **(A)–(F)**, the six images are calculated using phases of 0, 0.6π, 0.65π, 0.75π, 0.8π, and π.

scattering distribution changes in a spectacular way as the axis orientation changes from VSARP (a) to XSARP (d) with rotation of the angle α by90°.

CONCLUSION

We have shown that a coherent superposition of degenerate m states within a single rovibrational eigenstate behaves like a multi-slit interferometer for molecular scattering. To illustrate this idea, we considered the $\Delta j = 2$ rotationally inelastic scattering of HD prepared in coherent superpositions of m states within a single ($v = 1$, $j = 2$) eigenstate using SARP. The m sublevel coherence breaks the symmetry about the collision velocity direction. Each m state in the superposition provides a quantum mechanical pathway connecting the initial and final state in the collision process that gives rise to the interference pattern in the azimuthal angle φ, the coordinate canonically connected to the Z component of the angular momentum. In particular, we showed that the coherently mixed $m = \pm 1$ biaxial state of HD behaves like an optical interferometer producing interference fringes for the scattered intensity as a function of φ. The two phase-locked orientations of the molecular axis create two distinct quantum mechanical pathways, and so this molecular interferometer provides a proof of fundamental quantum mechanical principles. The biaxial state has already been prepared and used in scattering experiments in our laboratory, and so demonstration of these interference effects is highly experimentally feasible. We further showed that the phase of the scattering matrix can be measured using such a molecular interferometer. We also demonstrated that the coherent superposition can be used to control molecular scattering by spatially directing the scattered molecules in much the same way a multi-slit grating interferometer diffracts optical waves. Because the polarization directions of the pump and Stokes laser pulses determine the m state superposition, they can be used to control the interference effects in the scattering process. Such control is not limited to inelastic scattering, the m state superposition

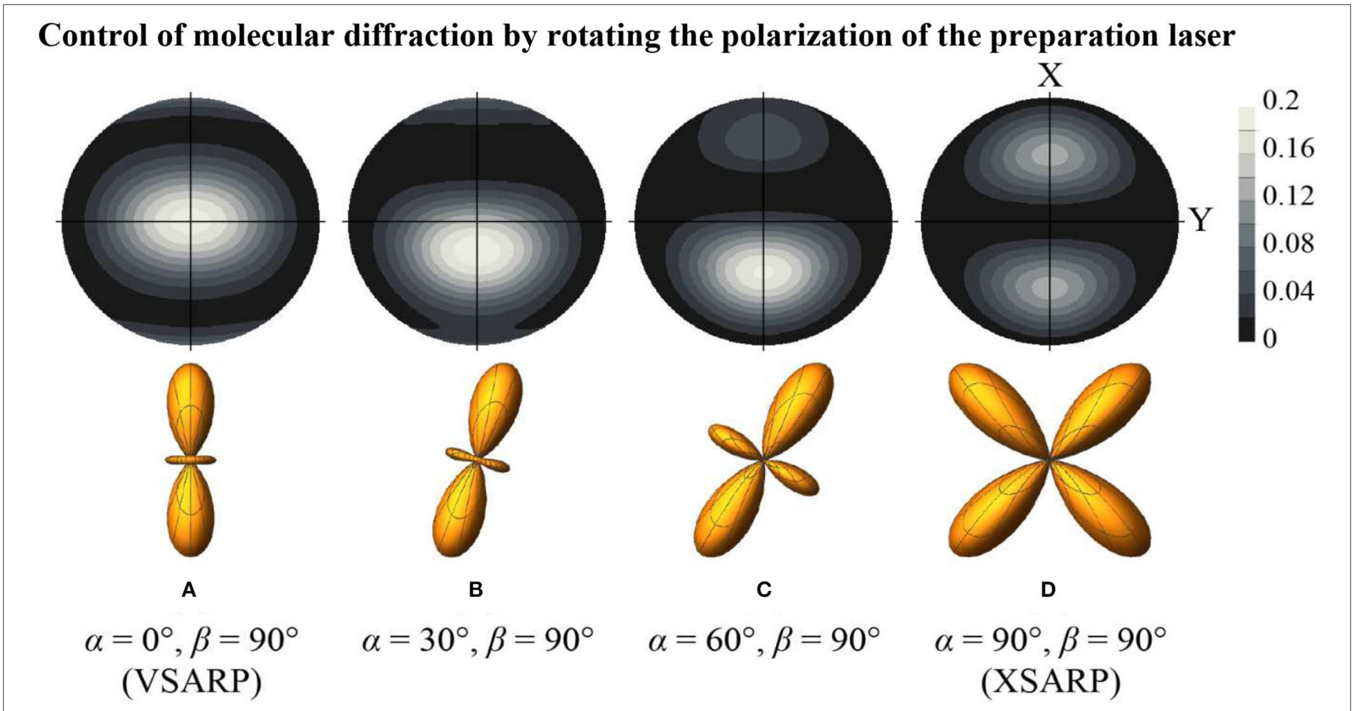

FIGURE 5 | Control of molecular scattering by laser polarizations. Here, the pump laser polarization is kept fixed parallel to the X axis, corresponding to $\beta = 90^\circ$, while the Stokes laser polarization is rotated from $\alpha = 0$ **(A)**, 30 **(B)**, 60 **(C)**, to 90° **(D)**. The axis distributions shown in the bottom panel are given with the plane of the page as the XZ plane. The top panel shows the calculated scattering images of rotationally relaxed HD ($v = 1$, $j_f = 0$, $m_f = 0$), demonstrating that the maxima of the scattering can be directed at different positions.

can control elastic and reactive scattering processes as well [9, 37, 38].

DATA AVAILABILITY STATEMENT

The original contributions presented in the study are included in the article/**Supplementary Material**, further inquiries can be directed to the corresponding author/s.

AUTHOR CONTRIBUTIONS

All authors discussed and wrote this manuscript.

FUNDING

This work has been supported by the U.S. Army Research Office under ARO Grant Nos. W911NF-19-1-0163 and W911NF-19-1-0283.

SUPPLEMENTARY MATERIAL

The Supplementary Material for this article can be found online at: https://www.frontiersin.org/articles/10.3389/fphy.2021.671997/full#supplementary-material

REFERENCES

1. Feynman RP, Leighton RB, Sands ML. *Feynman Lectures on Physics, Vol. 3*. Boston, MAL Addison Wesley Publishing Co (1963).
2. Gong J, Brumer P. Indistinguishability and interference in the coherent control of atomic and molecular processes. *J Chem Phys.* (2010) 132:054306. doi: 10.1063/1.3304921
3. Tavabi AH, Boothroyd CB, Yücelen E, Frabboni S, Gazzadi GC, Dunin-Borkowski RE, et al. The young-feynman controlled double-slit electron interference experiment. *Sci Rep.* (2019) 9:2–9. doi: 10.1038/s41598-019-43323-2
4. Frabboni S, Gazzadi GC, Pozzi G. Young's double-slit interference experiment with electrons. *Am J Phys.* (2007) 75:1053–5. doi: 10.1119/1.2757621
5. Arndt M, Nairz O, Vos-Andreae J, Keller C, Van der Zouw G, Zeilinger A. Wave-particle duality of C_{60}. *Nature.* (1999) 401:680–2. doi: 10.1038/44348
6. Canton SE, Plésiat E, Bozek JD, Rude BS, Decleva P, Martín F. Direct observation of young's double-slit interferences in vibrationally resolved photoionization of diatomic molecules. *Proc Natl Acad Sci USA.* (2011) 108:7302–6. doi: 10.1073/pnas.1018534108
7. Akoury D, Kreidi K, Jahnke T, Weber T, Staudte A, Schöffler M, et al. The simplest double slit : interference and entanglement in double photoionization of H_2. *Science.* (2007) 318:949–52. doi: 10.1126/science.1144959
8. Nichols B, Chadwick H, Gordon SD, Eyles CJ, Hornung B, Brouard M, et al. Steric effects and quantum interference in the inelastic scattering of NO(X) + Ar. *Chem Sci.* (2015) 6:2202–10. doi: 10.1039/C4SC03842H
9. Sha G, He J, Jiang B, Zhang C. Evidence for quantum interference in collision-induced intramolecular energy transfer within CO singlet-triplet mixed states. *J Chem Phys.* (1995) 102:2772–9. doi: 10.1063/1.468653
10. Onvlee J, Gordon SD, Vogels SN, Auth T, Karman T, Nichols B, et al. Imaging quantum stereodynamics through fraunhofer scattering of NO radicals with rare-gas atoms. *Nat Chem.* (2017) 9:226–33. doi: 10.1038/nchem.2640

11. Chen XL, Chen HM, Li J, Liu YM, Dai XC, Sha GH, et al. Quantum interference effect on collisional energy transfer within singlet ∼ triplet mixed states of Na_2. *Chem Phys Lett.* (2000) 318:107–12. doi: 10.1016/S0009-2614(99)01432-3
12. Jambrina PG, Herráez-Aguilar D, Aoiz FJ, Sneha M, Jankunas J, Zare RN. Quantum interference between H + D 2 quasiclassical reaction mechanisms. *Nat Chem.* (2015) 7:661–7. doi: 10.1038/nchem.2295
13. Jambrina PG, Aldegunde J, Aoiz FJ, Sneha M, Zare RN. Effects of reagent rotation on interferences in the product angular distributions of chemical reactions. *Chem Sci.* (2016) 7:642–9. doi: 10.1039/C5SC03373J
14. Sneha M, Gao H, Zare RN, Jambrina PG, Menéndez M, Aoiz FJ. Multiple scattering mechanisms causing interference effects in the differential cross sections of H + D2 → HD($v' = 4$, j') + D at 3.26 eV collision energy. *J Chem Phys.* (2016) 145:024308. doi: 10.1063/1.4955294
15. Xie Y, Zhao H, Wang Y, Huang Y, Wang T, Xu X, et al. Quantum interference in H + HD → H2 + D between direct abstraction and roaming insertion pathways. *Science.* (2020) 368:767–71. doi: 10.1126/science.abb1564
16. Kendrick BK, Li H, Li M, Kotochigova S, Croft JF, Balakrishnan N. Non-adiabatic quantum interference in the ultracold Li + LiNa → Li2 + Na reaction. *Phys Chem Chem Phys.* (2021) 23:5096–112. doi: 10.1088/1742-6596/1412/12/122016
17. Brumer P, Abrashkevich A, Shapiro M. Laboratory conditions in the coherent control of reactive scattering. *Faraday Discuss.* (1999) 113:291–302. doi: 10.1039/a902135c
18. Arango CA, Shapiro M, Brumer P. Coherent control of collision processes: penning versus associative ionization. *J Chem Phys.* (2006) 125:094315. doi: 10.1063/1.2336430
19. Král P, Thanopulos I, Shapiro M. Colloquium: coherently controlled adiabatic passage. *Rev Mod Phys.* (2007) 79:53–77. doi: 10.1103/RevModPhys.79.53
20. Krause JL, Shapiro M, Brumer P. Coherent control of bimolecular chemical reactions. *J Chem Phys.* (1990) 92:1126–31. doi: 10.1063/1.458174
21. Seideman T. Revival structure of aligned rotational wave packets. *Phys Rev Lett.* (1999) 83:4971–4. doi: 10.1103/PhysRevLett.83.4971
22. Dooley PW, Litvinyuk IV, Lee KF, Rayner DM, Spanner M, Villeneuve DM, et al. Direct imaging of rotational wave-packet dynamics of diatomic molecules. *Phys Rev A.* (2003) 68:023406. doi: 10.1103/PhysRevA.68.023406
23. Yang J, Guehr M, Vecchione T, Robinson MS, Li R, Hartmann N, et al. Diffractive imaging of a rotational wavepacket in nitrogen molecules with femtosecond megaelectronvolt electron pulses. *Nat Commun.* (2016) 7:11232. doi: 10.1038/ncomms11232
24. Bergmann K, Theuer H, Shore BW. Coherent population transfer among quantum states of atoms and molecules. *Rev Mod Phys.* (1998) 70:1003–25. doi: 10.1103/RevModPhys.70.1003
25. Vitanov NV, Rangelov AA, Shore BW, Bergmann K. Stimulated raman adiabatic passage in physics, chemistry, and beyond. *Rev Mod Phys.* (2017) 89:1–66. doi: 10.1103/RevModPhys.89.015006
26. Vitanov NV, Halfmann T, Shore BW, Bergmann K. Laser-Induced population transfer by adiabatic passage techniques. *Annu Rev Phys Chem.* (2001) 52:763–809. doi: 10.1146/annurev.physchem.52.1.763
27. Vewinger F, Heinz M, Garcia Fernandez R, Vitanov NV, Bergmann K. Creation and measurement of a coherent superposition of quantum states. *Phys Rev Lett.* (2003) 91:213001. doi: 10.1103/PhysRevLett.91.213001
28. Mukherjee N, Dong W, Zare RN. Coherent superposition of M-states in a single rovibrational level of H_2 by Stark-induced adiabatic raman passage. *J Chem Phys.* (2014) 140:074201. doi: 10.1063/1.4865131
29. Mukherjee N, Zare RN. Stark-induced adiabatic Raman passage for preparing polarized molecules. *J Chem Phys.* (2011) 135:024201 doi: 10.1063/1.3599711
30. Mukherjee N, Perreault WE, Zare RN. Stark-Induced adiabatic passage processes to selectively prepare vibrationally excited single and superposition of quantum states. In: Jaan L, editor. *Frontiers and Advances in Molecular Spectroscopy.* Amsterdam: Elsevier Inc (2018). p. 1–46. doi: 10.1016/B978-0-12-811220-5.00001-0
31. Devolder A, Tscherbul T, Brumer P. Coherent control of reactive scattering at low temperatures: signatures of quantum interference in the differential cross sections for F+ H2 and F+ HD coherent control of reactive scattering at devolder, tscherbul, and brumer. *Phys Rev A.* (2020) 102:31303. doi: 10.1103/PhysRevA.102.031303
32. Perreault WE, Mukherjee N, Zare RN. Quantum control of molecular collisions at 1 Kelvin. *Science.* (2017) 358:356–9. doi: 10.1126/science.aao3116
33. Perreault WE, Mukherjee N, Zare RN. Stark-induced adiabatic Raman passage examined through the preparation of D2 ($v = 2$, $j = 0$) and D2 ($v = 2$, $j = 2$, $m = 0$). *J Chem Phys.* (2019) 150:234201. doi: 10.1063/1.5109261
34. Perreault WE, Zhou H, Mukherjee N, Zare RN. Harnessing the power of adiabatic curve crossing to populate the highly vibrationally excited H_2 ($v = 7$, $j = 0$) level. *Phys Rev Lett.* (2020) 124:163202. doi: 10.1103/PhysRevLett.124.163202
35. Perreault WE, Mukherjee N, Zare RN. HD ($v = 1$, $j = 2$, m) orientation controls HD-He rotationally inelastic scattering near 1 K. *J Chem Phys.* (2019) 150:174301. doi: 10.1063/1.5096531
36. Perreault WE, Mukherjee N, Zare RN. Quantum controlled rotationally inelastic scattering of HD with H_2 and D_2 near 1 Kelvin reveals collisional partner reorientation. *Nat Chem.* (2018) 10:561–7. doi: 10.1038/s41557-018-0028-5
37. Gong J, Shapiro M, Brumer P. Entanglement-assisted coherent control in nonreactive diatom-diatom scattering. *J Chem Phys.* (2003) 118:2626–36. doi: 10.1063/1.1535428
38. Rice SA. Interfering for the good of a chemical reaction. *Nature.* (2001) 409:422–6. doi: 10.1038/35053211

Conflict of Interest: The authors declare that the research was conducted in the absence of any commercial or financial relationships that could be construed as a potential conflict of interest.

frontiers in Physics

ORIGINAL RESEARCH
published: 31 May 2021
doi: 10.3389/fphy.2021.627826

Laser-Induced Control of the Optical Response of Aluminum Phthalocyanine Chloride Complexes Dissolved in Ethanol

*Carina da Costa Castanheira *, Andreas Persch, Paul Birk, Christian Ott * and Thomas Pfeifer **

Max Planck Institute for Nuclear Physics, Heidelberg, Germany

We show that absorption spectra of aluminum chloride phthalocyanine (AlClPc) in the liquid phase can be dynamically modified through the time-resolved interaction with a second laser pulse during a time window on the order of 100 fs. The observed effects can be explained by laser-induced coherent coupling dynamics between the ground state and a bath of excited states as reproduced by a few-level toy model. The presented results help to understand how intense laser fields interact with complex molecules in solution, but in their laser-controlled response still much alike isolated atoms in the gas phase. This understanding can, in the future, be used to modify and control the dynamics in complex systems.

Keywords: transient absorption spectroscopy, coherence in the liquid phase, atom-like multi-level simulation, laser-induced control of the optical response, aluminum phthalocyanine chloride

Edited by:
Philip Bucksbaum,
Stanford University, United States

Reviewed by:
Arkaprabha Konar,
Kent State University, United States
Marcos Dantus,
Michigan State University,
United States

****Correspondence:***
Carina da Costa Castanheira
dacosta@mpi-hd.mpg.de
Christian Ott
christian.ott@mpi-hd.mpg.de
Thomas Pfeifer
thomas.pfeifer@mpi-hd.mpg.de

Specialty section:
This article was submitted to
Physical Chemistry and
Chemical Physics,
a section of the journal
Frontiers in Physics

Received: *10 November 2020*
Accepted: *04 May 2021*
Published: *31 May 2021*

Citation:
da Costa Castanheira C, Persch A, Birk P, Ott C and Pfeifer T (2021) Laser-Induced Control of the Optical Response of Aluminum Phthalocyanine Chloride Complexes Dissolved in Ethanol.
Front. Phys. 9:627826.
doi: 10.3389/fphy.2021.627826

1 INTRODUCTION

Coherent laser-control concepts are widely used to efficiently control matter [1–3]. In the gaseous phase the optical response of atomic and molecular targets can be controlled by XUV-NIR multi-pulse experiments which have been understood through laser-induced couplings between isolated electronic states [4–7], and also including vibrational couplings [8–12]. This approach also includes the possibility to selectively modify and control the dipole response with intense fields [13–15]. For more complex systems of molecules dissolved in the liquid phase, the intricacy of coherent light-matter interaction increases, where typically the coupling to a bath leads to rather rapid decoherence effects [16–20]. Nevertheless, coherent control concepts have been realized in these systems [21–23] and can also be understood through atom-like modeling [24, 25]. Based on existing dynamic coherent-control concepts which have been already established in the XUV-NIR spectral region on gas phase targets [14, 26, 27] it is the goal of this work to expand the dynamic control of absorption spectra to the liquid phase using time-resolved absorption spectroscopy in the visible (VIS) to near-infrared (NIR) regime.

The conceptual idea of measuring and controlling the optical dipole response of the system is presented in **Figure 1**. A weak excitation pulse induces a freely decaying dipole moment at time $t = 0$, which itself interferes with the electric field of the excitation pulse. This interference leads to the characteristic (unperturbed) static absorption spectrum of the system that is imprinted on the excitation pulse spectrum. When a control pulse subsequently interacts (at time $t = \tau > 0$) with the initially induced dipole moment it can be coherently modified, which is also known as perturbed free-induction decay [28–30]. This leads to characteristic spectral modifications of the absorption spectrum of the excitation pulse [5, 7, 14]. Hereby it should be noted that a grating-based

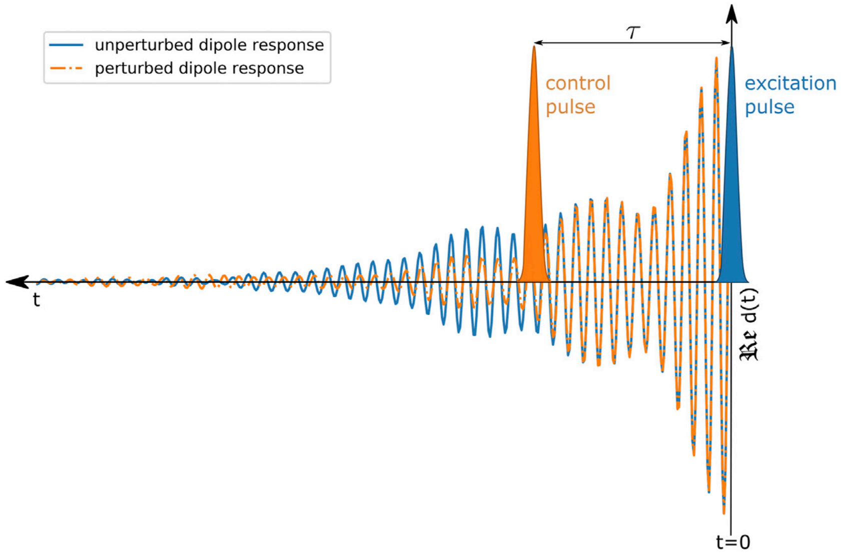

FIGURE 1 | Schematic illustration of controlling the optical dipole response. The excitation pulse (depicted in blue) initiates the system's dipole response $d(t)$ at time $t = 0$ which thereafter evolves freely in time (blue solid curve) for $t > 0$. At time $t = \tau$ a control pulse (depicted in orange) interacts with the dipole response, leading to a perturbed dipole response (orange dashed curve), which thereafter deviates from the unperturbed dipole response (evolving in absence of the control pulse) for $t > \tau$. See also Ref. [14] for further discussions of this concept.

spectrometer (not shown in **Figure 1**) intrinsically performs the Fourier transform and thus a time-integrated spectral measurement is carried out, which includes both the excitation pulse at $t = 0$ and its (possibly perturbed; in the presence of the control pulse) dipole response for $t > 0$. This concept thus invokes a time-domain picture of light-matter interaction where the absorption of light is understood in the impulsive limit of a time-domain (dipole) response function, the laser control of which is only possible while the system still reacts coherently upon the initial (excitation-induced) impulsive stimulus, which is here realized experimentally. The full real-time action of the control pulse on the system's dynamics can in principle be retrieved from the measured absorption spectrum provided a sufficiently short excitation pulse is used [15].

With this understanding laser-induced coupling dynamics can be extracted across isolated atomic [6, 13, 31], molecular [9, 10] and also more complex resonances [25]. Here, we apply these laser-control concepts of absorption spectra and the dipole response to a larger system of an organo-metallic complex in the liquid phase to explore new possibilities to dynamically control the system's absorption properties. Therefore we experimentally and computationally explore the impact of a laser field on a molecular coherence, which is encoded in the weak-field excitation-only absorption spectrum, by applying the concept of the induced dipole moment and its manipulation. We further confirm this approach by reproducing the measured coherent effects of the dynamically modified dipole response by using a numerical atom-like few-level toy model.

In this work our target of interest are aluminum phthalocyanine chloride (AlClPc) complexes dissolved in ethanol. Due to their outstanding electronic and optical properties phthalocyanines in general enjoy a variety of industrial and medical applications such as solar cells [32, 33] and photodynamic therapy (PDT) of tumors [34–36]. Phthalocyanines are thermally and chemically stable and can therefore sustain also slightly more intense electromagnetic radiation, which makes them adequate candidates for the interaction with intense laser fields in the liquid phase. Their absorption is mostly governed by a $\pi - \pi^*$ transition of the 18 delocalized π-electrons of the phthalocyanine ring resulting in two characteristic absorption bands, the Soret- (300–350 nm) and the Q-band (600–700 nm) [37]. The Q-band of AlClPc shows a substructure consisting of the strong Q3 and weak Q2 and Q1 bands which are maintained also in solution in ethanol [38].

2 MATERIALS AND METHODS

To exert laser-induced control of the optical response of AlClPc in the liquid phase we use a transient-absorption measurement scheme "in reverse": A weak (excitation) pulse to excite the system, and a second stronger pulse—referred to as control pulse—arriving later. Both pulses are in the visible spectral range.

The measurement concept is depicted in **Figure 2**. The preceding weak pulse induces in the sample a freely decaying dipole moment (blue) which can be understood as the coupling between the ground state GS and the excited states of the Q-band. The interference of the induced dipole response in time with the weak pulse itself—both are in a fixed phase relationship—leads to an (unperturbed) absorption spectrum which is dispersed by a

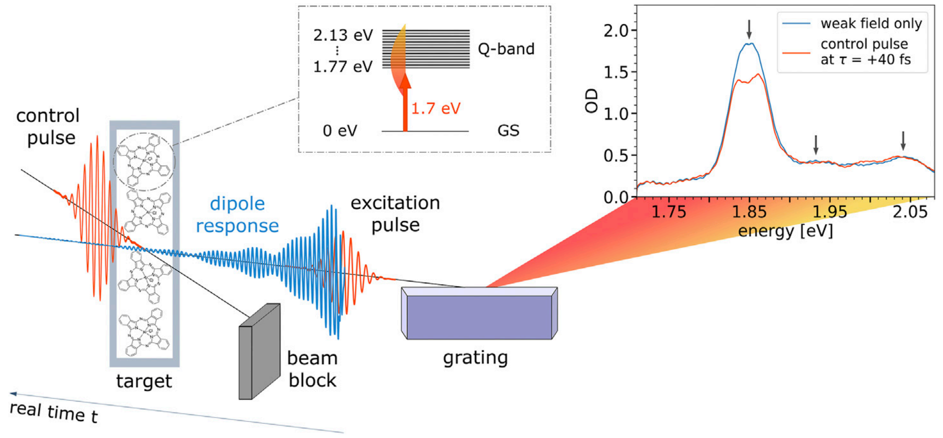

FIGURE 2 | Measurement concept. Pulses propagate from left to right, so, if considered temporally, real time increases from right to left. Therefore, the depicted pulse arrangement shows a configuration for positive delay times, where the delayed control pulse modifies the excitation-pulse-induced dipole moment (depicted in blue). Exemplary absorption spectra are shown for the case of very late control delays in blue (effectively "weak field only") where the control pulse does not change the dipole response anymore, as well as for the time delay τ = +40 fs, where the control pulse significantly perturbs the induced dipole moment. Black arrows denote the position of the Q3-, Q2-, and Q1-band. The inset shows an atom-like level scheme which is used for our toy model.

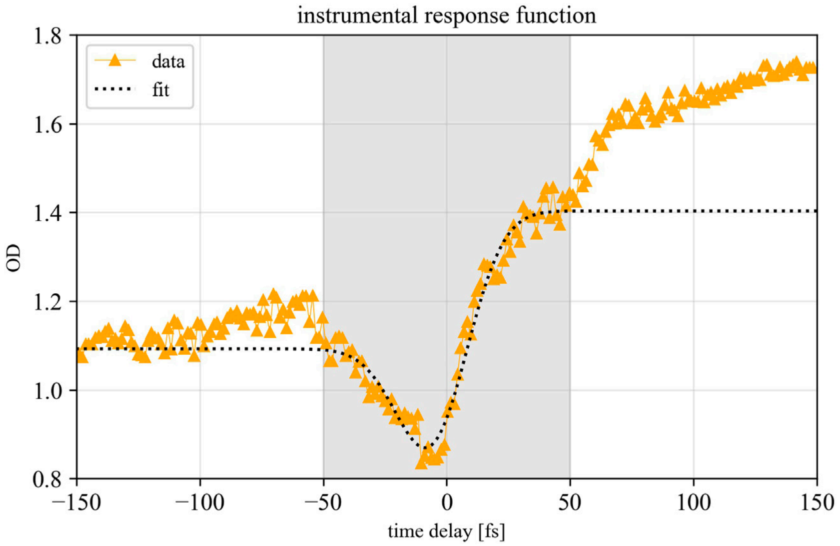

FIGURE 3 | Fit of the instrumental response function on the mean lineout of the Q3-band as a function of the time delay. The fit function (1) was applied in the grey shaded pulse-overlap area.

grating and measured as a function of energy (see the corresponding blue spectrum). If the control pulse arrives in time before the coherent dipole response has decayed completely, it is able to disturb the system by modifying the dipole response, leading to changes in the measured weak-field absorption spectrum (depicted in red color).

For the case of control-pulse first, that pulse does induce a dipole moment with which the later arriving weak pulse can interact. This effect is not seen in our measurements, since the control pulse (and therefore the co-propagating control-induced dipole moment) is spatially blocked after the sample. This is the reason why in our case we are only sensitive to the weak-field induced dipole moment. The difference in our experiment is thus rooted in the slightly non-collinear geometry where in the far field (after the sample) the pulses are detected spatially separate. Please note, due to the non-collinear geometry, measuring the excitation pulse together with its dipole response perturbed by the control pulse, any higher-order coherent effects induced by the control pulse itself, including stimulated emission induced by the control pulse [39], are not observed in the measurement direction of the excitation pulse.

To generate broadband ultrashort laser pulses in the visible spectral range we use a commercially available Ti:Sapphire

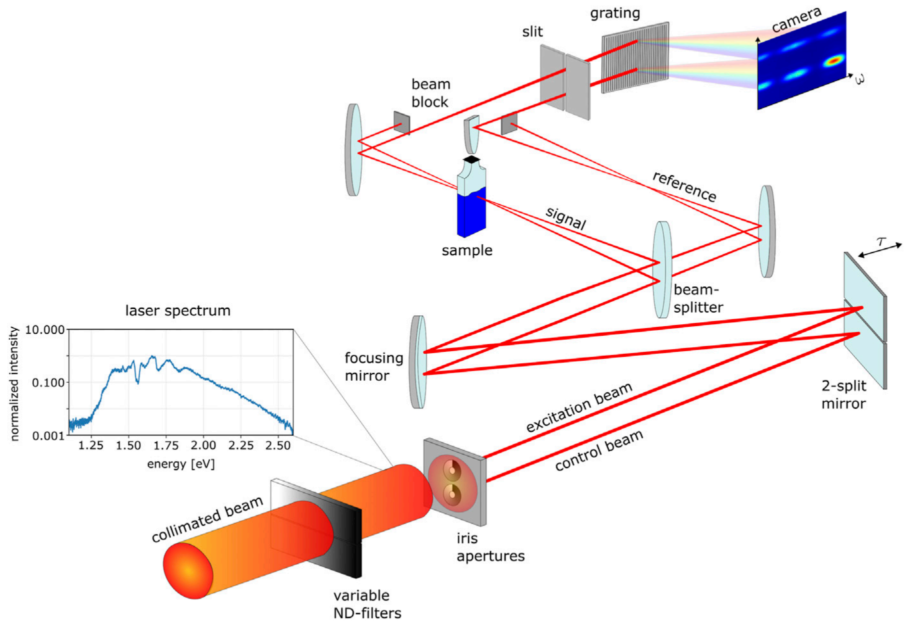

FIGURE 4 | Experimental response-control setup. See text for details.—Note: The 2-split mirror, as well as the focusing mirror are experimentally hit under close-to-normal angle of incidence. Increased angles are depicted in the illustration for a better schematic overview of the experimental setup.

multi-pass amplifier laser system (Femtolasers FEMTOPOWER™ HE/HR CEP4) with a 3 kHz repetition rate, approximately 3 mJ pulse energy and a pulse duration of 20 fs full-width at half maximum (FWHM). After nonlinear propagation in a hollow-core fiber, a supercontinuum is generated which approximately covers the spectral range from 500 to 1000 nm. Subsequently the pulses are compressed with chirped mirrors. For this measurement we use chirped supercontinuum pulses of 32.7 ± 0.8 fs (FWHM), determined by fitting the instrumental response function on the lineout of the ground-state bleach of the Q3-band over the time delay, as can be seen in **Figure 3**. This helps to attenuate the peak intensities of the laser pulses to avoid permanent damage of the sample. As a fit function we used a convolution between a Gaussian, a Heaviside and an exponential function:

$$f_{fit}(t) = \left(\left(\frac{A}{\sqrt{2\pi\sigma^2}} e^{-\frac{t^2}{2\sigma^2}} \right) * \left(\Theta(t) \cdot \left(c + B \cdot e^{-\frac{t}{\tau}} \right) \right) \right) + b \qquad (1)$$

with c and b being constants representing the depth and the total offset of the step, while A and B are constants for the amplitude of the instrumental response function (IRF) and the exponential decay, respectively, and σ denotes the width of the IRF and τ the exponential relaxation time. We apply this fit in the gray shaded pulse overlap area (**Figure 3**) near temporal overlap, i.e. before the onset of more complex molecular dynamics at later times.

The experimental response-control setup is depicted in detail in **Figure 4**. The collimated beam is divided into phase-synchronized excitation and control beams by a custom-built array of two iris apertures. The iris parameters are adjusted for the control beam to obtain a bigger focus diameter than the excitation beam. This ensures that the excitation-pulse-induced dipole response can be globally modified by the control beam, fully illuminating the excited sample volume. The preceding variable metallic neutral-density (ND) filters allow for an independent adjustment of the intensity of the beams. The time delay between both beams is introduced by a two-component mirror consisting of two mirrors separately mounted on piezo micrometer delay stages (PIHera Piezo Linearstage P-622.1CD, Physik Instrumente) which are hit by the laser beams under close-to normal angle of incidence, allowing to access time delays up to ±1.7 ps. Shortly after the focusing mirror (with a focal length of 50 cm), both beams pass a broadband beamsplitter (Layertech 110105) which reflects 80% and transmits 20% of the two beamlets. The transmitted part is used as a reference while the reflected part is guided into the sample where control and excitation beams spatially overlap with an intersection angle of 1.72 degree and a spot size of 150 µm FWHM diameter for the excitation beam and 400 µm for the control beam. In both pathways the control beam is blocked and only the excitation beam and its reference replica are refocussed using two additional focusing mirrors with a focal length of 50 cm each onto the slit of a Czerny-Turner-type spectrometer (Acton SpectraPro, Princeton Instruments). The excitation signal and reference beams are spectrally resolved with a resolution of 1.7 meV by a concave grating of 600 grooves/mm and detected with a spatial offset on the same CCD camera chip (CoolSnap K4, Teledyne Photometrics) as a function of the excitation-control time delay.

As a sample container, cyclic olefin copolymer cuvettes (SpecVette™ manufactured by Aline Inc.) with 0.5 mm path length and 25 µl volume were used. The solution of AlClPc was prepared by dissolving 0.0042 g of AlClPc (purchased

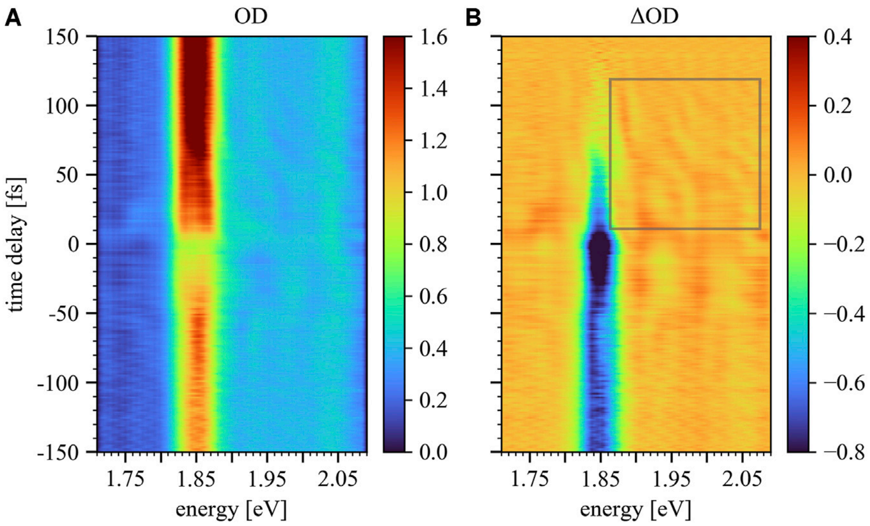

FIGURE 5 | Time-delay trace OD (ω, τ) **(A)** and ΔOD (ω, τ) **(B)** of AlClPc complexes dissolved in ethanol. The ΔOD **(B)** underlines the control-induced changes of the excitation-pulse induced dipole response in AlClPc. Faint rapid fringes along the time-delay axis are due to residual stray light of the control beam which optically interferes with the excitation beam and occur symmetrically for both positive and negative times. At negative/positive times, the control pulse arrives before/after the excitation pulse, where the latter is centered at time $t = 0$ and induces a coherent dipole response for times $t > 0$. The grey box marks the area of interest where slow spectro-temporal modulations of the measured absorption are visible. The color bars represent the magnitude of OD.

from Sigma Aldrich) in 0.01 ml of 99.9% ethanol (Uvasol® by Sigma Aldrich) and was further diluted with distilled water with a ratio of 3:1 which results in a solution with a concentration of 55 nmol/ml.

3 RESULTS

3.1 Experimental Results

For the measurements the excitation-beam average power was set to 0.28 mW and the control average power to 4.0 mW which correspond to on-target peak intensities of $3.2 \cdot 10^{10}$ and $1.7 \cdot 10^{11}$ W/cm^2 respectively. The transmitted signal and reference spectra were recorded for excitation-control time delays between −180 and +150 fs with a step size of 1.33 fs, where positive delays denote the excitation pulse preceding the control pulse. Laser-induced modifications of the excitation-pulse induced dipole response can therefore only take place for positive time delays $(\tau > 0)$. With this in mind the optical density OD (ω, τ) is calculated according to Beer-Lambert's law:

$$\mathrm{OD}(\omega, \tau) = -\log_{10} \frac{I_{sig}(\omega, \tau)}{c(\omega) \cdot I_{ref}(\omega, \tau)} \tag{2}$$

with the signal and reference spectral intensity I_{sig} and I_{ref} depending on both time delay τ and frequency ω. The factor $c(\omega)$ is a calibration factor which corrects for the relative intensities between the signal and reference beams which are dependent on ω and mainly introduced by the beamsplitter. To determine $c(\omega)$ a measurement is conducted beforehand with an empty cyclic olefin copolymer cuvette in the focus. To additionally ensure that the solvent does not introduce effects which might be interpreted as a contribution from the coherent response of the AlClPc complexes, a time-delay scan in the neat solvent was conducted which showed no significant time-dependent spectro-temporal structures. After this step the actual measurement in the AlClPc complexes in ethanol are conducted with the same settings.

The static absorption of AlClPc's Q-band is depicted in blue in **Figure 2** and spans the spectral range between 1.80 and 2.08 eV. The highest contribution to the ground-state absorption is attributed to the Q3-band centered at 1.85 eV. The Q1-band is centered at 2.04 eV, while the Q2-band at 1.93 eV is only faintly visible. The measured time-delay-dependent absorption $OD(\omega, \tau)$ can be seen in **Figure 5**. For a better visibility of the dynamic changes the relative optical density $[\Delta\mathrm{OD}(\omega, \tau)]$ was calculated by subtracting the weak-field static absorption spectrum. The latter has been determined through the average of the optical density for control-pulse time delays between +150 and +140 fs, where the excitation-pulse induced absorption is no longer influenced as can be seen in **Figure 5A**. This can be rationalized since for late time delays the laser control of the dipole response is no longer possible. The most prominent feature which can be observed in **Figure 5** is the decrease in absorption of the Q3-band for negative time delays. This effect can be explained by a ground-state bleach [40, 41]. In this case the control pulse itself, when arriving first, triggers a significant amount of population transfer into the excited states, which then leads to a lowered ground-state absorption of the excitation pulse as expected in conventional pump-probe transient absorption spectroscopy. For positive times (control pulse arrives later than the excitation pulse) a time-dependent modulation in the measured absorption spectrum between 1.85 and 2.10 eV is observed. For a better visibility the area of interest is marked in **Figure 5B** with a grey box. These slow modulations can be observed for positive time delays only and up to approximately +100 fs which implies that coherent modification of

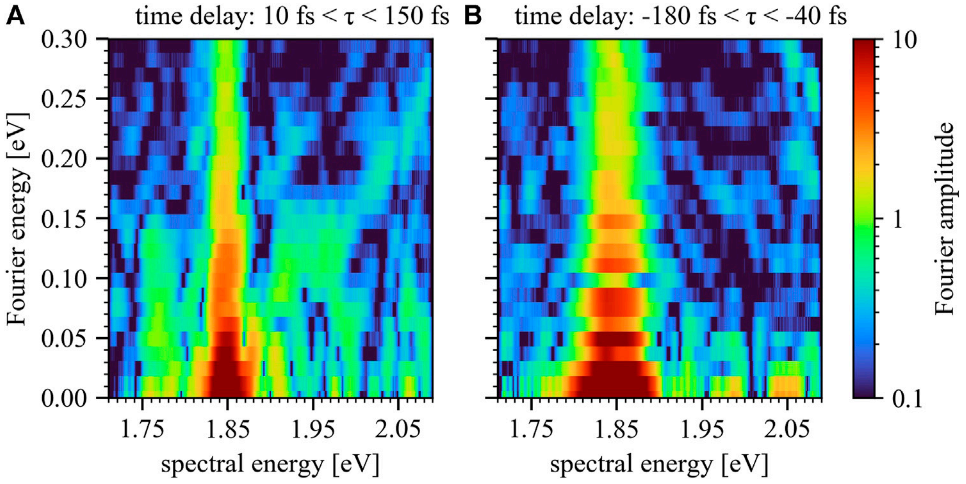

FIGURE 6 | Fourier plot for positive **(A)** and negative **(B)** time delays of the $\Delta\mathrm{OD}(\omega, \tau)$ depicted in **Figure 5B**. Diagonals of slope ±1 pointing at a spectral energy of approximately 1.84 eV can be observed in the Fourier plot only for positive time delays.

the excitation-pulse induced dipole response is still possible at these relatively long time scales even in the liquid phase. In addition a slight splitting of the Q3-band for positive time delays between 0 and +50 fs can be found.

To verify the origin of the observed effects a Fourier transform along the time-delay axis for positive and negative times of the ΔOD trace is performed separately and depicted in **Figure 6**. In atoms, this procedure was used to reveal couplings of different energy levels by plotting the Fourier energy over absorption spectral energy [14, 26, 31]. In these two-dimensional Fourier energy vs. spectral energy representations, diagonals of slope ±1 that intersect the energy axis have been previously identified to indicate the modification of the coherent dipole response of that particular state for a variable time delay between excitation and control pulses [14]. Furthermore, enhancements in the Fourier amplitude along these diagonals are indicative of a coherent coupling between different states [31]. Such diagonals of slope ±1 can be observed in **Figure 6A** which arise at a spectral energy of approximately 1.84 eV and hence can be further associated to the Q3-band. Comparing the Fourier plots for positive and negative time delays, **Figure 6A** shows rich structure, while in **Figure 6B** only a globally enhanced signal around the Q3-band is visible.

The significant qualitative difference between both Fourier plots confirms that the observed diagonal features are associated with laser-driven excited-state dipoles: for positive time delays the control field is able to modify the freely evolving dipole response of the excitation pulse. This qualitative difference between **Figure 6A,B** therefore strongly suggests that the previously introduced mechanism (**Figure 1**, **2**) plays a significant role. Further confirmation of the underlying origin of the observed effects will be discussed in the following section by employing an atom-like multi-level model calculation.

3.2 Atom-Like Multi-Level Toy Model

We implement a numerical toy model through the propagation of the time-dependent Schrödinger equation in a multi-level system. Hereby we approximate the Q-bands through an ensemble of $N = 300$ closely spaced states with respective energy widths of 2.2 meV each. We have ascertained that this choice of linewidth is sufficiently small to reproduce quantum interferences over the time-delay range of the measured data. In order to approximate the weak-field-only white-light absorption spectrum (depicted by the blue curve in the inset of **Figure 2**), the 300 states are brought to a mutual overlap and are equidistantly distributed over an energy range between 1.61 and 2.21 eV. Their respective real-valued transition dipole moments to the ground state are set such that the simulated white-light absorption spectrum agrees with the measurement, which is shown for comparison in **Figure 7A**. To solve the time-dependent Schrödinger equation

$$i\frac{\partial}{\partial t}\left|\psi(t)\right\rangle = \mathcal{H}\left|\psi(t)\right\rangle \tag{3}$$

with

$$\mathcal{H} = \mathcal{H}_0 + \mathcal{H}_{\mathrm{int}} \tag{4}$$

a split-step algorithm [42] has been used. Under the assumption that the Hamiltonian $\mathcal{H}$ is constant during each time step, this routine solves the equations of motion iteratively for every time step by changing between the diagonalized Hilbert spaces of the unperturbed Hamiltonian $\mathcal{H}_0$ and the interaction Hamiltonian $\mathcal{H}_{\mathrm{int}} = \hat{d}\cdot E(t)$ in the dipole approximation with the dipole operator $\hat{d}$ and the time-dependent electric field $E(t)$. The wavefunction $\left|\psi(t)\right\rangle = \sum_i c_i(t)|\Phi_i\rangle$ can be represented as a sum of time-dependent state coefficients $c_i(t)$ and the spatial eigenstates of the system $|\Phi_i\rangle$. The dipole response $d(t)$ of the system can therefore be calculated by

$$d(t) = \langle\psi(t)|\hat{d}|\psi(t)\rangle = \sum_{m,n} d_{nm} c_n(t) c_m^*(t) + c.c., \tag{5}$$

where $d_{nm} = \langle\Phi_m|\hat{d}|\Phi_n\rangle$. The d_{nm} are chosen with the aim to reproduce the measured (weak-field, excitation pulse only)

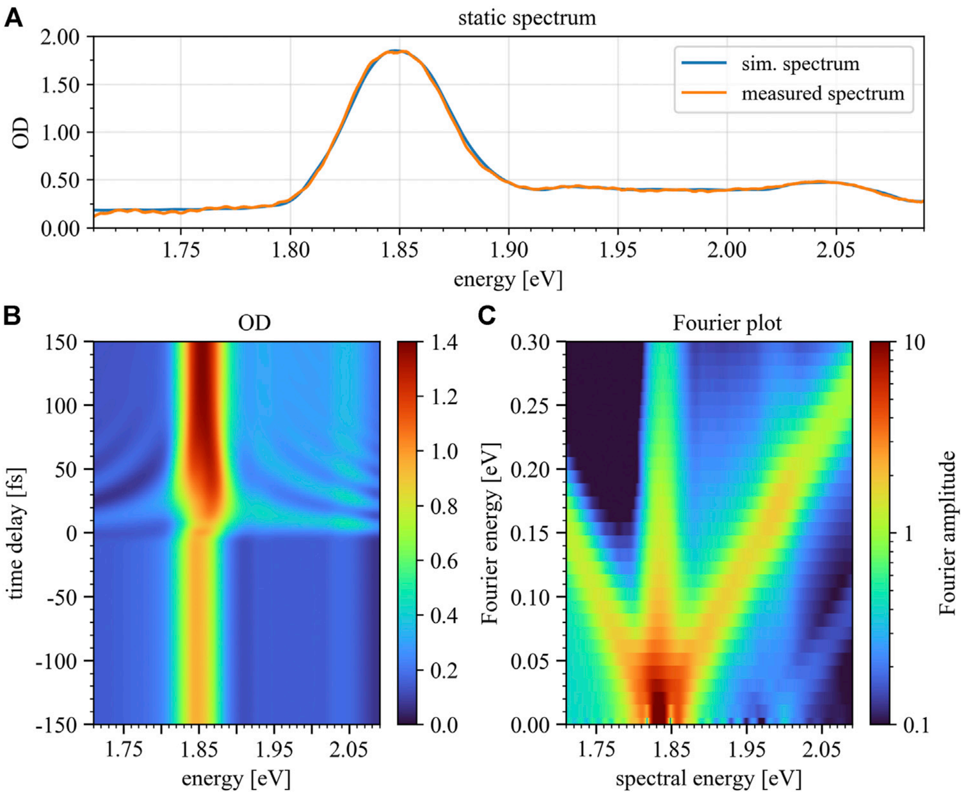

FIGURE 7 | Simulated static absorption spectrum **(A)**, time-delay trace **(B)** and Fourier plot **(C)** for positive time delays only. Panel 7B depicts the modeled optical density over a time-delay range of 300 fs, where the color bar marks the magnitude of OD. The Fourier plot (Panel 7C) reveals diagonals with slope ±1 in a similar fashion as seen in the experimental data. Negative time delays refer to control-pulse first, positive to excitation-pulse first.

absorption spectrum. Therefore the dipole matrix elements were set such that the thereby generated absorption spectrum closely matches the experimental data (**Figure 7A**). The final Hamiltonian matrix then reads

$$\mathcal{H} = \begin{bmatrix} \omega_0 & d_{1,0}E(t) & d_{2,0}E(t) & \dots & d_{300,0}E(t) \\ d_{0,1}E(t) & \omega_1 & 0 & \dots & 0 \\ d_{0,2}E(t) & 0 & \omega_2 & \dots & 0 \\ \vdots & \vdots & \vdots & \ddots & 0 \\ d_{0,300}E(t) & 0 & 0 & 0 & \omega_{300} \end{bmatrix}, \tag{6}$$

where $E(t) = E_{excitation}(t) + E_{control}(t-\tau)$ is the sum electric fields of both excitation and control pulses, and ω_i represent the complex eigenenergies of the states. The arrival time of the excitation pulse is kept constant at $t = 0$ while the control pulse is temporally varied with the relative time delay τ. The pulses are implemented with a Gaussian envelope, an intensity FWHM of 3 fs and a central photon energy of 1.70 eV.

The dipole spectrum $\tilde{d}(\omega)$ is obtained by Fourier-transforming the dipole response $d(t)$, and together with the spectral representation of the electric field $\tilde{E}_s(\omega)$, the absorption cross section $\sigma(\omega)$ can be calculated according to

$$\sigma(\omega) \propto \omega \cdot \mathrm{Im}\left[\frac{\tilde{d}(\omega)}{\tilde{E}_s(\omega)}\right], \tag{7}$$

which reflects the interference of the excitation-pulse induced dipole response with the excitation pulse itself, and their propagation through the medium according to Maxwell's equations. The OD is in turn proportional to the absorption cross section *via*

$$\mathrm{OD}(\omega) = -\log_{10}\left(\frac{I(\omega)}{I_0(\omega)}\right) = \frac{N_a l \sigma(\omega)}{\ln(10)}, \tag{8}$$

where N_a represents the number density of absorbers (i.e. AlClPc molecules) and l is the length of the absorption volume. A more detailed derivation of **Eqs 7**, **8** can be found [7].

To mimic the non-collinear experimental setup, an additional wave-front averaging { Refs. [43, 44]} is performed by calculating the absorption spectra with different carrier-envelope-phase (CEP) values for the control pulse, while keeping the CEP of the excitation pulse fixed, and subsequently taking the average of the resulting absorption spectra. Using this procedure the optical interference (heterodyne effect) between both optical pulses is suppressed in the toy model. Experimentally this optical interference is suppressed by the intersection angle of 1.72 degree which corresponds, together with the focal size of 150 µm, to a spread in delay of approximately seven full cycles of the wavelength. Finally, the simulated time-delay trace was convoluted with the instrumental response function, to account

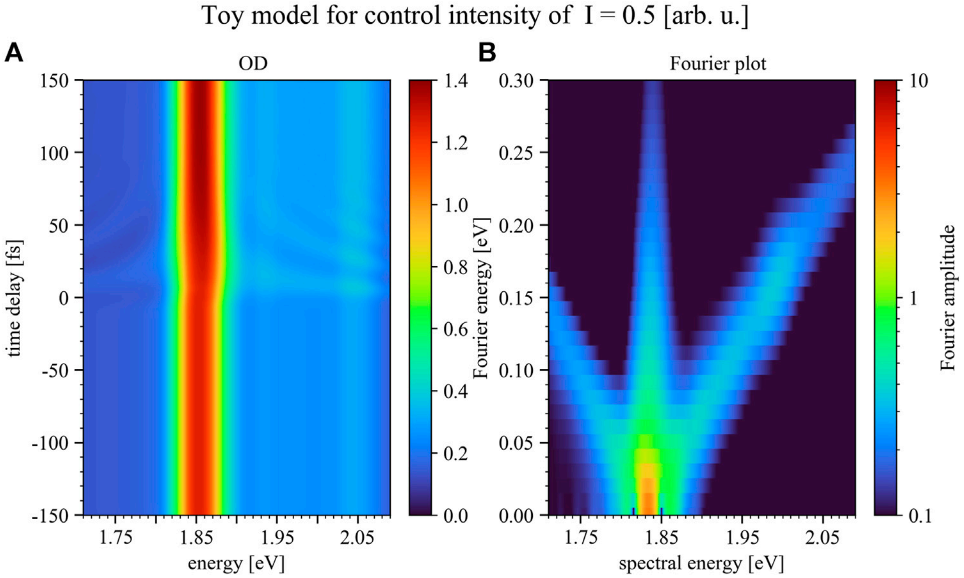

FIGURE 8 | Simulated time delay trace **(A)** and Fourier plot **(B)** for positive time delays only, but for the case of half the control-pulse intensity compared to **Figure 7**. Panel 8A depicts the modeled optical density over a time-delay range of 300 fs, where the color bar marks the magnitude of the OD. The Fourier plot (Panel 8B) reveals less pronounced diagonals with slope ±1 compared to the experimental data. As can be seen by lowering the intensity of the control pulse the structures upon the absorption decrease. Negative time delays refer to control-pulse first, positive to excitation-pulse first.

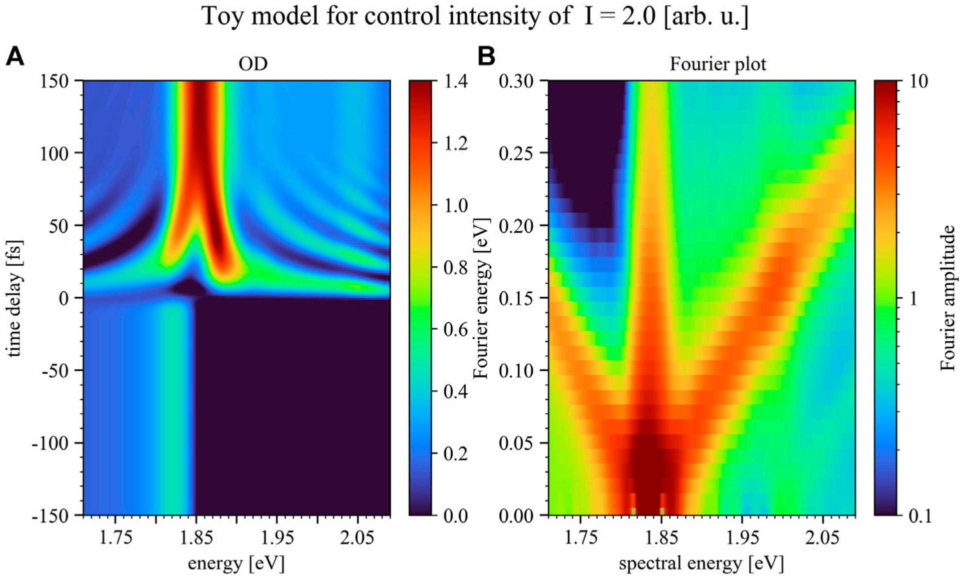

FIGURE 9 | Simulated time delay trace **(A)** and Fourier plot **(B)** for positive time delays only, but for the case of double the control-pulse intensity of **Figure 7**. Panel 9A depicts the modeled optical density over a time-delay range of 300 fs, where the color bar marks the magnitude of the OD. The Fourier plot (Panel 9B) reveals diagonals with slope ±1 in a more pronounced fashion compared to the experimental data. The Rabi-/Autler-Townes splitting for small time delays near resonance can be observed to set in and grow with increasing control pulse intensity. Negative time delays refer to control-pulse first, positive to excitation-pulse first.

for the finite temporal and spectral resolution of the experiment. The resulting time-delay trace, as well as the corresponding Fourier plot (see discussion of **Figure 5** above) are depicted in **Figures 7B,C**.

To show the impact of the control-pulse intensity on the manipulation of the excitation-pulse induced dipole response the numerical toy model was additionally conducted for two more intensities, half (**Figure 8**) and double (**Figure 9**) of the case shown in **Figure 7**. Hereby the results shown in **Figure 7** reproduce the experimental results best.

As can be seen in **Figure 8** by lowering the intensity of the control pulse the structures upon the absorption decrease, while for increasing the control-pulse intensity one enters the strong-coupling limit. In this intensity region the control pulse is able to strongly modify the excitation-pulse induced dipole moment, leading to the splitting of the Q3-band which can already be seen in **Figure 7B** and increases toward higher control-pulse intensity (**Figure 9**). This band splitting is a Rabi-/Autler-Townes splitting involving light-induced level shifts of strongly coupled states, which can be observed to set in and grow with increasing control-pulse intensity.

In our toy model we only consider states up to a total excitation energy of 2.21 eV. Excitation of higher-lying states might also take place in our measurement but were neglected in the toy model due to lower relative population and thus have only a minor effect on the strong coupling of the lower-lying states. A prominent representative of such energetically higher-lying states is the Soret-band, which could imprint coupling signatures induced by the strong control pulse, which one could also try to identify by measuring its subsequently decay to the Q-band by fluorescence emission [40, 45]. Additional influence due to the coupling to higher excited states, like the Soret-band, may give rise to additional fine structures of the observed time-delay dependent interference.

4 DISCUSSION

Comparing the measured time-delay-dependent absorbance (**Figure 5A**) with the simulated trace (**Figure 7B**), a good qualitative agreement can be observed for energies > 1.80 eV. A discrepancy between the experimental and simulated data in the low-energy region is present since not all coupling channels are taken into account yet in the toy model to fully describe the experiment. Including more couplings currently lies outside the scope of this first study. Nevertheless the model reproduces the slight splitting of the Q3-band between 0 and 50 fs, the decrease in the overall absorption for negative time delays as well as the hyperbolic structures converging toward the Q3-band. Furthermore, also the Fourier energy plot in **Figure 7C** reveals diagonals of slope ±1 linked to the center of the Q3 band at spectral energy 1.84 eV, in qualitative agreement with the experiment. All these effects can thus be realized and understood with the described simplified atom-like multi-level toy model, with its level scheme depicted in **Figure 2**. The good structural agreement between experimental observation and the model results shows that the dynamical mechanism at work in this laser-driven AlClPc solution can be effectively approximated in the coupled system of ground and excited states.

To summarize, we have observed time-dependent coherent modifications of the ground-state absorption spectrum attributed to the Q-band of AlClPc complexes in the liquid phase. By comparing our measurements with an atom-like multi-level toy model, we were able to qualitatively reproduce and identify the spectro-temporal structures in the optical density as a laser-induced coupling between the ground state and a bath of excited states. Thus, by controlling the dipole response with a time-delayed laser pulse it is possible to understand the coherent ultrafast dynamics of complex systems in solution under the influence of intense light fields.

DATA AVAILABILITY STATEMENT

The raw data supporting the conclusion of this article will be made available by the authors, without undue reservation.

AUTHOR CONTRIBUTIONS

CC and AP conducted the experiment and evaluated the experimental data together. CC wrote the paper manuscript, while AP conducted the numerical simulation using a part of the code provided from PB. CO and TP supervised the research project and gave input to the manuscript.

REFERENCES

1. Shapiro M, and Brumer P. Coherent Control of Atomic, Molecular, and Electronic Processes. *Adv At Mol Opt Phys* (2000) 42:287–345. doi:10.1016/S1049-250X(08)60189-5
2. Dantus M. Coherent Nonlinear Spectroscopy: From Femtosecond Dynamics to Control. *Annu Rev Phys Chem* (2001) 52:639–79. doi:10.1146/annurev.physchem.52.1.639
3. Ohmori K. Wave-packet and Coherent Control Dynamics. *Annu Rev Phys Chem* (2009) 60:487–511. doi:10.1146/annurev.physchem.59.032607.093818
4. Wang H, Chini M, Chen S, Zhang CH, He F, Cheng Y, et al. Attosecond Time-Resolved Autoionization of Argon. *Phys Rev Lett* (2010) 105:143002. doi:10.1103/PhysRevLett.105.143002
5. Chen S, Bell MJ, Beck AR, Mashiko H, Wu M, Pfeiffer AN, et al. Light-induced States in Attosecond Transient Absorption Spectra of Laser-Dressed Helium. *Phys Rev A* (2012) 86:063408. doi:10.1103/PhysRevA.86.063408
6. Kaldun A, Ott C, Blättermann A, Laux M, Meyer K, Ding T, et al. Extracting Phase and Amplitude Modifications of Laser-Coupled Fano Resonances. *Phys Rev Lett* (2014) 112:103001. doi:10.1103/PhysRevLett.112.103001
7. Wu M, Chen S, Camp S, Schafer KJ, and Gaarde MB. Theory of Strong-Field Attosecond Transient Absorption. *J Phys B: At Mol Opt Phys* (2016) 49:062003. doi:10.1088/0953-4075/49/6/062003
8. Reduzzi M, Chu WC, Feng C, Dubrouil A, Hummert J, Calegari F, et al. Observation of Autoionization Dynamics and Sub-cycle Quantum Beating in Electronic Molecular Wave Packets. *J Phys B: At Mol Opt Phys* (2016) 49:065102. doi:10.1088/0953-4075/49/6/065102
9. Warrick ER, Cao W, Neumark DM, and Leone SR. Probing the Dynamics of Rydberg and Valence States of Molecular Nitrogen with Attosecond Transient Absorption Spectroscopy. *J Phys Chem A* (2016) 120:3165. doi:10.1021/acs.jpca.5b11570
10. Cheng Y, Chini M, Wang X, González-Castrillo A, Palacios A, Argenti L, et al. Reconstruction of an Excited-State Molecular Wave Packet with Attosecond Transient Absorption Spectroscopy. *Phys Rev A* (2016) 94:23403. doi:10.1103/PhysRevA.94.023403
11. Warrick ER, Fidler AP, Cao W, Bloch E, Neumark DM, and Leone SR. Multiple Pulse Coherent Dynamics and Wave Packet Control of the Dark State by Attosecond Four-Wave Mixing. *Faraday Discuss* (2018) 212:157–74. doi:10.1039/C8FD00074C
12. Drescher L, Reitsma G, Witting T, Patchkovskii S, Mikosch J, and Vrakking MJJ. State-resolved Probing of Attosecond Timescale

Molecular Dipoles. *J Phys Chem Lett* (2019) 10:265–9. doi:10.1021/acs.jpclett.8b02878

13. Ott C, Kaldun A, Raith P, Meyer K, Laux M, Evers J, et al. Lorentz Meets Fano in Spectral Line Shapes: A Universal Phase and its Laser Control. *Science* (2013) 340:716–20. doi:10.1126/science.1234407
14. Blättermann A, Ott C, Kaldun A, Ding T, and Pfeifer T. Two-dimensional Spectral Interpretation of Time-dependent Absorption Near Laser-Coupled Resonances. *J Phys B: At Mol Opt Phys* (2014) 47:124008. doi:10.1088/0953-4075/47/12/124008
15. Stooß V, Cavaletto S, Donsa S, Blättermann A, Birk P, Keitel C, et al. Real-Time Reconstruction of the Strong-Field-Driven Dipole Response. *Phys Rev Lett* (2018) 121:173005. doi:10.1103/PhysRevLett.121.173005
16. Nuernberger P, Ruetzel S, and Brixner T. Multidimensional Electronic Spectroscopy of Photochemical Reactions. *Angew Chem Int Edition* (2015) 54:11368–86. doi:10.1002/anie.201502974
17. Nairat M, Webb M, Esch MP, Lozovoy VV, Levine BG, and Dantus M. Time-resolved Signatures across the Intramolecular Response in Substituted Cyanine Dyes. *Phys Chem Chem Phys* (2017) 19:14085–95. doi:10.1039/C7CP00119C
18. Kumpulainen T, Lang B, Rosspeintner A, and Vauthey E. Ultrafast Elementary Photochemical Processes of Organic Molecules in Liquid Solution. *Chem Rev* (2017) 117:10826–939. doi:10.1021/acs.chemrev.6b00491
19. Oliver TAA. Recent Advances in Multidimensional Ultrafast Spectroscopy. *R Soc Open Sci* (2018) 5:171425. doi:10.1098/rsos.171425
20. Buckup T, and Léonard J. *Multidimensional Time-Resolved Spectroscopy*. Switzerland: Springer (2018).
21. Brixner T, Damrauer NH, Niklaus P, and Gerber G. Photoselective Adaptive Femtosecond Quantum Control in the Liquid Phase. *Nature* (2001) 414:57–60. doi:10.1038/35102037
22. Pearson BJ, White JL, Weinacht TC, and Bucksbaum PH. Coherent Control Using Adaptive Learning Algorithms. *Phys Rev A* (2001) 63:063412. doi:10.1103/PhysRevA.63.063412
23. Herek JL, Wohlleben W, Cogdell RJ, Zeidler D, and Motzkus M. Quantum Control of Energy Flow in Light Harvesting. *Nature* (2002) 417:533–5. doi:10.1038/417533a
24. Schneider J, Wollenhaupt M, Winzenburg A, Bayer T, Köhler J, Faust R, et al. Efficient and Robust Strong-Field Control of Population Transfer in Sensitizer Dyes with Designed Femtosecond Laser Pulses. *Phys Chem Chem Phys* (2011) 13:8733–46. doi:10.1039/C0CP02723E
25. Meyer K, Liu Z, Müller N, Mewes JM, Dreuw A, Buckup T, et al. Signatures and Control of Strong-Field Dynamics in a Complex System. *Proc Natl Acad Sci* (2015) 112:15613–8. doi:10.1073/pnas.1509201112
26. Chini M, Wang X, Cheng Y, Wu Y, Zhao D, Telnov DA, et al. Sub-cycle Oscillations in Virtual States Brought to Light. *Scientific Rep* (2013) 3:1105.
27. Ott C, Kaldun A, Argenti L, Raith P, Meyer K, Laux M, et al. Reconstruction and Control of a Time-dependent Two-Electron Wave Packet. *Nature* (2014) 516:374–8. doi:10.1038/nature14026
28. Brito Cruz CH, Gordon JP, Becker PC, Fork RL, and Shank CV. Dynamics of Spectral Hole Burning. *IEEE J Quan Electron* (1988) 24:261–9. doi:10.1109/3.122
29. Sasaki F, and Kobayashi S. Femtosecond Dynamics of Frenkel Excitons in Pseudoisocyanine J Aggregates. *Jpn J Appl Phys* (1995) 34:188. doi:10.7567/jjaps.34s1.188
30. Bengtsson S, Larsen EW, Kroon D, Camp S, Miranda M, Arnold CL, et al. Space–time Control of Free Induction Decay in the Extreme Ultraviolet. *Nat Photon* (2017) 11:252–8. doi:10.1038/nphoton.2017.30
31. Ding T, Ott C, Kaldun A, Blättermann A, Meyer K, Stooss V, et al. Time-resolved Four-Wave-Mixing Spectroscopy for Inner-Valence Transitions. *Opt Lett* (2016) 41:709–12. doi:10.1364/OL.41.000709
32. de la Torre G, Claessens CG, and Torres T. Phthalocyanines: Old Dyes, New Materials. Putting Color in Nanotechnology. *Chem Commun* (2007) 2000–15. doi:10.1039/B614234F
33. Walter MG, Rudine AB, and Wamser CC. Porphyrins and Phthalocyanines in Solar Photovoltaic Cells. *J Porphyrins Phthalocyanines* (2010) 14:759–92. doi:10.1142/S1088424610002689
34. Bonnett R. Photosensitizers of the Porphyrin and Phthalocyanine Series for Photodynamic Therapy. *Chem Soc Rev* (1995) 24:19–33. doi:10.1039/CS9952400019
35. Py-Daniel KR, Namban JS, de Andrade LR, de Souza PEN, Paterno LG, Azevedo RB, et al. Highly Efficient Photodynamic Therapy Colloidal System Based on Chloroaluminum Phthalocyanine/pluronic Micelles. *Eur J Pharm Biopharm* (2016) 103:23–31. doi:10.1016/j.ejpb.2016.03.028
36. Jayme CC, Calori IR, and Tedesco AC. Spectroscopic Analysis of Aluminum Chloride Phthalocyanine in Binary Water/ethanol Systems for the Design of a New Drug Delivery System for Photodynamic Therapy Cancer Treatment. *Spectrochimica Acta A: Mol Biomol Spectrosc* (2016) 153:178–83. doi:10.1016/j.saa.2015.08.027
37. Edwards L, and Gouterman M. Porphyrins: XV. Vapor Absorption Spectra and Stability: Phthalocyanines. *J Mol Spectrosc* (1970) 33:292–310. doi:10.1016/0022-2852(70)90040-8
38. Vilsinski B, Gerola A, Lemos É, Magalhães Barbosa P, Katieli C, Cesar G, et al. Spectroscopic Study of Aluminum Phthalocyanine Chloride (AlPcCl) in Homogeneous and Micro-heterogeneous Media Consisting of P-123 and F-127 Polymeric Micelles. *Química Nova* (2015) 38:631–9. doi:10.5935/0100-4042.20150056
39. Konar A, Shah JD, Lozovoy VV, and Dantus M. Optical Response of Fluorescent Molecules Studied by Synthetic Femtosecond Laser Pulses. *J Phys Chem Lett* (2012) 3:1329–35. doi:10.1021/jz300363t
40. Gan Q, Li S, Morlet-Savary F, Wang S, Shen S, Xu H, et al. Photophysical Properties and Optical Limiting Property of a Soluble Chloroaluminum-Phthalocyanine. *Opt Express* (2005) 13:5424–33. doi:10.1364/OPEX.13.005424
41. Melnikov MY. Aluminum Phthalocyanine on Silica Nanoparticles: Aggregation and Excited States. *Macroheterocycles* (2015) 8:279–83. doi:10.6060/mhc150459l
42. Feit MD, and Fleck JA. Solution of the Schrödinger Equation by a Spectral Method II: Vibrational Energy Levels of Triatomic Molecules. *J Chem Phys* (1983) 78:301–8. doi:10.1063/1.444501
43. Liu Z, Cavaletto SM, Ott C, Meyer K, Mi Y, Harman Z, et al. Phase Reconstruction of Strong-Field Excited Systems by Transient-Absorption Spectroscopy. *Phys Rev Lett* (2015) 115:033003. doi:10.1103/PhysRevLett.115.033003
44. Becquet V, and Cavaletto SM. Transient-absorption Phases with Strong Probe and Pump Pulses. *J Phys B: At Mol Opt Phys* (2018) 51:035501. doi:10.1088/1361-6455/aa8e6a
45. Chahraoui D, Valat P, and Kossanyi J. Fluorescence of Phthalocyanines: Emission from an Upper Excited State. *Res Chem Intermediates* (1992) 17:219–32. doi:10.1163/156856792X00146

Conflict of Interest: The authors declare that the research was conducted in the absence of any commercial or financial relationships that could be construed as a potential conflict of interest.

frontiers in Physics

ORIGINAL RESEARCH
published: 14 June 2021
doi: 10.3389/fphy.2021.675375

Electronic Currents and Magnetic Fields in H_2^+ Induced by Coherent Resonant Bichromatic Circularly Polarized Laser Pulses: Effects of Orientation, Phase, and Helicity

André D. Bandrauk[1]*, *Szczepan Chelkowski*[1] and *Kai-Jun Yuan*[1,2]†

[1]*Laboratoire de Chimie Théorique, Faculté des Sciences, Université de Sherbrooke, Sherbrooke, QC, Canada,* [2]*Institute of Atomic and Molecular Physics, Jilin University, Jilin, China*

We theoretically study pulse phase and helicity effects on ultrafast magnetic field generation in intense bichromatic circularly polarized laser fields. Simulations are performed on the aligned molecular ion H_2^+ from numerical solutions of corresponding time-dependent Schrödinger equations. We demonstrate how electron coherent resonant excitation influences the phase and helicity of the optically induced magnetic field generation. The dependence of the generated magnetic field on the pulse phase arises from the interference effect between multiple excitation and ionization pathways, and is shown to be sensitive to molecular alignment and laser polarization. Molecular resonant excitation induces coherent ring electron currents, giving enhancement or suppression of the phase dependence. Pulse helicity effects control laser-induced electron dynamics in bichromatic circular polarization excitation. These phenomena are demonstrated by a molecular attosecond photoionization model and coherent electron current theory. The results offer a guiding principle for generating ultrafast magnetic fields and for studying coherent electron dynamics in complex molecular systems.

Keywords: magnetic field generation, intense laser pulses, coherent ring currents, multiple ionization pathways, bichromatic circularly polarized pulse

OPEN ACCESS

Edited by:
Robert Gordon,
University of Illinois at Chicago,
United States

Reviewed by:
Hirohiko Kono,
Tohoku University, Japan
Joern Manz,
Freie Universität Berlin, Germany

Correspondence:
André D. Bandrauk
Andre.Dieter.Bandrauk@usherbrooke.ca

†*Deceased*

Specialty section:
This article was submitted to Physical Chemistry and Chemical Physics,
a section of the journal
Frontiers in Physics

Received: *03 March 2021*
Accepted: *14 May 2021*
Published: *14 June 2021*

Citation:
Bandrauk AD, Chelkowski S and Yuan K-J (2021) Electronic Currents and Magnetic Fields in H_2^+ *Induced by Coherent Resonant Bichromatic Circularly Polarized Laser Pulses: Effects of Orientation, Phase, and Helicity.*
Front. Phys. 9:675375.
doi: 10.3389/fphy.2021.675375

1 INTRODUCTION

Imaging and manipulating molecular electron dynamics is one of the main goals in photophysical processes and photochemical reactions. Advances in synthesizing ultrashort intense laser pulses [1, 2] allow one to visualize and control electrons on their natural attosecond (1 as = 10^{-18} s) timescale and sub-nanometer dimension [3–6]. One important application of ultrashort circularly polarized attosecond pulses is to produce strong magnetic field pulses from electronic ring currents in atomic and molecular systems [7–13]. By creating unidirectional constant valence-type electronic currents in molecules with circularly polarized UV laser pulses, static magnetic fields [7–9] can be efficiently generated by the excitation of resonant degenerate orbitals. These laser-induced magnetic fields are much larger than those obtained by traditional static field methods [14]. In [8], it has been found that for the hydrogen-like atom, the existence of ring currents is related to the presence of the states having nonzero magnetic orbital momentum magnetic quantum numbers. Surprisingly, the strongest magnetic field originates from the $2p_\pm$ orbital in the hydrogen-like atom, which can be prepared *via* resonant $1s \rightarrow 2p_\pm$ transition. One also finds that, in general, ring electronic currents are dependent on the symmetry of the molecular orbitals. The helicity of driving circularly polarized pulses [15] can be used to reconstruct attosecond charge migration [16–19]. Linearly polarized laser pulses can also induce excited ring currents by controlling the rotation direction of π electrons in planar/nonplanar aromatic molecules [20–22]. We have proposed methods previously to create “spinning” continuum electrons which can be generated and remain localized on sub-nanometer molecular dimensional scales [23, 24], offering a way to produce high-order harmonic generation (HHG). Time-dependent circular coherent electron wave packets (CEWPs) and currents are created as superposition of bound-continuum states. They thus become the source of intense time-dependent internal magnetic fields generated on attosecond timescale. The induced attosecond magnetic fields have been shown to be a function of various laser pulse parameters, such as the pulse intensity, wavelength, and duration [25, 26], thus providing new tools for control of ultrafast optical magnetism generation [27–31].

Investigating ultrafast electron dynamics by bichromatic circularly polarized attosecond laser pulses with corotating or counter-rotating components has been attracting considerable attention in the field of light–matter interactions. It has already been shown that counter-rotating intense ultrafast circularly polarized pulses can induce re-collision, thus ensuring efficient HHG [32–35], the new source of circularly polarized X-ray attosecond pulses. These counter-rotating laser fields are now being adopted to produce circularly polarized HHG with nonzero initial angular momenta [36–38]. With counter-rotating circularly polarized laser pulses, the technique of double optical gating can be efficiently employed for producing isolated elliptically polarized attosecond pulses [39]. Bichromatic laser fields have also been adopted to probe atomic and molecular structure by photoelectron momentum distributions [40]. By combination of two circularly polarized attosecond ultraviolet (UV) pulses, spiral electron vortices in photoionization momentum distributions have been predicted theoretically in both atomic [41–43] and molecular systems [44–46], which are shown to be sensitive to the helicity of the bichromatic fields. Recent experiments have demonstrated this fact by focusing on multiphoton femtosecond ionization of potassium atoms [47, 48]. Most recently, above-threshold ionization obtained previously by a bicircular field has been reported [49–52].

In this work, we present attosecond magnetic field generation and electron currents under molecular resonant excitation in bichromatic attosecond circular polarization processes. Such ultrafast attosecond pulses have been generated by current laser techniques from circularly polarized HHG [53–55]. Numerical simulations are performed on the aligned molecular ion H_2^+ at equilibrium by numerically solving the corresponding three-dimensional (3D) time-dependent Schrödinger equation (TDSE). Ultrafast magnetic field generation has been studied previously by bichromatic circularly polarized laser pulses [56, 57]. It has shown that the interference effect between multiple ionization pathway influences the magnetic field generation. However, the effect of the coherent electron currents in bicircular magnetic field processes under molecular resonant excitation has not been presented. We focus here on the pulse phase and helicity-dependent magnetic field generation. We demonstrate molecular resonant excitation effects by comparing the dependence of the generated ultrafast magnetic field on the relative carrier-envelope phase (CEP) and the helicity of pulses at different molecular alignments. It is also found that attosecond charge migration arising from coherent resonant excitation induces coherent electron ring currents in molecules, leading to an absence of the CEP dependence. Induced electron ring currents resulting from molecular coherent resonant excitation are shown to be an important factor in bichromatic magnetic field generation. These results allow to control ultrafast magnetic fields, leading to molecular attosecond charge migration dynamics. Since molecular vibrational and rotational effects occur on the femtosecond ($1\,\text{fs} = 10^{-15}\,\text{s}$) and picosecond ($1\,\text{ps} = 10^{-12}\,\text{s}$) timescales, fixed nuclei simulations are valid and used to describe ultrafast magnetic field generation processes on the attosecond timescale.

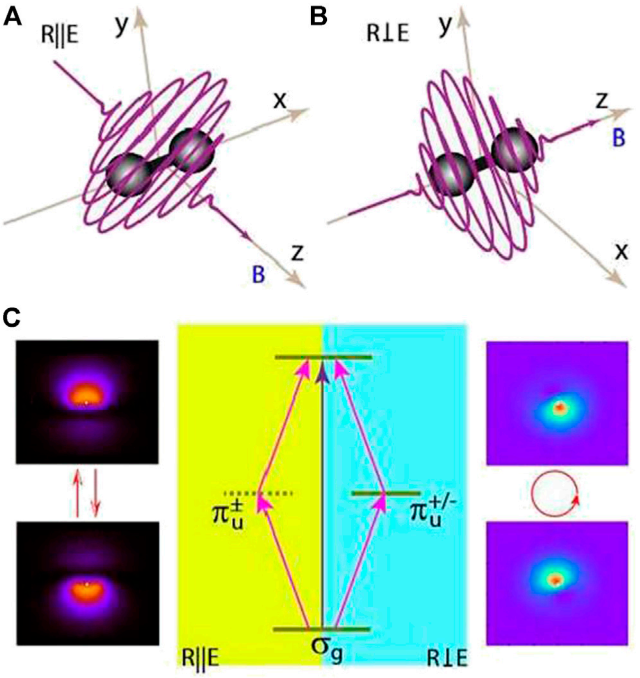

FIGURE 1 | Illustration of ultrafast magnetic field generation **B** under resonant excitation of H_2^+ aligned along the *x/z* axis by bichromatic co- and counter-rotating circularly polarized XUV pulses $\mathbf{E}(t)$ with their field vectors polarized in the (x, y) plane. Two excitation processes for the molecule axis parallel and perpendicular to the laser (x, y) polarization plane, that is, **(A)** in plane $\mathbf{R} \parallel \mathbf{E}$ and **(B)** around axis $\mathbf{R} \perp \mathbf{E}$, are compared. **(C)** Molecular $\sigma_g - \pi_u^\pm$ resonant excitation and ionization are shown for different molecular alignments, and corresponding evolutions of coherent electron wave packet density distributions at different times. Protons are at ±R/2 = ±1 a.u.

The article is organized as follow: We briefly describe the computational method for solving TDSEs of the aligned molecular ion H_2^+ to simulate electron currents and magnetic field generation in **Section 2**. The results of ultrafast magnetic fields by intense bichromatic circularly polarized attosecond XUV laser pulses are presented and discussed in **Section 3**. In **Section 4**, we finally summarize our findings. Throughout this article, atomic units (au) which are defined by setting $\hbar = e^2 = m_e = 1$ are used unless otherwise stated.

2 NUMERICAL METHODS

For the aligned molecule ion H_2^+ within Born–Oppenheimer approximation static nuclear frames, the corresponding 3D TDSE in the cylindrical coordinate $\mathbf{r} = (\rho, \theta, z)$ reads as

$$i\frac{\partial}{\partial t}\psi(\mathbf{r},t) = \left[-\frac{1}{2}\nabla_r^2 + V_{en}(\mathbf{r},\mathbf{R}) + V_L(\mathbf{r},t)\right]\psi(\mathbf{r},t), \qquad (1)$$

with the Laplacian

$$-\frac{1}{2}\nabla_{\mathbf{r}}^2 = -\frac{1}{2\rho}\frac{\partial}{\partial\rho}\left(\rho\frac{\partial}{\partial\rho}\right) - \frac{1}{2\rho^2}\frac{\partial^2}{\partial\theta^2} - \frac{1}{2}\frac{\partial^2}{\partial z^2}, \qquad (2)$$

where $V_{en}(\mathbf{r},\mathbf{R})$ is the electron-nuclear potential in which we fixed the internuclear separation to the equilibrium separation and $|\mathbf{R}| = 2$ au. The circularly polarized laser pulse propagates along the z axis, perpendicular to the (x,y) plane, with $x = \rho\cos\theta$ and $y = \rho\sin\theta$, as shown in **Figure 1**. The radiative interaction between the laser field and the electron $V_L(\mathbf{r}) = \mathbf{r}\cdot\mathbf{E}(t)$ is described in the length gauge for circularly polarized pulses of frequencies ω_1 and ω_2.

$$\begin{aligned}\mathbf{E}(t) &= \mathbf{E}_1(t) + \mathbf{E}_2(t)\\ &= Ef(t)\begin{cases}\widehat{e}_x\left[\cos(\omega_1 t + \phi_1) + \cos(\omega_2 t + \phi_2)\right]\\ \widehat{e}_y\left[\sin(\omega_1 t + \phi_1) + \epsilon\sin(\omega_2 t + \phi_2)\right]\end{cases},\end{aligned} \qquad (3)$$

where $\widehat{e}_{x/y}$ is the laser polarization direction, and the symbol $\epsilon = \pm 1$ denotes the helicity of combined fields, that is, corotating ($\epsilon = +1$) or counter-rotating ($\epsilon = -1$) components. ϕ_1 and ϕ_2 are CEPs of the pulses $\mathbf{E}_1(t)$ and $\mathbf{E}_2(t)$, respectively. A smooth $\sin^2(\pi t/T_{lp})$ pulse envelope $f(t)$ for maximum amplitude E, intensity $I = I_x = I_y = c\varepsilon_0 E^2/2$, and duration $T_{lp} = n\tau$ is adopted, where one optical cycle period $\tau_{1,2} = 2\pi/\omega_{1,2}$.

The 3D TDSE in **Eq. 1** is propagated by a second-order split operator method which conserves unitarity in each time step Δt combined with a fifth-order finite difference method and Fourier transform technique in the spatial steps $\Delta\rho$, Δz, and $\Delta\theta$ [59, 60]. The initial electron wave function $\psi(\mathbf{r}, t = 0)$ is prepared in the ground $1s\sigma_g$ state calculated by propagating an initial appropriate wave function in imaginary time using the zero-field TDSE in **Eq. 1**. The time step is taken to be $\Delta t = 0.01$ au $= 0.24$ as. The spatial discretization is $\Delta\rho = \Delta z = 0.25$ au for a radial grid range $0 \le \rho \le 128$ au (6.77 nm) and $|z| \le 32$ au (1.69 nm), and the angle grid size $\Delta\theta = 0.025$ radian. To prevent unphysical effects due to the reflection of the wave packet from the boundary, we multiply $\psi(\rho,\theta,z,t)$ by a "mask function" or absorber in the radial coordinate ρ with the form $\cos^{1/8}[\pi(\rho - \rho_a)/2\rho_{abs}]$. For all results reported here, we set the absorber domain at $\rho_a = \rho_{max} - \rho_{abs} = 104$ au with $\rho_{abs} = 24$ au, exceeding well the field-induced electron oscillation $\alpha_d = E/\omega_{1/2}^2$ of the electron [25]. The time-dependent probability current density is defined by the quantum expression in the length gauge,

$$\mathbf{j}(\mathbf{r},t) = \frac{i\hbar}{2m_e}\left[\psi(\mathbf{r},t)\nabla_{\mathbf{r}}\psi^*(\mathbf{r},t) - \psi^*(\mathbf{r},t)\nabla_r\psi(\mathbf{r},t)\right], \qquad (4)$$

where $\psi(\mathbf{r},t)$ is the exact Born–Oppenheimer (static nuclei) electron wave function obtained from the TDSE in **Eq. 1**, and $\nabla_{\mathbf{r}} = e_\rho\nabla_\rho + e_\theta\nabla_\theta/\rho + e_z\nabla_z$ is the momentum operator in cylindrical coordinates. Then the corresponding *time-dependent* magnetic field is calculated using the following classical Jefimenko equation [61]:

$$\mathbf{B}(\mathbf{r},t) = -e\frac{\mu_0}{4\pi}\int\left[\frac{\mathbf{j}(\mathbf{r}',t_r)}{|\mathbf{r}-\mathbf{r}'|^3} + \frac{1}{|\mathbf{r}-\mathbf{r}'|^2 c}\frac{\partial\mathbf{j}(\mathbf{r}',t_r)}{\partial t}\right]\times(\mathbf{r}-\mathbf{r}')d^3\mathbf{r}', \qquad (5)$$

where $t_r = t - r/c$ is the retarded time and $\mu_0 = 4\pi\times10^{-7}$ NA^{-2} (6.692×10^{-4} au) is the permeability of free space. Units of $B(\mathbf{r},t)$ are teslas (1 T $= 10^4$ Gauss) if the elementary charge e is in Coulombs. For the static zero-field time-independent conditions occurring after the pulse duration, **Eq. 5** reduces to the classical Biot–Savart law, that is, $B(\mathbf{r},t) = -e(\mu_0/4\pi)(v\times r)/r^3$ [61]. Note that the retardation effects due to r/c = 0.35 attoseconds (where for an estimate r = R = 2 au. is used) are negligible.

Of note is that equation **Eq. 4** defines the quantum probability current (not the electric current) as defined in any quantum mechanics textbook. The electron electric current used in the Biot–Savart law in **Eq. 5** is therefore $\mathbf{j}_{\text{electric}} = -e\mathbf{j}$. This explains the sign (−) in **Eq. 5**, e = 1 in atomic units.

3 RESULTS AND DISCUSSIONS

The ground and excited states of H_2^+ ion and its electron potentials, $1s\sigma_g$, $1s\sigma_u$, $2s\sigma_g$, $2s\sigma_g$, $1\pi_u$, *etc.*, are well documented in [65]. Numerical solutions of the TDSE for H_2^+ aligned with the laser polarization (x–y) plane, that is, $\mathbf{R} \parallel$ to the x-axis with the electric field vector $\mathbf{E}(t)$ rotating in the (x,y) plane (**Figure 1A**), are used for obtaining time-dependent probabilities P(t) of the $1s\sigma_g$ and $2p\pi_u$ states at equilibrium R = 2 au. excited by a 70-nm pulse at two different intensities, $I = 2\times10^{14}$ W/cm^2 and $I = 1\times10^{15}I = 1\times10^{15}$ W/cm^2, by a five-cycle pulse (one cycle = 0.234 fs = 234 as). Thus, at $I = 2\times10^{14}$, **Figure 2A**, one sees no significant ionization, whereas at $I = 1\times10^{15}$ W/cm^2, **Figure 2B**, the $2p\pi_u$ state is 85% occupied, and still one sees little ionization. In conclusion, short few-cycle intense and resonant pulses contribute little ionization with major excitation of the resonant state, such as the $2p\pi_u$ state at 70 nm and some Rydberg states above the $2p\pi_u$ state shown in 1.

We investigate laser-induced highly nonlinear optical effects using pairs of bichromatic circularly polarized laser pulses. We use $\lambda_1 = 70$ nm ($\omega_1 = 0.65$ au) circularly polarized pulse in combination with $\lambda_2 = 35$ nm ($\omega_2 = 2\omega_1 = 1.3$ au) circularly polarized pulse. Pairs of circularly polarized harmonics of different frequency and helicity can easily be prepared by a combination of pairs of counter-rotating circularly polarized laser pulses at different frequencies [62]. The molecular ion H_2^+ is aligned along the x/z axis, the two X-ray ultra violet (XUV) pulses with their field polarization vectors in the (x,y) plane propagate along the z axis, as illustrated in **Figure 1A**, for

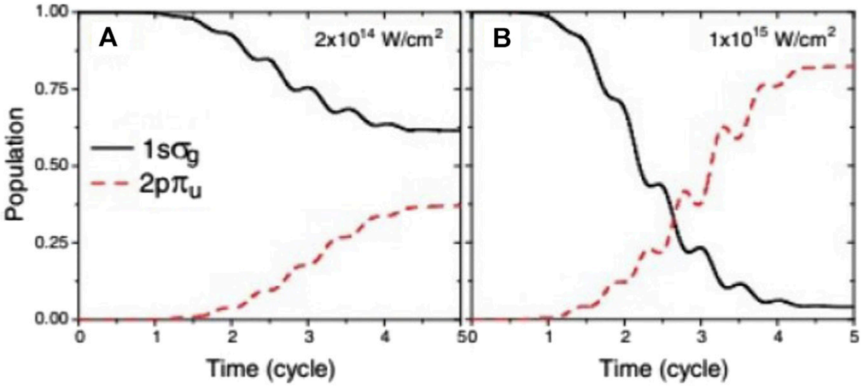

FIGURE 2 | Time-dependent probability density $\mathcal{D}(t)$ for in-plane excitation of (black solid line) the ground $1s\sigma_g$ state and of (red dashed line) the excited $2p\pi_u$ by λ_1 = 70 nm (ω_1 = 0.65 au) and 580 as FWHM circularly polarized UV laser pulses at two different pulse intensities: **(A)** $I = 2 \times 10^{14}$ W/cm^2 and **(B)** $I = 1 \times 10^{15}$ W/cm^2. 1-cycle = 234 as.

in-plane excitation, and **Figure 1B** for around axis excitation. With the pulse frequency$\omega_1 = \Delta E$ and the energy difference $\Delta E = E_{\pi_u} - E_{\sigma_g} = 0.65$ au, a resonant excitation with the ground $1s\sigma_g$ state and the excited π_u electronic states occurs. Moreover, with $\omega_2 = 2\omega_1$, such bichromatic laser pulses can also produce CEWPs with the same kinetic energies, $E_e = 2\omega_1 - I_p = \omega_2 - I_p$, by combination of multiple multiphoton transitions to Rydberg and the continuum state, thus leading to electron interference between the two ionization pathways. Since the induced electron currents are localized in the laser (x, y) polarization plane, the generated magnetic field is concentrated along the z axis. We therefore only present the results of the magnetic field B along the z axis.

As illustrated in **Figure 1C**, the coherent resonant excitation between the ground $1s\sigma_g$ state and the excited π_u state by the λ_1 = 70 nm circularly polarized laser pulse is dependent on the molecular alignment. In the case of $\mathbf{R} \parallel \mathbf{E}$, the in-plane degenerates perpendicular excitation, $\pi_u^{\pm} \leftarrow \sigma_g$ for different angular momenta $\Delta m = \pm 1$ dominates, and the electron density distribution evolves nearly perpendicular to the molecular axis [63], whereas in the case of $\mathbf{R} \perp \mathbf{E}$, the produced electron wave packets move around the molecular axis due to individual $\pi_u^{+/-} \leftarrow \sigma_g$ transitions $\Delta m = 1$ or -1 [64]. Meanwhile, two ω_1 and single ω_2 transitions to the continuum ($2\omega_1 = \omega_2 > I_p$) occur, leading to interference effects between these two excitation ionization channels. We show how coherent resonant excitation influences the interference effect on the magnetic field generation. We present the effects of the pulse phase on the attosecond magnetic field generation under the resonant excitation with various molecular alignments. Processes with different helicities ϵ, that is, corotating ($\epsilon = +1$) and counter-rotating ($\epsilon = -1$) pulse combinations, are compared as well.

3.1 Dependence of Generated Magnetic Fields on Circular Error Probability and Molecular Alignments

We first present the counter-rotating ($\epsilon = -1$) dynamics. **Figure 3** shows results of the generated maximum magnetic field B at the molecular center $\mathbf{r} = 0$ by intense single and bichromatic circularly polarized attosecond pulses described in **Eq. 3** [57]. Two cases of molecular excitation–ionization processes in the molecular ion H_2^+ aligned along a) the x axis, $\mathbf{R} \parallel \mathbf{E}$, and b) the z axis, $\mathbf{R} \perp \mathbf{E}$, are compared for the bichromatic laser pulses with their field polarization vectors in the (x,y) plane, as illustrated in **Figure 1**. The corresponding generated magnetic fields mainly lie in both cases along the z axis. The pulse wavelengths are, respectively, λ_1 = 70 nm (ω_1 = 0.65 au) and λ_2 = 35 nm (ω_2 = 1.3 au). We always fix the pulse intensities $I = 1 \times 10^{14}$ W/cm^2 (E = 0.0534 au) and durations T_{lp} = 48.3 au = 1.16 fs, corresponding to 580 as FWHM (full width at half maximum), that is, $5\tau_1$ for ω_1 pulse and $10\tau_2$ for ω_2 pulse. We also set the pulse CEP $\phi_1 = 0$ and vary the CEP ϕ_2 from 0 to 2π, that is, the relative CEP is $\phi = \phi_2 - \phi_1 = \phi_2$. **Figure 3** shows the CEP ϕ dependence of the generated magnetic fields with different molecular alignments.

3.1.1 Resonant Excitation in the Case of In-Plane R ∥ E

For the case of in-plane excitation with the molecule axis parallel to the laser (x, y) polarization plane as shown in **Figure 1A**, the generated magnetic field B at the molecular center is critically sensitive to the relative pulse CEP ϕ, as shown in **Figure 3A**. It is found that as the CEP ϕ varies from 0 to 2π, B oscillates periodically as $\cos(\phi)$. The maximum and minimum values of the magnetic field are B = 0.225 T and 0.165 T at $\phi \approx 0$ (or 2π) and π, respectively. For comparison, we also simulate the results of the induced magnetic field B with single-color circularly polarized attosecond pulses at separated wavelengths λ = 70 and 35 nm. The other parameters are the same as those used in **Figure 3A**. For the two single-pulse processes, the corresponding maximum strengths of induced magnetic fields at the molecular center are, respectively, $B_{\omega_1}^{\parallel}$ = 0.194 T and $B_{\omega_2}^{\parallel}$ = 0.022 T. Due to the $\sigma_g - \pi_u^+$ resonant excitation, the magnetic field induced by the resonant 70 pulse is much stronger than that induced by the nonresonant 35-nm pulse, $B_{\omega_1}^{\parallel} \approx 8.8 B_{\omega_2}^{\parallel}$. The sum value of the generated magnetic fields $B_s^{\parallel} = B_{\omega_1}^{\parallel} + B_{\omega_2}^{\parallel}$ is slightly smaller than the

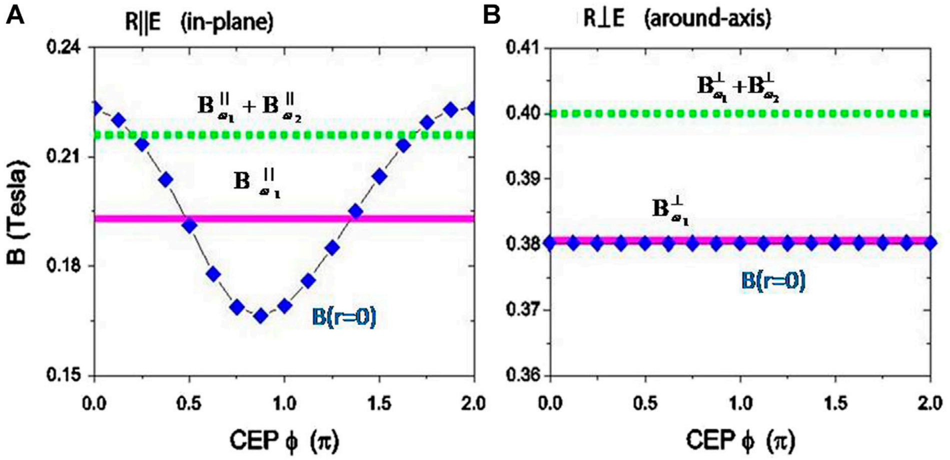

FIGURE 3 | Maximum magnetic fields $B(\mathbf{r}=0)$ (blue diamond) at the molecular center as a function of CEP $\phi=\phi_2-\phi_1$ for the aligned molecule H_2^+ in bichromatic counter-rotating ($\epsilon=-1$) circularly polarized laser pulses with their field vectors polarized in the (x,y) plane. Two cases are compared for the molecule aligned along **(A)** the x axis, in plane $\mathbf{R}\parallel\mathbf{E}$, and **(B)** the z axis, around axis $\mathbf{R}\perp\mathbf{E}$. Pulse wavelengths $\lambda_1=70$ nm ($\omega_1=0.65$ au) and $\lambda_2=35$ nm ($\omega_2=1.3$ au), intensities $I=1\times10^{14}$ W/cm^2 ($E=0.0534$ au), and duration $T_{lp}=5\tau_1=10\tau_2$ (580 as FWHM) are fixed. Red solid lines denote the generated magnetic field $B^{\|}_{\omega_1}=0.194$ T and $B^{\perp}_{\omega_1}=0.382$ T by a single $\lambda=70$ nm circularly polarized laser pulse, and green dashed lines present the sum values of the magnetic fields $B^{\|}_{S}=B^{\|}_{\omega_1}+B^{\|}_{\omega_2}=0.216$ T and $B^{\perp}_{S}=B^{\perp}_{\omega_1}+B^{\perp}_{\omega_2}=0.401$ T.

maximum field $B=0.225$ T of the bicircular process. Comparing to the single-color circular processes, one notes that the sensitivity of the induced magnetic field B to the CEP ϕ in **Figure 3A** results from the interference effects between $\lambda_1=70$ nm and $\lambda_2=35$ nm optical processes.

From **Eq. 4**, **5**, for a simple ring current flowing in the ring having the radius r, one can derive a simple relation:

$$B\sim \mathcal{D}v/r^2, \tag{6}$$

where $\mathcal{D}$ is the probability density and v is the electron speed. This simple relation can be obtained in the following way: from the quantum definition of the current given in **Eq. 4** in which we assume that ψ is the plane wave, that is, $\psi=\sqrt{\mathcal{D}}\exp(i\mathbf{p}\cdot\mathbf{r}/\hbar)$, where $\mathbf{p}$ is the electron momentum tangent to the ring, one gets after performing the ∇ derivation a simple relation $j=\mathcal{D}\frac{p}{m_e}=\mathcal{D}v$ as shown in [58]. Next, for the case of the electron current mainly localized in a plane one gets from **Eq. 5**, that is, $B\sim j/r^2\sim\mathcal{D}v/r^2$, we thus derived **Eq. 6**.

Thus, in **Eq. 6**, the magnetic field is proportional to the electron probability density $\mathcal{D}$ and the electron velocity which originates from the electron current density $j=\mathcal{D}v$ [58]. Density $\mathcal{D}$ for the case of resonant transitions corresponds to the excited state transition probability, which is determined by the intrinsic transition dipole of molecules and the electric field strength as discussed in detail in **Supplementary Appendix A2**. Therefore, the dependence of the generated magnetic field in **Figure 3** on the pulse CEP ϕ mainly comes from the transition probability $\mathcal{D}$ which is influenced by the interference effect between color $\lambda_1=70$ nm and $\lambda_2=35$ nm pulse nonlinear optical responses, as presented in **Supplementary Appendix A1**.

With the bichromatic counter-rotating circularly polarized pulse at $\lambda_1=70$ nm and $\lambda_2=35$ nm, two nonlinear responses can be triggered. By the $\lambda_1=70$ nm pulse, resonance-enhanced excitation ionization occurs where the molecule is resonantly excited from the σ_g state to the degenerate $\pi_u^{\pm}$ state with $\omega_1=E_e-E_g$ *via* a perpendicular transition. Meanwhile, the absorptions of two ω_1 photons and one $\omega_2=2\omega_1$ photon give rise to photoelectron wave packets with the same kinetic energies E_e in the continuum. The total photoionization probability is the sum of the two ionization excitation processes and their interference. As shown in **Supplementary Appendix A1**, the two ionization probabilities $\mathcal{D}^{(1)}$ and $\mathcal{D}^{(2)}$ are insensitive to the pulse phases, whereas the interference term $\mathcal{D}^{(1,2)}$ depends on the relative phase of the laser pulses and on the relative phase of the electron wave packets in the continuum. As a result, the total excitation probability density $\mathcal{D}=\mathcal{D}^{(1)}+\mathcal{D}^{(2)}+\mathcal{D}^{(1,2)}$ is also a cosine function of the relative pulse phase ϕ with the form $\mathcal{D}\sim\cos(\phi)$. The interference effect between the two processes modulates the total transition and current probabilities. Combining **Eq. 6** with Eqs 19 and 20 in **Supplementary Appendix A1**, one obtains $B\sim\cos(\phi)$, giving rise to a CEP dependence of the generated magnetic field, as illustrated in **Figure 3A** (blue diamond), B (r = 0).

3.1.2 Resonant Excitation in the Case of Around-Axis R ⊥ E

For around R axis excitation, **Figure 3B** shows phase-dependent magnetic field B generation in the process of molecule axis perpendicular to the laser (x,y) polarization plane, leading to around-axis currents. Comparing to the in-plane $\mathbf{R}\parallel\mathbf{E}$ case in **Figure 3A**, one sees that the oscillation of the magnetic field B with the relative phase ϕ is, however, strongly suppressed. As shown in **Figure 3B**, the magnetic field is almost insensitive to the phase ϕ, with a constant value of $B=0.38$ T. The magnetic fields generated by the individual bichromatic pulses are less than the sum of the two single 70 and 35 nm processes, that is, $B < B_s^{\perp} = B_{\omega_1}^{\perp} + B_{\omega_2}^{\perp} = 0.4$ T, where $B_{\omega_1}^{\perp} = 0.382$ T and $B_{\omega_2}^{\perp} = 0.019$ T. The bichromatic magnetic fields mainly arise from the single-photon 70 nm process, $B = B_{\omega_1}^{\perp}$, whereas the contribution from the absorption of single 35 nm (ω_2) or two 70 nm (ω_1) photons is weak and negligible, as shown in **Figure 3B**. This implies that the interference effect between the two ionization processes does not influence the bichromatic magnetic field generation. Of note is that for the single ω_1/ω_2 pulse case, the generated magnetic fields are also dependent on the molecular alignments and the pulse wavelength. At $\lambda = 70$ nm, $B_{\omega_1}^{\perp} \approx 2B_{\omega_1}^{\parallel}$, the perpendicular case is stronger, whereas at 35 nm, the generated magnetic fields are nearly equivalent, $B_{\omega_2}^{\perp} \approx B_{\omega_2}^{\parallel}$. The difference indicates essentially the importance of the around R axis ring electron currents in the resonant intermediate π_u electronic state.

For the optical responses in **Figure 3B** of the molecule H_2^+ perpendicular to the laser (x, y) polarization plane, $\mathbf{R} \perp \mathbf{E}$, **Figure 1B**, by a single 70-nm circularly polarized pulse, resonant excitation between the ground σ_g state and the excited π_u^+ state with magnetic quantum number $\Delta m = 1$ leads to ring electron currents in molecules [64, 67]. As shown in **Supplementary Appendix A2**, using the electronic angular continuity equation [16, 17],

$$\frac{d}{dt}\mathcal{D}(\mathbf{r}, t) + \frac{d}{d\theta} j_{\theta}^{\perp}(\mathbf{r}, t) = 0. \tag{7}$$

One obtains the laser-induced electron current $j_{\theta}^{\perp}(r, t)$ in the following form

$$j_{\theta}^{\perp}(\mathbf{r}, t) \sim \cos(\Delta E t + \theta). \tag{8}$$

Eq. 8 combined with Eqs. 21 and 26 shows that for the superposition electron state $\psi_c(r, t)$, the time-dependent electronic density $\mathcal{D}(r, t)$ and the induced angular current $j_{\theta}^{\perp}(r, t)$ evolve in time with the electron coherence period of $\Delta\tau^{(0)} = 2\pi/\Delta E$. Therefore, the total magnetic field B in the bichromatic circularly laser field is mainly generated from the electron currents in the coherent electron wave packet $\psi_c(r, t)$ in Eq. 21 by the λ =70 nm pulse. The contributions from the continuum electron wave packets with energy E_e by the 35-nm pulse are clearly very weak, that is, $B_{\omega_1}^{\perp} \approx 20B_{\omega_2}^{\perp}$, and therefore negligible. As a result, altering the relative CEP ϕ does not lead to a variance of the generated magnetic field B.

3.1.3 Laser-Induced Electron Currents in Molecules

For the magnetic field B generated by coherent electron currents in molecules, the evolution of the induced electron currents $j_{\boldsymbol{\theta}}(\mathbf{r}, t)$ with time t is determined by the coherent resonant excitation and the molecular alignments. **Figure 4** illustrates snapshots of angular electron probability currents $j_{\theta}^{\perp}(x, y, z = 0, t)$ at the center of H_2^+ obtained from **Eq. 4** at different times t (unit of $\tau = 2\pi/\omega_1 = \tau_1$) for the molecule H_2^+ perpendicular to the laser (x, y) polarization plane, $\mathbf{R} \perp \mathbf{E}$, **Figure 1**, leading to around R axis currents, $j_{\theta}^{\perp}(x, y, z = 0, t) = j_{\theta}^{\perp}(\rho\cos\theta, \rho\sin\theta, z = 0, t)$. The bichromatic counter-rotating ($\epsilon = -1$) circularly polarized XUV pulse at CEPs $\phi_1 = \phi_2 = 0$ is used to excite the molecule. It is found that the induced electron currents are asymmetric with respect to the molecular center and rotate with a period of τ around the z or molecular R axis in the (x, y) polarization plane with an anticlockwise direction, as predicted in **Eq. 8**. This confirms that the ring electron currents mainly arise from the coherent resonant excitation between the ground σ_g state and the excited π_u^+ state by the 70-nm circularly polarized pulse [64]. From such coherent electron currents, the generated magnetic fields are unidirectional, along the z/R axis. At the molecular center $z = 0$, the magnetic field is the sum of those at the two nuclei, $\pm R/2$. In the bichromatic circular polarized processes, the contributions of the magnetic field generation from the 70 nm pulse are dominant, which do not depend on the pulse phase. Therefore, varying the relative pulse CEP ϕ does not influence the generated magnetic field B, as illustrated in **Figure 3B**.

For comparison, in **Figure 5**, we also plot the in-plane electron probability current $j_{\theta}^{\parallel}(x, y, z = 0, t)$ at the center of the molecule H_2^+ aligned along the x axis, parallel to the laser polarization (x, y) plane, $\mathbf{R} \parallel \mathbf{E}$ in **Figure 1A**, of bichromatic counter-rotating circularly polarized pulses. Combining **Figure 4** with **Figure 5**, one sees that these time-dependent electron currents are sensitive to the molecular alignments. The joint $\sigma_g - \pi_u^{\pm}$ resonant excitations induce coherent electron currents. The induced electron probability currents are mainly localized along the molecular internuclear axis, that is, the resonant perpendicular atomic ($p_y \leftarrow s$) transitions dominate during the excitation processes. In this case, the coherent exited electronic state is given by

$$\pi_u^c(\mathbf{r}) = -i\left[\pi_u^+(\mathbf{r}) - \pi_u^-(\mathbf{r})\right]/2 = \pi_u^y(\mathbf{r}), \tag{9}$$

where $\pi_u^{\pm}(\mathbf{r}) = [\pi_u^x(\mathbf{r}) \pm i\pi_u^y(\mathbf{r})]/\sqrt{2}$ and $|\tilde{\pi}_u^{\pm}(\mathbf{r})|^2 = [|\pi_u^x(\mathbf{r})|^2 + |\pi_u^y(\mathbf{r})|^2]/2$. Then the corresponding interference term in the time-dependent electron density becomes (in cylindrical coordinates (ρ, θ, z) as shown in [9, 64] and in **Supplementary Appendix A2**)

$$\mathcal{D}_{(e,g)}(r, t) = 2c_g c_e \psi_g(r)\tilde{\psi}_e^{\pm}(\rho, z)\cos(\Delta E t)\sin(\theta), \tag{10}$$

and the time-dependent current

$$j_{\theta}^{\parallel}(r, t) = -2c_g c_e \psi_g(r)\tilde{\psi}_e^{\pm}(\rho, z)\Delta E\sin(\Delta E t)\cos(\theta), \tag{11}$$

where $\tilde{\psi}_e^{\pm}(\rho, z)$ is the absolute value of $\psi_e^{\pm}$ (see Eq. 23). It is found that the coherent density and current superposition terms in **Eqs. 10** and **11** follow the forms $\sim\sin(\theta)$ and $\cos(\theta)$. As a result, the coherent wave packets due to the $\sigma_g - \pi_u^{\pm}$ superposition oscillate along the y direction, perpendicular to the molecular axis, **Figure 1C**, whereas the corresponding currents oscillate mainly along the molecular axis, **Figure 4**. The generated magnetic field at the two molecular nuclear centers $\pm R/2$ has opposite phases [70]. Their overlap leads to a weak magnetic field at the molecule center $z = 0$. The generated magnetic field in **Figure 3A** therefore mainly results from the coherent excitation by bichromatic circularly polarized laser pulses.

3.2 Influence of the Pulse Helicity

We next study the process with a bichromatic corotating ($\epsilon = +1$) circularly polarized laser pulse. **Figure 6** shows the maximum generated magnetic field B at various relative pulse phases ϕ. The other laser parameters are the same as those

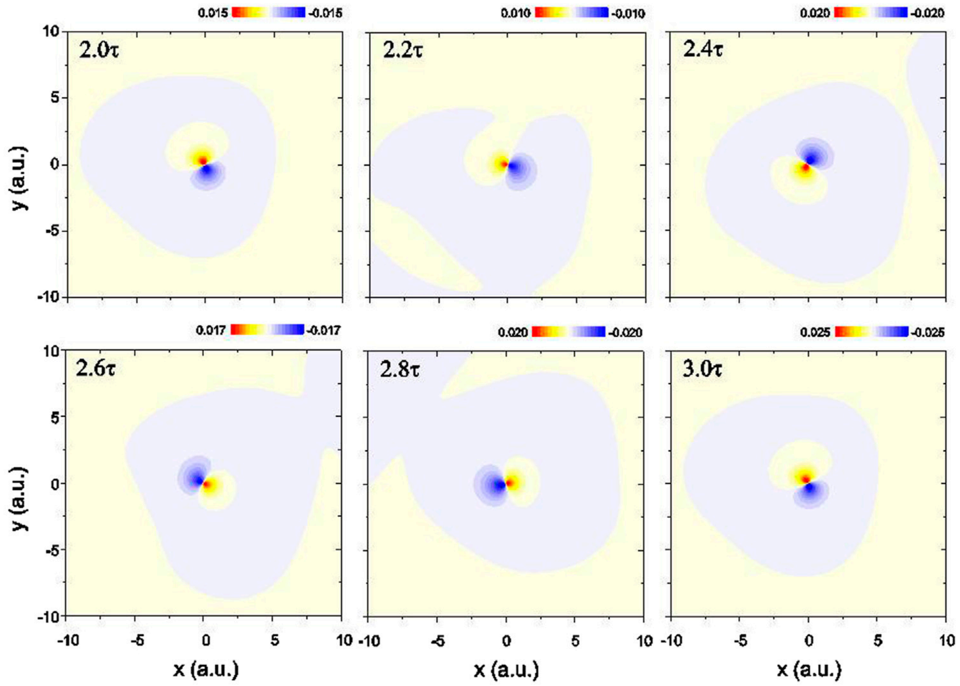

FIGURE 4 | Evolutions of the induced angular electron probability current density $j_{\theta}^{\perp}(x, y, z = 0, t)$ at different times t (unit of $\tau = \tau_1 = 2\pi/\omega_1$) for the molecule perpendicular to the laser polarization (x, y) plane, that is, around-axis $\mathbf{R} \perp \mathbf{E}$, by bichromatic counter-rotating $(\epsilon = -1)$ circularly polarized laser pulses at wavelengths $\lambda_1 = 70$ nm $(\omega_1 = 0.65$ au) and $\lambda_2 = 35$ nm $(\omega_2 = 1.3$ au), intensities $I = 1 \times 10^{14}$ W/cm^2 (E = 0.0534 au), duration $T_{lp} = 5\tau_1 = 10\tau_2$ (580 as FWHM), and relative CEP $\phi = 0$. Units of induced angular electron currents are arbitrary.

used in **Figure 3**. It was found that similar results are obtained in **Figure 6**, as the counter-rotating $(\epsilon = -1)$ case in **Figure 3**. For the case of $\mathbf{R} \parallel \mathbf{E}$, the magnetic field B varies as a sine function of the phase ϕ, as predicted in **Supplementary Appendix A1**. A phase $\pi/2$ shift occurs in the CEP ϕ-dependent magnetic field generation by the corotating bichromatic pulses. This mainly results from the different electron dynamics induced by the two pulses with opposite helicity. It was also found for the corotating $(\epsilon = +1)$ case the generated magnetic field depends on the molecular alignment. In **Figure 6B**, we see that for the case of **R⊥E**, the total generated magnetic field (blue diamond) is shown to be almost insensitive to the relative CEP ϕ, similar as in **Figure 3B**. At various pulse phases ϕ, the magnetic field $B = 0.38$ T is obtained. The $\sigma_g - \pi_u^+$ resonant excitation with $\Delta m = 1$ gives rise to unidirection ring electron currents, as illustrated in **Figure 3**. The contribution from the coherent electron wave packets $\psi_0(\mathbf{r}, t)$ in Eq. 21 dominates. The effects of the multiple pathway $(2\omega_1$ and $\omega_2)$ excitation interference can be neglected. Consequently, the generated magnetic field does not depend on the pulse CEP ϕ. The independence of the generated magnetic field on the pulse helicity ϵ also confirms the importance of the charge migration. This offers an approach to explore molecular structure and orbitals.

It should be noted that in the case of $\mathbf{R} \parallel \mathbf{E}$ in the general pulse $\mathbf{E}(t)$ with its field polarization vectors in the (x, y) plane, the strength of the generated magnetic field is slightly sensitive to the pulse helicity ϵ. As shown in **Figure 6A**, at $\epsilon = +1$ for corotating cases, the maximum magnetic field is $B = 0.206$ T at $\phi = 0.4\pi$, which is slightly weaker than that at $\epsilon = -1$ for counter-rotating cases in **Figure 3A**, where $B = 0.225$ T at $\phi = 0$. **Eq. 6** predicts that the induced magnetic field, in general, is proportional to the ratio of the electron velocity v and inversely proportional to r^2, where r is the radius of the excitation state of an electron under the influence of a strong laser field. The difference between the corotating and counter-rotating generated magnetic fields in **Figures 3A,6A** results from the laser-induced dynamics, which depends on the helicity of driving pulses.

According to the classical laser-induced electron motion models [68, 69], the electron velocity and radius are determined by the pulse amplitude E, frequency $2\omega_1 = \omega_2$, and helicity ϵ, which are given by

$$\dot{x}(t) = -\frac{E}{\omega_1}\left\{\sin(\omega_1 t) - \sin(\omega_1 t_0) + \frac{1}{2}\left[\sin(\omega_2 t) - \sin(\omega_2 t_0)\right]\right\},$$
$$\dot{y}(t) = -\frac{E}{\omega_1}\left\{\cos(\omega_1 t_0) - \cos(\omega_1 t) + \frac{\epsilon}{2}\left[\cos(\omega_2 t_0) - \cos(\omega_2 t)\right]\right\}, \tag{12}$$

and the corresponding electron displacements are

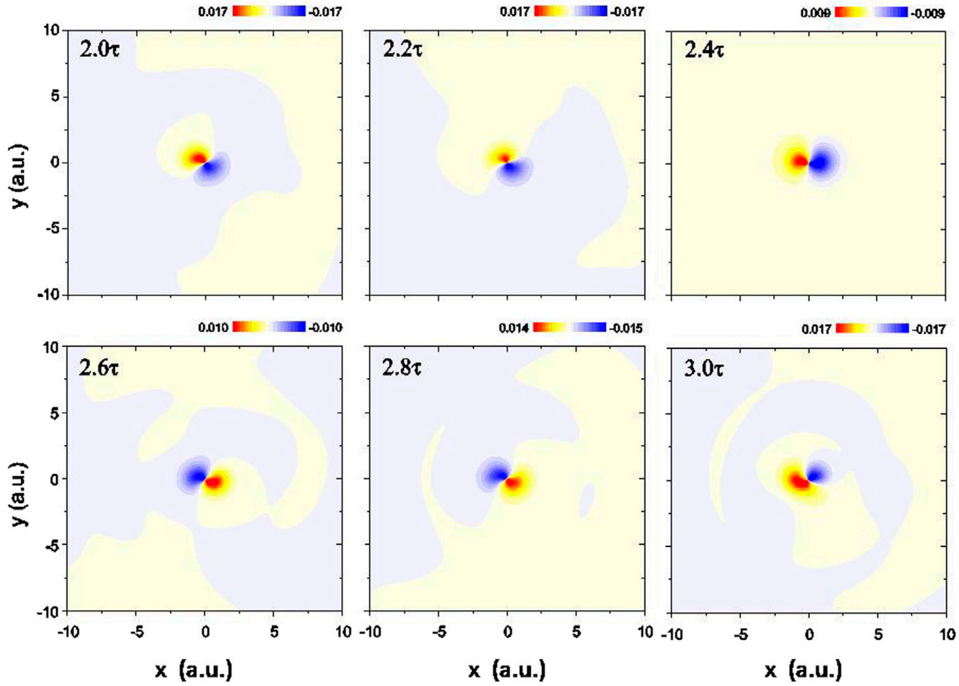

FIGURE 5 | Time dependence of the induced angular probability electron current $j_\theta^{\parallel}(x, y, z = 0, t)$ at different moments t (unit of $\tau = \tau_1 = 2\pi/\omega_1$) for the molecular axis parallel to the laser polarization (x, y) plane, that is, in-plane $\mathbf{R} \parallel \mathbf{E}$, by bichromatic counter-rotating ($\epsilon = -1$) circularly polarized laser pulses at wavelengths $\lambda_1 = 70$ nm ($\omega_1 = 0.65$ au) and $\lambda_2 = 35$ nm ($\omega_2 = 1.3$ au), intensities $I = 1 \times 10^{14}$ W/cm^2 (E = 0.0534 au), duration $T_{lp} = 5\tau_1 = 10\tau_2$ (580 as FWHM), and CEP $\phi = 0$. Units of induced angular electron probability currents are arbitrary.

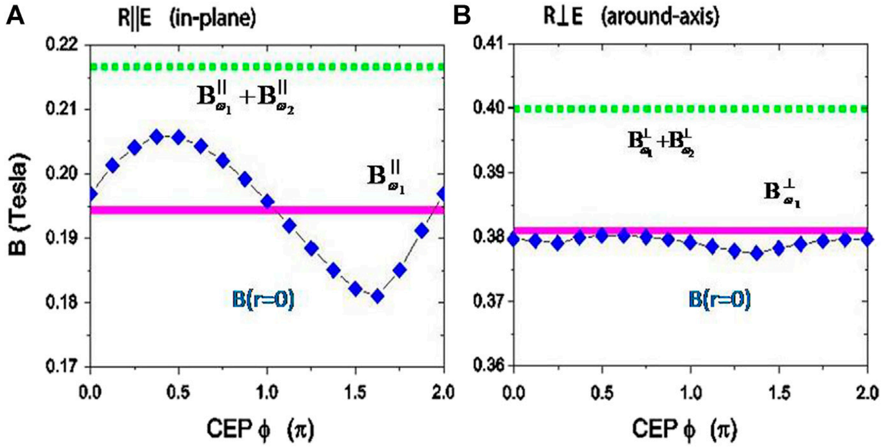

FIGURE 6 | Dependence of the maximum magnetic field B (blue diamond) at the molecular center, $r = 0$ on the relative pulse CEP $\phi = \phi_2 - \phi_1$ for the aligned molecule H_2^+ by bichromatic corotating ($\epsilon = +1$) circularly polarized laser pulses with their field vectors polarized in the (x, y) plane. Two cases are compared for the molecule aligned parallel to **(A)** the x axis and **(B)** the z axis, that is, parallel $\mathbf{R} \parallel \mathbf{E}$ in **Figure 1A** and perpendicular $\mathbf{R} \perp \mathbf{E}$ in **Figure 1B**, to the laser (x, y) polarization plane. Pulse wavelengths $\lambda_1 = 70$ nm ($\omega_1 = 0.65$ au) and $\lambda_2 = 35$ nm ($\omega_2 = 1.3$ au), intensities $I = 1 \times 10^{14}$ W/cm^2 ($E = 0.0534$ au), and duration $T_{lp} = 5\tau_1 = 10\tau_2$ (580 as FWHM) are fixed. Magenta solid lines denote the generated magnetic field $B^{\parallel}_{\omega_1} = 0.194$ T and $B^{\perp}_{\omega_1} = 0.382$ T by a single $\lambda = 70$ nm circularly polarized laser pulse, and green dashed lines are the sum values of the magnetic fields $B^{\parallel}_S = B^{\parallel}_{\omega_1} + B^{\parallel}_{\omega_2} = 0.216$ T and $B^{\perp}_S = B^{\perp}_{\omega_1} + B^{\perp}_{\omega_2} = 0.401$ T.

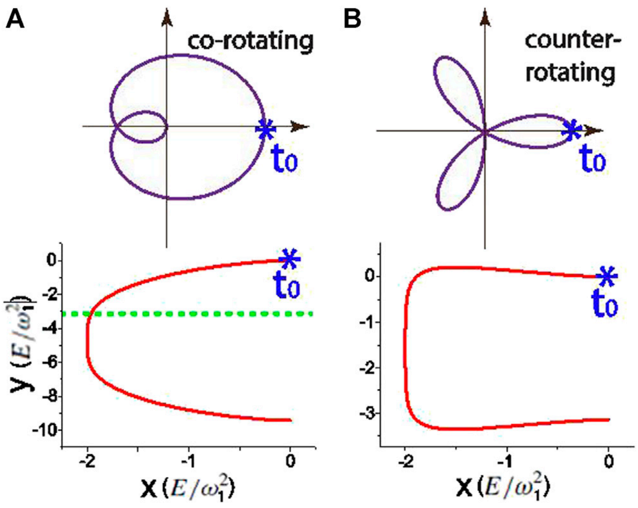

FIGURE 7 | Bichromatic ($\omega_2 = 2\omega_1$) circularly polarized (top row) electric field vectors and (bottom row) corresponding laser-induced displacement trajectories $[x(t), y(t)]$ of free electrons for **(A)** corotating ($\epsilon = +1$) and **(B)** counter-rotating ($\epsilon = -1$) helicity schemes. The initial position is $x(t_0) = y(t_0) = 0$, where t_0^* indicates the ionization time at the maxima of the combined fields. Green line corresponds to the minimum laser-induced radius r_0 of an ionized electron at frequency ω_1 and circular field amplitude E, $r_0 = (2E/\omega_1^2)\sqrt{1 + (\pi/2)^2}$ as shown in [23].

$$
\begin{aligned}
x(t) &= -\frac{E}{\omega_1^2}\{\cos(\omega_1 t_0) - \cos(\omega_1 t) - \omega_1 (t - t_0)\sin(\omega_1 t_0) \\
&\quad + \frac{1}{4}[\cos(\omega_2 t_0) - \cos(\omega_2 t) - \omega_2 (t - t_0)\sin(\omega_2 t_0)]\}, \\
y(t) &= -\frac{E}{\omega_1^2}\{\sin\omega_1 t_0 - \sin\omega_1 t + \omega_1 (t - t_0)\cos(\omega_1 t_0) \\
&\quad + \frac{\epsilon}{4}[\sin\omega_2 t_0 - \sin(\omega_2 t) + \omega_2 (t - t_0)\cos(\omega_2 t_0)]\},
\end{aligned}
\tag{13}
$$

where t_0 is the ionization time. **Figure 7** shows bichromatic circularly polarized laser field vectors with corotating and counter-rotating components and corresponding induced electron displacements, where zero initial position of one ionized electron is assumed, that is, $x(t_0) = y(t_0) = 0$. Such electron displacements can be measured by interfering spirals in photoelectron momentum distributions [71]. With the XUV pulses, a multiphoton ionization process occurs since the Keldysh parameter $\gamma > 1$ [72]. The initial electron velocities are nearly equivalent with $\sqrt{2(\omega_2 - I_p)}$. As shown in **Figure 7**, for the corotating $\epsilon = 1$ case, the radius of the continuum electron is much larger than that of the counter-rotating $\epsilon = -1$ case. The electron moves way quickly in the corotating field, whereas the counter-rotating field restricts the ionized electron around the molecular center. Because $B \sim j/r^2$ in **Eq. 5**, **6**, weaker maximum magnetic field is generated in the corotating case in **Figure 5A**. The dependence of generated magnetic fields on the pulse helicity ϵ reflects the laser-induced electron dynamics in bichromatic fields. The present simulation confirms that steering the radius of the induced electron currents allows to control generated magnetic fields with bichromatic circularly polarized pulses.

4 CONCLUSION

We present the ultrafast magnetic field generation in molecules from one electron molecular TDSE simulation under effects of coherent resonant excitation in bichromatic ($\omega_2 = 2\omega_1$) co- and counter-rotating circularly polarized laser fields. Numerical results are obtained for the aligned molecular ion H_2^+, which can be fully and exactly studied. We evaluate the generated magnetic field $B(\mathbf{r} = 0)$ at the molecular center at different relative CEP ϕ of the two circularly polarized pulses with both counter-rotating and corotating combinations. It is found that altering the CEP ϕ varies the maximum values of the generated magnetic field, $B(\mathbf{r} = 0)$, which is shown to be dependent on the molecule alignment, and is maximum for in-plane bichromatic excitation.

In a bichromatic (frequency $\omega_1 \neq \omega_2$) circularly polarized field, a $\sigma_g - \pi_u^\pm$ resonant excitation of individual magnetic components $m = \pm 1$ is triggered by the resonant ω_1 (70 nm) pulse. As a result, coherent electron currents between the ground σ_g state and the degenerate excited $\pi_u^\pm$ electronic state are induced in molecules. We compare two nonlinear responses for different molecular alignments:

- For the around-axis case, $\mathbf{R} \perp \mathbf{E}$, the molecule aligned along the z axis, perpendicular to the laser (x, y) polarization plane, **Figure 1B**, and the magnetic field mainly results from the coherent electron currents which are induced by one resonant ω_1 photon around R. The contribution from two ω_1 photons or one ω_2 photon is negligible. Varying the relative CEP ϕ does not influence the generated magnetic field. Similar results are obtained for both counter-rotating $\varepsilon = -1$, **Figure 3B**, and corotating $\varepsilon = +1$, **Figure 6B**, excitations, confirming the main role of the around-axis circular coherent electron current.
- For the in-plane case, $\mathbf{R} \parallel \mathbf{E}$, the molecule aligned parallel to the laser (x, y) polarization plane, **Figure 1A**, and the magnetic field generation is shown to be strongly dependent on the pulse phase ϕ, confirming the effects of multiple pathway ionization. The in-plane coherent electron currents generate the magnetic fields in the two nuclei with opposite phases and evolve perpendicular to the molecular R axis. Their superposition suppresses the magnetic field generation at the molecular center, **Figure 3**. The results we present arise mainly from the total electron currents by one ω_1 photon absorption, that is, the $\sigma_g - \pi_u^\pm$ resonant excitation, and two ω_1 or one ω_2 transition to the continuum. The generated magnetic field depends on the photoionization probability which is a function of the relative CEP ϕ Eq. 20. As a consequence of interference effects between the ω_1 and ω_2 photoionization pathways, altering their relative phase ϕ gives rise to a modulation of the generated magnetic field $B(\mathbf{r} = 0)$ at the molecular center with forms $\sim \cos(\phi)$ for counter-rotating and

$\sin(\phi)$ for corotating combinations. It is also shown that the maximum of the magnetic field for the counter-rotating case is larger than that for the corotating case because of the difference in laser-induced electron displacements, which depends strongly on the helicity of the driving pulse, **Figure 6**.

The present results in principle provide the importance of coherent electron dynamics and of control magnetic fields by bichromatic circularly polarized laser pulses. The dependence of the generated magnetic field on the relative phase and helicity of driving laser pulses also allows to characterize the property of laser pulses and probe coherent electron currents and to charge migration in molecules. Although a simple single electron molecular ion H_2^+ is used, similar electron dynamics phenomena should be predicted in more complex molecular systems [7, 27, 30, 73], thus offering an approach for controlling ultrafast magnetic field generation.

The above laser-induced molecular magnetic field generation on the electron's quantum timescale, the asec, was studied in the Born–Oppenheimer Approximation, that is, with static nuclei. Nuclear motion effects, that is, non–Born–Oppenheimer, are now being pursued on the near femtosecond timescale in order to include nuclear motion effects with bound and dissociation molecular states [83], de-and re-coherence in charge migration [84] and isotope effects in HD+ ultrafast ionization [85]. In the case of laser pulses propagating perpendicular to the molecular R-axis with the pulse electric fields in the molecular plane, **Figure 1A**, re-collision of electron currents with nuclei is an important nonlinear optical effect shown in **Figure 6** to be examined in detail for moving nuclei. Finally, the strong magnetic fields generated by intense ultrafast laser pulses are expected to interact with the electron currents themselves. Proton beams have been shown recently to be useful tools to measure intense magnetic field directions generated by current solenoids [86], thus confirming that laser-generated magnetic fields can interact also with nuclei in matter.

AUTHOR CONTRIBUTIONS

AB as a research leader directed this research formulated research goals and contributed in the scientific interpretation of results. KY wrote codes, executed codes, and prepared graphics but died last March before completing this research. SC participated in initial algorithm preparation for computer codes and did final preparation.

FUNDING

This work is supported in part by the National Natural Science Foundation of China (Grant Nos. 11974007 and 11574117) and the NSERC-RGPIN2019-05291.

ACKNOWLEDGMENTS

The authors also thank Compute Canada for access to massively parallel computer clusters, and the Natural Sciences and Engineering Research Council of Canada and the Fonds de Recherche du Québec-Nature et Technologies for supporting their research work.

SUPPLEMENTARY MATERIAL

The Supplementary Material for this article can be found online at: https://www.frontiersin.org/articles/10.3389/fphy.2021.675375/full#supplementary-material

REFERENCES

1. Krausz F., and Ivanov M. Attosecond Physics. *Rev Mod Phys* (2009) 81:163, 234. doi:10.1103/revmodphys.81.163
2. Chang Z., Corkum P. B., and Leone S. R. Attosecond optics and technology: progress to date and future prospects [Invited]. *J Opt Soc Am B* (2016) 33:1081. doi:10.1364/josab.33.001081
3. Chelkowski S., Yudin G. L., and Bandrauk A. D. Observing Electron Motion in Molecules. *J Phys B At Mol Opt Phys* (2006) 39:S409, S417. doi:10.1088/0953-4075/39/13/s14
4. Niikura H, Villeneuve DM, and Corkum PB. Mapping Attosecond Electron Wave Packet Motion. *Phys Rev Lett* (2005) 94:083003. doi:10.1103/physrevlett.94.083003
5. Shao HC, and Starace AF. Detecting Electron Motion in Atoms and Molecules. *Phys Rev Lett* (2010) 105:263201. doi:10.1103/physrevlett.105.263201
6. Vrakking M. J. J., and Elsaesser T.. X-rays inspire electron movies. *Nature Photon* (2012) 6:645, 647. doi:10.1038/nphoton.2012.247
7. Barth I., Manz J., Shigeta Y., and Yagi K.. Unidirectional Electronic Ring Current Driven by a Few Cycle Circularly Polarized Laser Pulse: Quantum Model Simulations for Mg–Porphyrin. *J Am Chem Soc* (2006) 128:7043, 7049. doi:10.1021/ja057197l
8. Barth I, and Manz J. Electric Ring Currents in Atomic Orbitals and Magnetic fields Induced by Short Intense Circularly Polarized π Laser Pulses. *Phys Rev A* (2007) 75:012510. doi:10.1103/physreva.75.012510
9. Barth I., Serrano-Andrés L., and Seideman T. Nonadiabatic Orientation, Toroidal Current, and Induced Magnetic Field in BeO Molecules. *The Journal of Chemical Physics* (2008) 129:164303. doi:10.1063/1.2994737
10. Barth I, and Manz J. Quantum Switching of Magnetic Fields by Circularly Polarized Optimized Laser Pulses. In: K Yamanouchi, G Gerber, and AD Bandrauk, editors. *Progress in Ultrafast Intense Laser Science VI*, 2021. Springer Verlag Berlin (2010) p. 2.
11. Barth I., Manz J., and Serrano-Andrés L. Quantum Simulations of Toroidal Electric Ring Currents and Magnetic fields in Linear Molecules Induced by Circularly Polarized Laser Pulses. *Chemical Physics* (2008) 347:263–271. doi:10.1016/j.chemphys.2007.09.037
12. Köksal K., and Koç F. The Effect of Twisted Light on the Ring-Shaped Molecules: The Manipulation of the Photoinduced Current and the Magnetic Moment by Transferring Spin and Orbital Angular Momentum of High Frequency Light. *Computational and Theoretical Chemistry* (2017) 1099:203, 208. doi:10.1016/j.comptc.2016.11.031
13. Zhang G, Murakami M, Lefkidis G, Hübner W, and George TF. *Introduction to Ultrafast , From Femtosecond Magnetism to High-Harmonic Generation*. CRC Press, Taylor & Francis Group (2020) doi:10.1201/9780429194832

14. Nobusada K, and Yabana K. Photoinduced Electric Currents in Ring-Shaped Molecules by Circularly Polarized Laser Pulses. *Phys Rev A* (2007) 75:032518. doi:10.1103/physreva.75.032518
15. Jia D., Manz J., Paulus B., Pohl V., Tremblay J. C., and Yang Y. Quantum Control of Electronic Fluxes during Adiabatic Attosecond Charge Migration in Degenerate Superposition States of Benzene. *Chemical Physics* (2017) 482:146, 159. doi:10.1016/j.chemphys.2016.09.021
16. Hermann G., Liu C., Manz J., Paulus B., Pérez-Torres J. F., Pohl V., et al. Multidirectional Angular Electronic Flux during Adiabatic Attosecond Charge Migration in Excited Benzene. *J Phys Chem A* (2016) 120:5360, 5369. doi:10.1021/acs.jpca.6b01948
17. Hermann G., Liu C., Manz J., Paulus B., Pohl V., and Tremblay J. C. Attosecond Angular Flux of Partial Charges on the Carbon Atoms of Benzene in Non-aromatic Excited State. *Chemical Physics Letters* (2017) 683:553, 558. doi:10.1016/j.cplett.2017.01.030
18. Ding H., Jia D., Manz J., and Yang Y. Reconstruction of the electronic flux during adiabatic attosecond charge migration in HCCI+. *Molecular Physics* (2017) 115:1813, 1825. doi:10.1080/00268976.2017.1287967
19. Jia D., Manz J., and Yang Y.. Generation of electronic flux during the femtosecond laser pulse tailored to induce adiabatic attosecond charge migration in. *Journal of Modern Optics* (2017) 64:960, 970. doi:10.1080/09500340.2016.1269216
20. Kanno M, Kono H, Fujimura Y, and Lin SH. Nonadiabatic Response Model of Laser-Induced Ultrafast π-electron Rotations in Chiral Aromatic Molecules. *Phys Rev Lett* (2010) 104:108302. doi:10.1103/physrevlett.104.108302
21. Mineo H., Lin S. H., and Fujimura Y. Coherent π-electron dynamics of (P)-2,2′-biphenol induced by ultrashort linearly polarized UV pulses: Angular momentum and ring current. *The Journal of Chemical Physics* (2013) 138:074304. doi:10.1063/1.4790595
22. Kanno M., Kono H., and Fujimura Y. Laser-Control of Ultrafast π-Electron Ring Currents in Aromatic Molecules: Roles of Molecular Symmetry and Light Polarization. *Applied Sciences* (2018) 8:2347. doi:10.3390/app8122347
23. Yuan K.-J., and Bandrauk A. D. Circularly polarized attosecond pulses from molecular high-order harmonic generation by ultrashort intense bichromatic circularly and linearly polarized laser pulses. *J Phys B At Mol Opt Phys* (2012) 45:074001. doi:10.1088/0953-4075/45/7/074001
24. Yuan KJ, Lu H, and Bandrauk AD. High-order-harmonic Generation in Molecular Sequential Double Ionization by Intense Circularly Polarized Laser Pulses. *Phys Rev A* (2015) 92:023415. doi:10.1103/physreva.92.023415
25. Yuan KJ, and Bandrauk AD. Attosecond-magnetic-field-pulse Generation by Intense Few-Cycle Circularly Polarized UV Laser Pulses. *Phys Rev A* (2013) 88:013417. doi:10.1103/physreva.88.013417
26. Yuan KJ, and Bandrauk AD. Attosecond-magnetic-field-pulse Generation by Coherent Circular Molecular Electron Wave Packets. *Phys Rev A* (2015) 91:042509. doi:10.1103/physreva.91.042509
27. Zhang G. P., Hübner W., Lefkidis G., Bai Y., and George T. F. Paradigm of the Time-Resolved Magneto-Optical Kerr Effect for Femtosecond Magnetism. *Nature Phys* (2009) 5:499, 502. doi:10.1038/nphys1315
28. Zhang GP, and George TF. Total Angular Momentum Conservation in Laser-Induced Femtosecond Magnetism. *Phys Rev B* (2008) 78:052407. doi:10.1103/physrevb.78.052407
29. Kim J-W, Vomir M, and Bigot J-Y. Ultrafast Magnetoacoustics in Nickel Films. *Phys Rev Lett* (2012) 109:166601. doi:10.1103/physrevlett.109.166601
30. Bigot J.-Y.. Down to the nanometre scale. *Nature Mater* (2013) 12:283, 284. doi:10.1038/nmat3605
31. Zhang X, Zhu X, Wang D, Li L, Liu X, Liao Q, et al. Ultrafast Oscillating-Magnetic-Field Generation Based on Electronic-Current Dynamics. *Phys Rev A* (2019) 99:013414. doi:10.1103/physreva.99.013414
32. Zuo T., and Bandrauk A. D.. High-order Harmonic Generation in Intense Laser and Magnetic fields. *J Nonlinear Optic Phys Mat* (1995) 04:533, 546. doi:10.1142/s0218863595000227
33. Bandrauk AD, and Lu HZ. Controlling Harmonic Generation in Molecules with Intense Laser and Static Magnetic fields: Orientation Effects. *Phys Rev A* (2003) 68:043408. doi:10.1103/physreva.68.043408
34. Long S., Becker W., and McIver J. K.. Model Calculations of Polarization-dependent Two-Color High-Harmonic Generation. *Phys Rev A* (1995) 52:2262, 2278. doi:10.1103/physreva.52.2262
35. Milošević DB, Becker W, and Kopold R. Generation of Circularly Polarized High-Order Harmonics by Two-Color Coplanar Field Mixing. *Phys Rev A* (2000) 61:063403.
36. Fleischer A., Kfir O., Diskin T., Sidorenko P., and Cohen O.. Spin Angular Momentum and Tunable Polarization in High-Harmonic Generation. *Nature Photon* (2014) 8:543, 549. doi:10.1038/nphoton.2014.108
37. Medišauskas L, Wragg J, van der Hart H, and Ivanov MY. Generating Isolated Elliptically Polarized Attosecond Pulses Using Bichromatic Counterrotating Circularly Polarized Laser fields. *Phys Rev Lett* (2015) 115:153001. doi:10.1103/PhysRevLett.115.153001
38. Milošević DB. Circularly Polarized High Harmonics Generated by a Bicircular Field from Inert Atomic Gases in the P State: A Tool for Exploring Chirality-Sensitive Processes. *Phys Rev A* (2015) 92:043827.
39. Chang Z. Single Attosecond Pulse and Xuv Supercontinuum in the High-Order Harmonic Plateau. *Phys Rev A* (2004) 70:043802. doi:10.1103/physreva.70.043802
40. Mancuso CA, Hickstein DD, Grychtol P, Knut R, Kfir O, Tong X-M, et al. Strong-field Ionization with Two-Color Circularly Polarized Laser fields. *Phys Rev A* (2015) 91:031402(R). doi:10.1103/physreva.91.031402
41. Ngoko Djiokap JM, Hu SX, Madsen LB, Manakov NL, Meremianin AV, and Starace AF. Electron Vortices in Photoionization by Circularly Polarized Attosecond Pulses. *Phys Rev Lett* (2015) 115:113004. doi:10.1103/physrevlett.115.113004
42. Ngoko Djiokap JM, Meremianin AV, Manakov NL, Hu SX, Madsen LB, and Starace AF. Multistart Spiral Electron Vortices in Ionization by Circularly Polarized UV Pulses. *Phys Rev A* (2016) 91:013408.
43. Li M., Zhang G., Kong X., Wang T., Ding X., and Yao J.. Dynamic Stark Induced Vortex Momentum of Hydrogen in Circular fields. *Opt Express* (2018) 26:878. doi:10.1364/oe.26.000878
44. Yuan KJ, Chelkowski S, and Bandrauk AD. Photoelectron Momentum Distributions of Molecules in Bichromatic Circularly Polarized Attosecond UV Laser fields. *Phys Rev A* (2016) 93:053425. doi:10.1103/physreva.93.053425
45. Yuan K.-J., Lu H., and Bandrauk A. D.. Photoionization of triatomic molecular ions H_3^{2+} by intense bichromatic circularly polarized attosecond UV laser pulses. *J Phys B At Mol Opt Phys* (2017) 50:124004. doi:10.1088/1361-6455/aa72fa
46. Ngoko Djiokap JM, Meremianin AV, Manakov NL, Madsen LB, Hu SX, and Starace AF. Dynamical Electron Vortices in Attosecond Double Photoionization of H. *Phys Rev A* (2018) 98:063407. doi:10.1103/physreva.98.063407
47. Pengel D, Kerbstadt S, Johannmeyer D, Englert L, Bayer T, and Wollenhaupt M. Electron Vortices in Femtosecond Multiphoton Ionization. *Phys Rev Lett* (2017) 118:053003. doi:10.1103/physrevlett.118.053003
48. Pengel D, Kerbstadt S, Englert L, Bayer T, and Wollenhaupt M. Control of Three-Dimensional Electron Vortices from Femtosecond Multiphoton Ionization. *Phys Rev A* (2017) 96:043426. doi:10.1103/physreva.96.043426
49. Hasovic E, Becker W, and Milosevic DB. Electron Rescattering in a Bicircular Laser Field. *Opt Express* (2016) 24:6413.
50. Mancuso CA, Hickstein DD, Dorney KM, Ellis JL, Hasovic E, Knut R, et al. Controlling Electron-Ion Rescattering in Two-Color Circularly Polarized Femtosecond Laser fields. *Phys Rev A* (2016) 93:053406. doi:10.1103/physreva.93.053406
51. Li M, Jiang W-C, Xie H, Luo S, Zhou Y, and Lu P. Strong-field Photoelectron Holography of Atoms by Bicircular Two-Color Laser Pulses. *Phys Rev A* (2018) 97:023415. doi:10.1103/physreva.97.023415
52. Yuan KJ, and Bandrauk AD. Above-threshold Ionization in Molecules by Intense Multiple-Frequency Circularly Polarized Laser Pulses. *Phys Rev A* (2018) 98:023413. doi:10.1103/physreva.98.023413
53. Xie X, Scrinzi A, Wickenhauser M, Baltuška A, Barth I, and Kitzler M. Internal Momentum State Mapping Using High Harmonic Radiation. *Phys Rev Lett* (2008) 101:033901. doi:10.1103/physrevlett.101.033901
54. Yuan KJ, and Bandrauk AD. Single Circularly Polarized Attosecond Pulse Generation by Intense Few Cycle Elliptically Polarized Laser Pulses and Terahertz fields from Molecular media. *Phys Rev Lett* (2013) 110:023003. doi:10.1103/physrevlett.110.023003
55. Hernández-García C, Durfee CG, Hickstein DD, Popmintchev T, Meier A, Murnane MM, et al. Schemes for Generation of Isolated Attosecond Pulses of

Pure Circular Polarization. *Phys Rev A* (2016) 93:043855. doi:10.1103/physreva.93.043855
56. Yuan KJ, and Bandrauk AD. Attosecond-magnetic-field-pulse Generation by Electronic Currents in Bichromatic Circularly Polarized UV Laser fields. *Phys Rev A* (2015) 92:063401. doi:10.1103/physreva.92.063401
57. Guo J, Yuan KJ, Lu H, and Bandrauk AD. Spatiotemporal Evolution of Ultrafast Magnetic Field Generation in Molecules with Intense Bichromatic Circularly Polarized Uv Laser Pulses. *Phys Rev A* (2019) 99:053416. doi:10.1103/physreva.99.053416
58. Sederberg S, Kong F, and Corkum PB. Tesla-scale Terahertz Magnetic Impulses. *Phys Rev X* (2020) 10:011063. doi:10.1103/physrevx.10.011063
59. Bandrauk A. D., and Shen H. Exponential split operator methods for solving coupled time-dependent Schrödinger equations. *The Journal of Chemical Physics* (1993) 99:1185, 1193. doi:10.1063/1.465362
60. Bandrauk A. D., and Lu H. Exponential Propagators (Integrators) for the Time-dependent Schrödinger Equation. *J Theor Comput Chem* (2013) 12:1340001. doi:10.1142/s0219633613400014
61. Jefimenko OD. *Electricity and Magnetism: An Introduction to the Theory of Electric and Magnetic Fields*. 2nd ed. Star City, West Virginia: Electret Scientific Co. (1989)
62. Yuan KJ, and Bandrauk AD. Symmetry in Circularly Polarized Molecular High-Order Harmonic Generation with Intense Bicircular Laser Pulses. *Phys Rev A* (2018) 97:023408. doi:10.1103/physreva.97.023408
63. Yuan K.-J., and Bandrauk A. D. Time-resolved Photoelectron Imaging of Molecular Coherent Excitation and Charge Migration by Ultrashort Laser Pulses. *J Phys Chem A* (2018) 122:2241, 2249. doi:10.1021/acs.jpca.7b11669
64. Yuan K.-J., Shu C.-C., Dong D., and Bandrauk A. D. Attosecond Dynamics of Molecular Electronic Ring Currents. *J Phys Chem Lett* (2017) 8:2229, 2235. doi:10.1021/acs.jpclett.7b00877
65. Sharp T. E. Potential-energy curves for molecular hydrogen and its ions. *Atomic Data and Nuclear Data Tables* (1970) 2:119, 169. doi:10.1016/s0092-640x(70)80007-9
66. Juan KJ, Guo J, and Bandrauk AD. Circularly Polarized Attosecond Pulse Generation and Applications to Ultrafast Magnetism. *J Opt* (2017) 19:124016.
67. Yuan K.-J., and Bandrauk A. D. *Applied Sciences* (2019) Probing Attosecond Electron Coherence in Molecular Charge Migration by Ultrafast X-Ray Photoelectron Imaging 9:1941. doi:10.3390/app9091941
68. Corkum P. B., Burnett N. H., and Brunel F. Above-threshold Ionization in the Long-Wavelength Limit. *Phys Rev Lett* (1989) 62:1259, 1262. doi:10.1103/physrevlett.62.1259
69. Corkum P. B. Plasma Perspective on strong Field Multiphoton Ionization. *Phys Rev Lett* (1993) 71:1994, 1997. doi:10.1103/physrevlett.71.1994
70. Yuan KJ, Guo J, and Bandrauk AD. Generation of Ultrafast Magnetic fields from Molecular Coherent Electron Currents. *Phys Rev A* (2018) 98:043410. doi:10.1103/physreva.98.043410
71. Xiao X R, Wang M X, Liang H, Gong Q, and Peng L-Y. Proposal for Measuring Electron Displacement Induced by a Short Laser Pulse. *Phys Rev Lett* (2019) 122:053201. doi:10.1103/physrevlett.122.053201
72. Keldysh LV. Ionization in the Field of a strong Electromagnetic Wave. *Sov Phys JETP* (1965) 20:1307.
73. Mineo H., and Fujimura Y. Quantum Design of π-Electron Ring Currents in Polycyclic Aromatic Hydrocarbons: Parallel and Antiparallel Ring Currents in Naphthalene. *J Phys Chem Lett* (2017) 8:2019, 2025. doi:10.1021/acs.jpclett.7b00704
74. Pronin EA, Starace AF, Frolov MV, and Manakov NL. Perturbation Theory Analysis of Attosecond Photoionization. *Phys Rev A* (2009) 80:063403. doi:10.1103/physreva.80.063403
75. Pronin EA, Starace AF, and Peng LY. Perturbation-theory Analysis of Ionization by a Chirped Few-Cycle Attosecond Pulse. *Phys Rev A* (2011) 84:013417. doi:10.1103/physreva.84.013417
76. Yuan K-J, and Bandrauk AD. Molecular Above-Threshold-Ionization Angular Distributions with Attosecond Bichromatic Intense XUV Laser Pulses. *Phys Rev A* (2012) 85:013413. doi:10.1103/physreva.85.013413
77. Bakos J., Kiss A., Szabó L., and Tendler M. Light Intensity Dependence of the Multiphoton Ionization Probability in the Resonance Case. *Physics Letters A* (1972) 41:163, 164. doi:10.1016/0375-9601(72)91095-x
78. Agostini P., and Bensoussan P. Resonant three-photon ionization of potassium with circularly and linearly polarized light. *Appl Phys Lett* (1974) 24:216, 219. doi:10.1063/1.1655158
79. Yuan K.-J., and Bandrauk A. D. Exploring Coherent Electron Excitation and Migration Dynamics by Electron Diffraction with Ultrashort X-ray Pulses. *Phys Chem Chem Phys* (2017) 19:25846, 25852. doi:10.1039/c7cp05067d
80. Yuan K.-J., and Bandrauk A. D. Ultrafast X-ray Photoelectron Imaging of Attosecond Electron Dynamics in Molecular Coherent Excitation. *J Phys Chem A* (2019) 123:1328, 1336. doi:10.1021/acs.jpca.8b12313
81. Leone S. R., McCurdy C. W., Burgdörfer J., Cederbaum L. S., Chang Z., Dudovich N., et al. What will it take to observe processes in 'real time'? *Nature Photon* (2014) 8:162, 166. doi:10.1038/nphoton.2014.48
82. Kraus PM, Mignolet B, Baykusheva D, Rupenyan A, Horný L, Penka EF, et al. Measurement and Laser Control of Attosecond Charge Migration in Ionized Iodoacetylene. *Science* (2015) 350:790, 5. doi:10.1126/science.aab2160
83. Bandrauk AD, Chelkowski S, Corkum PB, Manz J, and Yudin GL. Attosecond Photoinization of Coherent Superpositions of Bound-Dissociative Molecular States-Effects of Nuclear Motion. *J Phys* (2009) B42:143001.
84. Jia D., Manz J., and Yang Y. De- and Recoherence of Charge Migration in Ionized Iodoacetylene. *J Phys Chem Lett* (2019) 10:4273, 4277. doi:10.1021/acs.jpclett.9b01687
85. Paramonov GK, Klamroth T, Lu HZ, and Bandrauk AD. Quantum Dynamic Isotope Effects and Power Spectra of H2+ and HD+ in Strong One-Cycle Laser Pulses". *Phys Rev* (2018) A98:063431.
86. Zhu BJ, et al. 30 Co-authors), Strong Magnetic fields with Simple Coils Irradiated by High Power Lasers. *Appl Phys Lett* (2015) 107:2619003. doi:10.1063/1.4939119

Conflict of Interest: The authors declare that the research was conducted in the absence of any commercial or financial relationships that could be construed as a potential conflict of interest.

frontiers in Physics

ORIGINAL RESEARCH
published: 30 June 2021
doi: 10.3389/fphy.2021.691727

Controlling H_3^+ Formation From Ethane Using Shaped Ultrafast Laser Pulses

Tiana Townsend[1], Charles J. Schwartz[1], Bethany Jochim[2], Kanaka Raju P.[2,3], T. Severt[2], Naoki Iwamoto[1], J. L. Napierala[1], Peyman Feizollah[2], S. N. Tegegn[1], A. Solomon[1], S. Zhao[1], K. D. Carnes[2], I. Ben-Itzhak[2] and E. Wells[1]*

[1]Department of Physics, Augustana University, Sioux Falls, SD, United States, [2]J. R. Macdonald Laboratory, Physics Department, Kansas State University, Manhattan, KS, United States, [3]School of Quantum Technology, DIAT(DU), Pune, India

An adaptive learning algorithm coupled with 3D momentum-based feedback is used to identify intense laser pulse shapes that control H_3^+ formation from ethane. Specifically, we controlled the ratio of D_2H^+ to D_3^+ produced from the $D_3C\text{-}CH_3$ isotopologue of ethane, which selects between trihydrogen cations formed from atoms on one or both sides of ethane. We are able to modify the D_2H^+:D_3^+ ratio by a factor of up to three. In addition, two-dimensional scans of linear chirp and third-order dispersion are conducted for a few fourth-order dispersion values while the D_2H^+ and D_3^+ production rates are monitored. The optimized pulse is observed to influence the yield, kinetic energy release, and angular distribution of the D_2H^+ ions while the D_3^+ ion dynamics remain relatively stable. We subsequently conducted COLTRIMS experiments on C_2D_6 to complement the velocity map imaging data obtained during the control experiments and measured the branching ratio of two-body double ionization. Two-body D_3^+ + $C_2D_3^+$ is the dominant final channel containing D_3^+ ions, although the three-body D + D_3^+ + $C_2D_2^+$ final state is also observed.

Keywords: coherent control, molecular dynamics, bond rearrangement, laser physics, imaging, ultrafast science

Edited by:
Tamar Seideman,
Northwestern University,
United States

Reviewed by:
Arkaprabha Konar,
Kent State University, United States
Balakrishnan Naduvalath,
University of Nevada, Las Vegas,
United States

****Correspondence:***
E. Wells
eric.wells@augie.edu

Specialty section:
This article was submitted to Physical Chemistry and Chemical Physics,
a section of the journal Frontiers in Physics

Received: *06 April 2021*
Accepted: *10 June 2021*
Published: *30 June 2021*

Citation:
Townsend T, Schwartz CJ, Jochim B, P. KR, Severt T, Iwamoto N, Napierala J L, Feizollah P, Tegegn SN, Solomon A, Zhao S, Carnes KD, Ben-Itzhak I and Wells E (2021) Controlling H_3^+ Formation From Ethane Using Shaped Ultrafast Laser Pulses. Front. Phys. 9:691727. doi: 10.3389/fphy.2021.691727

1 INTRODUCTION

The intramolecular migration of hydrogen continues to be an active area of investigation in ultrafast science [1–11] with implications for topics ranging from combustion [12] to peptide dissociation [13] and characterizing conformational differences in molecules [14, 15]. In some cases the migration of hydrogen leads to the formation of new molecular ions, such as H_3^+ [5, 16–21], by processes such as H_2 roaming or double hydrogen migration [18, 19, 22, 23].

The formation of H_3^+ is usually a multi-step process that often involves the association of hydrogen atoms from different sites of the parent molecule. In allene (C_3H_4), at least one hydrogen migration to the other side of the molecule is required [24, 25]. Even in molecules that contain a methyl group with three hydrogen atoms close together, there are H_3^+ formation pathways that involve hydrogen atoms from other parts of the parent molecule. Methanol is perhaps the best studied example of this behavior [5, 16–21, 26–29]. In methanol (CH_3OH), there is clear evidence that H_3^+ may form when a roaming H_2 from the methyl side abstracts the hydroxyl proton in addition to alternative mechanisms that only involve the methyl side. For ethanol (CH_3CH_2OH) and several slightly longer alcohol molecules, multiple pathways to H_3^+ formation exist that involve hydrogen migration, although the relative importance of these pathways decreases as the carbon chain length increases [19, 20].

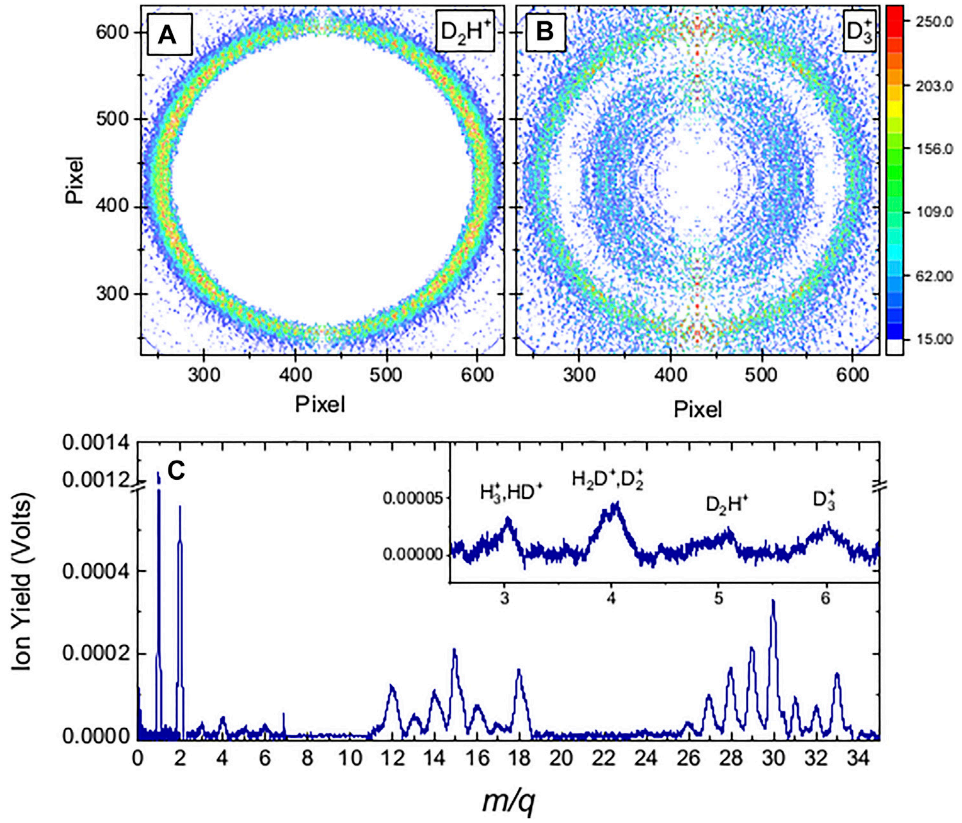

FIGURE 1 | Molecular fragmentation data obtained with 35 fs FWHM, 1.3 × 10^{14} W/cm^2 pulses centered at 785 nm, the conditions used in the closed-loop experiment. **(A)** Inverse Abel transformed VMI of D_2H^+ ions. **(B)** Inverse Abel transformed VMI of m/q = 6, which contains D_3^+ and C^{2+} ions. At this intensity, the two features are separated, with the C^{2+} ions inside the D_3^+ ring. The laser polarization is vertical for the VMI data. **(C)** Current mode time-of-flight (shown as a function of m/q) showing that the integrated yield of the m/q = 5 and m/q = 6 peaks are similar. When only the yield from the higher momentum feature in the m/q = 6 is considered, the ratio of D_2H^+ to D_3^+ is approximately 7:1, in agreement with the results of Kanya et al. [32]. The laser polarization is perpendicular to the time-of-flight axis in **(C)**.

Ethane (C_2H_6) is composed of two back-to-back methyl groups, and thus it is an excellent baseline system for examining hydrogen-related bond rearrangement. H_3^+ formation following double ionization of ethane has been examined in several previous experimental and theoretical studies [16, 30–35]. Kraus and co-workers theoretically identified a minimum-energy-path transition state with a neutral hydrogen molecule attached to a $C_2H_4^{2+}$ ion that led to the H_3^+ + $C_2H_3^+$ final state [31]. Their calculations were in good agreement with the measured kinetic energy release (KER) of these final products, in which the KER is essentially the reverse activation energy along the proposed reaction path. Kanya et al. showed, using different isotopologues of ethane, that hydrogen atoms are statistically scrambled between the initial and final states following double ionization [32]. In a later study, Boran et al. proposed a pathway that begins with hydrogen elimination (H + $C_2H_5^{2+}$) and continues through a sequence of transition states leading to a neutral hydrogen molecule attached to a $C_2H_3^{2+}$ ion followed by dissociation into $C_2H_2^+$ + H_3^+ [34]. Recent electron impact studies by Zhang et al. suggest the presence of an additional roaming-induced isomerization pathway that leads to H_3^+ formation on a longer timescale than the transition-state pathways [35].

Motivated by significant H_3^+ yields from the dissociation of ethane dications, the suggestions of multiple pathways that lead to H_3^+ formation following double ionization of ethane, and the sensitivity of the H_3^+ production to laser pulse parameters reported by Schirmel and co-workers [33], this article reports our efforts to manipulate the formation of H_3^+ using shaped ultrafast laser pulses.

2 EXPERIMENTAL METHOD

The experimental techniques applied in this study have recently been discussed elsewhere [21, 36], and in this section we will only highlight a few key points. Two different approaches are used to examine the interactions of intense laser pulses with ethane gas: First, the laser pulses are shaped using an acousto-optic programmable dispersive filter (AOPDF) [37] and the ethane reaction products are measured using velocity map imaging (VMI) [38, 39]. Second, COLd Target Recoil Ion Momentum

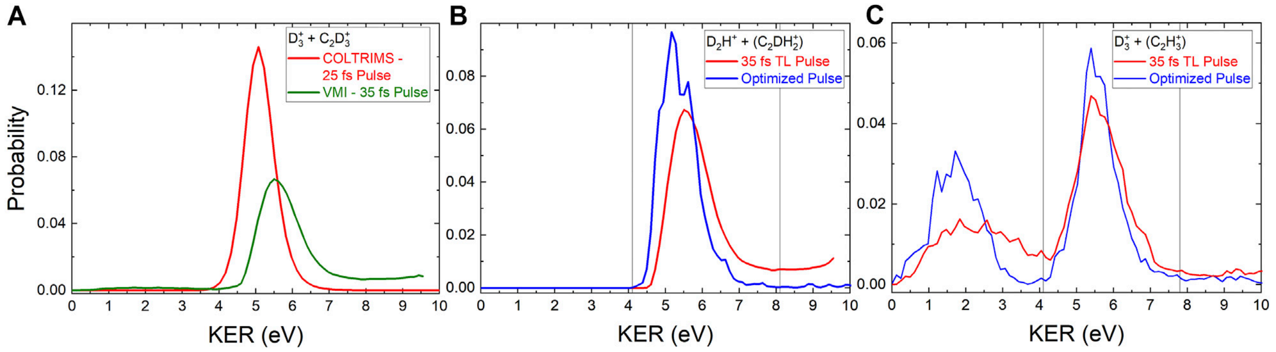

FIGURE 2 | (A) The red line shows the probability for two-body $D_3^+ + C_2D_3^+$ fragmentation as a function of kinetic energy release (KER) measured with COLTRIMS. To compare the COLTRIMS and VMI measurements, we added the D_2H^+ and D_3^+ ions measured with VMI in a 7:1 ratio and plotted the combined probability for dissociation as a function of KER (olive line). **(B)** The VMI-derived KER distribution for D_2H^+ ions assuming two-body breakup of $D_3C\text{-}CH_3$ into $D_2H^+ + C_2DH_2^+$. The red line represents the KER distribution produced by the transform limited (TL) pulse. The blue line is the KER distribution produced by the optimized pulse. The peak of the KER distribution from the optimized pulse is 0.3 eV lower than the peak of the KER distribution from the TL pulse. **(C)** The KER distributions for the D_3^+ channel assuming two-body breakup into $D_3^+ + C_2H_3^+$ initiated by a TL (red) and optimized (blue) pulse. The vertical lines in **(B)** and **(C)** indicate the edges of the regions used to calculate the fragment yield in the adaptive control experiment. The lower-KER structure in **(C)** is thought to be C^{2+}.

Spectroscopy (COLTRIMS) [40, 41] characterizes the dissociation dynamics of the ethane molecule following strong-field ionization.

2.1 Shaped Pulses and Velocity Map Imaging

In the shaped pulse/VMI portion of the experiment linearly polarized pulses with a duration of 35 fs full-width at half-maximum (FWHM) in intensity and a center wavelength of 785 nm are generated at 1 kHz by a Ti:Sapphire laser system named KLS. In this laser system, the compressor grating pair is in the Treacy configuration [42] while the stretcher gratings are in the Martinez configuration [43]. The amplified pulse energy of about 1.5 mJ was attenuated to the levels needed in the experiment. These near-Fourier-transform limited pulses will be denoted as TL pulses in this article. The acousto-optic programmable dispersive filter [37] was placed between the laser oscillator and multi-pass amplifier. In this experiment, we controlled only the spectral phase of the laser pulse. Pulse characteristics were determined using a second-harmonic-generation frequency-resolved-optical-grating (SHG-FROG) [44] device. Our version of VMI [45–47] integrates the momentum image of a given m/q time-of-flight peak over many laser shots by fully powering the detector within a specific time window. For a typical trial pulse, we collected VMI data for 5,000 laser shots for D_2H^+ and 35,000 laser shots for D_3^+ in order to obtain similar statistics for each ion. While our VMI approach does not measure correlated information about all the products from a specific laser-molecule interaction, it enables rapid data acquisition, making adaptive control experiments possible [48, 49]. Typical VMI data obtained with the online inversion method [47] are shown in **Figures 1A,B**.

In the closed-loop adaptive control approach, ion-specific three-dimensional momentum information provides the

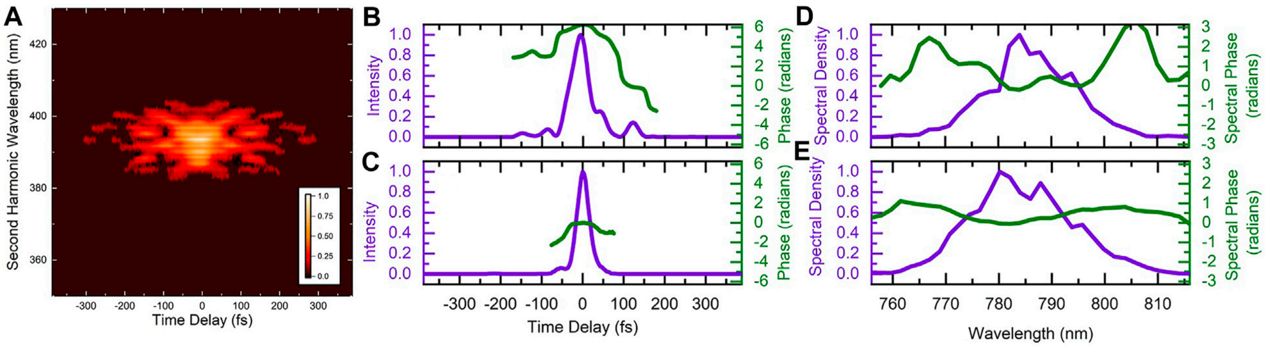

FIGURE 3 | (A) Measured frequency-resolved-optical-grating trace of the laser pulse optimized to increase the $D_2H^+:D_3^+$ ratio. **(B)** The retrieved intensity (violet) and temporal phase (green) of the optimized pulse. While second-harmonic-generation is symmetric with respect to time, this ambiguity can be removed with the additional information from the pulse shape parameters. **(C)** The retrieved intensity and temporal phase of an unshaped laser pulse for comparison, using the same color scheme. **(D)** The retrieved spectral density (violet) and phase (green) of the optimized pulse. **(E)** The unshaped spectral density and phase for comparison, again with the same color scheme.

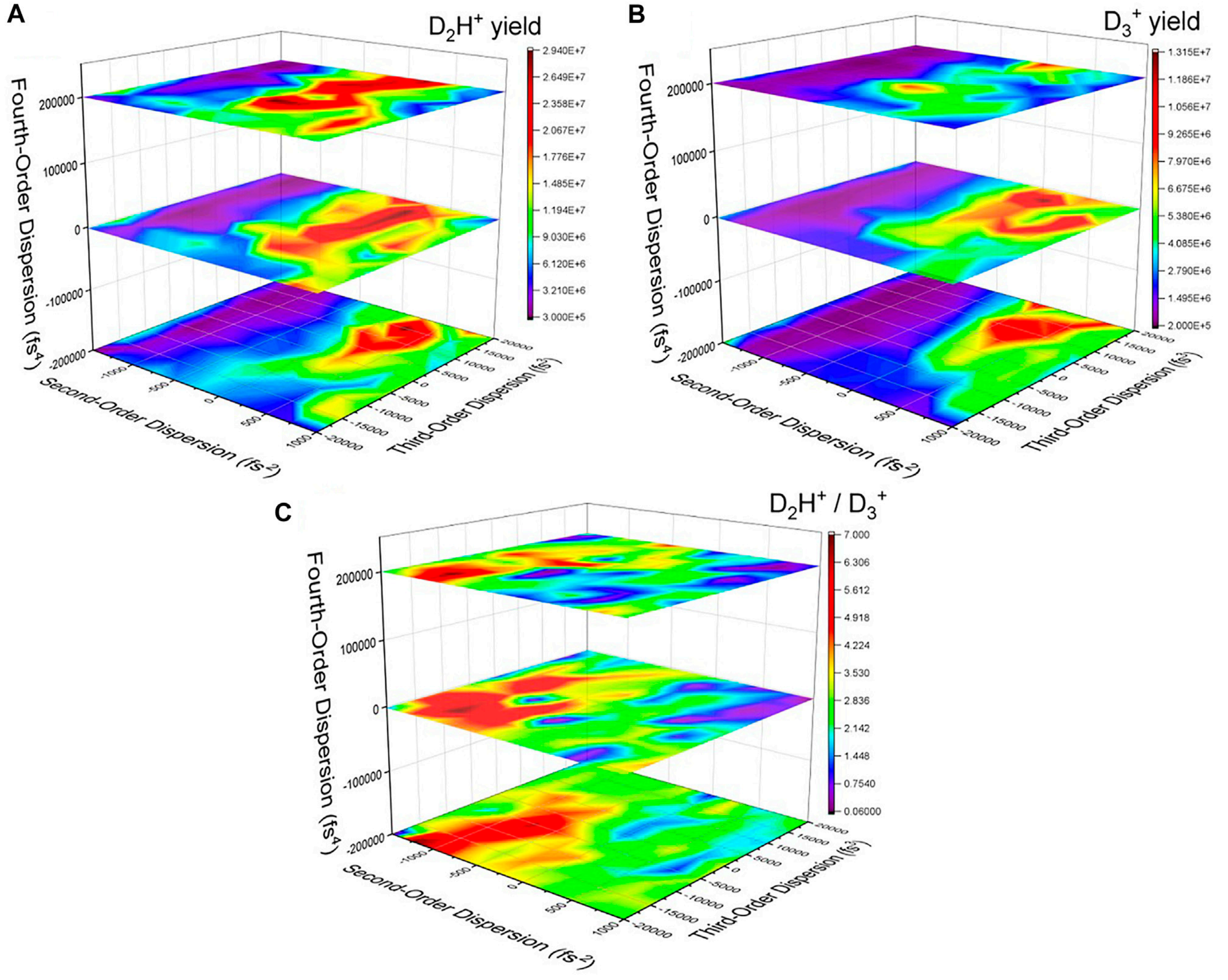

FIGURE 4 | The yield of **(A)** D_2H^+ and **(B)** D_3^+ as a function of second—and third-order dispersion for three values of fourth-order dispersion. In these measurements, the pulse energy is kept constant, so the intensity decreases as the dispersion lengthens the pulses. **(C)** The D_2H^+:D_3^+ ratio as a function of the same pulse parameters. The ratio is defined to be 1.0 at $\varphi^{(2)} = \varphi^{(3)} = \varphi^{(4)} = 0$.

feedback to drive a genetic algorithm that optimizes the pulse shapes to a control objective [46, 47]. The raw VMI data is inverted on-the-fly to recover a slice through the center of the three-dimensional momentum distribution using a modified "onion-peeling" algorithm as described by Rallis et al. [47]. The yield within user-defined regions of interest on the momentum plot is then evaluated, resulting in a numerical value that defines the "fitness" of the laser pulse being examined. The adaptive search parameterizes the pulse characteristics in terms of the spectral phase, which is broken into 16 evenly spaced segments between 734 and 830 nm. Since a portion of this range is beyond the pulse bandwidth, the effective number of search parameters is somewhat smaller than 16. Linear interpolation fills in the values between the adjacent phases. The algorithm is allowed to adjust each phase value between 0 and 2π.

To complement the closed-loop studies, systematic scans of the second- and third-order pulse dispersion were made for a few values of fourth-order dispersion. In this pulse-parameterization scheme [21, 50, 51], we describe the spectral phase, $\varphi(\omega)$, as a Taylor series expansion [52]:

$$\varphi(\omega) = \varphi^{(0)} + \frac{\varphi^{(1)}(\omega-\omega_0)}{1!} + \frac{\varphi^{(2)}(\omega-\omega_0)^2}{2!} + \frac{\varphi^{(3)}(\omega-\omega_0)^3}{3!} + \frac{\varphi^{(4)}(\omega-\omega_0)^4}{4!} + \cdots. \qquad (1)$$

2.2 Coincidence Momentum Imaging

In the COLTRIMS [40, 41] measurement, the laser pulses are produced by the PULSAR laser [53] at 10 kHz, with 25-fs (FWHM in intensity) pulse duration, a central wavelength of 790 nm, and maximum pulse energy of 2 mJ. The laser pulses were again characterized with SHG-FROG. The pulses are focused by a $f = 7.5$-cm spherical mirror onto randomly oriented target molecules in the supersonic molecular beam of the COLTRIMS apparatus. Following the laser-molecule interaction within the electric field of the spectrometer, all the

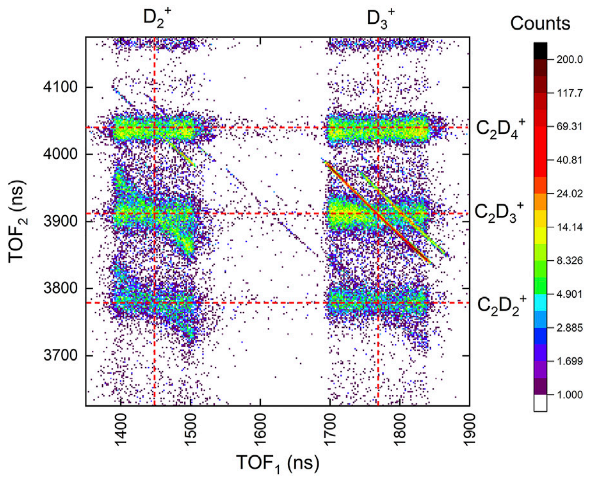

FIGURE 5 | The portion of the coincidence-time-of-flight map of two-body channels including D_2^+ and D_3^+ fragments from C_2D_6 exposed to a 25-fs, 790-nm, 1.5 × 10^{14} W/cm^2 laser pulse.

TABLE 1 | Ethane (C_2D_6) branching ratios for two-body double ionization by 25-fs, 1.5 × 10^{14}-W/cm^2 laser pulses centered at 790-nm.

Dissociation channel	Branching ratio (%)
$D^+ + C_2D_5^+$	1.00 ± 0.03
$D_2^+ + C_2D_4^+$	4.91 ± 0.08
$D_3^+ + C_2D_3^+$	69.80 ± 0.15
$CD_2^+ + CD_4^+$	1.01 ± 0.04
$CD_3^+ + CD_3^+$	23.27 ± 0.71

charged ethane photofragments are directed toward a time- and position-sensitive detector where they are measured in coincidence. The base pressure in the spectrometer region was below 2 × 10^{-10} Torr. Since the charged fragments are recorded on an event-by-event basis, we can use the measured time and position of all the charged fragments along with conservation of momentum to determine the three-dimensional momentum distributions.

3 RESULTS AND DISCUSSION

The experiments on D_3C-CH_3 (1,1,1-d$_3$ ethane, 98% pure) with shaped pulses and VMI detection used both an adaptive search strategy and a systematic search of pulse parameters. With this target, D_3^+ fragments must originate from only one side of the parent molecule, while D_2H^+ fragment formation must involve both sides of the parent molecule. While the D_3C-CH_3 target allows us to determine which hydrogen atoms participate in the bond rearrangement process, the $m/q = 6$ channel contains both the D_3^+ channel of interest and C^{2+} fragments [30]. At laser intensities that did not have a significant yield of C^+ ions (around 8×10^{13} W/cm^2), for which we could assume there was no C^{2+} signal, the D_3^+ signal rate was too low for adaptive control experiments.

As the intensity was increased, the VMI of the $m/q = 6$ ions began to have two features, as shown in **Figure 1B**. The outer feature, corresponding to a KER of around 5 eV, remained at that KER as the intensity increased. In contrast, both the signal size of the inside feature relative to the ≈5 eV feature and the radius of the inner feature in **Figure 1B** increased with intensity. We assume this inner feature, which is more aligned with the laser polarization at higher intensities, is caused by C^{2+} ions. At 1.3 × 10^{14} W/cm^2, the total yields of $m/q = 5$ and $m/q = 6$ are similar, as shown in **Figure 1C**. Using the VMI information, we can separate the two features in momentum space. The range of interest is shown by the vertical lines in **Figures 2B,C**. After separation of the C^{2+} from the D_3^+ and correction for different image exposure times, the ratio of D_2H^+ to D_3^+ is approximately 7: 1, as expected from the time-of-flight studies performed by Kanya et al. on different isotopologues of ethane [32].

3.1 Pulse Shaping and Control

We were able to increase the D_2H^+:D_3^+ ratio by a factor of 3.2 ± 0.7 using adaptive control. With phase-only shaping the pulse energy is kept constant at around 11 μJ/pulse, which corresponds to a peak intensity of 1.3 × 10^{14} W/cm^2. Experiments at slightly higher pulse energy also resulted in a D_2H^+:D_3^+ ratio higher than obtained with a TL pulse, but we observed significant overlap between the C^{2+} and D_3^+ fragments making it difficult to evaluate these results. When attempting to optimize the inverse D_3^+:D_2H^+ ratio, we did not observe any improvement over the TL 35-fs pulse.

Figure 2 shows the KER distributions obtained for the D_2H^+ and D_3^+ fragments with the optimized pulses and TL pulses. For the VMI data, we calculate the KER by assuming a two-body breakup of the D_3C-CH_3 parent molecule into an ion pair. For comparison, the KER distribution of $C_2D_6^{2+} \rightarrow D_3^+ + C_2D_3^+$ directly measured with COLTRIMS is shown in **Figure 2A**. The KER distributions are similar, although the COLTRIMS measurement is slightly lower. This could be due to small differences in the respective momentum/energy calibration or the slightly different pulse characteristics. As described in the introduction, Kraus et al. [31] and Boran et al. [34] have examined the dissociation pathways leading to H_3^+ formation from ethane and found KER values peaked between 5.2 and 5.5 eV. Zhang and co-workers have observed a slightly lower KER in recent electron-impact studies and suggested a different dissociation pathway [35].

Notably, the D_2H^+ KER distribution obtained with the pulse optimized to increase the D_2H^+:D_3^+ ratio is shifted about 0.3 eV lower than the KER distribution obtained with the TL pulse. The corresponding KER distribution for the D_3^+ yield, which is in the denominator of the control objective, shows no significant shift. In addition, the increase in the D_2H^+:D_3^+ ratio was due to an increase in D_2H^+ yield, not a reduction of D_3^+ yield. In some similar experiments, this combination of indicators has been a signature of a barrier-suppression mechanism [46]. Several of the theoretical efforts with ethane [31, 34, 35] identified one or more transition states in the dissociation process. If the energy of the transition state was modified by the field at an appropriate time, it could promote D_2H^+ production.

The characteristics of the optimized pulse are shown in **Figure 3**. While there is indeed a trailing secondary pulse around 125 fs after the main pulse, there are other features of the pulse shape that could be significant. To try and determine which pulse parameters are important for the manipulation of the control objective, we systematically scanned the linear chirp and third-order dispersion for three values of fourth-order dispersion. During these systematic scans we recorded the D_2H^+ and D_3^+ yields, shown in **Figure 4**, using the same gates on the VMI data as in the adaptive control experiment.

From a time-domain perspective, the second–and fourth-order dispersions lengthen the pulse symmetrically, while the third-order dispersion adds a pedestal either before or after the main pulse (see, e.g., Ref. 50). Thus, some of the temporal characteristics of the optimized pulse (**Figure 3**) can be reproduced, but the secondary pulse would be more difficult to construct using dispersive pulse parameters. As shown in **Figure 4C**, there are a number of combinations of pulse parameters that reach nearly the same level of effectiveness at manipulating the D_2H^+:D_3^+ ratio as the optimized pulse. The highest values of the D_2H^+:D_3^+ ratio are seen at negative values of both $\varphi^{(2)}$ and $\varphi^{(3)}$. In this region of parameter space, the yield of the individual channels have both been reduced by roughly a factor of 10. Therefore, while the adaptive and systematic search strategies can both find pulses that improve the control objective, and thus distinguish between formation of trihydrogen cations from one side of the parent molecule or both sides of the parent molecule, the adaptive search result maintains the overall yield better than the systematic search. This result is similar to the observations in a recent methanol experiment [21].

One curious element of the dispersion scan is the comparison to the previous work of Schirmel et al., who also examined H_3^+, D_2H^+, and D_3^+ yields from various isotopologues of ethane as a function of second-order dispersion (linear chirp) [33]. Our results match the results of Schirmel et al. in the sense that the sign of the linear chirp matters in the production of H_3^+. This is somewhat unusual, since dissociation rates rarely seem to depend on the sign of the chirp [54]. Our results show increases in D_2H^+ and D_3^+ yields, as well as an increasing D_2H^+:D_3^+ ratio, for positive linear chirp, with a maximum around $\varphi^{(2)} = +250\,\text{fs}^2$. This is in direct contrast to the result of Shirmel and co-workers who reported that negative linear chirp increases the yield of H_3^+ and other fragments from ethane, with a maximum at $\varphi^{(2)} \approx -1000\,\text{fs}^2$. They also report an essentially constant D_2H^+:D_3^+ ratio as a function of chirp.

One possible explanation for the seemingly conflicting results is that different intensities lead to different dissociation dynamics. The TL intensity of 1.3×10^{14} W/cm^2 used in this experiment is higher by about a factor of two than the highest intensity pulses used by Schirmel et al. [33]. In both our scans of the dispersion parameters and those of Schirmel et al., the pulse energy was kept constant. Schirmel et al. also noted that as the pulse energy increased in their experiments, the value of linear chirp that produced the most fragmentation became closer to zero (more positive). It is possible that our results simply continue this trend, although if the intensity is becoming the dominant factor in the dynamics it is unclear why zero dispersion does not produce a maximum or a minimum. We note that our D_2H^+ and D_3^+ yields also increased for $\varphi^{(3)} > 0$ and changing $\varphi^{(4)}$ had limited effect. Additional work, including a more detailed study of how dispersion and intensity combine to influence the dissociation dynamics, is needed to resolve these issues.

3.2 Branching Ratio

Another factor potentially confounding our understanding of how the production of H_3^+ can be manipulated with shaped laser pulses is the likelihood that more than one dissociation pathway

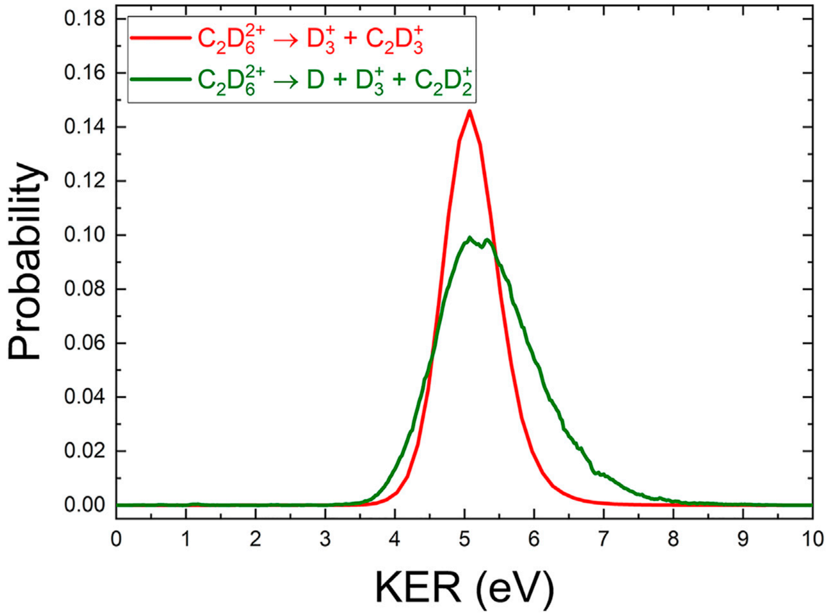

FIGURE 6 | A comparison of the (COLTRIMS-derived) KER spectrum of $D_3^+ + C_2D_3^+$ (red) and $D + D_3^+ + C_2D_2^+$ (olive) produced by 25 fs, 1.5×10^{14} W/cm^2 laser pulses centered at 790 nm.

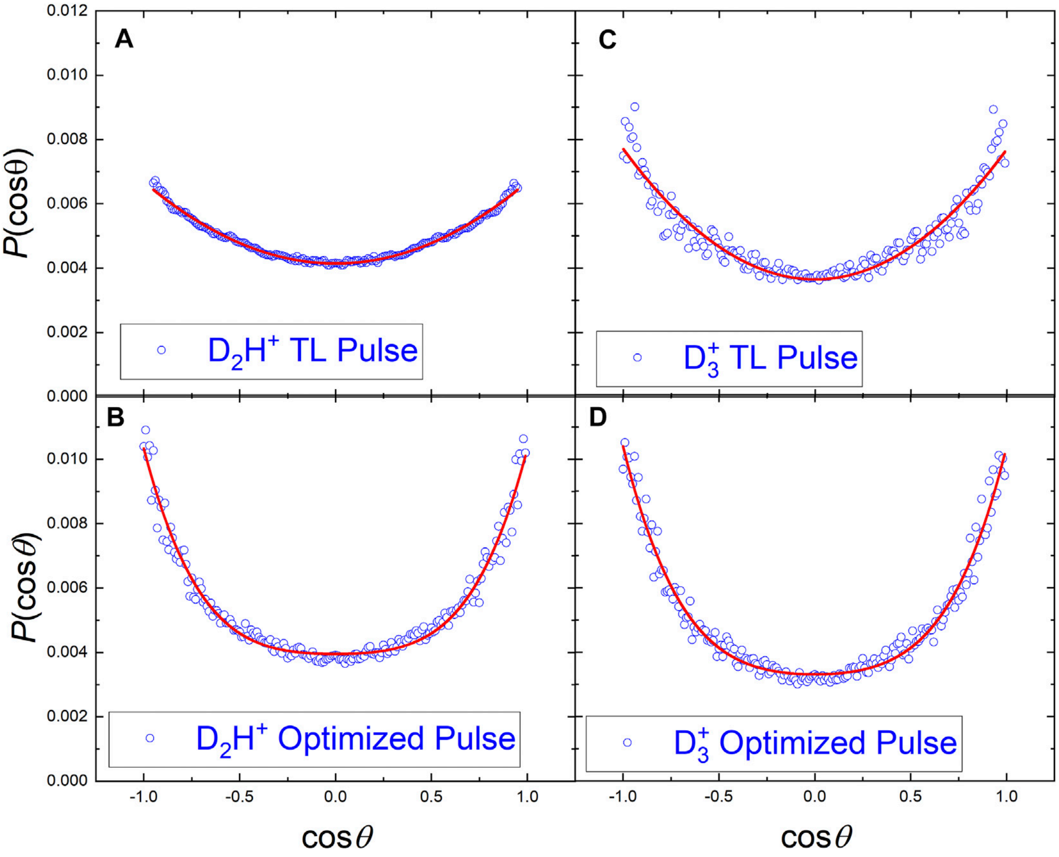

FIGURE 7 | The angular distributions of D_2H^+ and D_3^+ from VMI measurements of D_3C-CH_3 dissociation. **(A)** D_2H^+ fragments from a TL pulse. **(B)** D_2H^+ fragments produced from pulses optimized to increase the D_2H^+:D_3^+ ratio. In the right column are the same distributions for D_3^+ fragments by the **(C)** TL and **(D)** optimized pulses. The molecular ions forming the angular distributions are from within the areas on interest shown in **Figure 2**. The angle θ is between the laser polarization direction and the fragment dissociation direction. The solid lines in each panel are fits of the data to a Legendre polynomial in cosθ. The fit coefficients are shown in **Table 2**.

TABLE 2 | Legendre polynomial coefficients, a_n, obtained by fitting the probability of dissociation of D_2H^+ and D_3^+ as a function of cosθ.

Dissociation channel	Pulse type	a_0	a_2	a_4
D_2H^+	TL	0.0050	0.0017	-
D_2H^+	Optimized	0.0054	0.0038	0.0012
D_3^+	TL	0.0050	0.0027	-
D_3^+	Optimized	0.0050	0.0043	0.0012

is active. To partially address this issue, we performed COLTRIMS measurements of laser-induced dissociation of C_2D_6. We selected C_2D_6 as a target because D_3C-CH_3 was financially prohibitive for use in a supersonic jet without a buffer gas. While the peak intensities were similar in the COLTRIMS and VMI measurements, the pulse duration in the COLTRIMS measurements was 25 fs, i.e., significantly shorter than the 35 fs in the VMI case. As an approximate guide, we note that the Keldysh parameter [55] is approximately 0.9 for 1.3×10^{14} W/cm^2 pulses and the 11.52 eV ionization potential of ethane [56]. When the pulses are lengthened by pulse shaping the corresponding decrease in intensity raises the Keldysh parameter. The quasi-static approximation used in tunnel ionization is therefore not clearly valid in any of the experiments described here. **Figure 5** shows the relevant portion of the coincidence-time-of-flight (CTOF) plot. Following the procedure outlined in Ref. 36 for removing false coincidences, we use this data to obtain the two-body double-ionization branching ratio reported in **Table 1**.

We also analyzed the three-body D + D_3^+ + $C_2D_3^+$ channel. While the D_3^+ + $C_2D_2^+$ ion pair is visible in **Figure 5**, the momentum carried by the neutral deuterium atom smears out the corresponding island in the CTOF plot compared to the sharp two-body channels. The detailed corrections needed to reach the level of precision given in **Table 1** for three-body channels is time-consuming because of contributions from three-body channels containing three ions. By making some simplifying assumptions about which channels provide the most significant background, however, we estimate the D + D_3^+ + $C_2D_2^+$ yield is 16 times smaller than the main D_3^+ +$C_2D_3^+$ channel.

Using momentum conservation to deduce the contribution from the deuterium atom gives a KER distribution for this three-body channel, shown in **Figure 6**. The KER distribution is similar to the $C_2D_6^{2+} \rightarrow D_3^+ + C_2D_3^+$ KER distribution shown in **Figure 2C** and also the prediction of Boran et al. [34] for a $C_2D_6^{2+} \rightarrow D + C_2D_5^{2+} \rightarrow D + D_3^+ + C_2D_2^+$ process.

In addition, we did not find any significant evidence for D_3^+ production from the monocation, that is, D_3^+ + neutral fragments. Such a process would typically have low KER and there are negligibly few D_3^+ ions at low kinetic energy. Thus, we can conclude that we observe two, and only two, final channels that result in D_3^+ ions: two-body $D_3^+ + C_2D_3^+$ and three-body $D + D_3^+ + C_2D_2^+$. Of these, the two-body channel has the larger yield. When considering the results of our control experiments, it is likely that the main channel involved is a two-body double ionization process.

3.3 Angular Distributions

Since the control experiments with the D_3C-CH_3 isotopologue of ethane are designed to distinguish between the involvement of the hydrogen atoms on one or both sides of the molecule, the angular distributions from the VMI data might provide information about the dissociation dynamics beyond the KER shift shown in **Figure 2B**. Since the angular COLTRIMS data can be readily corrected using available experimental symmetries [36], we compared the COLTRIMS-measured $D_3^+ + C_2D_3^+$ angular distribution to the weighted sum of the D_2H^+ and D_3^+ VMI angular distributions to derive a function that ensured uniform detection efficiency across the VMI detector.

The angular distributions of the D_2H^+ and D_3^+ ions are shown in **Figure 7** for both TL and optimized pulses. These angular distributions were fit using a Legendre polynomial in cosθ, and the resulting coefficients are shown in **Table 2**. The most notable difference between the TL and optimized pulses is that the latter pulses produce a D_2H^+ distribution that is much more aligned with the laser polarization direction than the TL pulses. This trend is also apparent in the D_3^+ results, although to a lesser extent. In addition, both of the optimized pulses yield angular distributions that are better fit to 4th-order Legendre polynomials, while adding a 4th-order term does not improve the fit of the angular distributions produced by TL pulses.

The optimized pulse, therefore, is observed to have a significant impact on the yield, KER, and angular distribution of the D_2H^+ ions. In contrast, the D_3^+ ions display relatively similar dynamics for the optimized and TL pulses. A close comparison of **Figures 4A,B** shows that while the D_3^+ yield changes by a factor of 65 over the range of the dispersion scan, the D_2H^+ yield changes by a factor of 122 over the same parameter space. The relative stability of the D_3^+ formation process under the range of laser conditions may be a result of the limited combinations of atoms that could be involved. The greater multiplicity available for D_2H^+ formation might make that process more flexible and therefore more susceptible to the influence of the laser pulse changes.

4 SUMMARY

By using the D_3C-CH_3 isotopologue of ethane we were able to separate two different types of dissociation processes leading to the formation of trihydrogen cations: D_3^+ formation which involves atoms from only one side of the molecule and D_2H^+ that involves atoms from both sides of the molecule. Using shaped laser pulses, we increased the D_2H^+:D_3^+ ratio by a factor of up to three. The laser pulses optimized with an adaptive search strategy were more effective at improving the D_2H^+:D_3^+ ratio while maintaining the overall ion yield than the most effective pulses found with a systematic scan of pulse dispersion parameters. Using coincident ion detection available in a COLTRIMS measurement of C_2D_6, we verified that while three-body $D + D_3^+ + C_2D_3^+$ is observed, two-body $D_3^+ + C_2D_3^+$ is the dominant fragmentation channel containing D_3^+ ions. The pulse optimized with an adaptive search produces D_2H^+ fragments with a lower KER and an angular distribution more strongly peaked along the laser polarization direction than the TL pulse. This could be a signature of a barrier suppression mechanism. A multiple-pulse experiment probing the time dependence of H_3^+ formation in this process could be informative, as could further theoretical investigation of the timescales of some of the proposed H_3^+ formation mechanisms.

DATA AVAILABILITY STATEMENT

The raw data supporting the conclusions of this article will be made available by the authors, without undue reservation.

AUTHOR CONTRIBUTIONS

TT and TS led the analysis of the COLTRIMS measurements, while CS led the VMI analysis with assistance from TT, NI, and ST. BJ led the adaptive control experiments and KP led the dispersion scan experiments with assistance from NI, CS, JN, AS, TS, PF, ST, and EW. TS, BJ, SZ, KC, IB-I, and EW carried out the COLTRIMS experiment. IB-I and EW mentored the students and postdocs. EW wrote the manuscript with assistance from TT, TS, BJ, KP, KC, and IB-I. All authors reviewed the manuscript prior to submission.

FUNDING

Augustana University personnel and equipment are supported by the National Science Foundation grant PHYS-2011864. JR Macdonald Laboratory personnel and equipment are supported by the Chemical Sciences, Geosciences, and Biosciences Division, Office of Basic Energy Science, Office of Science, United States Department of Energy under award #DE-FG02-86ER1349.

ACKNOWLEDGMENTS

We thank Charles Fehrenbach for assistance with the PULSAR laser and the members of Vinod Kumarappan's group for assistance with the KLS laser.

REFERENCES

1. Endo T, Neville SP, Wanie V, Beaulieu S, Qu C, Deschamps J, et al. Capturing Roaming Molecular Fragments in Real Time. *Science* 370 (2020) 1072–7. doi:10.1126/science.abc2960
2. Kling NG, Díaz-Tendero S, Obaid R, Disla MR, Xiong H, Sundberg M, et al. Time-resolved Molecular Dynamics of Single and Double Hydrogen Migration in Ethanol. *Nat Commun* 10 (2019). doi:10.1038/s41467-019-10571-9
3. Ando T, Shimamoto A, Miura S, Iwasaki A, Nakai K, and Yamanouchi K. Coherent Vibrations in Methanol Cation Probed by Periodic H3+ Ejection after Double Ionization. *Commun Chem* 1 (2018). doi:10.1038/s42004-017-0006-7
4. Kübel M, Siemering R, Burger C, Kling NG, Li H, Alnaser AS, et al. Steering Proton Migration in Hydrocarbons Using Intense Few-Cycle Laser fields. *Phys Rev Lett* 116 (2016) 193001.doi:10.1103/physrevlett.116.193001
5. Livshits E, Luzon I, Gope K, Baer R, and Strasser D. Time-resolving the Ultrafast H_2 Roaming Chemistry and $H_3{}^+$ Formation Using Extreme-Ultraviolet Pulses. *Commun Chem* 3 (2020). doi:10.1038/s42004-020-0294-1
6. Ma P, Wang C, Li X, Yu X, Tian X, Hu W, et al. Ultrafast Proton Migration and Coulomb Explosion of Methyl Chloride in Intense Laser fields. *J Chem Phys* 146 (2017) 244305. doi:10.1063/1.4989565
7. Xu S, Zhao H, Zhu X, Guo D, Feng W, Lau K-C, et al. Dissociation of $[HCCH]^{2+}$ to $H_2{}^+$ and $C_2{}^+$: a Benchmark Reaction Involving H Migration, H-H Combination, and C-H Bond Cleavage. *Phys Chem Chem Phys* 20 (2018) 27725–9. doi:10.1039/c8cp05780j
8. Michie MJ, Ekanayake N, Weingartz NP, Stamm J, and Dantus M. Quantum Coherent Control of $H_3{}^+$ Formation in strong fields. *J Chem Phys* 150 (2019) 044303. doi:10.1063/1.5070067
9. Jochim B, Berry B, Severt T, Feizollah P, Zohrabi M, and P KR, Dependence on the Initial Configuration of strong Field-Driven Isomerization of C_2H_2 Cations and Anions. *J Phys Chem Lett* 10 (2019) 2320–7. doi:10.1021/acs.jpclett.9b00520
10. McDonnell M, LaForge AC, Reino-González J, Disla M, Kling NG, Mishra D, et al. Ultrafast Laser-Induced Isomerization Dynamics in Acetonitrile. *J Phys Chem Lett* 11 (2020) 6724–9. doi:10.1021/acs.jpclett.0c01344
11. Wang E, Shan X, Chen L, Pfeifer T, Chen X, Ren X, et al. Ultrafast Proton Transfer Dynamics on the Repulsive Potential of the Ethanol Dication: Roaming-Mediated Isomerization versus Coulomb Explosion. *The J Phys Chem A* 124 (2020) 2785–91. doi:10.1021/acs.jpca.0c02074
12. Sharma S, Raman S, and Green WH. Intramolecular Hydrogen Migration in Alkylperoxy and Hydroperoxyalkylperoxy Radicals: Accurate Treatment of Hindered Rotors. *J Phys Chem A* 114 (2010) 5689–701. doi:10.1021/jp9098792
13. Zhao J, Song T, Xu M, Quan Q, Siu KWM, Hopkinson AC, et al. Intramolecular Hydrogen Atom Migration along the Backbone of Cationic and Neutral Radical Tripeptides and Subsequent Radical-Induced Dissociations. *Phys Chem Chem Phys* 14 (2012) 8723. doi:10.1039/c2cp40708f
14. Hoerner JK, Xiao H, Dobo A, and Kaltashov IA. Is There Hydrogen Scrambling in the Gas Phase? Energetic and Structural Determinants of Proton Mobility within Protein Ions. *J Am Chem Soc* 126 (2004) 7709–17. doi:10.1021/ja049513m
15. Shen Y, Zhao X, Wang G, and Chen DDY. Differential Hydrogen/deuterium Exchange during Proteoform Separation Enables Characterization of Conformational Differences between Coexisting Protein States. *Anal Chem* 91 (2019) 3805–9. doi:10.1021/acs.analchem.9b00558
16. Hoshina K, Furukawa Y, Okino T, and Yamanouchi K. Efficient Ejection of H_3^+ from Hydrocarbon Molecules Induced by Ultrashort Intense Laser fields. *J Chem Phys* 129 (2008) 104302. doi:10.1063/1.2973588
17. Ando T, Iwasaki A, and Yamanouchi K. Strong-field Fourier Transform Vibrational Spectroscopy of Methanol Cation and its Isotopologues Using Few-Cycle Near-Infrared Laser Pulses. *Mol Phys* 117 (2019) 1732–40. doi:10.1080/00268976.2019.1572244
18. Ekanayake N, Nairat M, Kaderiya B, Feizollah P, Jochim B, Severt T, et al. Mechanisms and Time-Resolved Dynamics for Trihydrogen Cation (H_3^+) Formation from Organic Molecules in strong Laser fields. *Scientific Rep* 7 (2017). doi:10.1038/s41598-017-04666-w
19. Ekanayake N, Severt T, Nairat M, Weingartz NP, Farris BM, Kaderiya B, et al. H_2 Roaming Chemistry and the Formation of H_3^+ from Organic Molecules in strong Laser fields. *Nat Commun* 9 (2018). doi:10.1038/s41467-018-07577-0
20. Ekanayake N, Nairat M, Weingartz NP, Michie MJ, Levine BG, and Dantus M. Substituent Effects on H_3^+ Formation *via* H_2 Roaming Mechanisms from Organic Molecules under strong-field Photodissociation. *J Chem Phys* 149 (2018) 244310. doi:10.1063/1.5065387
21. Iwamoto N, Schwartz CJ, Jochim B, PK R, Feizollah P, Napierala JL, et al. Strong-field Control of H_3^+ Production from Methanol Dications: Selecting between Local and Extended Formation Mechanisms. *J Chem Phys* 152 (2020) 054302. doi:10.1063/1.5129946
22. Townsend D, Lahankar SA, Lee SK, Chambreau SD, Suits AG, Zhang X, et al. The Roaming Atom: Straying from the Reaction Path in Formaldehyde Decomposition. *Science* 306 (2004) 1158–61. doi:10.1126/science.1104386
23. Luzon I, Livshits E, Gope K, Baer R, and Strasser D. Making Sense of Coulomb Explosion Imaging. *J Phys Chem Lett* 10 (2019) 1361–7. doi:10.1021/acs.jpclett.9b00576
24. Mebel AM, and Bandrauk AD. Theoretical Study of Unimolecular Decomposition of Allene Cations. *J Chem Phys* 129 (2008) 224311. doi:10.1063/1.3037204
25. Xu H, Okino T, and Yamanouchi K. Tracing Ultrafast Hydrogen Migration in Allene in Intense Laser fields by Triple-Ion Coincidence Momentum Imaging. *J Chem Phys* 131 (2009) 151102. doi:10.1063/1.3251032
26. Furukawa Y, Hoshina K, Yamanouchi K, and Nakano H. Ejection of Triatomic Hydrogen Molecular Ion from Methanol in Intense Laser fields. *Chem Phys Lett* 414 (2005) 117–21. doi:10.1016/j.cplett.2005.07.108
27. Kotsina N, Kaziannis S, and Kosmidis C. Phase Dependence of OD^+, HOD^+, and H_3^+ Ions Released from the Deuterated Dication of Methanol under $\omega/2\omega$ Laser Field Irradiation. *Int J Mass Spectrom* 380 (2015) 34–9. doi:10.1016/j.ijms.2015.03.001
28. Nakai K, Kato T, Kono H, and Yamanouchi K. Communication: Long-Lived Neutral H_2 in Hydrogen Migration within Methanol Dication. *J Chem Phys* 139 (2013) 181103. doi:10.1063/1.4830397
29. Kotsina N, Kaziannis S, and Kosmidis C. Hydrogen Migration in Methanol Studied under Asymmetric Fs Laser Irradiation. *Chem Phys Lett* 604 (2014) 27–32. doi:10.1016/j.cplett.2014.04.040
30. Hoshina K, Kawamura H, Tsuge M, Tamiya M, and Ishiguro M. Metastable Decomposition and Hydrogen Migration of Ethane Dication Produced in an Intense Femtosecond Near-Infrared Laser Field. *J Chem Phys* 134 (2011) 064324. doi:10.1063/1.3549137
31. Kraus PM, Schwarzer MC, Schirmel N, Urbasch G, Frenking G, and Weitzel KM. Unusual Mechanism for H_3^+ Formation from Ethane as Obtained by Femtosecond Laser Pulse Ionization and Quantum Chemical Calculations. *J Chem Phys* 134 (2011) 114302. doi:10.1063/1.3561311
32. Kanya R, Kudou T, Schirmel N, Miura S, Weitzel KM, Hoshina K, et al. Hydrogen Scrambling in Ethane Induced by Intense Laser fields: Statistical Analysis of Coincidence Events. *J Chem Phys* 136 (2012) 204309. doi:10.1063/1.4720503
33. Schirmel N, Reusch N, Horsch P, and Weitzel KM. Formation of Fragment Ions (H^+, H_3^+, CH_3^+) From Ethane in Intense Femtosecond Laser fields – From Understanding to Control. *Faraday Discuss* 163 (2013) 461. doi:10.1039/c3fd20152j
34. Boran Y, Gutsev GL, Kolomenskii AA, Zhu F, Schuessler A, and Strohaber J. Dissociative Ionization of Ethane with Femtosecond Pulses of Radiation. *J Phys B: At Mol Opt Phys* 51 (2018) 035003. doi:10.1088/1361-6455/aa98d4
35. Zhang Y, Ren B, Yang CL, Wei L, Wang B, Han J, et al. Formation of H_3^+ from Ethane Dication Induced by Electron Impact. *Commun Chem* 3 (2020). doi:10.1038/s42004-020-00415-9
36. Zhao S, Jochim B, Feizollah P, Rajput J, Ziaee F, P KR, et al. Strong-field-induced Bond Rearrangement in Triatomic Molecules. *Phys Rev A* 99 (2019). doi:10.1103/physreva.99.053412
37. Verluise F, Laude V, Cheng Z, Spielmann C, and Tournois P. Amplitude and Phase Control of Ultrashort Pulses by Use of an Acousto-Optic Programmable Dispersive Filter: Pulse Compression and Shaping. *Opt Lett* 25 (2000) 575. doi:10.1364/ol.25.000575
38. Chandler DW, and Houston PL. Two-dimensional Imaging of State-Selected Photodissociation Products Detected by Multiphoton Ionization. *J Chem Phys* 87 (1987) 1445–7. doi:10.1063/1.453276

39. Eppink ATJB, and Parker DH. Velocity Map Imaging of Ions and Electrons Using Electrostatic Lenses: Application in Photoelectron and Photofragment Ion Imaging of Molecular Oxygen. *Rev Scientific Instr* 68 (1997) 3477–84. doi:10.1063/1.1148310
40. Dörner R, Mergel V, Jagutzki O, Spielberger L, Ullrich J, Moshammer R, et al. Cold Target Recoil Ion Momentum Spectroscopy: a 'momentum Microscope' to View Atomic Collision Dynamics. *Phys Rep* 330 (2000) 95–192. doi:10.1016/s0370-1573(99)00109-x
41. Ullrich J, Moshammer R, Dorn A, Dörner R, Schmidt LPH, and Schmidt-Böcking H. Recoil-ion and Electron Momentum Spectroscopy: Reaction-Microscopes. *Rep Prog Phys* 66 (2003) 1463.doi:10.1088/0034-4885/66/9/203
42. Treacy E. Optical Pulse Compression with Diffraction Gratings. *IEEE J Quan Electronics* 5 (1969) 454–8. doi:10.1109/jqe.1969.1076303
43. Martinez O. Design of High-Power Ultrashort Pulse Amplifiers by Expansion and Recompression. *IEEE J Quan Electronics* 23 (1987) 1385–7. doi:10.1109/jqe.1987.1073518
44. Trebino R. *Frequency-Resolved Optical Gating* (Kluwer Academic Publishers) (2000).
45. Kling NG, Paul D, Gura A, Laurent G, De S, Li H, et al. Thick-lens Velocity-Map Imaging Spectrometer with High Resolution for High-Energy Charged Particles. *J Instrumentation* 9 (2014) P05005. doi:10.1088/1748-0221/9/05/P05005
46. Wells E, Rallis C, Zohrabi M, Siemering R, Jochim B, Andrews P, et al. Adaptive strong-field Control of Chemical Dynamics Guided by Three-Dimensional Momentum Imaging. *Nat Commun* 4 (2013) 2895. doi:10.1038/ncomms3895
47. Rallis CE, Burwitz TG, Andrews PR, Zohrabi M, Averin R, De S, et al. Incorporating Real Time Velocity Map Image Reconstruction into Closed-Loop Coherent Control. *Rev Scientific Instr* 85 (2014) 113105. doi:10.1063/1.4899267
48. Judson RS, and Rabitz H. Teaching Lasers to Control Molecules. *Phys Rev Lett* 68 (1992) 1500–3. doi:10.1103/PhysRevLett.68.1500
49. Brif C, Chakrabarti R, and Rabitz H. Control of Quantum Phenomena: Past, Present and Future. *New J Phys* 12 (2010) 075008.doi:10.1088/1367-2630/12/7/075008
50. Lev U, Graham L, Madsen CB, Ben-Itzhak I, Bruner BD, Esry BD, et al. Quantum Control of Photodissociation Using Intense, Femtosecond Pulses Shaped with Third Order Dispersion. *J Phys B: At Mol Opt Phys* 48 (2015) 201001. doi:10.1088/0953-4075/48/20/201001
51. Nairat M, Lozovoy VV, and Dantus M. Order of Magnitude Dissociative Ionization Enhancement Observed for Pulses with High Order Dispersion. *J Phys Chem A* 120 (2016) 8529–36. doi:10.1021/acs.jpca.6b08659
52. Weiner A *Ultrafast Optics* (WILEY) (2009).
53. Ren X, Summers AM, P KR, Vajdi A, Makhija V, Fehrenbach CW, et al. Single-shot Carrier-envelope-phase Tagging Using an F–2f Interferometer and a Phase Meter: a Comparison. *J Opt* 19 (2017) 124017. doi:10.1088/2040-8986/aa9865
54. Lozovoy VV, Zhu X, Gunaratne TC, Harris DA, Shane JC, and Dantus M. Control of Molecular Fragmentation Using Shaped Femtosecond Pulses. *J Phys Chem A* 112 (2008) 3789–812. doi:10.1021/jp071691p
55. Joachain CJ, Kylstra NJ, and Potvliege RM. *Atoms in Intense Laser Fields* (Cambridge University Press) (2011).
56. [Dataset] Linstrom P. NIST Chemistry Webbook, NIST Standard Reference Database 69 (2018). doi:10.18434/T4D303

Conflict of Interest: The authors declare that the research was conducted in the absence of any commercial or financial relationships that could be construed as a potential conflict of interest.

ORIGINAL RESEARCH
published: 08 July 2021
doi: 10.3389/fphy.2021.677671

Manipulation of Multielectron Dynamics of Molecules by Fourier-Synthesized Intense Laser Pulses: Effective Potential Analysis of CO

Shu Ohmura*[1], *Hideki Ohmura*[2], *Tsuyoshi Kato*[3] and *Hirohiko Kono*[4]

[1]Department of Physical Science and Engineering, Nagoya Institute of Technology, Nagoya, Japan, [2]National Institute of Advanced Industrial Science and Technology (AIST), Tsukuba, Japan, [3]Department of Chemistry, School of Science, The University of Tokyo, Bunkyo-ku, Japan, [4]Department of Chemistry, Graduate School of Science, Tohoku University, Sendai, Japan

We present a theoretical investigation as to how multielectron dynamics of CO are manipulated by Fourier-synthesized intense laser pulses. The pulses used are assumed to be comprised of harmonics up to the fourth order. The multiconfiguration time-dependent (TD) Hartree-Fock (MCTDHF) method, where the multielectron wavefunction $\Psi(t)$ is expressed as a linear combination of various electron configurations, is employed to simulate the dynamics of CO interacting with Fourier-synthesized pulses. The multielectron nature such as electron correlation is quantified by using our effective potential approach. To begin with, the time-dependent natural orbitals $\{\phi_j(\boldsymbol{r},t)\}$ which diagonalize the first order reduced density matrix are obtained from $\Psi(t)$, where $\boldsymbol{r}$ is the one-electron coordinate. The effective potentials $v_j^{\mathrm{eff}}(\boldsymbol{r},t)$ that determine the dynamics of $\phi_j(\boldsymbol{r},t)$ are then derived from the equations of motion for $\{\phi_j(\boldsymbol{r},t)\}$. $v_j^{\mathrm{eff}}(\boldsymbol{r},t)$ consists of the one-body part $v_1(t)$ including the interaction with the laser electric field $\boldsymbol{\varepsilon}(t)$ and the two-body part $v_{2,j}(t)$ originating from electron-electron interaction. In this way, the role of electron correlation can be quantified by comparing $v_j^{\mathrm{eff}}(\boldsymbol{r},t)$ with those obtained by the TDHF method, where $\Psi(t)$ is approximated by a single Slater determinant. We found a very similar profile in $v_{5\sigma}^{\mathrm{eff}}(\boldsymbol{r},t)$ of the 5σ highest occupied molecular orbital for both near-infrared one-color (ω) and directionally asymmetric $\omega+2\omega$ two-color pulses; when $\boldsymbol{\varepsilon}(t)$ points from the nucleus C to O, a hump appears in $v_{5\sigma}^{\mathrm{eff}}(\boldsymbol{r},t)$ only 2 bohrs outward from C. The hump formation, which originates from the field-induced change in $v_{2,5\sigma}(t)$ (especially, due to electron correlation), is responsible for preferential electron ejection from the C atom side (experimentally observed anisotropic ionization). A coherent superposition of ω and 2ω fields with an appropriate relative phase thus works as a one-color pulse of which either positive or negative peaks are filtered out. More sophisticated manipulation is possible by adding higher harmonics to a synthesized field. We show that the 5σ orbital can be squeezed toward the inside of the potential valley in $v_{5\sigma}^{\mathrm{eff}}(\boldsymbol{r},t)$, which encloses the molecule at a radius of ~7 bohrs (semicircle in the region of $z<0$), by adjusting the phases of a $\omega+2\omega+3\omega+4\omega$ field. The hump and valley formation in $v_{5\sigma}^{\mathrm{eff}}(\boldsymbol{r},t)$ are closely correlated with domains of increasing and decreasing electron density, respectively.

Keywords: muliticonfiguration time-dependent Hartree-Fock theory, natural orbital dynamics, time-dependent effective potential, multielectron dynamics, tunnel ionization, intense laser pulse, multicolor superposition

OPEN ACCESS

Edited by:
Robert Gordon,
University of Illinois at Chicago,
United States

Reviewed by:
Andre Bandrauk,
Université de Sherbrooke, Canada
Arkaprabha Konar,
Kent State University, United States

****Correspondence:***
Hirohiko Kono
hirohiko.kono.d6@tohoku.ac.jp

Specialty section:
This article was submitted to
Physical Chemistry and Chemical
Physics,
a section of the journal
Frontiers in Physics

Received: *08 March 2021*
Accepted: *28 May 2021*
Published: *08 July 2021*

Citation:
Ohmura S, Ohmura H, Kato T and
Kono H (2021) Manipulation of
Multielectron Dynamics of Molecules
by Fourier-Synthesized Intense Laser
Pulses: Effective Potential Analysis
of CO.
Front. Phys. 9:677671.
doi: 10.3389/fphy.2021.677671

INTRODUCTION

Coherence is the succinct but vital word in modern science that features a wave of definite phase such as a laser field. The coherence of light [1] can be engraved in matter. Interaction of a coherent laser field with matter induces unique phenomena such as molecular alignment [2, 3] and high-order harmonic generation (HHG) of emission by intense near-infrared laser pulses [4]. Molecules can be aligned by intense near-infrared (IR) laser fields along a given space-fixed axis or plane, depending on the choice of light polarization through the anisotropic interaction of the electric field vector of intense laser radiation with the induced dipole moment. For a polarizable molecule, the major principal axis of the polarizability tensor is forced parallel to the polarization direction of a linearly polarized laser field. The mechanism of HHG is associated with the dynamics of an electron in field-dressed continuum states: Electrons freed by tunnel ionization (TI) [5–7] are pulled away from, pulled back near to, and recollided with parent ions within one optical cycle (the well-known three-step model [8]), while synchronized with the oscillating field. High energy photons even up to the soft x-ray range are emitted upon radiative recombination of an electron in field-driven quiver motion with the parent ion. In HHG, electronic continuum states in atoms or molecules are coherently excited with certain phases (described by a linear superposition of states), which leads to quantum interference between different electron trajectories (such as short and long trajectories) in the applied laser field [9, 10]. The HHG intensity is provided by the Fourier components of the induced dipole moment associated with individual trajectories. Coherent electronic motion in an ensemble of atoms or molecules, characterized by a definite dipole phase, is prerequisite for coherent emission of soft x-rays.

Phase coherence is the key concept in the optical control of quantum systems with high accuracy. Constructive and destructive interference between the wave packets created by a phase-locked pump-probe sequence can be controlled by varying the delay between the two pulses with interferometric precision [11, 12]. Various schemes for the control of optical phases have been devised to manipulate the wave functions or dynamics of quantum systems directly through the coherent nature of a laser field. This extensively growing research area is called coherent (or quantum) control [13–15]. Among various coherent control scenarios is utilization of a two-color phase-controlled laser field consisting of fundamental light and its harmonic light, which has been theoretically explored by Brumer and Shapiro [14]. For laser fields of moderate light intensity (below ~10^{12} W/cm^2), the population of a target state $|f\rangle$ can be controlled through quantum interference between two photo-induced transitions to $|f\rangle$, which is achieved by adjusting the relative phase between fundamental and harmonic fields [14]. In contrast, for the high intensity regime (above ~10^{12} W/cm^2), phase-controlled two-color fields can steer the motion of charges or dipoles with large amplitude. Such intense fields are used to induce asymmetric dynamics such as selective C-O bond breaking of ionized CO_2 [16, 17] and also to control the nonlinear coherent motion in TI [18–27] or HHG [28–31] of atoms and molecules.

An ultimate extension of this kind of methodology is Fourier synthesis of arbitrary light waveforms constructed of a fundamental frequency of light and its harmonics [32]. Sophisticated Fourier syntheses of laser fields have been reported [33–36]. Light wave engineering based on Fourier synthesis enables precise manipulation of electron motion beyond the case of single-frequency excitation; e.g., trajectory control of the HHG electrons in atoms and molecules by intense laser fields with various waveforms has been investigated theoretically [37] and achieved experimentally [38, 39]. Directionally asymmetric molecular TI induced by Fourier-synthesized four-color laser fields, consisting of fundamental, second-, third-, and fourth-harmonic light, can make possible orientation-selective molecular TI [40–43].

For a few-cycle single-frequency (one-color) pulse, carrier-envelope phase (CEP), i.e., the phase between the carrier wave and envelope peak of the pulse, also plays a significant role in electron dynamics such as TI and HHG. CEP stabilization has been achieved by the active feedback control which uses the combination of an f-to-2f interferometer to detect CEP drifts and a stereo-ATI (Above Threshold Ionization) phasemeter [44] to determine the value of CEP [45–48]. Few-cycle intense laser pulses with a stable CEP enable one to steer the electronic motion of atoms and molecules with an ultimate precision. Consequently, the HHG spectrum exhibits unique features depending on the CEP [49, 50].

Intense laser fields of light intensity above $I \approx 10^{12}$–10^{13} Wcm^{-2} initiate large amplitude electronic motion in atoms, molecules, etc., which triggers various physical or chemical phenomena in a wide range of timescale. Such systems can then be excited to high-lying electronic states or ionized in a nonperturbative manner. A typical phenomenon is TI, which is the source of the HHG upon recombination with the parent ion, as mentioned above. TI occurs mainly in the sub-femotosecond or attosecond (1 as = 10^{-18} s) region, owing to a highly nonlinear optical response, when the electric field of the laser reaches its maximum values. A number of experimental and theoretical studies have been devoted to profoundly understanding the intense-field induced electron dynamics in atoms [51], molecules [52], solids [53], and biological systems [54].

Different types of theoretical approaches beyond perturbation theory have been developed to deal with nonperturbative electronic dynamics of molecules. Epoch-making is the one proposed by Keldysh [55], in which the intense-field ionization rate or probability of an atom is formulated as an electronic transition from the ground state to continuum states of an electron liberated in a driving laser electric field (Volkov states) [56]. In this approach, the detailed atomic energy structure, such as information on excited states or electron correlation, is not taken into account and the Coulomb interaction of the released electron in the laser field with the remaining ion core is neglected. In the Perelemov-Popov-Terent'ev (PPT) approach [57], the long-range Coulomb interaction is incorporated into the Keldysh approach as the first-order correction in the quasi-classical action of the electron. These types of approaches can be integrated into S-matrix theory in which the transition amplitude of a quantum process is formulated by the projection of the total wave function of the system onto the final state. Several versions of the S-matrix approach have been developed which are together known as the Keldysh-Faisal-Reiss (KFR) theory or Strong Field Approximation (SFA) [58, 59].

Ionization induced by intense fields is characterized by the Keldysh parameter $\gamma = (\omega/f_{\max})(2I_P)^{1/2}$ [55] (in atomic units), where ω is the angular frequency of the applied laser electric field $\boldsymbol{\varepsilon}(t)$, $f_{\max}$ is the maximum of the envelop $f(t)$ of $\boldsymbol{\varepsilon}(t)$ and I_P is the ionization potential of the system. As $f(t)$ becomes larger and/or its optical period $2\pi/\omega$ becomes longer (i.e., $\gamma < 1$), an electron penetrates (or goes beyond) the "quasistatic" distorted barrier for ionization before the sign of the laser field reverses. The opposite case of $\gamma > 1$ is the multiphoton regime. In the case of $\gamma < 1$, the Ammosov–Delone–Krainov (ADK) model [60], which is the quasistatic limit $\gamma \to 0$ of the PPT approach, is most commonly used for atoms. A molecular version of the ADK model is developed by Lin et al. (called MO-ADK theory) [61].

In the above theoretical approaches, only one atomic or molecular orbital is considered as the main ionizing orbital and is allowed to interact with the applied field [61–63]. This is the so-called single active electron (SAE) approximation, where the time-dependent (TD) Schrödinger equation to be solved for the least-bound one-electron is constructed by modelling an "effective potential" after the interaction with the remaining electrons, the nuclei, and the applied fields. In [64, 65], model effective potentials for the ionizing orbital of a CO molecule were constructed by semiempirically formulating the dynamic multielectron polarization effects induced by the applied field [66–68]. The TD version of the Hartree-Fock (HF) method, which is a first-principles approach, can be used to describe the time evolution of a multielectron system (beyond the above SAE approximation). In this TDHF, the multielectron wave function $\Psi(t)$ at time t is however approximated by a single Slater determinant and the atomic or molecular orbitals involved therein evolve in time under the mean field approximation for electron-electron interaction; electron correlation (correlated electron motion) is thus not taken into account, as in the case of the HF method.

Correlated multielectron dynamics such as simultaneous double ionization of atoms and molecules is currently one of the primary targets in the research field of attosecond science [50, 52, 69, 70]. Among related subjects are correlated intramolecular electron dynamics [71, 72] and channel interference in HHG [73]. To describe such dynamics properly, one has to go beyond the computationally inexpensive SAE approximation or TDHF method. The multiconfiguration time-dependent Hartree-Fock (MCTDHF) method [74–83] has been developed in the past two decades as a legitimate method for including electron correlation in dynamics. In the MCTDHF, the multielectron wave function $\Psi(t)$ is expanded in terms of Slater determinants corresponding to various electron configurations, as in the case of time-independent quantum chemistry; both the orbitals and the coefficients of Slater determinants are optimized in compliance with TD variational schemes such as the Dirac-Frenkel variational principle [84, 85]. As the number of Slater determinants used increases, the quantitative accuracy is systematically improved.

As the level of the theory employed is higher, numerical results obtained become more detailed and reliable; accordingly, what is acquired to unveil the intrinsic physics underlying behind the numerical results becomes more complicated. The TD orbitals in the MCTDHF method evolves under the effects of electron correlation, but it is hard to extract the information of electron correlation from the time evolution of each orbital. For example, the temporal change in MCTDHF orbitals cannot be linearly decomposed into the change due to the one-body interaction (interaction of an electron with nuclei and external fields) and that due to the two-body interaction.

In our previous papers [86–90], a novel approach, i.e., a single orbital picture was established under the framework of the MCTDHF. We adopted the representation of TD natural spin-orbitals (SOs) $\{\phi_j(t)\}$ (see, for the natural SO, [91]), which diagonalizes the first-order reduced density matrix of electrons constructed from the MCTDHF multielectron wave function $\Psi(t)$. The orbital-dependent effective potentials $\{v_j^{\mathrm{eff}}(t)\}$ that govern the time evolution of $\{\phi_j(t)\}$ under the influence of electron correlation were then derived as a function of the spatial coordinate of an electron, $\boldsymbol{r}$ [88–90]. The obtained effective potential $v_j^{\mathrm{eff}}(\boldsymbol{r}, t)$ for $\phi_j(t)$ can be partitioned into $v_j^{\mathrm{eff}}(t) = v_1(t) + v_{2,j}(t)$, where $v_1(t)$ is the one-body interaction and $v_{2,j}(t)$ originates from the two-body interaction between electrons. We have investigated the mechanisms of the directional anisotropy in intense-field induced ionization of heteronuclear diatomic molecules CO [88–90] and LiH [90] by scrutinizing the temporal change in their effective potentials. The results of CO effective potentials are summarized in the second last paragraph of this section.

Directional anisotropy in the intense-field induced ionization of CO has been extensively investigated [20, 21, 26, 92] by using space-asymmetric ω+2ω two-color fields. The emission direction of C^+ or O^+ from CO in two-color field ionization experiments indicates that ionization is enhanced when the laser electric field $\boldsymbol{\varepsilon}(t)$ points from C to O [20, 21, 26, 92] (ionization from the C atom side). Intense-field ionization of CO mainly proceeds from the highest occupied molecular orbital (HOMO). It has been suggested, e.g., in the SAE approximation or single active orbital treatment [20, 21, 26, 61] that for CO the large-amplitude lobe of the HOMO around C is the origin of the preferential TI from C.

The direction of anisotropic ionization does not always agree with the prediction based solely on the shape of the HOMO. For OCS, the HOMO has a large amplitude around the C-S axis but ionization in a circularly polarized field is enhanced when the electric field turns to the direction from O to S [93]. This anisotropy is attributed to the linear Stark effect for polar molecules which increases (or reduces) the ionization potential of HOMO when $\boldsymbol{\varepsilon}(t)$ is parallel (or antiparallel) to the HOMO permanent dipole moment. In the linearly polarized ω+2ω two-color experiment reported by Ohmura et al. [27], the preferential direction was however from the S atom side (opposite to the case for circularly polarized pulses [93]). The linear Stark effect on intense-field-induced ionization has yet to be fully elucidated [94–100].

The results obtained by the conventional MO-ADK theory [61] are in agreement with the experimental result that the ionization rate of the HOMO of CO takes the maximum when $\boldsymbol{\varepsilon}(t)$ points from C to O. The Stark-shift-corrected MO-ADK theory, on the contrary, indicates the opposite trend [21], which directly reflects the tendency that the linear Stark effect increases the ionization potential of CO when $\boldsymbol{\varepsilon}(t)$ points from C to O and is therefore apt to reduce the HOMO ionization rate from the C atom side. The prediction by the Stark-shift-corrected molecular SFA [21] is in accord with the experimental observation. The diversity of theoretical predictions requires further investigation of the anisotropic ionization of CO.

Among other relevant factors to be considered for intense field ionization are the combined contribution from multiple orbitals [101, 102], field-induced multielectron correlation effects [87], and dynamic electron polarization [64, 99]. Although the emission direction of C^+ or O^+ from CO in the two-color ionization experiments [20, 21, 26] suggests that the main channel of the TI in CO is the 5σ HOMO, next lower lying orbitals such as 1π HOMO-1 and 4σ HOMO-2 can contribute to the ionization yield [88, 101]. These factors also affect the HHG process. The effects of dynamic electron polarization on HHG have also been discussed in [103, 104].

In previous studies [88–90], we calculated the effective potentials for natural orbitals of CO in an intense near-IR field ($\lambda = 760$ nm, $I = 10^{14}$ $\mathrm{Wcm^{-2}}$) from the MCTDHF wave function and investigated the mechanism of anisotropic ionization of CO. The analysis of the 5σ HOMO effective potential $v_{5\sigma}^{\mathrm{eff}}(t) = v_1(t) + v_{2,5\sigma}(t)$ obtained indicates that when $\boldsymbol{\varepsilon}(t)$ points to the direction from C to O, TI from the C atom side is enhanced and a thin hump barrier then emerges in $v_1(0) + v_{2,5\sigma}(t)$. A hump formed in $v_{5\sigma}^{\mathrm{eff}}(t)$, of which the location is only 2 bohrs away outside from the nucleus C, originates from the interaction between the electron leaving the ion core and the electrons swarming to the region of hump formation (ionization exit). We attributed the origin of the anisotropic TI in CO to this thin hump barrier, through which an ionizing electron penetrates. This kind of hump structure due to electron correlation is general and cannot be described by the TDHF. We simulated the dynamics of LiH interacting with an intense pulse of $\lambda = 1{,}520$ nm, which also indicates that a hump structure emerges in the 2σ HOMO effective potential and brings about anisotropic ionization.

We have so far shown how useful the effective potential approach is to unveil the intrinsic nature of multielectron dynamics [88–90]. In this paper, we examine the role of electron-electron interaction or electron correlation in CO interacting with Fourier-synthesized intense laser pulses by monitoring the temporal change in effective potentials, though the effective potential itself comes from a single-electron picture. The structure of this paper is as follows. The MCTDHF method for the calculation of multielectron dynamics is outlined in *Methodology for Effective Potential*, together with a brief derivation of the effective potentials for time-dependent natural orbitals. The results and discussion on the ionization and multielectron dynamics of CO in one-color to four-color phase-controlled fields are presented in *Results and Discussion*. Finally, conclusions about the manipulation of multielectron dynamics of CO by Fourier-synthesized pulses are given in *Conclusion*.

METHODOLOGY FOR EFFECTIVE POTENTIAL

In this section, we outline the MCTDHF method developed for the simulation of multielectron dynamics of atoms and molecules. In our approach, the multielectron wave function $\Psi(t)$ of a target system is obtained by numerically solving the equations of motion (EOMs) for time-dependent SOs and configuration interaction (CI) expansion coefficients in the MCTDHF method. We then convert the set of SOs in $\Psi(t)$ to an appropriate set of natural orbitals. The effective potential for each natural orbital is derived from the EOMs for natural orbitals; in this way, the role of multielectron dynamics or electron correlation can be quantified in a single orbital picture.

Outline of the Multiconfiguration Time-Dependent Hartree-Fock Method

The dynamics of an N_e-electron system is governed by the TD Schrödinger equation for the wave function $\Psi(t)$

$$i\hbar\frac{\partial\Psi(t)}{\partial t} = \widehat{H}(t)\Psi(t) \tag{1}$$

where $\widehat{H}(t)$ is the total electronic Hamiltonian including the interaction with the applied radiation field $\boldsymbol{\varepsilon}(t)$. We solve **Eq. 1** by using the MCTDHF method where $\Psi(t)$ is approximated as a liner combination of different electron configurations $\{\Phi_I(t)\}$ (represented by Slater determinants or configuration state functions) [74–83]:

$$\Psi(t) = \sum_{I=1}^{M} C_I(t)\Phi_I(t) \tag{2}$$

where $C_I(t)$ are the CI coefficients for $\Phi_I(t)$ and M is the total number of $\Phi_I(t)$. Each electron configuration is constructed of N_e spin-orbitals (SOs) $\{\psi_k(t)\}$; $\psi_k(t)$ is the product of a one-electron spatial orbital and a one-electron spin eigenfunction for the kth single-orbital state $|k(t)\rangle$. One may write $\psi_k(t)$ as $\psi_k(t) = \langle \boldsymbol{x}|k(t)\rangle$, where $\boldsymbol{x}$ consists of the spatial coordinate $\boldsymbol{r}$ and the spin coordinate μ of an electron. In the present study, the spin state of $\Psi(t)$ is assumed to be a singlet. The SOs used in the expansion of $\Psi(t)$ are here referred to as occupied orbitals. The number of the occupied orbitals, denoted by N_o, satisfies the relation $N_\mathrm{o} \geq N_\mathrm{e}$ in general; $N_\mathrm{o} = N_\mathrm{e}$ for TDHF.

The working EOMs for $\{\psi_k(t)\}$ and $\{C_I(t)\}$ have been derived by means of the Dirac-Frenkel TD variational principle [84, 85]:

$$\langle\delta\Psi(t)|\left[\widehat{H}(t) - i\hbar\frac{\partial}{\partial t}\right]|\Psi(t)\rangle = 0 \tag{3}$$

where $\delta\Psi(t)$ represents possible variations of $\{\psi_k(t)\}$ and $\{C_I(t)\}$ in the wave function (2). The EOMs for $\{\psi_k(t)\}$ are derived by inserting $\langle\delta\Psi(t)| = \langle\partial\Psi(t)/\partial\psi_k|\delta\psi_k$ into **Eq. 3**, whereas the EOMs for CI-coefficients are derived by instead using $\langle\delta\Psi(t)| = \langle\partial\Psi(t)/\partial C_I|\delta C_I$. Once the EOMs for $\{\psi_k(t)\}$ and $\{C_I(t)\}$ are solved, various quantities such as the first-order reduced density matrix (1RDM) $\rho(\boldsymbol{x},\boldsymbol{x}',t)$ can be calculated from $\{\psi_j(t)\}$ and $\{C_I(t)\}$.

$$\rho(\boldsymbol{x},\boldsymbol{x}',t) = \sum_{ij}^{N_{\mathrm{O}}} A_{ij}(t)\psi_i^*(\boldsymbol{x},t)\psi_j(\boldsymbol{x}',t) \tag{4}$$

where the (i,j) matrix element of the 1RDM, $A_{ij}(t)$, is expressed by using the annihilation operator $\hat{a}_j(t)$ and creation operator $\hat{a}_j^\dagger(t)$ for an electron in each $\psi_j(t)$

$$A_{ij}(t) = \langle\Psi(t)|\hat{a}_i^\dagger(t)\hat{a}_j(t)|\Psi(t)\rangle \tag{5}$$

Up to this point, $A_{ij}(t) \neq 0$ in general ($\{\psi_k(t)\}$ are not natural orbitals). The expectation value $\boldsymbol{u}(t)$ of any one-body operator $\hat{\boldsymbol{u}}$, such as the dipole moment operator $\hat{\boldsymbol{d}}$, is given by

$$\boldsymbol{u}(t) = \sum_{ij}^{N_{\mathrm{O}}} A_{ij}(t)\langle\psi_i(t)|\hat{\boldsymbol{u}}|\psi_j(t)\rangle \tag{6}$$

We now show briefly how to derive the effective potential for each SO. To begin with, we present in this paragraph the EOM for $\psi_k(t)$ derived in [88]:

$$i\hbar\frac{\partial|\psi_k(t)\rangle}{\partial t} = \left[\hat{h}(t) - \hat{g}(t)\right]|\psi_k(t)\rangle + \hat{Q}(t)\left[\hat{g}(t)|\psi_k(t)\rangle + \sum_{ij}^{N_{\mathrm{O}}} A^{-1}(t)_{ki}\hat{V}_{ij}(\boldsymbol{r},t)|\psi_j(t)\rangle\right] \tag{7}$$

where $\hat{h}(t)$ is the one-body Hamiltonian including the electric dipole interaction $\boldsymbol{r}\cdot\boldsymbol{\varepsilon}(t)$, $\hat{Q}(t) = 1 - \sum_k^{N_{\mathrm{O}}}|\psi_k(t)\rangle\langle\psi_k(t)|$ is the projector onto the complement to the current orbital space $\{\psi_k(t)\}$, $\hat{V}_{ij}(\boldsymbol{r},t)$ represents the orbital coupling between i and j mediated by other orbitals [76] (which depends on $\{C_I(t)\}$), and $\hat{g}(t)$ is to be determined so that the orthonormalization condition $\langle\psi_j(t)|\psi_k(t)\rangle = \delta_{jk}$ is maintained. Since **Eq. 7** leads to the following relation

$$i\hbar\langle\psi_j(t)|\frac{\partial}{\partial t}|\psi_k(t)\rangle = \langle\psi_j(t)|\left[\hat{h}(t) - \hat{g}(t)\right]|\psi_k(t)\rangle \tag{8}$$

the time propagation of $\{\psi_k(t)\}$ is unitary if $\hat{g}(t)$ is a Hermitian operator like $\hat{g}(t) = \sum_{mn}^{N_{\mathrm{O}}}|\psi_m(t)\rangle g_{mn}(t)\langle\psi_n(t)|$ with $g_{mn}(t) = g_{nm}^*(t)$. The EOM for $C_I(t)$, coupled with **Eq. (7)**, contains $\{C_I(t)\}$, $\{g_{km}(t)\}$ and the matrix elements of electron-electron interaction among SOs [75–77]. We choose $\hat{g}(t) = \hat{h}(t)$ to ensure that solving the EOMs for $\{\psi_j(t)\}$ and $\{C_I(t)\}$ is numerically stable; then, because of $\langle\psi_i(t)|\partial\psi_j(t)/\partial t\rangle = 0$ (for $i = j$ and $i \neq j$), the orthonormalization condition $\langle\psi_i(t)|\psi_j(t)\rangle = \delta_{ij}$ holds in the time-propagation of $|\psi_j(t)\rangle$.

How to Derive the Effective Potentials for Natural Orbitals

In the case of $\hat{g}(t) = \hat{h}(t)$, the off-diagonal elements of the 1RDM are in general nonzero, i.e., $A_{ij}(t) \neq 0$ for $i \neq j$. Diagonalization of the rhs of **Eq. 4** is equivalent to find a unitary transformation which converts $\{\psi_j(t)\}$ to an orbital set $\{\phi_j(t)\}$ that satisfies $A_{ij}(t) = 0$ for $i \neq j$. These orbitals $\{\phi_j(t)\}$ are called natural orbitals [91]. The diagonal element, $n_j(t) = A_{jj}(t)$, is the occupation number of $\phi_j(t)$. For $\{\phi_j(t)\}$, **Eq. 6** becomes the sum of the diagonal ones $\boldsymbol{u}_j(t) = \langle\phi_j(t)|\hat{\boldsymbol{u}}|\phi_j(t)\rangle$ as $\boldsymbol{u}(t) = \sum_j^{N_{\mathrm{O}}} n_j(t)\boldsymbol{u}_j(t)$ [86, 87].

The elements $\{A_{km}(t)\}$ of **Eq. 5** can be expressed by using CI-coefficients. We have derived the EOM for $A_{km}(t)$ in the natural orbital representation [88–90]:

$$\frac{\mathrm{d}A_{km}(t)}{\mathrm{d}t} = -\frac{i}{\hbar}\{W_{mk}(t) - W_{km}^*(t) + g_{mk}(t)[n_k(t) - n_m(t)]\} \tag{9}$$

where $W_{km}(t)$ is given in atomic units by [105, 106]

$$W_{km}(t) = \sum_{pqr}\int \mathrm{d}\boldsymbol{x}_1\mathrm{d}\boldsymbol{x}_2\phi_k^*(\boldsymbol{x}_1)\phi_q(\boldsymbol{x}_1)|\boldsymbol{r}_1 - \boldsymbol{r}_2|^{-1}\phi_r^*(\boldsymbol{x}_2)\phi_p(\boldsymbol{x}_2)\langle\Psi(t)|\hat{a}_m^\dagger(t)\hat{a}_r^\dagger(t)\hat{a}_p(t)\hat{a}_q(t)|\Psi(t)\rangle \tag{10}$$

We start with the natural orbitals at $t = t_0$, i.e., $\psi_j(t_0) = \phi_j(t_0)$, which are obtained from the MCTDHF wave function $\Psi(t)$ at $t = t_0$. To satisfy $A_{km}(t) = 0$ at $t \geq t_0$ for $k \neq m$, we have to set $g_{mk}(t)$ for $m \neq k$ in **Eq. 9** as

$$g_{mk}(t) = \frac{W_{mk}(t) - W_{km}^*(t)}{n_m(t) - n_k(t)} \tag{11}$$

The constraint that $A_{km}(t) = 0$ for $k \neq m$ does not fix the values of the diagonal elements $g_{kk}(t)$. The phases of $\{C_I(t)\}$ and the global phases of $\{\phi_j(t)\}$ are consistently determined through **Eq. 7** and EOMs for $\{C_I(t)\}$. For simplicity, we set the diagonal elements to be $g_{kk}(t) = 0$.

By substituting **Eq. 11** and $g_{kk}(t) = 0$ into **Eq. 7**, we reach the EOMs for natural SOs [88]

$$i\hbar\frac{\partial\phi_k(\boldsymbol{r},t)}{\partial t} = \left[\hat{t} + v_k^{\mathrm{eff}}(\boldsymbol{r},t)\right]\phi_k(\boldsymbol{r},t) \tag{12}$$

where $\hat{t}$ is the kinetic energy operator of an electron. Here, the one-body orbital-dependent effective potential $v_k^{\mathrm{eff}}(\boldsymbol{r},t)$, which determines the time evolution of $\phi_k(t)$ under multielectron interaction, is comprised of the one-body term $v_1(\boldsymbol{r},t)$ including the electric dipole interaction $\boldsymbol{r}\cdot\boldsymbol{\varepsilon}(t)$ and the two-body interaction term $v_{2,k}(\boldsymbol{r},t)$:

$$v_k^{\mathrm{eff}}(\boldsymbol{r},t) = v_1(\boldsymbol{r},t) + \sum_j^{N_{\mathrm{O}}}\frac{\langle\boldsymbol{r}|\hat{U}_{kj}(t)|\phi_j(t)\rangle}{\phi_k(\boldsymbol{r},t)} = v_1(\boldsymbol{r},t) + v_{2,k}(\boldsymbol{r},t) \tag{13}$$

where $\hat{U}_{kj}(t)$ is the coupling between $\phi_k(t)$ and $\phi_j(t)$

$$\hat{U}_{kj}(t) = \left(1 - \delta_{kj}\right)\frac{W_{jk}(t) - W_{kj}^*(t)}{n_k(t) - n_j(t)} + Q(t)\frac{\hat{V}_{kj}(t)}{n_k(t)} \tag{14}$$

We designate the expectation value of $\hat{t} + v_k^{\mathrm{eff}}(\boldsymbol{r},t)$ over $\phi_k(t)$ as a real-valued effective orbital energy $E_k(t)$. $v_k^{\mathrm{eff}}(\boldsymbol{r},t)$ is proved to be a Hermitian [88]. In practice, we calculate the "instantaneous" (orthonormal) natural orbitals $\{\phi_j(t)\}$ at time t from $\{\psi_j(t)\}$ and $\{C_I(t)\}$ obtained under the condition of

$\widehat{g}(t) = \widehat{h}(t)$. $v_k^{\mathrm{eff}}(\boldsymbol{r}, t)$ can be plotted as a function of $\boldsymbol{r}$ by inserting $\{\phi_j(t)\}$ and the corresponding $\{C_I(t)\}$ (different from those for $\widehat{g}(t) = \widehat{h}(t)$) into **Eq. 13**. Multielectron dynamics can be examined by plotting the temporal change in $v_1(\boldsymbol{r}, t)$ and that in $v_{2,k}(\boldsymbol{r}, t)$ separately. Electron correlation in dynamics can be quantified by the difference in $v_k^{\mathrm{eff}}(\boldsymbol{r}, t)$ between TDHF and MCTDHF.

RESULTS AND DISCUSSION

In addition to a one-color (ω) two-cycle pulse with different carrier-envelope phases [88–90], we theoretically investigated the response of CO to intense multicolor pulses; two-color (ω+2ω), three-color (ω+2ω+3ω), and four color (ω+2ω+3ω+4ω) pulses with different relative phases. We present the numerical results of ionization dynamics of a CO molecule interacting with the above four types of pulses to extract how laser field coherence affects multielectron dynamics from the spatial profiles of TD effective potentials of the 5σ HOMO natural orbital.

Applied Pulses

The C-O axis is assumed to be parallel to the polarization direction of the applied electric field $\boldsymbol{\varepsilon}(t)$. The frequency ω is chosen to be the fundamental of a Ti:Sapphire laser: here, $\hbar\omega = 0.06E_{\mathrm{h}} = 1.64\,\mathrm{eV}$ (wavelength $\lambda = 760\,\mathrm{nm}$), where E_{h} is the Hartree. The electric field of the one-color pulse, $\varepsilon_1(t)$, is assumed to have the form:

$$\varepsilon_1(t) = f(t)\cos(\omega t + \varphi_1) \tag{15}$$

where φ_1 is the CEP and $f(t)$ is the envelope function (The definition of φ_1 is shifted by π, compared to that in [88–90]). For all pulses presented in this paper, we use the same shape for $f(t)$

$$f(t) = F\sin^2(\pi t/2T_{\mathrm{c}}) \quad \text{for} \quad 0 \le t \le 2T_{\mathrm{c}} \tag{16}$$

and otherwise $f(t) = 0$. Here F is the maximum of $f(t)$ and $T_{\mathrm{c}} = 2\pi/\omega = 2.53$ fs is the optical period for the fundamental. The pulse length is 5.06 fs for all pulses. If $f(t) = 0.0534\ E_{\mathrm{h}}/(ea_0) = 2.74 \times 10^{10}\ \mathrm{Vm}^{-1}$, where e is the elementary charge and a_0 is the Bohr radius, the corresponding light intensity is $I = 1.0\times10^{14}\ \mathrm{W\,cm}^{-2}$. We use the following general form for multi-color pulses:

$$\begin{aligned}\varepsilon(t) = f(t)\big[&\cos(\omega t + \varphi_1) + a_2\cos(2\omega t + \varphi_2) + a_3\cos(3\omega t + \varphi_3) \\ &+ a_4\cos(4\omega t + \varphi_4)\big]\end{aligned} \tag{17}$$

These four phases φ_1,φ_2,φ_3, and φ_4 are chosen so that the main profile of $\varepsilon(t)$ is built in the middle of the pulse (Experimentally available is a pulse train of $\varepsilon(t)$). $\varepsilon_1(t)$ is given by setting $a_2 = a_3 = a_4 = 0$ in $\varepsilon(t)$. F in $f(t)$ is defined as

$$F = F_T/(1 + a_2 + a_3 + a_4) \tag{18}$$

where F_T is determined so that the maximum peak F_p of the electric field $|\varepsilon(t)|$ is the same as $F_p = 0.0378\ E_{\mathrm{h}}/(ea_0) = 1.94\times10^{10}\ \mathrm{Vm}^{-1}$ throughout this paper, unless otherwise noted. This field of F_p, which corresponds to $I = 5.0\times10^{13}\ \mathrm{Wcm}^{-2}$ in the case of one-color pulses, is weaker than in previous studies [88–90].

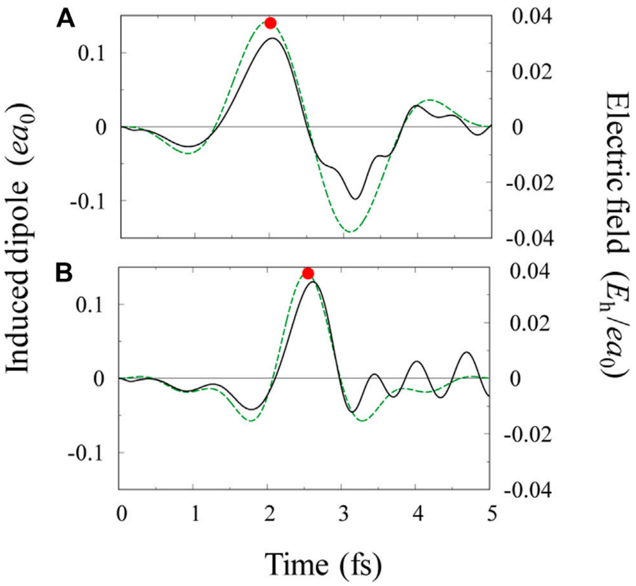

FIGURE 1 | (A) Electric field profile $\varepsilon_1(t)$ of the applied two-cycle pulse (15) of $\omega = 0.06E_{\mathrm{h}}/\hbar$ with CEP of $\varphi_1 = 0.5\pi$; **(B)** the asymmetric ω+2ω two-color field with $\varphi_1 = \varphi_2 = 0$ and $a_2 = 2/3$ (both are denoted by green broken lines). $\varepsilon_2(t)$ is defined by **Eq. 17**. The value of F_T in **Eq. 18** is chosen to be $0.0437E_{\mathrm{h}}/(ea_0)$ for $\varepsilon_1(t)$ and $0.0378E_{\mathrm{h}}/ea_0$ for $\varepsilon_2(t)$. The induced dipole moment $d_{5\sigma}(t)$ of the 5σ natural orbital of CO, obtained by TD-CASSCF, is superimposed in each panel (black solid lines).

TD-CASSCF Calculation

In *One-Color Pulses*, *Two-Color Pulses*, *Three-Color Pulses*, *Four-Color Pulses*, we discuss the characteristic features of the ionization of CO for one- and multi-color pulses. The effects of electron correlation is in detail examined on the basis of the TD effective potentials for the 5σ natural orbitals obtained in the MCTDHF framework. We trace the temporal change in effective potentials to investigate how distinctly electron correlation influences the electronic dynamics.

In the numerical simulations for CO in one-color pulses of $\lambda = 760$ nm [88–90], we considered 10 spatial orbitals 1σ, 2σ, 3σ, 4σ, 2×1π, 5σ HOMO, 2×2π LUMO (lowest unoccupied molecular orbital) and 6σ. There is a limit to the number of molecular orbitals (MOs) that we can handle in practical applications of the MCTDHF. The most commonly used scheme is the complete active space (CAS) method, where the orbitals used in the Slater determinants (or configuration state functions) are divided into inactive (core) and active orbitals. The two inactive spin-orbitals (SOs) with the same spatial function are singly occupied respectively in all electron configurations; all possible electron configurations are generated by distributing the other electrons among the active orbitals. This type of expansion scheme is called the time-dependent complete-active-space self-consistent-field (TD-CASSCF) method [107, 108]. Various wave-function-based multiconfigurational TD approaches to the dynamics of

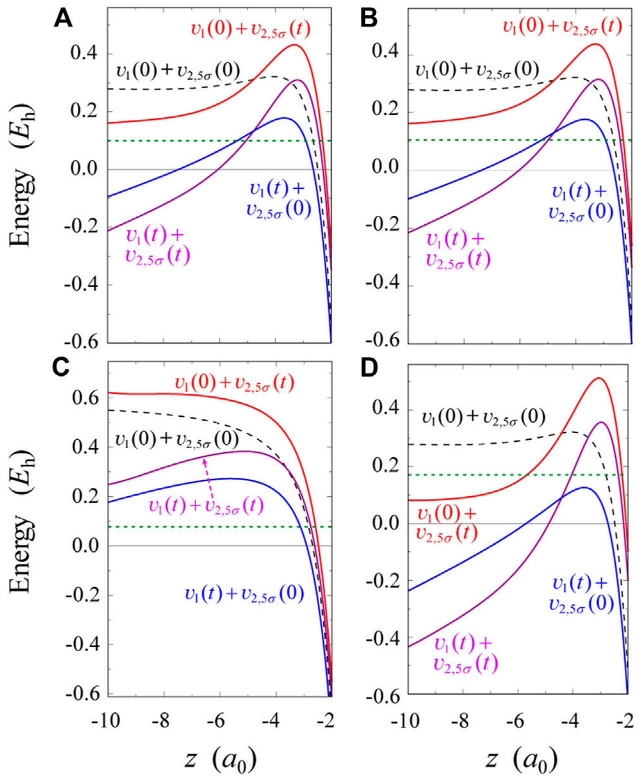

FIGURE 2 | Four kinds of 5σ effective potentials plotted parallel to the z-axis at the fixed value of $\rho = 0.755a_0$: **(A)** potentials obtained by TD-CASSCF at $t = t_1 \approx 2$ fs under the interaction with $\varepsilon_1(t)$ in **Figure 1A**; **(B)** TD-CASSCF potentials at $t \approx 2.53$ fs for $\varepsilon_2(t)$ in **Figure 1B**; **(C)** TDHF potentials at $t = t_1 \approx 2$ fs for $\varepsilon_1(t)$, i.e., the same pulse as in **Figure 1A**; **(D)** TD-CASSCF potentials at $t = t_1 \approx 2$ fs for the pulse (15) with a higher strength of $F_T = 0.06$ $E_h/(ea_0)$. $v_1(t)$ and $v_{2,5\sigma}(t)$ are respectively the one-body part and two-body part in $v_{5\sigma}^{\mathrm{eff}}(t)$. In each panel, the black broken, blue, red, and purple lines denote $v_1(0)+v_{2,5\sigma}(0)$, $v_1(t)+v_{2,5\sigma}(0)$, $v_1(0)+v_{2,5\sigma}(t)$, and $v_{5\sigma}^{\mathrm{eff}}(t) = v_1(t)+v_{2,5\sigma}(t)$, repectively. For reference, the level of the effective orbital energy $E_{5\sigma}(t)$ is given by a green horizontal dotted line. The time point t at which the effective potentials are calculated is indicated by a red filled circle in each panel in **Figure 1**.

indistinguishable particles are compiled in a recent review [109]. We adopted the following TD-CASSCF scheme in the present study; the lower lying core SOs up to 4σ were treated to be occupied by one electron and the shapes of the orbitals are allowed to vary according to the EOMs derived for the core SOs. The high lying 6 SOs, i.e., 2×1π, 5σ, 2×2π, 6σ, were treated as active orbitals that constitute the CAS to accommodate 14−8=6 electrons (the expansion length $M = 400$).

Since the molecular axis is parallel to the polarization direction, cylindrical symmetry is maintained; then, the cylindrical coordinates z and ρ are convenient for the numerical grid point representation of spatial orbitals; z is chosen parallel to the molecular axis. The nuclei C is placed at $z = -1.066$ a_0 and O is placed at $z = 1.066$ a_0 ($\rho = 0$). The C-O difference is equal to the equilibrium internuclear distance $R_e = 2.132$ a_0. The parameters necessary to describe MOs such as grid intervals are given in [88]. To estimate the ionization probability, we simply set an absorbing boundary that eliminate outgoing ionizing currents from propagating molecular orbitals. The details are explained in [87, 88].

One-Color Pulses

The temporal change in induced dipole moments characterizes the overall electronic dynamics of a molecule. Shown in **Figure 1A** are the one-color pulse $\varepsilon_1(t)$ (i.e., **Eq. 15**) with $\varphi_1 = 0.5\pi$ and the induced dipole moment of the 5σ HOMO natural orbital $\phi_{5\sigma}(t)$, denoted by $d_{5\sigma}(t)$. F_T in **Eq. 18** is chosen to be 0.04374 $E_h/(ea_0)$ so that the maximum peak is the target value of $F_p = 0.0378$ $E_h/(ea_0)$ (of which the value is used in all figures except **Figure 2D**). Up to around the end of the first optical cycle, the electronic response is quasi-adiabatic with respect to temporal change in $\varepsilon_1(t)$: the change in $d_{5\sigma}(t)$ is nearly proportional to $\varepsilon_1(t)$. This quasi-adiabatic feature is related to the fact that the energies of the excited singlet states of CO are higher than 8.5 eV [110]. The total induced dipole moment is nearly proportional to $d_{5\sigma}(t)$. In the adiabatic regime, the induced dipole moment is represented by a function of the applied filed $\varepsilon_1(t)$ (not necessarily a linear function of $\varepsilon(t)$). In the second optical cycle, electrons go back and forth during a half cycle to some extent (continuum states are also involved); the response becomes nonadiabatic and more complex as the interaction proceeds.

We have numerically confirmed that ionization exclusively occurs from the 5σ orbital when the electric field points from C to O, i.e., $\varepsilon_1(t) > 0$, for instance, at $t \approx 2$ fs in **Figure 1A**. At $\varepsilon_1(t) > 0$, the electric field then exerts a force on electrons toward the direction from O to C. The calculated ionization rate around the second peak of $\varepsilon_1(t)$ at $t \approx 2$ fs is roughly a few times larger for $\varphi_1 = 0.5\pi$ than for the phase reversed case of $\varphi_1 = -0.5\pi$ (The ionization from 5σ was significantly suppressed when $\varepsilon_1(t) < 0$.). This tendency, already found in the case of $F_T{\sim}0.06$ $E_h/(ea_0)$ [88], is in agreement with the experimentally observed anisotropy [26]. A criterion as to whether the ionization is adiabatic or not is given by the Keldysh parameter γ. For the pulse $\varepsilon_1(t)$, $\gamma{\sim}1.6$. It has been reported that TI remains as the dominant mechanism up to $\gamma \sim 3$ for few-cycle laser pulses [111]. The ionization process for $\varepsilon_1(t)$ is thus categorized as TI.

The origin of anisotropic ionization of CO in near-IR fields has been argued mostly in connection with the fact that the 5σ HOMO natural orbital has a large lobe around the C atom. In what follows, we examine what role electron correlation plays in the anisotropic ionization process. We investigate the mechanism of anisotropic near-IR induced ionization of CO by tracing the TD effective potentials of natural orbitals, defined by **Eq. 13**, which are changing every moment. More generally, the (correlated) multielectron nature intrinsic in intense-field-induced phenomena can be extracted from the analysis of the temporal change in the effective potential of each natural orbital.

Figure 2 display different types of 5σ HOMO effective potentials $v_{5\sigma}^{\mathrm{eff}}(t) = v_1(t) + v_{2,5\sigma}(t)$ for four cases, which are one-dimensional cuts parallel to the z-axis. The value of ρ is fixed at $\rho = 0.755a_0$, around which the electron density integrated over z takes a maximum. For the pulse in **Figure 1A** with $\varphi_1 = 0.5\pi$, the effective potentials at $t \approx t_1 = 2$ fs obtained by TD-CASSCF are shown in **Figure 2A** and those obtained by

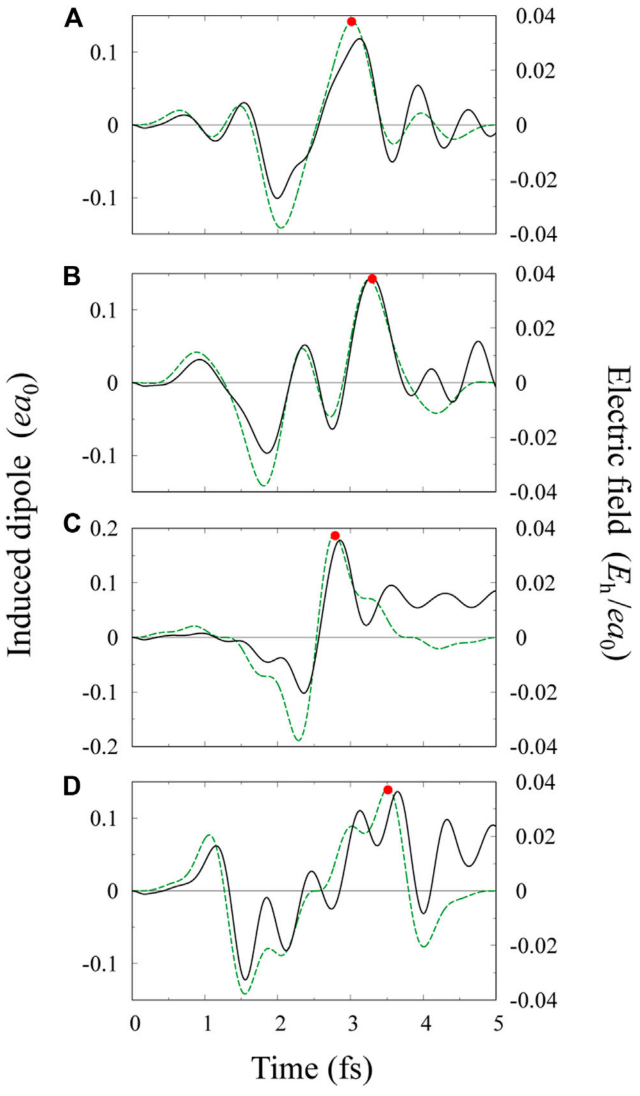

FIGURE 3 | Electric field profiles for multi-color pulses (green broken lines): **(A, B)** three-color pulses with relative intensities $a_2 = 2/3$ and $a_3 = 1/3$; **(C, D)** four-color pulses with relative intensities $a_2 = 1/2$, $a_3 = 1/3$, and $a_4 = 1/4$. The relative pahses and the intensity parameter F_T in **Eq. 18** are given as follows: **(A)** $\varphi_1 = \varphi_2 = -\pi/2, \varphi_3 = \pi/2$, and $E_T = 0.0541E_h/(ea_0)$; **(B)** $\varphi_1 = -\pi/2$, $\varphi_2 = \varphi_3 = \pi/2$, and $F_T = 0.0611E_h/(ea_0)$; **(C)** $\varphi_1 = \varphi_2 = \varphi_3 = \varphi_4 = -\pi/2$ and $F_T = 0.0528E_h/(ea_0)$; **(D)** $\varphi_1 = \varphi_3 = -\pi/2$, $\varphi_2 = \varphi_4 = \pi/2$, and $F_T = 0.0778E_h/(ea_0)$. The induced dipole mements $d_{5\sigma}(t)$ of the 5σ natural orbital for each pulse, denoted by a black solid line, is obtained by TD-CASSCF.

TDHF ($M = 1$) are shown in **Figure 2C**. The electric field $\boldsymbol{\varepsilon}_1(t)$ at $t \approx t_1$ points from C to O for the case of $\varphi_1 = 0.5\pi$ (i.e., $\varepsilon(t_1) > 0$). The one-body part $v_1(t)$ changes according to the dipole interaction, i.e., $v_1(t) = v_1(0) + z\varepsilon_1(t)$; $v_1(t_1) + v_{2,5\sigma}(0)$ in **Figures 2A,C** therefore exhibit the same linear slant in the asymptotic region of large $|z|$. On the other hand, the change in $v_{2,5\sigma}(t)$ is distinctly different between the two methods. The effective potential of $v_1(0) + v_{2,5\sigma}(t_1)$ obtained by TD-CASSCF has a hump around $z = -3a_0$ and crosses $v^{\mathrm{eff}}_{5\sigma}(0)$ at $z \approx -5a_0$; $v_1(0) + v_{2,5\sigma}(t_1)$ asymptotically approaches $v^{\mathrm{eff}}_{5\sigma}(0)$ as z goes negative. As a result, the total one $v^{\mathrm{eff}}_{5\sigma}(t_1) = v_1(t_1) + v_{2,5\sigma}(t_1)$ in **Figure 2A** has also a hump (extra thin barrier) around $z = -3a_0$ in comparison with $v_1(t_1) + v_{2,5\sigma}(0)$.

When the sign of $\varepsilon_1(t)$ is reversed in the next half cycle at $t \approx t_2 = 3$ fs, the two-body part $v_1(0) + v_{2,5\sigma}(t_2)$ monotonically increases up to $z \approx 11a_0$ ($v^{\mathrm{eff}}_{5\sigma}(t_2)$ is even slightly higher than $v^{\mathrm{eff}}_{5\sigma}(0)$ up to $z \approx 11a_0$, albeit the presence of the applied electric field of $\varepsilon_1(t_2) < 0$). A tunnel barrier in $v^{\mathrm{eff}}_{5\sigma}(t_2)$ is thus formed in the region of $z > 10a_0$, far away from the nuclei. Long propagation is required for an electron to reach the barrier located at $z \approx 10a_0$. We found that these features are responsible for the suppression of TI when $\varepsilon_1(t) < 0$ [88–90]. The fact that the tunnel barrier is far distant from the O atom when the electric field points from O to C can be also clearly demonstrated by the TD-CASSCF effective potential $v^{\mathrm{eff}}_{5\sigma}(t_1)$ for the opposite case of $\varphi_1 = -0.5\pi$. For this choice of φ_1, $\varepsilon_1(t_1) < 0$; the upward slope in $v^{\mathrm{eff}}_{5\sigma}(t_1)$ shifts downward around $z \approx 13a_0$. Another example for the opposite CEP is shown in Figure 5 in [90] (where the field strength is about one and a half times of the present one). The temporal change in the spatial profile of $v^{\mathrm{eff}}_{5\sigma}(t)$ is consistent with the experimentally observed anisotropic TI of CO.

To quantify the role of electron correlation, we compare the effective potentials in **Figure 2A** with TDHF ones shown in **Figure 2C**. In **Figure 2C**, $v_1(0) + v_{2,5\sigma}(t_1)$ increases gradually with decreasing z and is higher than $v_1(0) + v_{2,5\sigma}(0)$ by a constant of ~$0.1E_h$. Accordingly, $v^{\mathrm{eff}}_{5\sigma}(t_1)$ is nearly parallel to $v_1(t_1) + v_{2,5\sigma}(0)$. The tunnel barrier in $v^{\mathrm{eff}}_{5\sigma}(t_1)$ is higher and wider in **Figure 2C** than in **Figure 2A**. As expected from the tunnel barriers in **Figures 2A,C** the ionization probability obtained by TDHF was less than 1/30 of the TD-CASSCF value (~0.0008 for the whole pulse of $\varepsilon_1(t)$ with $\varphi_1 = 0.5\pi$). More importantly, hump formation in $v_1(0) + v_{2,5\sigma}(t_1)$ is not observed in **Figure 2C**. Hump formation is hence ascribed to the effects of multielectron interaction beyond the mean field approximation, i.e., the electron correlation originating from the interaction with the applied field. To grasp the appearance of the hump more comprehensively, we present 5σ effective potentials for a higher field strength of F_T=0.06 $E_h/(ea_0)$ in **Figure 2D** [88–90]. Comparison in $v_1(0) + v_{2,5\sigma}(t_1)$ between **Figures 2A,D** shows that the hump grows and the peak position in $v_1(0) + v_{2,5\sigma}(t_1)$ slightly shifts toward the nucleus C with increasing field strength ($\varepsilon_1(t_1) > 0$). The resulting thin barrier formed around $z = -3a_0$ in $v^{\mathrm{eff}}_{5\sigma}(t_1)$, which is not reproduced by TDHF, clearly indicates preferential ionization from the C atom side. The hump formation in $v_1(0) + v_{2,5\sigma}(t_1)$ reflects the process that an electron penetrates through the potential barrier due to a field-induced local rise of electron density, of which area may be called an ionization exit.

In *Four-Color Pulses*, we provide a more concrete picture to understand the root of hump formation in $v^{\mathrm{eff}}_{5\sigma}(t)$ and the mechanism of anisotropic ionization of CO.

Two-Color Pulses

The one-color field $\varepsilon_1(t)$ is directionally symmetric: the absolute value of $\varepsilon_1(t)$ is the same for its positive and negative extremes. The TOF fragment analyses of ω +2ω experiments for CO [20, 21,

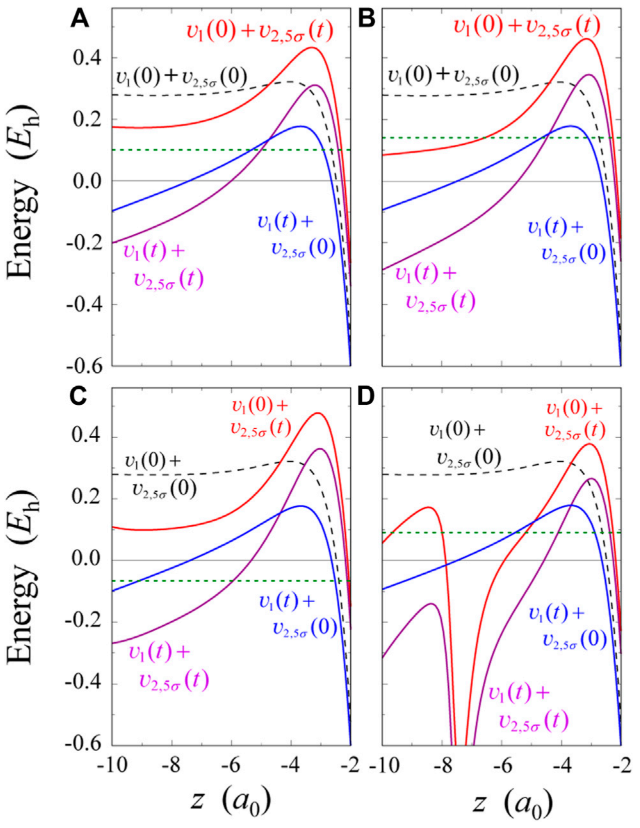

FIGURE 4 | Four kinds of 5σ effective potentials plotted parallel to the z-axis at the fixed value of $\rho = 0.755a_0$. The pulses used in four panels **(A–D)** correspond to those in **Figure 3(A–D)**, respectively. $v_1(t)$ and $v_{2,5\sigma}(t)$ are respectively the one-body part and two-body part in $v_{5\sigma}^{\mathrm{eff}}(t)$. The definitions of effective potentials are designated in each panel. The effective potentials in these panels are all calculated by TD-CASSCF. The green horizontal dotted line denotes the effective orbital energy $E_{5\sigma}(t)$. The time point at which the effective potentials are calculated is indicated by a red filled circle in each panel in **Figure 3**.

26] have indicated that the ionization rate takes the maximum when the field points from C to O and takes the minimum when the field is reversed. To reveal more explicitly the correlation in anisotropy between the ionization of CO and the applied field, we here employ two-color fields that provide asymmetric fields. **Figure 1B** is an example of an asymmetric two-color field $\varepsilon_2(t)$. The parameters in **Eq. 17** are chosen for $\varepsilon_2(t)$ as $a_2 = 2/3$, $\varphi_1 = \varphi_2 = 0$, and $F_T = F_p = 0.0378\,E/ea_0$ ($a_3 = a_4 = 0$). The sign of the electric field $\varepsilon_2(t)$ is reversed by setting $\varphi_1 = \varphi_2 = \pi$. Similar parameter sets of φ_1,φ_2, a_2 and E_T are experimentally feasible as demonstrated in [20, 21, 26].

The largest peak in $\varepsilon_2(t)$ of **Figure 1B** appears in the positive side. The central peak at $t \approx 2.53$ fs is overwhelmingly high and the effects of the other peaks are expected to be minute. The induced dipole moment of the 5σ orbital, calculated by TD-CASSCF, is also plotted in **Figure 1B**, indicating that the orbital responds to the two-color field mainly near the central peak. The TD-CASSCF effective potential $v_{5\sigma}^{\mathrm{eff}}(t)$ at $t \approx 2.5$ fs is shown in **Figure 2B**, which quantitatively agrees with that in the one-color case of **Figure 2A**. The positive peak of $\varepsilon_2(t)$ in **Figure 1B** has therefore almost the same effect on ionization as the positive peak of $\varepsilon_1(t)$ in **Figure 1A** does. The ionization probabilities for the pulses in **Figures 1A,B** are nearly the same as ~0.0008. This results again suggests that the ionization probability induced by the negative peak is much smaller than that by the positive peak, under the assumption that the effects of individual peaks in $\varepsilon_1(t)$ on TI are separable from each other. What ionization dynamics the positive or negative peak of a one-color pulse brings about can be separately examined by employing two-color pulses that are per se directionally asymmetric like $\varepsilon_2(t)$. The ionization probability for the sign-reversed pulse, i.e., $-\varepsilon_2(t)$, is about one-third as small as that for $\varepsilon_2(t)$. This approach has already been realized experimentally, as mentioned above.

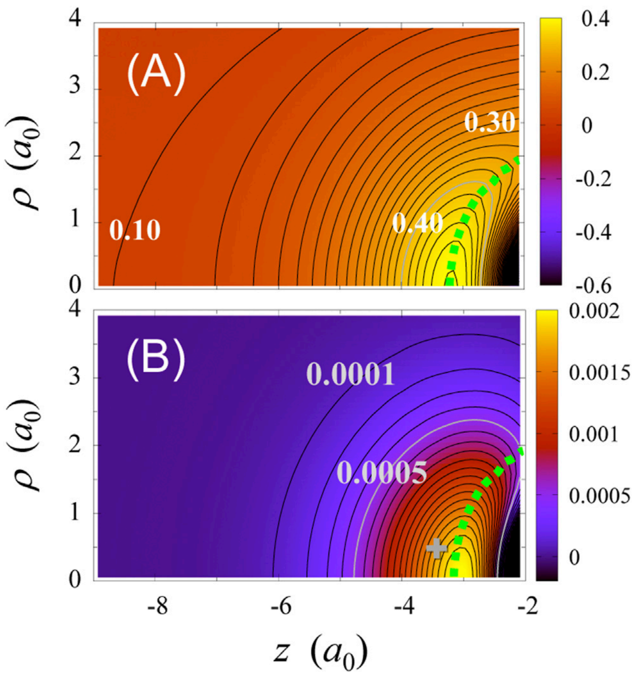

FIGURE 5 | TD-CASSCF results for the pulse in **Figure 3C**: **(A)** 2D contour plot of $v_1(0) + v_{2,5\sigma}(t)$ at $t \approx 2.8$ fs; **(B)** Contour plot of the difference in total electron density between $t \approx 2.8$ and $t = 0$. The contour lines in **(A)** are drawn at height intervals of $0.02E_h$. The numbers near contour lines indicate the heights (in units of E_h). The contour lines in **(B)** are drawn at intervals of 0.0001 a_0^{-3}. The symbol "+" designates that the electron density increases in the region. The hump ridgeline in $v_1(0) + v_{2,5\sigma}(t)$ is schematically illustrated in **(A)** by a light green dotted line, which is also drawn on the contour plot **(B)** as a dotted line.

Three-Color Pulses

Multicolor fields can be used to manipulate the modulation between the peaks of the electric field. In this subsection, we present $d_{5\sigma}(t)$ and $v_{5\sigma}^{\mathrm{eff}}(t)$ for three-color pulses with relative amplitudes $a_2 = 2/3$ and $a_3 = 1/3$. Two three-color pulses and corresponding $d_{5\sigma}(t)$ are shown in **Figures 3A,B**. The relative phases and the intensity parameter F_T in **Eq. 18** are as follows: (A)$\varphi_2 = -\pi/2$ and $F_T = 0.0541E_h/(ea_0)$; (B)$\varphi_2 = \pi/2$, and $F_T = 0.0611E_h/(ea_0)$. For both cases, $\varphi_1 = -\pi/2$ and $\varphi_3 = \pi/2$.

In the case of (A), the time difference between the negative maximum at $t = 2.05$ fs and positive maximum at $t = 3.02$ fs is 0.97 fs. This may be converted to an optical period as $2 \times 0.97=1.94$ fs, which is a little shorter than the period of a one-color field and longer than that of a two-color field, i.e., $2\pi/(2\omega) = 1.27$ fs. For the case of (B), an additional wiggle intervenes between the negative maximum at $t = 1.81$ fs and positive maximum at $t = 3.26$ fs. The time difference between the two peaks corresponds to the optical period of $2 \times 1.45=2.90$ fs, which is slightly longer than the one-color period of $T_c = 2.53$ fs. The period of the wiggle around $t = T_c$ is ~0.8 fs, which corresponds to the period of a 3ω field, i.e., $2\pi/(3\omega) = 0.84$ fs.

The induced dipole moment $d_{5\sigma}(t)$ in **Figure 3A** shows a quasiadiabatic response and the maximum value is as large as in **Figure 1A**. Corresponding effective potentials of the 5σ HOMO at $t \approx 3.0$ fs, shown in **Figure 4A**, are almost the same as in **Figure 2A**. These similarities to the case of the one-color pulse in **Figure 1A** may be attributed to the fact that the period between the main negative and positive peaks, i.e., 1.94 fs, is close to the period of one-color field, i.e., $T_c = 2.53$ fs. As a matter of fact, the ionization probability for the pulse in **Figure 3A** is nearly the same as that for $\varepsilon_1(t)$ in **Figure 1A**. Although a wiggle intervenes between the main negative and positive peaks in the electric field in **Figure 3B**, the corresponding induced dipole moment $d_{5\sigma}(t)$ also behaves nearly adiabatic, especially around $t = 3.3$ fs,. The present calculation for CO indicates that the response to three-color pulses is still more or less adiabatic. The peaks in $d_{5\sigma}(t)$ nearly coincide temporally with the peaks of the applied three-color field. The adiabatic character of three-color pulses is consistent with the recently reported experimental results for CO using femtosecond $\omega + 2\omega + 3\omega$ laser fields [43], where the phase-dependent behavior of ionization was explained by the phase-dependence and directional anisotropy of the instantaneous maxima of applied three-color fields. The maximum value of $d_{5\sigma}(t)$ in **Figure 3B** is slightly larger than that in **Figure 3A** and the hump in $v_1(0) + v_{2,5\sigma}(t)$ at $t \approx 3.3$ fs in **Figure 4B** becomes more prominent, compared to **Figure 2A** or **Figure 4A**. The wiggle in the applied field of **Figure 3B**, which appears around $t = 2.53$ fs with a short period of ~0.8 fs (≈the period of the 3ω field), exerts influence on the effective potential $v_{5\sigma}^{\text{eff}}(t)$ at a later time $t \approx 3.3$ fs, though the wiggle is relatively small and the overall response is almost adiabatic. The ionization barrier of $v_{5\sigma}^{\text{eff}}(t)$ in **Figure 4B** is thus largely different from that of $v_1(t) + v_{2,5\sigma}(0)$. The ionization probability for the pulse in **Figure 3B** is larger than that for **Figure 3A**. The former is ~0.0013 and the latter is ~0.0008.

Four-Color Pulses

The effects of sawtooth wave forms on multielectron dynamics can be investigated by using four-color fields. The relative amplitudes are fixed as $a_2 = 1/2$, $a_3 = 1/3$, and $a_4 = 1/4$ in this subsection. We show the responses to two four-color pulses in **Figures 3C,D**: (C)$\varphi_2 = \varphi_4 = -\pi/2$ and $E_T = 0.0528E_h/(ea_0)$; (D) $\varphi_2 = \varphi_4 = \pi/2$ and $E_T = 0.0778E_h/(ea_0)$. For both cases, $\varphi_1 = \varphi_3 = -\pi/2$. These sets lead to $E_p = 0.0378E_h/(ea_0)$. In the case of **Figure 3C**, the time difference between the negative maximum at $t = 2.29$ fs and positive maximum at $t = 2.78$ fs is 0.49 fs. This may be converted to an optical period as $2\times0.49 = 0.98$ fs, which is shorter than the optical period of a two-color field and longer than that of a three-color field ($2\pi/(3\omega) = 0.84$ fs). The electric field increases steeply and almost linearly from the negative maximum to the positive maximum. For the case of **Figure 3D**, an additional undulation intervenes between the negative maximum at $t = 1.55$ fs and positive maximum at $t = 3.52$ fs. The time difference between the two main peaks corresponds to the optical period of 3.94 fs, which is one and a half times as long as the one-color period of $T_c = 2.53$ fs. The period of the sawtooth-like undulation between the two peaks is 0.56 fs, which is close to the period of a 4ω field, i.e., $2\pi/(4\omega) = 0.63$ fs.

The induced dipole moment $d_{5\sigma}(t)$ in **Figure 3C** behaves rather nonadiabatically even in the initial region up to $t = 2$ fs, though the appled field $\varepsilon(t)$ as a whole seems a single cycle pulse with two dominant peaks at $t = 2.29$ fs and $t = 2.78$ fs. In fact, $d_{5\sigma}(t)$ in **Figure 3C** sensitively reflects how much high frequency components (in the present case, up to the fourth harmonic) are included in $\varepsilon(t)$. Notice that the induced dipole moment $d_{5\sigma}(t)$ rises steeply from $t \approx 2.3$ fs to $t \approx 2.8$ fs, while the abolute value of $d_{5\sigma}(t)$ prior to the midpoint of the pulse ($t = 2.53$ fs) is relatively small. The maximum value of $d_{5\sigma}(t)$ at $t \approx 2.8$ fs is as large as 0.18 ea_0, much larger than in the other cases of the same F_p. In **Figure 3D**, $d_{5\sigma}(t)$ increases with undulation from $t = 1.55$ fs to $t = 3.52$ fs, while reflecting the modulation in the applied pulse $\varepsilon(t)$. The resulting undulation amplitude in $d_{5\sigma}(t)$ is much larger than that in $\varepsilon(t)$, which indicates that the electron motion in $\phi_{5\sigma}(t)$ is sensitive to the presence of high frequency componets in $\varepsilon(t)$ even when the change in $\varepsilon(t)$ is moderate. Peaks in $d_{5\sigma}(t)$ are delayed from the corresponding peaks in $\varepsilon(t)$, which is a proof of nonadiabatic character.

Four types of 5σ effective potentials at $t \approx 2.8$ fs for the pulse in **Figure 3C** are shown in **Figure 4C**. The difference between $v_1(0) + v_{2,5\sigma}(t)$ and $v_1(0) + v_{2,5\sigma}(0)$ in **Figure 4C** is striking in comparison with the cases of **Figures 2A,B**: A hump is more clearly observed around $z = -3a_0$ in $v_1(0) + v_{2,5\sigma}(t)$ at $t \approx 2.8$ fs. The induced dipole moment of $\phi_{5\sigma}(t)$ responds to the steep rise in $\varepsilon(t)$ in the time span from $t = 2.3$ fs to $t = 2.8$ fs, and increases to a large maximum value (~0.18 ea_0) as shown in **Figure 3C**; concurrently, the other electrons also enter or appraoch the ionization exit. This is the reason why the hump become more distinct in **Figure 4C**, which is attributed to the electron correlation (stronger electron-electron interaction) induced by the coherent four-color pulse in **Figure 3C**. A more concrete evidence will be presnted below.

In the present treatment, the effective potential of CO is a two-dimensional (2D) function, i.e., a function of z and ρ. We have already examined TD-CASSCF effective potentials in 2D representation for a one-color pulse [90]. In **Figure 5A**, we present a 2D contour plot of $v_1(0) + v_{2,5\sigma}(t)$ at $t \approx 2.8$ fs for the four-color pulse in **Figure 3C**. On the whole, the hump height in $v_{5\sigma}^{\text{eff}}(t)$ drops from $(z, \rho) = (-3a_0, 0)$ with increasing ρ; i.e., the hump is formed around the molecular axis. The ridgeline of the hump slides down along a curve line from $(z, \rho) = (-3a_0, 0)$ toward $(-2a_0, 2a_0)$, which is schematically illustrated in **Figure 5A** by a dotted line.

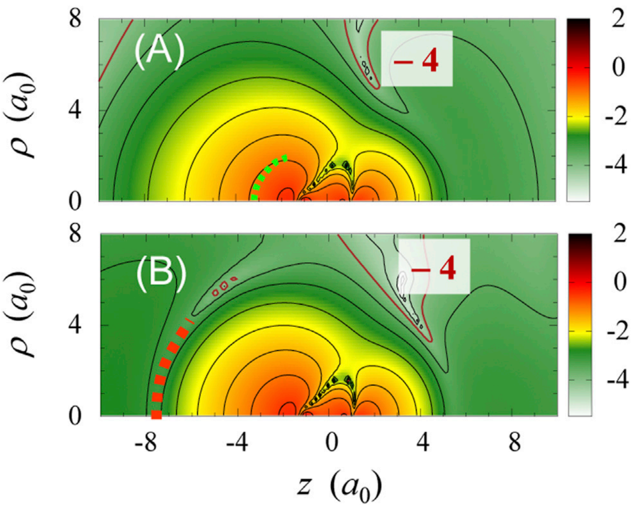

FIGURE 6 | 2D contour plots of $\phi_{5\sigma}(t)$ for four-color fields: (A) $\log_{10}|\phi_{5\sigma}(t)|$ at $t \approx 2.8$ fs for the pulse in **Figure 3C**; (B) $\log_{10}|\phi_{5\sigma}(t)|$ at $t \approx 3.5$ fs for the pulse in **Figure 3D**. The brown line represents the height of $|\phi_{5\sigma}(t)| = 10^{-4} a_0^{-3/2}$. The contour interval on the logarithmic scale is 0.5. The light green dotted line in **(A)** denotes the hump ridgeline in **Figure 5A**. The red dotted line in **(B)** denotes the valley in $v_{5\sigma}^{\mathrm{eff}}(t)$ for **Figure 4D**, along which a groove runs in the contour map of $\log_{10}|\phi_{5\sigma}(t)|$.

The change in field-induced electron-electron interaction is definitely affected by the spatial change in total electron density $P(z, \rho; t)$ or by the induced dipole moment. We present in **Figure 5B** a 2D plot of the difference $P(z, \rho; t) - P(z, \rho; 0)$ at $t \approx 2.8$ fs for the pulse in **Figure 3C**. A positive peak emerges around $(z, \rho) = (-3a_0, 0)$. Electrons mostly move along the C-O axis in the case where it is parallel to the polarization direction of the applied field. This buildup zone in the electron density $P(z, \rho; t) - P(z, \rho; 0)$ overlaps with the hump in **Figure 5A**, as indicated by the hump ridgeline superimposed on **Figure 5B**. The hump formation is hence ascribed to the interactions between electrons swarming to the buildup zone or between orbitals, which cannot be described by the TDHF level of theory. In conclusion, the hump in $v_1(0) + v_{2,5\sigma}(t)$ results from the penetration of an electron into the potential barrier formed by a field-induced local rise of electron density. When $\varepsilon(t) < 0$, $P(z, \rho; t) - P(z, \rho; 0)$ exhibits no distinct peaks in the region en route to ionization.

The hump ridge elevates as the field strength $\varepsilon(t)$ (> 0) increases, which sharply incises the protruding lobe of the 5σ natural orbital $\phi_{5\sigma}(t)$ around the C atom (See the light green dotted line in **Figure 6A**). This mechanism accelerates the ionization from $\phi_{5\sigma}(t)$ in the area outside the hump ridge. The area of the newly emerging hump is regarded as a TI exit in the presence of electron correlation or a crowd of electrons. We have confirmed that the hump height from the asymptotic value of $v_1(0) + v_{2,5\sigma}(t_1)$ at $z = -\infty$ is nearly proportional to the induced dipole moment of $\phi_{5\sigma}(t)$ associated with the spatial change in electron density [90]. For TDHF, the buildup zone in electron density spreads vaguely in comparison with the TD-CASSCF case, in agreement with the fact that no hump appears in **Figure 2C**.

For the pulse of **Figure 3D**, effective potentials at $t \approx 3.5$ fs are shown in **Figure 4D**. The potential $v_1(0) + v_{2,5\sigma}(t)$ at $t \approx 3.5$ fs exhibits a very unique feature, i.e., a deep dent around $z = -7.5a_0$. The dents connected in the (z, ρ) space form a deep valley in $v_{5\sigma}^{\mathrm{eff}}(t)$, which significantly distorts the profile of $v_{5\sigma}^{\mathrm{eff}}(t)$. The time span where $\varepsilon(t) > 0$ in the latter half of the pulse ($t > 2.53$ fs) is as long as 1.3 fs and the ionization barrier of $v_{5\sigma}^{\mathrm{eff}}(t)$ is then largely shifted down. Considering these facts and following a primitive picture of TI, we expected that the ionization probability for the pulse in **Figure 3D** is rather large. However, it is only slightly larger than that for **Figure 3C**; the ratio is ca. 0.008:0.006 (Overall, the ionization probabilities for the four-color pulses are about one order of magnitude larger than in the pulses comprised of harmonics up to the third order.). The ionization probaility for **Figure 3D** includes the additional contribution from the positive field area around $t = 1$ fs. We add that the effective potential $v_{5\sigma}^{\mathrm{eff}}(t)$ at $t \approx 3.5$ fs obtained by TDHF levels off in the range from $z = -4a_0$ to $z = -7a_0$ (as high as 0.4 E_{h}) and exhibits only a shallow valley at $z \approx -8a_0$ (The depth is ~0.1E_{h}). The TDHF ionization probabilities for **Figures 3C,D** were one order of magnitude smaller than the TD-CASSCF values.

An interpretation based on the present single-electron picture is that the valley in $v_{5\sigma}^{\mathrm{eff}}(t)$ of **Figure 4D** serves to block the electron current from the bound region (by reflection). This interpretation can be evidenced by the 2D contour plot of $|\phi_{5\sigma}(t)|$. **Figure 6A** represents $\log_{10}|\phi_{5\sigma}(t)|$ at $t \approx 2.8$ fs for the pulse in **Figure 3C**; **Figure 6B** represents $\log_{10}|\phi_{5\sigma}(t)|$ at $t \approx 3.5$ fs for the pulse in **Figure 3D**. **Figure 6A** simply shows a typical feature of TI that electron density leaks out from the bound region toward the negative z direction (for $\varepsilon(t) > 0$). On the other hand, **Figure 6B** shows that the bound component of $\phi_{5\sigma}(t)$ is encircled by the valley in $v_{5\sigma}^{\mathrm{eff}}(t)$, which is indicated by the red dotted line. The four-color pulse $\varepsilon(t)$ in **Figure 3D** behaves as if it squeezes $\phi_{5\sigma}(t)$ toward the inside of the valley, i.e., toward the center of the molecule, though at this moment the field $\varepsilon(t)$ pushes an electron toward the negative z direction. We found that the difference $P(z, \rho; t) - P(z, \rho; 0)$ at $t \approx 3.5$ fs becomes slightly negative in the area along the valley in $v_{5\sigma}^{\mathrm{eff}}(t)$ and it rises around the hump near $(z, \rho) = (-3a_0, 0)$ in $v_{5\sigma}^{\mathrm{eff}}(t)$, of which rise is more prominent than in the other cases with the same F_{p}. The valley in $v_{5\sigma}^{\mathrm{eff}}(t)$, associated with a diminution in electron density, is regarded as a signature of strong electron correlation induced by the four-color pulse. This type of coherent control of $\phi_{5\sigma}(t)$ works in forvor of ionization suppression. Since $\phi_{5\sigma}(t)$ in **Figure 6B** is spatially squeezed, $d_{5\sigma}(t)$ at $t \approx 3.5$ fs in **Figure 3D** is smaller than $d_{5\sigma}(t)$ at $t \approx 2.8$ fs in **Figure 3C**. The former is ~$0.13ea_0$ and the latter is ~$0.18ea_0$. The "squeezed" $\phi_{5\sigma}(t)$ orbital might be associated with the formation of a localized excited or resonance state as discussed in the next subsection.

On the Information out of High-Order Harmonic Generation Spectra

We here discuss the connection of the present results of TI with HHG. The HHG spectra of asymmetric molecules, which reflect the presence and motion of the charges in applied fields, can be utilized to investigate the mechanism of coherent control and to assess the degree of controllability. The ionization potential for a polar molecule in an intense field is a time-dependent one, as denoted by $I_p(t)$, which is due to the Stark-shift of the ground state; for HeH^{2+}, $I_p(t)$ is approximately given by $I_p(t) \approx I_0 + R\boldsymbol{\varepsilon}(t)/2$ [112–114], where I_0 is the field-free ionization potential and R is the internuclear distance. The Stark-shifted ionization potential leads to a cutoff energy in HHG that is higher than the widely accepted prediction by the three-step model, i.e. $E_{\text{cutoff}}^{(0)} = I_0 + 3.17 f_{\max}^2/4\omega^2$ [8], for the one-color applied field with a frequency ω, where $f_{\max}$ is the maximum field envelope. Etches and Madsen [115] have shown theoretically for a polar molecule CO that HHG components are generated beyond the predicted value of $E_{\text{cutoff}}^{(0)}$. The cutoff energy experimentally measured can serve as an index to quantify how the Fourier-synthesized fields manipulate the electronic wave function.

Another feature inherent in the HHG spectra of asymmetric molecules was pointed out by Bandrauk et al. [113, 114], who theoretically investigated the role of excited states in HHG for HeH^{2+}. They found that a transient localized state (Stark-shifted or field-dressed first excited state of HeH^{2+}) is resonantly populated prior to ionization by laser induced electron transfer from the He^{2+} side to the H^+ side. This field-dressed excited state is able to get back directly to the ground state with emission. A resulting new HHG channel, regarded as the quasi two-step pathway, gives birth to an intense resonance peak ($<E_{\text{cutoff}}^{(0)}$) near the field-dressed energy gap between the transient excited state and the ground state. In the case where the resonance state has long lifetime, the ionization via the resonance state is expected to be delayed, which for short laser pulses, redshifts the HHG spectrum in the plateau region [113]. This type of resonance channel is also investigated in [116]. A four-step model was thus proposed for the HHG of asymmetric molecules [113, 114], in which the representative transient state is incorporated into the three-step model as an additional step in the HHG. The extension of the cutoff energy mentioned in the above paragraph can also be interpreted by the following four-step pathway in the four-step model: i) An electron is pumped from the ground state to the localized long lifetime excited state (field-induced electron transfer from the He^{2+} side to the H^+ side), ii) then, part of the population is transferred to field-dressed continuum states, iii) the freed electron is accelerated in the laser field, and iv) recombination with the ground state (the neighboring He^{2+}) [114]. The cutoff extension is attributed to the difference in electric field potential between (ii) the ionization site (H^+) and (iv) recombination site (He^{2+}). The four-step pathway interferes in HHG with the quasi two-step pathway. It has been theoretically demonstrated that distinct vestiges of the interference between the two pathways appear in the HHG spectrum if the amplitudes of the two pathways are comparable with each other [114].

Intermediate states prepared by tailored multi-color fields, such as represented by a “squeezed” orbital in **Figure 6B**, may work as such transient excited states leading to resonance HHG. A realistic attempt to confirm the existence of such resonance states and to assess the controllability of the wave function is to examine how the HHG spectrum (regarding the cutoff energy, individual peak positions and intensities, etc.) changes by varying the relative phases among multi-color fields. In line with this, it is necessary to quantify how long the intermediate states (orbitals) prepared live. We would like to take on the applications of the effective potential approach to the setup of new experimental schemes and to the search of possible results, as discussed in [90].

CONCLUSION

We presented the results of theoretical investigation of the multielectron dynamics of CO in intense laser fields and discussed various manipulation schemes by Fourier-synthesized coherent fields comprised of harmonics up to the fourth order. The multielectron wavefunction $\Psi(t)$ to describe the electron dynamics are obtained by using the MCTDHF method, where $\Psi(t)$ is expanded in terms of various electron configurations or Slater determinants $\{\Phi_I(t)\}$. In the MCTDHF, both the CI coefficients $\{C_I(t)\}$ and molecular orbitals $\{\psi_j(\boldsymbol{r},t)\}$ in $\{\Phi_I(t)\}$ obey the coupled EOMs derived from the Dirac-Frenkel TD variational principle, where $\boldsymbol{r}$ is a one-electron coordinate. In actual numerical simulations for the dynamics of CO interacting with Fourier-synthesized pulses, we employed the TD-CASSCF scheme where the orbital space in the Slater determinants is split into inactive (core) and active orbitals. The peak of the applied field is fixed at $F_p = 0.0378\ E_h/(ea_0) = 1.94\times10^{10}\ \text{Vm}^{-1}$ throughout this paper except that in **Figure 2D**, of which the light intensity corresponds to $I = 5.0\times10^{13}\ \text{Wcm}^{-2}$ in the case of one-color pulses.

We then quantified the multielectron nature such as electron correlation by using our effective potential approach: the time-dependent natural orbitals $\{\phi_j(\boldsymbol{r},t)\}$, which diagonalize the first order reduced density matrix, are obtained from $\{\psi_j(\boldsymbol{r},t)\}$; next, the EOMs for $\{\phi_j(\boldsymbol{r},t)\}$ are derived, which define the effective single-electron potentials $v_j^{\text{eff}}(\boldsymbol{r},t)$ that determine the dynamics of $\phi_j(\boldsymbol{r},t)$ under the influence of electron-electron interaction. The effective potentials $\{v_j^{\text{eff}}(t)\}$ consist of two terms: $v_j^{\text{eff}}(t) = v_1(t) + v_{2,j}(t)$, where $v_1(t)$ is the one-body interaction including that with the applied laser field $\boldsymbol{\varepsilon}(t)$ and $v_{2,j}(t)$ represents an effective two-body electron-electron interaction for a single electron. The TD effective potentials as functions of a one-electron spatial coordinate $\boldsymbol{r}$ are thus obtained from the natural orbitals $\{\phi_j(\boldsymbol{r},t)\}$ and CI expansion coefficients $\{C_I(t)\}$ of the calculated $\Psi(t)$. In this approach, the role of electron correlation can be quantitatively analyzed by comparing $v_j^{\text{eff}}(\boldsymbol{r},t)$ with those obtained by the TDHF method.

Two-body interaction $v_{2,5\sigma}(t)$ can dramatically change the shape of the tunnel barrier in the 5σ HOMO effective potential $v_{5\sigma}^{\text{eff}}(\boldsymbol{r},t)$, whereas the one-body potential $v_1(t)$ is simply slanted by the electric dipole interaction. For near-IR one-color pulses, as the field strength increases when $\boldsymbol{\varepsilon}(t)$ points from C to O ($\varepsilon(t) > 0$), a hump is formed ~2 a_0 away outside from C ($z < 0$) in $v_1(0) + v_{2,5\sigma}(t)$. Around this region, the lobe of $\phi_{5\sigma}(t)$ spreads out extensively. Electron density is then transferred from the interior to the exterior region outside the hump ridge (which is considered the border between the interior and exterior regions), and ionization proceeds together with a bound component already distributed in the exterior region. The experimentally observed anisotropic ionization in CO is ascribed to the hump formation, which brings about preferential electron ejection from the C atom side. Hump formation originates from the field-induced change in $v_{5\sigma}^{\text{eff}}(\boldsymbol{r},t)$

mainly due to electron correlation. Upon the reversal of the sign of $\varepsilon(t)$, ionization is relatively suppressed, because the tunnel barrier is then located far away ($>13a_0$) from the O atom. This is the mechanism we proposed for the anisotropic ionization of CO [88–90].

We found that $v_{5\sigma}^{\mathrm{eff}}(\boldsymbol{r},t)$ for an optimized asymmetric ω+2ω two-color pulse exhibits a very similar profile as in $v_{5\sigma}^{\mathrm{eff}}(\boldsymbol{r},t)$ for one-color pulses. A coherent superposition of ω and 2ω fields with an appropriate relative phase works as if either positive or negative peaks are filtered out from a one-color pulse. The induced dipole moments $d_{5\sigma}(t)$ for three-color pulses behave almost adiabatic. The peaks in $d_{5\sigma}(t)$ nearly coincide temporally with the peaks of the applied three-color field. This suggests that the main ionization mechanism in three-color fields is still TI. More sophisticated manipulation can be realized by adding higher harmonics to a synthesized field. The controllability of electron dynamics is higher in four-color fields than in three-color fields. By adjusting the relative phases of a ω+2ω+3ω+4ω field, one can create, in addition to a hump, a deep potential valley in the negative z region of $v_{5\sigma}^{\mathrm{eff}}(\boldsymbol{r},t)$ which encloses the molecule at a radius of ~7 a_0. The 5σ orbital of CO is then squeezed toward the inside of the potential valley in $v_{5\sigma}^{\mathrm{eff}}(\boldsymbol{r},t)$. It is of much interest to reveal what is the origin of this "squeezed" orbital. We would like to point out again that a hump and valley in $v_{5\sigma}^{\mathrm{eff}}(\boldsymbol{r},t)$ are closely correlated with domains of increasing and decreasing electron density, respectively. As a first step to establish robust control schemes for multielectron dynamics by Fourier-synthesized coherent laser fields, we are planning to extract the information of two-body parts $\{v_{2,\mathrm{j}}(\mathrm{t})\}$ from phase-dependent quantities (functions of relative phases among harmonics), e.g., HHG spectra as well as the yields and release-direction propensities of fragment ions and electrons.

The final point to be discussed here concerns the future extension of the present effective potential approach to chemical reactions. The strong coupling between intense fields and valence electrons dramatically distorts the potential hypersurfaces which determine the motion of the nuclei and brings about decisive changes in reaction pathways [17, 117, 118]. Kübel et al. [118] ionized H_2 by a few-cycle visible pulse and prepared a wave packet on the σ_g state of H_2^+. The behavior of H_2^+ was controlled by a mid-infrared pulse with a delay that couples the σ_g state with the σ_u state by one-, three-, and five-photon absorption. They analyzed a strongly modulated angular distribution of protons by using two-color Floquet theory and proved the existence of complex light-induced (field-dressed) potential surfaces that multiphoton couplings afford. These potentials can be shaped by the amplitude, phase, and duration of the applied fields, which allows for manipulating the dissociation or reaction dynamics of small molecules.

A feasible extension along with this line is to include the nuclear coordinates $\{Q_k\}$ as adiabatic parameters into the present approach, i.e., to define or calculate "adiabatic" natural orbitals $\{\phi_j(\boldsymbol{r},\{Q_k\},t)\}$. The effective potential for $\phi_j(\boldsymbol{r},\{Q_k\},t)$ are then expressed as $v_j^{\mathrm{eff}}(\boldsymbol{r},\{Q_k\},t)$, which might connect more tightly the two pictures of molecular orbital and molecular dynamics. Another conceivable approach is to use a more fundamental method, namely, the extended MCTDHF method where the nuclear coordinates in the total wave function $\Psi(\{\boldsymbol{r}_j\},\{Q_k\},t)$ are dealt with as quantum mechanical variables (e.g., each nucleus is expressed by a single-particle function, like in the treatment of electrons as molecular orbitals) [89, 109, 119–121]. The molecular orbitals used in the extended MCTDHF are functions of a one-electron coordinate alone (i.e., $\{\psi_j(\boldsymbol{r},t)\}$); $\{Q_k\}$ are not involved, unlike in the conventional Born-Hung expansion [122]. An effective potential for each nucleus could in principle be derived from the non-Born-Oppenheimer wave function $\Psi(\{\boldsymbol{r}_j\},\{Q_k\},t)$, which would provide a single nucleus picture in the presence of correlated nuclear motion. The extended MCTDHF method also offers a novel concept of potential surfaces (extended-MCTDHF potentials). So far, the effective potential curves of the ground and excited states defined in this method are obtained for a 1D model H_2 [89, 120, 121] and the time-dependent system of 3D H_2^+ [123]. The memory size used in this method is shown to be about two orders of magnitude smaller than in the Born-Hung expansion method when the same accuracy is required for the lowest vibronic energy. It is intriguing, especially for polyatomic molecules, to construct multiphoton field-dressed potentials based on Floquet theory from extended-MCTDHF potentials.

The various effective potential approaches abovementioned would help reveal the entire picture of the quantum electronic and nuclear dynamics of molecules and help contribute to further development of coherent control of chemical reactions. Challenges are widespread ahead of the frontier of the research on Coherent Phenomena in Molecular Physics.

DATA AVAILABILITY STATEMENT

The raw data supporting the conclusions of this article will be made available by the authors, without undue reservation.

AUTHOR CONTRIBUTIONS

SO: Computation, preparation of figures. HO: conceptual proposal based on experimental feasibility, preparation of manuscript. TK: development of theoretical framework. HK: project coordination, preparation of manuscript. All authors developed the concept of the control of multielectron dynamics by multicolor fields and contributed to the article and approved the submitted version.

FUNDING

This work was supported in part by JSPS KAKENHI Grant Number JP16H04091.

ACKNOWLEDGMENTS

The authors would like to thank Prof. S. Koseki for providing us results of the electronic structure calculation of CO.

REFERENCES

1. Glauber RJ. *Quantum Theory of Optical Coherence: Selected Papers and Lectures*. Weinheim, Germany: Wiley VCH (2007). doi:10.1002/9783527610075.ch16
2. Friedrich B, and Herschbach DR. Alignment and Trapping of Molecules in Intense Laser Fields. *Phys Rev Lett* (1995) 74:4623. doi:10.1103/PhysRevLett.74.4623–6
3. Stapelfeldt H, and Seideman T. Colloquium: Aligning Molecules with Strong Laser Pulses. *Rev Mod Phys* (2003) 75: 543–57. doi:10.1103/RevModPhys.75.543
4. Agostini P, Fabre F, Mainfray G, Petite G, and Rahman NK. Free-free Transitions Following Six-Photon Ionization of Xenon Atoms. *Phys Rev Lett* (1979) 42: 1127–30. doi:10.1103/PhysRevLett.42.1127
5. Chin SL, Yergeau F, and Lavigne P. Tunnel Ionisation of Xe in an Ultra-intense CO_2 Laser Field (10^{14} Wcm^{-2}) with Multiple Charge Creation. *J Phys B: Atom Mol Phys* (1985) 18:L213–5. doi:10.1088/0022-3700/18/8/001
6. Augst S, Meyerhofer DD, Strickland D, and Chint SL. Laser Ionization of Noble Gases by Coulomb-Barrier Suppression. *J Opt Soc Am B* (1991) 8:858. doi:10.1364/josab.8.000858
7. DeWitt MJ, and Levis RJ. Observing the Transition from a Multiphoton-Dominated to a Field-Mediated Ionization Process for Polyatomic Molecules in Intense Laser Fields. *Phys Rev Lett* (1998) 81:5101–4. doi:10.1103/PhysRevLett.81.5101
8. Corkum PB. Plasma Perspective on Strong Field Multiphoton Ionization. *Phys Rev Lett* (1993) 71:1994. 10.1103/PhysRevLett.71.1994
9. Lewenstein M, Salières P, and L'Huillier A. Phase of the Atomic Polarization in High-Order Harmonic Generation. *Phys Rev A* (1995) 52: 4747–54. doi:10.1103/PhysRevA.52.4747
10. Becker W, Grasbon F, Kopold R, Milošević DB, Paulus GG, and Walther H. Above-threshold Ionization: From Classical Features to Quantum Effects. *Adv At Mol Opt Phys* (2002) 48: 35–98. doi:10.1016/S1049-250X(02)80006-4
11. Scherer NF, Carlson RJ, Matro A, Du M, Ruggiero AJ, Romero-Rochin V, et al. Fluorescence-detected Wave Packet Interferometry: Time Resolved Molecular Spectroscopy with Sequences of Femtosecond Phase-Locked Pulses. *J Chem Phys* (1991) 95: 1487–511. doi:10.1063/1.461064
12. Katsuki H, Chiba H, Girard B, Meier C, and Ohmori K. Visualizing Picometric Quantum Ripples of Ultrafast Wave-Packet Interference. *Science* (2006) 311: 1589–92. doi:10.1126/science.1121240
13. Rice SA, and Zhao M. *Optical Control of Molecular Dynamics*. New York: Wiley (2000). doi:10.1021/ja015259b
14. Shapiro M, and Brumer P. *Principles of the Quantum Control of Molecular Processes*. 2nd ed. New York: Wiley (2011). doi:10.1002/9783527639700
15. Gordon RJ, Zhu L, and Seideman T. Coherent Control of Chemical Reactions. *Acc Chem Res* (1999) 32:1007–16. doi:10.1021/ar970119l
16. Endo T, Fujise H, Kawachi Y, Ishihara A, Matsuda A, Fushitani M, et al. Selective Bond Breaking of CO_2 in Phase-Locked Two-Color Intense Laser Fields: Laser Field Intensity Dependence. *Phys Chem Chem Phys* (2017) 19: 3550–6. doi:10.1039/c6cp07471e
17. Sato Y, Kono H, Koseki S, and Fujimura Y. Description of Molecular Dynamics in Intense Laser Fields by the Time-Dependent Adiabatic State Approach: Application to Simultaneous Two-Bond Dissociation of CO_2 and its Control. *J Am Chem Soc* (2003) 125:8019–31. doi:10.1021/ja0344819
18. Schafer KJ, and Kulander KC. Phase-dependent Effects in Multiphoton Ionization Induced by a Laser Field and its Second Harmonic. *Phys Rev A* (1992) 45: 8026–33. doi:10.1103/PhysRevA.45.8026
19. Schumacher DW, Weihe F, Muller HG, and Bucksbaum PH. Phase Dependence of Intense Field Ionization: A Study Using Two Colors. *Phys Rev Lett* (1994) 73: 1344–7. doi:10.1103/PhysRevLett.73.1344
20. De S, Znakovskaya I, Ray D, Anis F, Johnson NG, Bocharova IA, et al. Field-free Orientation of CO Molecules by Femtosecond Two-Color Laser Fields. *Phys Rev Lett* (2009) 103:153002. doi:10.1103/PhysRevLett.103.153002
21. Li H, Ray D, De S, Znakovskaya I, Cao W, Laurent G, et al. Orientation Dependence of the Ionization of CO and NO in an Intense Femtosecond Two-Color Laser Field. *Phys Rev A* (2011) 84:043429. doi:10.1103/PhysRevA.84.043429
22. Kaziannis S, Kotsina N, and Kosmidis C. Interaction of Toluene with Two-Color Asymmetric Laser Fields: Controlling the Directional Emission of Molecular Hydrogen Fragments. *J Chem Phys* (2014) 141:104319. doi:10.1063/1.4895097
23. Ohmura H, Saito N, and Tachiya M. Selective Ionization of Oriented Nonpolar Molecules with Asymmetric Structure by Phase-Controlled Two-Color Laser Fields. *Phys Rev Lett* (2006) 96:173001. doi:10.1103/PhysRevLett.96.173001
24. Ohmura H, and Tachiya M. Robust Quantum Control of Molecular Tunneling Ionization in the Space Domain by Phase-Controlled Laser Fields. *Phys Rev A* (2008) 77:023408. doi:10.1103/physreva.77.023408
25. Ohmura H, Saito N, Nonaka H, and Ichimura S. Dissociative Ionization of a Large Molecule Studied by Intense Phase-Controlled Laser Fields. *Phys Rev A* (2008) 77:053405. doi:10.1103/PhysRevA.77.053405
26. Ohmura H, Saito N, and Morishita T. Quantum Control of Molecular Tunneling Ionization in the Spatiotemporal Domain. *Phys Rev A* (2011) 83:063407. doi:10.1103/PhysRevA.83.063407
27. Ohmura H, Saito N, and Morishita T. Molecular Tunneling Ionization of the Carbonyl Sulfide Molecule by Double-Frequency Phase-Controlled Laser Fields. *Phys Rev A* (2014) 89:013405. doi:10.1103/PhysRevA.89.013405
28. Kitzler M, and Lezius M. Spatial Control of Recollision Wave Packets with Attosecond Precision. *Phys Rev Lett* (2005) 95:253001. doi:10.1103/PhysRevLett.95.253001
29. Kim IJ, Kim CM, Kim HT, Lee GH, Lee YS, Park JY, et al. Highly Efficient High-Harmonic Generation in an Orthogonally Polarized Two-Color Laser Field. *Phys Rev Lett* (2005) 94:243901. doi:10.1103/PhysRevLett.94.243901
30. Mashiko H, Gilbertson S, Li C, Khan SD, Shakya MM, Moon E, et al. Double Optical Gating of High-Order Harmonic Generation with Carrier-Envelope Phase Stabilized Lasers. *Phys Rev Lett* (2008) 100:103906. doi:10.1103/PhysRevLett.100.103906
31. Brugnera L, Hoffmann DJ, Siegel T, Frank F, Zaïr A, Tisch JWG, et al. Trajectory Selection in High Harmonic Generation by Controlling the Phase between Orthogonal Two-Color Fields. *Phys Rev Lett* (2011) 107:153902. doi:10.1103/PhysRevLett.107.153902
32. Hänsch TW. A Proposed Sub-femtosecond Pulse Synthesizer Using Separate Phase-Locked Laser Oscillators. *Opt Commum* (1990) 80:71. doi:10.1016/0030-4018(90)90509-R
33. Shverdin MY, Walker DR, Yavuz DD, Yin GY, and Harris SE. Generation of a Single-Cycle Optical Pulse. *Phys Rev Lett* (2005) 94:033904. doi:10.1103/PhysRevLett.94.033904
34. Yoshitomi D, Kobayashi Y, and Torizuka K. Characterization of Fourier-Synthesized Optical Waveforms from Optically Phase-Locked Femtosecond Multicolor Pulses. *Opt Lett* (2008) 33:2925. doi:10.1364/OL.33.002925
35. Chan H-S, Hsieh Z-M, Liang W-H, Kung AH, Lee C-K, Lai C-J, et al. Synthesis and Measurement of Ultrafast Waveforms from Five Discrete Optical Harmonics. *Science* (2011) 331:1165–8. doi:10.1126/science.1198397
36. Yoshii K, Kiran Anthony J, and Katsuragawa M. The Simplest Route to Generating a Train of Attosecond Pulses. *Light Sci Appl* (2013) 2:e58. doi:10.1038/lsa.2013.14
37. Chipperfield LE, Robinson JS, Tisch JWG, and Marangos JP. Ideal Waveform to Generate the Maximum Possible Electron Recollision Energy for Any Given Oscillation Period. *Phys Rev Lett* (2009) 102:063003. doi:10.1103/PhysRevLett.102.063003
38. Wei P, Miao J, Zeng Z, Li C, Ge X, Li R, et al. Selective Enhancement of a Single Harmonic Emission in a Driving Laser Field with Subcycle Waveform Control. *Phys Rev Lett* (2013) 110:233903. doi:10.1103/PhysRevLett.110.233903
39. Haessler S, Balčiunas T, Fan G, Andriukaitis G, Pugžlys A, Baltuška A, et al. Optimization of Quantum Trajectories Driven by Strong-Field Waveforms. *Phys Rev X* (2014) 4:021028. doi:10.1103/PhysRevX.4.021028
40. Ohmura H, and Saito N. Quantum Control of a Molecular Ionization Process by Using Fourier-Synthesized Laser Fields. *Phys Rev A* (2015) 92:053408. doi:10.1103/PhysRevA.92.053408
41. Yoshida T, Saito N, and Ohmura H. Robust Generation of Fourier-Synthesized Laser Fields and Their Estimation of the Optical Phase by Using Quantum Control of Molecular Tunneling Ionization. *J Phys B: Mol Opt Phys* (2018) 51:065601. doi:10.1088/1361-6455/aaac20

42. Ohmura H, Yoshida T, and Saito N. Four-mode Multi-Selection in the Dual Phase Control of a Molecular Ionization Induced by Fourier-Synthesized Laser Fields. *Appl Phys Lett* (2019) 114:054101. doi:10.1063/1.5082578
43. Ohmura H, and Saito N. Sub-Optical-Cycle Attosecond Control of Molecular Ionization by Using Fourier-Synthesized Laser Fields. *Phys Rev A* (2020) 101: 043419. doi:10.1103/PhysRevA.101.043419
44. Paulus GG, Lindner F, Walther H, Baltuška A, Goulielmakis E, Lezius M, et al. Measurement of the Phase of Few-Cycle Laser Pulses. *Phys Rev Lett* (2003) 91:253004. doi:10.1103/PhysRevLett.91.253004
45. Apolonski A, Poppe A, Tempea G, Spielmann C, Udem T, Holzwarth R, et al. Controlling the Phase Evolution of Few-Cycle Light Pulses. *Phys Rev Lett* (2000) 85:740–3. doi:10.1103/PhysRevLett.85.740
46. Jones DJ, Diddams SA, Ranka JK, Stentz A, Windeler RS, Hall JL, et al. Carrier-Envelope Phase Control of Femtosecond Mode-Locked Lasers and Direct Optical Frequency Synthesis. *Science* (2000) 288:635–9. doi:10.1126/science.288.5466.635
47. Baltuska A, Fuji T, and Kobayashi T. Controlling the Carrier-Envelope Phase of Ultrashort Light Pulses with Optical Parametric Amplifiers. *Phys Rev Lett* (2002) 88:133901. doi:10.1103/PhysRevLett.88.13390110.1103
48. Kakehata M, Takada H, Kobayashi Y, Torizuka K, Takamiya H, Nishijima K, et al. Carrier-Envelope-Phase Stabilized Chirped-Pulse Amplification System Scalable to Higher Pulse Energies. *Opt Express* (2004) 12:2070–80. doi:10.1364/OPEX.12.002070
49. Baltuška A, Udem T, Uiberacker M, Hentschel M, Goulielmakis E, Gohle C, et al. Attosecond Control of Electronic Processes by Intense Light Fields. *Nature* (2003) 421:611–5. doi:10.1038/nature01414
50. Krausz F, and Ivanov M. Attosecond Physics. *Rev Mod Phys* (2009) 81: 163–234. doi:10.1103/RevModPhys.81.163
51. Joachain CJ, Kylstra NJ, and Potvliege RM. *Atoms in Intense Laser Fields*. Cambridge: Cambridge University Press (2011). doi:10.1017/CBO9780511993459
52. Nisoli M, Decleva P, Calegari F, Palacios A, and Martín F. Attosecond Electron Dynamics in Molecules. *Chem Rev* (2017) 117: 10760–825. doi:10.1021/acs.chemrev.7b00226
53. Schiffrin A, Paasch-Colberg T, Karpowicz N, Apalkov V, Gerster D, Mühlbrandt S, et al. Optical-Field-Induced Current in Dielectrics. *Nature* (2013) 493: 70–4. doi:10.1038/nature11567
54. Vasa P, and Mathur D. *Ultrafast Biophotonics*. Cham, Switzerland: Springer (2016). doi:10.1007/978-3-319-39614-9
55. Keldysh LV. Ionization in the Field of a Strong Electromagnetic Wave. *Sov Phys JETP* (1964) 20: 1307–14.
56. Wolkov DM. Über eine Klasse von Lösungen der Diracschen Gleichung. *Z Phys* (1935) 94: 250–60. doi:10.1007/BF01331022
57. Perelemov AM, Popov VS, and Terent'ev MV. Ionization of Atoms in an Alternating Electric Filed. *Soviet Phys JETP* (1966) 23: 924–34.
58. Faisal FHM. Multiple Absorption of Laser Photons by Atoms. *J Phys B: Mol Phys* (1973) 6:L89–L92. doi:10.1088/0022-3700/6/4/011
59. Reiss HR. Effect of an Intense Electromagnetic Field on a Weakly Bound System. *Phys Rev A* (1980) 22: 1786–813. doi:10.1103/PhysRevA.22.1786
60. Ammosov MV, Delone NB, and Krainov VP. Tunnel Ionization of Complex Atoms and of Atomic Ions in an Alternating Electromagnetic Field. *Soviet Phys JETP* (1986) 64: 1191–4.
61. Tong XM, Zhao Z, and Lin CD. Theory of Molecular Tunneling Ionization. *Phys Rev A* (2002) 66:033402. doi:10.1103/PhysRevA.66.033402
62. Abu-samha M, and Madsen LB. Single-Active-Electron Potentials for Molecules in Intense Laser Fields. *Phys Rev A* (2010) 81:033416. doi:10.1103/PhysRevA.81.033416
63. Awasthi M, and Saenz A. Breakdown of the Single-Active-Electron Approximation for One-Photon Ionization of the $B^1\Sigma_u^+$ State of H_2 Exposed to Intense Laser Fields. *Phys Rev A* (2010) 81:063406. doi:10.1103/PhysRevA.81.063406
64. Zhang B, Yuan J, and Zhao Z. Dynamic Core Polarization in Strong-Field Ionization of CO Molecules. *Phys Rev Lett* (2013) 111:163001. doi:10.1103/PhysRevLett.111.163001
65. Abu-samha M, and Madsen LB. Multielectron Effects in Strong-Field Ionization of the Oriented OCS Molecule. *Phys Rev A* (2020) 102:013433. doi:10.1103/PhysRevA.102.063111
66. Zhao Z, and Brabec T. Tunnel Ionization in Complex Systems. *J Mod Opt* (2007) 54: 981–97. doi:10.1080/09500340601043413
67. Hoang V-H, Zhao S-F, Le V-H, and Le A-T. Influence of Permanent Dipole and Dynamic Core-Electron Polarization on Tunneling Ionization of Polar Molecules. *Phys Rev A* (2017) 95:023407. doi:10.1103/physreva.95.023407
68. Kang H-P, Xu S-P, Wang Y-L, Yu S-G, Zhao X-Y, Hao X-L, et al. Polarization Effects in Above-Threshold Ionization with a Mid-infrared Strong Laser Field. *J Phys B: Mol Opt Phys* (2018) 51:105601. doi:10.1088/1361-6455/aabce0
69. Kling MF, and Vrakking MJJ. Attosecond Electron Dynamics. *Annu Rev Phys Chem* (2008) 59: 463–92. doi:10.1146/annurev.physchem.59.032607.093532
70. Vrakking MJJ, and Lepine F. *Attosecond Molecular Dynamics*. London: Royal Society of Chemistry (2018). doi:10.1039/9781788012669
71. Harumiya K, Kawata I, Kono H, and Fujimura Y. Exact Two-Electron Wave Packet Dynamics of H_2 in an Intense Laser Field: Formation of Localized Ionic States H^+H^-. *J Chem Phys* (2000) 113: 8953–60. doi:10.1063/1.1319348
72. Harumiya K, Kono H, Fujimura Y, Kawata I, and Bandrauk AD. Intense Laser-Field Ionization of H_2 Enhanced by Two-Electron Dynamics. *Phys Rev A* (2002) 66:043403. doi:10.1103/PhysRevA.66.043403
73. Smirnova O, Mairesse Y, Patchkovskii S, Dudovich N, Villeneuve D, Corkum P, et al. High Harmonic Interferometry of Multi-Electron Dynamics in Molecules. *Nature* (2009) 460: 972–7. doi:10.1038/nature08253
74. Zanghellini J, Kitzler M, Fabian C, and Brabec SA. An MCTDHF Approach to Multielectron Dynamics in Laser Fields. *Laser Phys* (2003) 13: 1064–8.
75. Kato T, and Kono H. Time-Dependent Multiconfiguration Theory for Electronic Dynamics of Molecules in an Intense Laser Field. *Chem Phys Lett* (2004) 392: 533–40. doi:10.1016/j.cplett.2004.05.106
76. Kato T, and Kono H. Time-Dependent Multiconfiguration Theory for Electronic Dynamics of Molecules in Intense Laser Fields: A Description in Terms of Numerical Orbital Functions. *J Chem Phys* (2008) 128:184102. doi:10.1063/1.2912066
77. Nest M, and Klamroth T. Correlated Many-electron Dynamics: Application to Inelastic Electron Scattering at a Metal Film. *Phys Rev A* (2005) 72:012710. doi:10.1103/PhysRevA.72.012710
78. Jordan G, Caillat J, Ede C, and Scrinzi A. Strong Field Ionization of Linear Molecules: a Correlated Three-Dimensional Calculation. *J Phys B: Mol Opt Phys* (2006) 39:S341–S347. doi:10.1088/0953-4075/39/13/S07
79. Nest M, Padmanaban R, and Saalfrank P. Time-Dependent Approach to Electronically Excited States of Molecules with the Multiconfiguration Time-Dependent Hartree-Fock Method. *J Chem Phys* (2007) 126:214106. doi:10.1063/1.2743007
80. Sukiasyan S, McDonald C, Destefani C, Ivanov MY, and Brabec T. Multielectron Correlation in High-Harmonic Generation: A 2D Model Analysis. *Phys Rev Lett* (2009) 102:223002. doi:10.1103/PhysRevLett.102.223002
81. Nguyen-Dang T-T, Peters M, Wang S-M, and Dion F. Toward Ab-Initio Simulations of Multiple Ionization Processes in Intense Laser Field. *Chem Phys* (2009) 366: 71–84. doi:10.1016/j.chemphys.2009.09.007
82. Redkin P, and Ganeev R. Simulation of Resonant High-Order Harmonic Generation in a Three-Dimensional Fullerenelike System by Means of a Multiconfigurational Time-Dependent Hartree-Fock Approach. *Phys Rev A* (2010) 81:063825.
83. Hochstuhl D, Bauch S, and Bonitz M. Multiconfigurational Time-Dependent Hartree-Fock Calculations for Photoionization of One-Dimensional Helium. *J Phys Conf Ser* (2010) 220(10):012019. doi:10.1088/1742-6596/220/1/012019
84. Dirac PAM. The Principles of Quantum Mechanics, *International Series of Monographs on Physics*. 4th ed. 27. Oxford: Oxford Science (1958).
85. Frenkel J. *Wave Mechanics, Advanced General Theory*. Oxford: Claredon Press (1934).
86. Kato T, and Kono H. Time-Dependent Multiconfiguration Theory for Ultrafast Electronic Dynamics of Molecules in an Intense Laser Field: Electron Correlation and Energy Redistribution Among Natural Orbitals. *Chem Phys* (2009) 366: 46–53. doi:10.1016/j.chemphys.2009.09.017
87. Ohmura S, Kono H, Oyamada T, Kato T, Nakai K, and Koseki S. Characterization of Multielectron Dynamics in Molecules: A Multiconfiguration Time-Dependent Hartree-Fock Picture. *J Chem Phys* (2014) 141:114105. doi:10.1063/1.4894505

88. Ohmura S, Kato T, Oyamada T, Koseki S, Ohmura H, and Kono H. A Single-Electron Picture Based on the Multiconfiguration Time-Dependent Hartree-Fock Method: Application to the Anisotropic Ionization and Subsequent High-Harmonic Generation of the CO Molecule. *J Phys B: Mol Opt Phys* (2018) 51: 034001. doi:10.1088/1361-6455/aa9e45
89. Kato T, Yamanouchi K, and Kono H. *Attosecond Molecular Dynamics*. London: Royal Society of Chemistry (2018). p. 139–81. doi:10.1039/9781788012669
90. Ohmura S, Kato T, Ohmura H, Koseki S, and Kono H. Analysis of the Multielectron Dynamics in Intense Laser-Induced Ionization of CO by the Time-Dependent Effective Potentials for Natural Orbitals. *J Phys B: Mol Opt Phys* (2020) 53:184001. doi:10.1088/1361-6455/ab9f0e
91. Löwdin P-O. Quantum Theory of Many-particle Systems. I. Physical Interpretations by Means of Density Matrices, Natural Spin-Orbitals, and Convergence Problems in the Method of Configurational Interaction. *Phys Rev* (1955) 97: 1474–89. doi:10.1103/PhysRev.97.1474
92. Kraus PM, Baykusheva D, and Wörner HJ. Two-pulse Orientation Dynamics and High-Harmonic Spectroscopy of Strongly-Oriented Molecules. *J Phys B: Mol Opt Phys* (2014) 47:124030. doi:10.1088/0953-4075/47/12/124030
93. Holmegaard L, Hansen JL, Kalhøj L, Louise Kragh S, Stapelfeldt H, Filsinger F, et al. Photoelectron Angular Distributions from Strong-Field Ionization of Oriented Molecules. *Nat Phys*. (2010) 6: 428–32. doi:10.1038/nphys1666
94. Majety VP, and Scrinzi A. Static Field Ionization Rates for Multi-Electron Atoms and Small Molecules. *J Phys B: Mol Opt Phys* (2015) 48:245603. doi:10.1088/0953-4075/48/24/245603
95. SakemiMinemoto YS, Minemoto S, and Sakai H. Orientation Dependence in Multichannel Dissociative Ionization of OCS Molecules. *Phys Rev A* (2017) 96:011401. doi:10.1103/PhysRevA.96.011401
96. Johansen R, Bay KG, Christensen L, Thøgersen J, Dimitrovski D, Madsen LB, et al. Alignment-dependent Strong-Field Ionization Yields of Carbonyl Sulfide Molecules Induced by Mid-infrared Laser Pulses. *J Phys B: Mol Opt Phys* (2016) 49:205601. doi:10.1088/0953-4075/49/20/2056010.1088/0953-4075/49/20/205601
97. Sándor P, Sissay A, Mauger F, Abanador PM, Gorman TT, Scarborough TD, et al. Angle Dependence of Strong-Field Single and Double Ionization of Carbonyl Sulfide. *Phys Rev A* (2018) 98:043425. doi:10.1103/PhysRevA.98.043425
98. Madsen LB, Jensen F, Tolstikhin OI, and Morishita T. Structure Factors for Tunneling Ionization Rates of Molecules. *Phys Rev A* (2013) 87:013406. doi:10.1103/PhysRevA.87.013406
99. Śpiewanowski MD, and Madsen LB. Alignment- and Orientation-dependent Strong-Field Ionization of Molecules: Field-Induced Orbital Distortion Effects. *Phys Rev A* (2015) 91:043406. doi:10.1103/PhysRevA.91.043406
100. Dimitrovski D, Martiny CPJ, and Madsen LB. Strong-field Ionization of Polar Molecules: Stark-Shift-Corrected Strong-Field Approximation. *Phys Rev A* (2010) 82:053404. doi:10.1103/PhysRevA.82.053404
101. Wu J, Schmidt LPH, Kunitski M, Meckel M, Voss S, Sann H, et al. Multiorbital Tunneling Ionization of the CO Molecule. *Phys Rev Lett* (2012) 108:183001. doi:10.1103/PhysRevLett.108.183001
102. Akagi H, Otobe T, and Itakura R. Deformation of an Inner Valence Molecular Orbital in Ethanol by an Intense Laser Field. *Sci Adv* (2019) 5:eaaw1885. doi:10.1126/sciadv.aaw1885
103. Le C-T, Hoang V-H, Tran L-P, and Le V-H. Effect of the Dynamic Core-Electron Polarization of CO Molecules on High-Order Harmonic Generation. *Phys Rev A* (2018) 97:043405. doi:10.1103/PhysRevA.97.043405
104. Zhang B, Yuan J, and Zhao Z. Dynamic Orbitals in High-Order Harmonic Generation from CO Molecules. *Phys Rev A* (2014) 90:035402. doi:10.1103/PhysRevA.90.035402
105. Pernal K, Gritsenko O, and Baerends EJ. Time-Dependent Density-Matrix-Functional Theory. *Phys Rev A* (2007) 75:012506. doi:10.1103/PhysRevA.75.012506
106. Benavides-Rivero CL, and Marques MAL. On the Time Evolution of Fermionic Occupation Numbers. *J Chem Phys* (2019) 151:044112. doi:10.1063/1.5109009
107. Sato T, and Ishikawa KL. Time-Dependent Complete-Active-Space Self-Consistent-Field Method for Multielectron Dynamics in Intense Laser Fields. *Phys Rev A* (2013) 88:023402. doi:10.1103/PhysRevA.88.023402
108. Miyagi H, and Madsen LB. Time-Dependent Restricted-Active-Space Self-Consistent-Field Theory for Laser-Driven Many-electron Dynamics. *Phys Rev A* (2013) 87:062511. doi:10.1103/PhysRevA.87.062511
109. Lode AUJ, Lévêque C, and Madsen LB. Colloquium: Multiconfigurational Time-Dependent Hartree Approaches for Indistinguishable Particles. *Rev Mod Phys* (2020) 92:011001. doi:10.1103/RevModPhys.92.011001
110. Nielsen ES, Jo/rgensen P, and Oddershede J. Transition Moments and Dynamic Polarizabilities in a Second Order Polarization Propagator Approach. *J Chem Phys* (1980) 73: 6238–46. doi:10.1063/1.440119
111. Uiberacker M, Uphues T, Schultze M, Verhoef AJ, Yakovlev V, Kling MF, et al. Attosecond Real-Time Observation of Electron Tunnelling in Atoms. *Nature* (2007) 446: 627–32. doi:10.1038/nature05648
112. Kamta GL, and Bandrauk ADAD. Phase Dependence of Enhanced Ionization in Asymmetric Molecules. *Phys Rev Lett* (2005) 94:203003. doi:10.1103/PhysRevLett.94.203003
113. Bian X-B, and Bandrauk AD. Nonadiabatic Molecular High-Order Harmonic Generation from Polar Molecules: Spectral Redshift. *Phys Rev A* (2011) 83(R): 041403. doi:10.1103/PhysRevA.83.041403
114. Bian X-B, and Bandrauk AD. Multichannel Molecular High-Order Harmonic Generation from Asymmetric Diatomic Molecules. *Phys Rev Lett* (2010) 105: 093903. doi:10.1103/PhysRevLett.105.093903
115. Etches A, and Madsen LB. Extending the Strong-Field Approximation of High-Order Harmonic Generation to Polar Molecules: Gating Mechanisms and Extension of the Harmonic Cutoff. *J Phys B: Mol Opt Phys* (2010) 43: 155602. doi:10.1088/0953-4075/43/15/155602
116. Strelkov V. Role of Autoionizing State in Resonant High-Order Harmonic Generation and Attosecond Pulse Production. *Phys Rev Lett* (2010) 104: 123901. doi:10.1103/PhysRevLett.104.123901
117. Kono H, Sato Y, Kanno M, Nakai K, and Kato T. Theoretical Investigations of the Electronic and Nuclear Dynamics of Molecules in Intense Laser Fields: Quantum Mechanical Wave Packet Approaches. *Bcsj* (2006) 79:196–227. doi:10.1246/bcsj.79.196
118. Kübel M, Spanner M, Dube Z, Naumov AY, Chelkowski S, Bandrauk AD, et al. Probing Multiphoton Light-Induced Molecular Potentials. *Nat Commun* (2020) 11:2596. doi:10.1038/s41467-020-16422-2
119. Kato T, and Yamanouchi K. Time-Dependent Multiconfiguration Theory for Describing Molecular Dynamics in Diatomic-like Molecules. *J Chem Phys* (2009) 131:164118. doi:10.1063/1.3249967
120. Ide Y, Kato T, and Yamanouchi K. Non-Born-Oppenheimer Molecular Wave Functions of H2 by Extended Multi-Configuration Time-Dependent Hartree-Fock Method. *Chem Phys Lett* (2014) 595-596:180–4. doi:10.1016/j.cplett.2014.01.055
121. Kato T, Ide Y, and Yamanouchi K. Molecular Wave Function and Effective Adiabatic Potentials Calculated by Extended Multi-Configuration Time-Dependent Hartree-Fock Method. *AIP Conf Proceed* (2015) 1702:090024. doi:10.1063/1.4938832
122. Azumi T, and Matsuzaki K. What Does the Term “Vibronic Coupling” Mean? *Photochem Photobiol* (1977) 25:315–26. doi:10.1111/j.1751-1097.1977.tb06918.x
123. Lötstedt E, Kato T, and Yamanouchi K. Time-Dependent Multiconfiguration Method Applied to Laser-Driven H_2^+. *Phys Rev A* (2019) 99:013404. doi:10.1103/PhysRevA.99.013404

Conflict of Interest: The authors declare that the research was conducted in the absence of any commercial or financial relationships that could be construed as a potential conflict of interest.

frontiers in Physics

ORIGINAL RESEARCH
published: 14 July 2021
doi: 10.3389/fphy.2021.700283

Decoherent Excitation of Transverse Free Currents in Dielectric Liquids *via* Inter-Molecular Interactions

C. S. DiLoreto[1] *and C. Rangan*[2]*

[1]*Department of Natural Sciences, Northwest Missouri State University, Maryville, MO, United States,* [2]*Department of Physics, University of Windsor, Windsor, ON, Canada*

We present a theoretical model for a class of optical scattering experiments in which short-duration, linearly-polarized electromagnetic pulses scatter off dielectric liquids. The pattern of scattering, particularly in the transverse direction, indicates that significant free currents are generated in the direction orthogonal to the polarization of the incident light. Modelling the target as a dense cluster of two-level systems, we show that transverse free currents are produced by short duration, electric-dipole interactions between proximate molecules, and result in scattering patterns similar to those observed in the experiments. Calculations provide a rationale for why these scattering patterns are not observed in the same molecules at lower densities or with lower field intensities. These features make this model a relevant alternative to proposed transverse optical magnetism theories.

Keywords: femtosecond pulse scattering, inter-molecular interactions, transverse scattering, lindblad master equation, ensemble scattering

Edited by:
Robert Gordon,
University of Illinois at Chicago,
United States

Reviewed by:
Huiqin Zhang,
University of Pennsylvania,
United States
Vladimir Malinovsky,
United States Army Research
Laboratory, United States

****Correspondence:***
C. Rangan
rangan@uwindsor.ca

Specialty section:
This article was submitted to
Optics and Photonics,
a section of the journal
Frontiers in Physics

Received: *25 April 2021*
Accepted: *28 June 2021*
Published: *14 July 2021*

Citation:
DiLoreto CS and Rangan C (2021)
Decoherent Excitation of Transverse
Free Currents in Dielectric Liquids via
Inter-Molecular Interactions.
Front. Phys. 9:700283.
doi: 10.3389/fphy.2021.700283

1 INTRODUCTION

Optical or artificial magnetism is typically seen in specifically-engineered, nanofabricated metamaterials such as thin metallic strip pairs [1], split-ring resonators [2], and hyperbolic metamaterials [3]. As the name metamaterial implies, these devices are specifically engineered to have properties beyond those traditionally found in naturally-occuring materials, and typically contain nanostructures with precise geometries. Over the last decade, a series of experiments [4–7] have reported observing optical magnetism in dielectric liquids. These experiments have generated significant interest due to the prospect of observing magneto-optic interactions in naturally-occurring, non-magnetic materials [8]. These experiments, in which a dielectric liquid (such as water or carbon tetrachloride) is excited by a short-duration ($\approx 100-150$ fs), high-intensity ($\approx 1\times10^8 - 4\times10^8$ W/cm^2) electromagnetic pulse, have shown that the scattered, free-emitted light in the propagation direction orthogonal to that of the incident light, has a significant intensity in the polarization direction orthogonal to the incident polarization. These results, suggestive of magnetic dipole radiation patterns, have led to the theory that intense optical fields induce magnetism in individual molecules, that lead to the generation of significant transverse free currents, which in turn generate the observed radiation patterns [9–12]. This "transverse optical magnetism" theory has encountered a number of criticisms, primarily centered around the need for a large relative magnetic permeability $\mu_r \approx c$ for agreement with experiments [9, 10, 13–16].

In this paper, we present an alternate theoretical model that can explain the experimental observations in Refs. [4–7] by including inter-molecular effects. In this model, strong, transverse free currents are produced through inter-molecular electric-dipole interactions without invoking magneto-optic effects in single molecules. Because the strength of inter-particle interactions decreases directly as the density of emitters decreases, this model can explain experiments in which scattering effects exhibit a strong density dependence. For example, it explains why these intensity patterns are not observed in scattering experiments that use low molecular density phases (such as the gas phase) [17].

2 THEORETICAL MODEL AND CALCULATIONS

When a linearly-polarized electromagnetic pulse is incident on a dense ensemble of molecules, the light absorbed by an individual molecule creates a free current in the initial polarization direction. Upon spontaneous emission, this light is re-emitted in a well-known dipole pattern. In a dense medium, this light is reabsorbed by neighboring molecules located at different spatial positions. This subsequent absorption by neighboring molecules leads to a free current that is not necessarily in the same direction as the incident polarization direction. By exciting radiating dipoles perpendicular to the polarization of the incident field, the ensemble will emit photons in multiple polarization directions. This creates radiation patterns similar to those observed in the experiments.

In our calculations, we model the scattering of a strong, electromagnetic pulse by the target molecular liquid in the experiments by a single-particle model of a dense, driven ensemble of quantum dipoles (two-level systems) [18]. We assume that the incident electromagnetic pulse is near-resonant with a single optical transition in the molecule. Since the quantum dipoles are excited by the local electromagnetic field, the excitation direction of each dipole can be different from each other and from the initial polarization of the incident electromagnetic field. To model excitations in directions other than the incident polarization direction, the state of the ensemble is represented by the density matrix of a four-level quantum system with one ground energy level \ketg and three excited "directional" states $|e_x\rangle$, $|e_y\rangle$ and $|e_z\rangle$, an idea first proposed for a single atom in Ref. [19]. The three excited states $|e_x\rangle$, $|e_y\rangle$ and $|e_z\rangle$ represent the excited energy levels when an x, y or z-polarized photon is absorbed by the ensemble in the ground state. We assume that the polarization of the incident electromagnetic field is in the y-direction. The inter-molecular interactions are modelled by decoherences that arise from nearest-neighbor dipolar energy transfers [18, 20]. The ensemble density matrix representing a cluster of molecules is therefore a 4×4 matrix, and its evolution can be calculated quickly. This model requires no *a priori* assumptions about the specific quantum levels of the target molecules other than the applied field being near-resonant with a single transition, therefore the conclusions are generalized to a wide class of molecules.

The Hamiltonian of the ensemble of two-level molecules, after making the rotating wave approximation as in Ref. [18] is:

$$H_{ens} = \begin{pmatrix} 0 & \frac{\hbar\Omega_x}{2} & \frac{\hbar\Omega_y}{2} & \frac{\hbar\Omega_z}{2} \\ \frac{\hbar\Omega_x^*}{2} & -\triangle & 0 & 0 \\ \frac{\hbar\Omega_y^*}{2} & 0 & -\triangle & 0 \\ \frac{\hbar\Omega_z^*}{2} & 0 & 0 & -\triangle \end{pmatrix}, \qquad (1)$$

where $\triangle$ represents the detuning between the molecular transition frequency and the frequency of the incident light, and the Rabi frequency-like terms ($\Omega_i = \mu_i E_i, i = x, y, z$) are proportional to the electric field amplitudes in each of the three Cartesian directions (E_i) and the transition dipole moment (μ_i). The incident electromagnetic pulse is polarized in the y-direction, and propagates along the x-direction. The electric field in the y-direction is dominated by the incident field, while the electric fields in the x and z directions represent the dipolar emission from a quantum emitter due to spontaneous emission, and are about an order of magnitude smaller than that of the incident field [18]. Note that we ignore the magnetic component of the electromagnetic field since it is much smaller than the electric field component, and the value of the relative magnetic permeability of the molecules is assumed to be 1.

In our four-level model, the spontaneous emission from the $|e_x\rangle$, $|e_y\rangle$, and $|e_z\rangle$ excited directional states to the ground state $|g\rangle$ have rates γ_{xg}, γ_{yg} and γ_{zg} respectively. These emission rates are determined using Fermi's Golden Rule [20]. An individual molecule in the ensemble can spontaneously emit in all directions, and this radiation can excite a neighbouring molecule. These "inter-particle interactions" are modelled by adding in additional decoherence rates between all three excited states, represented by the set of all possibleδ_{ij}'s ($i, j = x, y, z$) [18]. These rates represent the transfer of energy between molecules in which the energy emitted by one molecule transitioning to the ground state ($|i\rangle \rightarrow |g\rangle$) is absorbed and causes a nearby molecule in the ground state to transition to an excited state ($|g\rangle \rightarrow |j\rangle$). This model of the intermolecular energy transfer as a decoherence rate is inspired by models of the Forster-Resonance Energy Transfer (FRET) process commonly seen in biophysical systems [20]. These δ's do not result in a loss of energy from the ensemble, therefore, they act like dephasing rates for the ensemble density matrix.

The magnitude of these dephasing rates associated with energy transfer between molecules (δ_{ij}) are calculated by modelling the radiation emitted by a molecule as electric dipole radiation that is absorbed by the nearest neighbors (separated by **r**) in a square lattice. The expressions are derived in [18] and are of the form:

$$\frac{\delta_{ij}}{\gamma_0} = \frac{N_a \pi c^3}{4\omega^3} \left(3\left(\hat{u}_i \cdot \hat{r}_i\right)\left(\hat{u}_j \cdot \hat{r}_i\right) - \hat{u}_j \cdot \hat{u}_i\right)\left(\sqrt{\bar{\rho}_{ii}\bar{\rho}_{gg}}\,\sqrt{\bar{\rho}_{jj}\bar{\rho}_{gg}}\right), \qquad (2)$$

where N_a is the number density of the ensemble, ω is the natural frequency of the transition dipole, $\gamma_0 = \gamma_{ig} = \gamma_{jg}$ is the spontaneous emission rate of the involved transitions and $\hat{u}_i$ is the direction of the transition dipole moment.

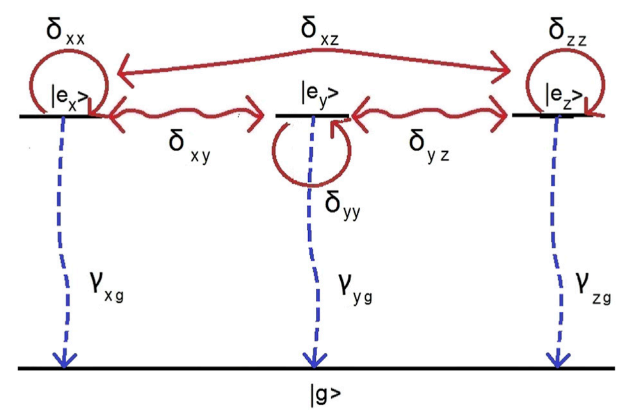

FIGURE 1 | Decoherence structure in a single-particle approximation of a driven molecular ensemble. Inter-molecular energy transfer due to reabsorption of spontaneously emitted photons (γ_{ig}'s in dashed/blue) are modelled as decoherent dephasing terms (δ_{ij}'s in solid/red) For details on how the decoherence rates are calculated, see Ref. [18].

The term $\sqrt{\bar{\rho}_{ii}\bar{\rho}_{gg}}\sqrt{\bar{\rho}_{jj}\bar{\rho}_{gg}}$, modifies the decoherence rate by estimating how many dipoles are undergoing transitions that experience the $|i\rangle \rightarrow |j\rangle$ energy transfer. Since $\bar{\rho}_{gg}$, $\bar{\rho}_{ii}$ and $\bar{\rho}_{jj}$ are functions of time, and depend on the intensity of the applied field, the dephasing rates exhibit an intensity-dependence. If the intensity of the applied field is significantly low, the ensemble state will simply oscillate around the ground state and these dephasing rates will remain close to zero.

A diagram of all the decoherence processes in the single-particle quantum model of the ensemble is provided in **Figure 1**. The Lindblad superoperator representing the spontaneous emission, and dephasing due to intermolecular energy transfer has the form:

$$L(\bar{\rho}) = \sum_{i=x,y,z} \frac{\gamma_{ig}}{2}\left(\sigma_{ig}^{\dagger}\sigma_{ig}\bar{\rho} + \bar{\rho}\sigma_{ig}^{\dagger}\sigma_{ig} - 2\sigma_{ig}\bar{\rho}\sigma_{ig}^{\dagger}\right) \tag{3}$$

$$+\sum_{i=x,y,z}\sum_{j=x,y,z} \frac{\delta_{ij}}{2}\left(\sigma_{ij}^{\dagger}\sigma_{ij}\bar{\rho} + \bar{\rho}\sigma_{ij}^{\dagger}\sigma_{ij} - 2\sigma_{ij}\bar{\rho}\sigma_{ij}^{\dagger}\right),$$

with $\sigma_{ij} = |j\rangle\langle i|$.

The density matrix of the ensemble, $\bar{\rho}$, is evolved in time using the Lindblad-von Neumann equation:

$$\dot{\bar{\rho}} = -\frac{i}{\hbar}\left[H_{ens}, \bar{\rho}\right] - L(\bar{\rho}). \tag{4}$$

As shown in Ref. [18], the time-dependent behavior of the density matrix of an ensemble in a four-level basis, agrees very well with the numerically calculated, average time-dependent behavior of ≈ 4000 two-level molecules calculated via a mean-field solution of Maxwell-Lindblad equations.

After calculating the time-dependent density matrix elements, we determine the Emission Ratio (R), the ratio of the intensity perpendicular the incident polarization (called I_M as in the experimental papers) to the intensity parallel to the incident polarization (I_E). In comparison to the experiments, this ratio is calculated at a point along the transverse z-direction. The instantaneous intensities will be proportional to the ratio of the square of the modulus of the free currents ($\mathbf{J}_i$)in the driving field polarization direction ($i = y$) and an orthogonal direction ($i = x$) [5], that is,

$$\frac{I_M(t)}{I_E(t)} = \frac{|J_x(t)|^2}{|J_y(t)|^2}. \tag{5}$$

This ratio can be expressed in terms of the ensemble density matrix elements since $J_i = \dot{\mu}_i = Tr\left(\dot{\bar{\rho}}\underline{\mu_i}\right) = Tr\left(\dot{\bar{\rho}}\frac{\partial H}{\partial E_i}\right)$. The observed Emission Ratio is the ratio of the intensities integrated over time. Therefore,

$$\overline{R} = \frac{\int dt\left|\mu_x\left(\dot{\bar{\rho}}_{xg} + \dot{\bar{\rho}}_{gx}\right)\right|^2}{\int dt\left|\mu_y\left(\dot{\bar{\rho}}_{yg} + \dot{\bar{\rho}}_{gy}\right)\right|^2}, \tag{6}$$

which yields a simple relationship between calculated elements of the ensemble density matrix, and the measured Emission Ratio. We assume that the transition dipole moments are the same in each direction, $\mu_x = \mu_y$, and as in **Eq. 2**, $\bar{\rho}_{ig} \approx \sqrt{\bar{\rho}_{ii}\bar{\rho}_{gg}}$. Note that the Emission Ratio scales with the dipole moment of the transition as $\left(\frac{\mu}{\mu_0}\right)^2$.

This model is sensitive to both the density of molecules in the ensemble as well as the intensity of the applied field. Under low intensities or low densities these inter-molecular effects are not significant. Over long time periods, these effects die out very quickly. However at high intensities, high densities and short time periods these effects can lead to significant excitation and free currents generated in orthogonal polarization directions [18]. This is similar to experiments in coherent atomic ensembles that have shown that inter-atomic interactions affect resonance frequencies and scattering polarizations, in a way that is dependent on both the density of emitters and the incident intensity [21].

3 EMISSION RATIOS FROM A DENSE ENSEMBLE

We now calculate the Emission Ratio R generated in response to a strong incident pulse similar to the experiments in Refs. [5, 6]. A 100fs pulse with an intensity of 8×10^8 W/cm^2 and a central wavelength of 775 nm excites an ensemble of molecules with a molecular number density N_A, assumed to have a value similar to that of water ($N_A = 3.3 \times 10^{28} m^{-3}$). Our model makes the approximation that there is a single, optical transition that is resonantly excited by the pulse. We make the simplification that the pulse amplitude is a constant over its duration (i.e., it is a rectangular pulse). This simplification takes advantage of the pulse-area theorem used in quantum control frameworks, in which only the area under the pulse significantly affects excitation [22]. We also assume that all the molecules are initially in the ground state. The dipole moment of system was taken to be $\approx 1.8D = 3.7 \times 10^{-11} em$, based on the net dipole of a single water molecule [23],

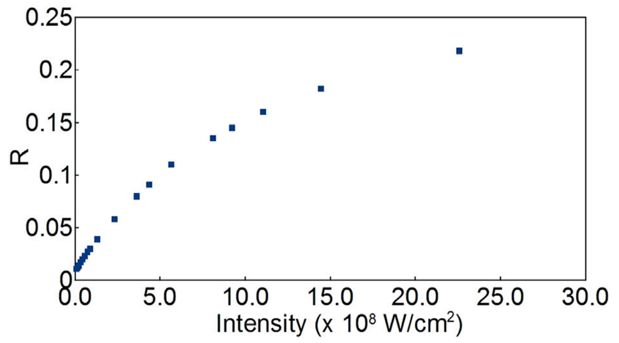

FIGURE 2 | Emission Ratio of water as a function of increasing intensity of the applied 100fs pulse. As the intensity increases, the transition to the excited state of each molecule is driven more strongly, and the probability of inter-molecular energy transfer increases, thus increasing the Emission Ratio.

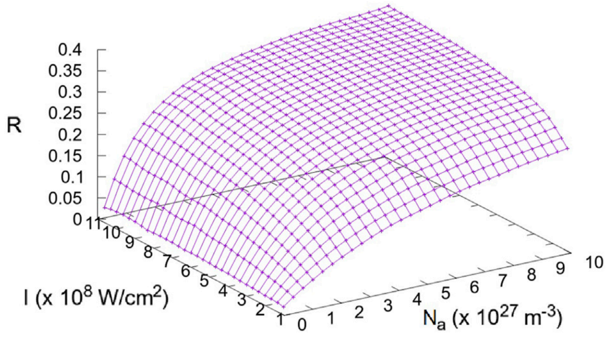

FIGURE 3 | Density dependence of the Emission Ratio of an ensemble of molecules with electric dipole transition moment $\mu = 10^{-10}em$ as a function of increasing number density in the ensemble. As the number density is increased, the probability of inter-molecular interactions increases, thus increasing the Emission Ratio.

however this value may actually be higher due to water being in a condensed phase [24].

Figure 2 shows the dependence of the emission ratio for water on the intensity of the applied 100fs pulse. The range of pulse intensities was chosen to match the overall range found in the experiments in Refs. [5, 6].

From this figure, it is seen that for the emission ratio to become significant for 100fs pulses, the average field intensity needs to be higher than $\approx 10^7$ W/cm^2). This minimum intensity limit is seen in experiments [5]. The curve is similar to the measured experimental curves in that it shows a linear increase at low intensities [6]. At higher intensities, we predict the emission will reach a saturation value. We find that the calculated emission ratio for a dielectric liquid similar to water is fairly significant with a value of 0.15, close to the experimentally measured emission ratio of approximately 0.22 [6].

This quantitative difference is not surprising as our model treats the molecules as dipole emitters and looks at no other interactions between molecules. However, given the generality of our model and the fact that the Emission Ratio under this mechanism is similar in strength to what is measured, it suggests that this alternate pathway from transverse free currents and scattered intensities should represent a significant step in understanding short-pulse scattering experiments from dielectric liquids.

In addition to intensity-dependent effects, our model also predicts that there should be a strong dependence on the density of the medium. This dependence is an attractive feature of this alternate model as strong transverse free currents are typically not seen in gas-phase scattering experiments [17].

Using our simplified model, **Figure 3** shows the predicted density dependence of the Emission Ratio of a general molecular ensemble with electric dipole transition moment around $\mu_0 = 10^{-10}em$. As the density of the liquid increases (thus increasing the probability of intermolecular energy transfer), the emission ratio increases. Quantitative comparison to the experiments is made challenging since our model assumes that the molecules are infinitesimally small in size, whereas the size of molecules such as carbon tetra chloride or benzene is large, and the atoms in the molecules are actually much closer together than the number density suggests. Thus for larger molecules such as CCl_4, the Emission Ratio would reach saturation at lower intensities than predicted by the number density alone, which appears to be the case in experiments [6].

Due to the presence of this density dependence, we suggest two possible experiments that could validate our model. The first involves performing the same experiments as described in Refs. [4–7] by using systems with varying molecular densities. If the transverse free currents are caused by inter-molecular electric interactions, the Emission Ratio should clearly increase as a function of density (whereas a single-molecule magneto-optic effect will not be effected by density). This may be accomplished by performing these short-pulse scattering experiments on the same liquids at different temperatures and pressures. The second suggested experiment is a measurement of the time-dependence of the scattered signal. Since out model involves absorption and re-emission between molecules, it is naturally time-dependent and thus the Emission Ratio should change as a function of time, and also be fairly sensitive to different pulse widths at the same intensity.

4 CONCLUSION

For optical scattering experiments in dense media, the interactions between molecules can have a significant effect on the observed scattering intensity patterns. We have proposed a theoretical model wherein significant transverse currents are generated in optical scattering experiments on dielectric liquids due to inter-molecular electric-dipole interactions. Using our model, we show that the strength of these inter-molecular interactions increase with both density and incident intensity. The calculated dependence of the transverse currents on the intensity of the incident electromagnetic pulse agrees with experimental results. The density dependence provides a direct explanation for why these effects do not appear in scattering experiments involving less-dense targets such as gases. We provide suggestions for future scattering experiments that can validate our model.

DATA AVAILABILITY STATEMENT

The raw data supporting the conclusions of this article will be made available by the authors, without undue reservation.

REFERENCES

1. Chettiar UK, Kildishev AV, Klar TA, and Shalaev VM. Negative index Metamaterial Combining Magnetic Resonators with Metal Films. *Opt Express* (2006) 14:7872. doi:10.1364/oe.14.007872
2. Zhou J, Koschny T, Kafesaki M, Economou EN, Pendry JB, and Soukoulis CM. Saturation of the Magnetic Response of Split-Ring Resonators at Optical Frequencies. *Phys Rev Lett* (2005) 95:223902. doi:10.1103/physrevlett.95.223902
3. Poddubny A, Iorsh I, Belov P, and Kivshar Y. Hyperbolic Metamaterials. *Nat Photon* (2013) 7:948–57. doi:10.1038/nphoton.2013.243
4. Oliveira SL, and Rand SC. Intense Nonlinear Magnetic Dipole Radiation at Optical Frequencies: Molecular Scattering in a Dielectric Liquid. *Phys Rev Lett* (2007) 98. doi:10.1103/PhysRevLett.98.093901
5. Rand SC, Fisher WM, and Oliveira SL. Optically Induced Magnetization in Homogeneous, Undoped Dielectric media. *J Opt Soc Am B* (2008) 25:1106. doi:10.1364/josab.25.001106
6. Fisher WM, and Rand SC. Dependence of Optically Induced Magnetism on Molecular Electronic Structure. In: international Conference on Luminescence and Optical Spectroscopy of Condensed Matter (ICL'08); JUL 07-11, 2008, 129. Lyon, France: . Univ Lumiere Lyon 2 (2009). p. 1407–9. doi:10.1016/j.jlumin.2009.02.036*J Lumin*
7. Fisher AA, Dreyer EFC, Chakrabarty A, and Rand SC. Optical Magnetization, Part I: Experiments on Radiant Optical Magnetization in Solids. *Opt Express* (2016) 24:26055. doi:10.1364/oe.24.026055
8. Papadakis GT, Fleischman D, Davoyan A, Yeh P, and Atwater HA. Optical Magnetism in Planar Metamaterial Heterostructures. *Nat Commun* (2018) 9: 296. doi:10.1038/s41467-017-02589-8
9. Rand SC. Quantum Theory of Coherent Transverse Optical Magnetism. *J Opt Soc Am B* (2009) 26:B120. doi:10.1364/josab.26.00b120
10. Fisher WM, and Rand SC. Light-induced Dynamics in the Lorentz Oscillator Model with Magnetic Forces. *Phys Rev A* (2010) 82:013802. doi:10.1103/physreva.82.013802
11. Fisher AA, Cloos EF, Fisher WM, and Rand SC. Dynamic Symmetry-Breaking in a Simple Quantum Model of Magneto-Electric Rectification, Optical Magnetization, and Harmonic Generation. *Opt Express* (2014) 22:2910. doi:10.1364/oe.22.002910
12. Fisher AA, Dreyer EFC, Chakrabarty A, and Rand SC. Optical Magnetization, Part II: Theory of Induced Optical Magnetism. *Opt Express* (2016) 24:26064. doi:10.1364/oe.24.026064

AUTHOR CONTRIBUTIONS

CD performed the calculations, interpreted the results and co-wrote the manuscript. CR oversaw the project, advised CD, assisted in the analysis, and co-wrote the paper.

FUNDING

CD greatly acknowledges computing resources made available through the National Science Foundation under Grant No. 1624416. CR gratefully acknowledges support from the Discovery Grant program of the Natural Sciences and Engineering Research Council of Canada (funding reference number RGPIN-2019-06387).

13. Palffy-Muhoray P. Comment on "Intense Nonlinear Magnetic Dipole Radiation at Optical Frequencies: Molecular Scattering in a Dielectric Liquid". *Phys Rev Lett* (2007) 99:189401. doi:10.1103/physrevlett.99.189401
14. Oliveira SL, and Rand SC. Oliveira and Rand Reply:. *Phys Rev Lett* (2007) 99: 189402. doi:10.1103/physrevlett.99.189402
15. Sharma NL. *Phys Rev Lett* (2009) 102:119403.
16. Oliveira SL, and Rand SC. Oliveira and Rand Reply:. *Phys Rev Lett* (2009) 102: 119404. doi:10.1103/physrevlett.102.119404
17. Murphy WF. The Rayleigh Depolarization Ratio and Rotational Raman Spectrum of Water Vapor and the Polarizability Components for the Water Molecule. *J Chem Phys* (1977) 67:5877–82. doi:10.1063/1.434794
18. DiLoreto CS, and Rangan C. Single-particle Model of a Strongly Driven, Dense, Nanoscale Quantum Ensemble. *Phys Rev A* (2018) 97:013812. doi:10.1103/physreva.97.013812
19. Fratalocchi A, Conti C, and Ruocco G. Three-dimensional Ab Initio Investigation of Light-Matter Interaction in Mie Lasers. *Phys Rev A* (2008) 78:013806. doi:10.1103/physreva.78.013806
20. Novotny L, and Hecht B. *"emph "Bibinfo Title Principles of Nano-Optics*, 8. Cambridge University Press (2006).
21. Bromley SL, Zhu B, Bishof M, Zhang X, Bothwell T, Schachenmayer J, et al. Collective Atomic Scattering and Motional Effects in a Dense Coherent Medium. *Nat Commun* (2016) 7:11039. doi:10.1038/ncomms11039
22. Tannor DJ. *Introduction to Quantum Mechanics: A Time-dependent Perspective*. Mill Valley, CA: University Science Books (2007).
23. Lovas FJ. Microwave Spectral Tables II. Triatomic Molecules. *J Phys Chem Reference Data* (1978) 7:1445–750. doi:10.1063/1.555588
24. Gregory JK, Clary DC, Liu K, Brown MG, and Saykally RJ. The Water Dipole Moment in Water Clusters. *Science* (1997) 275:814–7. doi:10.1126/science.275.5301.814

Conflict of Interest: The authors declare that the research was conducted in the absence of any commercial or financial relationships that could be construed as a potential conflict of interest.

frontiers in Physics

REVIEW
published: 16 July 2021
doi: 10.3389/fphy.2021.675134

Quantum Control of Coherent π-Electron Dynamics in Aromatic Ring Molecules

Hirobumi Mineo[1,2]*, *Ngoc-Loan Phan*[3] *and Yuichi Fujimura*[4]*

[1]*Atomic Molecular and Optical Physics Research Group, Advanced Institute of Materials Science, Ton Duc Thang University, Ho Chi Minh City, Vietnam,* [2]*Faculty of Applied Sciences, Ton Duc Thang University, Ho Chi Minh City, Vietnam,* [3]*Department of Physics, Ho Chi Minh City University of Education, Ho Chi Minh City, Vietnam,* [4]*Department of Chemistry, Graduate School of Science, Tohoku University, Sendai, Japan*

Herein we review a theoretical study of unidirectional π-electron rotation in aromatic ring molecules, which originates from two quasi-degenerate electronic excited states created coherently by a linearly polarized ultraviolet/visible laser with a properly designed photon polarization direction. Analytical expressions for coherent π-electron angular momentum, ring current and ring current-induced magnetic field are derived in the quantum chemical molecular orbital (MO) theory. The time evolution of the angular momentum and the ring current are expressed using the density matrix method under Markov approximation or by solving the time-dependent Schrödinger equation. In this review we present the results of the following quantum control scenarios after a fundamental theoretical description of coherent angular momentum, ring current and magnetic field: first, two-dimensional coherent π-electron dynamics in a non-planar (*P*)-2,2’-biphenol molecule; second, localization of the coherent π-electron ring current to a designated benzene ring in polycyclic aromatic hydrocarbons; third, unidirectional π-electron rotations in low-symmetry aromatic ring molecules based on the dynamic Stark shift of two relevant excited states that form a degenerate state using the non-resonant ultraviolet lasers. The magnetic fields induced by the coherent π-electron ring currents are also estimated, and the position dependence of the magnetic fluxes is demonstrated.

Keywords: quantum control, electron dynamics, coherent ring current, ring current localization, angular momentum, quantum switching, Stark-induced degenerate electronic state

Edited by:
Philip Bucksbaum,
Stanford University, United States

Reviewed by:
Sheng Meng,
Institute of Physics (CAS), China
Luca Evangelisti,
University of Bologna, Italy

***Correspondence:**
Hirobumi Mineo
mineo@tdtu.edu.vn
Yuichi Fujimura
fujimurayuichi@m.tohoku.ac.jp

Specialty section:
This article was submitted to Physical Chemistry and Chemical Physics, a section of the journal Frontiers in Physics

Received: *02 March 2021*
Accepted: *23 June 2021*
Published: *16 July 2021*

Citation:
Mineo H, Phan N-L and Fujimura Y (2021) Quantum Control of Coherent π-Electron Dynamics in Aromatic Ring Molecules.
Front. Phys. 9:675134.
doi: 10.3389/fphy.2021.675134

1 INTRODUCTION

Recent progress in laser science and technology has facilitated the coherent control of ultrafast charge migration dynamics in molecular systems [1–21]. Controlled charge migration can generate unidirectional currents and current-induced magnetic fields, which can be used as a guiding principle for the next-generation ultrafast optoelectronic devices [22, 23]. Laser control of π-electron rotations in aromatic ring molecules is a typical example. Pioneering studies on the generation of coherent π-electron rotations in high-symmetry ring molecules such as Mg porphyrin having degenerate excited states have been reported by the Manz group [24–26]. π-Electron rotations were induced by degenerate electronic excited states, which were coherently created by circularly polarized ultraviolet (UV) lasers. The generation mechanism of the photon angular momentum involves the photon transfer from the circularly polarized UV lasers to the π-electrons, thereby the left- or right-handed circular polarization of the applied laser defines the rotational direction of the angular momentum [27]. In contrast in ring molecules with low-symmetry π-electrons cannot be rotated by using the circularly polarized lasers, due to the absence of electronic excited states degenerate, that would receive the photon angular momentum. Thus, it was commonly understood that coherent π-electron rotations could not be generated in low-symmetry aromatic ring molecules. However, Kanno et al. [28–31] have invalidated this long-established understanding by demonstrating that π-electrons in oriented chiral aromatic ring molecules can be rotated by the coherent excitation of a pair of quasi-degenerate π-electronic excited states using a linearly polarized UV/vis laser pulse with a properly designed photon polarization direction [28, 29]; the polarization direction of the pulse determines the initial direction of the π-electron rotation, whether right- or left-handed one. The duration of the unidirectional rotation is inversely proportional to the energy difference between the two quasi-degenerate excited states, and inverse rotation begins after the duration because the coherent state is not a nonstationary state rather than an eigenstate. Pump and dump laser pulses with their properly designed polarization directions for these lasers are applied to eliminate the reverse rotation. The number of unidirectional rotations during the duration can be estimated from the energy difference between the quasi-degenerate excited and ground states. This only applies to the ideal case in which any dephasing processes disturbing the electronic coherence are omitted. It is expected that unidirectional ring currents produce much stronger magnetic fields than traditional static magnetic fields [32, 33].

The concept of the conventional ring current has already been established previously and plays an important role in interpreting the magnetic properties and aromaticity of conjugated molecular systems [34, 35]. The molecules investigated based on the ring current are in the ground state, and the current densities for evaluation of the ring current are calculated using the first-order electronic wave function in the time-independent magnetic field and in a permanent magnetic dipole. Such a conventional ring current should be called an incoherent current.

In this article, we present the most recent results of our theoretical studies on the quantum control of coherent π→electron rotations in low-symmetry aromatic ring molecules. Low-symmetry aromatic ring molecules are not rare, but rather common: high-symmetry aromatic molecules often become low-symmetry ones by substitution of a functional group, or under environment conditions. In the next section, the fundamental theory for the quantitative analysis of coherent π-electrons in a low-symmetry aromatic ring molecule is introduced. Here, the time-dependent coherent angular momentum, ring current, and ring current-induced magnetic field are analytically derived in a closed form in the quantum chemical MO theory. Time-evolutions of these quantities are derived by the density matrix method [36–39]. The temporal behavior of coherence is determined by the off-diagonal element of density matrix. Then, the Markov approximation is ultilized for considering the dephasing effects on the conherent angular momenta and ring currents. The magnitudes of the electronic angular momenta and ring currents are expressed as the summation of the expectation values of the corresponding one-electron operators in the aromatic rings. The bond current between the nearest neighbor carbon atoms, C_i and C_j, is defined as an electric current flowing through a half plane perpendicular to the $C_i - C_j$ bond. The coherent bond current in an aromatic ring is defined as the average of all bond currents. The application of this theory to a nonplanar chiral aromatic molecule, (*P*)-2,2'-biphenol, is briefly described. (*P*)-2,2'-biphenol has four patterns of coherent π-electron rotations along with the two phenol rings because of its nonplanar geometrical structure [39, 40]. A sequence of the four rotational patterns can be controlled through a coherent excitation of two electronic states with two requirements: the symmetry of the two electronic states, and their relative phase. Quantum switching of coherent π-electron rotations is proposed [40]. In **Section 3**, the key points are summarized for the application of the quantum optimal control method for controlling coherent ring currents in polycyclic aromatic hydrocarbons (PAHs). These molecules exhibit several localization patterns of coherent π-electron rotations. Therefore, how to set up the target state for a desired localization pattern is crucial [41, 42]. However, we demonstrate that the target state can easily be set up using the Lagrange multiplier method. As examples, two types of current localizations for the simplest PAH, anthracene, are adopted [42]: current localization to the designated benzene ring, and the perimeter ring current. In **Section 4**, a convenient scenario involving unidirectional π-electron rotations in low-symmetry aromatic ring molecules is described [43]. The basic idea behind unidirectional electron rotations is to degenerate two nondegenerate excited states by utilizing dynamic Stark shifts. A degenerate state induced by dynamic Stark shifts is called a dynamic Stark-induced degenerate electronic state (DSIDES). Two linearly polarized continuous lasers with different frequencies and phases are used to form a DSIDES, where each laser is set to selectively interact with each electronic state through non-resonant excitation. As a result, the unidirectional π-electron rotation is driven by the lasers. This scenario was applied to toluene. The resulting angular momenta can be represented by a pulse train having an angular momentum. Each angular momentum pulse represents the unidirectional π-electrons rotation, which begins with acceleration and ends with deceleration.

2 COHERENT π-ELECTRON DYNAMICS IN LOW-SYMMETRY AROMATIC RING MOLECULES

In this section we present the theoretical formalism for the coherent π-electrons in a low-symmetry aromatic ring molecule to derive analytical expressions for the coherent angular momentum, ring current and the current-induced magnetic field within the framework of the quantum chemical MO treatment [39, 40].

2.1 Equations of Motion for Coherent π-Electron Rotations Induced by Ultrashort UV/Vis Lasers

The expectation values of the coherent π–electron angular momentum and the ring current operators in an aromatic molecule are generally expressed as

$$\langle \hat{O}(t)\rangle = n\int d^3\mathbf{r}_1\cdots d^3\mathbf{r}_n \Psi^*(t)\hat{O}(r)\Psi(t). \tag{1}$$

Here, $\hat{O}(r)$ is a single-electron operator for the angular momentum or current. $\Psi(t)$ is the wave function of the π–electrons in laser field $\mathbf{F}(t)$ at time t, n denotes the number of electrons, and $\mathbf{r}_i$ express the ith electron coordinates. Since the optically-allowed electronic excited states of the conjugated aromatic rings are of our interest, the electronic wave function can be expanded by the two electronic configurations, i.e., the ground configuration $\mathbf{\Phi}_0$, and the singly excited ones $\mathbf{\Phi}_\alpha$ as

$$\Psi(t) = c_0(t)\mathbf{\Phi}_0 + \sum_\alpha c_\alpha(t)\mathbf{\Phi}_\alpha, \tag{2}$$

where $\mathbf{\Phi}_0$ is defined by a single Slater determinant as $\Phi_0(\mathbf{r}_1,\cdots,\mathbf{r}_n) = \|\phi_1\cdots\phi_a\cdots\phi_b\cdots\phi_n\|$ with $\phi_n \equiv \phi_n(\mathbf{r}_n)$. Here, ϕ_a and ϕ_b are the occupied orbitals, Φ_α is the electronic wave function for a single electron excited configuration $\alpha : a \to a'$, i.e., the single electron transition from the occupied molecular orbital (MO) a to the unoccupied MO a', when $\Phi_\alpha(\mathbf{r}_1,\cdots,\mathbf{r}_n) = \|\phi_1\cdots\phi_{a'}\cdots\phi_b\cdots\phi_n\|$.

The coherent and incoherent temporal behaviors of the electrons induced by a laser field $\mathbf{F}(t)$ can be obtained directly by solving the coupled electronic equations of motion expressed by the density matrix elements $\rho_{\alpha\beta}(t)$ under the initial population conditions $\rho_{00}(0) = 1$ and $\rho_{\alpha\alpha}(0) = 0$ for $\alpha \neq 0$ and $\rho_{\alpha\beta}(0) = 0$ for $\alpha \neq \beta$, that is, there is no electronic coherence at the initial time such that

$$\frac{d\rho_{\alpha\beta}(t)}{dt} = -\frac{i}{\hbar}\sum_\gamma\left(V_{\alpha\gamma}(t)\rho_{\gamma\beta}(t) - \rho_{\alpha\gamma}(t)V_{\gamma\beta}(t)\right) - \left(i\omega_{\alpha\beta} + \gamma_{\alpha\beta}\right)\rho_{\alpha\beta}(t). \tag{3}$$

Here, $\rho_{\alpha\beta}(t) \equiv c_\alpha(t)c_\beta^*(t)$ is the density matrix element, and $V_{\alpha\gamma}(t)$ is the coupling matrix element between states α and γ *via* the molecule-laser interaction $\hat{V}(t) = -\boldsymbol{\mu}\cdot\mathbf{F}(t)$, where $\boldsymbol{\mu}$ denotes the transition dipole moment operator, $\gamma_{\alpha\beta}\left(=\frac{1}{2}(\gamma_\alpha+\gamma_\beta) + \gamma^{(d)}{}_{\alpha\gamma}\right)$ are the dephasing constants in the Markov approximation [38, 39] and $\omega_{\beta\alpha}$is the frequency difference between the two electronic states α and β. Here, $\gamma_\alpha(\gamma_\beta)$ is the non-radiative transition rate constant of the electronic state $\alpha(\beta)$, and $\gamma^{(d)}{}_{\alpha\beta}$ are the pure dephasing constants induced by the elastic interaction between the heat bath and molecule of interest.

Because we are interested in the coherent behaviors of dipole-allowed quasi-degenerate π-electronic excited states in the visible or UV region of an aromatic ring molecule, **Eq. 1** can be rewritten in terms of singly excited configurations $\{\Phi_\kappa\}$ if $\kappa \neq 0$ as

$$\langle O(t)\rangle = n\int d^3\mathbf{r}_1\cdots d^3\mathbf{r}_n \mathrm{Tr}\left(\rho(t)O(r)\right), \tag{4}$$

where $O_{\alpha\beta}(r) = \langle\Phi_\alpha|\hat{O}(r)|\Phi_\beta\rangle$.

In **Eq. 4**, the coherence between singly excited state configurations is considered, and the coherence between the ground state and the excited state is neglected because this coherence is much shorter compared to that between the singly excited state configurations. In this case, the coherence time is proportional to the inverse of the energy gap between the two electronic states.

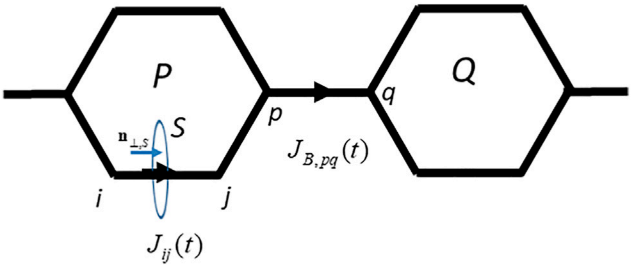

FIGURE 1 | The interatomic bond current $J_{ij}(t)$ and bridge bond current $J_{B,pq}(t)$ are depicted. Here, i and j indicate the positions of two atomic sites in the bond $C_i - C_j$, and each carbon atom C_p, or C_q belongs to a different aromatic ring P or Q, which are in neighbors.

The coherent π-electron angular momentum is formulated in the quantum chemical MO theory, and the π-orbital ϕ_k associated with the optical transition is expanded in terms of a linear combination of atomic orbitals χ_i as

$$\phi_k = \sum_i c_{k,i}\chi_i, \quad (k = a, a', b, b'), \tag{5}$$

where χ_i denotes the atomic orbital, and $c_{k,i}$ indicates the molecular orbital coefficient.

Equation 4 can be expressed by using the **Eq. 5** as

$$\langle\hat{O}(t)\rangle = 2n\sum_{\alpha<\beta}\mathrm{Im}\,\rho_{\beta\alpha}(t)\sum_{ij}\left(\delta_{ab}c^*_{a'i}c_{b'j} + \delta_{a'b'}c^*_{ai}c_{bj}\right)\int d^3r\chi_i^* i\hat{O}(r)\chi_j. \tag{6}$$

Here, the temporal behavior of the expectation value $\langle\hat{O}(t)\rangle$ can be expressed using the off-diagonal density matrix element $\rho_{\beta\alpha}(t)$. The suffixes (a, a') ((b, b')) corresponds to the electronic configurations $\alpha(\beta)$, respectively.

2.2 Coherent π-Electron Angular Momentum

Consider the spatially fixed aromatic ring molecule with N aromatic rings. The electron angular momentum operator is defined as $\hat{O}(\mathbf{r}) = \mathbf{l}_Z = \sum_K \hat{O}_K(\mathbf{r})$ with $\hat{O}_K(\mathbf{r}) = \mathbf{l}_{Z,K} = -i\hbar(x_K\partial/\partial y_K - y_K\partial/\partial x_K)\mathbf{n}_{\perp,K}$. Here $\mathbf{l}_{Z,K}$is the electronic angular momentum operator of the component perpendicular to ring K. Coordinates x_K and y_K are defined on the aromatic ring K, and $\mathbf{n}_{\perp,K}$ is the unit vector perpendicular to the aromatic ring. The expectation value of Kth angular momentum operator is given in terms of a $2p_z$ carbon atomic orbitals (AOs) as

$$\begin{aligned}\mathbf{l}_{Z,K}(t) &\equiv \int d^3r_K\langle\Psi(t)|\mathbf{l}_{Z,K}|\Psi(t)\rangle \\ &= -2n_e\hbar\,\mathbf{n}_{\perp,K}\sum_{\alpha<\beta}\mathrm{Im}\,\rho_{\beta\alpha}(t)\sum_{ij\in K}\left(\delta_{ab}c^*_{a'i}c_{b'j} + \delta_{a'b'}c^*_{ai}c_{bj}\right) \\ &\times\int d^3r\chi_i^*\left(x\frac{\partial}{\partial y} - y\frac{\partial}{\partial x}\right)\chi_j,\end{aligned} \tag{7}$$

where n_e is the total number of electrons in the system.

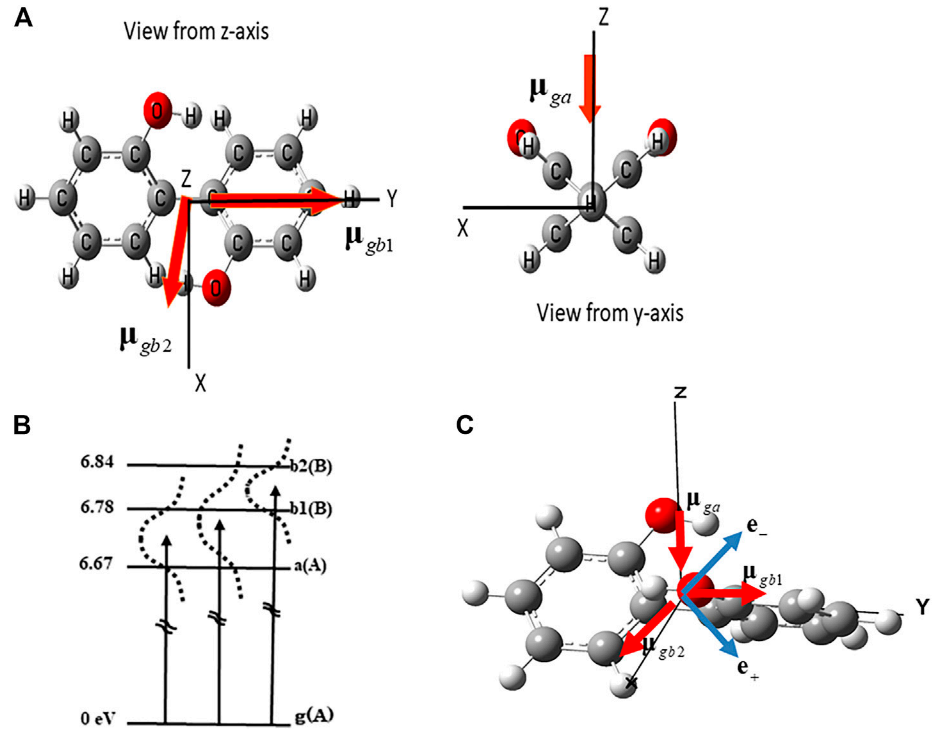

FIGURE 2 | (A) Geometrical structure of (*P*)-2,2'-biphenol belonging to point group C_2 and the transition dipole moments between the ground state (g) and three excited states *a*, b_1 and b_2. **(B)** Three electronic excited states and the dipole allowed transitions used to create the coherent electronic states. A and B are the irreducible representations of point group C_2. Dotted lines indicate the laser band widths that cover the superpositions of two electronic excited states (a b_1), (a b_2) and (b_1 b_2) respectively. **(C)** Linearly polarized unit vector of laser $\mathbf{e}_+$ ($\mathbf{e}_-$) used to generate the in-phase superposition (a+b_1) (out-of-phase superposition (a-b_1)).

Note that in **Eq. 7** the dependence of the electron angular momentum on the laser intensity is reflected in the imaginary part of the off-diagonal density matrices Im $\rho_{\beta\alpha}(t)$.

2.3 Coherent π-Electron Ring Current

From **Eq. 6**, the perpendicular component of the time-dependent electric current flowing through a surface *S* (*See* **Figure 1**) is generally defined as

$$\langle J(t)\rangle = 2n_e\sum_{\alpha<\beta}\mathrm{Im}\,\rho_{\beta\alpha}(t)\sum_{ij}\left(\delta_{ab}c^*_{a'i}c_{b'j}+\delta_{a'b'}c^*_{ai}c_{bj}\right)\int d^3r\chi^*_i\hat{J}(\mathbf{r})\chi_j. \tag{8}$$

Here $\hat{J}(\mathbf{r})=\frac{e\hbar}{2m_ei}(\overrightarrow{\nabla}-\overleftarrow{\nabla})$ is the current density operator. $\overrightarrow{\nabla}(\overleftarrow{\nabla})$ is the nabla operating on the atomic orbital on the right-hand side (left-hand side).

Equation 8 can be expressed as

$$\langle J(t)\rangle=\sum_{i<j}J_{ij}(t), \tag{9}$$

where

$$J_{ij}(t)=2n_e\sum_{\alpha<\beta}\mathrm{Im}\,\rho_{\beta\alpha}(t)\left(\delta_{ab}\left(c^*_{a'i}c_{b'j}-c^*_{b'i}c_{a'j}\right)+\delta_{a'b'}\left(c^*_{ai}c_{bj}-c^*_{bi}c_{aj}\right)\right)J_{ij}, \tag{10a}$$

with

$$J_{ij}=\int_S d^2r_\perp\chi^*_i\mathbf{n}_{\perp,S}\cdot\overrightarrow{\nabla}\chi_j, \tag{10b}$$

where $\mathbf{n}_{\perp,S}$ is a unit vector perpendicular to a surface *S*, which is given as $\mathbf{n}_{\perp,S}=\frac{\mathbf{r}_j-\mathbf{r}_i}{|\mathbf{r}_j-\mathbf{r}_i|}$, and the surface *S* is set at the center of the carbon bond C_i-C_j. The surface integrations in **Eqs. 8**, **10b** are carried out over the half-plane *S* (*see* **Figure 1**). Using Slater type AOs for $\{\chi_i\}$, J_{ij} in **Eq. 10b** can be expressed in analytical form [40].

We introduce the *bridge bond current* $J_{B,pq}(t)$ which is a specific case of an interatomic bond current, and is defined as the current bridging two aromatic rings *P* and *Q*, passing from the nearest neighbor carbon atom at site *p* to *q*. Here, each carbon atom C_p, or C_q belongs to a different aromatic ring *P* or *Q* which are in the neighbors. (*see* **Figure 1**).

The bridge bond current is given in terms of the interatomic current, $J_{pq}(t)$, as

$$J_{B,pq}(t)=-J_{pq}(t)\cos\theta_d. \tag{11}$$

Here, θ_d is the dihedral angle between the two rings *P* and *Q* [39].

We now define an averaged ring current along ring *K*, $J_K(t)$, which is defined by taking the average of all bond currents as

$$J_K(t)\equiv\frac{1}{n_K}\sum_{(i<j)\subset K}^{n_K}J_{ij}(t), \tag{12}$$

where n_K is the number of bonds in ring *K*.

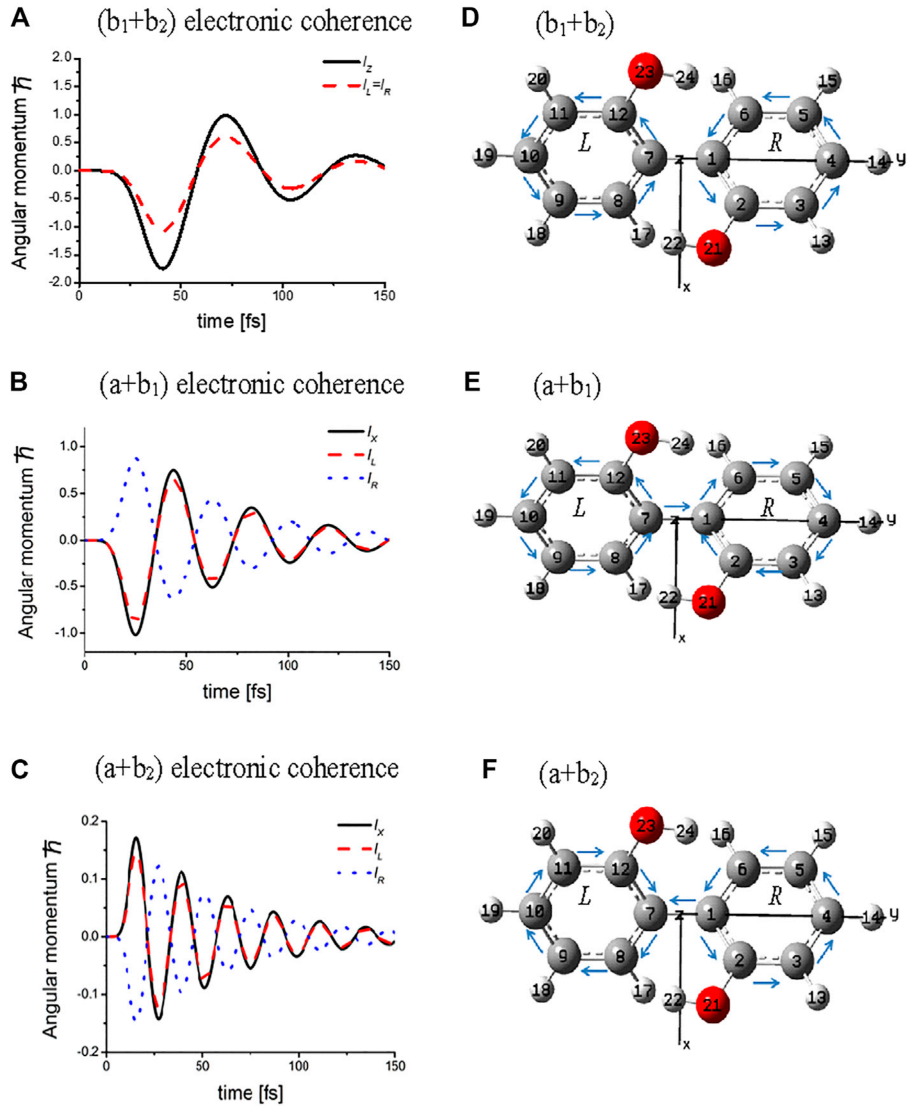

FIGURE 3 | Temporal behaviors of the coherent angular momenta, total values l_Z (l_X), and components, l_L (l_R) of *L* (*R*) ring for three types of the electronic coherence and the directions of the bond currents at the initial time: upper panel for ($b_1 + b_2$) electronic coherence excited by laser pulse with amplitude of 0.19 TW/cm^2; middle panel for ($a + b_1$) electronic coherence excited by laser pulse with amplitude of 0.83 TW/cm^2; lower panel for ($a + b_2$) electronic coherence excited by the laser pulse with amplitude of 3.32 TW/cm^2. The dephasing constants were set as $\gamma_{b1b2} = \gamma_{ab1} = \gamma_{ab2} = 0.01$ eV (~1/50 fs $^{-1}$). The arrows above the C – C bonds indicate the initial directions of the currents. Note that the bridge bond current $J_{1,7} = 0$ for the ($b_1 + b_2$) electronic coherence, while $J_{1,7} \neq 0$ for the ($a + b_1$) and ($a + b_2$) electronic coherences. Reprinted with permission from Ref. [39] Copyright (2013) American Institute of Physics.

2.4 Application to Nonplanar (*P*)-2,2'-biphenol

(*P*)-2,2'-biphenol is one of the typical nonplanar chiral aromatic ring molecules, which has two aromatic rings connected through the C-C bridge bond. For convenience, hereafter, we denote *L* (*R*) for the left- (right-) hand side phenol ring of (*P*)-2,2'-biphenol. **Figure 2A** exhibits the geometrical structure of (*P*)-2,2'-biphenol with the transition dipole moments vectors between the ground and excited states. (*P*)-2,2'-biphenol was assumed to be fixed on a surface by a non-conjugated chemical bond or was oriented in the space by the molecular orientation techniques by laser [44–46]. The laboratory-fixed *Y*-axis was set parallel to the single chemical bond bridging two phenol molecules, and the rotational axis of the molecule belonging to point group C_2 was set along the laboratory-fixed *Z*-axis which was parallel to the surface normal. The ground state geometry of (*P*)-2,2'-biphenol was optimized using the DFT-B3LYP level theory with the 6-31G+(d,p) basis set in the GAUSSIAN09 code [47]. The dihedral angle θ_d between the two phenol rings, was found to be 108.9° based on the density functional theory (DFT) calculations. The calculated geometrical structures are provided in Refs. [39, 40].

TABLE 1 | Angular momenta of the two phenol rings $l_L \equiv \mathbf{l}_L(t*) \cdot \mathbf{n}_L$ and $l_R \equiv \mathbf{l}_R(t*) \cdot \mathbf{n}_R$, and the resulting angular momenta l_X and l_Z at the maximum coherence time $t = t^{*1)}$.

	$l_L/\hbar$	$l_R/\hbar$	$l_X/\hbar$	$l_Z/\hbar$
$(a+b_1)$	–1.09	1.09	–1.27	0
$(a+b_2)$	0.17	–0.17	0.20	0
(b_1+b_2)	–1.44	–1.44	0	–2.34

1) The maximum coherence occurs at $\mathrm{Im}\,\rho_{b2,b1} = \mathrm{Im}\,\rho_{b1,a} = \mathrm{Im}\,\rho_{b2,a} = -1/2$.$l_X = 2l_L \cos\frac{\theta_d}{2} = 1.163 l_L = -1.163 l_R$ *for the* (a+b$_1$) *or* (a+b$_2$) *electronic coherences;* $l_Z = 2l_L \sin\frac{\theta_d}{2} = 1.627 l_L = 1.627 l_R$ *for the* (b$_1$+b$_2$) *electronic coherence with dihedral angle* θ_d (= 108.9°) *between the two phenol rings. Reprinted with permission from Ref. [39] Copyright (2013) American Institute of Physics.*

To create the coherent angular momenta and ring currents in (*P*)-2,2'-biphenol, we focused on the three dipole-allowed electronic excited states (a, b_1, and b_2) as shown in **Figure 2B**. The transition energies from the ground (g) to the a, b_1, and b_2 states, which were calculated under the optimized ground state geometry using the TD-DFT B3LYP level of theory [39, 40] were 6.67, 6.78, and 6.84 eV, respectively.

2.4.1 Generation of Two-state Electronic Coherence Using Linearly Polarized UV Pulses

For a creation of the coherent angular momentum and ring current using linearly polarized laser pulses, it is essential to prepare for an electronic coherence with a fixed relative phase between two electronic states, a and b_1, i.e., in-phase $(a + b_1)$ or out-of-phase $(a - b_1)$. The principle behind the preparation of the electronic coherence $(a + b_1)$ $((a - b_1))$ using a linearly polarized laser with polarization unit vector $\mathbf{e}_+$ ($\mathbf{e}_-$) is schematically demonstrated in **Figure 2C** [39, 40].

In the frame work of the three-excited state model, there are three types of two-electronic coherent states represented as $b_1 \pm b_2$, $a \pm b_1$ and $a \pm b_2$, respectively. At the initial time each electronic coherence can be generated by applying a linearly polarized UV laser with a properly selected laser polarized direction. Because of the non-planar geometry of the molecule, the angular momentum is two-dimensional, and the two ring currents flow are on the two different planes, the direction of total angular momentum is dependent on the symmetry of the coherent state created by the laser: The Z-directional angular momentum (ring current) is generated for the created coherent state with the A-irreducible representation of the C_2 point group, while the X-directional angular momentum (ring current) is generated for the coherent state with B.

It is remarkable that even though the third excited state is located between the two excited states in the three-excited states system, the coherent electronic state can still be created if the applied linearly polarized lasers satisfy the following conditions. For example, for the $(a \pm b_2)$ electronic coherence, the conditions for the linearly polarized lasers with polarization vectors $\mathbf{e}_\pm$ are given as

$$\boldsymbol{\mu}_{ga} \cdot \mathbf{e}_\pm = \pm \boldsymbol{\mu}_{gb2} \cdot \mathbf{e}_\pm \text{ and } \boldsymbol{\mu}_{gb1} \cdot \mathbf{e}_\pm = 0, \tag{13}$$

or equivalently,

$$\mathbf{e}_\pm = \boldsymbol{\mu}_{gb1} \times \left(\boldsymbol{\mu}_{gb2} \mp \boldsymbol{\mu}_{ga}\right) \Big/ \left|\boldsymbol{\mu}_{gb1} \times \left(\boldsymbol{\mu}_{gb2} \mp \boldsymbol{\mu}_{ga}\right)\right|. \tag{14}$$

Thus, if the laser overlaps the electronic states a, b_1, and b_2, the $(a + b_2)$ or $(a - b_2)$ electronic coherent state can be created selectively.

2.4.2 Coherent Angular Momentum Quantum Beats and Bond Currents

Figure 3 exhibits the temporal behaviors of the angular momenta calculated for three types of electronic coherences, (b_1+b_2), $(a + b_1)$ and $(a + b_2)$, each of which is created by a linearly polarized UV laser pulse with a properly selected polarization direction of laser. For the (b_1+b_2) electronic coherence, the total angular momentum parallel to the Z-axis, l_Z, is created together with two ring components $l_L = l_R$, whereas for both the $(a + b_1)$ and $(a + b_2)$ electronic coherences, the total angular momenta parallel to the X-axis, l_X, are generated with $l_L = -l_R$, with a π-phase shift. Similarly, for out-of-phase electronic coherences, $(b_1 - b_2)$, $(a - b_1)$ and $(a - b_2)$, the angular momentum can be given by the corresponding in-phase electronic coherence with a π-phase shift. The simple sinusoidal temporal behavior originates from the coherence of two electronic states with the oscillation period corresponding to a frequency difference between the two-electronic states. This is referred to as the angular momentum quantum beats, which are similar to the fluorescence quantum beats which originate from the vibronic coherence [48]. We note that π-electrons rotate a few times in a unidirectional manner within a half cycle of the oscillation. This unidirectional π-electron rotation can produce a unidirectional ring current and corresponding current-induced magnetic flux. In principle, this enables the design of ultrafast switching devices which consist of organic aromatic ring molecules.

The angular momenta $l_Z(t)$ and $l_X(t)$, shown in **Figure 3**, are obtained by the summation of the angular momenta created in the L and R aromatic rings $\mathbf{l}_L(t)$ and $\mathbf{l}_R(t)$ using the following relationship $l_Z(t) = 2\mathbf{l}_L(t) \cdot \mathbf{e}_Z \sin\frac{\theta_d}{2}$ with $\mathbf{l}_L(t) \cdot \mathbf{e}_Z = \mathbf{l}_R(t) \cdot \mathbf{e}_Z$, and $l_X(t) = 2\mathbf{l}_L(t) \cdot \mathbf{e}_X \cos\frac{\theta_d}{2}$ (where $\mathbf{l}_L(t) \cdot \mathbf{e}_X = -\mathbf{l}_R(t) \cdot \mathbf{e}_X$). **Table 1** lists the angular momenta of (*P*)-2,2'-biphenol with the dihedral angle $\theta_d = 108.9°$ where the electronic coherence is maximum at time $t = t*$, i.e., when the magnitude of the imaginary part of the density matrix element is maximized ($\mathrm{Im}\,\rho_{\alpha\beta}(t*) = -\frac{1}{2}$) and dephasing effects are neglected. This results in $l_X(t*) > 0$ or $l_X(t*) < 0$ for the $(a + b_1)$ and $(a + b_2)$ electronic coherences, respectively, and in $l_Z(t*) < 0$ for the $(b_1 + b_2)$ electronic coherence.

The magnitudes of the bond current, J_{ij} calculated at the maximum coherence time, are presented in detail in [40]. The magnitudes of the averaged ring current over the C-C bonds at the maximum coherence time, $\bar{J}$ are on the order of tens of μA, i.e., $\bar{J}$ = 161, 86.5 and 63.4 μA for $(b_1 + b_2)$, $(a + b_1)$, and $(a + b_2)$ coherences, respectively.

Effects of dephasings on coherent π-electron angular momentum and ring currents were treated in the Markov approximation, and time-independent dephasing constants were used under the assumption of instantaneous interactions between the system and phonon baths. In a system such as condensed phases, the Markov approximation is broken down. Non-Markov

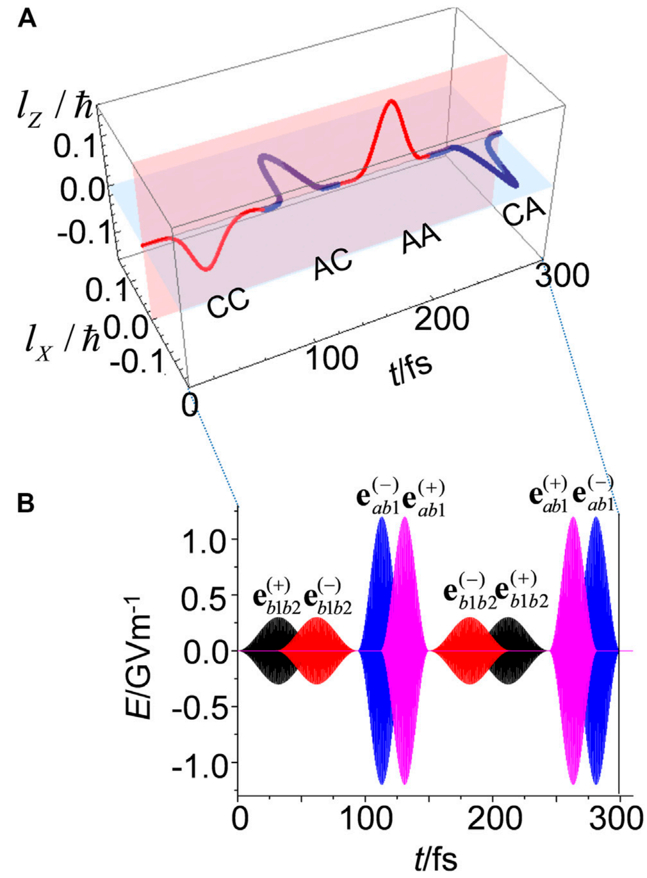

FIGURE 4 | (A) Sequential four-step quantum switching of π-electron rotations in (*P*)-2,2'-biphenol. **(B)** The sequential overlapped pump and dump laser pulses. Reprinted with permission from Ref. [40] Copyright (2012) American Chemical Society.

response of coherent should be essential. Time evolution of coherent ring currents were calculated in a hierarchical master equation approach beyond the Markov approximation has been treated [49].

2.4.3 Ultrafast Quantum Switching of Angular Momentum

Consider the quantum control of π-electron rotations for two-dimensional angular momentum switching based on the results shown in **Table 1**. Here, two-dimensional quantum switching is defined as a sequential pulse of the electronic angular momentum with its constant sign (positive or negative) along the *Z*- or *X*-axis. Note that any quantum switching step should be completed before the reverse rotation of the π-electrons begins, because it may otherwise disturb the signal. Consider a sequential four-step control, which is expressed as $l_Z(-) \rightarrow l_X(+) \rightarrow l_Z(+) \rightarrow l_X(-)$. This indicates the switching of rotational patterns in the order CC → AC → AA → CA, where the symbol C (A) means clockwise (anti-clockwise) direction, and for example, CA rotation means clockwise and anti-clockwise rotations along the phenol rings *L* and *R*, respectively. Here, $l_X(+)$ $(l_Z(-))$ means the π-electron angular momentum along the *X*- (*Z*-) axis with a positive (negative) sign, i.e., anti-clockwise (clockwise) rotation of π-electrons around the corresponding axis.

Figure 4A presents a 3D plot of the angular momentum as it switches based on the sequential four-step control scheme. From **Figure 4A**, we can see that the π-electron rotations are successfully manipulated by the pulses depicted in **Figure 4B**. That is, both the rotational axis parallel to the Z- or X-axis and the rotational directions around those axes, clockwise or anti-clockwise, are manipulated by the sequential four-step process. In **Figure 4B**, each switching step of control was performed using pump and dump pulses with specific polarization directions and phases. The laser pulse with an amplitude of 1.2 GV/m ($= 1.9 \times 10^{11}$ W/cm^2) was used in the second and fourth steps. The dynamic Stark shifts between electronic states a, b_1 and b_2 were on the order of 0.01 eV [39], indicating that the Stark effects could be omitted in **Figure 4A**.

The pulses shown in **Figure 4B** have two features. The first feature is that the pump (dump) pulse for each step has polarizations, $\mathbf{e}_{\alpha\beta}^{(-)}(\mathbf{e}_{\alpha\beta}^{(+)})$ or $\mathbf{e}_{\alpha\beta}^{(+)}$ $(\mathbf{e}_{\alpha\beta}^{(-)})$. Each pulse has an energy width that is large enough to coherently excite two quasi-degenerate electronic excited states, as shown in **Figure 2**. The second feature is that the pump and dump laser pulses partially overlap. In the creation of the CC rotation, for example, the electric field of the pump pulse was $\boldsymbol{E}^{(+)}_{b1b2}(t) = \boldsymbol{e}^{(+)}_{b1b2}E^{0}_{b1b2}\sin^2(\pi t/T_{b1b2})\sin(\omega_{c,b1b2}t)$, while the electric field of the dump pulse was $\boldsymbol{E}^{(-)}_{b1b2}(t) = \boldsymbol{e}^{(-)}_{b1b2}E^{0}_{b1b2}\sin^2(\pi(t - t^{pd}_{b1b2})/T_{b1b2})\sin(\omega_{c,b1b2}t + \pi/2)$. Here, T_{b1b2} (= 60.9 fs) indicates the oscillation period between b_1 and b_2 states, E^{0}_{b1b2} is the amplitude of the laser pulse, $\omega_{c,b1b2}$ is the central frequency between the two excited states b_1 and b_2; and t^{pd}_{b1b2} (the time interval between the pump and dump laser pulses) was set to $T_{b1b2}/2$ (Supporting information in Ref. [39]). The angle between the two polarization vectors, $\mathbf{e}^{(+)}_{b1b2}$ and $\mathbf{e}^{(-)}_{b1b2}$, was 113.5°.

With respect to ultrafast quantum switching, it is crucial to create the overlap of the pump and dump pulses, where the resulting electric field rotates as an elliptically polarized electric field in the overlapped time domain, and the dump laser pulse reverse the rotation that occurs during this region. As a result, the angular momentum of the π-electrons is nullified.

2.4.4 Coherent Ring Current-Induced Magnetic Field

There have been interesting reports on the evaluation of the magnetic fields of atoms and oriented heteronuclear diatomic molecules, AlCl and BeO [32, 50, 51]. Strong and unidirectional magnetic fields are generated from the degenerate electronic states of these atoms and molecules excited by circularly polarized intense laser pulses. We estimated the magnetic fields (magnetic field flux density) generated by the coherent ring currents of (*P*)-2,2'-biphenol. The results may provide fundamental information for designing ultrafast switching devices controlled by current-induced magnetic fields as well as coherent ring currents [52–54].

As an example, consider the magnetic field induced by the ring current for the $(b_1 + b_2)$ electronic coherence. In **Figure 5**, $B_K(t*, h)$ represents the current-induced magnetic field along the central axis perpendicular to ring K (L or R) as a function of the height h above the Z-axis at $t = t*$ under the maximum coherence condition (when $\text{Im}\,\rho_{b_1b_2}(t*) = -1/2$). An expression for the magnetic field $B_K(t*, h)$ was derived by taking into account the interatomic bond currents with the $2p_z$ Slater AOs [40]. Note that $B_L(t*, h) = B_R(t*, h)$ for the $(b_1 + b_2)$ electronic coherence (**Table 1**). It is interesting to compare the behaviors of $B_K(t*, h)$ with those calculated using

$$B^{SRL}_K(t, h) = \frac{\mu_0 J_K(t)}{2r}\sin^3\eta, \tag{15}$$

which was derived using a simple ring loop (SRL) model. Here, $\mu_0 = 4\pi \cdot 10^{-7}\,[\mathrm{W}_b/(\mathrm{A}\cdot\mathrm{m})]$ is the magnetic constant, $r\ (= r_{ij})$ is the ring radius, and $\eta\ (= \sin^{-1}(r/\sqrt{r^2 + h^2}))$ is defined as the angle between the Z-axis and a straight line depicted from the point on ring K that crosses the Z-axis. $B_K(t, 0)$ at $\eta = \pi/2$ is the magnetic field measured at the center of ring K. The magnitude of $B_K(t^*, 0)$ induced by $J_K(t^*) = 100\,\mu\mathrm{A}$ is 448 mT at the center of the ring K with $r =$ 0.14 nm. It can be found from **Figure 5** that the magnitudes of $B^{SRL}_K(t^*, h)$ are overestimated near the aromatic ring plane $0 \leq h < 1$ Å, while the magnitudes are reasonable for $h > 1$ Å, although slightly different results can be observed between the two magnetic fields for large values of h. At the center of the aromatic ring, $B_K(t^*, h = 0) = 0.66B^{SRL}_K(t^*, h = 0)$. This can be understood from the result that the π-electron current density is densely distributed over the aromatic ring. A subtle difference between $B^{SRL}_K(t*, h)$and $B_K(t*, h)$ is observed for large h, although both magnetic fields $B^{SRL}_K(t*, h \to \infty) = 0$ and $B_K(t*, h \to \infty) = 0$ approach zero. This deviation originates from the approximation that the aromatic ring is not a considered to be a perfect ring.

It is necessary to check whether the value of $B_K(t, 0)$ is larger than the one corresponding to the magnetic field B_{Laser} induced by the applied laser field F when the induced magnetic fields are created during an ultrasfast laser pulse excitation at the early time regime. The magnitude of magnetic field B_{Laser} can be estimated from a simple formula $|B_{\mathrm{Laser}}| = |F|/c$ with $c = 3.0 \times 10^8\,\mathrm{ms}^{-1}$. The calculated magnitude of magnetic field B_{Laser} with $|F| = 1.0$ GV/m is approximately $7.4B_K(t*, h)$, which is on the same order as the field induced by the ring current $J = 100\,\mu\mathrm{A}$. This implies that we need a careful examination to observe the current-induced magnetic flux, or to use the electro-magnetic device as a switching control tool.

Thus far, we have taken into account the ring current-induced magnetic fields of the low-symmetry aromatic ring molecule (*P*)-2,2'-biphenol, in which nondegenerate two electronic excited states are coherently excited by the linearly polarized UV lasers. Here we briefly discuss the ring current-induced magnetic field for the *degenerate* electronic excited states of an aromatic molecule induced by the intense *circularly polarized* UV laser pulse. Yuan and Bandrauk [2, 33] have numerically demonstrated that the circularly polarized ultrashort pulses are generated from the molecular high-order harmonic generation using the intense linearly and circularly polarized laser pulses. This indicates a possibility for the ultrashort circularly polarized UV laser pulses to create the ring current-induced magnetic fields in high symmetric aromatic ring molecules. We can estimate the magnitude of the ring current-induced magnetic field of benzene within the SRL model using **Eq. 15**. Here, $J(t)$ is the electric ring current of the degenerated electronic state. The electronic spectrum of benzene is characterized by the dipole-allowed transition from the ground state to the third singlet electronic excited state ($^1\mathrm{E}_{1u}$). For an equal population between the two states at $t = t*$, $B^{SRL}(t*, 0) = 874\,\mathrm{mT}$ is obtained using the maximum value of the coherent ring current $J(t*) = 195\,\mu\mathrm{A}$ evaluated under the π-electron approximation [40, 55]. For comparison, we obtained $B^{SRL}_K(t*, 0) = 874\,\mathrm{mT}$ and $B_K(t*, 0) = 579\,\mathrm{mT}$when $J(t*) = 195\,\mu\mathrm{A}$for (*P*)-2,2'-biphenol. Note that the same magnitudes of the induced magnetic field $B^{SRL}_K(t*, 0)$ for (*P*)-2,2'-biphenol and $B^{SRL}(t*, 0) = 874\,\mathrm{mT}$ for benzene were obtained in the SRL model because the two parameters in the SRL model, the radius of the ring r, and the ring current $J(t^*)$ have the same values for both types of ring molecules. The same tendency in the magnitudes between $B^{SRL}_K(t^*, 0)$ and $B_K(t^*, 0)$ is also observed for benzene.

3 CURRENT LOCALIZATION IN POLYCYCLIC AROMATIC HYDROCARBONS

In this section we consider a localization of coherent ring current in polyatomic aromatic hydrocarbons (PAH) [41, 42]. There exist

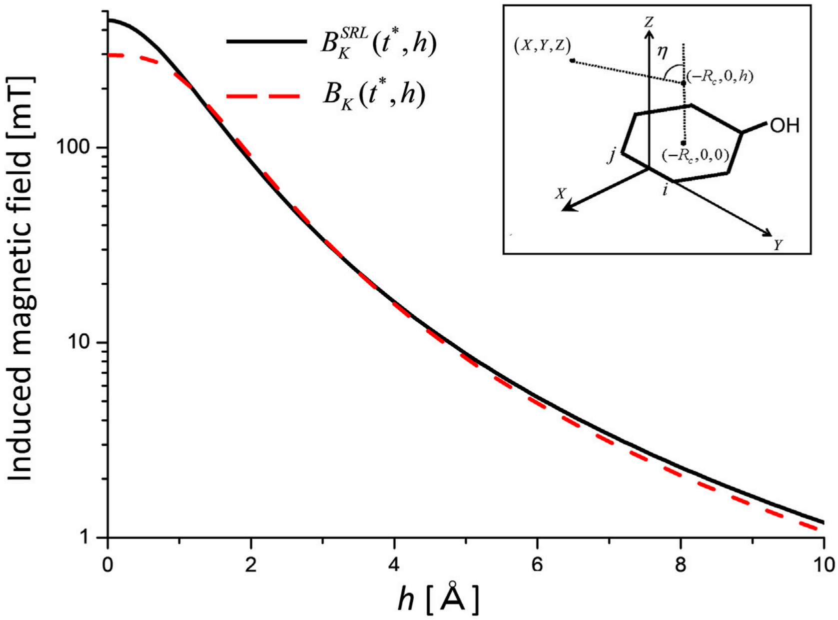

FIGURE 5 | Induced magnetic fields for the $(b_1 + b_2)$ electronic coherence as a function of height h measured from the center of aromatic ring K at the maximum coherence time $t = t*$. $B_K^{SRL}(t*,h)$ and $B_K(t*,h)$ represent the induced magnetic field calculated by a simple ring loop model, and the field calculated by the expression that explicitly takes into account the coherent ring currents, respectively. The inset panel defines the coordinate system for height h and angle η. R_c denotes the center of the phenol ring.

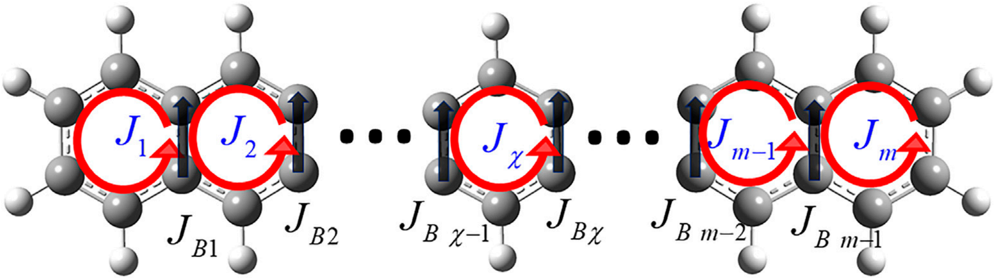

FIGURE 6 | π-Electron ring currents J_l and bridge bond currents $J_{Bl'}$ $(1 \le l \le m,\ 1 \le l' \le m - 1)$ in a linear planar polycyclic aromatic hydrocarbon (PAH). J_χ refers to the π-electron ring current localized on aromatic ring χ.

various current localization patterns in PAH simply because of their geometrical structures consisting of many benzene units. Quantum optimal control method is a general and reliable one to choose a desired current localization pattern from the various patterns using control lasers. The quantum control method has successfully been applied to manipulation of molecules such as coherent control of chemical reactions [56, 57]. After a brief introduction of quantum optimal control method [41, 42, 58], we demonstrate how the target state is set up for the designated ring current using the Lagrange multiplier method. Here, the π-electron ring current is expressed in terms of the interatomic bond currents between two adjoining C–C atoms. At final, the target states are derived for the two types of current localization: the localized ring current, which indicates that the ring current is localized to the designated aromatic ring in linear PAH, and the perimeter ring current in linear PAH [41, 42].

3.1 Quantum Optimal Control Approach

The objective functional to be maximized, is defined as [59–61].

$$J[\mathbf{F}] = \left\langle \Psi(T) \middle| \hat{O}_T \middle| \Psi(T) \right\rangle - \alpha_0 \int_0^T dt\,(\mathbf{F}(t))^2$$
$$-2\,\mathrm{Im}\left[\int_0^T dt \left\langle \xi(t) \middle| i\hbar\frac{\partial}{\partial t} - \left(H_0 - \boldsymbol{\mu}\cdot\mathbf{F}(t)\right) \middle| \Psi(t) \right\rangle \right], \quad (16)$$

where H_0 is a Hamiltonian in absence of field, and $\Psi(t)$ is the time-dependent wave function in the electric field $\mathbf{F}(t)$. Here, the target operator $\widehat{O}_T$ is expressed as $\widehat{O}_T = |\Psi_T > < \Psi_T|$, where Ψ_T is the target state wave function at the final time T, defined as $\Psi_T = \sum_a c_a(T)\Phi_a$, and is equal to $\Psi(T)$ under the optimal condition, $\widehat{O}_T = |\sum_a c_a(T)\Phi_a\rangle\langle\sum_b c_b(T)\Phi_b|$. The penalty factor α_0 is introduced to suppress the magnitude of the electric field $\mathbf{F}(t)$. $\xi(t)$is the time-dependent Lagrange multiplier. The third term in **Eq. 16** is added to decouple the boundary conditions of the equations for $\Psi(t)$ and $\xi(t)$ as indicated in **Eq. 17.** Taking the variational condition $\delta J[\mathbf{F}] = 0$, the following coupled equations are obtained,

$$i\hbar\frac{\partial}{\partial t}\Psi(t) = (H_0 - \boldsymbol{\mu}\cdot\mathbf{F}(t))\Psi(t), \tag{17a}$$

$$i\hbar\frac{\partial}{\partial t}\xi(t) = (H_0 - \boldsymbol{\mu}\cdot\mathbf{F}(t))\xi(t), \tag{17b}$$

where

$$\mathbf{F}(t) = -\frac{1}{\alpha_0}\mathrm{Im}\langle\xi(t)|\boldsymbol{\mu}|\Psi(t)\rangle. \tag{17c}$$

Here, $\Psi(t)$ satisfies the initial condition $\Psi(0) = \Phi_0$, and $\xi(T)$ satisfies the condition, $\xi(T) = \widehat{O}_T\Psi(T)$ at final time T. Note that by solving **Eq. 17**, we obtain the optimal solution $\Psi(T)$, which is equal to Ψ_T.

3.2 Setup of Target Operators

Consider the ring current localization to a designated ring χ in a PAH, as shown in **Figure 6**. From **Eqs. 10a**, **12**, the ring current on ring κ at the target time T is expressed as

$$\begin{aligned} J_\kappa(T) &\equiv \frac{1}{n_\kappa}\sum_{\alpha=1}^{n}\sum_{\beta=1}^{n}\sum_{(i<j)\subset\kappa}^{n_\kappa} J_{ij,\alpha\beta}(T) \\ &= \sum_{\alpha=1}^{n}\sum_{\beta=1}^{n} J_{\kappa,\alpha\beta}\mathrm{Im}\left(c_\alpha(T)c_\beta^*(T)\right) \\ &= J_\kappa(c_1, c_2, \cdots c_n),\ (1 \le \kappa \le m) \end{aligned} \tag{18a}$$

with $c_i \equiv c_i(T)$, and

$$J_{\kappa,\alpha\beta} = \frac{2n_e e\hbar}{m_e}\sum_{(i<j)\subset\kappa}^{n_\kappa}\left\{\left(\delta_{ab}\left(c_{a'i}^* c_{b'j} - c_{b'i}^* c_{a'j}\right) + \delta_{a'b'}\left(c_{ai}^* c_{bj} - c_{bi}^* c_{aj}\right)\right)J_{ij}\right\}. \tag{18b}$$

Here, n is the number of electronic excited states. Hereafter, we write $c_\alpha(T)$ as c_α for simplicity.

The target state $\Psi_T = \sum_\alpha c_\alpha\Phi_\alpha$ can be determined by applying the Lagrange multiplier method to the ring currents at the target time T in **Eq. 18a**, which provides the coupled equations in terms of the configuration interaction coefficients with $\{\mathrm{Re}c_\alpha, \mathrm{Im}c_\alpha\}$. The target operator is given as $\widehat{O}_T = |\Psi_T > < \Psi_T|$.

The coupled equations for the ring current localization to aromatic ring χ can be expressed as

$$\sum_{\beta=1}^{n} J_{\chi,\beta\alpha}\,\mathrm{Im}c_\beta + \sum_{\kappa\ne\chi}^{m}\sum_{\beta=1}^{n}\lambda_\kappa J_{\kappa,\beta\alpha}\,\mathrm{Im}c_\beta + \lambda_\chi\mathrm{Re}c_\alpha = 0,\ (1 \le \alpha \le n) \tag{19a}$$

$$-\sum_{\beta=1}^{n} J_{\chi,\beta\alpha}\mathrm{Re}c_\beta - \sum_{\kappa\ne\chi}^{m}\sum_{\beta=1}^{n}\lambda_\kappa J_{\kappa,\beta\alpha}\,\mathrm{Re}c_\beta + \lambda_\chi\mathrm{Im}c_\alpha = 0,\ (1 \le \alpha \le n) \tag{19b}$$

$$\sum_{\alpha=1}^{n}\left((\mathrm{Re}c_\alpha)^2 + (\mathrm{Im}c_\alpha)^2\right) - 1 = 0, \tag{19c}$$

and

$$\sum_{\beta=1}^{n}\sum_{\alpha=1}^{n} J_{\kappa,\alpha\beta}\left(\mathrm{Im}c_\alpha\mathrm{Re}c_\beta - \mathrm{Re}c_\alpha\mathrm{Im}c_\beta\right) = 0\,. \tag{19d}$$

A brief derivation of **Eq. 19** is summarized in **Appendix A**.

The coefficients $\{\mathrm{Re}c_\alpha, \mathrm{Im}c_\alpha\}$with λ_l included are numerically determined by applying the Newton-Raphson method to the coupled equations in **Eq. 19**. The target operator for the localization is obtained as $\widehat{O}_T = |\sum_\alpha c_\alpha\Phi_\alpha\rangle\langle\sum_\beta c_\beta\Phi_\beta|$.

Now consider the bridge bond currents $J_{Bl'}$ shown in **Figure 6**, and the perimeter ring current of a PAH with m aromatic rings, $J_P \equiv \frac{1}{m}\sum_{l=1}^{m} J_l$, which is defined as the average of the π-electron ring currents at each aromatic ring site. For the perimeter ring current, the bridge bond currents $J_{Bl'}(1 \le l' \le m-1)$ flowing among the nearest neighbor aromatic rings, should be zero at the target time. The target operators for the bridge bond currents, $J_{Bl'}(1 \le l' \le m-1)$, and perimeter ring current, J_P, can be derived from **Eq. 19** by replacing $J_{\kappa,\beta\alpha}$ with $J_{Bl',\beta\alpha}$ and $J_{P,\beta\alpha}$, respectively, because $J_{Bl'}$ and J_P can be written in terms of $\{\mathrm{Re}c_\alpha, \mathrm{Im}c_\alpha\}$ as

$$J_P = \sum_{\beta=1}^{n}\sum_{\alpha=1}^{n} J_{P,\alpha\beta}\left(\mathrm{Im}\,c_\alpha\,\mathrm{Re}c_\beta - \mathrm{Re}c_\alpha\,\mathrm{Im}\,c_\beta\right), \tag{20a}$$

and

$$J_{Bl'} = \sum_{\beta=1}^{n}\sum_{\alpha=1}^{n} J_{Bl',\alpha\beta}\left(\mathrm{Im}\,c_\alpha\,\mathrm{Re}c_\beta - \mathrm{Re}c_\alpha\,\mathrm{Im}\,c_\beta\right), \tag{20b}$$

respectively.

Similar to **Eq. 19**, the coupled equations for the perimeter ring current are derived in **Appendix B**.

3.3 Application of Current Localization Control to Anthracene

We applied the quantum optimal control (QOC) method described in the preceding section to anthracene, one of the smallest PAHs [42]. Anthracene (D_{2h}) was assumed to be fixed on a surface (the XY plane), or oriented spatially by lasers The molecular geometry was optimized in the MP2/6-311+g(d,p) level theory using the GAUSSIAN09 code [47]. As demonstrated in **Figure 7A**, anthracene consists of three aromatic rings, which are called *L*-, *M*-, and *R*- rings respectively.

Consider the two types of π-electron localized ring currents of anthracene: the perimeter current flowing along the outside chemical bonds of anthracene, and the middle ring current localized to the *M*-ring. Both types of localized ring currents belong to the irreducible representation B_{1g} of the D_{2h} point group, which are symmetry-adapted. The excited states contributing to the two ring currents need to belong to the B_{3u} and B_{2u} representations, because each corresponding electronic coherence created by the two excited states belongs to the B_{1g} representation. The excited state for the localized ring

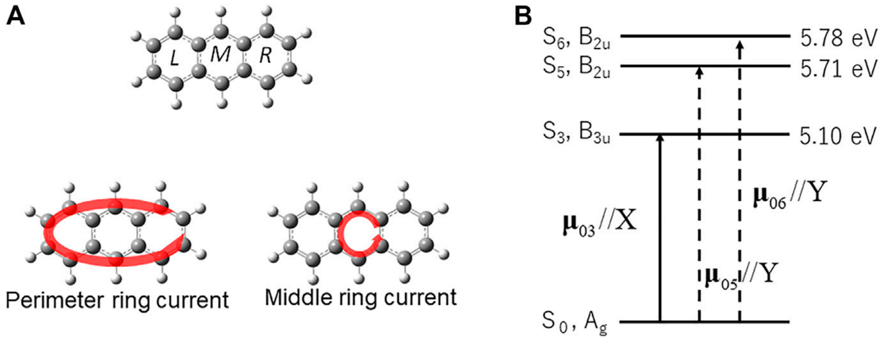

FIGURE 7 | (A) Symmetry-adapted ring currents (B_{1g}) in anthracene, perimeter ring current, and middle ring current. **(B)** The electronic excited states adapted for laser control of π-electron ring in anthracene (D_{2h}), and the non-zero transition dipole moments between the ground/excited-excited states. The solid (dashed) arrows represent the transition dipole moments which are parallel to the X (Y) axis.

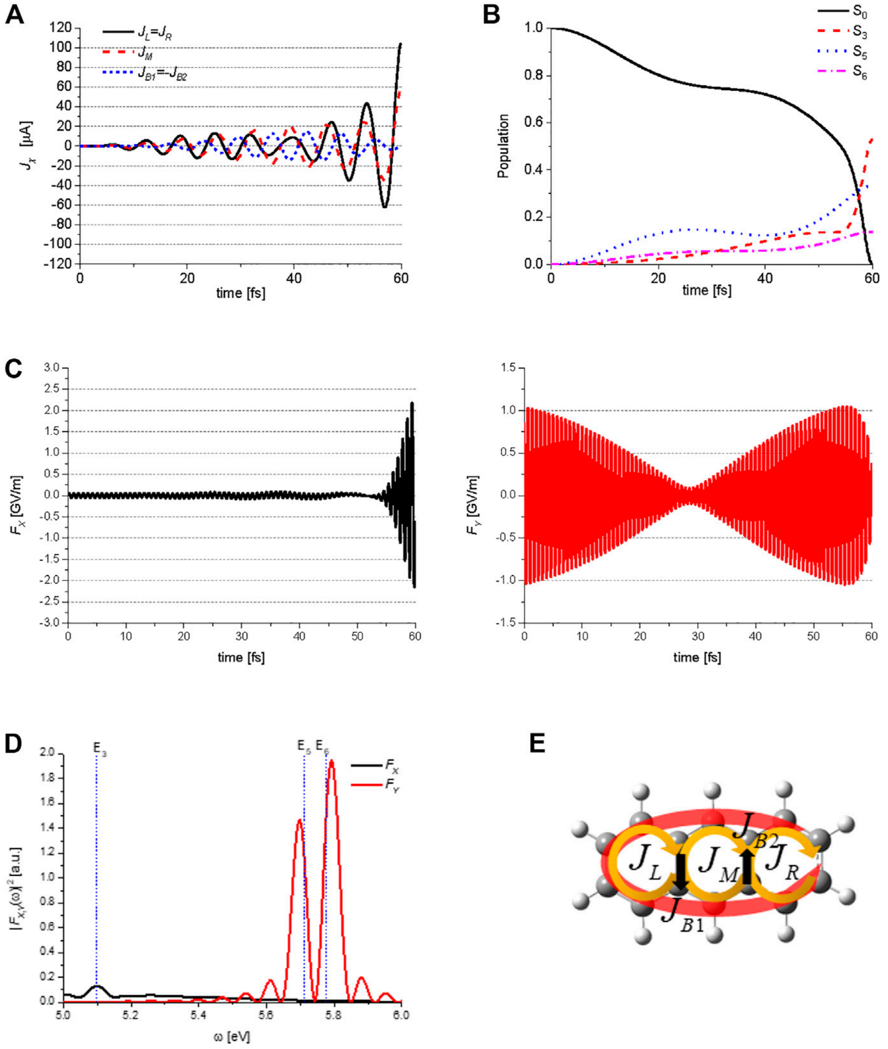

FIGURE 8 | Quantum optimal control simulations for generation of the perimeter ring current in anthracene: **(A)** temporal behavior of the three ring currents $J_L(t) = J_R(t)$ (solid line), $J_M(t)$ (broken line), and those of the two bridge bond currents $J_{B1}(t) = -J_{B2}(t)$ (dotted line); **(B)** temporal behavior of the population in S_0, and those in the three excited states: $S_3(B_{2u})$, $S_5(B_{2u})$, and $S_6(B_{2u})$; **(C)** optimized X- polarized laser pulse field $F_X(t)$ **(left-hand side)** and Y-polarized $F_Y(t)$ **(right-hand side)**; **(D)** Fourier transformed spectra of the two laser fields $F_X(\omega)$ and $F_Y(\omega)$; **(E)** five components of the perimeter ring current at an arbitrary time. Reprinted with permission from Ref. [40] Copyright (2012) American Chemical Society.

TABLE 2 | Matrix elements of the coherent π-electron ring currents for the three aromatic rings of anthracene, $J_{x,\alpha\beta}$(X = L, M, R), and those of the coherent bond currents shared by the two adjacent aromatic rings, $J_{Bi,\alpha\beta}$ (i = 1, 2) (*see* **Figure 8E**).

α	β	$J_{L,\alpha\beta}$ (μA)	$J_{M,\alpha\beta}$ (μA)	$J_{R,\alpha\beta}$ (μA)	$J_{B1,\alpha\beta}$ (μA)	$J_{B2,\alpha\beta}$ (μA)
S_3 (B_{3u})	S_5 (B_{2u})	82.2	80.8	82.2	–32.5	32.5
S_3 (B_{3u})	S_6 (B_{2u})	65.4	−18.0	65.4	49.0	–49.0

L (R) indicate the left (right)-hand side ring, M corresponds to the middle ring. Here a positive current denotes that the ring current flows (the π-electron rotates) in an anti-clockwise (clockwise) direction. Reprinted with permission from Ref. [42] Copyright (2017) American Institute of Physics.

current is S_3 with B_{3u} representation, and the other two excited states S_5 and S_6 with B_{2u} representation as shown in **Figure 7B**. This defines a "symmetry-adapted ring current" [41, 42].

The excited state energies in **Figure 7B** were calculated to be E_3 = 5.10 eV, E_5 = 5.71 eV, and E_6 = 5.78 eV. Here, S_4 (B_{3u}) with E_4 = 5.13 eV was excluded because the oscillator strength was negligibly small (f = 0.0013) in our numerical simulation. The non-zero transition dipole moments relevant to the coherent π-electron ring current control were calculated using the time-dependent density functional theory (TDDFT) method as, $\boldsymbol{\mu}_{S0,S3} = (-3.98, 0, 0)$, $\boldsymbol{\mu}_{S0,S5} = (0, -0.64, 0)$, and $\boldsymbol{\mu}_{S0,S6} = (0, -0.44, 0)$ (in a.u.) for the ground and excited states. The vapor absorption spectrum of anthracene shows the strongest absorption peak at 5.30 eV [62], which corresponds to E_3 = 5.10 eV in the TDDFT calculation.

Figure 8 shows the QOC results for the generation of an anti-clockwise perimeter ring current in anthracene. The target state is expressed from the results obtained using the Lagrange multiplier method as

$$\Psi_{\mathrm{AAA}} = 0.717i\Phi_{S3} + 0.581\Phi_{S5} + 0.385\Phi_{S6}. \tag{21}$$

Here, the subscripts specifying the target state, for example, ACA for Ψ_{ACA}, indicates the anti-clockwise ring currents in two aromatic rings, L and R, and a clockwise ring current in aromatic ring M. It should be noted that the target state for a generation of any coherent ring current is expressed in terms of its complex form. The control target time was set to T = 60 fs. The matrix elements of π-electron ring currents $J_{X,\alpha\beta}$ (X = L, M, R) and the bond current $J_{Bi,\alpha\beta}$ (i = 1, 2), for two excited states α, β are presented in **Table 2**. Here the π-electron ring current flowing in an anticlockwise direction is defined as positive, whereas the bond current flowing toward the Y direction is defined as positive (*See* **Figure 6**). **Figure 8A** shows the temporal evolutions of the coherent ring currents J_χ for the three aromatic rings of anthracene, χ = L, M, R, and those for $B1$ and $B2$. It can be observed from **Figure 8A** that the two bond currents $J_{B1,\alpha\beta}$ and $J_{B2,\alpha\beta}$ vanish at the target control time of T = 60 fs, and all ring currents in three aromatic rings exhibit positive. This indicates that the coherent π-electrons rotate clockwise along the outside (perimeter) of the aromatic ring. The laser-controlled π-electrons includes a ring current averaged over the three aromatic rings, $J_p \equiv (J_L + J_M + J_R)/3$ = 89.0 μA, which is the perimeter ring current.

Figure 8B shows the temporal behavior of the ground state S_0, and three excited states S_3 (B_{3u}), S_5 (B_{2u}), and S_6 (B_{2u}) populations during the QOC process, which are induced by the two control lasers. **Figure 8C** shows the X and Y-components of the electric field $\mathbf{F}(t)$ generated by the control lasers, and **Figure 8D** shows the Fourier transformed spectra $F_X(\omega)$ and $F_Y(\omega)$ in the ultraviolet (UV) frequency domain. By analyzing the temporal behavior of the electric field $\mathbf{F}(t)$ of the control lasers in **Figure 8C** and the Fourier transformed spectra of the control laser fields in **Figure 8D**, the mechanisms of the laser-controlled ring currents in anthracene can be clarified. It is evident that from the modulation in **Figure 8C** the two linearly (Y-) polarized lasers with a relative phase zero induce the electronic coherence between the two excited states S_5 (B_{2u}) and S_6 (B_{2u}), and that the linearly polarized laser pulse parallel to the X-axis creates the perimeter ring current on the molecular plane.

Thus far, we have considered the QOC procedure for generating an anti-clockwise perimeter current. The QOC procedure for generating a clockwise perimeter current can be carried out in the same manner as described above (*See* **Eq. 21**) by considering the target state,

$$\Psi_{\mathrm{CCC}} = \Psi^*_{\mathrm{AAA}} = -0.717i\Phi_{S3} + 0.581\Phi_{S5} + 0.385\Phi_{S6}. \tag{22}$$

We carry out the QOC procedure to generate the anticlockwise ring current localized to the middle ring of anthracene. The target state is expressed as

$$\Psi_{0A0} = 0.707\Phi_{S3} - 0.440i\Phi_{S5} + 0.553i\Phi_{S6}. \tag{23}$$

The target state for the middle ring current with the clockwise flow is given by the relationship $\Psi_{0C0} = \Psi^*_{0A0}$. **Figure 9** exhibits the QOC results, where **Figure 9A** displays the temporal evolutions of ring current localization control to the three aromatic rings, indicating that J_M is a ring current with 64.4 μA at the target control time of 60 fs, but on the other hand the ring currents J_L and J_R of the other two aromatic rings vanish. This indicates that the ring current localized to the middle aromatic ring is created by the control laser pulses presented in **Figures 9C,D**. The temporal behaviors of the populations shown in **Figure 9B** are nearly the same as those of the perimeter ring currents as shown in **Figure 8B**. As presented in **Figure 9C**, the two linearly (Y-) polarized lasers induce the electronic coherence between the two excited states S_5 and S_6 with a definite relative phase π, in contrast to the results presented in **Figure 8C**. In the mechanism of generation between the perimeter and the middle ring currents there is no difference except the phase difference between the two excited states S_5 and $S_{6,}$ because the temporal behavior in both **Figure 8B** and **Figure 9B** and the temporal behavior in the X-polarized laser pulse in both **Figure 8C** and **Figure 9C** are similar to each other.

Main difference between the temporal behaviors of the Y-polarized lasers in **Figure 8C** and **Figure 9C** can be explained briefly in the following. The two coherent states created by the Y-polarized lasers can be expressed as

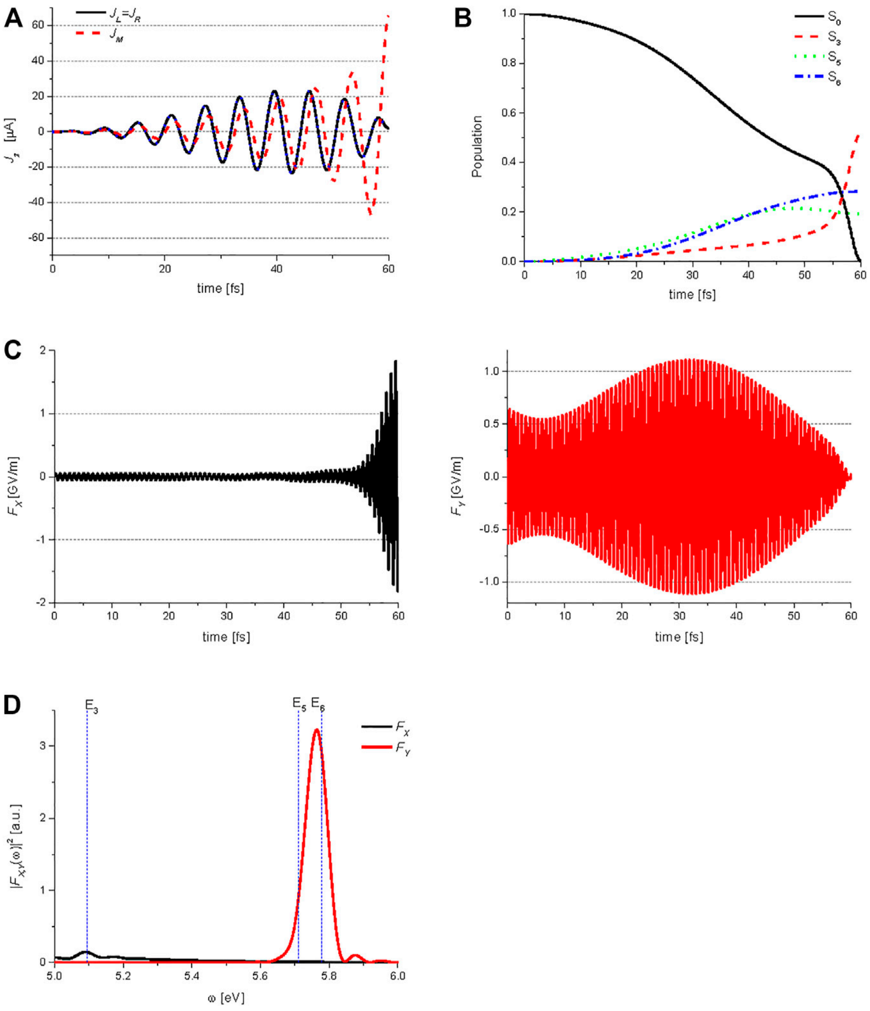

FIGURE 9 | Quantum optimal control simulations for generation of the middle ring current in anthracene: **(A)** temporal behavior of the ring currents $J_L(t) = J_R(t)$ (solid line) and $J_M(t)$ (broken line); **(B)** temporal behavior of the S_0 population and those of the three excited state $S_3(B_{2u})$, $S_5(B_{2u})$ and $S_6(B_{2u})$ populations; **(C)** optimized X- and Y-polarized laser pulse fields $F_X(t)$ **(left-hand side)** and $F_Y(t)$ **(right-hand side)**; **(D)** Fourier transformed spectra of the laser pulse fields $F_X(\omega)$ and $F_Y(\omega)$. Reprinted with permission from Ref. [42] Copyright (2017) American Institute of Physics.

$$F_+(t) = F_{S5}\, sin(\omega_{S5}t) + F_{S6}\, sin(\omega_{S6}t), \tag{24a}$$

and

$$F_-(t) = F_{S5}\, sin(\omega_{S5}t) - F_{S6}\, sin(\omega_{S6}t). \tag{24b}$$

For simplicity, the amplitudes of the two coherent states are assumed to have the same value, i.e., $F_{S5} = F_{S6} \equiv F_Y$. The above expressions can then be simplified to

$$F_+(t) = F_Y sin\left[\frac{(\omega_{S5} + \omega_{S6})t}{2}\right]\cos\left[\frac{(\omega_{S5} - \omega_{S6})t}{2}\right], \tag{25a}$$

and

$$F_-(t) = F_Y cos\left[\frac{(\omega_{S5} + \omega_{S6})t}{2}\right]\sin\left[\frac{(\omega_{S5} - \omega_{S6})t}{2}\right]. \tag{25b}$$

Here, the frequency difference $|\omega_{S5} - \omega_{S6}|/2$ yields an oscillation beating period of 120 fs, which is nearly the same as that of the quantum beat frequency observed in **Figure 8C** and **Figure 9C**.

Having clarified the control mechanism of the coherent ring current generation, we can semi-quantitatively reproduce the above results in **Figures 8**, **9** by using an analytical method [42]. This indicates, in principle, that two types of ring current localizations, the perimeter ring current and the middle ring current in linear PAHs, can be generated in experiment using three coherent UV lasers without a sophisticated QOC device.

For QOC numerical simulations of the ring current localization control in anthracene, we have only considered the perimeter and the middle ring currents generations, which are symmetry-adapted, while we did not consider a ring current localization to the L- or R-ring of anthracene, which are created by a symmetry-broken procedure, as demonstrated for naphthalene in Ref. [41]. That is, other excited state(s) with gerade symmetry must be considered in addition to the excited

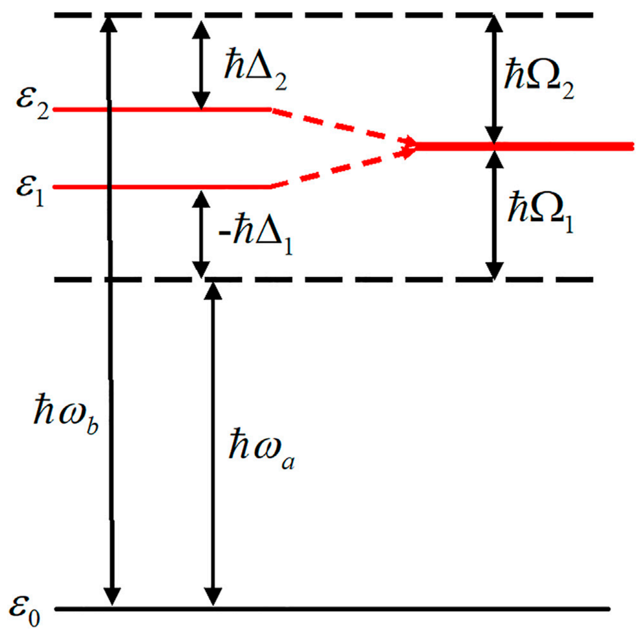

FIGURE 10 | Dynamic Stark-induced degenerate state with the Rabi frequencies (Ω_1 and Ω_2) using two stationary linearly-polarized lasers with the frequencies, ω_a and ω_b, and detuning frequencies Δ_1 andΔ_2 respectively.

states with ungerade symmetry as described in the previous subsection.

It is important to consider how to observe the ultrafast coherent ring currents in PAHs. We proposed a method to detect the direction of the atto-second coherent ring current by tracking the femtosecond molecular vibrational motions that can induce the nonadiabatic couplings [30]. Rodriguez and Mukamel [63] have proposed measuring the circular dichroism (CD) of the ring current using the pump-probe method. Recently, two methods have been proposed for the detection of the ultrafast coherent ring currents. One method, recently proposed by Yuan et al., Bandrauk's group [64], is utilizing the atto-second detection method of the coherent electronic dynamics in molecules with the temporal and spatial resolutions using the circularly polarized ultrashort UV pump and X-ray probe laser pulses. The other method is to utilize the time-resolved scanning microscopy (STM) and the magnetic force microscopy (MFM) to detect the ring current-induced magnetic fields during the ultrashort time [65–67].

It is also expected that to apply our methods to planar or non-planar extended molecular systems, such as graphene sheets. In principle, our method can be extended to these large systems, by considering the symmetry of the molecular system and the constraints on the π-electron ring currents.

Using laser control, it is also essential to maintain the created ring current at the target region (path) at least during one vibrational period of the PAH [68]. Otherwise, the created ring current would dissipate quickly because of the vibronic interactions and/or the nonadiabatic couplings between the two electronic excited states [30, 69–71].

4 DYNAMIC STARK-INDUCED π-ELECTRON ROTATIONS IN LOW-SYMMETRY AROMATIC RING MOLECULES

In this section, we present a convenient method for inducing unidirectional π-electron rotations in aromatic ring molecules with low symmetry [43]. The basic idea behind the induction of unidirectional electron rotations is to degenerate two nondegenerate excited states by utilizing dynamic Stark shifts, as demonstrated in **Figure 10**. We refer to this as the dynamic Stark-induced degenerate electronic state (DSIDES) [43]. Two linearly polarized continuous lasers operating at different frequencies and phases are used to form DSIDES: Each laser is set to selectively interact with each electronic state through non-resonant excitation. The lower and higher excited states are shifted up and down with the same population, respectively, and the DSIDES is formed at the center between them. As a result, unidirectional π-electron rotation is driven by two lasers. In the laser control scenario, only one input parameter out of the four possible parameters (frequency and intensity for each laser), is required to induce the DSIDES formation.

First, the DSIDES formation is described in a three-electronic state model under the fixed nuclei condition, and the time-dependent expectation value of the angular momentum operator of π-electrons is derived and analytically expressed. Next, to demonstrate the applicability of the control scenario, the results of the DSIDES treatment for toluene, which is a typical aromatic ring molecule of low symmetry belonging to Cs point group, are presented.

4.1 Formation of Dynamic Stark-Induced Degenerate Electronic State DSIDES and the Resulting Angular Momentum

Consider the coherent π-electron angular momentum in an aromatic ring molecule with low symmetry excited by non-resonant, stationary UV/visible lasers. The molecule of our interest is one oriented in a space or attached to a surface, as mentioned in the preceding sections. We adopt a three-electronic state model in the frozen nuclei approximation. The three electronic states including the ground state specified by the energy $\varepsilon_0\,(\equiv \hbar\omega_0)$, and two excited states specified by $\varepsilon_1\,(\equiv \hbar\omega_1)$ and $\varepsilon_2\,(\equiv \hbar\omega_2)$, as shown in **Figure 10**. Here, DSIDES can be formed by two stationary linearly polarized lasers with detuning frequencies $\Delta_1 = \omega_a - \omega_{10} < 0$ and $\Delta_2 = \omega_b - \omega_{20} > 0$. The frequency difference between the two excited states is expressed as $\omega_{21} = \omega_2 - \omega_1$. The dynamic Stark shifts are denoted by the Rabi frequencies Ω_1 and Ω_2, as presented in **Figure 10**. The wave function of the total system in the stationary lasers is defined through laser-molecular interactions as

$$\Phi(t) = c_0(t)\exp(-i\omega_0 t)\phi_0 + c_1(t)\exp(-i\omega_1 t)\phi_1 + c_2(t)\exp(-i\omega_2 t)\phi_2. \tag{27}$$

Here, the normalization condition for the coefficients $c_0(t)$, $c_1(t)$, and $c_2(t)$ are as follows,

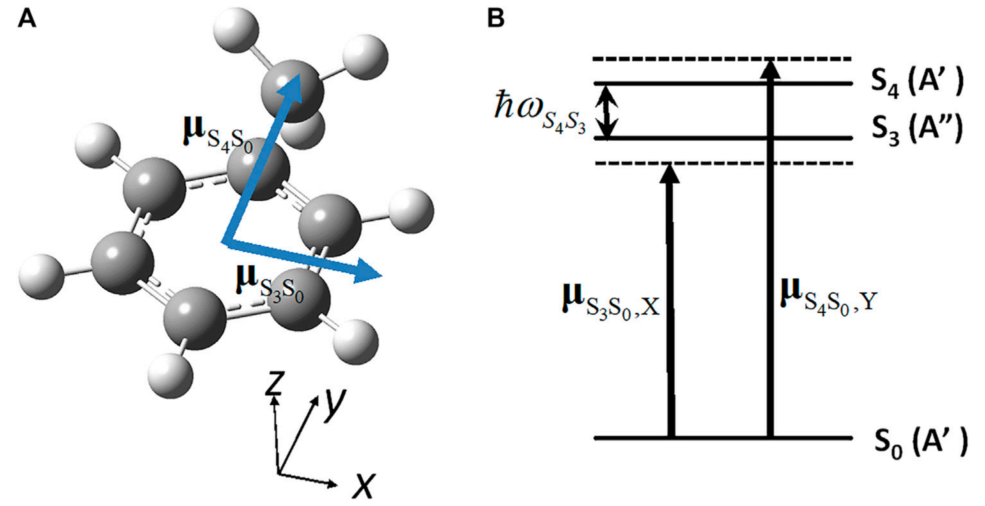

FIGURE 11 | (A) Geometrical structure of toluene molecule (C_S) in the ground state (S_0) with the directions of the two electronic transition dipole moments; **(B)** Parameters for the three electronic states adopted to induce the unidirectional angular momentum: $\hbar\omega_{S_4S_3} = 0.10$ eV as the energy difference between S_4 and S_3, $\mu_{S_3S_0,X} = 5.27$ D, and $\mu_{S_4S_0,Y} = 5.67$ D as the transition dipole moments, $E_{S_3} = 8.2$ eV and $E_{S_4} = 8.3$ eVas the vertical transition energies. The angular momentum matrix element between S_3 and S_4, $\ell_{Z,S_3S_4} = 0.672i$, is perpendicular to the aromatic ring.

$$\left|c_0(t)\right|^2 + \left|c_1(t)\right|^2 + \left|c_2(t)\right|^2 = 1. \tag{28}$$

The system Hamiltonian interacting with the electric fields is given as

$$H(t) = H_0 + V(t), \tag{29}$$

where H_0 satisfies $H_0\phi_i = \varepsilon_i\phi_i$ for i =0, 1, and 2. In **Eq. 29**, the interaction Hamiltonian $V(t)$ between the system and the two electric fields is written as

$$V(t) = -\boldsymbol{\mu}\cdot\mathbf{F}_a\cos(\omega_a t - \zeta_a) - \boldsymbol{\mu}\cdot\mathbf{F}_b\cos(\omega_b t - \zeta_b). \tag{30}$$

Here $\boldsymbol{\mu} = -e\mathbf{r}$ is the electronic dipole moment operator, where $\mathbf{r}$ means the electron coordinate. $\mathbf{F}_\alpha = F_\alpha\mathbf{e}_\alpha$ $(\alpha = a, b)$ is the electric field with amplitude F_α and photo-polarization vector $\mathbf{e}_\alpha$, ζ_α is the initial phase, and ω_α is the central frequency. In **Eq. 30**, the two electric fields denoted by a and b induce non-resonant transitions from the ground state to the two excited states. The selective transition conditions are set by the choice of the laser polarization vectors ($\mathbf{e}_a$ and $\mathbf{e}_b$) satisfying $\boldsymbol{\mu}_{02}\perp\mathbf{e}_a$ and $\boldsymbol{\mu}_{01}\perp\mathbf{e}_b$, respectively.

The time-dependent Schrödinger equation can be written as

$$i\hbar\frac{\partial\Phi(t)}{\partial t} = H(t)\Phi(t). \tag{31}$$

The coefficients must satisfy the coupled differential equation

$$i\hbar\frac{\partial}{\partial t}\begin{pmatrix} c_0(t) \\ c_1(t) \\ c_2(t) \end{pmatrix} = \boldsymbol{H}(t)\begin{pmatrix} c_0(t) \\ c_1(t) \\ c_2(t) \end{pmatrix}, \tag{32}$$

where the interaction Hamiltonian,

$$\boldsymbol{H}(t) = \begin{pmatrix} 0 & V_{01}^a(t) & V_{02}^b(t) \\ V_{10}^a(t) & 0 & 0 \\ V_{20}^b(t) & 0 & 0 \end{pmatrix}, \tag{33}$$

is applied with $V_{01}^a(t) = <\phi_0|\boldsymbol{\mu}\cdot\mathbf{F}_a|\phi_1> \cos(\omega_a t - \zeta_a)exp(-i\omega_{10}t)$ and $V_{02}^b(t) = <\phi_0|\boldsymbol{\mu}\cdot\mathbf{F}_b|\phi_2> \cos(\omega_b t - \zeta_b)exp(-i\omega_{20}t)$.

Equation 32 can be rewritten in the rotating approximation (RWA) and solved under the following restriction conditions to obtain the analytical solutions for the time-dependent coefficients $\{c_i(t)\}$. For this purpose, we introduce three conditions that can be set experimentally:

i. $V \equiv V_{01}^a = V_{02}^b$ for the transition magnitudes, (34a)
ii. $\Delta \equiv \Delta_2 = -\Delta_1 > 0$ for detuning frequencies, (34b)

And

iii. $\Delta = \Omega - \frac{\omega_{21}}{2}$ to induce the degeneracy condition, (34c)

where the transition magnitudes are $V_{01}^a \equiv -\boldsymbol{\mu}_{01}\cdot\mathbf{F}_a/(2\hbar)$, and $V_{02}^b \equiv -\boldsymbol{\mu}_{02}\cdot\mathbf{F}_b/(2\hbar)$.

In **Eq. 34c**, the two dressed states are assumed to have equal energies, i.e., $\Omega \equiv \Omega_1 = \Omega_2 (= \sqrt{\Delta^2 + 2V^2})$, which is called the Rabi frequency [43]. The three conditions lead to a reduction of the input parameters of the two lasers, such that the two amplitudes (F_a and F_b), and two central frequencies (ω_a and ω_b) are reduced to one input parameter. We take $F_a \equiv F$ hereafter. Analytical expressions for time-dependent coefficients $\{c_i(t)\}$ are given in **Appendix C**.

The time-dependent angular momentum defined as an expectation value of an angular momentum operator $\hat{L}_Z = -i\hbar\frac{\partial}{\partial\varphi} = \left(\hbar\hat{l}_Z, \hat{l}_Z = -i\frac{\partial}{\partial\varphi}\right)$, can be expressed,

$$\begin{aligned} L_Z(t) &= <\Phi(t)|\hat{L}_Z|\Phi(t)> \\ &= -2\hbar\mathrm{Im}(l_{Z,12})\mathrm{Im}[c_1*(t)c_2(t)exp(-i\omega_{21}t)]. \end{aligned} \tag{35}$$

Here, $l_{Z,12} = <\phi_1|\hat{l}_Z|\phi_2> = -<\phi_2|\hat{l}_Z|\phi_1> = -l_{Z,21}$ and $l_{Z,12} = i\mathrm{Im}l_{Z,12}$.

4.2 Unidirectional π-Electron Rotations in Toluene

We calculate $L_Z(t)$ (derived in the preceding subsection) in a real molecule, toluene. The simplest three-electronic state model is applied for toluene because the quasi-degenerate states S_3 (A") and S_4 (A′) in toluene (C_s) correspond to the doubly degenerate state S_3 (E_{1u}) in benzene (D_{6h}): Note that the S_3 (E_{1u}) state is a dipole-allowed excited state in benzene (D_{6h}), whereas the other two lower excited states, $S_2(B_{1u})$ and $S_1(B_{2u})$, are dipole-forbidden. The geometry optimization of toluene was carried out with the MP2 level of theory [43]. The C_S symmetry of toluene indicates that one of the hydrogen atoms belonging to the methyl group is perpendicular to an aromatic ring plane (**Figure 11A**).

Figure 12A shows the calculated time-dependent angular momentum expectation values $L_Z(t)$ with respect to the relative phase $\zeta = -\pi/2$ ($\zeta = +\pi/2$) between the two lasers for the left (right) panel. These were calculated using **Eq. 35** combined with **Eq. 34**. Here, the amplitude of the electric field F_a is adopted as the input parameter F ($\equiv F_a$). Other parameters are shown in **Table 3A**, while **Table 3B** shows the time-dependent populations in the three electronic states.

The time-dependent angular momenta plotted in **Figure 12A** are comprised of angular momentum pulse trains of the same shape for each value of F. Each angular momentum pulse corresponds to the unidirectional π-electron rotation, which begins with acceleration and ends with deceleration. The direction of the π-electron rotations is determined by the relative phase ζ between the two lasers: clockwise rotation for ζ=+π/2, and anti-clockwise rotation for ζ=−π/2. Here we discuss how the unidirectional π-electron rotations are created. We first note that $L_Z(t)$ can be rewritten under the two conditions, **Eq. 34a** and **Eq. 34b**, for $\Omega \approx \Delta$ as

$$L_Z(t) \approx 4\hbar \mathrm{Im}\left(l_{Z,12}\right)\frac{V^2\Delta^2}{\Omega^4}\left(1-\cos\Omega t\right)\sin\left(\left(2\Delta+\omega_{21}-\Omega\right)t+\zeta\right). \tag{36}$$

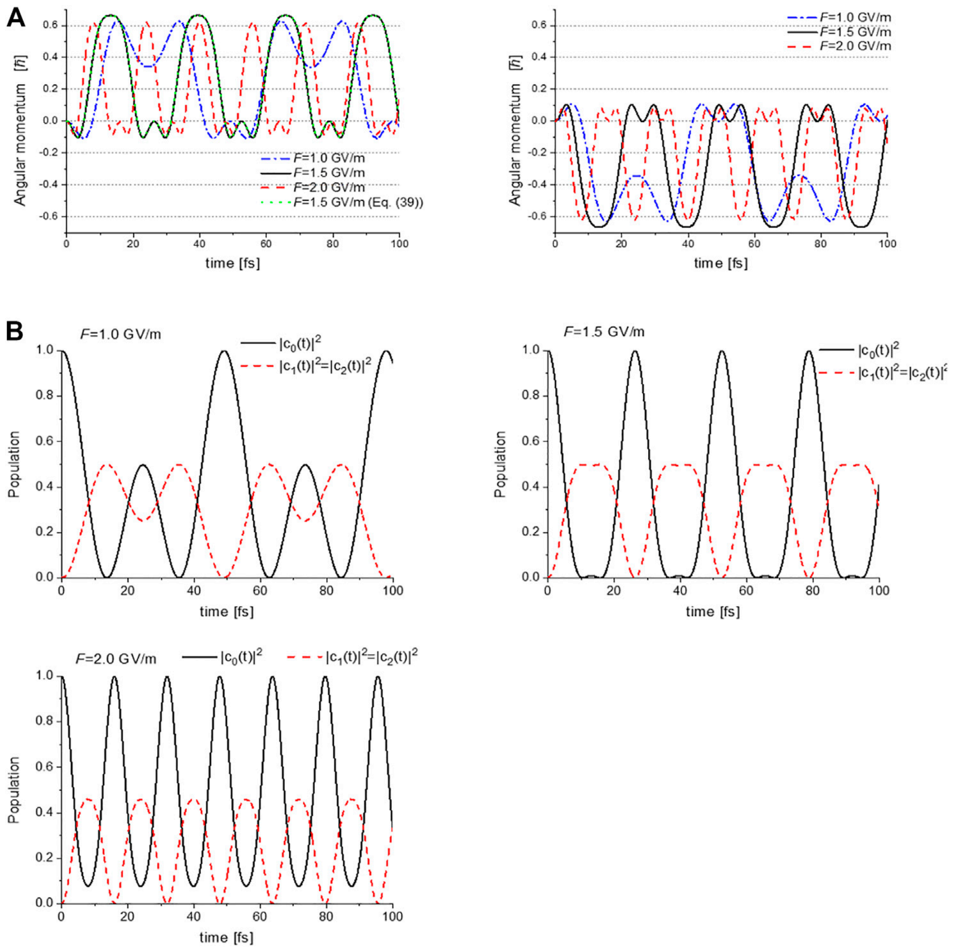

FIGURE 12 | (A) Expectation values of the angular momentum operator $L_Z(t)$ for toluene, calculated with the laser input parameter values F = 1.0, 1.5 and 2.0 GV/m. The left **(right)** panel shows $L_Z(t)$ with respect to the relative phase between two lasers $\zeta = -\pi/2$ ($\zeta = +\pi/2$); **(B)** Temporal evolutions of the populations in S_0, S_3, and S_4 for F = 1.0, 1.5 and 2.0 GV/m. Reprinted with permission from Ref. [43] Copyright (2016) Royal Society of Chemistry.

TABLE 3A | Input parameter *F* (≡ F_a) and other parameters for a generation of unidirectional π-electron rotation in toluene.

F [GV/m] ([W/cm^2])	**2|V| [eV]**	**Ω [eV]**	**|V|/Ω**	**Δ [eV]**	**ω_a [eV]**	**ω_b [eV]**
1.0 (0.13 × 10^{12})	0.110	0.084	0.655	0.032	8.16	8.33
1.5 (0.30 × 10^{12})	0.165	0.157	0.525	0.105	8.09	8.40
2.0 (0.53 × 10^{12})	0.220	0.260	0.423	0.208	7.99	8.51

Reprinted with permission from Ref. [43] Copyright (2016) Royal Society of Chemistry.

Table 3B | Calculated physical properties of the unidirectional π-electron rotation in toluene.

F [GV/m]	**T [fs]**[a]	**τ [fs]**[a]	**$\bar{L}_Z[\hbar]$**[a]	**J [μA]**	**N_r**
1.0	49.2	12.6	0.084	16.8	3.90
1.5	26.3	6.40	0.166	33.2	4.10
2.0	15.9	6.87	0.155	31.0	2.32

[a] *Parameters V, Δ, Ω, ω_a, and ω_b, were calculated for three values of F using **Eq. 34**. These parameters used for the calculation of the following physical quantities: T as a period of Rabi oscillation; $\bar{L}_Z$ is the angular momentum averaged over one cycle period of Rabi oscillation, $\tau = 2\pi m_e r/p = 2\pi m_e r^2/|\bar{L}_Z|$ as the rotational period of a π-electron, J as a ring current, and $N_r \equiv T/\tau$ as one cycle count of π-electron rotations.*

Equation 36 expresses no unidirectional π-electron rotations. By introducing the third condition, **Eq. 34c**, which provides for the formation of the doubly degenerate dressed states with $\zeta = \pm\pi/2$, **Eq. 36** can be expressed as

$$L_Z(t) \approx 4\hbar \mathrm{Im}(l_{Z,12}) \frac{V^2\Delta^2}{\Omega^4}(1-\cos\Omega t)\sin(\Omega t+\zeta). \quad (37)$$

This indicates a unidirectional π-electron rotation whose direction is determined by the relative phase ζ, that is, $L_Z(t) > 0$ for $\zeta = -\pi/2$ and $L_Z(t) < 0$ for $\zeta = +\pi/2$, as demonstrated in **Figure 12**. The dotted line shown in **Figure 12A** represents $L_Z(t)$ for $F = 1.5$ GV/m as calculated by **Eq. 37**, which well reproduces $L_Z(t)$ curve calculated using **Eq. 35** without the approximation of Ω≈Δ approximation. Thus, the unidirectional π-electron rotation originates from the DSIDES formed by the two non-resonant lasers with a definite relative phase of ±π/2.

As demonstrated in **Figure 12A**, the oscillation periods of the angular momentum pulses become shorter (higher Rabi frequency Ω), and those amplitudes decrease as *F* increases. These two behaviors result from the third restriction condition for degeneracy (**Eq. 35c**) used in the derivation of $L_Z(t)$. This degeneracy condition should be satisfied for the two dressed states with equal energies to maintain their energies located at the center of the two excited states, even though the laser intensities of two lasers increase. This results in an increase in the detuning parameter Δ of the two lasers, that is, a decrease (increase) in ω_a (ω_b), as shown in **Table 3A**.

Figure 12A exhibits that the maximum magnitude of the angular momentum occurs in the vicinity of $F = 1.5$ GV/m. This can be explained by noting that the constant in **Eq. 37**, $V^2\Delta^2/\Omega^4$, with Rabi frequency of $\Omega = \sqrt{\Delta^2 + 2V^2}$, reaches its maximum at $\Delta^2 = 2V^2$, which in turn provides the maximum angular momentum. Using the relationship $\Delta^2 = 2V^2$for the dressed states with equal energies in **Eq. 34c**, the electric field *F* is estimated as $F = \sqrt{2}\hbar\Delta/(\boldsymbol{\mu}_{10})_X = 1.52$ GV/m with $\Delta = 0.118$ eV, which is close to the $F = 1.5$ GV/m value shown in **Figure 12A**.

Figure 12B shows the *F*-dependence of the $|c_{S_0}(t)|^2$, $|c_{S_3}(t)|^2$ and $|c_{S_4}(t)|^2$ populations in toluene, which were calculated using Eqs. (B2). The relationship between the excited state populations, $|c_{S_3}(t)|^2 = |c_{S_4}(t)|^2$, is maintained because the conditions represented by **Eqs. 34a**, **34b**, were used for a derivation of $L_Z(t)$. Inversion of populations between the ground and excited states occurs for $F = 1.5$ GV/m and 2.0 GV/m, as demonstrated in **Figure 12B**. By comparing **Figures 12A,B**, it can be observed that major components of the unidirectional angular momentum pulse are created during when the population inversion occurs.

We now estimate the physical constants associated with π-electron rotations, which are listed in **Table 3B**: one cycle count of π-electron rotation N_r, and the magnitude of ring current *J* in one cycle of Rabi oscillation with periodicity $T \equiv 2\pi/\Omega$. In particular for aromatic molecules the ring current is an important physical quantity because it is directly related to the magnetic field induced by the ring current. For simplicity, we consider the classical model of π-electron rotation, in which N_r is defined as $N_r \equiv T/\tau$. Here $\tau = 2\pi m_e r/p = 2\pi m_e r^2/|\bar{L}_Z|$ is the rotational period of a π-electron having an angular momentum averaged over one cycle period of Rabi oscillation ($\bar{L}_Z$). m_e is the electron mass, and *r* indicates the radius of the aromatic ring. $\bar{L}$ was calculated using **Eq. 37** substituting for $L_Z(t)$ as

$$\bar{L}_Z = \frac{1}{T}\int_0^T dt L_Z(t) = -\frac{2\hbar \mathrm{Im} l_{Z,12}}{\Omega^4} V^2\Delta^2 \sin\zeta. \quad (38)$$

The ring current can be approximately expressed as $J \approx \bar{L}_Z J_0/\hbar$ [39–41, 43]. Here on a single aromatic ring, $J_0 = 200$ μA was a typical value of the ring current estimated with a unit angular momentum ℏ. **Table 3B** exhibits the calculated ring current *J*, cycle counts of π-electron rotations along the aromatic ring N_r and three values of *F* adopted in **Figure 12**, together with the parameters used in this model calculation. In **section 3**, we presented a pump-dump control procedure for the generation of sequential unidirectional ring currents in a 2,2'-biphenol molecule having non-degenerate excited states. The same order of magnitudes of the pump- and dump- pulse lasers were applied in the vicinity of ~1 GV/m, considering that the number of aromatic rings differs between biphenol and toluene. This can be explained by the point that the magnitudes of the ring current J or the angular momentum $\overline{L}_Z$ are proportional to that of the coherence between the two excited states, but not proportional to the number of aromatic rings. It is remarkable that in **Table 3B** J is not proportional to N_r, it is actually proportional to N_r/T. This is originated from the different behaviors between J and N_r related to the F-dependence shown in **Table 3B**.

5 SUMMARY AND PERSPECTIVE

This paper briefly provides an overview of the theoretical study of quantum laser control of coherent π-electron dynamics in low-symmetry aromatic ring molecules, which we have undertaken in recent several years [39–43, 68–73]. The essential principles to generate the π-electron angular momentum and ring current in a low symmetry aromatic ring molecule are first to create a superposition of two electronic excited (coherent) states using two linearly polarized lasers, and second to select the clockwise or anticlockwise rotational component from the non-stationary time evolution of the coherent state using pump and dump lasers with properly designed polarization directions. Here, the direct product of the irreducible representations of each excited states in the molecular point group belongs to that of the molecular rotation, (Rx, Ry or Rz), and the relative phase between the two linearly polarized lasers are fixed in order to determine the initial direction of the angular momentum and ring current. In additon to the laser conditions, aromatic ring molecules also need to satisfy the follwing conditions to generate the π-electron angular momentum and ring current. First two electronic excited states are nearly degenerate, and second, those states can be excited from the ground states using UV lasers, i.e., transitions between the electronic excited states and ground states are optically allowed.

On the basis of the above principles, analytical expressions for coherent π-electron angular momentum, ring current, and ring current-induced magnetic field are derived in the quantum chemical MO theory. A coherent π-electron ring current is defined as the average of the bond currents. Temporal behaviors of these coherent quantities are calculated using the density matrix method within the Markov approximation. Quantum simulations of the coherent quantuities have been performed for (*P*)-2,2'-biphenol. Based on the simulation results a new quantum control method for two-dimensional ultrafast angular momentum switching was proposed. The essential point of the quantum control is to use a sequence of the overlapped pump and dump pulses with a selected relative phase and selected polarization directions between the two lasers. The results for the (*P*)-2,2'-biphenol indicate that this new control scheme can potentially be used for the design and realization of ultrafast multi-dimensional electronic switching devices, or field-effect transistor devices.

The familiar quantum optimal control procedure was applied to an optiaml control of the coherent π-electron ring currents in planar PAHs with D_{2h} symmetry. For this purpose, we have to set up the target state for a desired ring current pattern. The final target wave functions are determined *via* the Lagrange multiplier method by solving the coupled equations of motion under the constraints that the ring currents must satisfy. The method was applied to anthracene. The creation of the perimeter current and the middle ring current in anthracene were successfully realized. The control mechanisms were elucidated by analyzing the time-dependent behaviors of the control laser puses and the populations of the relevant electronic states. Concerning the types of molecules used in the above laser control studies, polycyclic planar aromatic molecules like PAHs, coronene and benzoic acids dimers are applicable for a laser control of perimeter or localized ring currents.

Another laser control method for the π-electrons unidirectional rotation in low symmetric aromatic rings was presented. The basic idea of the control method is to degenerate two nondegenerate excited states by using dynamic Stark shifts. Doubly degenerate excited state was created by the Stark shift using the two linearly polarized non-resonant lasers with a definite relative phase of $\pm\frac{\pi}{2}$, which determines the angular momentum direction (clockwise or anti-clockwise π-electron rotation). Applying the RWA, the coherent π-electron angular momentum in a three-electronic state model was analytically expressed in a closed form, and the proposed control theory have been applied to toluene (Cs). The numerical simulations indicated that the resulting angular momentum comprised sequential angular momentum pulses with a positive or negative value depending on the relative phases between the two lasers.

Some theoretical studies on laser control of the coherent π-electron rotations that were not included in this review are noteworthy. Probing molecular chirality, right-handed or left-handed chiral molecules, is a central issue in natural science. E.x., Phenylalanine is an essential amino acid, and L-enantiomer is found in natural system. On the other hand, D-enantiomer is synthesized artificially, and racemate phenylalanine is used for dietary supplement. However, in conventional methods such as CD spectroscopy and optical rotatory dispersion (ORD) spectroscopy [74, 75], the signals are very week because these processes involve second-order evaluations. As a possible of laser control scheme of the unidirectional π-electron rotations in low symmetric aromatic ring molecules, we previously proposed an efficient enantiomer-probing scenario for chiral aromatic molecule [71, 72]. A pair of nondegenerate excited states becomes degenerate by applying the dynamic Stark shift in the presence of two non-resonant UV lasers, producing an enantiomer-specific angular momentum. In that study, phenylalanine was adopted as an example for the numerical simulation. The resulting enantiomer-specific magnetic fluxes were on the order of a few Tesla, with periods of several tens of femtoseconds.

The contribution of vibrational motion to coherent π-electron rotations is also an important research topic that was not discussed in this review. In our previous research, vibrational effects on the coherent π-electron rotations in (*P*)-2,2'-biphenol were theoretically studied in the adiabatic approximation [73]. It was found that the low-frequency torsion mode around the bridge causes modulations in the beat of the ring current [73]. The vibrational effects on dynamic Stark-induced π-electron rotations in aromatic ring molecules with low symmetry were also studied using the displaced harmonic oscillator (DHO) model in the adiabatic approximation [72]. A pair of the lowest vibronic state in the two electronic excited states was degenerated using the two linearly polarized UV lasers. The two potential displacements between the ground state and the two electronic excited states were used as the parameters. The shapes of the sequential angular momentum pulses were affected by the potential displacements.

From one perspective, theoretical treatments beyond the adiabatic approximation [28, 31, 74–77] are expected to be incorporated such that other electronic excited states interact with the two relevant excited states through nonadiabatic couplings. It is crucial to clarify the effect of nonadiabatic couplings to the unidirectional π-electron rotations and determine how to maintain π-electron rotations by way of quantum optimal control techniques. In large PAHs, once π-electron rotation is realized at a localized ring site and once a site-selective coherent ring current is generated, the localized ring current is transferred from site to site using the laser pulses, i.e., transferred ring currents, which allow for an ultrafast switching function at the selected local site. Furthermore, the site-selective coherent ring current and transferred ring current can create the induced magnetic fields. These electromagnetic fields are expected to provide ultrafast probing of local sites in large molecular systems, biomolecules with chiral aromatic ring molecules, and PAHs. Further development of theoretical treatments involving photon-induced electronic coherence in molecular systems would be promising in the near future.

AUTHOR CONTRIBUTIONS

The authors made a substantial, direct, and intellectual contribution to the work and approved it for publication. Original draft preparation, software, formal analysis, and funding acquisition, HM; Conceptualization, supervision, project administration, and validation, YF; Writing—original draft preparation, HM and YF; Investigation, writing—review and editing, HM, N-LP, and YF.

ACKNOWLEDGMENTS

HM and YF are grateful to Dr. M. Yamaki, and Professors Y. Teranishi, G-S. Kim, Y.J. Yan, and H. Nakamura for their contribution in earlier works. YF would like to thank Professor S. H. Lin for his critical comments and financial support.

REFERENCES

1. Goulielmakis E, Loh Z-H, Wirth A, Santra R, Rohringer N, Yakovlev VS, et al. Real-time Observation of Valence Electron Motion. *Nature* (2010) 466: 739–43. doi:10.1038/nature09212
2. Yuan K-J, and Bandrauk AD Circularly Polarized Attosecond Pulses from Molecular High-Order Harmonic Generation by Ultrashort Intense Bichromatic Circularly and Linearly Polarized Laser Pulses. *J Phys B: Mol Opt Phys* (2012) 45:074001. doi:10.1088/0953-4075/45/7/074001
3. Chen S, Gilbertson S, Wang H, Chini M, Zhao K, Khan SD, et al. Attosecond Pulse Generation, Characterization and Application. *Adv Multiphoton Process. Spectrosc* (2011) 20:127–74. doi:10.1142/9789814343992_0004
4. Remacle F, and Levine RD Attosecond Pumping of Nonstationary Electronic States of LiH: Charge Shake-Up and Electron Density Distortion. *Phys Rev A* (2011) 83:013411. doi:10.1103/PhysRevA.83.013411
5. Tzallas P, Skantzakis E, Kruse JE, and Charalambidis D On the Generation of Intense Isolated Attosecond Pulses by Many-Cycle Laser Fields. In: *Progress in Ultrafast Intense Laser Science*. Heidelberg: Springer (2011). p. 163–90. doi:10.1007/978-3-642-18327-0_8
6. Ulusoy IS, and Nest M Correlated Electron Dynamics: How Aromaticity Can Be Controlled. *J Am Chem Soc* (2011) 133:20230–6. doi:10.1021/ja206193t
7. Fujimura Y, and Sakai H *Electronic and Nuclear Dynamics in Molecular Systems*. Singapore: World Scientific (2011). p. 117–32.
8. Singh KP, He F, Ranitovic P, Cao W, De S, Ray D, et al. Control of Electron Localization in Deuterium Molecular Ions Using an Attosecond Pulse Train and a Many-Cycle Infrared Pulse. *Phys Rev Lett* (2010) 104:023001. doi:10.1103/PhysRevLett.104.023001
9. Krausz F, and Ivanov M Attosecond Physics. *Rev Mod Phys* (2009) 81:163–234. doi:10.1103/RevModPhys.81.163
10. Nest M, Remacle F, and Levine RD Pump and Probe Ultrafast Electron Dynamics in LiH: A Computational Study. *New J Phys* (2008) 10:025019. doi:10.1088/1367-2630/10/2/025019
11. Kling MF, and Vrakking MJJ Attosecond Electron Dynamics. *Annu Rev Phys Chem* (2008) 59:463–92. doi:10.1146/annurev.physchem.59.032607.093532
12. Skourtis SS, Beratan DN, Naaman R, Nitzan A, and Waldeck DH Chiral Control of Electron Transmission through Molecules. *Phys Rev Lett* (2008) 101:238103. doi:10.1103/PhysRevLett.101.238103
13. NabekawaMidorikawa YK, and Midorikawa K Nonlinear Optics for Characterizing XUV/Soft X-ray High-Order Harmonic Fields in Attosecond Regime. *Adv Multiphoton Process. Spectrosc* (2008) 18:1–67. doi:10.1142/9789812791740_0001
14. Lein M, and Chirilă CC Signatures of Molecular Structure and Dynamics in High-Order Harmonic Generation. *Adv Multiphoton Process. Spectrosc* (2008) 18:69–106. doi:10.1142/9789812791740_0002
15. Corkum PB, and Krausz F Attosecond Science. *Nat Phys* (2007) 3:381–7. doi:10.1038/nphys620
16. Remacle F, Nest M, and Levine RD Laser Steered Ultrafast Quantum Dynamics of Electrons in LiH. *Phys Rev Lett* (2007) 99:183902. doi:10.1103/PhysRevLett.99.183902
17. Räsänen E, Castro A, Werschnik J, Rubio A, and Gross EKU Optimal Control of Quantum Rings by Terahertz Laser Pulses. *Phys Rev Lett* (2007) 98:157404. doi:10.1103/PhysRevLett.98.157404
18. Klamroth T Optimal Control of Ultrafast Laser Driven many-electron Dynamics in a Polyatomic Molecule: N-Methyl-6-Quinolone. *J Chem Phys* (2006) 124:144310. doi:10.1063/1.2185633
19. Pershin YV, and Piermarocchi C Laser-controlled Local Magnetic Field with Semiconductor Quantum Rings. *Phys Rev B* (2005) 72:245331. doi:10.1103/PhysRevB.72.245331
20. Niikura H, Légaré F, Hasbani R, Ivanov MY, Villeneuve DM, and Corkum PB Probing Molecular Dynamics with Attosecond Resolution Using Correlated Wave Packet Pairs. *Corkum PBNature* (2003) 421:826–9. doi:10.1038/nature01430
21. Haruyama K, kono H, Fujimura Y, Kawata I, and Bandrauk AD Intense Laser-Field Ionization of H2 Enhanced by Two-Electron Dynamics. *Phys Rev A* (2002) 66:043403. doi:10.1103/PhysRevA.66.043403

22. Anthony JE Functionalized Acenes and Heteroacenes for Organic Electronics. *Chem Rev* (2006) 106:5028–48. doi:10.1021/cr050966z
23. Bonifas AP, and McCreery RL 'Soft' Au, Pt and Cu Contacts for Molecular Junctions through Surface-Diffusion-Mediated Deposition. *Nat Nanotech* (2010) 5:612–7. doi:10.1038/nnano.2010.115
24. BarthManz IJ, and Manz J Periodic Electron Circulation Induced by Circularly Polarized Laser Pulses: Quantum Model Simulations for Mg Porphyrin. *Angew Chem Int Ed* (2006) 45:2962–5. doi:10.1002/anie.200504147
25. Barth I, Manz J, Shigeta Y, and Yagi K Unidirectional Electronic Ring Current Driven by a Few Cycle Circularly Polarized Laser Pulse: Quantum Model Simulations for Mg−Porphyrin. *J Am Chem Soc* (2006) 128:7043–9. doi:10.1021/ja057197l
26. Barth I, and Manz J Quantum Switching of Magnetic Fields by Circularly Polarized Re-optimized π Laser Pulses: From One-Electron Atomic Ions to Molecules. In: *Progress in Ultrafast Intense Laser Science VI*. Berlin, Heidelberg: Springer (2010). p. 21–44. doi:10.1007/978-3-642-15054-8_2
27. Nobusada K, and Yabana K Photoinduced Electric Currents in Ring-Shaped Molecules by Circularly Polarized Laser Pulses. *Phys Rev A* (2007) 75:032518. doi:10.1103/PhysRevA.75.032518
28. Kanno M, Kono H, and Fujimura Y Control of π-Electron Rotation in Chiral Aromatic Molecules by Nonhelical Laser Pulses. *Angew Chem Int Ed* (2006) 45: 7995–8. doi:10.1002/anie.200602479
29. Kanno M, Hoki K, Kono H, and Fujimura Y Quantum Optimal Control of Electron Ring Currents in Chiral Aromatic Molecules. *J Chem Phys* (2007) 127: 204314. doi:10.1063/1.2806180
30. Kanno M, Kono H, Fujimura Y, and Lin SH Nonadiabatic Response Model of Laser-Induced Ultrafastπ-Electron Rotations in Chiral Aromatic Molecules. *Phys Rev Lett* (2010) 104:108302. doi:10.1103/PhysRevLett.104.108302
31. Kanno M, Kono H, and Fujimura Y Control of π-Electron Rotations in Chiral Aromatic Molecules Using Intense Laser Pulses. In: *Progress in Ultrafast Intense Laser Science VII*. Berlin, Heidelberg: Springer (2011). p. 53–78. doi:10.1007/978-3-642-18327-0_3
32. Barth I, Manz J, and Serrano-Andrés L Quantum Simulations of Toroidal Electric Ring Currents and Magnetic fields in Linear Molecules Induced by Circularly Polarized Laser Pulses. *Chem Phys* (2008) 347:263–71. doi:10.1016/j.chemphys.2007.09.037
33. Yuan K-J, and Bandrauk AD Attosecond-magnetic-field-pulse Generation by Coherent Circular Molecular Electron Wave Packets. *Phys Rev A* (2015) 91: 042509. doi:10.1103/PhysRevA.91.042509
34. Steiner E, and Fowler PW Patterns of Ring Currents in Conjugated Molecules: A Few-Electron Model Based on Orbital Contributions. *J Phys Chem A* (2001) 105:9553–62. doi:10.1021/jp011955m
35. Lazzerretti P Ring Currents. *Prog Nucl Magn Reson Spectrosc* (2000) 36:1–88. doi:10.1016/S0079-6565(99)00021-7
36. Redfield AG The Theory of Relaxation Processes. *Adv Magn Reson* (1965) 1: 1–32. doi:10.1016/B978-1-4832-3114-3.50007-6
37. Lindblad G On the Generators of Quantum Dynamical Semigroups. *Commun.Math Phys* (1976) 48:119–30. doi:10.1007/BF01608499
38. Lin SH, Chang CH, Liang KK, Chang R, Shiu YJ, Zhang JM, et al. Ultrafast Dynamics and Spectroscopy of Bacterial Photosynthetic Reaction Centers. *Adv Chem Phys* (2002) 12:1–88. doi:10.1002/0471264318.ch1
39. Mineo H, Lin SH, and Fujimura Y Coherent π-electron Dynamics of (P)-2,2′-biphenol Induced by Ultrashort Linearly Polarized UV Pulses: Angular Momentum and Ring Current. *J Chem Phys* (2013) 138:074304. doi:10.1063/1.4790595
40. Mineo H, Yamaki M, Teranishi Y, Hayashi M, Lin SH, and Fujimura Y Quantum Switching of π-Electron Rotations in a Nonplanar Chiral Molecule by Using Linearly Polarized UV Laser Pulses. *J Am Chem Soc* (2012) 134: 14279–82. doi:10.1021/ja3047848
41. Mineo H, and Fujimura Y Quantum Design of π-Electron Ring Currents in Polycyclic Aromatic Hydrocarbons: Parallel and Antiparallel Ring Currents in Naphthalene. *J Phys Chem Lett* (2017) 8:2019–25. doi:10.1021/acs.jpclett.7b00704
42. Mineo H, and Fujimura Y Quantum Control of Coherent π-electron Ring Currents in Polycyclic Aromatic Hydrocarbons. *J Chem Phys* (2017) 147: 224301. doi:10.1063/1.5004504
43. Mineo H, Yamaki M, Kim G-S, Teranishi Y, Lin SH, and Fujimura Y Induction of Unidirectional π-electron Rotations in Low-Symmetry Aromatic Ring Molecules Using Two Linearly Polarized Stationary Lasers. *Phys Chem Chem Phys* (2016) 18:26786–95. doi:10.1039/C6CP04254F
44. Oda K, Hita M, Minemoto S, and Sakai H All-Optical Molecular Orientation. *Phys Rev Lett* (2010) 104:213901. doi:10.1103/PhysRevLett.104.213901
45. Stapelfeldt H, and Seideman T Colloquium: Aligning Molecules With strong Laser Pulses. *Rev Mod Phys* (2003) 75:543–57. doi:10.1103/RevModPhys.75.543
46. Kanai T, Minemoto S, and Sakai H Quantum Interference during High-Order Harmonic Generation From Aligned Molecules. *Nature* (2005) 435:470–4. doi:10.1038/nature03577
47. Frisch MJ, Trucks GW, Schlegel HB, Scuseria GE, Robb MA, Cheeseman JR, et al. *Gaussian 09, Revision E.01*. Wallingford, CT: Gaussian, Inc. (2009).
48. Baskin JS, Felker PM, and Zewail AH Doppler-free Time-resolved Polarization Spectroscopy of Large Molecules: Measurement of Excited State Rotational Constants. *J Chem Phys* (1986) 84:4708–10. doi:10.1063/1.449998
49. Mineo H, Lin SH, Fujimura Y, Xu J, Xu RX, and Yan YJ Non-Markovian Response of Ultrafast Coherent Electronic Ring Currents in Chiral Aromatic Molecules in a Condensed Phase. *J Chem Phys* (2013) 139:214306. doi:10.1063/1.4834035
50. Barth I, and Manz J Electric Ring Currents in Atomic Orbitals and Magnetic Fields Induced by Short Intense Circularly Polarizedπlaser Pulses. *Phys Rev A* (2007) 75:012510. doi:10.1103/PhysRevA.75.012510
51. Barth I, Serrano-Andrés L, and Seideman T Nonadiabatic Orientation, Toroidal Current, and Induced Magnetic Field in BeO Molecules. *J Chem Phys* (2008) 129:164303. doi:10.1063/1.2994737
52. Acremann Y, Buess M, Back CH, Dumm M, Bayreuther G, and Pescia D A Single Ion as a Nanoscopic Probe of an Optical Field. *Nature* (2001) 414:49–51. doi:10.1038/35102129
53. Kruglyak VV, Portnoi ME, and Hicken RJ Use of the Faraday Optical Transformer for Ultrafast Magnetization Reversal of Nanomagnets. *J Nanophoton* (2007) 1:013502. doi:10.1117/1.2516174
54. Kirilyuk A, Kimel AV, and Rasing T Ultrafast Optical Manipulation of Magnetic Order. *Rev Mod Phys* (2010) 82:2731–84. doi:10.1103/RevModPhys.82.2731
55. Kanno M, Ono Y, Kono H, and Fujimura Y Laser-Polarization Effects on Coherent Vibronic Excitation of Molecules with Quasi-Degenerate Electronic States. *J Phys Chem A* (2012) 116:11260–72. doi:10.1021/jp305284w
56. Bandrauk AD, Fujimura Y, and Gordon RJ *Laser Control and Manipulation of Molecules*. Washington, DC: American Chemical Society (2002). p. 821. doi:10.1021/bk-2002-0821.fw001
57. Gordon R, Zhu LC, and Seideman T Coherent Control of Chemical Reactions. *Acc Chem Res* (1999) 12:1007–16. doi:10.1021/ar970119l
58. Krause P, Klamroth T, and Saalfrank P Time-dependent Configuration-Interaction Calculations of Laser-Pulse-Driven Many-electron Dynamics: Controlled Dipole Switching in Lithium Cyanide. *J Chem Phys* (2005) 123: 074105. doi:10.1063/1.1999636
59. Zhu W, Botina J, and Rabitz H Rapidly Convergent Iteration Methods for Quantum Optimal Control of Population. *J Chem Phys* (1998) 108:1953–63. doi:10.1063/1.475576
60. Zhu W, and Rabitz H A Rapid Monotonically Convergent Iteration Algorithm for Quantum Optimal Control over the Expectation Value of a Positive Definite Operator. *J Chem Phys* (1998) 109:385–91. doi:10.1063/1.476575
61. Ohtsuki Y, Zhu W, and Rabitz H Monotonically Convergent Algorithm for Quantum Optimal Control with Dissipation. *J Chem Phys* (1999) 110:9825–32. doi:10.1063/1.478036
62. Ferguson J, Reeves LW, and Schneider WG VAPOR ABSORPTION SPECTRA AND OSCILLATOR STRENGTHS OF NAPHTHALENE, ANTHRACENE, AND PYRENE. *Can J Chem* (1957) 35:1117–36. doi:10.1139/v57-152
63. Rodriguez JJ, and Mukamel S Probing Ring Currents in Mg-Porphyrins by Pump-Probe Spectroscopy. *J Phys Chem A* (2012) 116:11095–100. doi:10.1021/jp3035874
64. Yuan K-J, Shu C-C, Dong D, and Bandrauk AD Attosecond Dynamics of Molecular Electronic Ring Currents. *J Phys Chem Lett* (2017) 8:2229–35. doi:10.1021/acs.jpclett.7b00877
65. Rugar D, Budakian R, Mamin HJ, and Chui BW Single Spin Detection by Magnetic Resonance Force Microscopy. *Nature* (2004) 430:329–32. doi:10.1038/nature02658
66. Repp J, Meyer G, Stojković SM, Gourdon A, and Joachim C Molecules on Insulating Films: Scanning-Tunneling Microscopy Imaging of Individual

Molecular Orbitals. *Phys Rev Lett* (2005) 94:026803. doi:10.1103/PhysRevLett.94.026803

67. Sloan PA Time-resolved Scanning Tunnelling Microscopy for Molecular Science. *J Phys Condens Matter* (2010) 22:264001. doi:10.1088/0953-8984/22/26/264001
68. Yamaki M, Teranishi Y, Nakamura H, Lin SH, and Fujimura Y The Generation of Stationary π-electron Rotations in Chiral Aromatic Ring Molecules Possessing Non-degenerate Excited States. *Phys Chem Chem Phys* (2016) 18:1570–7. doi:10.1039/C5CP05467B
69. Mineo H, Lin SH, and Fujimura Y Vibrational Effects on UV/Vis Laser-Driven π-electron Ring Currents in Aromatic Ring Molecules. *Chem Phys* (2014) 442: 103–10. doi:10.1016/j.chemphys.2014.02.011
70. Mineo H, Phan N-L, La D-K, and Fujimura Y Theoretical Study of Dynamic Stark-Induced π-Electron Rotations in Low-Symmetry Aromatic Ring Molecules Beyond the Frozen Nuclear Approximation. *J Phys Chem A* (2021) 125:1476–89. doi:10.1021/acs.jpca.0c10216
71. Mineo H, Kim G-S, Lin SH, and Fujimura Y Dynamic Stark-Induced Coherent π-Electron Rotations in a Chiral Aromatic Ring Molecule: Application to Phenylalanine. *J Phys Chem A* (2019) 123:6399–410. doi:10.1021/acs.jpca.9b03083
72. Mineo H, Kim G-S, Lin SH, and Fujimura Y Quantum Design for Ultrafast Probing of Molecular Chirality through Enantiomer-specific Coherent π-Electron Angular Momentum. *J Phys Chem Lett* (2018) 9:5521–6. doi:10.1021/acs.jpclett.8b02137
73. Mineo H, Kanno M, Kono H, Chao SD, Lin SH, and Fujimura Y Ultrafast Coherent Dynamics of Nonadiabatically Coupled Quasi-Degenerate Excited States in Molecules: Population and Vibrational Coherence Transfers. *Chem Phys* (2012) 392:136–42. doi:10.1016/j.chemphys.2011.11.004
74. Barron LD *Molecular Light Scattering and Optical Activity*. Cambridge, UK: Cambridge University Press (1982).
75. JM Hicks, eds. *Chirality: Physical Chemistry*. Washington, DC; American Chemical Society, (2002) 1–16.
76. Nakamura H *Nonadiabatic Transition Concept, Basic Theories and Applications, Chapter 10. Multi-Dimensional Problems*. Singapore: World Scientific (2012) 212–44.
77. de Vivie-Riedle R, and Hofmann A Nonadiabatic Quantum Dynamics and Control Strategies. In: W Domcke, DR Yarkony, and H Köppel, eds. *Conical Intersections, Electronic Structure, Dynamics & Spectroscopy*. New Jersey: World Scientific, (2004) 803–27.

Conflict of Interest: The authors declare that the research was conducted in the absence of any commercial or financial relationships that could be construed as a potential conflict of interest.

APPENDIX

A BRIEF DERIVATION OF TARGET OPERATORS, CALCULATED USING THE COUPLED EQUATIONS FOR THE RING CURRENT LOCALIZATION (EQ. 19).

In general, the Lagrange function L_J consists of "the function to be maximized or minimized" and "all related constraint conditions of the system," For the localization of the π-electron ring current, J_χ in PAHs, $L_J(c_1,\cdots,c_n,\lambda_1,\cdots,\lambda_m)$ can be rewritten as

$$L_J(c_1,\cdots,c_n,\lambda_1,\cdots,\lambda_m) = J_\chi + \lambda_1 J_1 + \cdots + \lambda_{\chi-1}J_{\chi-1} + \lambda_\chi\left(\sum_{\alpha=1}^{n}|c_\alpha|^2 - 1\right) + \lambda_{\chi+1}J_{\chi+1} + \cdots + \lambda_m J_m, \tag{A1}$$

Where the first term J_χ is the target ring current to be maximized, while the other terms with Lagrange multiplier λ_κ, $J_\kappa \equiv J_\kappa(T)$, are irrelevant to the localization under the constraint conditions, such that $J_1 = \cdots = J_{\chi-1} = J_{\chi+1} = \cdots = J_m = 0$, and $(\sum_{\alpha=1}^{n}|c_\alpha|^2 - 1) = 0$, which indicates the number conservation of the π-electrons associated with the ring current.

The partial derivatives of **Eq. 19** with respect to $x_\alpha = (\mathrm{Re}c_\alpha, \mathrm{Im}c_\alpha)$, λ_χ and λ_κ are then

$$\frac{\partial L_J}{\partial x_\alpha} = \frac{\partial J_\chi}{\partial x_\alpha} + \sum_{\kappa\neq\chi}^{m}\lambda_\kappa\frac{\partial J_\kappa}{\partial x_\alpha} + \lambda_\chi\frac{\partial}{\partial x_\alpha}\left(\sum_{\beta=1}^{n}|c_\beta|^2 - 1\right) = 0,\ (1\leq\alpha\leq n), \tag{A2a}$$

$$\frac{\partial L_J}{\partial \lambda_\chi} = \sum_{\alpha=1}^{n}|c_\alpha|^2 - 1 = 0, \tag{A2b}$$

And

$$\frac{\partial L_J}{\partial \lambda_\kappa} = J_\kappa = 0,\ (1\leq\kappa\leq m,\ \kappa\neq\chi), \tag{A2c}$$

Respectively, where J_l(i.e.,$J_\chi$and J_κ) can be rewritten in terms of $\mathrm{Re}c_\alpha$ and $\mathrm{Im}c_\alpha$ as

$$J_l = \sum_{\alpha}^{n}\sum_{\beta}^{n}J_{l,\alpha\beta}\left(\mathrm{Im}c_\alpha\mathrm{Re}c_\beta - \mathrm{Re}c_\alpha\mathrm{Im}c_\beta\right)(1\leq l\leq m). \tag{A3}$$

By substituting the partial derivatives of J_l in **Eq. (A3)**, with respect to $\mathrm{Re}c_\alpha$ and $\mathrm{Im}c_\alpha$ into **Eq. (A2a)**, we obtain $2n$+m coupled equations with $2n$+m variables as

$$\sum_{\beta=1}^{n}J_{\chi,\beta\alpha}\mathrm{Im}c_\beta + \sum_{\kappa\neq\chi}^{m}\sum_{\beta=1}^{n}\lambda_\kappa J_{\kappa,\beta\alpha}\mathrm{Im}c_\beta + \lambda_\chi\mathrm{Re}c_\alpha = 0,\ (1\leq\alpha\leq n), \tag{A4a}$$

And

$$-\sum_{\beta=1}^{n}J_{\chi,\beta\alpha}\mathrm{Re}c_\beta - \sum_{\kappa\neq\chi}^{m}\sum_{\beta=1}^{n}\lambda_\kappa J_{\kappa,\beta\alpha}\mathrm{Re}c_\beta + \lambda_\chi\mathrm{Im}c_\alpha = 0,\ (1\leq\alpha\leq n). \tag{A4b}$$

Equations (A2b), **(A2c)** can be expressed as

$$\sum_{\alpha=1}^{n}\left((\mathrm{Re}c_\alpha)^2 + (\mathrm{Im}c_\alpha)^2\right) - 1 = 0, \tag{A4c}$$

And

$$\sum_{\beta=1}^{n}\sum_{\alpha=1}^{n}J_{\kappa,\alpha\beta}\left(\mathrm{Im}c_\alpha\mathrm{Re}c_\beta - \mathrm{Re}c_\alpha\mathrm{Im}c_\beta\right) = 0\,. \tag{A4d}$$

Equation (A4) contains the final equations, which are the same as those in **Eq. 19**.

B BRIEF DERIVATION OF TARGET OPERATORS, CALCULATED USING THE COUPLED EQUATIONS FOR THE PERIMETER RING CURRENT (EQ. 20).

Similar to the ring current localization, the Lagrange functional for the perimeter ring current is given as

$$L_J^P(c_1,\cdots,c_n,\lambda_1,\cdots,\lambda_m) = J_P + \lambda_1 J_{B,1} + \cdots + \lambda_{m-1}J_{B,m-1} + \lambda_m\left(\sum_{\alpha=1}^{n}|c_\alpha|^2 - 1\right), \tag{B1}$$

Where J_P is the perimeter ring current (**Eq. 20a**) to be maximized, and $J_{B,l'}$ are the bridge bond currents (*see* **Eq. 20b**), which should be zero at the target time $t = T$, $J_{B,l'} = 0$ where $1\leq l'\leq m-1$. The last term indicates the normalization condition for the total target wave function $\sum_{\alpha=1}^{n}|c_\alpha|^2 - 1 = 0$.

In the same manner as the ring current is localized to a designated ring, the coupled equations for the perimeter ring current are obtained by taking partial derivatives of the Lagrange functional L_J^P (Eq. (B1)) with respect to $\mathrm{Re}c_\alpha$, $\mathrm{Im}c_\alpha$, and λ_l.

The coupled equations for the perimeter ring current can then be expressed as

$$\sum_{\beta=1}^{n}J_{\beta\alpha}^{P}\mathrm{Im}c_\beta + \sum_{l'=1}^{m-1}\sum_{\beta=1}^{n}\lambda_{l'}J_{\beta\alpha}^{B,l'}\mathrm{Im}c_\beta + \lambda_m\mathrm{Re}c_\alpha = 0,\ (1\leq\alpha\leq n) \tag{B2a}$$

$$-\sum_{\beta=1}^{n}J_{\beta\alpha}^{P}\mathrm{Re}c_\beta - \sum_{l'=1}^{m-1}\sum_{\beta=1}^{n}\lambda_{l'}J_{\beta\alpha}^{B,l'}\mathrm{Re}c_\beta + \lambda_m\mathrm{Im}c_\alpha = 0,\ (1\leq\alpha\leq n) \tag{B2b}$$

$$\sum_{\alpha,\beta=1}^{n}J_{\alpha\beta}^{B,l'}\left(\mathrm{Im}c_\alpha\mathrm{Re}c_\beta - \mathrm{Re}c_\alpha\mathrm{Im}c_\beta\right) = 0,\ \left(1\leq l'\leq m-1\right) \tag{B2c}$$

And

$$\sum_{\alpha=1}^{n}\left((\mathrm{Re}c_\alpha)^2 + (\mathrm{Im}c_\alpha)^2\right) - 1 = 0. \tag{B2d}$$

C CALCULATED RESULTS OF TIME-DEPENDENT COEFFICIENTS $\{c_i(t)\}$ IN EQ. 31.

Equation 32 can be rewritten in the rotating approximation (RWA) as

$$\dot{c}_0(t) = -iV^a_{01}\exp(i\Delta_1 t)c_1(t) - iV^b_{02}\exp(i\Delta_2 t + i\zeta)c_2(t), \quad \text{(C1a)}$$

$$\dot{c}_1(t) = -iV^a_{01}\exp(-i\Delta_1 t)c_0(t), \quad \text{(C1b)}$$

$$\dot{c}_2(t) = -iV^b_{02}\exp(-i\Delta_2 t - i\zeta)c_0(t), \quad \text{(C1c)}$$

Where $\zeta \equiv \zeta_a - \zeta_b$ is the laser relative phase between the two lasers. Note that the laser phases ζ_a and ζ_b are transferred to the electronic states.

The coupled differential equations in Eq. (B1) are analytically solved under the two conditions described by **Eqs. 34a**, **34b** by setting the initial condition: $c_0(0) = 1,\ c_1(0) = c_2(0) = 0$ [43] such that

$$c_0(t) = \frac{\Delta^2 + V^2\left(e^{-i\Omega t} + e^{i\Omega t}\right)}{\Omega^2}, \quad \text{(C2a)}$$

$$c_1(t) = \frac{V}{2\Omega^2}\left[2\Delta e^{i\Delta t} + (\Omega - \Delta)e^{i(\Omega+\Delta)t} - (\Omega - \Delta)e^{-i(\Omega-\Delta)t}\right], \quad \text{(C2b)}$$

$$c_2(t) = -e^{-i\zeta}\frac{V}{2\Omega^2}\left[2\Delta e^{-i\Delta t} + (\Omega - \Delta)e^{-i(\Omega+\Delta)t} - (\Omega - \Delta)e^{i(\Omega-\Delta)t}\right]. \quad \text{(C2c)}$$

frontiers
in Physics

ORIGINAL RESEARCH
published: 16 July 2021
doi: 10.3389/fphy.2021.689635

Long-Lasting Orientation of Symmetric-Top Molecules Excited by Two-Color Femtosecond Pulses

Long Xu†, Ilia Tutunnikov*†, Yehiam Prior* and Ilya Sh. Averbukh**

AMOS and Department of Chemical and Biological Physics, The Weizmann Institute of Science, Rehovot, Israel

Impulsive orientation of symmetric-top molecules excited by two-color femtosecond pulses is considered. In addition to the well-known transient orientation appearing immediately after the pulse and then reemerging periodically due to quantum revivals, we report the phenomenon of *field-free long-lasting* orientation. Long-lasting means that the time averaged orientation remains non-zero until destroyed by other physical effects, e.g., intermolecular collisions. The effect is caused by the combined action of the field-polarizability and field-hyperpolarizability interactions. The dependence of degree of long-lasting orientation on temperature and pulse parameters is considered. The effect can be measured by means of second (or higher-order) harmonic generation, and may be used to control the deflection of molecules traveling through inhomogeneous electrostatic fields.

Keywords: long-lasting orientation, symmetric-top, two-color laser pulses, polarizability interaction, hyperpolarizability interaction

Correspondence:
Long Xu
long.xu@weizmann.ac.il
Ilia Tutunnikov
ilia.tutunnikov@weizmann.ac.il
Yehiam Prior
yehiam.prior@weizmann.ac.il
Ilya Sh. Averbukh
ilya.averbukh@weizmann.ac.il

†These authors have contributed equally to this work

Specialty section:
This article was submitted to Physical Chemistry and Chemical Physics,
a section of the journal Frontiers in Physics

Received: *01 April 2021*
Accepted: *18 June 2021*
Published: *16 July 2021*

Citation:
Xu L, Tutunnikov I, Prior Y and Averbukh IS (2021) Long-Lasting Orientation of Symmetric-Top Molecules Excited by Two-Color Femtosecond Pulses.
Front. Phys. 9:689635.
doi: 10.3389/fphy.2021.689635

1 INTRODUCTION

Over the years, diverse optical methods have been developed to align and orient molecules of varying complexity and many applications related to studies of molecular and photon-induced processes are based on the ability to control the absolute orientation of the molecules. For reviews, see [1–6].

There are several laser-based strategies for achieving molecular orientation in the gas phase, including using a combination of intense non-resonant laser and weak electrostatic fields [7–15], and using strong single-cycle terahertz (THz) pulses [16–23], alone or together with optical pulses [24–26]. In addition, laser and THz pulses with twisted polarization were shown to be effective for inducing enantioselective orientation of chiral molecules [27–33].

The techniques listed above rely on the laser-dipole and/or laser-polarizability interactions. Another route to molecular orientation stems from higher-order laser-molecule interactions, e.g., the laser field-hyperpolarizability interaction. Non-resonant phase-locked two-color laser pulses consisting of the fundamental wave (FW) and its second harmonic (SH) were used for inducing molecular orientation by interacting with the molecular hyperpolarizability [34–49].

Here, we investigate the orientation dynamics of symmetric-top molecules excited by single two-color femtosecond laser pulses. In addition to the well-known transient orientation appearing immediately as a response to the laser excitation, we predict the existence of *long-lasting orientation*. Long-lasting means that the time-averaged orientation remains non-zero, within the model, indefinitely or until destroyed by additional physical effects, e.g., by collisions. The long-lasting orientation induced by a two-color pulse has an intricate dependence on *both* the molecular polarizability and hyperpolarizability. Related effects have been recently observed in chiral molecules excited by one-color laser pulses with twisted polarization [30, 32] and investigated in non-linear molecules excited by THz pulses [23, 33].

The paper is organized as follows. In the next section, we describe our numerical approaches for simulating the laser-driven molecular rotational dynamics. In **Section 3**, we present the long-lasting orientation, which is the main result of this work. **Section 4** is devoted to a qualitative analysis of the effect, and a derivation of the approximate classical formula for the degree of long-lasting orientation. Additional results are presented in **Section 5**.

2 NUMERICAL METHODS

In this work, the rotational dynamics of symmetric-top molecules is treated within the rigid rotor approximation. We performed both classical and quantum mechanical simulations of molecular rotation driven by two-color laser fields. This section outlines the theoretical approaches used in both cases.

2.1 Classical Simulation

In the classical limit, the rotational dynamics of a single rigid top is described by Euler's equations [50]

$$\mathbf{I}\dot{\mathbf{\Omega}} = (\mathbf{I}\mathbf{\Omega})\times\mathbf{\Omega} + \mathbf{T}, \tag{1}$$

where $\mathbf{I} = \mathrm{diag}(I_a, I_b, I_c)$ is the moment of inertia tensor, $\mathbf{\Omega} = (\Omega_a, \Omega_b, \Omega_c)$ is the angular velocity, and $\mathbf{T} = (T_a, T_b, T_c)$ is the external torque resulting from the interaction between field-induced dipole moment and the electric field. All the quantities in **Eq. 1** are expressed in the rotating molecular frame of reference, equipped with a basis set including the three principal axes of inertia, *a*, *b*, and *c*.

In the laboratory frame of reference, the electric field of a two-color laser pulse is defined by

$$\mathbf{E}(t) = \varepsilon_1(t)\cos(\omega t)\mathbf{e}_Z + \varepsilon_2(t)\cos(2\omega t + \varphi)\mathbf{e}_{\mathrm{SH}}, \tag{2}$$

where the two terms correspond to the FW and its SH, respectively. ω is the carrier frequency of the FW field, φ is the relative phase of the second harmonic, $\varepsilon_n(t) = \varepsilon_{n,0}\exp[-2\ln 2\,(t/\sigma_n)^2]$, $n = 1, 2$, is the field's envelope with $\varepsilon_{n,0}$ as the peak amplitude, and σ_n is the full width at half maximum (FWHM) of the laser pulse intensity profile. The polarization direction of the SH field is given by $\mathbf{e}_{\mathrm{SH}} = \cos(\phi_{\mathrm{SH}})\mathbf{e}_Z + \sin(\phi_{\mathrm{SH}})\mathbf{e}_X$, where ϕ_{SH} is its angle with respect to the Z axis, $\mathbf{e}_Z$ and $\mathbf{e}_X$ are the unit vectors along laboratory Z and X axes, respectively. The electric field in the molecular frame of reference can be expressed as

$$\mathbf{E}(t) = \varepsilon_1(t)\cos(\omega t)\mathbf{e}_1 + \varepsilon_2(t)\cos(2\omega t + \varphi)\mathbf{e}_2, \tag{3}$$

where $\mathbf{e}_1 = Q\mathbf{e}_Z$ and $\mathbf{e}_2 = Q\mathbf{e}_{\mathrm{SH}}$ are the unit vectors expressed in the molecular frame of reference. Q is a 3×3 time-dependent orthogonal matrix relating the laboratory and the molecular frames of reference. It is parametrized by a quaternion, q which has an equation of motion $\dot{q} = q\Omega/2$, with $\Omega = (0, \mathbf{\Omega})$ being a pure quaternion [51, 52]. Considering laser-polarizability and laser-hyperpolarizabiltiy interactions, the torque induced by a two-color field has two contributions $\mathbf{T} = \mathbf{T}^{\alpha} + \mathbf{T}^{\beta}$, where [53]

$$\mathbf{T}^{\alpha} = \overline{(\boldsymbol{\alpha}\mathbf{E}\times\mathbf{E})} = \frac{\varepsilon_1^2}{2}(\boldsymbol{\alpha}\mathbf{e}_1)\times\mathbf{e}_1 + \frac{\varepsilon_2^2}{2}(\boldsymbol{\alpha}\mathbf{e}_2)\times\mathbf{e}_2, \tag{4}$$

$$\begin{aligned}\mathbf{T}_i^{\beta} &= \frac{1}{2}\overline{[(\mathbf{E}\boldsymbol{\beta}\mathbf{E})\times\mathbf{E}]}_i \\ &= \sum_{m,n,j,k}\frac{\varepsilon_1^2\varepsilon_2}{4}\epsilon_{ijk}\beta_{mnj}e_{1m}e_{2n}e_{1k} + \sum_{m,n,j,k}\frac{\varepsilon_1^2\varepsilon_2}{8}\epsilon_{ijk}\beta_{mnj}e_{1m}e_{1n}e_{2k}.\end{aligned} \tag{5}$$

Here, the overline $\overline{(\cdots)}$ represents averaging over the optical cycle, $\boldsymbol{\alpha}$ and $\boldsymbol{\beta}$ are the polarizability and hyperpolarizability tensors, respectively. ϵ_{ijk} is the Levi-Civita symbol, β_{mnj} is a component of the hyperpolarizability tensor, e_{1m} and e_{2m} are the components of the FW and SH fields, respectively.

To simulate the behavior of an ensemble of non-interacting molecules, we use the Monte Carlo approach. For each molecule, the Euler's equations [**Eq. 1**] with the torques in **Eqs. 4**, **5** are solved numerically using the standard fourth order Runge-Kutta algorithm. In the simulations we used ensembles consisting of $N \gg 1$ molecules. The initial uniform random quaternions, representing isotropically distributed molecules, were generated using the recipe from [54]. Initial angular velocities are distributed according to the Boltzmann distribution,

$$f(\mathbf{\Omega}) \propto \prod_i \exp\left(-\frac{I_i\Omega_i^2}{2k_BT}\right), \tag{6}$$

where $i = a, b, c$, T is the temperature and k_B is the Boltzmann constant.

2.2 Quantum Simulation

The Hamiltonian describing the rotational degrees of freedom of a molecule and the molecular polarizability and hyperpolarizability couplings to external time-dependent fields can be written as $H(t) = H_r + H_{\mathrm{int}}(t)$, where H_r is the field-free Hamiltonian [55], and $H_{\mathrm{int}}(t)$ is the molecule-field interaction potential, with two contributions $H_{\mathrm{int}}(t) = V_\alpha + V_\beta$, where [56]

$$V_\alpha = -\frac{1}{2}\sum_{i,j}\alpha_{ij}E_iE_j, \quad V_\beta = -\frac{1}{6}\sum_{i,j,k}\beta_{ijk}E_iE_jE_k. \tag{7}$$

Here E_i, α_{ij}, and β_{ijk} are the components of the field vector, polarizability tensor $\boldsymbol{\alpha}$, and hyperpolarizability tensor $\boldsymbol{\beta}$, respectively. Since the optical carrier frequency of the laser fields, ω [see **Eq. 2**], is several orders of magnitude larger than a typical rotational frequency of small molecules, the energy contribution due to the interaction with the molecular permanent dipole, $\boldsymbol{\mu}$, $-\boldsymbol{\mu}\cdot\mathbf{E}(t)$ is negligible.

We use the eigenstates of H_r, $|JKM\rangle$, describing the field-free motion of quantum symmetric-top [55], as the basis set in our numerical simulations. The three quantum numbers are J, K and M, where J is the total angular momentum, while K and M are its projections on the molecular a axis and the laboratory-fixed Z axis, respectively. The time-dependent Schrödinger equation $i\hbar\partial_t|\Psi(t)\rangle = H(t)|\Psi(t)\rangle$ is solved by numerical exponentiation of the Hamiltonian matrix (see Expokit [57]) with the initial state being one of the field-free eigenstates, $|\Psi(t=0)\rangle = |JKM\rangle$. The degree of molecular orientation is derived by calculating the induced polarization, the expectation

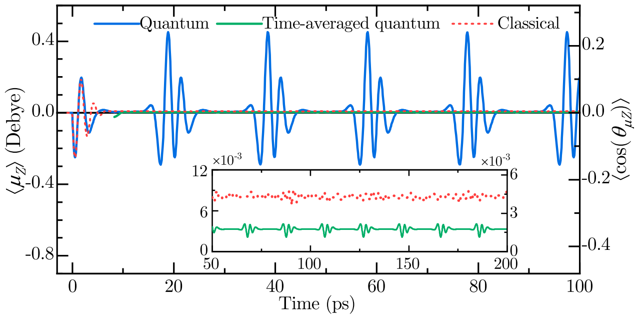

FIGURE 1 | Z-projection of the dipole moment, $\langle \mu_Z \rangle$ and the orientation factor, $\langle \cos(\theta_{\mu Z}) \rangle \equiv \langle \mu_Z \rangle / \mu$ as a function of time for CH_3F molecule at initial rotational temperature $T = 5\,\mathrm{K}$. Here μ is the magnitude of the dipole moment and $\theta_{\mu Z}$ denotes the angle between the dipole moment and laboratory Z axis. The solid blue and dotted red lines represent the results of quantum and classical simulations, respectively. The solid green line is the time average defined by $\overline{\langle \mu_Z \rangle (t)} = (\Delta t)^{-1} \int_{t-\Delta t/2}^{t+\Delta t/2} dt' \langle \mu_Z \rangle (t')$, where $\Delta t = 19.6\,\mathrm{ps}$. The inset shows a magnified portion of the signals.

value of the dipole projection. The polarization along each of the axes in the laboratory-fixed frame of reference is given by

$$\langle \mu_i^{(J,K,M)} \rangle (t) = \langle \Psi(t) | \boldsymbol{\mu} \cdot \mathbf{e}_i | \Psi(t) \rangle, \tag{8}$$

where $\mathbf{e}_i$ represents one of the unit vectors $\mathbf{e}_X, \mathbf{e}_Y, \mathbf{e}_Z$. Thermal effects are accounted for by computing the incoherent average of the time-dependent polarizations obtained for the various initial states $|JKM\rangle$. The relative weight of each of the projections $\langle \mu_i^{(J,K,M)} \rangle (t)$ is defined by the Boltzmann distribution,

$$\langle \mu_i \rangle (t) = \frac{1}{\mathcal{Z}} \sum_{J,K,M} \epsilon_K \exp\left[-\frac{\varepsilon_{J,K,M}}{k_B T} \right] \langle \mu_i^{(J,K,M)} \rangle (t), \tag{9}$$

where $\mathcal{Z} = \sum_{J,K,M} \epsilon_K \exp(-\varepsilon_{J,K,M}/k_B T)$ is the partition function, and $\varepsilon_{J,K,M}$ is the energy/eigenvalue corresponding to $|JKM\rangle$ state. For molecules with two or more identical atoms, an additional statistical factor ϵ_K must be included in the distribution [58]. For the case of methyl fluoride (CH_3F) molecule considered in this work, ϵ_K is given by

$$\epsilon_K = \frac{(2I_H + 1)^3}{3} \left[1 + \frac{2\cos(2\pi K/3)}{(2I_H + 1)^2} \right], \tag{10}$$

where $I_H = 1/2$.

In our simulations, the basis set included all the states with $J \leq 30$. For our sample molecule, CH_3F, at initial temperature of $T = 5\,\mathrm{K}$, this means that initial states with $J \leq 8$ were included. Additional details about the numerical simulations, including the matrix elements of the interaction Hamiltonian H_{int}, can be found in **Supplementary Appendix A**.

3 LONG-LASTING ORIENTATION

We continue to consider the methyl fluoride (CH_3F), as an example for a symmetric-top molecule. The molecule is excited by a two-color pulse in which the polarizations of the FW and SH are parallel and along Z axis [$\phi_{\mathrm{SH}} = 0$, see **Eq. 2**]. In addition, here we set the relative phase between them to be zero ($\varphi = 0$). Later on we discuss what changes when this phase changes. **Table 1** summarizes the molecular properties of CH_3F. Moments of inertia, dipole moment, and polarizability tensor components are taken from NIST, where they were computed within the density functional theory (DFT, method CAM-B3LYP/aug-cc-pVTZ) [59]. The hyperpolarizability values are literature values taken from [60].

Figure 1 shows the projection of the dipole moment along the laboratory Z axis, $\langle \mu_Z \rangle$, calculated classically and quantum mechanically (see Methods **Section 2**). In the classical case, the angle brackets $\langle \cdots \rangle$ denote ensemble average, that is the average of the dipole projections of $N = 10^8$ molecules, initially isotropically distributed in space and having random angular velocities [see **Eq. 6**]. In the quantum case, $\langle \cdots \rangle$ denotes incoherent average of initially populated rotational states [see **Eq. 9**]. Note that the averages $\langle \mu_X \rangle$ and $\langle \mu_Y \rangle$ are zero. Here, the initial temperature is $T = 5\,\mathrm{K}$, the peak intensities of the FW and SH fields are $I_{\mathrm{FW}} = 8 \times 10^{13}\,\mathrm{W/cm^2}$ and $I_{\mathrm{SH}} = 3 \times 10^{13}\,\mathrm{W/cm^2}$, respectively, and the duration (FWHM) of the pulses are $\sigma_1 = \sigma_2 = 120\,\mathrm{fs}$ [see **Eq. 2**]. On the short time scale (first $\approx 2\,\mathrm{ps}$), the classical and quantum results are in remarkable agreement, and show the expected immediate response to a kick by a two-color pulse. On the long time scale, the quantum mechanical simulation exhibits distinct quantum revivals of the orientation [61–65]. This transient orientation effect is well studied and was observed in the past [34–49].

In the case of symmetric-top molecules considered here, we observe *long-lasting (persistent)* orientation, a previously unreported phenomenon in two-color orientation schemes. The inset in **Figure 1** demonstrates that after the initial oscillations are washed out, the classical polarization/degree of orientation attains a constant, nonzero value. In the quantum case too, despite its being partially masked by the revivals, the sliding time average of the signal is approximately constant and it persists indefinitely within the adopted model. This long-lasting orientation is one of the main results of this work.

Several comments are in order. Additional physical effects can distort the long-term field-free picture of identical periodically appearing revivals seen in **Figure 1**. These include the centrifugal distortion and the radiation emission due to rapidly rotating molecular permanent dipole moment. Dephasing of the rotational states caused by the centrifugal distortion leads to the eventual decay of the revivals' peaks [21, 22]. Nevertheless, the average dipole remains almost unchanged (see [23]). The radiative emission results in the gradual decrease of the rotational energy [21, 22]. However, for a rarefied molecular gas, the estimated relative energy loss during a single revival is very small. The proper description of the behavior on an even longer timescale (nanoseconds), requires the inclusion of collisions and fine structure effects [66, 67], which is beyond the scope of the current work. Furthermore, it should be noted that higher laser pulse intensities lead to higher degree of orientation, but when the intensity is high enough for molecular ionization, another effect kicks in, namely

TABLE 1 | Molecular properties (in atomic units) of CH_3F: moments of inertia, nonzero elements of dipole moment, polarizability tensor, and hyperpolarizability tensor. All the quantities are represented in the reference frame of molecular principal axes of inertia.

Moments of inertia	Dipole components	Polarizability components	Hyperpolarizability components
$I_a = 20982$ $I_b = 129238$ $I_c = 129238$	$\mu_a = -0.736$	$\alpha_{aa} = 18.38$ $\alpha_{bb} = 16.76$ $\alpha_{cc} = 16.76$	$\beta_{aaa} = 40.449$ $\beta_{abb} = \beta_{acc} = 26.970$ $\beta_{bbb} = -\beta_{bcc} = -11.019$

orientation mechanism due to selective molecular ionization of molecules with specific orientation [43, 44]. Considering this kind of orientation is also beyond the scope of this work.

4 LONG-LASTING ORIENTATION - A QUALITATIVE DESCRIPTION

An explicit form of the interaction potential [**Eq. 7**] can be obtained by expressing the electric field vector in the rotating molecular frame of reference. For the sake of the current discussion, this can be done conveniently by using an orthogonal rotation matrix parameterized by the three Euler angles, $R(\phi, \theta, \chi)$. We use the definition convention adopted in [55], according to which, ϕ and θ are the standard azimuth and polar angles defining the orientation of the molecular frame z axis, and χ is the additional rotation angle about z axis. The basis set in the rotating molecular frame of reference consists of the three principal axes of inertia, a, b, c. For molecules belonging to the C_{3v} symmetry group (such as CH_3F), there are three non-zero polarizability components (two of them are equal), and 11 non-zero hyperpolarizability components (three of which are independent) [68]. For definiteness, we associate the axis of the three-fold rotational symmetry with the most polarizable molecular principal axis a (z axis in the rotating frame), having the smallest moment of inertia, I_a. In this case, the non-zero polarizability elements are $\alpha_{aa} > \alpha_{bb} = \alpha_{cc}$, and the independent hyperpolarizability elements are β_{aaa}, $\beta_{abb} = \beta_{acc}$, $\beta_{bbb} = -\beta_{bcc}$. The other non-zero hyperpolarizability elements are obtained by permuting the indices of the independent elements [68]. The parameters of the CH_3F molecule are listed in **Table 1**.

We consider the case of a two-color pulse in which both the FW and SH are polarized along Z axis. The interaction potential is obtained by carrying out the summation in **Eq. 7** (where all the quantities are expressed in the basis of principal axes of inertia) and we average over the optical cycle. The resulting potential has two contributions,

$$\overline{V}_\alpha(\theta) = -\frac{\varepsilon_1^2(t) + \varepsilon_2^2(t)}{4}(\alpha_{aa} - \alpha_{bb})\cos^2(\theta), \tag{11}$$

$$\begin{aligned}\overline{V}_\beta(\theta, \chi) = &-\frac{\varepsilon_1^2(t)\varepsilon_2(t)}{8}\cos(\varphi)\sin^3(\theta)\cos(3\chi)\beta_{bcc} \\ &-\frac{\varepsilon_1^2(t)\varepsilon_2(t)}{8}\cos(\varphi)\left[3\sin^2(\theta)\cos(\theta)\beta_{abb}\right. \\ &\left.+\cos^3(\theta)\beta_{aaa}\right].\end{aligned} \tag{12}$$

To facilitate the qualitative discussion in this section, we let $\beta_{bbb} = \beta_{bcc} = 0$. These elements of the hyperpolarizability tensor are the smallest (see **Table 1**), and their omission does not affect the qualitative features of the discussed phenomena. Thus, the hyperpolarizability interaction becomes

$$\overline{V}_\beta^\star(\theta) = -\frac{\varepsilon_1^2(t)\varepsilon_2(t)}{8}\cos(\varphi)\left[3\sin^2(\theta)\cos(\theta)\beta_{abb} + \cos^3(\theta)\beta_{aaa}\right]. \tag{13}$$

And $\overline{V} = \overline{V}_\alpha + \overline{V}_\beta^\star$ is a function of a single variable θ—the polar angle between the symmetry axis of the molecule (a axis) and the laboratory Z axis (axis of laser polarization).

The two parts of the interaction potential lead to two distinct effects. $\overline{V}_\alpha(\theta)$ is a symmetric function of θ (about $\theta = \pi/2$), and a kick by such a potential results in molecular alignment (for reviews, see [1–6]). The second part, $\overline{V}_\beta^\star(\theta)$ is an asymmetric function of θ, causing molecular orientation. Transient orientation of linear molecules excited by two-color laser pulses has been observed [38–40, 42, 44] and is being studied theoretically [45–49]. **Figure 2** shows the angular dependence of $\overline{V}_\beta^\star(\theta)$, $\cos(\varphi)[3b\sin^2(\theta)\cos(\theta) + \cos^3(\theta)]$, see **Eq. 13**. The orienting potential is proportional to $\cos(\varphi)$, such that the orientation is zero for $\varphi = \pi/2$. Also, the relative phase can be used to control the orientation direction. To simplify the following expressions, we set $\varphi = 0$.

4.1 Approximate Classical Formula

In the case of weak excitation, we can derive an approximate classical formula for the degree of long-lasting orientation. Since the long-lasting orientation manifests itself under field-free conditions, we begin by considering the free motion of a single classical symmetric top. The free motion of the unit vector **a**, pointing along the rotational symmetry axis of the molecule, is given by a simple vectorial differential equation

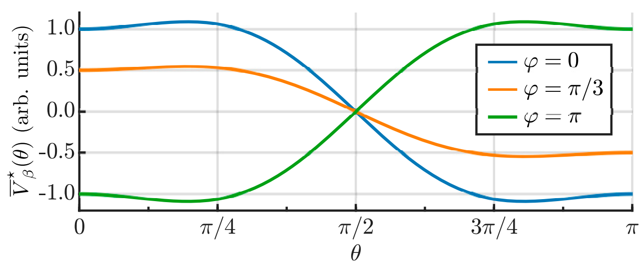

FIGURE 2 | Angle dependence of the potential $\overline{V}_\beta^\star(\theta)$, $\cos(\varphi)[3b\sin^2(\theta)\cos(\theta) + \cos^3(\theta)]$, see **Eq. 13**, for different relative phases, φ. Here, $b = \beta_{abb}/\beta_{aaa} = 2/3$.

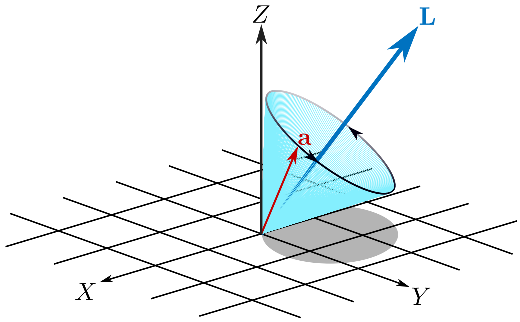

FIGURE 3 | Illustration of precession of the vector **a** about the angular momentum vector **L**. The tip of **a** describes a circle, while the arrow lies on the surface of a cone. The angular frequency of the precession is *L*/*I*, see **Eq. 14**.

$\dot{\mathbf{a}} = (\mathbf{L}/I)\times\mathbf{a}$. Here, $\mathbf{L}$ is the conserved angular momentum vector, I is the moment of inertia along the orthogonal axes b and c ($I_a < I_b = I_c \equiv I$). The solution of this equation is given by

$$\mathbf{a}(t) = \mathbf{L}\frac{\mathbf{L}\cdot\mathbf{a}(0)}{L^2} + \left[\mathbf{a}(0) - \mathbf{L}\frac{\mathbf{L}\cdot\mathbf{a}(0)}{L^2}\right]\cos\left(\frac{L}{I}t\right) + \frac{\mathbf{L}}{L}\times\mathbf{a}(0)\sin\left(\frac{L}{I}t\right), \tag{14}$$

where L is the magnitude of angular momentum and $\mathbf{a}(0)$ is vector $\mathbf{a}$ at $t = 0$. The above equation describes precession of $\mathbf{a}$ around $\mathbf{L}$ at a rate L/I (see **Figure 3**). In the special case of a linear molecule, $L_a = \mathbf{L}\cdot\mathbf{a}(0) = 0$, so that **Eq. 14** reduces to

$$\mathbf{a}(t) = \mathbf{a}(0)\cos\left(\frac{L}{I}t\right) + \frac{\mathbf{L}}{L}\times\mathbf{a}(0)\sin\left(\frac{L}{I}t\right). \tag{15}$$

Equation 15 describes a uniform rotation of $\mathbf{a}$ in a plane perpendicular to the angular momentum vector $\mathbf{L}$.

The degree of long-lasting orientation (see the inset of **Figure 1**) can be obtained by considering the ensemble average projection of the molecular axis $\mathbf{a}$ on the laboratory Z axis, $a_Z = \mathbf{e}_Z\cdot\mathbf{a}$, and then evaluating its time average

$$\overline{\langle a_Z\rangle} = \lim_{\tau\to\infty}\frac{1}{\tau}\int_0^\tau \langle \mathbf{e}_Z\cdot\mathbf{a}(t)\rangle dt, \tag{16}$$

where $t = 0$ defines the end of the two-color pulse (when the free motion begins). Note that for CH_3F the molecular dipole, $\boldsymbol{\mu}$ points along $-\mathbf{a}$ (see **Table 1**). Next, we exchange the order of the ensemble and time averaging. The time average of a_Z is obtained from **Eq. 14** and it reads

$$\overline{a_Z} = \frac{(L_Z)_f (L_a)_f}{L_f^2}, \tag{17}$$

where $L_Z = \mathbf{e}_Z\cdot\mathbf{L}$, $L_a = \mathbf{a}\cdot\mathbf{L}$, and subindex f denotes that all the quantities are taken after the pulse. With the potential in **Eqs. 11, 13**, both ϕ and χ are cyclic coordinates. Therefore, the canonically conjugate angular momenta L_Z and L_a are conserved. As a consequence, **Eq. 17** becomes

$$\overline{a_Z} = \frac{L_Z L_a}{L_f^2}, \tag{18}$$

where L_Z and L_a are taken before the pulse. At this stage, we can conclude that the long-lasting orientation is strictly zero when the initial temperature is zero and/or in the limit of a linear rotor. In the first case, $L_Z = L_a = 0$, while in the second case $L_a = 0$, because $I_a = 0$ for linear molecules.

For the ensemble averaging, it is advantageous to express all the quantities in the basis of principal axes of inertia. The magnitude of the angular momentum after the pulse, L_f^2, is given by

$$L_f^2 = (L_b + \delta L_b)^2 + (L_c + \delta L_c)^2 + L_a^2, \tag{19}$$

where L_a, L_b, L_c are the values before the pulse, while δL_b and δL_c are the changes in angular momentum components due to laser excitation. Explicit expressions for δL_b and δL_c can be obtained using the impulsive approximation. In this approximation, we assume that the duration of the two-color pulse is much shorter than the typical period of molecular rotation, such that the molecular orientation remains unchanged during the pulse. Using this approximation and the Euler-Lagrange equations, we derive the explicit expressions for δL_b and δL_c (the details are summarized in **Supplementary Appendix B**),

$$\delta L_b = f(\theta)\sin(\chi), \tag{20}$$

$$\delta L_c = f(\theta)\cos(\chi), \tag{21}$$

where

$$f(\theta) = P_1\sin(2\theta) + P_2\sin(\theta)\left[(3\cos(2\theta)+1)\beta_{abb} - 2\cos^2(\theta)\beta_{aaa}\right], \tag{22}$$

and

$$P_1 = \frac{\sigma}{4}\sqrt{\frac{\pi}{\ln(16)}}\left(\varepsilon_{1,0}^2 + \varepsilon_{2,0}^2\right)(\alpha_{bb} - \alpha_{aa}), \tag{23}$$

$$P_2 = \frac{3\sigma}{16}\sqrt{\frac{\pi}{\ln(64)}}\varepsilon_{1,0}^2\varepsilon_{2,0}. \tag{24}$$

Here $\sigma = \sigma_1 = \sigma_2$, $\varepsilon_{1,0}$, and $\varepsilon_{2,0}$ are the peak amplitudes of the FW and SH, respectively. L_Z is expressed in terms of the molecular frame components $L_{a,b,c}$ using the rotation matrix $R(\phi,\theta,\chi)$, such that

$$L_Z = -\sin(\theta)\cos(\chi)L_b + \sin(\theta)\sin(\chi)L_c + L_a\cos(\theta). \tag{25}$$

Finally, we carry out the ensemble average

$$\langle\overline{a_Z}\rangle = \frac{1}{\mathcal{Z}}\int_\Omega\int_{L^3}\frac{L_Z L_a}{L_f^2}\exp\left[-\frac{1}{2k_B T}\left(\frac{L_a^2}{I_a} + \frac{L_b^2}{I} + \frac{L_c^2}{I}\right)\right] \times \sin\theta\, d\theta\, d\chi\, d\phi\, dL_a\, dL_b\, dL_c, \tag{26}$$

where $\mathcal{Z}$ is the partition function. To simplify the integral, we assume that $|\delta L_b/L_b|, |\delta L_c/L_c| \ll 1$ [see **Eqs. 19–21**] and expand $1/L_f^2$ in powers of $f(\theta)$ [see **Eq. 22**]. Only terms proportional to even powers of $f(\theta)$ contribute to the integral. We consider the first non-vanishing term proportional to $f^2(\theta)$, such that [see **Supplementary Equation S26**]

$$\langle\overline{a_Z}\rangle \approx \frac{\tilde{I}_L(w)}{4k_B T I}\sqrt{\frac{w}{\pi}}\int f^2(\theta)\sin(2\theta)\,d\theta, \tag{27}$$

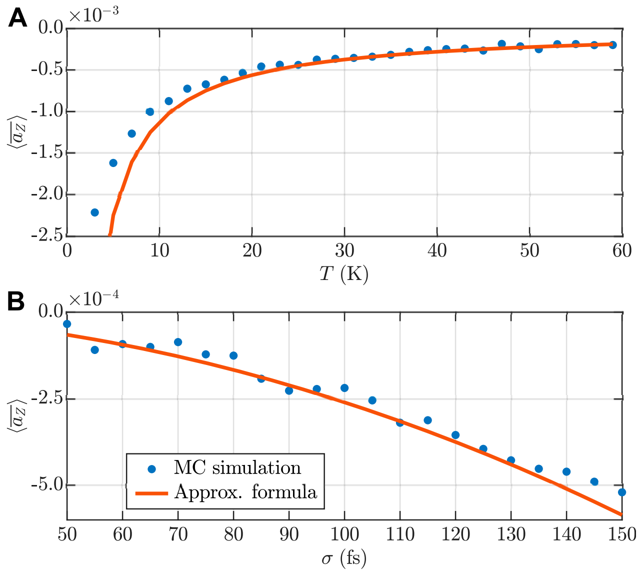

FIGURE 4 | (A) Temperature and **(B)** pulse duration dependence of the degree of long-lasting orientation obtained using the approximate formula in **Eq. 28** (red line) and numerically using the impulsive approximation (blue dots). Here $I_{FW} = 2 \times 10^{13}$ W/cm^2, $I_{SH} = 0.75 \times 10^{13}$ W/cm^2, and $\sigma = 120$ fs. Each point is an average of 10^8 sample molecules. In **B**, the temperature is fixed to $T = 30$ K.

where $w = I/I_a$, and $\tilde{I}_L(w)$ is a monotonic function of $w > 1$. In the limit of a linear molecule $(w \to \infty)$, $\tilde{I}_L(w) \to 0$ [see **Supplementary Equation S27 and Figure S1**].

For the polarizability interaction alone, $f(\theta) = P_1 \sin(2\theta)$, and $\int f^{2n}(\theta) \sin(2\theta)\, d\theta = 0$. For the hyperpolarizability interaction alone, $f(\theta) = P_2 \sin(\theta)[(3\cos(2\theta) + 1)\beta_{abb} - 2\cos^2(\theta)\beta_{aaa}]$ which is a symmetric function (about $\theta = \pi/2$), and therefore $\int f^n(\theta) \sin(2\theta)\, d\theta = 0$ for all n. Only when both polarizability and hyperpolarizability interactions are included, $\langle \overline{a_Z} \rangle \neq 0$. In this case,

$$\langle \overline{a_Z} \rangle \approx \frac{16\tilde{I}_L(w)}{105 k_B T I} \sqrt{\frac{w}{\pi}} P_1 P_2 (2\beta_{abb} - 3\beta_{aaa}), \qquad (28)$$

where P_1 and P_2 are given by **Eqs. 23**, **24**, and $\tilde{I}_L(w)$ is given by **Supplementary Equation S27**. The details of the derivation of **Eq. 28** are summarized in **Supplementary Appendix C**.

According to **Eq. 28**, the degree of long-lasting orientation scales as σ^2/T. In **Figure 4**, we compare the temperature (panel **A**) and pulse duration (panel **B**) dependencies of the long-lasting orientation obtained using the approximate formula in **Eq. 28** with the numerical results obtained by evaluating the formula in **Eq. 18** using the Monte Carlo approach as described in the Methods **Section 2** (using the impulsive approximation, see **Supplementary Appendix B**).

There is a good agreement between the numerical results and the results obtained using the approximate formula, especially at higher temperatures (higher initial angular momenta), where the assumption $|\delta L_b/L_b|, |\delta L_c/L_c| \ll 1$ is well satisfied. The pulse duration dependence shows the connection to the energy gained by the molecule from the laser pulse. In the limit of weak excitation (low pulse intensity and/or high temperature), the approximate formula also reveals the more involved dependence on the fields' amplitudes, according to **Eqs. 23**, **24**.

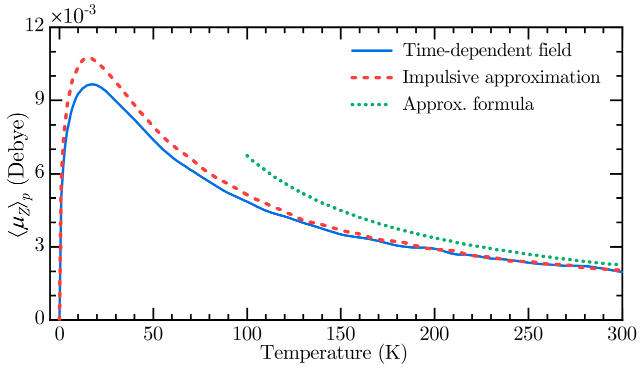

FIGURE 5 | Classically calculated permanent values of Z-projection of the dipole moment. The field parameters are similar to **Figure 1**. Cases of fully time-dependent field (solid blue) and using impulsive approximation (dashed red) are compared. The dotted green line is obtained using the approximate formula in **Eq. 28** with $\langle \mu_Z \rangle_p = -\mu \langle \overline{a_Z} \rangle$ (dipole moment points againts a axis, see **Table 1**).

The hyperpolarizability part of the interaction potential, $\overline{V}^{\star}_{\beta}(\theta)$ [see **Eq. 13**], is an asymmetric function of θ (about $\theta = \pi/2$, see **Figure 2**), similar to the orienting potential, which is proportional to $-\cos(\theta)$, due to a single THz pulse interacting with the molecular dipole, $\boldsymbol{\mu}$. As we show here and as it was shown in [23], excitation by such orienting potentials results in transient orientation followed by residual long-lasting orientation.

Despite the similarity, the mechanisms behind the long-lasting orientation induced by a femtosecond two-color and a picosecond THz pulse are not the same. It was shown in [23] that in the limit of vanishing THz pulse duration, the induced long-lasting orientation tends to zero. In other words, a δ-kick by a purely orienting potential doesn't lead to long-lasting orientation. In contrast, here we show that a δ-kick by a *combined, aligning and orienting*, potentials results in a long-lasting orientation [see the discussion under **Eq. 27**, also see **Figure 5**].

5 TEMPERATURE AND POLARIZATION DEPENDENCE OF THE LONG-LASTING ORIENTATION

Figure 5 depicts the long-lasting orientation of the dipole moment as a function of temperature for the case of collinearly polarized two-color pulse. Due to the short pulse duration ($\sigma = 120$ fs), the results of the fully time-dependent simulation (solid blue line) are well reproduced using the impulsive approximation (dashed red line). The impulsive approximation is described in **Supplementary Appendix B**. As mentioned in **Section 4**, the long-lasting orientation vanishes at $T = 0$ K, (see **Eq. 18**). At high temperatures, the long-lasting orientation decreases as $\propto T^{-1}$. Therefore, there should be an optimal temperature for which the long-lasting orientation is maximal. As is shown in **Figure 5**, for the field parameters used here, the optimal temperature is $T \approx 20$ K. In

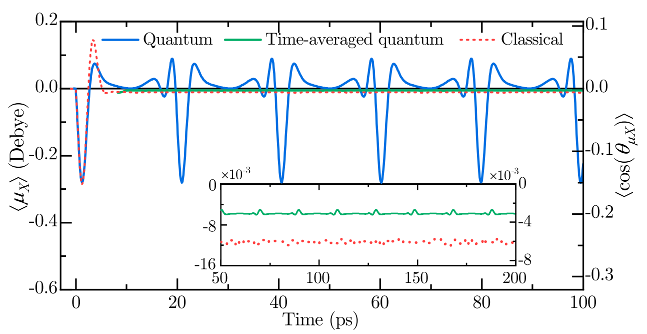

FIGURE 6 | X-projection of the dipole moment, $\langle\mu_X\rangle$ and the orientation factor, $\langle\cos(\theta_{\mu X})\rangle \equiv \langle\mu_X\rangle/\mu$ as a function of time. $\theta_{\mu X}$ denotes the angle between the dipole moment and laboratory X axis. The conditions used here are the same as in the case shown in **Figure 1**, except that the angle between the polarizations of FW and SH is $\phi_{SH} = \pi/2$ [see **Eq. 2**].

the derivation leading to the approximate formula in **Eq. 28**, we assumed $\beta_{bbb} = \beta_{bcc} = 0$. Nevertheless, the results obtained using **Eq. 28** qualitatively agree with the numerical results at higher temperatures as well (dotted green line).

As an additional example, we consider the case of a cross-polarized two-color pulse in which the polarizations of the FW and SH are along Z and X axes, respectively. **Figure 6** shows the dipole signal along the laboratory X axis. Note that the Y and Z-projections of the dipole moment, $\langle\mu_{Y,Z}\rangle$ are exactly zero. In this case, a similar transient dipole response along the polarization direction of SH can be seen. On the long time scale, it is followed by the long-lasting orientation. Notice that for the field parameters used here, the achieved degree of both transient and long-lasting orientation is higher in the case of cross-polarized FW and SH compared with **Figure 1** (also see [46]).

6 CONCLUSION

We have theoretically demonstrated a new phenomenon of long-lasting (persistent) orientation of symmetric-top molecules excited by a single two-color femtosecond pulse. The residual orientation was shown to last indefinitely (within the adopted model), or until destroyed by other physical effects, e.g., intermolecular collisions. We derived an approximate classical expression revealing several qualitative features of the phenomenon, including the scaling with temperature, pulse duration, and other field and molecular parameters. The predictions of the formula are in full agreement with the results of numerical simulations in the limit of weak excitation. A quick check for different polarizations showed that in the case of cross-polarized FW and SH, the achieved degree of both transient and long-lasting orientation may be higher than in the case of parallel configuration. The magnitude of the long-lasting dipole signal shown in this work is about 10×10^{-3} Debye, corresponding to a degree of molecular orientation of about 0.5%. This value is similar to typical experimental values observed by means of the Coulomb explosion technique, which is of the order of 0.1%, e.g., see [32, 44]. Further and careful optimization of the parameters of the two-color pulse may give rise to even higher degrees of long-lasting orientation. Moreover, it has been demonstrated before that the degree of molecular alignment/orientation can be enhanced when a sequence of several laser pulses is used instead of a single pulse [17, 69–74], and a similar approach may be beneficial for increasing the degree of the long-lasting orientation. The orientation may be measured with the help of second (or higher-order) harmonic generation [42]. In addition, the long-lasting orientation may be utilized in deflection experiments using inhomogeneous electrostatic fields [75–77], where the deflection angle of a molecular beam in a static electric field depends on the time-averaged directional cosine, $\overline{\langle\cos(\theta)\rangle}$. Therefore, although small compared to the peak value of the transient orientation, the long-lasting orientation may have a significant, observable effect on the deflection angle.

DATA AVAILABILITY STATEMENT

The raw data supporting the conclusions of this article will be made available by the authors, without undue reservation.

AUTHOR CONTRIBUTIONS

All the authors participated in formulating the problem and initiating this study. LX and IT equally contributed to the calculations and numerical simulations. All the authors participated in analyzing the results and writing the manuscript. YP and IA supervised and guided the work.

FUNDING

We gratefully acknowledge support by the Israel Science Foundation (Grant No. 746/15). IA acknowledges support as the Patricia Elman Bildner Professorial Chair. This research was made possible in part by the historic generosity of the Harold Perlman Family.

SUPPLEMENTARY MATERIAL

The Supplementary Material for this article can be found online at: https://www.frontiersin.org/articles/10.3389/fphy.2021.689635/full#supplementary-material

REFERENCES

1. Stapelfeldt H, and Seideman T. Colloquium: Aligning Molecules with strong Laser Pulses. *Rev Mod Phys* (2003) 75:543.
2. Ohshima Y, and Hasegawa H. Coherent Rotational Excitation by Intense Nonresonant Laser fields. *Int Rev Phys Chem* (2010) 29:619.
3. Fleischer S, Khodorkovsky Y, Gershnabel E, Prior Y, and Averbukh IS. Molecular Alignment Induced by Ultrashort Laser Pulses and its Impact on Molecular Motion. *Isr J Chem* (2012) 52:414.
4. Lemeshko M, Krems RV, Doyle JM, and Kais S. Manipulation of Molecules with Electromagnetic fields. *Mol Phys* (2013) 111:1648.
5. Koch CP, Lemeshko M, and Sugny D. Quantum Control of Molecular Rotation. *Rev Mod Phys* (2019) 91:035005.
6. Lin K, Tutunnikov I, Ma J, Qiang J, Zhou L, Faucher O, et al. Spatiotemporal Rotational Dynamics of Laser-Driven Molecules. *Adv Photon* (2020) 2:024002.
7. Friedrich B, and Herschbach D. Enhanced Orientation of Polar Molecules by Combined Electrostatic and Nonresonant Induced Dipole Forces. *J Chem Phys* (1999) 111:6157.
8. Sakai H, Minemoto S, Nanjo H, Tanji H, and Suzuki T. Controlling the Orientation of Polar Molecules with Combined Electrostatic and Pulsed, Nonresonant Laser fields. *Phys Rev Lett* (2003) 90:083001.
9. Goban A, Minemoto S, and Sakai H. Laser-field-free Molecular Orientation. *Phys Rev Lett* (2008) 101:013001.
10. Ghafur O, Rouzée A, Gijsbertsen A, Siu WK, Stolte S, and Vrakking MJJ. Impulsive Orientation and Alignment of Quantum-State-Selected NO Molecules. *Nat Phys* (2009) 5:289.
11. Holmegaard L, Nielsen JH, Nevo I, Stapelfeldt H, Filsinger F, Küpper J, et al. Laser-induced Alignment and Orientation of Quantum-State-Selected Large Molecules. *Phys Rev Lett* (2009) 102:023001.
12. Mun JH, Takei D, Minemoto S, and Sakai H. Laser-field-free Orientation of State-Selected Asymmetric Top Molecules. *Phys Rev A* (2014) 89:051402(R).
13. Takei D, Mun JH, Minemoto S, and Sakai H. Laser-field-free Three-Dimensional Molecular Orientation. *Phys Rev A* (2016) 94:013401.
14. Omiste JJ, and González-Férez R. Theoretical Description of the Mixed-Field Orientation of Asymmetric-Top Molecules: A Time-dependent Study. *Phys Rev A* (2016) 94:063408.
15. Thesing LV, Küpper J, and González-Férez R. Time-dependent Analysis of the Mixed-Field Orientation of Molecules without Rotational Symmetry. *J Chem Phys* (2017) 146:244304.
16. Harde H, Keiding S, and Grischkowsky D. THz Commensurate Echoes: Periodic Rephasing of Molecular Transitions in Free-Induction Decay. *Phys Rev Lett* (1991) 66:1834.
17. Averbukh IS, and Arvieu R. Angular Focusing, Squeezing, and Rainbow Formation in a Strongly Driven Quantum Rotor. *Phys Rev Lett* (2001) 87: 163601.
18. Machholm M, and Henriksen NE. Field-free Orientation of Molecules. *Phys Rev Lett* (2001) 87:193001.
19. Fleischer S, Zhou Y, Field RW, and Nelson KA. Molecular Orientation and Alignment by Intense Single-Cycle THz Pulses. *Phys Rev Lett* (2011) 107: 163603.
20. Kitano K, Ishii N, Kanda N, Matsumoto Y, Kanai T, Kuwata-Gonokami M, et al. Orientation of Jet-Cooled Polar Molecules with an Intense Single-Cycle THz Pulse. *Phys Rev A* (2013) 88:061405(R).
21. Damari R, Kallush S, and Fleischer S. Rotational Control of Asymmetric Molecules: Dipole- versus Polarizability-Driven Rotational Dynamics. *Phys Rev Lett* (2016) 117:103001.
22. Babilotte P, Hamraoui K, Billard F, Hertz E, Lavorel B, Faucher O, et al. Observation of the Field-free Orientation of a Symmetric-Top Molecule by Terahertz Laser Pulses at High Temperature. *Phys Rev A* (2016) 94:043403.
23. Xu L, Tutunnikov I, Gershnabel E, Prior Y, and Averbukh IS. Long-lasting Molecular Orientation Induced by a Single Terahertz Pulse. *Phys Rev Lett* (2020) 125:013201.
24. Daems D, Guérin S, Sugny D, and Jauslin HR. Efficient and Long-Lived Field-free Orientation of Molecules by a Single Hybrid Short Pulse. *Phys Rev Lett* (2005) 94:153003.
25. Gershnabel E, Averbukh IS, and Gordon RJ. Orientation of Molecules via Laser-Induced Antialignment. *Phys Rev A* (2006) 73:061401(R).
26. Egodapitiya KN, Li S, and Jones RR. Terahertz-induced Field-free Orientation of Rotationally Excited Molecules. *Phys Rev Lett* (2014) 112:103002.
27. Yachmenev A, and Yurchenko SN. Detecting Chirality in Molecules by Linearly Polarized Laser fields. *Phys Rev Lett* (2016) 117:033001.
28. Gershnabel E, and Averbukh IS. Orienting Asymmetric Molecules by Laser fields with Twisted Polarization. *Phys Rev Lett* (2018) 120:083204.
29. Tutunnikov I, Gershnabel E, Gold S, and Averbukh IS. Selective Orientation of Chiral Molecules by Laser fields with Twisted Polarization. *J Phys Chem Lett* (2018) 9:1105.
30. Milner AA, Fordyce JAM, MacPhail-Bartley I, Wasserman W, Milner V, Tutunnikov I, et al. Controlled Enantioselective Orientation of Chiral Molecules with an Optical Centrifuge. *Phys Rev Lett* (2019) 122:223201.
31. Tutunnikov I, Floß J, Gershnabel E, Brumer P, and Averbukh IS. Laser-induced Persistent Orientation of Chiral Molecules. *Phys Rev A* (2019) 100: 043406.
32. Tutunnikov I, Floß J, Gershnabel E, Brumer P, Averbukh IS, Milner AA, et al. Observation of Persistent Orientation of Chiral Molecules by a Laser Field with Twisted Polarization. *Phys Rev A* (2020) 101:021403(R).
33. Tutunnikov I, Xu L, Field RW, Nelson KA, Prior Y, and Averbukh IS. Enantioselective Orientation of Chiral Molecules Induced by Terahertz Pulses with Twisted Polarization. *Phys Rev Res* (2021) 3:013249.
34. Vrakking MJJ, and Stolte S. Coherent Control of Molecular Orientation. *Chem Phys Lett* (1997) 271:209.
35. Dion C, Bandrauk AD, Atabek O, Keller A, Umeda H, and Fujimura Y. Two-frequency IR Laser Orientation of Polar Molecules. Numerical Simulations for HCN. *Chem Phys Lett* (1999) 302:215.
36. Kanai T, and Sakai H. Numerical Simulations of Molecular Orientation Using strong, Nonresonant, Two-Color Laser fields. *J Chem Phys* (2001) 115:5492.
37. Takemoto N, and Yamanouchi K. Fixing Chiral Molecules in Space by Intense Two-Color Phase-Locked Laser fields. *Chem Phys Lett* (2008) 451:1.
38. De S, Znakovskaya I, Ray D, Anis F, Johnson NG, Bocharova IA, et al. Field-Free Orientation of CO Molecules by Femtosecond Two-Color Laser Fields. *Phys Rev Lett* (2009) 103:153002.
39. Oda K, Hita M, Minemoto S, and Sakai H. All-optical Molecular Orientation. *Phys Rev Lett* (2010) 104:213901.
40. Wu J, and Zeng H. Field-free Molecular Orientation Control by Two Ultrashort Dual-Color Laser Pulses. *Phys Rev A* (2010) 81:053401.
41. Zhang S, Shi J, Zhang H, Jia T, Wang Z, and Sun Z. Field-free Molecular Orientation by a Multicolor Laser Field. *Phys Rev A* (2011) 83:023416.
42. Frumker E, Hebeisen CT, Kajumba N, Bertrand JB, Wörner HJ, Spanner M, et al. Oriented Rotational Wave-Packet Dynamics Studies via High Harmonic Generation. *Phys Rev Lett* (2012) 109:113901.
43. Spanner M, Patchkovskii S, Frumker E, and Corkum P. Mechanisms of Two-Color Laser-Induced Field-free Molecular Orientation. *Phys Rev Lett* (2012) 109:113001.
44. Znakovskaya I, Spanner M, De S, Li H, Ray D, Corkum P, et al. Transition between Mechanisms of Laser-Induced Field-free Molecular Orientation. *Phys Rev Lett* (2014) 112:113005.
45. Mun JH, and Sakai H. Improving Molecular Orientation by Optimizing Relative Delay and Intensities of Two-Color Laser Pulses. *Phys Rev A* (2018) 98:013404.
46. Mun JH, Sakai H, and González-Férez R. Orientation of Linear Molecules in Two-Color Laser fields with Perpendicularly Crossed Polarizations. *Phys Rev A* (2019) 99:053424.
47. Mun JH, and Kim DE. Field-free Molecular Orientation by Delay- and Polarization-Optimized Two Fs Pulses. *Sci Rep* (2020) 10:18875.
48. Mellado-Alcedo D, Quintero NR, and González-Férez R. Linear Polar Molecule in a Two-Color Cw Laser Field: A Symmetry Analysis. *Phys Rev A* (2020) 102:023110.
49. Wang S, and Henriksen NE. Optimal Field-Free Molecular Orientation with Nonresonant Two-Color Adiabatic-Turn-On and Sudden-Turn-Off Laser Pulses. *Phys Rev A* (2020) 102:063120.
50. Goldstein H, Poole C, and Safko J. *Classical Mechanics*. San Francisco, CA: Addison-Wesley (2002).
51. Coutsias EA, and Romero L. *The Quaternions with an Application to Rigid Body Dynamics*. Sandia Technical Report (2004) SAND2004-0153.

52. Kuipers JB. *Quaternions and Rotation Sequences: A Primer with Applications to Orbits, Aerospace and Virtual Reality*. Princeton, N.J.: Princeton University Press (1999).
53. Lin K, Tutunnikov I, Qiang J, Ma J, Song Q, Ji Q, et al. All-optical Field-free Three-Dimensional Orientation of Asymmetric-Top Molecules. *Nat Commun* (2018) 9:5134.
54. LaValle SM. *Planning Algorithms*. New York: Cambridge University Press (2006).
55. Zare RN. *Angular Momentum: Understanding Spatial Aspects in Chemistry and Physics*. New York: Wiley (1988).
56. Buckingham AD. *Advances in Chemical Physics*. New York: John Wiley & Sons (2007). p. 107–42. Permanent and Induced Molecular Moments and Long-Range Intermolecular Forces.
57. Sidje RB. Expokit: A Software Package for Computing Matrix Exponentials. *ACM Trans Math Softw* (1998) 24:130.
58. McDowell RS. Rotational Partition Functions for Symmetric-top Molecules. *J Chem Phys* (1990) 93:2801.
59. Johnson RD. *NIST Computational Chemistry Comparison and Benchmark Database, Release 20*. Tech. Rep (2019).
60. Chong DP. Theoretical Calculations of Dipole Moments, Polarizabilities, and Hyperpolarizabilities of HF, OCS, O_3, CH_3F, and CH_3Cl by Local Density Approximation. *J Chin Chem Soc* (1992) 39:375.
61. Eberly JH, Narozhny NB, and Sanchez-Mondragon JJ. Periodic Spontaneous Collapse and Revival in a Simple Quantum Model. *Phys Rev Lett* (1980) 44:1323.
62. Parker J, and Stroud CR, Jr. Coherence and Decay of Rydberg Wave Packets. *Phys Rev Lett* (1986) 56:716.
63. Averbukh IS, and Perelman NF. Fractional Revivals: Universality in the Long-Term Evolution of Quantum Wave Packets beyond the Correspondence Principle Dynamics. *Phys Lett A* (1989) 139:449.
64. Felker PM. Rotational Coherence Spectroscopy: Studies of the Geometries of Large Gas-phase Species by Picosecond Time-Domain Methods. *J Phys Chem* (1992) 96:7844.
65. Robinett RW. Quantum Wave Packet Revivals. *Phys Rep* (2004) 392:1.
66. Thomas EF, Søndergaard AA, Shepperson B, Henriksen NE, and Stapelfeldt H. Hyperfine-structure-induced Depolarization of Impulsively Aligned I_2 Molecules. *Phys Rev Lett* (2018) 120:163202.
67. Thesing LV, Yachmenev A, González-Férez R, and Küpper J. The Effect of Nuclear-Quadrupole Coupling in the Laser-Induced Alignment of Molecules. *J Phys Chem A* (2020) 124:2225.
68. Buckingham AD, and Orr BJ. Molecular Hyperpolarisabilities. *Q Rev Chem Soc* (1967) 21:195.
69. Leibscher M, Averbukh IS, and Rabitz H. Molecular Alignment by Trains of Short Laser Pulses. *Phys Rev Lett* (2003) 90:213001.
70. Leibscher M, Averbukh IS, and Rabitz H. Enhanced Molecular Alignment by Short Laser Pulses. *Phys Rev A* (2004) 69:013402.
71. Lee KF, Litvinyuk IV, Dooley PW, Spanner M, Villeneuve DM, and Corkum PB. Two-pulse Alignment of Molecules. *J Phys B: Mol Opt Phys* (2004) 37:L43.
72. Bisgaard CZ, Poulsen MD, Péronne E, Viftrup SS, and Stapelfeldt H. Observation of Enhanced Field-free Molecular Alignment by Two Laser Pulses. *Phys Rev Lett* (2004) 92:173004.
73. Pinkham D, Mooney KE, and Jones RR. Optimizing Dynamic Alignment in Room Temperature CO. *Phys Rev A* (2007) 75:013422.
74. Zhang S, Lu C, Jia T, Wang Z, and Sun Z. Field-free Molecular Orientation Enhanced by Two Dual-Color Laser Subpulses. *J Chem Phys* (2011) 135: 034301.
75. Gershnabel E, and Averbukh IS. Electric Deflection of Rotating Molecules. *J Chem Phys* (2011) 134:054304.
76. Gershnabel E, and Averbukh IS. Deflection of Rotating Symmetric Top Molecules by Inhomogeneous fields. *J Chem Phys* (2011) 135: 084307.
77. Küpper J, Filsinger F, Meijer G, and Stapelfeldt H. Manipulating the Motion of Complex Molecules: Deflection, Focusing, and Deceleration of Molecular Beams for Quantum-State and Conformer Selection, in Methods in Physical Chemistry. John Wiley & Sons (2012). p. 1–28.

Conflict of Interest: The authors declare that the research was conducted in the absence of any commercial or financial relationships that could be construed as a potential conflict of interest.

frontiers in Physics

ORIGINAL RESEARCH
published: 03 August 2021
doi: 10.3389/fphy.2021.670750

Classical Limit of Quantum Mechanics for Damped Driven Oscillatory Systems: Quantum–Classical Correspondence

Jeong Ryeol Choi *

Department of Nanoengineering, Kyonggi University, Suwon, Korea

The investigation of quantum–classical correspondence may lead to gaining a deeper understanding of the classical limit of quantum theory. I have developed a quantum formalism on the basis of a linear invariant theorem, which gives an exact quantum–classical correspondence for damped oscillatory systems perturbed by an arbitrary force. Within my formalism, the quantum trajectory and expectation values of quantum observables precisely coincide with their classical counterparts in the case where the global quantum constant $\hbar$ has been removed from their quantum results. In particular, I have illustrated the correspondence of the quantum energy with the classical one in detail.

Keywords: quantum–classical correspondence, classical limit, Caldirola–Kanai Hamiltonian, quantum energy, invariant operator

Edited by:
Robert Gordon,
University of Illinois at Chicago,
United States

Reviewed by:
Chitra Rangan,
University of Windsor, Canada
Adélcio De Oliveira,
Universidade Federal de São João del-Rei, Brazil

***Correspondence:**
Jeong Ryeol Choi
choiardor@hanmail.net

Specialty section:
This article was submitted to Optics and Photonics, a section of the journal Frontiers in Physics

Received: *22 February 2021*
Accepted: *24 May 2021*
Published: *03 August 2021*

Citation:
Choi JR (2021) Classical Limit of Quantum Mechanics for Damped Driven Oscillatory Systems: Quantum–Classical Correspondence. Front. Phys. 9:670750. doi: 10.3389/fphy.2021.670750

1 INTRODUCTION

A fundamental issue in physics is to elucidate how classical mechanics (or Newtonian mechanics) emerges from a more general theory of physics, the so-called relativistic quantum mechanics. While the appearing of classical mechanics as a low velocity limit of relativistic mechanics is well known, the classical limit of quantum mechanics is a subtle problem yet. Planck's $\hbar \to 0$ limit [1] and Bohr's $n \to \infty$ limit [2] are the oldest proposals for the formulation of the classical limit of quantum theory. However, there has been controversy from the early epoch of quantum mechanics concerning this limit through different ideas and thoughts [3–9]. Accordingly, the mechanism on how to interlace the exact correspondence between the quantum and the classical theories has not yet been fully understood. Man'ko and Man'ko argued that the picture of extracting classical mechanics with the simple limitation $\hbar \to 0$ does not have universal applicability [4]. Some physicists believe that quantum mechanics is not concerned with a single particle problem but an ensemble of particles, and its $\hbar \to 0$ limit is not classical mechanics but classical statistical mechanics instead (see Ref. [5] and references therein). For more different opinions concerning the classical limit of quantum mechanics, refer in particular to Refs. [7, 8].

The purpose of this research is to establish a theoretical formalism concerning the classical limit of quantum mechanics for damped driven oscillatory systems, which reveals the quantum and classical correspondence, without any approximation or assumption except for the fundamental limitation $\hbar \to 0$. To deduce Newtonian mechanics from quantum one along this line, canonical quantum mechanics with fundamental Hamiltonian dynamics will be used. My theory is based on an invariant operator method [10–13] which is generally employed for mathematically treating quantum mechanical systems. This method enables us to derive exact quantum mechanical solutions for time-varying Hamiltonian systems. I will interpret and discuss the physical meanings of the consequences in order to derive insight into the correspondence principle.

2 INVARIANT-BASED DYNAMICS AND QUANTUM SOLUTIONS

To investigate quantum–classical correspondence, I consider a damped driven harmonic oscillator of mass m and frequency ω_0, whose Hamiltonian is given by [13–16]

$$\hat{H} = e^{-\gamma t}\frac{\hat{p}^2}{2m} + \frac{1}{2}e^{\gamma t}m\left[\omega_0^2\hat{q}^2 - 2f(t)\hat{q}\right], \tag{1}$$

where γ is a damping constant and $f(t)$ is a time-dependent driving force divided by m. From canonical Hamiltonian dynamics, one can confirm that this Hamiltonian gives an exact equation of motion for the damped driven harmonic oscillator. In the case of $f(t) = 0$, this becomes the conventional Caldirola–Kanai (CK) Hamiltonian [17, 18] which has been widely used in a phenomenological approach for the dissipation of the damped harmonic oscillator.

If I denote the classical solution of the system in configuration space as $Q(t)$, it can be written in the form $Q(t) = Q_{\mathrm{h}}(t) + Q_{\mathrm{p}}(t)$ where $Q_{\mathrm{h}}(t)$ is a homogeneous solution and $Q_{\mathrm{p}}(t)$ a particular solution. From the basic algebra in classical dynamics, we have [19]

$$Q_{\mathrm{h}}(t) = Q_0 e^{-\gamma t/2}\cos(\omega t + \varphi), \tag{2}$$

$$Q_{\mathrm{p}}(t) = \int_0^t [f(t')/\omega] e^{-\gamma(t-t')/2}\sin[\omega(t-t')]dt', \tag{3}$$

where Q_0 is the amplitude of the mechanical oscillation at $t = 0$, ω is a modified frequency which is $\omega = (\omega_0^2 - \gamma^2/4)^{1/2}$, and φ is an arbitrary phase. The canonical classical solution in the momentum space can also be represented in a similar form: $P(t) = P_{\mathrm{h}}(t) + P_{\mathrm{p}}(t)$, where $P_{\mathrm{h}}(t) = m\dot{Q}_{\mathrm{h}}(t)e^{\gamma t}$ and $P_{\mathrm{p}}(t) = m\dot{Q}_{\mathrm{p}}(t)e^{\gamma t}$.

In order to describe quantum solutions of the system, it is useful to introduce an invariant operator which is a powerful tool in elucidating mechanical properties of dynamical systems that are expressed by a time-dependent Hamiltonian like **Eq. 1**. A linear invariant operator of the system can be derived by means of the Liouville–von Neumann equation and it is given by (see **Appendix A**)

$$\hat{I} = c\left[e^{-\gamma t/2}\hat{p}_{\mathrm{p}} + m\left(\frac{\gamma}{2} - i\omega\right)e^{-\gamma t/2}\hat{q}_{\mathrm{p}}\right]e^{i\omega t}, \tag{4}$$

where $\hat{p}_{\mathrm{p}} = \hat{p} - P_{\mathrm{p}}(t)$, $\hat{q}_{\mathrm{p}} = \hat{q} - Q_{\mathrm{p}}(t)$ and $c = (2\hbar m\omega)^{-1/2}e^{i\chi}$ with a real constant phase χ. The eigenvalue equation of this operator can be expressed in the form

$$\hat{I}|\phi\rangle = \lambda|\phi\rangle, \tag{5}$$

where λ is the eigenvalue and $|\phi\rangle$ is the eigenstate. I have represented the formulae of λ and the eigenstate $\langle q|\phi\rangle$ in the configuration space in **Appendix A**, including detailed derivation of them.

According to the Lewis–Riesenfeld theory [10, 20], the wave function that satisfies the Schrödinger equation is closely related to the eigenstate of the invariant operator. In fact, the wave function of the system in the coherent state is represented in terms of $\langle q|\phi\rangle$ as [10]

$$\langle q|\psi\rangle = \langle q|\phi\rangle e^{i\theta(t)}, \tag{6}$$

where $\theta(t)$ is a time-dependent phase. If we insert this equation together with **Eq. 1** into the Schrödinger equation, we have $\theta(t) = -\omega t/2$. The wave function described here is necessary for investigating quantum–classical correspondence through the evolution of the system. It is notable that the probability density $|\langle q|\psi\rangle|^2$ is Gaussian and such a Gaussianity is maintained through the lapse of time as in the case of other Gaussian waves [21, 22] proposed in the literature. The fact that the wave function, **Eq. 6**, exactly satisfies the Schrödinger equation may guarantee the validity of the research unfolded in this work.

3 CORRESPONDENCE BETWEEN QUANTUM AND CLASSICAL TRAJECTORIES

Let us now see whether the expectation values of the position and the momentum operators under this formalism agree with the corresponding classical trajectories or not. Considering that the position operator is represented in terms of $\hat{I}$ as (see **Appendix A**)

$$\hat{q} = i\sqrt{\hbar/(2m\omega e^{\gamma t})}\left[\hat{I}e^{-i(\omega t+\chi)} - \hat{I}^\dagger e^{i(\omega t+\chi)}\right] + Q_{\mathrm{p}}(t), \tag{7}$$

and using **Eq. 6**, it can be easily verified that

$$\langle\hat{q}\rangle = Q(t), \tag{8}$$

where $\langle\cdot\rangle = \langle\psi|\cdot|\psi\rangle$. Hence, the quantum expectation value of the position operator is exactly the same as that of the classical trajectory $Q(t)$. In a similar way, the expectation value of the canonical momentum is also derived such that $\langle\hat{p}\rangle = m\dot{Q}(t)e^{\gamma t}$. However, in general, the physical momentum in a damped system is not equivalent to the canonical one. Because the physical momentum operator is defined in the form $\hat{p}_k = \hat{p}e^{-\gamma t}$ [23] in the present case, its expectation value is given by

$$\langle\hat{p}_k\rangle = m\dot{Q}(t)(\equiv P_k(t)), \tag{9}$$

where $P_k(t)$ is the classical physical momentum. We thus confirm that the linear invariant operator theory admits quantum expectation values of $\hat{q}$ and $\hat{p}_k$ in a simple manner, of which results precisely coincide with the corresponding classical values. We can regard this outcome as an initial step for verifying that the invariant formalism of quantum mechanics reconciles with the principle of quantum and classical correspondence.

The above consequence, however, does not mean that the quantum particle (oscillator) follows the exact classical trajectory that is uniquely defined. Quantum mechanics is basically nonlocal and there are numerous possible paths allowed, within the width of a wave packet, for a quantum particle that has a definite initial condition. It is impossible to indicate exactly which path the quantum particle actually follows, but some paths may be more likely than others, especially those close to the classically predicted path. As a consequence of the Ehrenfest's theorem [24], the trajectory of the quantum particle can be approximated to that of the classical one only when the width of the quantum wave packet is sufficiently narrow. Details of the Ehrenfest's theorem for a particular case of the system where the oscillator is driven by a sinusoidal force are shown in Ref. [25].

4 QUANTUM ENERGY AND ITS CLASSICAL LIMIT

As pointed out by Hen and Kalev [9] and some other authors [26], obtaining a quantum–classical correspondence from a test performed at the level concerned expectation values is the key for achieving the genuine correspondence. Hence, it is necessary to compare the expectation values of quantum observables with their counterpart classical quantities. I will now analyze the expectation value of the quantum energy which is one of the most common observables in the system. Notice that quantum energy $E(t)$ for a nonconservative system is different from the expectation value of the Hamiltonian and the expression of the energy operator, in the present case, is [16, 27]

$$\widehat{E} = e^{-2\gamma t}\widehat{p}^2\big/(2m) + (1/2)m\omega_0^2\widehat{q}^2. \tag{10}$$

After representing this operator in terms of $\widehat{I}$ and $\widehat{I}^\dagger$, it is able to evaluate the expectation value of $\widehat{E}$ with the help of **Eq. 6**. Through this procedure, I finally have (see **Appendix B**)

$$E(t) = \frac{1}{2}\hbar\Omega + e^{-2\gamma t}\frac{P^2(t)}{2m} + \frac{1}{2}m\omega_0^2 Q^2(t), \tag{11}$$

where $\Omega = (\omega_0^2/\omega)e^{-\gamma t}$. This is the main consequence of my present research. The first term that contains $\hbar$ is the zero-point energy that does not vanish even when the displacement of the oscillator is zero. Note that this term varies over time. Although q^2 (p^2) can be obtained by raising q (p) squared classically, the quantum expectation value $\langle\widehat{q}^2\rangle$ ($\langle\widehat{p}^2\rangle$) is different from $\langle\widehat{q}\rangle^2$ ($\langle\widehat{p}\rangle^2$) because it involves a zero-point quantity. Such zero-point quantities also act as the origin of the zero-point quantum energy. When it comes to a measure of energy, great care must be taken in order to distinguish its classicality from the quantum nature. Fundamentally, the behavior of energy and its variance are directly related to the uncertainty principle [28, 29]. The (quantum) energy is, in general, not conserved over time in dissipative systems like this, while it is possible to predict its amount at any given instant in time.

For better understanding of the time behavior of **Eq. 11**, let us consider a specific system which is the cantilever in the tapping mode atomic force microscopy (TMAFM) [30]. This system is widely used as a dynamic imaging technique. For a mechanical description of TMAFM, see **Appendix C**. The time evolutions of quantum energy for TMAFM are illustrated in **Figure 1** using **Eq. 11** with comparison to its counterpart classical one. This figure exhibits complete consistency between the quantum energy (with $\hbar \to 0$) and the corresponding classical one. I have also applied the present theory to another system which is the familiar damped harmonic oscillator driven by a periodic sawtooth force (see **Appendix D** and **Figure 2** for its mechanical description). Sawtooth forces or signals are typically observed from atomic force microscopy with biomolecules like proteins [31] and from a modulation of current density in a nuclear-fusion tokamak [32]. **Figure 3** shows that the quantum description of this system using my theory also coincides with the classical one. We thus confirm that the formalism of quantum mechanics based on the linear invariant yields exact quantum–classical correspondence.

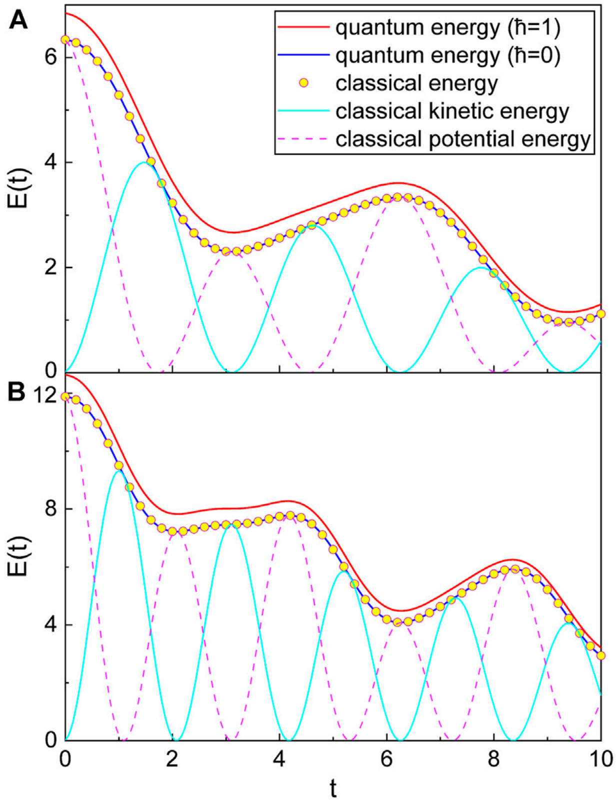

FIGURE 1 | Exact quantum energy (red line), quantum energy with $\hbar \to 0$ (blue line), and classical mechanical energy (circle) of the oscillating cantilever in TMAFM as a function of t where $k = 0.5$, $a_0 = 0.3$, $D_0 = 0.5$, $\hbar = 1$, $m_{\text{eff}} = 1$, $Q_0 = 3$, $\gamma = 0.1$, $F_{\text{ext}} = 0.3$, and $\varphi = 0$. The values of (ω_0, ω_d) are $(1, 0.3)$ for **(A)** and $(1.5, 0.6)$ for **(B)**. All values are taken to be dimensionless for convenience; this convention will also be used in subsequent figures.

For further analysis, let us consider the case where the driving force disappears ($f(t) \to 0$). We can then confirm using **Eq. 2** that **Eq. 11** reduces to that of Ref. [33], which is of the form

$$E(t) = \frac{1}{2}\hbar\Omega + E_0 e^{-\gamma t}\left(1 + \frac{\gamma}{2\omega_0}\cos\left[2(\omega t + \varphi) - \delta\right]\right), \tag{12}$$

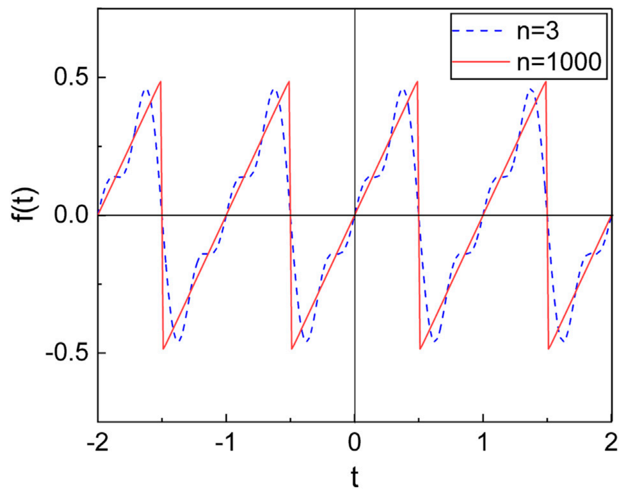

FIGURE 2 | Sawtooth driving force $f(t)$ with $f_0 = 1$, $m = 1$, and $\tau = 1$, where the mathematical formula of $f(t)$ with a period τ is defined in **Appendix D**. n is the natural number (see **Appendix D**). I have considered n up to three for the blue dashed line and up to 1,000 for the red solid line. As n increases, the form of the obtained sawtooth driving force becomes more exact.

where $E_0 = m\omega_0^2 Q_0^2/2$ and $\delta = \tan^{-1}(2\omega/\gamma)$. Except for the first term which is a purely quantum one, this is the well-known formula of the classical mechanical energy for the damped harmonic oscillator. Of course, for the high displacement limit $Q_0 \gg \hbar/(m\omega)$, it is possible to neglect the quantum effect via the use of the assumption $\hbar \sim 0$ and, consequently, the quantum energy can be successfully approximated to the classical one. Though the quantum energy is considered now as a model example in order to explain the correspondence principle, one can easily check, using the formalism developed here, that the analytical expectation values of other observables are also in precise congruence with their classical counterparts under the limit $\hbar \to 0$. For other formulae of quantum energies and their interpretation for this reduced system $(f(t) \to 0)$, which were derived using other methods such as the SU(1,1) Lie algebraic approach, refer to Ref. [34].

5 UNCERTAINTY AND THE CORRESPONDENCE PRINCIPLE

An important feature of quantum mechanics, which distinguishes it from classical mechanics, is the appearance of a minimum uncertainty product between the arbitrary two noncommutative operators. One cannot simultaneously know the values of position and momentum with an arbitrary precision from a quantum measurement, while the classical theory of measurement has nothing to do with such a limitation.

The quantum variance of an observable $\hat{\mathcal{O}}$ in the state $|\psi\rangle$ is given by $\Delta\hat{\mathcal{O}} = [\langle\hat{\mathcal{O}}^2\rangle - \langle\hat{\mathcal{O}}\rangle^2]^{1/2}$. From this identity and the use of **Eq. 6**, the quantum uncertainty product for position and momentum of the system can be directly derived as

$$\Delta\hat{q}\Delta\hat{p} = \hbar\omega_0/(2\omega). \tag{13}$$

Because this consequence is independent of the particular solutions, $Q_p(t)$ and $P_p(t)$, the driving force does not affect the uncertainty product. In other words, the uncertainty product of the system is the same as that of the undriven damped harmonic oscillator [12]. Due to the obvious inequality $\omega_0 \geq \omega$, the uncertainty principle holds in this case. For the case $\gamma \to 0$, this uncertainty product reduces to $\hbar/2$ which is its minimal value allowed in quantum mechanics for the harmonic oscillator. On the other hand, for $\hbar \to 0$, this becomes zero, showing the classical prediction.

6 OTHER FORMALISMS AND APPROACHES

There are several other quantum formalisms for describing the damped harmonic oscillator, such as the Lindblad dynamics

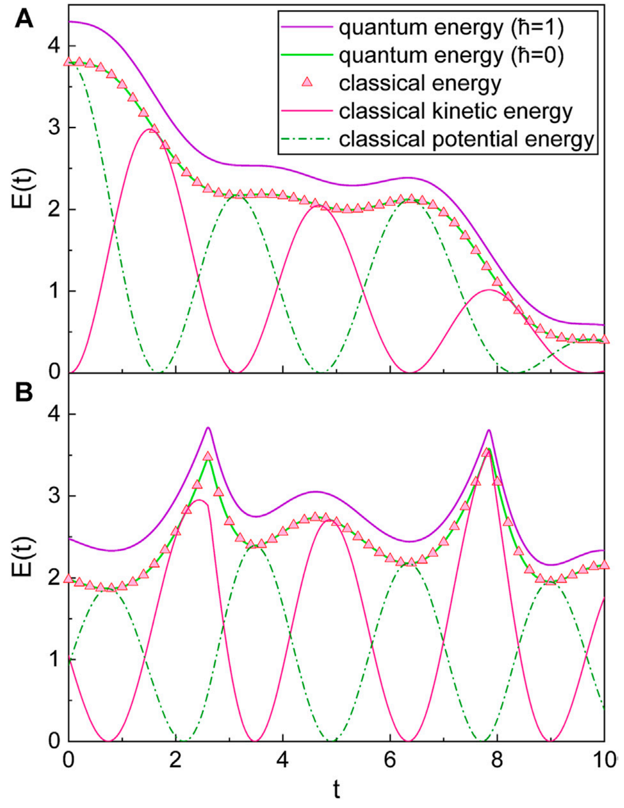

FIGURE 3 | Exact quantum energy (violet line), quantum energy with $\hbar \to 0$ (green line), and classical mechanical energy (triangle) of the oscillator driven by the sawtooth force as a function of t where $m = 1$, $\hbar = 1$, $\gamma = 0.1$, $\omega_0 = 1$, $\varphi = 0$, and $n = 1000$. The values of (Q_0, ω_d, f_0) are $(3, 0.3, 1)$ for **(A)** and $(1, 1.2, 2)$ for **(B)**.

[35–38], non-Hermitian Hamiltonian dynamics [39–41], and the Schwinger action method [15, 42]. Let's look into the relatively well-known Lindblad dynamics here. Whereas my approach uses invariant operators $\hat{I}$ and $\hat{I}^\dagger$ as basic tools for unfolding quantum theory, the approach based on the Lindblad theory uses an annihilation operator and its Hermitian adjoint operator (creation operator). The definition of the annihilation operator in that theory is given by $\hat{a} = \sqrt{m\omega/(2\hbar)}\hat{q} + i\hat{\mathsf{p}}/\sqrt{2m\omega\hbar}$, where $\hat{\mathsf{p}}$ is a momentum which is defined in terms of the notation in this work as (see Eq. 46 of Ref. [35])

$$\hat{\mathsf{p}} = \hat{p}_k + m(\gamma/2)\hat{q}. \tag{14}$$

Although the momentum given above seems similar to the physical momentum, it is not exactly the same due to the presence of the additional second term.

In particular, Korsch evaluated the expectation value of $\hat{a}^\dagger\hat{a}$ for the damped oscillator driven by a sinusoidal force of the form

$$f(t) = f_{\rm d}\cos(\omega_{\rm d}t). \tag{15}$$

If we denote the expectation value of an observable $\hat{\mathcal{O}}$ in the Lindblad theory as $\langle\hat{\mathcal{O}}\rangle_{\rm L}$, Korsch's result for $\hat{a}^\dagger\hat{a}$ with $\hbar = 1$ and $m = 1$ is given by (see Eq. 98 of Ref. [35])

$$\langle\hat{a}^\dagger\hat{a}\rangle_{\rm L} = \frac{1}{b(t)} - 1 + |\alpha(t)|^2, \tag{16}$$

where

$$b(t) = \frac{(\mu-\nu)(1-u_0)e^{\gamma t}}{\mu u_0 - \nu + \mu(1-u_0)e^{\gamma t}}, \tag{17}$$

$$\alpha(t) = \alpha_0 e^{-(i\omega+\gamma/2)t} - \frac{f_{\rm d}}{2\sqrt{2\omega}}\left(\frac{e^{-(i\omega+\gamma/2)t} - e^{i\omega_{\rm d}t}}{\omega+\omega_{\rm d}-i\gamma/2} + \frac{e^{-(i\omega+\gamma/2)t} - e^{-i\omega_{\rm d}t}}{\omega-\omega_{\rm d}-i\gamma/2}\right), \tag{18}$$

while $\mu = \gamma' + \gamma/2$ and $\nu = \gamma' - \gamma/2$, γ' is a diffusion constant [38], and u_0 is a constant chosen within the range $0 < u_0 < 1$.

Let us now compare the present result with Korsch's together with the classical one. The expectation value of $\hat{a}^\dagger\hat{a}$ in my theory is given by

$$\langle\hat{a}^\dagger\hat{a}\rangle = \frac{m\omega}{2\hbar}\langle\hat{q}^2\rangle + \frac{\langle\hat{\mathsf{p}}^2\rangle}{2m\omega\hbar} - \frac{1}{2}e^{-\gamma t}. \tag{19}$$

The expectation values $\langle\hat{q}^2\rangle$ and $\langle\hat{\mathsf{p}}^2\rangle$ are provided in **Appendix E**. On the other hand, a classical counterpart of the expectation value of $\hat{a}^\dagger\hat{a}$ can be defined as A^*A, where

$$A = \sqrt{m\omega/(2\hbar)}Q(t) + i\mathsf{P}(t)\big/\sqrt{2m\omega\hbar}, \tag{20}$$

with

$$\mathsf{P}(t) = P_k(t) + \frac{m\gamma}{2}Q(t). \tag{21}$$

Figures 4, **5** are the comparison of the time behavior between $\langle\hat{a}^\dagger\hat{a}\rangle$, $\langle\hat{a}^\dagger\hat{a}\rangle_{\rm L}$, and A^*A. The difference of **Figure 5** compared with **Figure 4** is the chosen amplitude α_0, that is, α_0 in **Figure 5** is relatively smaller than that used in **Figure 4**. Although the result in this work agrees well with the Korsch's one for the case of **Figure 4**, the two results in **Figure 5** are somewhat different from each other. Especially, the discrepancy between them is very large for the case $\omega_{\rm d} < \omega_0$ (see **Figure 5B**). By the way, my results in both **Figures 4**, **5** agree with the classical ones. From a lengthy calculation after substituting Equations E1 and E2 in **Eq. 19**, it can also be verified that $\langle\hat{a}^\dagger\hat{a}\rangle$ is exactly the same as A^*A analytically.

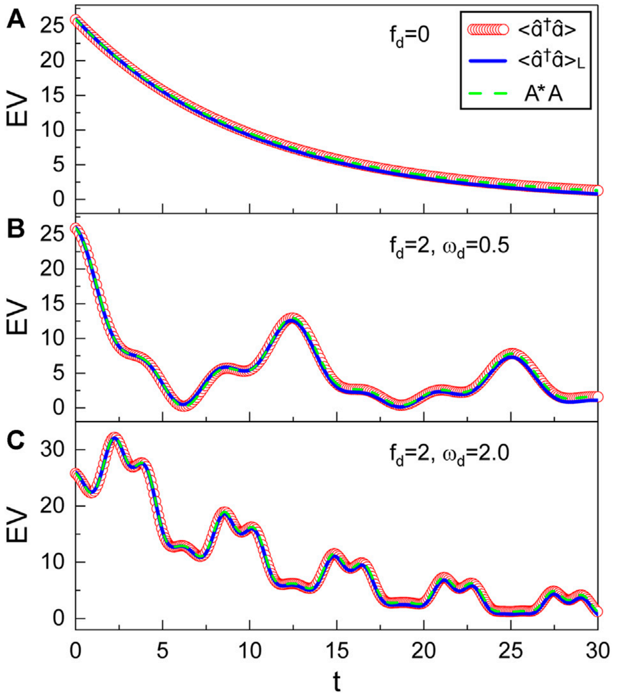

FIGURE 4 | Time evolution of the expectation values (EV), $\langle\hat{a}^\dagger\hat{a}\rangle$ (**Eq. 19**), $\langle\hat{a}^\dagger\hat{a}\rangle_{\rm L}$ (**Eq. 16**), and A^*A, for several different choices of the sinusoidal driving force characterized by $f_{\rm d}$ and $\omega_{\rm d}$. The chosen values of $f_{\rm d}$ and $\omega_{\rm d}$ are designated in each panel. I have used $\alpha_0 = 5$, $u_0 = 0.5$, $\omega_0 = 1$, $\gamma = 0.1$, $\gamma' = 0$, $m = 1$, $\hbar = 1$, $\chi = 0$, and $\varphi = 0$. The value of Q_0 is 7.21 for **A**, 4.54 for **B**, and 7.85 for **C**.

There are lots of different approaches for the classical limit of quantum mechanics with their own viewpoints. The problem of quantum–classical transition has been extensively investigated for the quartic oscillator by Oliveira *et al.* [29, 43–45]. They argued that quantum–classical correspondence can be achieved via the convergence of three factors, which are large classical actions, the object-environment interaction, and experimentally induced limitations. It was reported by Zurek [46] that the quantum–classical limit is governed by decoherence that takes place through environmental perturbations. As a quantum chaotic system is decohered, it restores classical behavior as a consequence of the destruction of quantum superpositions. Wiebe and Ballentine [47]

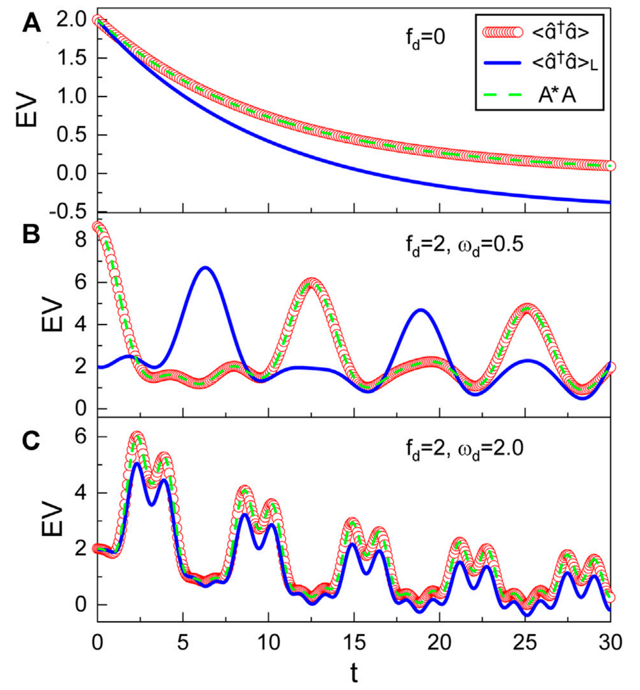

FIGURE 5 | Time evolution of $\langle \hat{a}^\dagger \hat{a} \rangle$, $\langle \hat{a}^\dagger \hat{a} \rangle_L$, and $A^* A$ for the case where the amplitude is relatively small ($\alpha_0 = 1$). The value of Q_0 is 2.00 for **A**, 1.50 for **B**, and 2.67 for **C**. Other unspecified values used here are the same as those of **Figure 4**.

examined quantum–classical differences by computing the chaotic tumbling of the satellite Hyperion from both classical and quantum points of view regarding the hypothesis of Zurek.

7 CONCLUSION

Classical limit of quantum mechanics for a driven damped harmonic oscillator has been investigated based on the linear invariant operator. The full wave function of the system was represented in terms of the eigenstate of the linear invariant operator according to the Lewis–Riesenfeld theory [10]. The expectation values of observables, such as position, momentum, and quantum energy, have been derived by using the wave function, and I have compared them with their classical counterparts. From this, it was shown that $\hbar \to 0$ limit of quantum mechanics for the system coincides with the counterpart classical mechanics within my formulation. The quantum formalism adopted here may be extended to other systems beyond the harmonic oscillator, provided that a given system admits a linear invariant quantity as a tool for its analysis.

The recent trend [48, 49] of the reimplementation of classical mechanics in particle optics using quantum particles is a clear testimony of the close relationship between quantum and classical mechanics. Some essential knowledge of quantum information theory is developed on the basis of classical-like wave properties, while the quantum nature of a physical system is unquestionable especially when nonlocal entanglement is concerned [50]. It may be the very common opinion that every new physical theory should not only precisely describe facts that cannot be covered by existing theories but must also reproduce the predictions of classical mechanics in an appropriate classical limit.

Quantum systems exhibit various nonclassical properties such as entanglement, superposition, nonlocality, and negative Wigner distribution function. While such nonclassicalities are important in the next-generation quantum information science, the description of nonclassical properties is valid and reliable only when the underlying quantum formalism used in such descriptions is precise and complete. A formalism of quantum theory may be acceptable only when it gives classical results in the classical limit ($\hbar \to 0$ limit). This is the reason why a complete quantum formalism that obeys quantum–classical correspondence is important. Such a formalism may admit to explaining the various characteristics of dynamical systems in a reasonable and consistent way from every possible angle. The result for a correspondence principle that I have developed in this research beyond simple static systems may provide a deep insight into understanding how classical mechanics emerges from quantum mechanics through a limiting situation.

8 METHODS

I considered a time-dependent Hamiltonian, which is composed of the basic CK Hamiltonian and an additional term associated with a time-varying driving force. This Hamiltonian corresponds to a damped driven harmonic oscillator.

The linear invariant operator of the system is constructed from the Liouville–von Neumann equation. The eigenvalue and the eigenstate of the linear invariant operator are derived by solving its eigenvalue equation through a fundamental mathematical procedure. If a system is described by a time-dependent Hamiltonian like the case given here, the eigenstate of the (linear) invariant operator is important because the full wave function of the system is expressed in terms of such an eigenstate [10]. More clearly speaking, the wave function in this case is represented by the eigenstate and a phase factor (see **Eq. 6** in the text). Because we now know the formula of the eigenstate, the phase of the wave function can be easily evaluated by means of the Schrödinger equation. In this way, we can derive the full wave function eventually. This wave function is necessary in order to investigate the $\hbar \to 0$ limit of quantum mechanics.

The quantum expectation values of observables, such as position, momentum, and the energy operator, are derived using the wave function. By comparing such expectation values with their classical counterparts, the correspondence principle between quantum and classical mechanics is analyzed.

DATA AVAILABILITY STATEMENT

The original contributions presented in the study are included in the article, and further inquiries can be directed to the corresponding author.

AUTHOR CONTRIBUTIONS

The author confirms being the sole contributor of this work and has approved it for publication.

FUNDING

This work was supported by the National Research Foundation of Korea(NRF) grant funded by the Korea government(MSIT) (No.: NRF-2021R1F1A1062849).

REFERENCES

1. Planck M. *Vorlesungen uber die Theorie der Wärmestralhung*. 978-0270103878. New York: Dover Publications (1959).
2. Bohr N. *The Theory of Spectra and Atomic Constitution*. 978-1107669819. London: Cambridge University Press (1922).
3. Liboff RL. On the Potential $x^{2N}$and the Correspondence Principle. *Int J Theor Phys* (1979) 18(3):185–91. doi:10.1007/BF00670395
4. Man’ko OV, and Man’ko VI. Classical Mechanics Is Not the Limit $\hbar\rightarrow 0$ of Quantum Mechanics. *J Russ Laser Res* (2004) 25(5):477–92. doi:10.1023/B:JORR.0000043735.34372.8f
5. Huang XY. Correspondence between Quantum and Classical Descriptions for Free Particles. *Phys Rev A* (2008) 78(2):022109. doi:10.1103/PhysRevA.78.022109
6. Kay KG. Hamiltonian Formulation of Quantum Mechanics with Semiclassical Implications. *Phys Rev A* (1990) 42(7):3718–25. doi:10.1103/PhysRevA.46.1213
7. Klein U. What Is the $\hbar \rightarrow 0$ Limit of Quantum Theory. *Am J Phys* (2012) 80(11):1009–16. doi:10.1119/1.4751274
8. Oliveira AC. Classical Limit of Quantum Mechanics Induced by Continuous Measurements. *Physica A* (2014) 393:655–68. doi:10.1016/j.physa.2013.09.025
9. Hen I, and Kalev A. Classical States and Their Quantum Correspondence. arXiv:0701015v2 [quant-ph] (2007).
10. Lewis HR, Jr., and Riesenfeld WB. An Exact Quantum Theory of the Time-dependent Harmonic Oscillator and of a Charged Particle in a Time-dependent Electromagnetic Field. *J Math Phys* (1969) 10(8):1458–73. doi:10.1063/1.1664991
11. Abdalla MS, and Choi JR. Propagator for the Time-dependent Charged Oscillator via Linear and Quadratic Invariants. *Ann Phys* (2007) 322(12): 2795–810. doi:10.1016/j.aop.2007.01.006
12. Choi JR, and Zhang S. Quantum and Classical Correspondence of Damped-Amplified Oscillators. *Phys Scr* (2002) 66(5):337–41. doi:10.1238/Physica.Regular.066a00337
13. Choi JR, and Ju S. Properties of the Geometric Phase in Electromechanical Oscillations of Carbon-Nanotube-Based Nanowire Resonators. *Nanoscale Res Lett* (2019) 14:44. doi:10.1186/s11671-019-2855-8
14. Yeon K-H, Kim S-S, Moon Y-M, Hong S-K, Um C-I, and George TF. The Quantum under-, Critical- and Over-damped Driven Harmonic Oscillators. *J Phys A: Math Gen* (2001) 34(37):7719–32. doi:10.1088/0305-4470/34/37/321
15. Urrutia LF, and Hernandez E. Calculation of the Propagator for a Time-dependent Damped, Forced Harmonic Oscillator Using the Schwinger Action Principle. *Int J Theor Phys* (1984) 23(12):1105–27. doi:10.1007/BF02213423
16. Um C-I, Yeon K-H, and George TF. The Quantum Damped Harmonic Oscillator. *Phys Rep* (2002) 362(2-3):63–192. doi:10.1016/S0370-1573(01)00077-1
17. Caldirola P. Porze Non Conservative Nella Meccanica Quantistica. *Nuovo Cimento* (1941) 18(9):393–400. doi:10.1007/BF02960144
18. Kanai E. On the Quantization of Dissipative Systems. *Prog Theor Phys* (1948) 3(4):440–2. doi:10.1007/BF01313310
19. Flores-Hidalgo G, and Barone FA. The One Dimensional Damped Forced Harmonic Oscillator Revisited. *Eur J Phys* (2011) 32(2):377–9. doi:10.1088/0143-0807/32/2/010
20. Choi JR, and Nahm IH. SU(1,1) Lie Algebra Applied to the General Time-dependent Quadratic Hamiltonian System. *Int J Theore Phys* (2006) 46(1): 1–15. doi:10.1007/s10773-006-9050-2
21. Schumaker BL. Quantum Mechanical Pure States with Gaussian Wave Functions. *Phys Rep* (1986) 135(6):317–408. doi:10.1016/0370-1573(86)90179-1
22. Marhic MF. Oscillating Hermite-Gaussian Wave Functions of the Harmonic Oscillator. *Lett Nuovo Cim* (1978) 22(9):376–8. doi:10.1007/BF02820587
23. Greenberger DM. A Critique of the Major Approaches to Damping in Quantum Theory. *J Math Phys* (1979) 20(5):762–70. doi:10.1063/1.524148
24. Ehrenfest P. Bemerkung über die angenäherte gültigkeit der klassischen mechanik innerhalb der quantenmechanik. *Z Phys* (1927) 45(7-8):455–7. doi:10.1007/BF01329203
25. Medjber S, Bekkar H, Menouar S, and Choi JR. Testing the Validity of the Ehrenfest Theorem beyond Simple Static Systems: Caldirola-Kanai Oscillator Driven by a Time-dependent Force. *Chin Phys B* (2016) 25(8), 080301. doi:10.1088/1674-1056/25/8/080301
26. Bolivar AO. In: *Quantum-Classical Correspondence: Dynamical Quantization and the Classical Limit*. 978-3-662-09649-9. New York: Springer (2004).
27. Colegrave RK, and Abdalla MS. A Canonical Description of the Fabry-Perot Cavity. *Optica Acta* (1981) 28(4):495–501. doi:10.1080/713820584
28. Caves CM, and Milburn GJ. Quantum-mechanical Model for Continuous Position Measurements. *Phys Rev A* (1987) 36(12):5543–55. doi:10.1103/PhysRevA.36.5543
29. Oliveira AC, Oliveira ZT, Jr., and Correia NS, Complementarity and Classical Limit of Quantum Mechanics: Energy Measurement Aspects. arXiv: 1307.0528v1 [quant-ph] (2013).
30. Legleiter J, Park M, Cusick B, and Kowalewski T. Scanning Probe Acceleration Microscopy (SPAM) in Fluids: Mapping Mechanical Properties of Surfaces at the Nanoscale. *PNAS* (2006) 103(13):4813–8. doi:10.1073/pnas.0505628103
31. Hornyak GL, Tibbals HF, Dutta J, and Moore JJ. *Introduction to Nanoscience & Nanotechnology* 978-1420047790. Boca Raton: CRC Press (2009).
32. Soltwisch H. Measurement of Current-Density Changes during Sawtooth Activity in a Tokamak by Far-Infrared Polarimetry. *Rev Sci Instrum* (1988) 59(8):1599–604. doi:10.1063/1.1140159
33. Choi JR. Interpreting Quantum States of Electromagnetic Field in Time-dependent Linear media. *Phys Rev A* (2010) 82(5):055803. doi:10.1103/PhysRevA.82.055803
34. Choi JR. Analysis of Quantum Energy for Caldirola-Kanai Hamiltonian Systems in Coherent States. *Results Phys* (2013) 3(1):115–21. doi:10.1016/j.rinp.2013.06.003
35. Korsch HJ. Lindblad Dynamics of the Damped and Forced Quantum Harmonic Oscillator. arXiv 1908.01187v2 [quant-ph] (2019).
36. Fujii K. Quantum Damped Harmonic Oscillator. In: P Bracken, editor. *Advances in Quantum Mechanics*. 978-953-51-1089-7. Rijeka: Intech (2013). p. 133–56.
37. Isar A. Uncertainty, Entropy and Decoherence of the Damped Harmonic Oscillator in the Lindblad Theory of Open Quantum Systems. *Fortschr Phys* (1999) 47(7-8):855–79. doi:10.1002/(SICI)1521-3978(199909)47:7/8¡855::AID-PROP855¿3.0.CO;2-Z
38. Piilo J, and Maniscalco S. Driven Harmonic Oscillator as a Quantum Simulator for Open Systems. *Phys Rev A* (2006) 74(3):032303. doi:10.1103/PhysRevA.74.032303

39. Graefe EM, Höning M, and Korsch HJ. Classical Limit of Non-Hermitian Quantum Dynamics—A Generalized Canonical Structure. *J Phys A: Math Theor* (2010) 43(7):075306. doi:10.1088/1751-8113/43/7/075306
40. Grimaldi A, Sergi A, and Messina A. Evolution of a Non-Hermitian Quantum Single-Molecule Junction at Constant Temperature. *Entropy* (2021) 23(2):147. doi:10.3390/e23020147
41. Nigam K, and Banerjee K. Quantum Dynamics of Complex Hamiltonians. arXiv:1602.00157v2 [quant-ph] (2016).
42. Pepore S, and Sukbot B. Schwinger Method for Dual Damped Oscillators. *Chin J Phys* (2015) 53(5):100002. doi:10.6122/CJP.20150803
43. Oliveira AC, Nemes MC, and Romero KMF. Quantum Time Scales and the Classical Limit: Analytic Results for Some Simple Systems. *Phys Rev E* (2003) 68(3):036214. doi:10.1103/PhysRevE.68.036214
44. Oliveira AC, de Faria JGP, and Nemes MC. Quantum-classical Transition of the Open Quartic Oscillator: The Role of the Environment. *Phys Rev E* (2006) 73(4):046207. doi:10.1103/PhysRevE.73.046207
45. Oliveira AC, de Magalhães ARB, and Faria JGP. Influence of Experimental Resolution on the Quantum-To-Classical Transition in the Quartic Oscillator. *Physica A* (2012) 391(21):5082–9. doi:10.1016/j.physa.2012.05.064
46. Zurek WH. Decoherence, Chaos, Quantum-Classical Correspondence, and the Algorithmic Arrow of Time. *Phys Scr* (1998) 1998(T76):186–98. doi:10.1238/Physica.Topical.076a00186
47. Wiebe N, and Ballentine LE. Quantum Mechanics of Hyperion. *Phys Rev A* (2005) 72(2):022109. doi:10.1103/PhysRevA.72.022109
48. Wang Y-M, and Liang J-Q. Repulsive Bound-Atom Pairs in an Optical Lattice with Two-Body Interaction of Nearest Neighbors. *Phys Rev A* (2010) 81(4):045601. doi:10.1103/PhysRevA.81.045601
49. Hawkes PW. Examples of Electrostatic Electron Optics: The Farrand and Elektros Microscopes and Electron Mirrors. *Ultramicroscopy* (2012) 119:9–17. doi:10.1016/j.ultramic.2011.11.009
50. Goldin MA, Francisco D, and Ledesma S. Classical Images as Quantum Entanglement: An Image Processing Analogy of the GHZ Experiment. *Opt Commun* (2011) 284(7):2089–93. doi:10.1016/j.optcom.2010.12.057
51. Louisell WH. *Quantum Statistical Properties of Radiation*. 0-471-54785-9. New York: John Wiley & Sons (1973). p. 104–9.
52. Choi JR. Exact Solution of a Quantized LC Circuit Coupled to a Power Source. *Phys Scr* (2006) 73(6):587–95. doi:10.1088/0031-8949/73/6/010

Conflict of Interest: The author declares that the research was conducted in the absence of any commercial or financial relationships that could be construed as a potential conflict of interest.

APPENDIX A: LINEAR INVARIANT OPERATOR AND ITS EIGENSTATE

From a straightforward evaluation of the Liouville-von Neumann equation,

$$d\hat{I}/dt = \partial\hat{I}/\partial t + \left[\hat{I}, \hat{H}\right]/(i\hbar) = 0, \tag{A1}$$

using the Hamiltonian given in **Eq. 1** in the text, we can easily derive the linear invariant operator $\hat{I}$ that is given in **Eq. 4** in the text (see Ref. 13). Notice that the Hermitian adjoint of this operator, $\hat{I}^\dagger$, is also an invariant operator. From a combined evaluation of the two equations for $\hat{I}$ and $\hat{I}^\dagger$, it is possible to eliminate $\hat{p}$ and, as a consequence, the expression for $\hat{q}$ which appeared in **Eq. 7** in the text can be obtained. From a similar method, we can also obtain the expression for $\hat{p}$. By solving the eigenvalue equation of the invariant operator, **Eq. 5**, in the configuration space on the basis of the technique adopted in Ref. 20, we obtain the eigenvalue as

$$\lambda = \beta e^{i\omega t}, \tag{A2}$$

where $\beta = -i\sqrt{m\omega/(2\hbar)}Q_0 e^{-i(\omega t+\varphi-\chi)}$, and the eigenstate of the form

$$\langle q|\phi\rangle = \sqrt{\frac{m\omega}{\hbar\pi}}\exp\left[e^{\gamma t/2}\frac{C_1 q_{\rm p} - C_2 q_{\rm p}^2}{\hbar} + C_3\right], \tag{A3}$$

where $q_{\rm p} = q - Q_{\rm p}(t)$ and

$$C_1 = \sqrt{2\hbar m\omega}\beta, \tag{A4}$$

$$C_2 = \frac{1}{2}me^{\gamma t/2}(\omega + i\gamma/2), \tag{A5}$$

$$C_3 = \frac{iP_{\rm p}(t)q}{\hbar} + \frac{\gamma t}{4} - \frac{\beta^2}{2} - \frac{|\beta|^2}{2}. \tag{A6}$$

APPENDIX B: EXPECTATION VALUE OF THE ENERGY OPERATOR

I present how to evaluate the expectation value of the energy operator. From a minor evaluation with the energy operator using the expression of $\hat{I}$ (and its Hermitian conjugate $\hat{I}^\dagger$), it is possible to represent the energy operator in terms of $\hat{I}$ and $\hat{I}^\dagger$ such that

$$\hat{E} = \left[\frac{\hbar}{4}\left(\frac{2\omega_0^2}{\omega}\left(2\hat{I}^\dagger\hat{I} + 1\right) - \varepsilon\hat{I}^2 - \varepsilon^*\hat{I}^{\dagger 2}\right) + \sqrt{\frac{\hbar}{2}}\left(\Theta\hat{I} + \Theta^*\hat{I}^\dagger\right)\right]e^{-\gamma t} + E_{\rm p}, \tag{B1}$$

where $\varepsilon = \gamma[\gamma/(2\omega) + i]e^{-2i(\omega t+\chi)}$ and

$$\Theta = \left[\sqrt{\frac{\omega}{m}}e^{-\gamma t/2}\eta P_{\rm p}(t) + ie^{\gamma t/2}\sqrt{\frac{m}{\omega}}\omega_0^2 Q_{\rm p}(t)\right]e^{-i(\omega t+\chi)}, \tag{B2}$$

$$E_{\rm p} = e^{-2\gamma t}\frac{P_{\rm p}^2(t)}{2m} + \frac{1}{2}m\omega_0^2 Q_{\rm p}^2(t), \tag{B3}$$

with $\eta = 1 - i\gamma/(2\omega)$. Here, I have used the relation $\hat{I}\hat{I}^\dagger = \hat{I}^\dagger\hat{I} + 1$, i.e., all $\hat{I}\hat{I}^\dagger$ are replaced by $\hat{I}^\dagger\hat{I} + 1$: this procedure of operator ordering is necessary when we manage a coherent state (see, for example, Ref. 51). Now by considering the fact that the eigenvalues of $\hat{I}$ and $\hat{I}^\dagger$ are λ and λ^* respectively, we can easily identify the expectation value of the energy operator, $\langle\psi|\hat{E}|\psi\rangle$, which is given in **Eq. 11** in the text. Notice that the $\hbar$ must not be taken simplistically to zero at the initial stage of the evaluation under the pretext of obtaining the classical limit. We should keep it until we arrive at the final representation, **Eq. 11**.

APPENDIX C: CANTILEVER SYSTEM

Description of the cantilever system appears in Ref. 30. If we denote the effective mass of the cantilever as $m_{\rm eff}$, the force acted on the lever is represented in the form

$$f(t) = [F_{\rm ext} + k(D_0 - a_0\sin\omega_{\rm d}t)]/m_{\rm eff}, \tag{C1}$$

where $F_{\rm ext}$ is the tip-sample force, $k(= m_{\rm eff}\omega_0^2)$ is the cantilever spring constant, D_0 is the resting position of the cantilever base, a_0 is the driving amplitude, and $\omega_{\rm d}$ is the drive frequency [30].

APPENDIX D: DAMPED HARMONIC OSCILLATOR WITH A SAWTOOTH FORCE

I regard the damped harmonic oscillator to which applied an external sawtooth force with the period $\tau = 2\pi/\omega_{\rm d}$. The sawtooth force can be represented as $f(t) = f_0 t/(m\tau)$ for a period $-\tau/2 < t < \tau/2$ (see **Figure 2**), where f_0 is a constant that represents the strength of the force. In this case, $f(t)$ can be rewritten in terms of an infinite series such that [52]

$$f(t) = [f_0/(\pi m)]\sum_{n=1}^{\infty}\frac{(-1)^{n+1}}{n}\sin(n\omega_{\rm d}t). \tag{D1}$$

APPENDIX E: EXPECTATION VALUES OF $\hat{q}^2$ AND $\hat{\rm p}^2$

The expectation values of $\hat{q}^2$ and $\hat{\rm p}^2$ in the state $|\psi\rangle$, which are necessary in the development of a consequence in **Section 6**, are given by

$$\langle\hat{q}^2\rangle = -\frac{\hbar}{2m\omega e^{\gamma t}}\left[\lambda^2 e^{-2i(\omega t+\chi)} + \lambda^{*2}e^{2i(\omega t+\chi)} - 2|\lambda|^2 - 1\right] + iQ_{\rm p}(t)\sqrt{\frac{2\hbar}{m\omega e^{\gamma t}}}\left[\lambda e^{-i(\omega t+\chi)} - \lambda^* e^{i(\omega t+\chi)}\right] + Q_{\rm p}^2(t), \tag{E1}$$

$$\langle\hat{\rm p}^2\rangle = \frac{m\omega\hbar}{2}e^{-\gamma t}\left[\lambda^2 e^{-2i(\omega t+\chi)} + \lambda^{*2}e^{2i(\omega t+\chi)} + 2|\lambda|^2 + 1\right] + G_{\rm p}(t)\sqrt{2m\omega\hbar}e^{-\gamma t/2}\left[\lambda e^{-i(\omega t+\chi)} + \lambda^* e^{i(\omega t+\chi)}\right] + G_{\rm p}^2(t), \tag{E2}$$

where $G_{\rm p}(t) = P_{\rm p}(t)e^{-\gamma t} + \gamma m Q_{\rm p}(t)/2$. The particular solutions that correspond to the driving force of **Eq. 15** are given by

$$Q_\mathrm{p}(t) = \frac{f_\mathrm{d}}{\sqrt{\left(\omega_0^2 - \omega_\mathrm{d}^2\right)^2 + \gamma^2\omega_\mathrm{d}^2}} \cos(\omega_\mathrm{d} t - \delta_\mathrm{d}), \tag{E3}$$

$$P_\mathrm{p}(t) = -\frac{m f_\mathrm{d}\omega_\mathrm{d}}{\sqrt{\left(\omega_0^2 - \omega_\mathrm{d}^2\right)^2 + \gamma^2\omega_\mathrm{d}^2}} e^{\gamma t} \sin(\omega_\mathrm{d} t - \delta_\mathrm{d}), \tag{E4}$$

where

$$\delta_\mathrm{d} = \mathrm{atan}\left(\omega_0^2 - \omega_\mathrm{d}^2, \gamma\omega_\mathrm{d}\right). \tag{E5}$$

Here, $\vartheta \equiv \mathrm{atan}(x, y)$ is a two-argument inverse function of $\tan\vartheta = y/x$. This function is defined in the range $0 \le \vartheta < 2\pi$.

frontiers
in Physics

REVIEW
published: 20 August 2021
doi: 10.3389/fphy.2021.675258

Multichromatic Polarization-Controlled Pulse Sequences for Coherent Control of Multiphoton Ionization

*Kevin Eickhoff, Lars Englert, Tim Bayer and Matthias Wollenhaupt**

Ultrafast Dynamics Group, Institut für Physik, Carl von Ossietzky Universität Oldenburg, Oldenburg, Germany

Edited by:
Robert Gordon,
University of Illinois at Chicago,
United States

Reviewed by:
Jianming Wen,
Kennesaw State University,
United States
David Ayuso,
Imperial College London,
United Kingdom
Nicolas Douguet,
Kennesaw State University,
United States

***Correspondence:**
Matthias Wollenhaupt
matthias.wollenhaupt@uni-oldenburg.de

Specialty section:
This article was submitted to
Optics and Photonics,
a section of the journal
Frontiers in Physics

Received: *02 March 2021*
Accepted: *23 July 2021*
Published: *20 August 2021*

Citation:
Eickhoff K, Englert L, Bayer T and Wollenhaupt M (2021) Multichromatic Polarization-Controlled Pulse Sequences for Coherent Control of Multiphoton Ionization.
Front. Phys. 9:675258.
doi: 10.3389/fphy.2021.675258

In this review, we report on recent progress in the generation and application of multichromatic polarization-tailored pulse sequences for the coherent control of multiphoton ionization (MPI) dynamics and present unpublished experimental results that complement our previous findings. Specifically, we utilize single-color, bichromatic, and trichromatic polarization-controlled pulse sequences generated by spectral amplitude, phase and polarization modulation of a carrier-envelope phase (CEP)-stable white light supercontinuum for MPI. The analysis of the number of ionization pathways and the number of distinct final free electron states shows that both increase significantly, but scale differently with the number of absorbed photons and the number of pulses in the sequence. In our experiments, ultrafast polarization shaping is combined with high-resolution photoelectron tomography to generate, control, and reconstruct three-dimensional photoelectron momentum distributions from atomic and molecular MPI. We discuss the use of polarization-controlled single-color and bichromatic pulse sequences in perturbative and non-perturbative coherent control of coupled electron-nuclear dynamics in molecules, atomic spin-orbit wave packet dynamics and the directional photoemission from atoms and chiral molecules. We compare the coherent control of CEP-insensitive intraband multipath interference in the MPI with a fixed number of photons with CEP-sensitive interband multipath interference in the ionization with a different number of photons. The generation and control of free electron vortices with even-numbered rotational symmetry by MPI with single-color pulse sequences is contrasted with the bichromatic control of CEP-sensitive electron vortices with odd-numbered rotational symmetry. To illustrate the potential of multichromatic pulse sequences for coherent control, we present a trichromatic scheme for shaper-based quantum state holography.

Keywords: coherent control, bichromatic polarization shaping, multiphoton ionization, photoelectron tomography, chiral molecules

1 INTRODUCTION

The basic principles of coherent control have been established more than 30 years ago [1–6]. Today many applications of coherent control have been demonstrated in various areas of physics and chemistry including multiphoton excitation [7–10] and ionization (MPI) of atoms [11, 12] and small molecules [13–15], electronic transitions in condensed matter [16], controlled molecular dissociation [17], spectroscopy [18, 19] and laser chemistry [20, 21]. Even in emerging fields such as high harmonic generation (HHG) [22, 23], material processing [24, 25], nonlinear microscopy [19], photoassociation [26], nanomaterial research [27] and quantum information [28] coherent control has proven its usefulness. A very effective method to control the dynamics of quantum systems is by specific manipulation of constructive and destructive quantum interferences [29] using ultrashort tailored laser pulses. Advanced techniques for generating tailored ultrashort laser pulses on the one hand and for highly differential detection on the other hand, have been key to experimental advances in coherent control. Since the implementation of the first single layer 128 pixel pulse shaping devices [30–40], remarkable advances have been achieved towards high precision pulse shaping using 640 pixel devices [41–50] and polarization shapers [51, 52], vector-field synthesizers [53–58] and supercontinuum pulse shaping [59–66]. Recently, we have introduced a scheme for polarization shaping of carrier-envelope phase (CEP)-stable over-octave-spanning white light supercontinua (WLS) to generate polarization-tailored bichromatic fields [65]. The latter work resulted in the experimental demonstration of a new class of cycloidal pulse shapes, such as counterrotating circularly polarized (CRCP) and corotating circularly polarized (COCP) cycloidal fields. In general, polarization-tailored multicolor femtosecond laser fields have opened up new perspectives in numerous applications ranging from HHG [67–72, 74, 75] over the coherent control of ultrafast electron dynamics in atoms and molecules [73, 76–78] to the manipulation of coherent excitations in nanostructures [79, 80].

The use of advanced polarization-shaped pulses for the generation of free electron wave packets by MPI has necessitated 3D detection to characterize the full 3D photoelectron momentum distribution (PMD). While time-of-flight techniques enabled the kinetic energy-resolved detection of photoelectrons from ultrafast MPI dynamics [81, 82], their angular distribution became available through the use of velocity map imaging (VMI) techniques [83–85]. Currently, the most sophisticated detection method is based on COLTRIMS [86, 87]. Cylindrically symmetric PMDs can be retrieved from the measured 2D projections using the Abel-inversion technique [88]. In order to image non-cylindrically symmetric PMDs, we have introduced a VMI-based photoelectron tomography technique [89]. By now, photoelectron tomography has become an established method with versatile applications including 3D imaging of PMDs from atomic strong-field ionization [90], the reconstruction of molecular PMDs in the laboratory [91] and molecular [92] frame, the retrieval of circularly polarized XUV fields from HHG [93] or the reconstruction of PMDs from strong-field photodetachment of negatively charged ions [94]. Applications of photoelectron tomography have ranged from the generation and characterization of designer electron wave packets [95, 96] and multiphoton photoelectron circular dichroism (PECD) measurements [97] to the extraction of transition matrix elements from tomographic data [98]. More recently, we have used photoelectron tomography to study free electron angular momentum wave packets [99], spin-orbit [100] and Rydberg wave packet dynamics [101] and photoelectron vortices with even [102–104] and odd [73] rotational symmetries. An overview of our recent photoelectron tomography studies of coherent control of atomic MPI can be found in [105, 106].

In this contribution, we review the application of shaper-generated multichromatic polarization-controlled fields for coherent control of atomic and molecular MPI. We study the quantum dynamics of atomic and molecular model systems induced by absorption of $\mathcal{N}$ photons from $\mathcal{M}$ pulses, focussing on the new opportunities offered by polarization-tailored multichromatic fields. The paper is organized as follows: In **Section 2**, we introduce the time-dependent laser electric field and summarize the theoretical methods that we have used to reproduce and analyze our experimental results. Details of our experimental setup for generating polarization-controlled multichromatic pulse sequences by spectral amplitude and phase modulation of a CEP-stable supercontinuum and the VMI-based photoelectron tomography technique are given in **Section 3**. In **Section 4** we present our results on coherent control of MPI with multichromatic pulse trains ordered by the type of pulse sequence we have used in the experiment. We start with experiments using single-color linearly polarized pulse sequences (**Section 4.1**) for perturbative and non-perturbative control of atomic and molecular MPI. By analyzing the 3D PMD, we rationalize the observed photoelectron spectra in an experiment on the interference of ultrashort free electron wave packets [11]. We review the generation of free electron vortices (FEVs) with c_4, c_6 and c_8 rotational symmetry using circularly polarized pulse sequences and present previously unpublished results on the vortex formation. The article's focus on intraband and interband coherent control scenarios using linearly and circularly polarized bichromatic pulse sequences is elaborated in **Section 4.2**. Examples include the control of frequency mixing contributions in the MPI with orthogonal linearly polarized (OLP) and CRCP bichromatic fields with applications to the observation of spin-orbit wave packets. In addition, we present the control of directional photoemission in the MPI of atoms and chiral molecules by bichromatic parallel linearly polarized (PLP) fields or few-cycle circularly polarized fields, and the use of cycloidal bichromatic fields to generate and manipulate 3D PMDs with c_1 and c_7 rotational symmetry. Finally, results on coherent control by trichromatic pulse sequences are presented in **Section 4.3**. The phase-sensitive combination of intra- and interband interferences is used for trichromatic shaper-based quantum state holography. We conclude with a summary and an outlook in **Section 5**.

2 THEORY

The MPI of atoms and molecules has been studied extensively both experimentally and theoretically. The fundamentals are documented in a vast body of literature, see for example [107–112]. In this section, we present the notation to describe multichromatic pulse sequences (**Section 2.1**) and summarize the theoretical concepts based on either non-perturbative description of the atomic and molecular neutral dynamics perturbatively coupled to the continuum (**Section 2.2**) or fully perturbative intraband and interband interference in MPI. The theoretical description is specifically adapted to reproduce the experimental results and discuss the relevant control aspects.

2.1 Ultrashort Polarization-Controlled Multichromatic Pulse Sequences

We start by describing the electric field of a pulse sequence consisting of $\mathcal{M}$ pulses, each of which with a different polarization state, e.g. linear, circular or in general elliptic. $\mathcal{E}_j(t-\tau_j)$ represents the complex valued time-delayed (τ_j) envelope of the jth pulse with a pulse-duration of Δt, which contains the effects due to higher-order spectral phase functions [113]. Here, Δt describes the full width at half maximum of the laser intensity. Taking into account the carrier oscillation with the central angular frequency ω_j, the relative phase φ_j, and the common CEP φ_{ce}, the scalar field of the jth pulse reads

$$E_j(t) = \mathcal{E}_j(t-\tau_j)e^{-i(\omega_j t+\varphi_j+\varphi_{ce})}. \tag{1}$$

The coefficients c_j^{-1} and c_j^{+1} in **Eq. 2** describe the weights of the respective right-handed circularly polarized (RCP) (−1) and left-handed circularly polarized (LCP) (+1) components

$$\begin{aligned} E_j^{-1}(t) &= E_j(t)c_j^{-1}, \\ E_j^{+1}(t) &= E_j(t)c_j^{+1}. \end{aligned} \tag{2}$$

For example, $\boldsymbol{c}_j = (c_j^{-1}, c_j^{+1}) = (1,0)$ denotes RCP light while $\boldsymbol{c}_j = (1,1)/\sqrt{2}$ represents horizontally linearly polarized light. Using the Jones vectors $\boldsymbol{e}_{-1} = \frac{1}{\sqrt{2}}(\boldsymbol{e}_x - i\boldsymbol{e}_y)$ for RCP and $\boldsymbol{e}_{+1} = -\frac{1}{\sqrt{2}}(\boldsymbol{e}_x + i\boldsymbol{e}_y)$ for LCP pulses, we obtain the time-dependent vectorial electric field of the jth pulse

$$\boldsymbol{E}_j(t) = E_j^{-1}(t)\boldsymbol{e}_{-1} + E_j^{+1}(t)\boldsymbol{e}_{+1}. \tag{3}$$

The total field is obtained by superposition of all $\mathcal{M}$ pulses in the sequence

$$\boldsymbol{E}(t) = \sum_{j=1}^{\mathcal{M}} \boldsymbol{E}_j(t) = \sum_{j=1}^{\mathcal{M}} \mathcal{E}_j(t-\tau_j)e^{-i(\omega_j t+\varphi_j+\varphi_{ce})}\left(c_j^{-1}\boldsymbol{e}_{-1} + c_j^{+1}\boldsymbol{e}_{+1}\right). \tag{4}$$

The physical field is given by $\mathrm{Re}[\boldsymbol{E}(t)]$. Schematic representations of single-color ($\mathcal{M}=2, \omega_1=\omega_2$), bichromatic ($\mathcal{M}=2, \omega_1 \neq \omega_2$) and trichromatic ($\mathcal{M}=3, \omega_i \neq \omega_j$) pulse sequences with different polarizations are depicted in **Figures 4**, **7**, **12**, respectively.

2.2 Simulation of Multiphoton Ionization

Many theoretical concepts and numerical methods are available to describe and simulate the quantum dynamics of atoms and molecules induced by the interaction with ultrashort laser pulses [4, 6, 114]. In the past two decades, we have used different methods to model ultrafast dynamics driven by shaped femtosecond pulses to model our experiments and interpret our observations. In parallel with our experimental studies, we have presented the corresponding theoretical descriptions and numerical simulations of the multilevel coherent control of atomic [115, 116] and molecular [117, 118] excitation. We have devised a resonant strong-field control mechanism based on the manipulation of dressed state populations and energies [119] and, in this context, developed a formalism to model photoelectron spectra from resonance-enhanced multiphoton ionization (REMPI) accounting for non-perturbative population dynamics and AC Stark shifts [118, 120]. In [48, 103], we provided a description for the calculation of sculpted 3D free electron wave packets from MPI, including the energy and angular distribution. Recently, we employed *ab initio* methods to numerically solve the time-dependent Schrödinger equation (TDSE) for a 2D model atom interacting with a polarization-tailored bichromatic femtosecond laser pulse sequence [121]. The model was applied to reproduce and analyze our experimental results reported in [73, 103] taking into account phase fluctuations in the CEP and the Gouy phase.

2.2.1 Non-Perturbative Neutral Dynamics Coupled to the Continuum

Resonant strong-field control of MPI dynamics is based on the non-perturbative manipulation of resonant bound state dynamics and the simultaneous perturbative mapping of those dynamics into the ionization continuum by absorption of additional photons. To model this type of non-perturbative REMPI processes we adapt the concept from Meier et al. [122] and divide the calculation into two steps. In the first step, we calculate the non-perturbative neutral dynamics of the time-dependent amplitudes $c_i(t)$ by solving the corresponding TDSE numerically for a multistate quantum system, including all relevant bound states. This procedure yields the time-dependent bound state populations $|c_i(t)|^2$. In the second step, we compute the photoelectron kinetic energy spectrum using time-dependent perturbation theory by inserting the amplitudes determined in the first step. This strategy is illustrated in **Figure 1A** for a generic atomic system and in (B) for the potassium molecule.

2.2.1.1 Atomic Multiphoton Ionization

To simulate our experiments, we have modeled atomic systems by multilevel schemes involving two [120, 123–125], three [48, 116] or more [115] bound states. As an example, we consider a two-level atom, consisting of a ground state $|1\rangle$ and an excited state $|2\rangle$ separated in energy by $\hbar\omega_{21} = \hbar\omega_2 - \hbar\omega_1$ and coupled by the transition dipole moment μ_{21}. The non-perturbative dynamics of the atom interacting with an intense near-resnant femtosecond laser pulse $E(t) = \mathcal{E}(t)e^{-i\omega_0 t}$, where ω_0 is the laser central frequency and $\mathcal{E}(t)$ is the generally complex-valued temporal envelope, is governed by the TDSE. Using both, the dipole

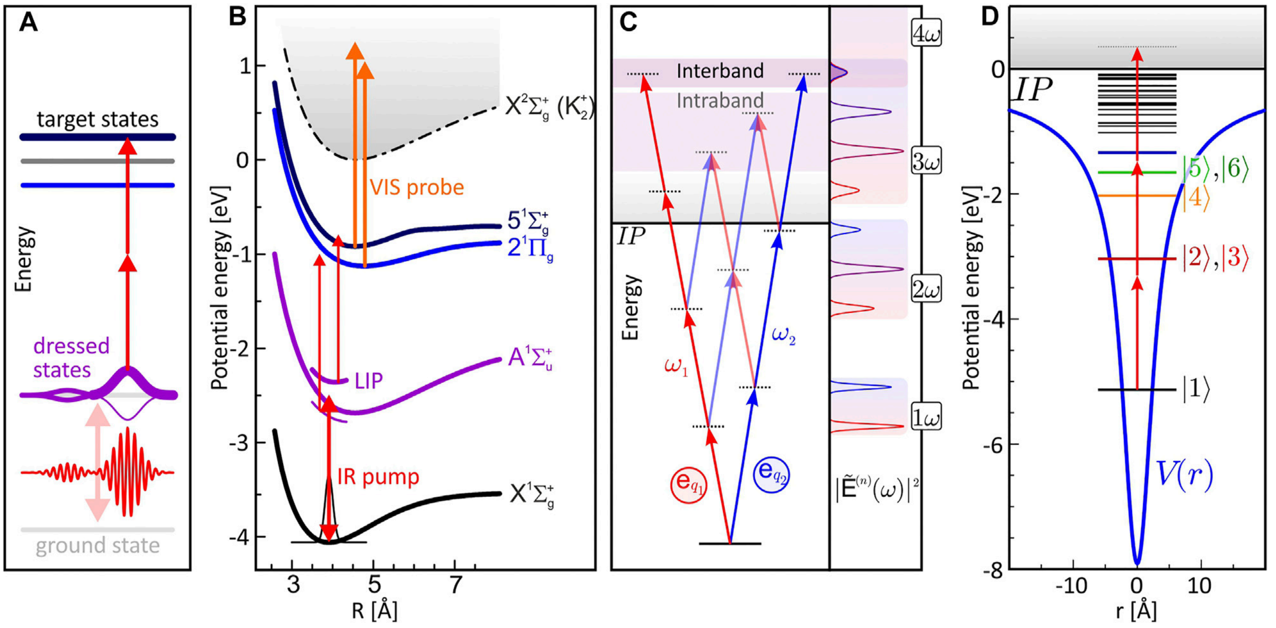

FIGURE 1 | Generic ionization schemes: **(A)** and **(B)** Non-perturbative neutral dynamics perturbatively coupled to the continuum [119]. **(A)** Generic scheme for the selective population of dressed states [119]. **(B)** Light-induced potentials of potassium dimers for ultrafast switching via the selective population of dressed states. **(C)** Scheme for perturbative control of intraband [73] and interband [105] MPI with polarization-shaped pulses along with multiphoton spectra. **(D)** Model potential for *ab initio* simulations of MPI with cycloidal laser pulses [121].

approximation and rotating wave approximation, the interaction picture TDSE for the time-dependent ground and excited state amplitudes $c_1(t)$ and $c_2(t)$ reads [5, 119, 126].

$$i\hbar\frac{d}{dt}\begin{bmatrix} c_1(t) \\ c_2(t) \end{bmatrix} = \frac{1}{2}\begin{bmatrix} 0 & -\mu_{21}\mathcal{E}^*(t)e^{i\delta t} \\ -\mu_{21}\mathcal{E}(t)e^{-i\delta t} & 0 \end{bmatrix}\begin{bmatrix} c_1(t) \\ c_2(t) \end{bmatrix}. \quad (5)$$

Herein, $\delta = \omega_0 - \omega_{21}$ is the detuning of the laser with respect to the atomic resonance. The TDSE in **Eq. 5** is solved numerically on a discrete temporal grid using short-time propagator methods [4]. This procedure yields the time evolution of the state vector $\boldsymbol{c}(t) = [c_1(t), c_2(t)]^T$. With the knowledge of the excited state amplitude $c_2(t)$, we calculate the amplitudes $c(\omega_k)$ of the free electrons, released with a kinetic energy of $\hbar\omega_k$ by perturbative $\mathcal{N}$-photon ionization from the excited state, by $\mathcal{N}$-th order time-dependent perturbation theory [115, 123, 127]

$$c(\omega_k) = \frac{\mu^{(\mathcal{N})}}{(i\hbar)^{\mathcal{N}}}\int_{-\infty}^{\infty} c_2(t)\, E^{\mathcal{N}}(t) e^{i(\omega_k-\omega_2)t} dt. \quad (6)$$

The notation was adapted from Dudovich et al. [128]. The multiphoton transition dipole moment $\mu^{(\mathcal{N})}$ for the bound-free transition is in general complex-valued and depends on the atomic structure. In the narrow energy windows considered here, we assume an unstructured continuum, i.e., treat the coupling as energy-independent. This numerical method was applied to reproduce the experimental photoelectron spectra obtained in our studies of basic physical mechanisms of resonant non-perturbative coherent control of atomic model systems using PLP single-color double pulse sequences [123, 124], multipulse sequences [117, 120, 129, 130], chirped pulses [115, 125, 130] and shaped pulses from spectral step-phase modulation [116, 127] (cf. **Section 4.1.1.2**).

2.2.1.2 Molecular Multiphoton Ionization

Molecular systems are modeled in the framework of the Born-Oppenheimer approximation by a set of N bound electronic states $|\phi_n\rangle$ characterized by the adiabatic potential energy curves $V_n(R)$. For simplicity, we restrict ourselves to the diatomic case, where the nuclear coordinate R denotes the internuclear separation of the atoms and describes the vibration of the molecule. In the electronic basis, the TDSE for the state vector $\boldsymbol{\psi}(R,t) = (\psi_1(R,t), .., \psi_n(r,t), .., \psi_N)^T$ reads [131]

$$i\hbar\frac{\partial}{\partial t}\boldsymbol{\psi}(R,t) = \hat{\mathcal{H}}(R,t)\boldsymbol{\psi}(R,t). \quad (7)$$

The time-dependent probability amplitudes $\psi_n(R, t)$ of the electronic states describe the nuclear wave packets in the electronic potentials $V_n(R)$. Making use of the dipole approximation, the Born-Oppenheimer Hamiltonian is given by [132]

$$\hat{\mathcal{H}}(R,t) = -\frac{\hbar^2}{2m_r}\frac{\partial^2}{\partial R^2}\hat{1} + \hat{\mathcal{V}}(R) - \boldsymbol{\mu}(R)\cdot\boldsymbol{E}(t), \quad (8)$$

with the reduced mass m_r of the molecule. Explicit expressions of the Hamiltonian matrix are provided in [118, 132]. The diagonal matrix $\mathcal{V}(R)$ contains the potentials $V_n(R)$. These potentials, as well as the R-dependent transition dipole matrix elements contained in $\boldsymbol{\mu}(R)$, were supplied by C. Meier and F. Spiegelman (see [118] for more information) and were recently confirmed by Petersen et al. [133]. The TDSE in **Eq. 7** is solved numerically by iterative propagation of the state vector on a temporal grid employing a Fourier-based split-operator method [134]. The time evolution of $\boldsymbol{\psi}(R, t)$ yields the coupled electron-nuclear (vibronic) wave packet dynamics in the bound molecular system. In a theoretical study, we demonstrated efficient ultrafast switching between different electronic target states in potassium dimers (**Figure 1B**) by resonant non-perturbative control of the vibronic dynamics in the $X^1\Sigma_g$ ground and $A^1\Sigma_u$ states using an intense PLP single-color pulse sequence [118, 131] (cf. **Section 4.1.1.2**).

To calculate the photoelectron contribution from a bound electronic state $V_n(R)$, produced by perturbative one-photon ionization with a probe pulse $E_{pr}(t) = \mathcal{E}_{pr}(t)e^{-i\omega_{pr}t}$, we pursue two alternative strategies. The first approach makes use of the semi-classical difference potential analysis technique by Mulliken [81, 135, 136]. The combination of energy conservation and the Franck-Condon principle provides a mapping $R \rightarrow \omega_k = \omega_k(R)$ of the internuclear distance R to the photoelectron excess energy $\hbar\omega_k$, which is mediated by the difference potential $\Delta V_n(R) = V_{ion}(R) - V_n(R)$. Here, $V_{ion}(R)$ is the Born-Oppenheimer potential of the ionic state. If this mapping is invertible, requiring that $\Delta V_n(R)$ is strictly monotonous throughout the ionization R-window, then the photoelectron contribution from state n can be written as

$$\mathcal{P}_n(\omega_k) \propto \left[\frac{d(\Delta V_n)}{dR}\right]^{-1} \int_{-\infty}^{\infty} \left|\psi_n(R(\omega_k), t)\right|^2 \cdot \left|\mathcal{E}_{pr}(t)\right|^2 dt. \tag{9}$$

If $\Delta V_n(R)$ is non-monotonous within the ionization window, i.e. $\Delta V_n{}'(R)$ vanishes locally, we decompose the wave packet into a set of Gaussian functions which are locally mapped into Gaussian-shaped photoelectron distributions with a narrow, but finite spectral width in the order of the experimental energy resolution. The second approach is based on a perturbative quantum mechanical treatment of the ionization process. Consider a transition from the bound vibrational eigenstate ν to an ionic vibrational eigenstate ν' with the transition frequency $\omega_{\nu'\nu} = \omega_{\nu'} - \omega_\nu$. For a fixed spectral component ω of the probe pulse spectrum $\tilde{E}_{pr}(\omega) = \mathcal{F}[E_{pr}(t)](\omega)$, the photoelectron excess energy is given by $\omega_k = \omega - \omega_{\nu'\nu}$. The photoelectron contribution from the nth electronic state is determined by the Franck-Condon factor $|\langle\nu'|\nu\rangle|^2$, the final population of the bound vibrational states $|\langle\nu|\psi_n^\infty\rangle|^2 = |\langle\nu|\psi_n\rangle_{t\rightarrow\infty}|^2$ and the spectral intensity of the probe pulse:

$$\mathcal{P}_n(\omega_k) \propto \sum_{\nu,\nu'} |\langle\nu'|\nu\rangle|^2 \cdot |\langle\nu|\psi_n^\infty\rangle|^2 \cdot \left|\tilde{\mathcal{E}}_{pr}(\omega_k + \omega_{\nu'\nu})\right|^2. \tag{10}$$

The quantum mechanical description was used to reproduce and analyze the experimental results in [132, 137]. Using intense PLP single-color multipulse sequences followed by an ionizing probe pulse with a different color, we were able to demonstrate the resonant non-pertubative control scheme described above experimentally [131, 132, 137].

2.2.2 Perturbative Intraband and Interband Interference in Multiphoton Ionization

In this section we consider perturbative atomic MPI with a pulse train consisting of $\mathcal{M}$ pulses. A schematic representation of the available intraband pathways for absorption of $\mathcal{N} = 2$ photons is shown in **Figure 2** for (A) single-color, (B) bichromatic, and (C) trichromatic ionization scenarios. The specific scheme for bichromatic intraband MPI reported in [99] and interband MPI by $(3\omega{:}4\omega)$ pulse sequences reported in [73] is presented in **Figure 1C**. To describe the general intraband case, we extend the perturbative description of non-resonant bichromatic MPI reported in [73, 105, 106] to photoionization with $\mathcal{N}$ photons from a multichromatic CEP-stable sequence of $\mathcal{M}$ pulses. To this end we consider absorption of r_j RCP and l_j LCP photons from the jth polarization components $E_j^{+1}(t)$ and $E_j^{-1}(t)$ introduced in **Eq. 2**, respectively. Representing the total number of absorbed RCP and LCP photons by r and l,

$$r = \sum_{j=1}^{\mathcal{M}} r_j \quad \text{and} \quad l = \sum_{j=1}^{\mathcal{M}} l_j, \tag{11}$$

the order of the MPI process is $\mathcal{N} = r + l$. We introduce $(\boldsymbol{l}, \boldsymbol{r}) = (l_1, \ldots, l_{\mathcal{M}}, r_1, \ldots, r_{\mathcal{M}})$ as a shorthand notation for the tuples of absorbed photon numbers to characterize the relevant temporal multiphoton field

$$E^{(\boldsymbol{l},\boldsymbol{r})}(t) = \prod_{j=1}^{\mathcal{M}} \left[E_j^{-1}(t)\right]^{r_j} \left[E_j^{+1}(t)\right]^{l_j}, \tag{12}$$

which is written down explicitly for a tricromatic field ($\mathcal{M} = 3$)

$$E^{(l_1,l_2,l_3,r_1,r_2,r_3)}(t) = \left[E_1^{-1}(t)\right]^{r_1} \left[E_1^{+1}(t)\right]^{l_1} \left[E_2^{-1}(t)\right]^{r_2} \left[E_2^{+1}(t)\right]^{l_2} \left[E_3^{-1}(t)\right]^{r_3} \left[E_3^{+1}(t)\right]^{l_3}. \tag{13}$$

Taking the Fourier transform of the temporal multiphoton field $E^{(\boldsymbol{l},\boldsymbol{r})}(t)$, we obtain the multiphoton spectrum $\mathcal{S}^{(\boldsymbol{l},\boldsymbol{r})}(\omega)$ to describe the absorption of $(\boldsymbol{l}, \boldsymbol{r})$ photons

$$\mathcal{S}^{(\boldsymbol{l},\boldsymbol{r})}(\omega) = \mathcal{F}\left[E^{(\boldsymbol{l},\boldsymbol{r})}(t)\right](\omega). \tag{14}$$

Taking into consideration the selection rules for absorption of RCP ($\Delta m = -1$) and LCP ($\Delta m = +1$) photons and ignoring for simplicity $\Delta l = -1$, the dipole moments $\mu_{(\boldsymbol{l},\boldsymbol{r})}$, the multiplicity of a specific $\mathcal{N}$-photon ionization pathway given by the multinomial coefficients $(\mathcal{N}, (\boldsymbol{l}, \boldsymbol{r}))$, the kinetic energy $\hbar\omega$ and ionization potential $\hbar\omega_{IP}$ as well as the angular distribution $Y_{\mathcal{N},l-r}(\theta, \phi)$ for the absorption of $\mathcal{N} = l + r$ photons, we obtain the photoelectron wave function

$$\begin{aligned}\psi_{\mathcal{N}}(\varepsilon, \theta, \phi) &= i^{\mathcal{N}} \sum_{\mathcal{N}=l+r} \begin{pmatrix} \mathcal{N} \\ (\boldsymbol{l}, \boldsymbol{r}) \end{pmatrix} \mu_{(\boldsymbol{l},\boldsymbol{r})}\, S^{(\boldsymbol{l},\boldsymbol{r})}(\hbar\omega + \hbar\omega_{IP})\, Y_{\mathcal{N},l-r}(\theta, \phi), \\ &= \sum_k \alpha_k \psi_{l,m_k}(\varepsilon, \theta, \phi),\end{aligned} \tag{15}$$

where we sum over all indices $(\boldsymbol{l}, \boldsymbol{r})$ such that $l + r = \mathcal{N}$. The α_k describe the complex-valued coefficients of the partial wave functions ψ_{l,m_k} including the multiphoton transition dipole moments and the electric field amplitudes and phases. In the discussion of the different control scenarios below, we use a shorthand notation based on **Eq. 15** including the amplitudes and phases of α_k relevant to the control scenario. In addition, since we focus on the field-induced variation of the wave function, the

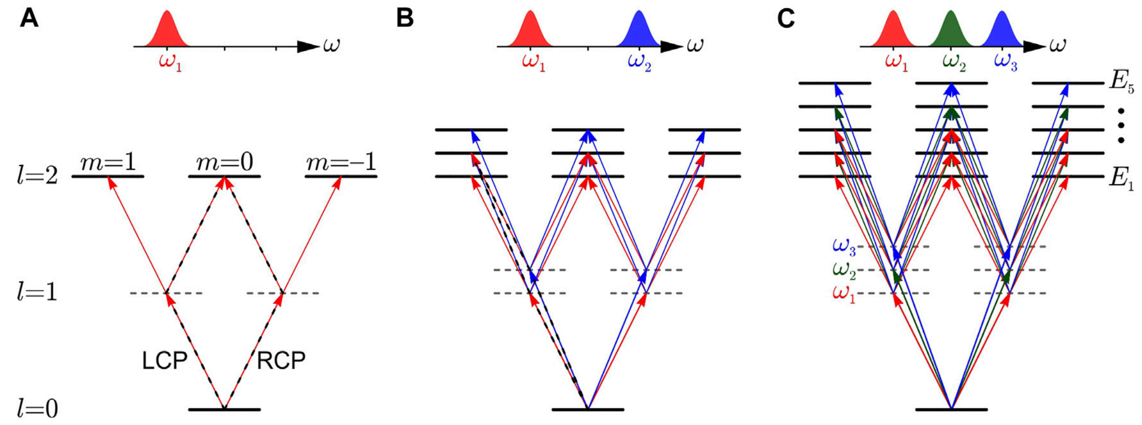

FIGURE 2 | Pathways for intraband MPI with $\mathcal{N} = 2$ photons using elliptically polarized multichromatic pulse sequences: **(A)** $\mathcal{M} = 1$ single-color, **(B)** $\mathcal{M} = 2$ bichromatic, **(C)** $\mathcal{M} = 3$ trichromatic pulses. The black dotted lines on top of the arrows indicate a pair of indistinguishable pathways.

intrinsic atomic phases and radial amplitudes of the dipole couplings are generally omitted. The geometric part of the dipole couplings, given by the Wigner 3-j symbols, is written explicitly whenever the amplitudes of the participating partial wave functions cannot be manipulated individually by the electric field amplitudes. Otherwise, the field amplitudes are generally adapted in the experiment to optimize the interference contrast. The optical phases are written explicitly whenever they are used as control parameters to manipulate the resulting photoelectron wave packet. A more comprehensive theoretical description is given for example in [107–109, 138].

Control of multiphoton processes by multichromatic pulse sequences is based on the interference of multiple pathways leading to the same final state. As we increase the number of pulses, both the number of available quantum pathways and the number of final states increase significantly, opening up more versatile options for control. **Figure 2** illustrates the pathways for absorption of $\mathcal{N} = 2$ photons in a single-color ($\mathcal{M} = 1$) scenario (A), a bichromatic ($\mathcal{M} = 2$) scheme (B), and trichromatic ($\mathcal{M} = 3$) (C) intraband MPI with elliptical polarization. Examples for indistinguishable pairs of pathways (see below) are indicated with black dotted lines on top of the arrows. The numbers of available pathways and final states scale differently with the number of absorbed photons ($\mathcal{N}$) and the number of pulses ($\mathcal{M}$) in the sequence, suggesting a change in the overall physical picture of MPI for single-color versus multichromatic pulse sequences. The total number of final states $\mathcal{C}_f(\mathcal{M},\mathcal{N})$ is the product of the number of available angular momentum states $\mathcal{C}_l(\mathcal{N})$ and the number of different energy levels. The former is $\mathcal{C}_l(\mathcal{N}) = \mathcal{N} + 1$ determined by the selection rules $\Delta m = \pm 1$ and the latter is given by all combinations of energies

$$\mathcal{C}_e(\mathcal{M},\mathcal{N}) = \frac{(\mathcal{M}+\mathcal{N}-1)!}{\mathcal{N}!(\mathcal{M}-1)!}, \tag{16}$$

some of which may be degenerate. For each absorption of a photon, there are $2\mathcal{M}$ different paths, i.e. two for the circularity (LCP and RCP) and $\mathcal{M}$ for the different colors, yielding $\mathcal{C}_p(\mathcal{M},\mathcal{N}) = (2\mathcal{M})^{\mathcal{N}}$ pathways for $\mathcal{N}$-photon ionization. Because the ordering of the photons in an absorption event, i.e. in a specific (non-resonant) pathway, cannot be distinguished, the number of the distinguishable pathways is given by the number of contributions in **Eq. 15** yielding

$$\mathcal{C}_d(\mathcal{M},\mathcal{N}) = \begin{pmatrix} \mathcal{N}+2\mathcal{M}-1 \\ 2\mathcal{M}-1 \end{pmatrix}. \tag{17}$$

An overview of the numbers of angular momentum states ($\mathcal{C}_l$), free electron energy states ($\mathcal{C}_e$), pathways ($\mathcal{C}_p$) and distinguishable pathways ($\mathcal{C}_d$) for ionization with $\mathcal{N} = 1, \ldots, 4$ and $\mathcal{M} = 1, 2, 3$ pulses is presented in **Table 1**.

In addition to the above discussed intraband interferences characterized by absorption of $\mathcal{N}$ photons, in multichromatic scenarios further interferences arise when pathways with a different number of absorbed photons $\mathcal{N}_1$ and $\mathcal{N}_2$ interfere. In this case the wave function is a superposition of both contributions

$$\psi(\varepsilon,\theta,\phi) = \psi_{\mathcal{N}_1}(\varepsilon,\theta,\phi) + \psi_{\mathcal{N}_2}(\varepsilon,\theta,\phi). \tag{18}$$

If both pathways address overlapping final continuum states, i.e. the energy gained by absorption of $\mathcal{N}_1$ photons with $\hbar\omega_1$ agrees within the bandwidth with the energy delivered by $\mathcal{N}_2$ photons with $\hbar\omega_2$, as shown in **Figure 1C** for a (3ω:4ω) bichromatic field, CEP-sensitive interband interferences occur. Bichromatic fields with commensurable frequencies $\omega_2 = \omega_1 \cdot \mathcal{N}_1/\mathcal{N}_2$ satisfy the above condition $\varepsilon = \hbar\mathcal{N}_1\omega_1 = \hbar\mathcal{N}_2\omega_2$. Examples for CEP-control of interband interferences in the MPI by linearly and circularly polarized bichromatic pulse sequences are presented in **Section 4.2.1.1** and **Section 4.2.1.2**.

2.2.3 2D *Ab Initio* Simulation of Atomic Multiphoton Ionization in Cycloidal Laser Fields

Another efficient method to simulate atomic photoionization dynamics by polarization-shaped ultrashort laser fields is based on solving of the TDSE numerically for a 2D model system

TABLE 1 | Overview of the total number of possible pathways for ionization with a given number of photons ($\mathcal{N}$) from ($\mathcal{M}$) pulses. Shown are the numbers of angular momentum states ($\mathcal{C}_l$), free electron energy states ($\mathcal{C}_e$), pathways ($\mathcal{C}_p$) and distinguishable pathways ($\mathcal{C}_d$).

	$\mathcal{N} = \mathbf{1}$		$\mathcal{N} = \mathbf{2}$		$\mathcal{N} = \mathbf{3}$		$\mathcal{N} = \mathbf{4}$	
$\mathcal{M} = 1$	$\mathcal{C}_l = 2$	$\mathcal{C}_e = 1$	$\mathcal{C}_l = 3$	$\mathcal{C}_e = 1$	$\mathcal{C}_l = 4$	$\mathcal{C}_e = 1$	$\mathcal{C}_l = 5$	$\mathcal{C}_e = 1$
	$\mathcal{C}_p = 2$	$\mathcal{C}_d = 2$	$\mathcal{C}_p = 4$	$\mathcal{C}_d = 3$	$\mathcal{C}_p = 8$	$\mathcal{C}_d = 4$	$\mathcal{C}_p = 16$	$\mathcal{C}_d = 5$
$\mathcal{M} = 2$	$\mathcal{C}_l = 2$	$\mathcal{C}_e = 2$	$\mathcal{C}_l = 3$	$\mathcal{C}_e = 3$	$\mathcal{C}_l = 4$	$\mathcal{C}_e = 4$	$\mathcal{C}_l = 5$	$\mathcal{C}_e = 5$
	$\mathcal{C}_p = 4$	$\mathcal{C}_d = 4$	$\mathcal{C}_p = 16$	$\mathcal{C}_d = 10$	$\mathcal{C}_p = 64$	$\mathcal{C}_d = 20$	$\mathcal{C}_p = 256$	$\mathcal{C}_d = 35$
$\mathcal{M} = 3$	$\mathcal{C}_l = 2$	$\mathcal{C}_e = 3$	$\mathcal{C}_l = 3$	$\mathcal{C}_e = 6$	$\mathcal{C}_l = 4$	$\mathcal{C}_e = 10$	$\mathcal{C}_l = 5$	$\mathcal{C}_e = 15$
	$\mathcal{C}_p = 6$	$\mathcal{C}_d = 6$	$\mathcal{C}_p = 36$	$\mathcal{C}_d = 21$	$\mathcal{C}_p = 216$	$\mathcal{C}_d = 56$	$\mathcal{C}_p = 1296$	$\mathcal{C}_d = 126$

aligned in the laser polarization plane. In [121], we employed the 2D model potential shown in **Figure 1D**

$$V(r) = -\frac{ze^2}{4\pi\varepsilon_0}\frac{\operatorname{erf}(r/a)}{r}, \tag{19}$$

with the error function erf and a soft-core parameter a, and solved the TDSE for the time-dependent Hamiltonian

$$\mathcal{H}(\boldsymbol{r}, t) = -\frac{\hbar^2}{2m_e}\Delta + V(r) + e\,\boldsymbol{r}\cdot\boldsymbol{E}(t) \tag{20}$$

on a 2D grid using the Fourier-based split-operator method [134]. Specifically, atomic MPI with cycloidal, i.e. COCP and CRCP, femtosecond laser pulse sequences was investigated. Employing single-color pulse sequences, we were able to reproduce selected recent experimental results on the generation of photoelectron vortices [102, 103] and to analyze the transient vortex formation dynamics in different physical pictures, including the bound state population dynamics, the time evolution of the free electron wave function and its asymptotic topological charge. Employing cycloidal bichromatic fields, we reproduced the experimental results on the generation of free electron wave packets with odd rotational symmetries [73]. We analyzed the final state wave function with respect to the relative orientation between field and PMD and extracted the azimuthal probability density current to validate the physical discussions in the experimental studies [73, 105, 106]. Furthermore, the simulations allowed us to examine the influence of experimental CEP and Gouy phase fluctuations on the measured PMD. Eventually, we applied the technique to investigate photoelectron vortices theoretically in so far unexplored intensity regimes.

3 EXPERIMENT

In this section, we introduce our experimental scheme for the coherent control of ultrafast MPI dynamics in atoms and molecules using polarization-tailored single-color or multichromatic fields. In the experimental studies, we combine advanced supercontinuum pulse shaping techniques with the highly differential detection of photoelectrons using a VMI spectrometer. The experimental setup is portrayed in **Figure 3**. CEP-stable polarization-shaped laser pulse sequences are generated using a phase-stabilized white light polarization shaper in 4*f* geometry. Photoelectron wave packets, released by the interaction of the shaped pulses with the atomic or molecular sample in the VMI spectrometer, are observed with energy and angular resolution. By rotating the pulses about the laser beam axis using a wave plate, the VMI spectrometer is turned into a photoelectron tomography apparatus, allowing us to retrieve the full 3D PMD. In the following, we give an overview of white light polarization shaping in **Section 3.1** and photoelectron tomography in **Section 3.2**. For a more detailed description of both techniques, we refer to [106].

3.1 Supercontinuum Polarization Pulse Shaping

Various experimental schemes for the generation of multicolor laser fields have been reported, including 4*f* pulse shapers adapted to an octave-spanning WLS [61, 64] and extensions to optical waveform synthesizers [139, 140] as well as four-wave mixing schemes [141] and molecular modulation [142–144]. Our method to generate multichromatic polarization-tailored pulse sequences is based on 4*f*-polarization pulse shaping of a white light supercontinuum. The primary light source of our experiments is an actively CEP-stabilized multipass chirped pulse amplifier system (FEMTOLASERS Rainbow 500, CEP 4 module, Femtopower HR 3 kHz) providing 20 fs infrared pulses centered at 790 nm with an energy of 1.0 mJ. These pulses are used to seed a neon-filled hollow-core fiber (absolute pressure ~ 2.0 bar) generating an over-octave spanning WLS which is amplitude- and phase-modulated in the spectral domain using a home-built 4*f* polarization pulse shaper [48, 50, 51, 145]. While traditional 4*f* pulse shaping allows for either independent amplitude and phase modulation or phase and polarization shaping [51, 145], recently we introduced a pulse shaping scheme specifically adapted for the independent shaping of amplitude, phase and polarization of bichromatic fields [65, 106, 146]. The bichromatic white light polarization shaper is shown on the lefthand side of **Figure 3**. Bichromatic amplitude profiles are sculptured from the WLS via combined amplitude and phase modulation using a traditional polarization shaping setup consisting of a 640 pixel dual-layer liquid crystal spatial light modulator (LC-SLM) in the Fourier plane of a folded 4*f* setup with holographic transmission gratings at the in- and output. A customized composite polarizer mounted directly behind the LC-SLM enables independent polarization control of both spectral bands (colors). Along the spectral axis, the polarizer is divided into two parts, each of which can be chosen in *s*- or *p*-configuration, resulting in the generation of either bichromatic PLP (both colors *s*- or *p*-polarized) or OLP

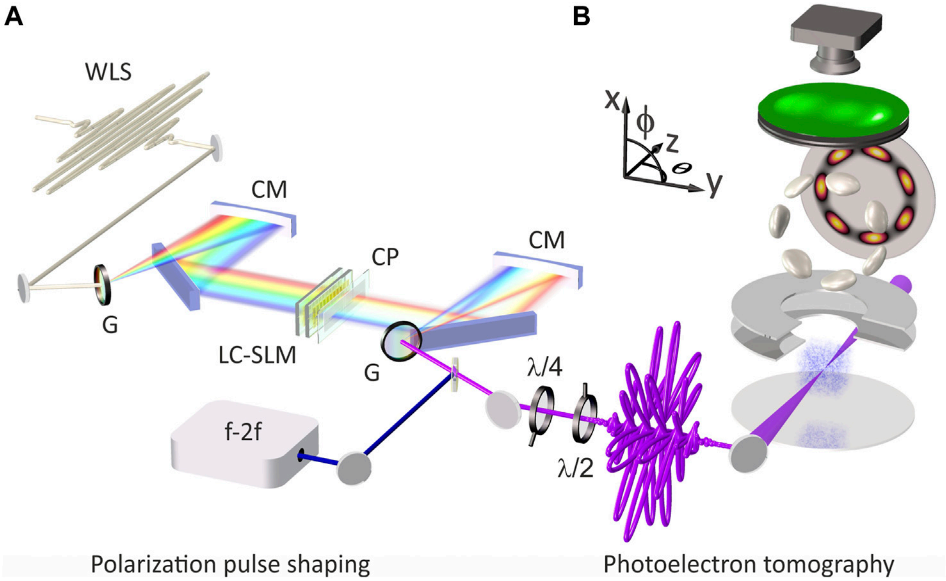

FIGURE 3 | Experimental setup for multichromatic coherent control of MPI utilizing a white light polarization pulse shaper **(A)** and a photoelectron VMI spectrometer **(B)**. Multichromatic amplitude, phase and polarization tailoring of an input WLS is implemented by a specifically adapted polarization shaper in folded 4*f* geometry. The WLS input beam is spectrally dispersed at the input grating (G), collimated at the cylindrical mirror (CM) and spectrally modulated in the Fourier plane by a dual-layer LC-SLM and a custom composite polarizer (CP). Active CEP-stabilization is realized by an *f*-2*f* interferometer feeding the control loop of the laser system. A superachromatic $\lambda/4$ wave plate at the output allows to generate circularly polarized pulse sequences. Using an additional $\lambda/2$ wave plate, the shaped laser pulse is rotated about the beam axis, which is the basis for VMI-based photoelectron tomography. The VMI spectrometer on the right consists of an electrostatic lens system projecting the PMD onto an microchannel plate detector attached to a phosphor screen. Images of the resulting 2D projections are recorded with a charge-coupled device camera. Exemplarily, a CRCP (3ω:4ω) output pulse is depicted in magenta along with the tomographically reconstructed 3D PMD created by MPI of potassium atoms.

(one color *s*-, the other one *p*-polarized) fields. The bichromatic pulse shaping approach allows us to control the center frequency ratio, spectral bandwidths and amplitude profiles of both spectral bands and, moreover, independently permits the application of arbitrary phase modulation functions. By use of a superachromatic quarter wave plate ($\lambda/4$) at the shaper output, we generate circularly polarized single-color or bichromatic pulse sequences. An additional half wave plate ($\lambda/2$) is used to rotate the polarization-shaped laser pulses about the propagation axis, which is the basis for the photoelectron tomography technique discussed in **Section 3.2**. To ensure the CEP-stability of the shaped pulses, we use the shaper to generate an additional (ω: 2ω) field which is split off the main beam by a dichroic mirror and sent to an *f*-2*f* interferometer. The interferometer feeds the active control loop of the amplifier, which stabilizes the CEP of the shaped pulses before they are focused into the VMI spectrometer. The root mean squared CEP stability after the shaper was measured over 11 h and is better than 215 mrad [101]. Finally, dispersion control and pulse characterization are implemented *in situ*, i.e. in the interaction region of the VMI spectrometer, by using the shaper for adaptive optimization of the highly nonlinear MPI of xenon atoms and to perform shaper-based cross-correlation measurements [146].

3.2 Photoelectron Tomography

In order to study the full 3D PMD caused by the interaction of atoms and molecules with polarization-tailored ultrashort laser pulses, we employ the VMI technique [83, 103] for the energy- and angle-resolved measurement of photoelectron wave packets. The VMI spectrometer is shown on the righthand side of **Figure 3**. The tailored laser pulses are focused via a broadband silver mirror with a focal length of 250 mm into the interaction region of the VMI spectrometer. The background pressure is typically in the order of 5×10^{-7} mbar. All experiments were carried out in the gas phase. Alkali atomic samples are supplied by dispenser sources (working pressure: $\sim 10^{-7}$ mbar), whereas rare gases or molecular samples are injected using an effusive gas-inlet (working pressure: $\sim 10^{-6}$ mbar). An electrostatic lens setup consisting of a repeller, an extractor and an Einzellens, projects the 3D PMD created by MPI of the sample by the incident laser pulses onto a chevron-type microchannel plate detector stacked with a phosphor screen. The resulting 2D image of the projected PMD is recorded by a charge-coupled device camera. PMDs created by MPI with either linearly or circularly polarized laser pulses are, in general, cylindrically symmetric and can therefore be reconstructed from a single 2D image via Abel inversion, e.g. using the pBASEX algorithm [88]. In contrast, PMDs created by polarization-shaped pulses typically exhibit no such symmetry. For the retrieval of 3D PMDs with arbitrary shape, we developed a tomographic reconstruction technique [89] based on the rotation of the laser pulse—and hence the PMD—using a superachromatic $\lambda/2$ wave plate. After acquiring numerous 2D projections of the PMD under various rotation angles, we retrieve the 3D PMD by application of tomographic techniques such as the Fourier slice algorithm [89, 147, 148] or the backprojection algorithm [90, 147, 149]. An advantage of the Fourier slice method is that the angular discretization inherent to the measurement appears only in the Fourier domain representation, whereas the retrieved real-space PMD is angularly smooth. For a typical tomographic measurement, we use about 45 different orientations of the $\lambda/2$ wave plate ranging from -90° to 86°. Energy calibration of the reconstructed 3D PMD is performed by taking 151 azimuthal 2D slices through the 3D data cube and convert the radial momentum distributions into corresponding energy distributions. We estimate an energy-resolution of better than 80 meV for photoelectrons with a kinetic energy of about 1 eV. Thus, our VMI-based photoelectron tomography technique is well suited to retrieve the highly structured 3D PMDs generally created by MPI with multichromatic polarization-shaped laser pulse sequences. Similar tomographic techniques have been applied, e.g., for the imaging of molecular orbitals [148], the discrimination of chiral molecules *via* the multiphoton PECD [150] and the time-resolved imaging of ultrafast laser-matter interactions inside transparent media [149].

4 RESULTS AND DISCUSSION

In this section, we discuss our experimental results on photoelectron tomography of 3D PMDs obtained by atomic and molecular MPI using multichromatic polarization-controlled pulse sequences. We present our findings in the order of the type of pulse sequence: We start with experiments on MPI with single-color pulse sequences in **Section 4.1** and focus on various coherent control scenarios by bichromatic pulse sequences in **Section 4.2**. New results on trichromatic pulse sequences are presented in **Section 4.3**.

4.1 Single-Color Pulse Sequences

Single-color pulses consist of a single connected spectral band with bandwidth $\Delta\omega$ centered around a carrier frequency ω_1. A set of single-color pulse sequences for different polarizations is depicted in **Figure 4**. These pulses are the starting point of our discussion.

4.1.1 Single-Color Linearly Polarized Pulse Sequences

Single-color PLP pulse sequences with variable time-delay τ, as shown in **Figure 4A**, are the standard tool in pump-probe experiments [151]. Even in the overlapping region $\tau \approx 0$, such pulses remain linearly polarized. In contrast, OLP pulse sequences, as shown in **Figure 4B**, additionally address the spatiotemporal aspect of the light-matter interaction due to their time-dependent polarization. Their application ranges from the phase-control of currents in semiconductors [152] to the steering of molecular rotation [153, 154]. Crossed polarizations demand a vectorial description of the field and thus provide access to the angular properties of the interaction energy $-\boldsymbol{\mu} \cdot \boldsymbol{E}$. Depending on the relative phase, OLP pulses are either linearly, elliptically or circularly polarized at $\tau = 0$.

4.1.1.1 Perturbative Multiphoton Ionization

In [11], Wollenhaupt et al. have used phase-locked pairs of linearly polarized single-color pulses to study the interference of ultrashort free electron wave packets generated by perturbative MPI of potassium atoms. By variation of the time delay in the PLP sequence, the interference pattern in the photoelectron kinetic energy spectrum from one-photon ionization of the excited $5p$ state was controlled. The observation of interferences in the photoelectron spectrum demonstrated that the coherence properties of the ultrashort laser pulses were transferred to the electrons. Using OLP sequences, i.e. crossed polarizations, no such interference fringes have been found in the threshold electrons. However, the quantum interferences reappeared at

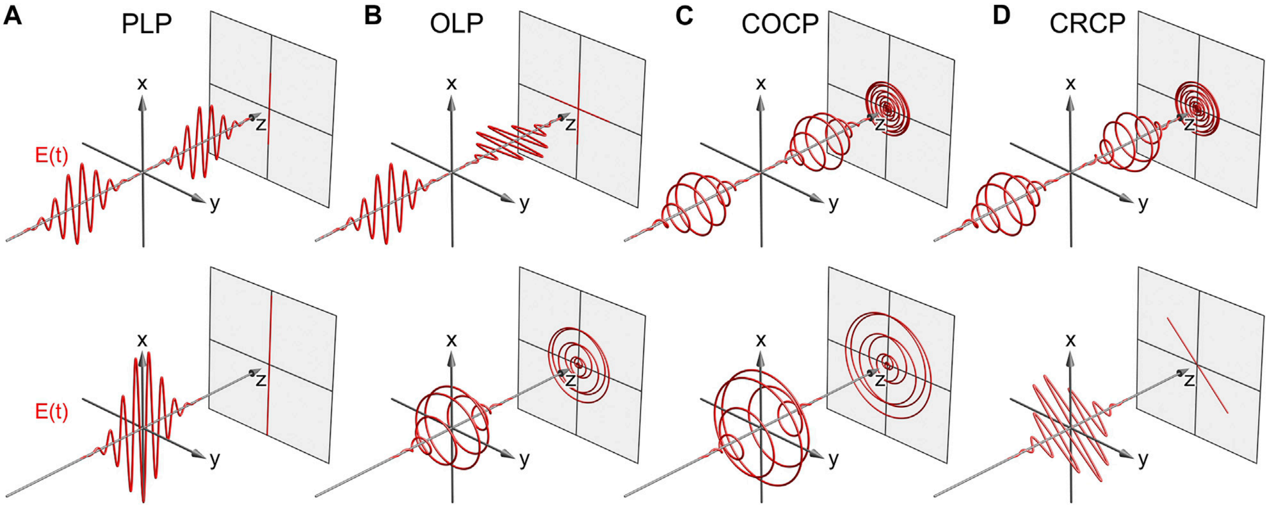

FIGURE 4 | Single-color pulse sequences. The projection in *z*-direction visualizes the time-dependent electric field vector at the position of the atom or molecule. **(A)** PLP, **(B)** OLP, **(C)** COCP and **(D)** CRCP single-color pulse sequences. Upper figures: Sequence with separated pulses $\tau > 2\Delta t$, lower figures: Coinciding pulses at $\tau = 0$.

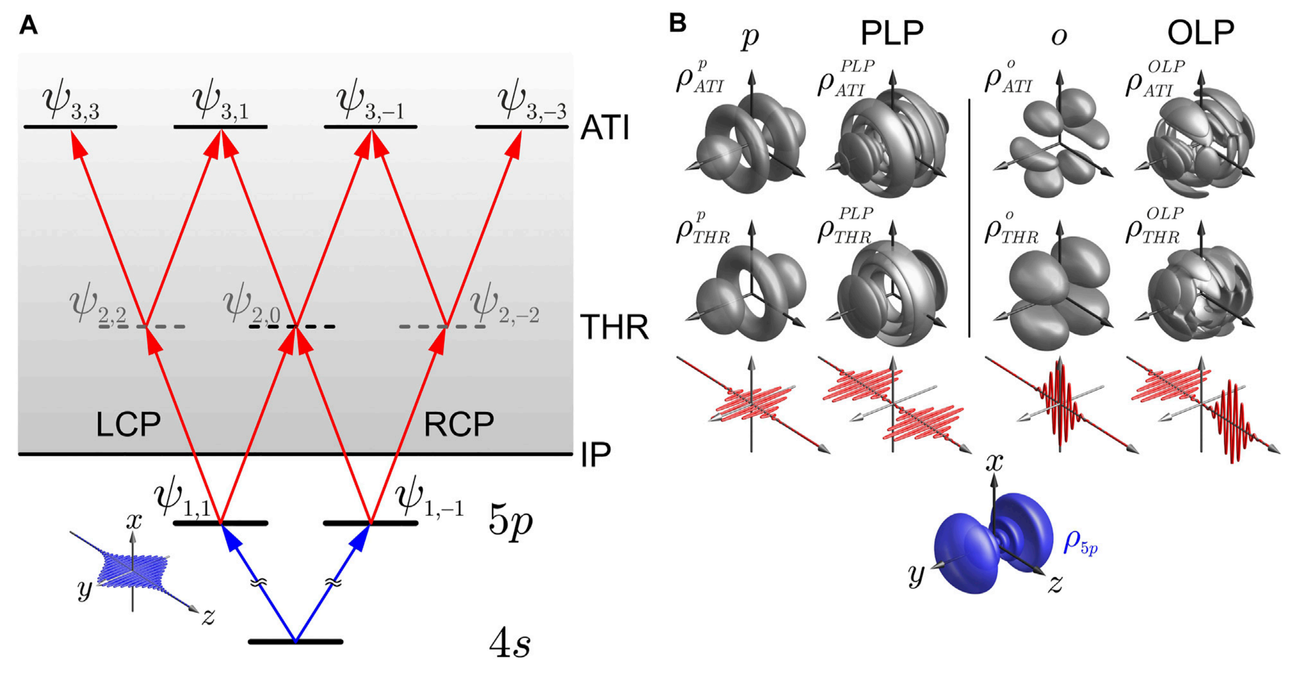

FIGURE 5 | One- and two-photon ionization of potassium atoms with an infrared PLP or OLP pulse sequence after preparation of the atom in the excited 5*p* state by a blue prepulse. **(A)** Energy level diagram for excitation and ionization in the spherical basis. **(B)** Simulated electron densities of the excited 5*p* state **(bottom)** and the emitted photoelectron at the threshold **(middle row)** and ATI **(top row)**. Left side of each column: Single pulse ionization at the threshold and the ATI for parallel ρ^p_{THR} (ρ^p_{ATI}) and orthogonal ρ^o_{THR} (ρ^o_{ATI}) polarized pulses, respectively. Right side of each column: Double pulse ionization at the threshold (ATI) for PLP $\rho^{\mathrm{PLP}}_{\mathrm{THR}}$ ($\rho^{\mathrm{PLP}}_{\mathrm{ATI}}$) and OLP $\rho^{\mathrm{OLP}}_{\mathrm{THR}}$ ($\rho^{\mathrm{OLP}}_{\mathrm{ATI}}$) pulse sequences.

twice the modulation frequency in the above-threshold ionization (ATI).

To rationalize the experimental findings reported in [11], we apply the general formalism discussed in **Section 2.2.2** to describe one- and two-photon ionization of a pre-excited atom with single-color PLP and OLP pulse sequences and analyze the full 3D PMD. **Figure 5A** shows a schematic energy level diagram of potassium atoms for the excitation of the 5*p* state and subsequent photoionization at the threshold (THR) and the ATI. The description in the spherical basis provides a consistent picture for excitation and ionization with both PLP and OLP sequences. Simulated PMDs at the ionization threshold and the ATI are depicted in **Figure 5B**. The left column shows the PMDs from ionization with either a single pulse or a PLP pulse sequence whose polarizations are parallel (*p*) to the initial blue excitation pulse. Ionization with a single orthogonal (*o*) polarized pulse or an OLP pulse sequence are depicted in the right column. To calculate the modulation of the interference in the photoelectron spectra, we first consider the wave function in the excited 5*p* state prepared by the initial, linearly polarized blue (405 nm) laser pulse. In the spherical basis, the *p* state is a superposition of the two $\psi_{1,\pm1}$ states

$$\Psi_{5p} = \psi_{1,1} + \psi_{1,-1}. \tag{21}$$

Taking into account the transition dipole moments determined by the Wigner 3-*j* symbols, the absorption of another parallel or orthogonal polarized photon from the 5*p* state yields the wave functions for the photoelectrons at the ionization threshold

$$\begin{aligned} \Psi^p_{\mathrm{THR}} &= \frac{1}{\sqrt{15}}\psi_{2,2} + \frac{2}{3\sqrt{10}}\psi_{2,0} + \frac{1}{\sqrt{15}}\psi_{2,-2}, \\ \Psi^o_{\mathrm{THR}} &= \frac{1}{\sqrt{15}}\psi_{2,2} + \frac{1}{\sqrt{15}}\psi_{2,-2}. \end{aligned} \tag{22}$$

By calculating the electron density $\rho(\varepsilon,\theta,\phi) = |\Psi(\varepsilon,\theta,\phi)|^2$, we see that ionization with a parallel polarized field yields the expected *d*-type electron density ρ^p_{THR} plotted on the left side of **Figure 5B**, whereas orthogonal ionization of the aligned 5*p* state gives rise to the $d_{x,y}$-type state due to the cancellation of the $\psi_{2,0}$ state via destructive quantum interference. The generation of such a $d_{x,y}$-type state in the continuum, exhibiting a c_4 rotational symmetry, has been experimentally demonstrated using a two-color OLP sequence to ionize potassium atoms [105]. Ionization with a single-color PLP sequence, i.e. two phase locked time-delayed parallel polarized pulses, leads to the superposition state

$$\Psi^{\mathrm{PLP}}_{\mathrm{THR}} = \left(1 + e^{-i\varepsilon\tau/\hbar}\right)\Psi^p_{\mathrm{THR}} \tag{23}$$

characterized by the interference structures in the electron density $\rho^{\mathrm{PLP}}_{\mathrm{THR}}$. By integration over the angular coordinates θ and ϕ, we obtain the energy-resolved photoelectron spectrum

$$I^{\mathrm{PLP}}_{\mathrm{THR}}(\varepsilon) \propto I^p_{\mathrm{THR}}(\varepsilon)\left[1 + \cos(\varepsilon\tau/\hbar)\right], \tag{24}$$

yielding the fully cosinusoidally modulated spectrum in agreement with the experimental results [11]. In contrast, in the OLP case, the superposition of two different wave functions

$$\Psi^{\mathrm{OLP}}_{\mathrm{THR}} = \Psi^{p}_{\mathrm{THR}} + \Psi^{o}_{\mathrm{THR}}\, e^{-i\varepsilon\tau/\hbar} \tag{25}$$

results in the highly patterned electron density $\rho^{\mathrm{OLP}}_{\mathrm{THR}}$ displayed on the right side of **Figure 5B**. Again, by angular integration we find that in the OLP case the interference in the photoelectron spectrum cancels out as reported in [11]. Consequently, the OLP-photoelectron spectrum at the ionization threshold is unstructured and independent of the time delay

$$I^{\mathrm{OLP}}_{\mathrm{THR}}(\varepsilon) \propto I_{\mathrm{THR}}(\varepsilon). \tag{26}$$

In the next step, we apply the same procedure to analyze the PMDs at the ATI. To this end, we write down the corresponding wave functions and densities and calculate the photoelectron spectra to rationalize the experimental findings in the ATI spectrum. Absorption of another parallel (orthogonal) linearly polarized photon from the threshold states given by **Eq. 22** yields the wave functions in the ATI

$$\begin{aligned} \Psi^{p}_{\mathrm{ATI}} &= \frac{1}{\sqrt{105}}\psi_{3,3} + \frac{3}{15\sqrt{7}}\psi_{3,1} + \frac{3}{15\sqrt{7}}\psi_{3,-1} + \frac{1}{\sqrt{105}}\psi_{3,-3}, \\ \Psi^{o}_{\mathrm{ATI}} &= \frac{1}{\sqrt{105}}\psi_{3,3} - \frac{1}{15\sqrt{7}}\psi_{3,1} - \frac{1}{15\sqrt{7}}\psi_{3,-1} + \frac{1}{\sqrt{105}}\psi_{3,-3}. \end{aligned} \tag{27}$$

The corresponding densities ρ^{p}_{ATI} and ρ^{o}_{ATI} are shown in the upper row of **Figure 5B**. Assuming the two pulses in the sequence are fully separated ($\tau \gg \Delta t$), i.e. the temporal overlap vanishes, there are no contributions from paths describing sequential ionization from different pulses, and hence the wave functions for PLP and OLP sequences read

$$\begin{aligned} \Psi^{\mathrm{PLP}}_{\mathrm{ATI}} &= \left(1 + e^{-2i\varepsilon\tau/\hbar}\right)\Psi^{p}_{\mathrm{ATI}}, \\ \Psi^{\mathrm{OLP}}_{\mathrm{ATI}} &= \Psi^{p}_{\mathrm{ATI}} + \Psi^{o}_{\mathrm{ATI}}\, e^{-2i\varepsilon\tau/\hbar}. \end{aligned} \tag{28}$$

Again, in the PLP case, the PMDs given by $\rho^{\mathrm{PLP}}_{\mathrm{ATI}}$, and hence the corresponding photoelectron spectra in the ATI are fully modulated by the delay-dependent interferences

$$I^{\mathrm{PLP}}_{\mathrm{ATI}}(\varepsilon) \propto I^{p}_{\mathrm{ATI}}(\varepsilon)\left[1 + \cos\left(2\varepsilon\tau/\hbar\right)\right]. \tag{29}$$

Using the above method to calculate the PMDs from two-photon ionization with an OLP sequence, given by $\rho^{\mathrm{OLP}}_{\mathrm{ATI}}$, and the respective photoelectron spectra, we obtain

$$I^{\mathrm{OLP}}_{\mathrm{ATI}}(\varepsilon) \propto I_{\mathrm{ATI}}(\varepsilon)\left[5 + 3\cos\left(2\varepsilon\tau/\hbar\right)\right]. \tag{30}$$

In contrast to the unmodulated photoelectron spectra from ionization with OLP pulses at the threshold (**Eq. 26**), the spectra in the ATI are indeed modulated—albeit more weakly—in the OLP case in agreement with the experimental work.

In another polarization-sensitive pump-probe experiment, single-color PLP and OLP pulse sequences have been used to control the perturbative MPI of potassium molecules [52]. It was demonstrated that the ionization efficiency is higher for OLP pulses than for PLP pulses. This result was rationalized by the orthogonality of transition dipole moments encountered along the major MPI pathways in the potassium dimer. The experiment, which included the first demonstration of control of molecular dynamics via ultrafast polarization shaping, showed that tailored polarization-shaped pulses are better suited than the corresponding linearly polarized fields to manipulate the spatiotemporal evolution of molecular wave functions.

4.1.1.2 Non-perturbative Resonance-Enhanced Multiphoton Ionization

The basic concept behind the non-perturbative control of REMPI processes is depicted in **Figure 1A**. The scheme is based on the selective population of dressed states (SPODS), recently reviewed in [119], by a sequence of PLP single-color femtosecond laser pulses. A relatively weak prepulse with a pulse area of $\pi/2$ [5] with respect to the resonant transition—typically between the ground and first excited state—is followed by an intense main pulse. Initially, the prepulse excites an electronic wave packet of maximum coherence, i.e., an efficient charge oscillation described by a time-dependent induced dipole moment $\boldsymbol{\mu}_i(t)$. After a time delay τ, the electric field $\boldsymbol{E}(t)$ of the main pulse couples to the induced charge oscillation. By suitable adaption of the optical phase to the electric dipole dynamics, the interaction energy $-\boldsymbol{\mu}_i(t)\cdot\boldsymbol{E}(t)$ is maximized (minimized), equivalent to the selective population of the upper (lower) dressed state in the strongly coupled resonant sub-system. This energy shift (resonant AC-Stark shift) opens up new multiphoton routes to higher-lying (lower-lying) target states which are inaccessible by perturbative excitation as shown in **Figure 1A**.

Resonant non-perturbative control via SPODS was first reported on 1 + 2 REMPI of potassium atoms [123]. Using interferometric double pulse sequences, we demonstrated efficient ultrafast switching between different ionization target channels by controlling the dressed state populations of the resonant $4s$–$4p$ transition via the relative optical phase. The interpretation of the scheme in a dressed state picture, was presented in [124]. On the same system, we also implemented SPODS with PLP single-color multipulse trains generated by sinusoidal spectral phase modulation [120]. In that work, dressed state control by all sine-parameters was demonstrated.

Subsequently, we applied SPODS to the non-perturbative control of coupled electron-nuclear dynamics in molecules. In the molecular case, the charge dynamics induced by the prepulse is altered due to the coupling between electronic and nuclear degrees of freedom. For example, the amplitude of the dipole oscillation depends on the overlap of vibrational wave packets launched in the resonant electronic states. Also, as the vibrational wave packets propagate, the electronic resonance frequency varies changing the eigenfrequency of the dipole and introducing an additional phase drift which the main pulse needs to adapt to. Our proof-of-principle studies were performed on the potassium dimer serving as a molecular prototype system. The corresponding excitation scheme is depicted in **Figure 1B**. The prepulse resonantly couples the $X^1\Sigma_g^+$ ground state and the $A^1\Sigma_u^+$ excited state, giving rise to two light-induced potentials (i.e. molecular dressed states) and launching the vibronic dynamics. By selective population of a single light-induced potential through the main pulse, population is transferred efficiently to a predefined target state out of a manifold of high-lying but bound electronic states. In a first theoretical study, we demonstrated ultrafast efficient (~ 80% population transfer) switching between the $2^1\Pi_g$ and $5^1\Sigma_g^+$ state using PLP single-color double pulse sequences [118]. The scenario was demonstrated experimentally employing single-color multipulse trains from sine-modulation [137].

4.1.2 Free Electron Vortices With Circularly Polarized Pulse Sequences

In this section we consider the creation of free electron wave packets by REMPI of potassium atoms with single-color circularly polarized pulse sequences (**Figures 4C,D**). First, in **Section 4.1.2.1**, we discuss the formation of a FEV by perturbative MPI at the ionization threshold with c_6 rotational symmetry and in the ATI with c_8 rotational symmetry. In addition, we study the evolution of the c_6 FEV into an angular momentum eigenstate as the time-delay in the sequence vanishes. Then, non-perturbative REMPI resulting in a FEV with c_4 rotational symmetry is examined in **Section 4.1.2.2**. We show, how the wave function of the latter FEV is reconstructed using a holographic method.

4.1.2.1 Perturbative Resonance-Enhanced Multiphoton Ionization

Recently, the generation of FEVs by photoionization with two time-delayed CRCP attosecond laser pulses has been theoretically predicted and termed "an unusual kind of Ramsey interference" [155]. FEVs with $c_{|m_1-m_2|}$ rotational symmetry arise from the interference of two free electron angular momentum states $\psi_{l,m}$ with different magnetic quantum numbers m_1 and m_2. In general, the wave function Ψ_{FEV} of this superposition state reads

$$\Psi_{\mathrm{FEV}} = \Psi_{|m_1-m_2|} \propto \psi_{l_1,m_1} + \psi_{l_2,m_2}\, e^{-i\varepsilon\tau/\hbar}. \tag{31}$$

Note that, in the single-color case $l_1 = l_2$. Motivated by the helical interference structures in the electron density, Starace and coworkers [155] coined the term "electron vortex" for this type of PMD. In general, this notion of an electron vortex is not identical with a vortex state defined by its non-vanishing azimuthal probability density current $\boldsymbol{j}$. The probability density current of the vortex state defined in **Eq. 31** has been derived in [106] and reads

$$\boldsymbol{j} \propto \mathrm{Im}\left[\Psi^*_{\mathrm{FEV}}\nabla\Psi_{\mathrm{FEV}}\right] = \frac{1}{2}|\Psi_{\mathrm{FEV}}|^2\left[\frac{\tau}{\hbar}\boldsymbol{e}_\varepsilon + \frac{(m_1+m_2)}{\varepsilon\sin(\theta)}\boldsymbol{e}_\phi\right], \tag{32}$$

where $\boldsymbol{e}_\varepsilon$ and $\boldsymbol{e}_\phi$ denote the respective unit vectors in energy and azimuthal direction. A detailed discussion of the probability density current of vortex states can be found in [105, 106, 156]. Interestingly, PMDs exhibiting simultaneously helical interference structures and a non-vanishing azimuthal probability density current (**Eq. 32**) have been experimentally demonstrated by bichromatic MPI using time-delayed CRCP pulses [73] and analyzed by TDSE simulations [121]. FEVs have recently attracted much attention, both theoretically [155, 157–174] and experimentally [73, 102–104]. In this section we discuss our experimental results on the creation and manipulation of FEVs from femtosecond atomic MPI using shaper-generated single-color femtosecond CRCP pulse sequences (**Figure 4D**). By combining ultrafast polarization pulse shaping with photoelectron tomography, Pengel *et al.* [102] were the first to experimentally demonstrate FEVs from REMPI of potassium atoms. Initially, it was shown that perturbative REMPI with a single-color CRCP sequence gives rise to the six-armed Archimedean spiral-shaped FEV depicted in **Figure 6B**. The corresponding wave function

$$\Psi_6 \propto \psi_{3,-3} + \psi_{3,3}\, e^{-i\varepsilon\tau/\hbar} \tag{33}$$

produces a vortex-shaped electron density distribution. In the same work, it was shown that changing from MPI with a time-delayed single-color CRCP sequence to the corresponding single-color COCP sequence (**Figure 4C**) results in the wave function

$$\Psi_0 \propto \psi_{3,3}\left(1 + e^{-i\varepsilon\tau/\hbar}\right), \tag{34}$$

corresponding to a toroidal PMD with spectral interference fringes in the radial (energy) direction spaced by h/τ. Subsequently, Pengel et al. [103] reported on the formation of FEVs from polarization-shaped supercontinua and on the generation of an eight-armed FEV in the ATI with the wave function

$$\Psi_8 \propto \psi_{4,-4} + \psi_{4,4}\, e^{-i\varepsilon\tau/\hbar}. \tag{35}$$

The c_8 rotationally symmetric FEV in the ATI is shown in **Figure 6C**. The time-dependent electric field of single-color CRCP sequences shown in **Figure 4D** reveals that, as the time delay vanishes, the sequence evolves into a linearly polarized field whose orientation is determined by the relative phase between the LCP and RCP components. In **Figure 6D** we present results from tomographic reconstruction of the PMDs as $\tau \to 0$. The initial c_6 rotationally symmetric FEV ($\tau = 20$ fs) evolves into a distorted vortex (14 fs) with more and more pronounced lobes in the vicinity of the x-axis at 10 fs and eventually turns into the rotated angular momentum state $\mathcal{R}_x(\pi/2)\psi_{3,0}$ at $\tau = 0$. Partially overlapping LCP and RCP pulses resulting in the non-vanishing product $[E_1^{-1}(t)]^{r_1}\cdot[E_1^{+1}(t)]^{l_1}$ give rise to the additional pathways with alternating circularity, e.g. LCP → RCP → LCP and RCP → LCP → RCP, shown in **Figure 1C** with light arrows for a bichromatic MPI scenario. These pathways populate the free electron angular momentum states $\psi_{3,-1}$ and $\psi_{3,1}$ in addition, leading to the superposition of four $\psi_{3,m}$ states with $m \in (-3, -1, 1, 3)$. MPI with the horizontally polarized pulse at $\tau = 0$ results in the rotated angular momentum state $\mathcal{R}_x(\pi/2)\psi_{3,0}$ which is a superposition of the four $\psi_{3,m}$ states according to

$$\mathcal{R}_x(\pi/2)\psi_{3,0}(\theta,\phi) \propto \frac{1}{\sqrt{105}}\psi_{3,3} + \frac{3}{15\sqrt{7}}\psi_{3,1} + \frac{3}{15\sqrt{7}}\psi_{3,-1} + \frac{1}{\sqrt{105}}\psi_{3,-3}, \tag{36}$$

where the amplitudes have been taken from **Eq. 27**. This result can be checked by decomposition of the rotated state into the unrotated basis

$$\mathcal{R}_x(\pi/2)\psi_{3,0}(\theta,\phi) = \sum_{m=-3,-1,1,3} D^{(3)}_{m,0}(\pi/2)\,\psi_{3,m}(\theta,\phi), \tag{37}$$

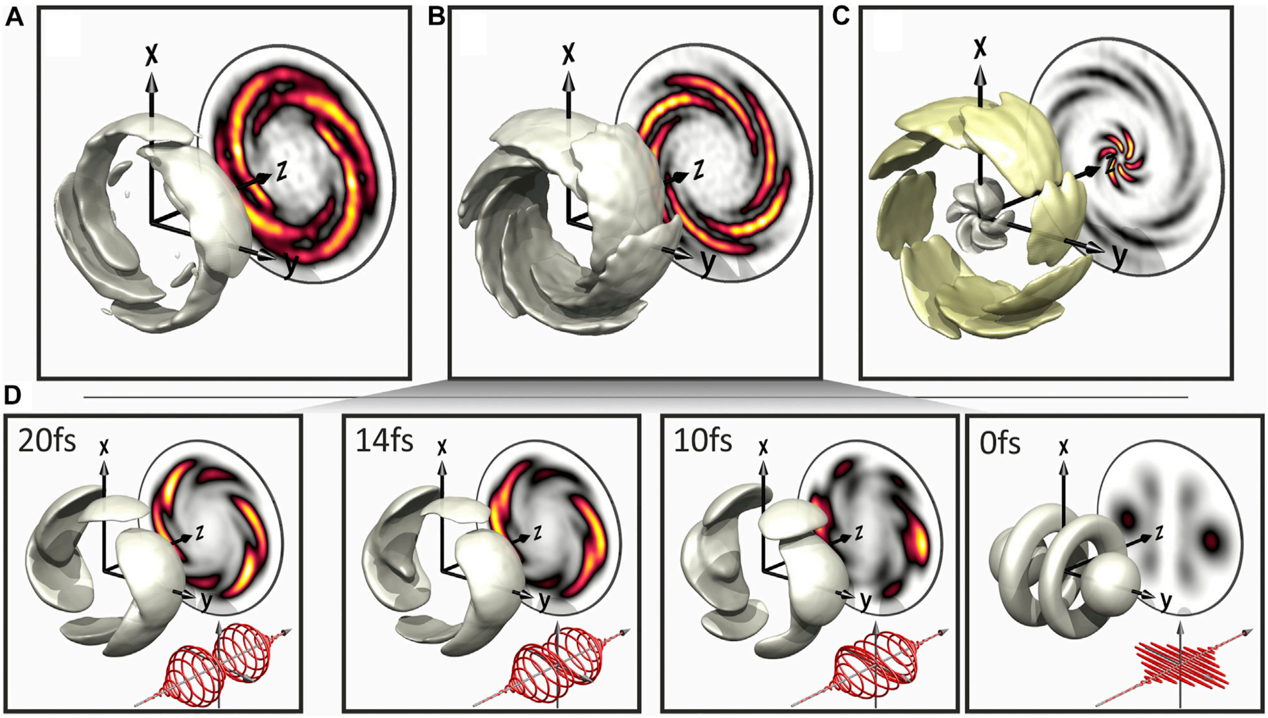

FIGURE 6 | Tomographically reconstructed Archimedean spiral-shaped FEVs with c_4, c_6 and c_8 rotational symmetry from 1 + 2 REMPI of potassium atoms using single-color CRCP pulses along with their projection in the *z*-direction [103]. **(A)** Non-perturbative REMPI with a sequence of two π pulses creates a FEV with four arms. **(B)** Perturbative REMPI gives rise to a six-armed FEV. **(C)** Absorption of an additional photon in the continuum results in an eight-armed FEV in the ATI. **(D)** Evolution of the c_6 FEV as the time delay decreases from τ = 20 fs to τ = 0 fs.

where $D^{(l)}_{m,m'}$ represent the Wigner-*D* coefficients [95, 138, 175, 176].

4.1.2.2 Non-Perturbative Resonance-Enhanced Multiphoton Ionization

So far, we discussed c_6 and c_8 rotationally symmetric FEVs generated by perturbative three- and four-photon ionization, respectively, with the intermediate resonant 4*p* state being only weakly populated and not contributing significantly to the vortex formation. In contrast, it was demonstrated that FEVs with c_4 rotational symmetry can be generated by non-perturbative REMPI [102]. By using CRCP pulse sequences with a pulse area of π [5], the 4*s* state was fully depleted and the 4*p* state fully populated. Hence, ionization with the second pulse started from the excited 4*p* state resulting in a wave function characterized by the superposition of angular momentum states with different values of $|m|$

$$\Psi_4 \propto \psi_{3,-1} + \psi_{3,3}\, e^{-i\epsilon\tau/\hbar}. \tag{38}$$

The tomographic reconstruction of the corresponding PMD depicted in **Figure 6A** shows a FEV with four arms. Using the same REMPI scheme, Pengel *et al.* [103] demonstrated a holographic method for direct measurement of the wave function of the non-perturbative c_4 vortex by measuring a π shift in the azimuthal interferences in the polar direction of the vortex due to the polar nodal line of the $\psi_{3,1}$ angular momentum state.

4.2 Bichromatic Pulse Sequences

In this section, we discuss a number of applications of bichromatic polarization-shaped pulse sequences for femtosecond spectroscopy and coherent control of ultrafast quantum dynamics [105, 106]. Bichromatic fields are characterized by two spectral bands with individual bandwidths of $\Delta\omega_1$ and $\Delta\omega_2$ centered around two different carrier frequencies ω_1 and ω_2, as detailed in [99]. The spectral band with the lower (higher) carrier frequency is typically referred to as red (blue) component. Our shaper-based approach for the generation of bichromatic fields offers independent control over the amplitude, phase and polarization profile of the field [65, 146]. Shaper-generated polarization-tailored bichromatic fields are therefore very versatile, not only regarding their use in bichromatic coherent control schemes but also in terms of their application in time-resolved studies of ultrafast dynamics. For example, employing a linear spectral phase function $(\omega - \omega_i) \cdot \tau$ allows us to introduce a variable time delay τ between the two colors to generate bichromatic pulse sequences for polarization-sensitive two-color pump-probe experiments [177]. Several examples of polarization-controlled bichromatic pulse sequences, with both

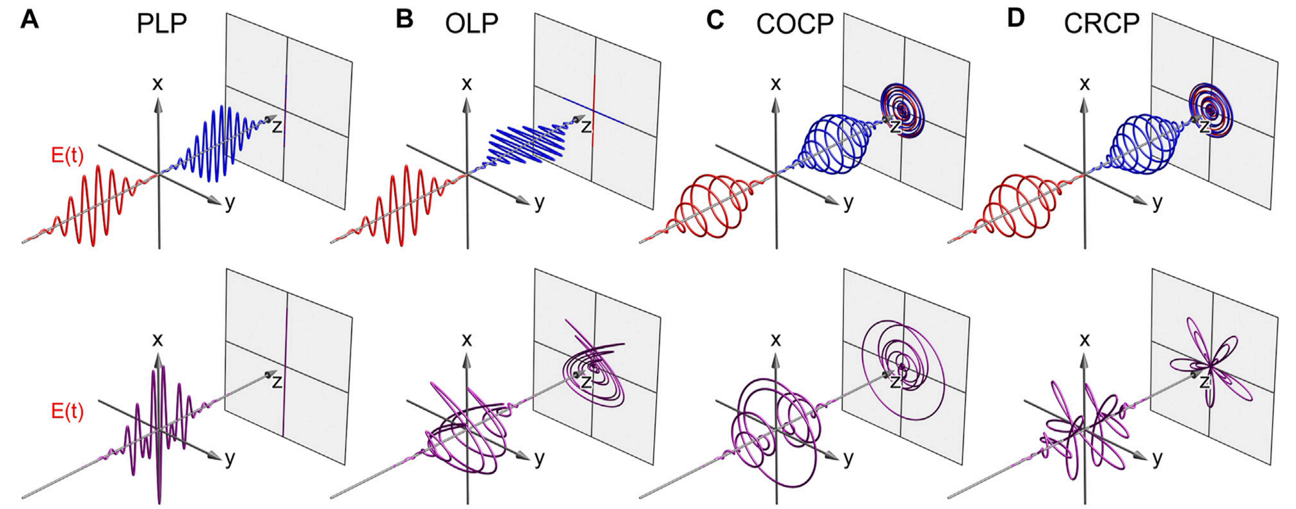

FIGURE 7 | Bichromatic pulse sequences. The projection in *z*-direction visualized the time-dependent electric field vector at the position of the atom or molecule. **(A)** PLP, **(B)** OLP, **(C)** COCP and **(D)** CRCP bichromatic pulse sequences. Upper figures: Sequence with separated pulses $\tau > 2\Delta t$, lower figures: Coinciding pulses at $\tau = 0$.

colors being fully separated in time, are depicted in the top row of **Figure 7**, including the prototypical PLP, OLP, COCP and CRCP fields. The bottom row illustrates the same sequences for $\tau = 0$. In contrast to the single-color case, temporally overlapping bichromatic fields occur in a plethora of shapes and symmetries, depending on the frequency ratio, polarization, amplitude and relative phase of the two colors. For example, in the OLP case shown in **Figure 7B**, the bichromatic polarization profile exhibits a Lissajous-type shape, while in the COCP and CRCP cases, shown in (C) and (D), the polarization profiles are cycloidally shaped. The applications of polarization-tailored bichromatic fields are as versatile as their shapes. For example, PLP bichromatic fields were applied to control plasmon-enhanced photoemission from silver clusters [178] and strong-field photoemission from gold nanotips [79]. OLP bichromatic fields with commensurable frequencies, characterized by Lissajous-type polarization profiles which exhibit a time-varying optical chirality, have been used to investigate sub-cycle variations in the PECD of chiral molecules [179, 180]. Commensurable CRCP bichromatic fields exhibit unique propeller shapes with distinct rotational symmetry. Currently, such fields play a prominent role in HHG [67, 68, 70–72, 181, 182], strong-field ionization [158, 183–186], and were employed for the time-resolved probing of molecular chirality [187]. In the perturbative regime, coherent control of bichromatic MPI is governed by the manipulation of intra- and interband interferences [105] (**Section 2.2.2**). In the following, we discuss examples for the bichromatic control of MPI in atoms (**Section 4.2.1**) and molecules (**Section 4.2.2**).

4.2.1 Atomic Multiphoton Ionization

Atomic model systems interacting with multichromatic pulse sequences are ideally suited to elucidate the physical mechanisms underlying the coherent control. In this section, we study two mechanisms of coherent control of multipath interference in the atomic MPI by polarization-tailored bichromatic fields. We compare the CEP-insensitive intraband MPI with $\mathcal{N}$ photons to the CEP-sensitive interband MPI with different numbers $\mathcal{N}_1 \neq \mathcal{N}_2$ of photons. Different bichromatic control scenarios are implemented using linearly (**Section 4.2.1.1**) and circularly (**Section 4.2.1.2**) polarized bichromatic fields.

4.2.1.1 Linearly Polarized Bichromatic Pulse Sequences

The two prototypes of linearly polarized bichromatic pulse sequences, PLP and OLP fields, are illustrated in **Figures 7A,B**, respectively. To illustrate the difference between interband and intraband interferences in optical phase-control, we discuss below the results from bichromatic MPI of alkali atoms using CEP-stable commensurable PLP (3ω:4ω) fields [73] on the one hand and incommensurable OLP bichromatic fields [99, 100] on the other hand. We start by investigating phase-sensitive interband interferences arising from the superposition of continuum states with opposite parity [73, 188]. MPI of sodium atoms with a PLP (3ω:4ω) field creates an *f*-type photoelectron wave packet ($\psi_{3,0}$) *via* 3-photon ionization by the blue pulse (ω_2) and a *g*-type wave packet ($\psi_{4,0}$) *via* 4-photon ionization in the continuum by the red pulse (ω_1). Both wave packets overlap at a kinetic energy of $\varepsilon = 4\hbar\omega_1 = 3\hbar\omega_2$ resulting in interband interferences. Because the difference between the number of photons absorbed by each partial wave is odd, the resulting photoelectron wave function is a superposition of two states with opposite parity

$$\Psi_{\mathrm{PLP}} \propto \psi_{3,0} + i\,\psi_{4,0}\,e^{-i\varphi_{\mathrm{ce}}}. \tag{39}$$

As illustrated in **Figure 8A**, this wave function exhibits a directional asymmetry along the laser polarization axis (*y*-axis), which is sensitive to the CEP. To study the CEP-

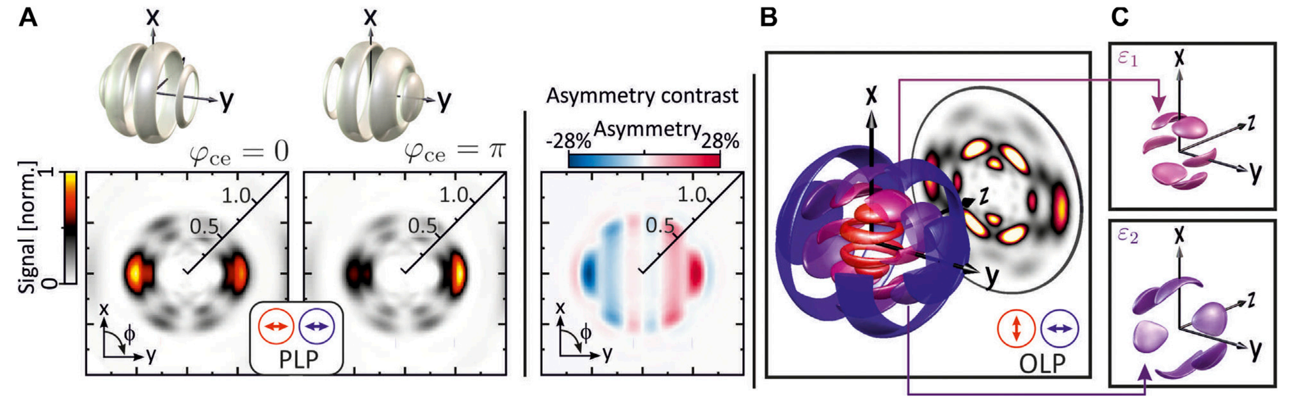

FIGURE 8 | Measured PMDs from bichromatic MPI of sodium and potassium atoms. **(A)** Retrieved (x, y)-sections from the photoemission of sodium atoms using CEP-stable $(3\omega{:}4\omega)$ PLP fields. The left and middle frames show the Abel-inverted sections for $\varphi_{\mathrm{ce}} = 0$ and $\varphi_{\mathrm{ce}} = \pi$, respectively. The top insets show the corresponding generic 3D PMDs of the wave packets. The calculated asymmetry contrast, depicted in the right frame, shows pronounced asymmetries in the laser polarization plane originating from CEP-sensitive interband interference. **(B)** Measured and tomographically reconstructed 3D PMD from three-photon ionization of potassium atoms using bichromatic fields with incommensurable frequencies. The PMD shows four energetically separated shells originating from single-color and frequency mixing contributions, equidistantly centered around energies ε_i $(i = 0, 1, 2, 3)$. **(C)** The partial wave packets from the intermediate energy channels ε_1 and ε_2, exhibit pseudo c_6 rotational symmetry resulting from intraband interference.

dependence of the asymmetry, we measured 2D projections of the PMD for $\varphi_{\mathrm{ce}} = 0$ and $\varphi_{\mathrm{ce}} = \pi$. The recorded projections were Abel-inverted using the pBASEX algorithm [88]. The retrieved 2D sections of the PMD through the (x, y) polarization plane are shown in the left and middle frames of **Figure 8A**. The sections display a pronounced left/right asymmetry which is inverted by switching the CEP from 0 to π. To quantify the asymmetry, we derived the asymmetry contrast [105, 189] directly from the measured projections. The result shown in the right frame of **Figure 8A** reveals a CEP-induced directional asymmetry of up to ±28%. A similar scheme for the control of directional photoemission from xenon atoms by bichromatic MPI with phase-modulated PLP $(7\omega{:}8\omega)$ fields was recently reported in [189, 190]. In that contribution, the bichromatic pulses were specifically tailored to induce phase-controlled 7- vs. 8-photon interband interference in the $5P_{3/2}$ ionization continuum of xenon. An alternative strategy to steer the directionality of ultrafast electronic processes in atoms [188, 189, 191, 192], molecules [193–195] or solids [196–201] is based on the use of CEP-stable few-cycle femtosecond laser pulses. In this case, however, the interpretation of the interference mechanism is generally complicated by the multitude of MPI pathways connecting the ground state to a specific energy target state. Using shaper-generated commensurable bichromatic fields tailored to the MPI process, has enabled us to excite specific asymmetric target states in the continuum by two-path interband interference, fully controllable via the CEP and the relative phase of the two colors. In contrast to the few-cycle approach, we were thus able to localize phase-controlled asymmetries in a preselected photoelectron energy window [189]. To demonstrate the concept of intraband interference, we employed temporally overlapping $(\tau < \Delta t)$ OLP bichromatic fields with incommensurable frequencies for 3-photon ionization of potassium atoms. While both the blue and the red component produce individual single-color signals centered at $\varepsilon_0 = 3\hbar\omega_1 - \hbar\omega_{\mathrm{IP}}$ and $\varepsilon_3 = 3\hbar\omega_2 - \hbar\omega_{\mathrm{IP}}$, third-order intrapulse frequency mixing leads to two additional contributions centered at $\varepsilon_1 = 2\hbar\omega_1 + \hbar\omega_2 - \hbar\omega_{\mathrm{IP}}$ and $\varepsilon_2 = \hbar\omega_1 + 2\hbar\omega_2 - \hbar\omega_{\mathrm{IP}}$, which are energetically disentangled from the single-color signals (cf. **Eq. 15**) [99, 100]. The measured and tomographically reconstructed 3D PMD is shown in the main frame of **Figure 8B**. The different above mentioned contributions are color-coded. Since each of the frequency mixing pathways is composed of three photons—albeit with different combinations of red and blue photons—the accumulated optical phase in each target state is identical, rendering the resulting intraband interference of all target states CEP-insensitive. Each of the photoelectron angular distributions within a given energy interval is determined by a specific coherent superposition of angular momentum states as described in **Eq. 15**. For example, the two single-color signals are described by rotated f-type wave packets perpendicularly to one another along the respective laser polarization axis, i.e. the x- and y-axis for the OLP pulse shown in **Figure 7B**. The two inner partial wave packets in the energy interval around ε_1 (magenta) and ε_2 (purple) resulting from intraband interference read

$$\Psi_{\mathrm{OLP}}^{\varepsilon_1/\varepsilon_2} \propto \psi_{3,3} \mp \frac{1}{\sqrt{15}}\psi_{3,1} - \frac{1}{\sqrt{15}}\psi_{3,1} \pm \psi_{3,-3}, \tag{40}$$

analogously to **Eq. 27**, where the upper and lower signs in the sum correspond to ε_1 and ε_2, respectively. Both reconstructed partial wave packets are shown separately in **Figure 8C**. They are also aligned perpendicularly with respect to one another and exhibit a pseudo c_6 rotational symmetry. Using $(\omega{:}2\omega)$ bichromatic OLP fields, we recently demonstrated the generation of a c_4 rotationally symmetric PMD in the 2-photon ionization of potassium atoms [105] similar to the $d_{x,y}$ state shown in **Figure 5B**. Again, the mechanism was based on the cancellation of specific quantum pathways by intraband interference. Due to the energetic disentanglement of the different photoelectron contributions from intraband interference, this scheme is suitable for pump-probe experiments featuring background-free detection of ultrafast dynamics. For example, employing shaper-generated linearly polarized bichromatic pump-probe pulse sequences, we investigated Rydberg [177] and spin-orbit [100] wave packet dynamics. The full potential of polarization-shaped bichromatic fields to generate and manipulate angular momentum superposition states via frequency mixing has been studied in [99]. Very recently, we introduced a shaper-based quantum state holography (SQuaSH) method by combining intra- and interband interferences using commensurable CEP-stable bichromatic fields for phase-sensitive pump-probe measurements [101].

4.2.1.2 Circularly Polarized Bichromatic Pulse Sequences

Circularly polarized bichromatic fields, with their cycloidal polarization profiles (**Figures 7C,D**), offer fascinating possibilities for the generation and control of electronic angular momentum wave packets with unusual physical properties, whether in the neutral system as in the case of spin-orbit wave packets (SOWPs) or in the ionization continuum as in the case of free electron wave packets. Similar to the linearly polarized case discussed in **Section 4.2.1.1**, the mechanism to control the spectrum, the symmetry and the rotation of the PMD is based on the manipulation of intraband and interband interference by the polarization state of the sequence (CRCP or COCP) and the optical phases. We illustrate the basic concepts with two examples. In the first example, we use bichromatic CRCP pulse sequences with incommensurable frequencies for MPI of potassium atoms and make use of the energetic disentanglement of the angular momentum states in the continuum. This ionization scheme is utilized for background-free observation of SOWP dynamics in the bound state. The second example deals with the creation and coherent control of FEVs with unusual rotational symmetry by interband interference in the MPI of sodium atoms with CEP-stable commensurable cycloidal bichromatic pulse sequences.

Recently, we demonstrated intraband frequency mixing by shaper-generated CRCP bichromatic fields in the three-photon ionization of potassium [99]. Using temporally overlapping ($\tau < \Delta t$) sequences of two colors with incommensurable frequencies, we showed that in the CRCP case, frequency mixing results in a complete energetic disentanglement of the different angular momentum target states in the ionization continuum. The reconstructed 3D PMD is depicted in **Figure 9A**. The two single-color contributions in the inner- (red) and outermost (blue) energy channels correspond to the torus-shaped partial waves $\psi_{3,\pm3}$. The two frequency mixing contributions in the intermediate energy channels ε_1 and ε_2 correspond to the partial waves

$$\Psi^{\varepsilon_1/\varepsilon_2}_{\mathrm{CRCP}} = \psi_{3,\pm1} \tag{41}$$

displayed in the insets. This result shows that in the CRCP case, bichromatic frequency mixing provides a unique mapping between the number of absorbed red and blue photons and the different continuum target states, enabling the selective excitation of individual angular momentum states which otherwise (e.g. in the single-color case) overlap inseparably in the energy spectrum (**Eq. 36**). As pointed out in **Section 4.2.1.1**, if the two colors are spectrally disjoint, the frequency mixing signals are insensitive to the optical phases implying that frequency mixing signals are inherently robust with respect to phase fluctuations of the CEP, the relative phase between the colors or the Gouy-phase. Moreover, the process of frequency mixing is very efficient due to the large number of pathways leading to the same final state (see **Figure 2**). These properties, i.e. efficiency, robustness and the disentanglement of target states, make frequency mixing a well-suited test-bed for bichromatic pump-probe studies. The potential of shaper-based bichromatic pump-probe spectroscopy was recently demonstrated on the examples of time- and angular-resolved measurement [177] and holographic observation [101] of ultrafast Rydberg dynamics and the time-resolved 3D imaging of ultrafast SOWP dynamics in potassium atoms [100].

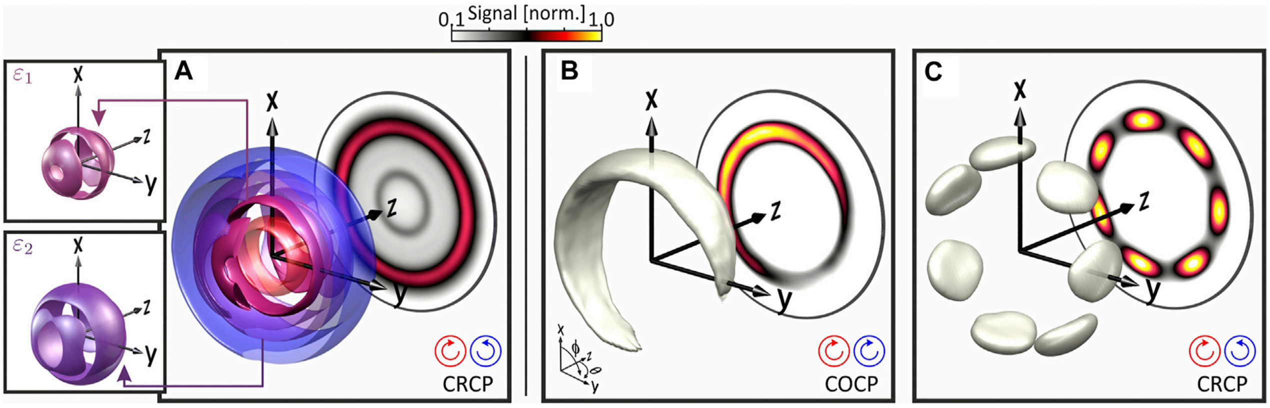

FIGURE 9 | Tomographically reconstructed 3D PMDs of free electron wave packets created by MPI of potassium and sodium atoms with circularly polarized bichromatic pulses. **(A)** Intraband interferences and single-color contributions from MPI of potassium using CRCP bichromatic fields with incommensurable frequencies. **(B)** FEV with c_1 rotational symmetry from interband interference in the MPI of sodium using CEP-stable COCP (3ω:4ω) bichromatic fields. **(C)** FEV with c_7 rotational symmetry created by MPI of sodium using CRCP (3ω:4ω) fields.

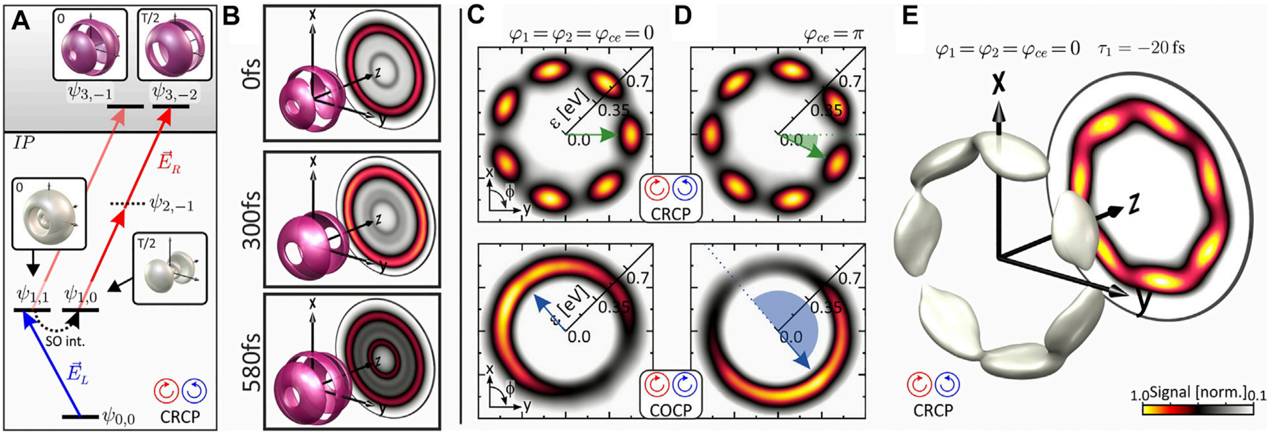

FIGURE 10 | Applications of intra- and interband interference in the MPI of potassium and sodium atoms using circularly polarized bichromatic pulse sequences. **(A)** Excitation scheme for the time-resolved 3D imaging of ultrafast SOWP dynamics in potassium using shaper-generated bichromatic pump-probe pulse sequences. **(B)** Reconstructed 3D PMDs for different stages of the SOWP cycle, revealing the orbital realignment dynamics in the excited 4*p* state due to the spin-orbit interaction. **(C)** and **(D)** Coherent control of the azimuthal rotation of the c_1 and c_7 rotationally symmetric FEVs from **Figures 9B,C**, respectively. **(E)** Reconstructed 3D PMD of a seven-arm Archimedean spiral-shaped FEV created by MPI of sodium using a time-delayed (τ_1 = −20 fs) CRCP (3ω:4ω) bichromatic pulse sequence.

In the latter experiment, the LCP blue pulse (pump) was tuned on resonance with the two 4*p* fine structure states $4p_{1/2}$ and $4p_{3/2}$. These states are separated energetically by $\Delta\varepsilon$ = 7 meV which corresponds to a SOWP oscillation period of $T = h/\Delta\varepsilon$ = 580 fs. The bandwidth of the pump was chosen sufficiently large to excite both states coherently and, thus, launch the SOWP in the neutral system. After a variable time delay τ, introduced experimentally by linear spectral phase modulation via the shaper, the RCP red pulse (probe) ionized the atom from the 4*p* states in a two-photon process, mapping the SOWP into the ionization continuum as depicted in **Figure 10A**. More specifically, the electron dynamics in the neutral atom were mapped into the ε_1-channel, where—due to the energetic disentanglement from other contributions—the time evolution of the SOWP could be observed without any interfering background. By tomographic reconstruction of the PMD as a function of time delay τ, we obtained 3D images of the spatiotemporal SOWP dynamics. The images are shown in **Figure 10B**. Initially, at τ = 0, the partial wave from the ε_1-channel displays $\psi_{3,-1}$ symmetry. This symmetry maps the torus-shaped $\psi_{1,1}$ state (4*p* (m = 1)) in the neutral system, which is consistent with the impulsive excitation of the 4*p* state by the circularly polarized pump pulse. At half-period $\tau \approx T/2$, the symmetry of the photoelectron angular distribution in the ε_1-channel evolves into that of a $\psi_{3,-2}$ state, mapping the dumbbell-shaped $\psi_{1,0}$ state [4*p* (m = 0)]. The time evolution of the SOWP between these two states is driven by the spin-orbit interaction which, in a semi-classical picture, is interpreted as the precession of the coupled spin and orbital angular momenta around the total angular momentum. After a full period T, the distribution in the ε_1-channel returns to $\psi_{3,-1}$ symmetry indicating the completion of the first SOWP oscillation cycle. These findings, along with additional results obtained for OLP bichromatic pump-probe sequences [99, 100], showcase the capabilities of bichromatic pump-probe spectroscopy, based on shaper-generated polarization-shaped tailored bichromatic pulse sequences in combination with photoelectron tomography, for the background-free 3D imaging of ultrafast spatiotemporal quantum dynamics.

Next, we discuss the application of circularly polarized bichromatic pulse sequences with commensurable frequencies for the coherent control of interband $\mathcal{N}_1$ vs. $\mathcal{N}_2$ MPI processes. When the different colored pulses overlap in time, i.e. at $\tau = 0$, the resulting field exhibits a cycloidal polarization profile with an $\mathcal{S}_{\text{opt}}$-fold rotational symmetry (**Figures 7C,D**) described by

$$\mathcal{S}_{\text{opt}} = (\mathcal{N}_1 \pm \mathcal{N}_2)/\text{gcd}(\mathcal{N}_1,\mathcal{N}_2). \tag{42}$$

Here, the upper and lower sign correspond to CRCP and COCP pulses, respectively, and gcd denotes the greatest common divisor. For the sake of clarity, we discuss below the case of $\text{gcd}(\mathcal{N}_1,\mathcal{N}_2) = 1$. The use of commensurable frequency cycloidal fields enables the creation of FEVs with unusual rotational symmetry by controlling the multipath interference in $\mathcal{N}_1$- vs. $\mathcal{N}_2$-photon ionization. The resulting FEV exhibits an $\mathcal{S}_{\text{FEV}}$-fold rotational symmetry with $\mathcal{S}_{\text{FEV}} = \mathcal{N}_1 \pm \mathcal{N}_2$, reflecting the field symmetry from **Eq. 42**. Due to the different photonic orders of the contributing ionization pathways, the resulting interband interference is sensitive to the optical phases (cf. **Eq. 39**). Both, the relative phases φ_1 and φ_2 of the two colors and the CEP φ_{ce} of the field induce an azimuthal rotation of the FEV, i.e. in the polarization plane, by different angles and in different directions. The general expression for the total rotation angle induced by the optical phases reads [73]

$$\alpha = \frac{1}{\mathcal{N}_2 \pm \mathcal{N}_1}\left(\Delta\mathcal{N}\varphi_{\text{ce}} + \mathcal{N}_2\varphi_1 - \mathcal{N}_1\varphi_2\right), \tag{43}$$

with $\Delta\mathcal{N} = \mathcal{N}_2 - \mathcal{N}_1$. Again, the upper and lower sign correspond to the CRCP and the COCP case, respectively. This relation first implies that for the observation of interband interference in the experiment, the stabilization of the CEP is crucial, otherwise the interference pattern is rotationally averaged out [73]. Apparently, the response of the quantum system to fluctuations of the CEP is different for interband interference compared to intraband frequency mixing (**Section 4.2.1.1**), which is robust with respect to optical phase variations. The second important implication of **Eq. 43** is that the orientation of the FEV in polarization plane is controllable by all optical phases, albeit to different extents. Recently, we have experimentally demonstrated the creation and manipulation of 1- and 7-fold rotationally symmetric FEVs by controlled interband interference in the 3- vs. 4-photon ionization of sodium atoms using CEP-stable (3ω: 4ω) circularly polarized pulses [73]. Similar to the linear case (cf. **Eq. 39**), the photoelectron wave function in the circular case is described by the coherent superposition of a partial wave $\psi_{4,4}$, created by absorption of four LCP photons from the red pulse, and a partial wave $\psi_{3,\pm3}$ created by absorption of three LCP (+: COCP case) or RCP (−: CRCP case) photons from the blue pulse

$$\Psi_{4\pm3} \propto \psi_{3,\pm3} + i\psi_{4,4}e^{-i(\Delta\varphi - \varepsilon\tau_1/\hbar)}. \tag{44}$$

The phase term $\Delta\varphi = 4\varphi_1 - 3\varphi_2 + \varphi_{ce}$ describes the optically induced relative phase between both partial waves. The phase term $\varepsilon\tau_1/\hbar$ accounts for an additional energy-dependent propagation phase accumulated if the red pulse is time-delayed by τ_1 relative to the blue pulse. The FEV described by Ψ_1, created by COCP ionization, exhibits a single azimuthal lobe reminiscent of a crescent, while the FEV with the wave function Ψ_7, created by CRCP ionization, displays seven lobes in the polarization plane. The corresponding tomographically reconstructed 3D PMDs, measured at the parameters $\Delta\varphi = 0$ and $\tau_1 = 0$, are shown in **Figures 9B,C**, respectively. To demonstrate the rotational control of both FEVs, we varied the CEP from $\varphi_{ce} = 0$ to $\varphi_{ce} = \pi$, analogously to the directional control discussed in **Section 4.2.1.1** (**Figure 8**). The resulting rotation of the PMD is depicted in **Figures 10C,D**, indicated by the green and blue angle segments, respectively. While the c_1 FEV is rotated by $\alpha^{\mathrm{COCP}} = \pi$, the c_7 FEV is rotated by an angle of $\alpha^{\mathrm{CRCP}} = \frac{\pi}{7}$, in agreement with **Eq. 43**. In addition, we demonstrated the generation of a vortex-shaped PMD with c_7 rotational symmetry by introducing a time-delay of $\tau_1 = -20$ fs between the two colors in the CRCP pulse sequence. The reconstructed corresponding 3D PMD of the c_7 rotationally symmetric FEV, shown in **Figure 10E**, exhibits the characteristic helical interference structure, causing the vortex-like tilt of the lobes. The results on the FEVs with odd rotational symmetry created by MPI with circularly polarized commensurable bichromatic fields demonstrate our ability to manipulate the properties of the PMD by precise control on multipath interband interference. The rotational symmetry of FEVs is determined by the selection of the MPI pathways via the polarization state (COCP or CRCP), while its azimuthal orientation is manipulated by the optical phases including the relative phase and the CEP.

4.2.2 Molecular Multiphoton Ionization

Two-color femtosecond pump-probe experiments are ideally suited to study ultrafast dynamics in molecules driven by femtosecond laser pulses [151]. In the following **Section 4.2.2.1** and **Section 4.2.2.2**, we discuss the application of this concept to the observation of non-Born-Oppenheimer dynamics in sodium dimers and the mapping of non-perturbative control of concerted electron-nuclear dynamics in potassium dimers. In **Section 4.2.2.3**, we present new results demonstrating axial and lateral asymmetries in the photoemission from chiral molecules induced by MPI with CEP-stable circularly polarized few-cycle pulses from a WLS.

4.2.2.1 Non-adiabatic Molecular Dynamics

In [202], we used a PLP two-color pump-probe sequence to study the effect of adiabatic (non-Born-Oppenheimer) dynamics in the $2^1\Sigma_u^+$ double-minimum state of the sodium dimer. The sequence consisted of a 340 nm pump pulse, to launch a vibrational wave packet in the $2^1\Sigma_u^+$ state by single photon excitation, and a time-delayed 265 nm probe pulse to interrogate the vibrating molecule by single photon ionization. Time- and energy-resolved photoelectron spectra were measured in order to map the time evolution of the nuclear wave packet along the vibrational coordinate R. The sodium double-minimum state arises from an avoided crossing of diabatic states [203]. Therefore, the electronic structure changes rapidly as a function of R suggesting a strong dependence of the ionization probability on the internuclear distance. This reasoning was supported by theoretical predictions in [204, 205]. In the experiment, the nuclear wave packets were used as local probes to determine R-dependent ionization probabilities. By comparison of the measured photoelectron spectra to numerical wave packet simulations a linear R-dependence of the dipole moment $\mu_{n\to i}(R)$ for the neutral-to-ionic transition was retrieved. The experiment demonstrated that PLP two-color pump-probe sequences combined with time-resolved photoelectron spectroscopy is a powerful technique for the observation and unraveling of ultrafast photochemical dynamics in molecules.

4.2.2.2 Non-perturbative Electron-Nuclear Dynamics

In the experiments reported in [132, 137], we applied a two-color pump-probe scheme to demonstrate efficient ultrafast switching between bound electronic target states in the potassium dimer, based on a detailed understanding of the underlying strong-field control mechanism. Intense femtosecond pulse sequences, shaped with attosecond precision [50], were used to switch the neutral excitation selectively between the $2^1\Pi_g$ and the $5^1\Sigma_g^+$ state (cf. **Section 4.1.1.2**). Employing a time-delayed 570 nm probe pulse, generated by an optical parametric amplifier and combined interferometrically with the pump pulse, the final population of the target states was mapped into the energy-resolved photoelectron spectrum *via* one-photon ionization. By careful choice of the probe wavelength, the target state signals were tuned to an almost background-free energy window within the crowded photoelectron spectrum. In the measurement of non-perturbative bound state dynamics, signatures of strong-field interaction are typically washed out by volume averaging over the intensity distribution of the pump beam focus [132]. One way to counteract this effect is the utilization of a non-linear probe step. Due to the non-linear decrease of efficiency towards the focal edges, the probe volume is effectively reduced [119, 120]. In this experiment however, dealing with a linear probe step, the probe beam was expanded to be focused more tightly into the interaction region than the pump. By this means, the probe mapped only the central part of the interaction region with an approximately homogeneous pump intensity distribution. Both the energetic disentanglement of the two-color probe signals from the broad single-color background and the minimization of the focal intensity averaging were key to the interference-free observation of the non-perturbative population dynamics induced in the target states by the intense tailored pump pulse sequence. The results demonstrated our ability to efficiently steer the coupled electron-nuclear dynamics of a molecule into different preselected target channels by controlling the delicate interplay between the quantum phase of the induced charge dynamics and the optical phase of the driving laser field.

4.2.2.3 Asymmetries in the Photoemission From Chiral Molecules

Polarization-shaped bichromatic fields are particularly suitable to chiral applications. Recent examples comprise the control of optical chirality [206], fundamental investigations on the PECD of chiral molecules [179, 180] and time-resolved studies of molecular chirality [187, 207]. Motivated by our experimental findings on the CEP-control of lateral asymmetries in the atomic MPI of sodium atoms by (3ω: 4ω) [73] and xenon atoms by (7ω: 8ω) [189] bichromatic PLP pulses (cf. **Section 4.2.1.1**), we investigated asymmetries in the PMD from MPI of the chiral fenchone molecule using CEP-stable few-cycle pulses. The manipulation of lateral asymmetries in chiral molecules is particularly interesting because these molecules also exhibit a pronounced axial, i.e., forward/backward asymmetry in the photoelectron emission due to the PECD [208]. Recent measurements of the PECD of (-)-fenchone molecules from MPI with circularly polarized 400 nm pulses, depicted in **Figure 11A**, reproduce our previous results [97, 150]. Displayed is the antisymmetric part of the PMD with respect to the polarization plane, showing the well-known asymmetries of up to ±12%. Using a CEP-stable circularly polarized bandwidth-limited white light pulse centered at 800 nm, we observed CEP-sensitive lateral, i.e., left/right asymmetries in the photoelectron emission of (-)-fenchone. In **Figure 11B** we plot the difference between the PMDs measured with a CEP of $\varphi_{ce} = 0$ and $\varphi_{ce} = \pi$. This representation yields the antisymmetric part of the spectrum with respect to the propagation direction (z-direction), revealing pronounced lateral asymmetries of up to ±15%. The CEP-dependence of this asymmetry is shown in **Figure 11C** in the form of an energy-resolved asymmetry map obtained by integrating the spectra over the angular coordinate in one half-plane. These results demonstrate that MPI of chiral molecules with circularly polarized few-cycle pulses can be used to control the axial asymmetry *via* the PECD and, moreover, the lateral asymmetry via the CEP. Very recently, fully 3D polarization-tailored laser fields, generated by superposition of two polarization-controlled multichromatic laser pulses propagating non-collinearly in different directions, have been proposed as novel tools for the investigation of chiral light-matter interactions [209–212]. These so-called superchiral light fields [213] promise an unprecedented enantio-sensitivity which makes them highly attractive for chiral discrimination applications.

4.3 Multichromatic Pulse Sequences

A natural extension of bichromatic white-light polarization pulse shaping (cf. **Section 3.1**) is to generate multichromatic polarization-controlled pulse sequences. As a first step towards more complex pulses, we consider a trichromatic application. Trichromatic fields offer enhanced possibilities for ultrafast applications such as multicolor spectroscopy [214], strong-field physics [215, 216], the generation of terahertz radiation [217, 218] and HHG [219]. Further examples of trichromatic pulse sequences are illustrated in **Figure 12**. Each sequence consists of a temporally overlapping polarization-tailored bichromatic pulse which is either preceded by a circularly polarized [(A) and (B)] or

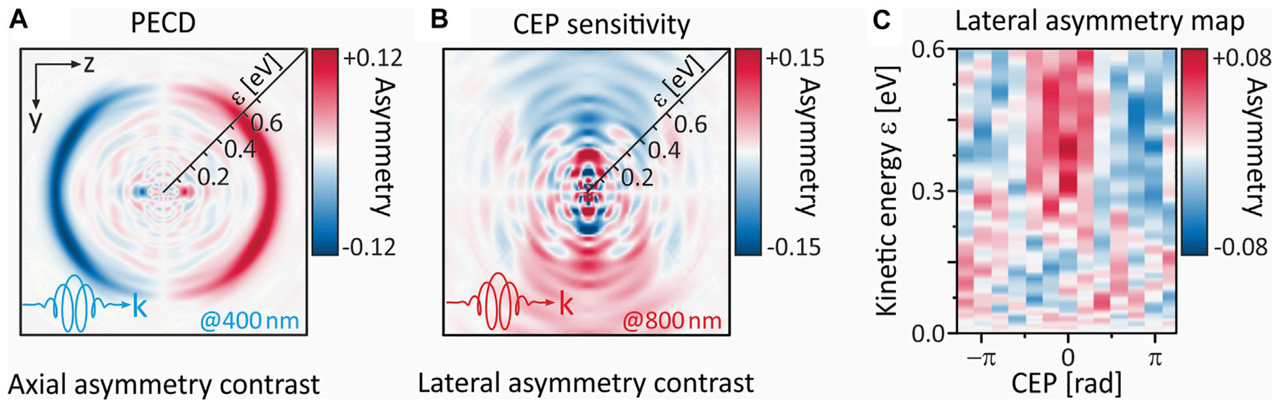

FIGURE 11 | PECD and lateral photoelectron asymmetries in the MPI of (-)-fenchone molecules using circularly polarized femtosecond laser pulses. **(A)** PECD observed at 400 nm. **(B)** Previously unpublished results on lateral asymmetries in the photoelectron emission using LCP few-cycle pulses with a duration of $\Delta t \approx 5$ fs centred at $\lambda_0 = 800$ nm. **(C)** CEP-dependence of the lateral asymmetry displayed as an energy-resolved asymmetry map.

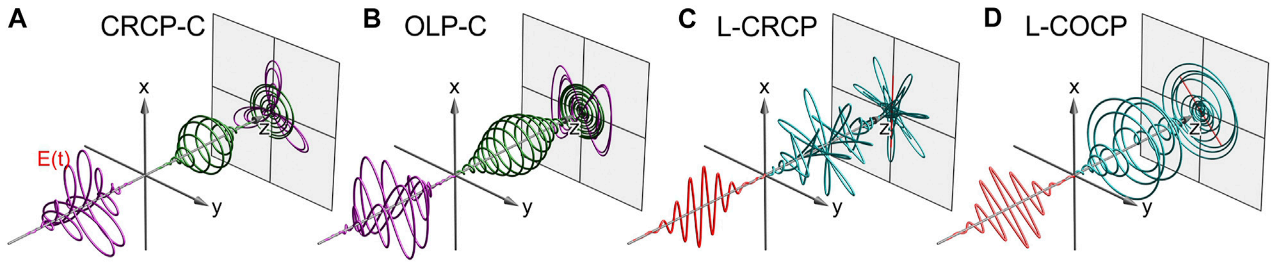

FIGURE 12 | Trichromatic pulse sequences. The projection in *z*-direction visualizes the time-dependent electric field vector at the position of the atom or molecule. **(A)** Circularly polarized single pulse followed by a CRCP pulse sequence, **(B)** Circularly polarized single pulse followed by an OLP pulse sequence, **(C)** CRCP pulse sequence followed by a linearly polarized (*s*) single pulse and **(D)** COCP pulse sequence followed by a linearly polarized single pulse tilted by 45°. In all figures the single pulse is separated by a delay $\tau > 2\Delta t$ from the coinciding pulse sequences.

followed by a linearly polarized [(C) and (D)] single pulse of a third color. The use of an additional color allows us to combine the bichromatic mechanism of intraband interference, e.g. for the background-free observation of ultrafast dynamics, with phase-sensitive interband interferences for the coherent control of the underlying multiphoton processes. For example, an auxiliary pulse can be used to provide a separate reference wave packet for an experimental implementation of wave packet holography. This extension opens up a manifold of coherent control scenarios ranging from multichromatic SQuaSH via the creation and manipulation of multiple FEVs to multichannel quantum-phase clocks [101, 220]. However, trichromatic MPI is not only an extension of bichromatic MPI but also changes the physical picture, since the number of available pathways and the number of target states scales differently with the number of pulses, as discussed in **Section 2.2.2**. So far, we have distinguished between intraband and interband interference in bichromatic MPI scenarios. Phase-sensitive interband interference was characterized by interfering pathways involving the absorption of a different number of photons per color, i.e. $\mathcal{N}_1 \neq \mathcal{N}_2$, resulting in the condition $\varepsilon = \hbar\mathcal{N}_1\omega_1 = \hbar\mathcal{N}_2\omega_2$. If more than two colors are present this condition can be generalized into

$$\varepsilon = \hbar\mathcal{N}_1\omega_1 + \hbar\mathcal{N}_2\omega_2 = \hbar\mathcal{N}_3\omega_3 \tag{45}$$

involving two distinct pathways, e.g., with three pairwise different numbers of photons $\mathcal{N}_1 \neq \mathcal{N}_2 \neq \mathcal{N}_3$. Building on the results of self-referenced bichromatic SQuaSH in [101], we devise a trichromatic scenario to study the interference of bichromatic 2 + 1 REMPI for the detection of a background free pump-probe signal with direct three photon ionization delivering a reference signal for wave packet holography. According to **Eq. 45**, the three frequencies are adjusted so that both contributions yield photoelectrons in the same energy window. In this particular scenario, we choose $\mathcal{N}_1 + \mathcal{N}_2 = \mathcal{N}_3$, such that the CEP-dependence in the final state cancels. Here we present previously unpublished data from SQuaSH on 2 + 1 REMPI of potassium atoms using a trichromatic PLP pulse sequence.

As shown in the excitation scheme in **Figure 13A** a photoelectron wave packet is created by resonant two-photon excitation of the 3*d* state by the red pump and subsequent one-photon ionization by the blue probe pulse. This wave packet interferes with the reference wave packet originating from off-resonant 3-photon ionization of the ground state by the green reference pulse to generate a phase-sensitive photoelectron hologram. We expect the hologram to be sensitive to the relative phases between the pump, the probe and the reference, but, because the same number of photons are absorbed in each pathway, the interference pattern should not depend on the CEP. To investigate this scheme experimentally, we apply spectral amplitude modulation of the WLS (cf. **Figure 13B**) to generate a tailored PLP trichromatic pulse sequence composed of a $\lambda_{\mathrm{pu}} = 928$ nm pump pulse (red band), followed by a $\lambda_{\mathrm{pr}} = 722$ nm probe (blue band) and $\lambda_{\mathrm{ref}} = 848$ nm reference pulse (green band). The time delays between the pulses are introduced via additional linear spectral phase modulation of the pump and probe band with $\tau_{\mathrm{pu}} = -215$ fs and $\tau_{\mathrm{pr}} = -15$ fs relative to the reference pulse. The wave function of the resulting photoelectron hologram reads

$$\Psi_{\mathrm{holo}} \propto \left(c_{\mathrm{pu}}c_{\mathrm{pr}}\, e^{-i(2\varphi_{\mathrm{pu}}+\varphi_{\mathrm{pr}})} + c_{\mathrm{ref}}\, e^{-i3\varphi_{\mathrm{ref}}}\right)\psi_{3,0}, \tag{46}$$

where c_{pu}, c_{pr} and c_{ref} denote the complex valued amplitudes including delay-dependent phases and φ_{pu}, φ_{pr} and φ_{ref} the relative optical phases corresponding to the pump-the probe- and the reference pulse, respectively. A tomographically reconstructed 3D PMD is depicted in **Figure 13C**. To evaluate the phase-dependence of the hologram, we measure the modulation of the integral cross-section in the SQuaSH channel of the photoelectron spectrum by variation of the relative optical phase $\varphi_{\mathrm{ref}} \in [-\pi, \pi]$. To this end, the measured PMDs are energy-calibrated [221] and integrated over the angular coordinates to yield the photoelectron spectra. In **Figures 13D,E** the resulting energy-resolved photoelectron spectra $I\,(\varepsilon; \varphi_{\mathrm{ref}})$ with $\varepsilon \in [0.01, 0.1]$ eV are plotted as a function of the relative phase of the reference pulse. The insets in the top frame show the measured projections for constructive ($\varphi_{\mathrm{ref}} = -1.64$ rad) and destructive interference (−0.77 rad). In agreement with **Eq. 46**, the interference signal shows a $\frac{2\pi}{3}$-periodic oscillation because the reference pulse ionizes the system by absorption of three photons. We invert the interference structure (**Figure 13E**) by introducing a phase of $\varphi_{\mathrm{pu}} = \frac{\pi}{2}$ to the pump pulse (**Eq. 46**), because the pump pulse

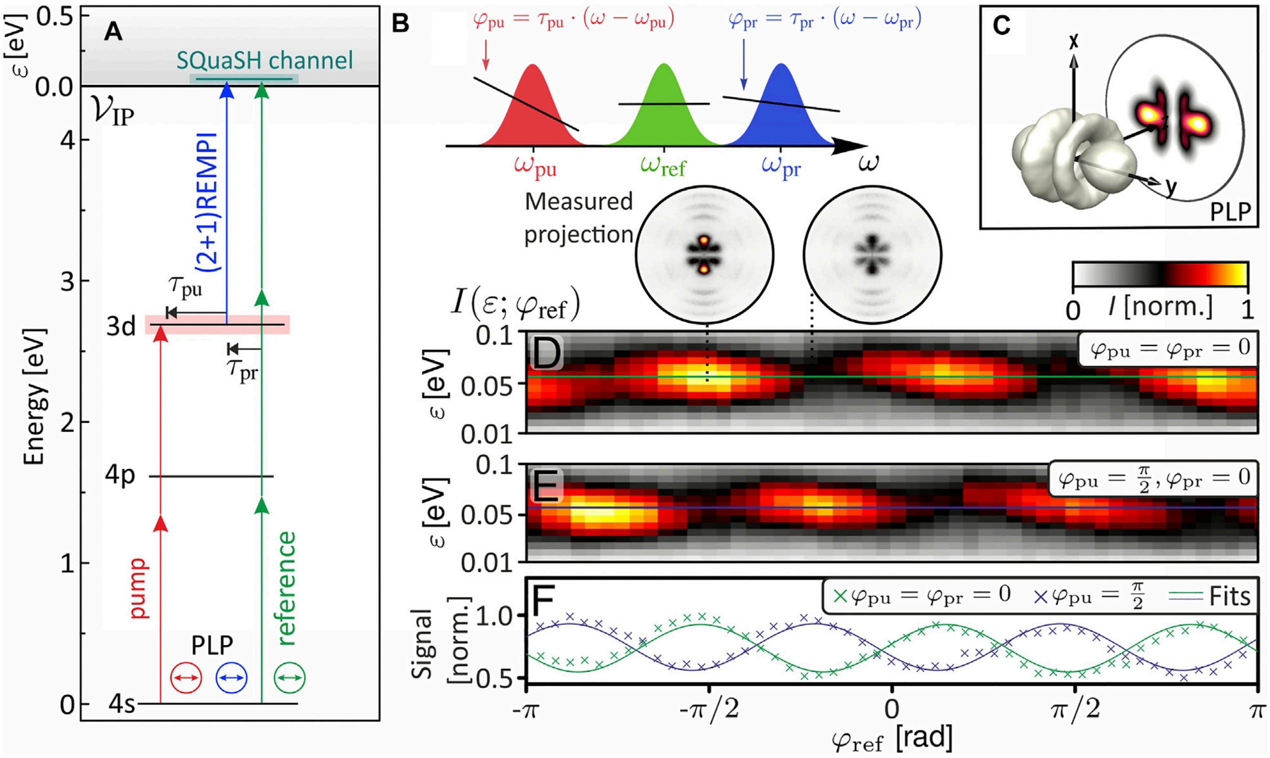

FIGURE 13 | SQuaSH on potassium atoms using PLP trichromatic pulse sequences. **(A)** Excitation scheme for the two-photon excitation (pump) and time-delayed one-photon ionization (probe) of the potassium 3*d* state. Interference of the resulting free electron wave packet with a reference wave packet created by three-photon ionization of the ground state by the reference pulse provides a phase-sensitive photoelectron hologram in the continuum. **(B)** The triple pulse sequence is generated by trichromatic WLS shaping applying linear spectral phases to introduce the time delays of pump and probe relative to the reference pulse. **(C)** Tomographically reconstructed 3D PMD from SQuaSH with PLP trichromatic pulses. **(D)** Angularly integrated photoelectron spectra $I(\varepsilon; \varphi_{\mathrm{ref}})$ versus the applied optical phase φ_{ref} of the reference pulse for $\varphi_{\mathrm{pu}} = 0$ showing a pronounced $\frac{2\pi}{3}$-periodic oscillation due to wave packet interferences. **(E)** same as **(D)** but for a relative phase of $\varphi_{\mathrm{pu}} = \frac{\pi}{2}$, resulting in an inversion of the interference pattern. **(F)** Sections through **(D)** and **(E)** along the phase axis, together with cosine-fits, highlighting the cosinusoidal oscillation.

contributes two photons to the REMPI process. The cosinusoidal oscillation is confirmed by showing sections through both interference patterns together with cosine-fits in **Figure 13F**.

5 SUMMARY AND OUTLOOK

In this review, we have reported on coherent control of MPI dynamics of atomic and molecular model systems using fully coherent polarization-tailored single-color, bichromatic and trichromatic pulse sequences. Building on previous experiments with single-color pulse sequences, we have shown that the advanced polarization shaping of CEP-stable supercontinua enables the generation of unprecedented bichromatic laser fields such as propeller-shaped CRCP pulses or Lissajous-like OLP pulses. Even more flexibility is achieved in trichromatic polarization shaping by the many possible combinations of linearly or circularly polarized pulses, resulting in an increasing number of final states and interfering pathways. These new pulse shapes enable the targeted use of CEP-insensitive intraband and CEP-sensitive interband multipath interference for quantum control. The experimental results on atomic and molecular MPI by multichromatic pulse sequences reviewed here, serve to illustrate the new options for coherent control. We have summarized the theoretical methods used to reproduce and analyze our experimental results and presented a powerful experimental technique combining supercontinuum polarization shaping and VMI-based high-resolution photoelectron tomography to reconstruct the full 3D PMD. The presented applications of single-color pulse sequences included perturbative and non-perturbative control of atomic and molecular MPI. We have analyzed the 3D PMD from a previous experiment on the interference of free electron wave packets created by PLP sequences and reported on free electron vortices with even-numbered rotational symmetry originating from MPI with single-color CRCP sequences. We have reviewed results on bichromatic coherent control by intraband and interband multipath interference on various examples including control of the directional photoemission in the MPI of atoms and chiral molecules by PLP and COCP fields, the use of COCP and CRCP cycloidal fields to generate and manipulate free electron vortices with odd-numbered rotational symmetry, and spin-orbit wave packets controlled by PLP pulses. Finally, we have introduced trichromatic shaper-based quantum state holography using a trichromatic PLP pulse sequence by adding a reference pulse to a bichromatic pump-probe sequence. As an example for the new options of trichromatic pulse shaping, we

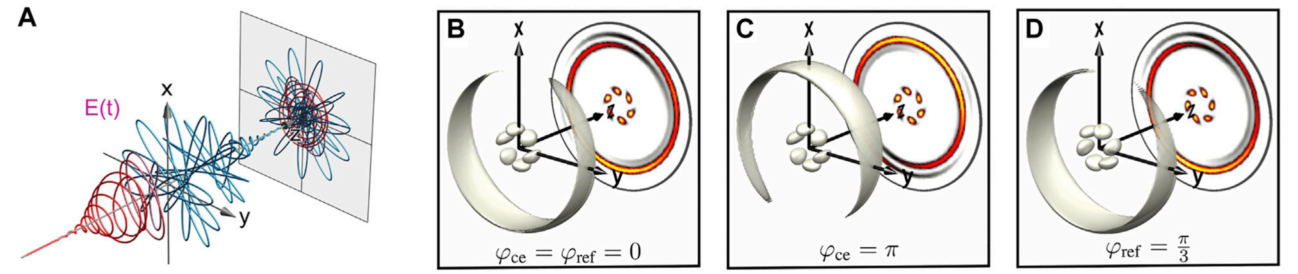

FIGURE 14 | (A) Trichromatic pulse sequence consisting of a circularly polarized single pulse temporally overlapping with a CRCP pulse sequence. While the pump-probe pulse sequence is given by a (3ω:4ω) bichromatic field, the additional green component exhibits a frequency ratio of 5:6 with respect to the probe field. **(B–D)** show the resulting PMDs displaying a CEP-insensitive 6-armed inner vortex surrounded by a CEP-sensitive 1-armed outer vortex, for selected values of the CEP and the relative optical phase φ_{ref}.

have devised an MPI scheme based on a polarization-tailored trichromatic CRCP pulse sequence which results in a CEP-insensitive c_6 rotationally symmetric inner vortex surrounded by a CEP-sensitive crescent-shaped wave-packet (**Figure 14**). Extensions of our shaping scheme towards the generation of independently polarization-controlled multichromatic multipulse sequences are currently explored in our labs.

Shaper-based multi-color 2D spectroscopy using fully coherent multichromatic CEP-stable pulse sequences is another emerging application of our technique. Taking advantage of the shaper's capability to additionally introduce higher order spectral phase modulation, the trichromatic scheme can be further developed into a powerful tool for coherent control spectroscopy by using sequences of tailored pulses, thus generalizing the concept of 2D spectroscopy. In addition, the tunability of the shaper-generated polarization-controlled multi-color fields makes them attractive for applications in quantum information [222], quantum metrology [109, 110, 223] and ultrafast nanotechnology [79, 178, 214, 224, 225]. In all the experiments reported above, the tailored polarization profile was confined to the (x, y)-plane perpendicular to the propagation direction of the pulse. Building on recent theoretical proposals [209–212, 226], we envision the next challenge in experimental coherent control to be the generation and tailoring of full 3D light fields by superimposing two polarization-shaped laser pulses propagating non-collinearly in different directions.

AUTHOR CONTRIBUTIONS

KE and MW developed the topic and idea, collected the data, and prepared the original manuscript. MW coordinated this review and managed the project. KE, LE, TB, and MW contributed to the conception and development of the narrative. KE, TB, and MW were responsible for data analysis and simulations. LE contributed to the drafting of the manuscript and prepared the illustrations. All authors contributed to manuscript revision, read, and approved the submitted version.

FUNDING

This research was funded by the Deutsche Forschungsgemeinschaft (DFG) *via* the priority program SPP1840 QUTIF. Open access publication fees are granted by the University Oldenburg Open-Access publication fond supported by the DFG program Wissenschaftliche Literaturversorgungs-und Informationssysteme.

ACKNOWLEDGMENTS

We thank Dominik Pengel and Stefanie Kerbstadt for providing previously unpublished data on the FEVs in **Figure 6** and the asymmetries in the PMDs of chiral molecules in **Figure 11**.

REFERENCES

1. Shapiro M, and Brumer P. Laser Control of Product Quantum State Populations in Unimolecular Reactions. *J Chem Phys* (1986) 84:4103–4. doi:10.1063/1.450074
2. Tannor DJ, Kosloff R, and Rice SA. Coherent Pulse Sequence Induced Control of Selectivity of Reactions: Exact Quantum Mechanical Calculations. *J Chem Phys* (1986) 85:5805–20. doi:10.1063/1.451542
3. Rice SA, and Zhao M. *Optical Control of Molecular Dynamics*. New York: Wiley (2000). p. 456.
4. Tannor D. *Introduction to Quantum Mechanics: A Time-dependent Perspective*. Sausalito: University Science Books (2007). p. 662.
5. Shore BW. *Manipulating Quantum Structures Using Laser Pulses*. Cambridge University Press (2011). p. 1–600.
6. Shapiro M, and Brumer P. *Quantum Control of Molecular Processes*. 2 edn.. New York: Wiley (2012). p. 562.
7. Meshulach D, and Silberberg Y. Coherent Quantum Control of Two-Photon Transitions by a Femtosecond Laser Pulse. *Nature* (1998) 396:239–42. doi:10.1038/24329
8. Dudovich N, Dayan B, Gallagher Faeder SM, and Silberberg Y. Transform-limited Pulses Are Not Optimal for Resonant Multiphoton Transitions. *Phys Rev Lett* (2001) 86:47–50. doi:10.1103/physrevlett.86.47
9. Dudovich N, Oron D, and Silberberg Y. Quantum Control of the Angular Momentum Distribution in Multiphoton Absorption Processes. *Phys Rev Lett* (2004) 92:103003. doi:10.1103/physrevlett.92.103003

10. Präkelt A, Wollenhaupt M, Sarpe-Tudoran C, and Baumert T. Phase Control of a Two-Photon Transition with Shaped Femtosecond Laser-Pulse Sequences. *Phys Rev A* (2004) 70:063407–10. doi:10.1103/physreva.70.063407
11. Wollenhaupt M, Assion A, Liese D, Sarpe-Tudoran C, Baumert T, Zamith S, et al. Interferences of Ultrashort Free Electron Wave Packets. *Phys Rev Lett* (2002) 89:173001. doi:10.1103/physrevlett.89.173001
12. Lee S, Lee HG, Cho J, Lim J, Park CY, and Ahn J. Coherent Control of Multiphoton-Ionization Passage of Excited-State Rubidium Atoms. *Phys Rev A* (2012) 86:045402. doi:10.1103/physreva.86.045402
13. Baumert T, Grosser M, Thalweiser R, and Gerber G. Femtosecond Time-Resolved Molecular Multiphoton Ionization: The Na_2 system. *Phys Rev Lett* (1991) 67:3753–6. doi:10.1103/physrevlett.67.3753
14. Park SM, Lu SP, and Gordon RJ. Coherent Laser Control of the Resonance-enhanced Multiphoton Ionization of HCl. *J Chem Phys* (1991) 94:8622–4. doi:10.1063/1.460047
15. Gordon RJ, Hu Z, Seideman T, Singha S, Sukharev M, and Zhao Y. Coherent Phase Control of Internal Conversion in Pyrazine. *J Chem Phys* (2015) 142: 144311. doi:10.1063/1.4916642
16. Singha S, Hu Z, and Gordon RJ. Closed Loop Coherent Control of Electronic Transitions in Gallium Arsenide. *J Phys Chem A* (2011) 115:6093–101. doi:10.1021/jp110869f
17. Assion A, Baumert T, Bergt M, Brixner T, Kiefer B, Seyfried V, et al. Control of Chemical Reactions by Feedback-Optimized Phase-Shaped Femtosecond Laser Pulses. *Science* (1998) 282:919–22. doi:10.1126/science.282.5390.919
18. Meshulach D, and Silberberg Y. Coherent Quantum Control of Multiphoton Transitions by Shaped Ultrashort Optical Pulses. *Phys Rev A* (1999) 60: 1287–92. doi:10.1103/physreva.60.1287
19. Silberberg Y. Quantum Coherent Control for Nonlinear Spectroscopy and Microscopy. *Annu Rev Phys Chem* (2009) 60:277–92. doi:10.1146/annurev.physchem.040808.090427
20. Dantus M, and Lozovoy VV. Experimental Coherent Laser Control of Physicochemical Processes. *Chem Rev* (2004) 104:1813–60. doi:10.1021/cr020668r
21. Gordon RJ, and Rice SA. Active Control of the Dynamics of Atoms and Molecules. *Annu Rev Phys Chem* (1997) 48:601–41. doi:10.1146/annurev.physchem.48.1.601
22. Bartels R, Backus S, Zeek E, Misoguti L, Vdovin G, Christov IP, et al. Shaped-pulse Optimization of Coherent Emission of High-Harmonic Soft X-Rays. *Nature* (2000) 406:164–6. doi:10.1038/35018029
23. Pfeifer T, Walter D, Winterfeldt C, Spielmann C, and Gerber G. Controlling the Spectral Shape of Coherent Soft X-Rays. *Appl Phys B* (2005) 80:277–80. doi:10.1007/s00340-005-1754-0
24. Englert L, Rethfeld B, Haag L, Wollenhaupt M, Sarpe-Tudoran C, and Baumert T. Control of Ionization Processes in High Band gap Materials via Tailored Femtosecond Pulses. *Opt Express* (2007) 15:17855–62. doi:10.1364/oe.15.017855
25. Stoian R, Wollenhaupt M, Baumert T, and Hertel IV. Temporal Pulse Tailoring in Ultrafast Laser Manufacturing Technologies. In: K Sugioka, M Meunier, and A Piqué, editors. *Laser Precision Micro Fabrication*, 135. Berlin Heidelberg: Springer Series in Material Science (2010). p. 121–44. doi:10.1007/978-3-642-10523-4_5
26. Salzmann W, Mullins T, Eng J, Albert M, Wester R, Weidemüller M, et al. Coherent Transients in the Femtosecond Photoassociation of Ultracold Molecules. *Phys Rev Lett* (2008) 100:233003––4. doi:10.1103/physrevlett.100.233003
27. Sukharev M, Seideman T, Gordon RJ, Salomon A, and Prior Y. Ultrafast Energy Transfer between Molecular Assemblies and Surface Plasmons in the strong Coupling Regime. *ACS Nano* (2014) 8:807–17. doi:10.1021/nn4054528
28. Glaser SJ, Boscain U, Calarco T, Koch CP, Köckenberger W, Kosloff R, et al. Training Schrödinger's Cat: Quantum Optimal Control. *Eur Phys J D* (2015) 69:279. doi:10.1140/epjd/e2015-60464-1
29. Rabitz H, de Vivie-Riedle R, Motzkus M, and Kompa K. Whither the Future of Controlling Quantum Phenomena?. *Science* (2000) 288:824–8. doi:10.1126/science.288.5467.824
30. Weiner AM, Heritage JP, and Kirschner EM. High-resolution Femtosecond Pulse Shaping. *J Opt Soc Am B* (1988) 5:1563–72. doi:10.1364/josab.5.001563
31. Meshulach D, Yelin D, and Silberberg Y. Adaptive Ultrashort Pulse Compression and Shaping. *Opt Commun* (1997) 138:345–8. doi:10.1016/s0030-4018(97)00090-4
32. Baumert T, Brixner T, Seyfried V, Strehle M, and Gerber G. Femtosecond Pulse Shaping by an Evolutionary Algorithm with Feedback. *Appl Phys B: Lasers Opt* (1997) 65:779–82. doi:10.1007/s003400050346
33. Yelin D, Meshulach D, and Silberberg Y. Adaptive Femtosecond Pulse Compression. *Opt Lett* (1997) 22:1793–5. doi:10.1364/ol.22.001793
34. Weiner AM. Femtosecond Pulse Shaping Using Spatial Light Modulators. *Rev Sci Instrum* (2000) 71:1929–60. doi:10.1063/1.1150614
35. Vajda Š, Bartelt A, Kaposta E-C, Leisner T, Lupulescu C, Minemoto S, et al. Feedback Optimization of Shaped Femtosecond Laser Pulses for Controlling the Wavepacket Dynamics and Reactivity of Mixed Alkaline Clusters. *Chem Phys* (2001) 267:231–9. doi:10.1016/s0301-0104(01)00275-0
36. Herek JL, Wohlleben W, Cogdell RJ, Zeidler D, and Motzkus M. Quantum Control of Energy Flow in Light Harvesting. *Nature* (2002) 417:533–5. doi:10.1038/417533a
37. Goswami D. Optical Pulse Shaping Approaches to Coherent Control. *Phys Rep* (2003) 374:385–481. doi:10.1016/s0370-1573(02)00480-5
38. Steinmeyer Gn.. A Review of Ultrafast Optics and Optoelectronics. *J Opt A: Pure Appl Opt* (2003) 5:R1–R15. doi:10.1088/1464-4258/5/1/201
39. Präkelt A, Wollenhaupt M, Assion A, Horn C, Sarpe-Tudoran C, Winter M, et al. Compact, Robust, and Flexible Setup for Femtosecond Pulse Shaping. *Rev Scientific Instr* (2003) 74:4950–3. doi:10.1063/1.1611998
40. Renard M, Chaux R, Lavorel B, and Faucher O. Pulse Trains Produced by Phase-Modulation of Ultrashort Optical Pulses: Tailoring and Characterization. *Opt Express* (2004) 12:473–82. doi:10.1364/opex.12.000473
41. Stobrawa G, Hacker M, Feurer T, Zeidler D, Motzkus M, and Reichel F. A New High-Resolution Femtosecond Pulse Shaper. *Appl Phys B* (2001) 72: 627–30. doi:10.1007/s003400100576
42. Dudovich N, Oron D, and Silberberg Y. Single-pulse Coherent Anti-stokes Raman Spectroscopy in the Fingerprint Spectral Region. *J Chem Phys* (2003) 118:9208–15. doi:10.1063/1.1568072
43. Monmayrant A, and Chatel B. New Phase and Amplitude High Resolution Pulse Shaper. *Rev Scientific Instr* (2004) 75:2668–71. doi:10.1063/1.1771492
44. Wohlleben W, Degert J, Monmayrant A, Chatel B, Motzkus M, and Girard B. Coherent Transients as a Highly Sensitive Probe for Femtosecond Pulse Shapers. *Appl Phys B* (2004) 79:435–9. doi:10.1007/s00340-004-1555-x
45. von Vacano B, Buckup T, and Motzkus M. Shaper-assisted Collinear Spider: Fast and Simple Broadband Pulse Compression in Nonlinear Microscopy. *J Opt Soc Am B* (2007) 24:1091–100. doi:10.1364/josab.24.001091
46. Zäh F, Halder M, and Feurer T. Amplitude and Phase Modulation of Time-Energy Entangled Two-Photon States. *Opt Express* (2008) 16:16452–8. doi:10.1364/oe.16.016452
47. Suchowski H, Natan A, Bruner BD, and Silberberg Y. Spatio-temporal Coherent Control of Atomic Systems: Weak to strong Field Transition and Breaking of Symmetry in 2d Maps. *J Phys B: Mol Opt Phys* (2008) 41:074008. doi:10.1088/0953-4075/41/7/074008
48. Wollenhaupt M, Krug M, Köhler J, Bayer T, Sarpe-Tudoran C, and Baumert T. Photoelectron Angular Distributions from strong-field Coherent Electronic Excitation. *Appl Phys B* (2009) 95:245–59. doi:10.1007/s00340-009-3431-1
49. Monmayrant A, Weber S, and Chatel B. A Newcomer's Guide to Ultrashort Pulse Shaping and Characterization. *J Phys B: Mol Opt Phys* (2010) 43: 103001––34. doi:10.1088/0953-4075/43/10/103001
50. Köhler J, Wollenhaupt M, Bayer T, Sarpe C, and Baumert T. Zeptosecond Precision Pulse Shaping. *Opt Express* (2011) 19:11638–53. doi:10.1364/oe.19.011638
51. Brixner T, and Gerber G. Femtosecond Polarization Pulse Shaping. *Opt Lett* (2001) 26:557–9. doi:10.1364/ol.26.000557
52. Brixner T, Krampert G, Pfeifer T, Selle R, Gerber G, Wollenhaupt M, et al. Quantum Control by Ultrafast Polarization Shaping. *Phys Rev Lett* (2004) 92: 208301. doi:10.1103/physrevlett.92.208301
53. Polachek L, Oron D, and Silberberg Y. Full Control of the Spectral Polarization of Ultrashort Pulses. *Opt Lett* (2006) 31:631–3. doi:10.1364/ol.31.000631

54. Plewicki M, Weise F, Weber SM, and Lindinger A. Phase, Amplitude, and Polarization Shaping with a Pulse Shaper in a Mach-Zehnder Interferometer. *Appl Opt* (2006) 45:8354–9. doi:10.1364/ao.45.008354
55. Ninck M, Galler A, Feurer T, and Brixner T. Programmable Common-Path Vector Field Synthesizer for Femtosecond Pulses. *Opt Lett* (2007) 32: 3379–81. doi:10.1364/ol.32.003379
56. Kupka D, Schlup P, and Bartels RA. Simplified Ultrafast Pulse Shaper for Tailored Polarization States Using a Birefringent Prism. *Rev Scientific Instr* (2009) 80:053110. doi:10.1063/1.3130046
57. Weise F, and Lindinger A. Full Control over the Electric Field Using Four Liquid crystal Arrays. *Opt Lett* (2009) 34:1258–12560. doi:10.1364/ol.34.001258
58. Schwarz C, Hüter O, and Brixner T. Full Vector-Field Control of Ultrashort Laser Pulses Utilizing a Single Dual-Layer Spatial Light Modulator in a Common-Path Setup. *J Opt Soc Am B* (2015) 32:933–45. doi:10.1364/josab.32.000933
59. Zeidler D, Witte T, Proch D, and Motzkus M. Optical Parametric Amplification of a Shaped white-light Continuum. *Opt Lett* (2001) 26: 1921–3. doi:10.1364/ol.26.001921
60. Binhammer T, Rittweger E, Ell R, Kärtner FX, and Morgner U. Prism-based Pulse Shaper for Octave Spanning Spectra. *IEEE J Quan Electron.* (2005) 41: 1552–7. doi:10.1109/jqe.2005.858781
61. Xu B, Coello Y, Lozovoy VV, Harris DA, and Dantus M. Pulse Shaping of Octave Spanning Femtosecond Laser Pulses. *Opt Express* (2006) 14:10939–44. doi:10.1364/oe.14.010939
62. Rausch S, Binhammer T, Harth A, Krtner FX, and Morgner U. Few-cycle Femtosecond Field Synthesizer. *Opt Express* (2008) 16:17410–9. doi:10.1364/oe.16.017410
63. Demmler S, Rothhardt J, Heidt AM, Hartung A, Rohwer EG, Bartelt H, et al. Generation of High Quality, 13 Cycle Pulses by Active Phase Control of an Octave Spanning Supercontinuum. *Opt Express* (2011) 19:20151–8. doi:10.1364/oe.19.020151
64. Hagemann F, Gause O, Wöste L, and Siebert T. Supercontinuum Pulse Shaping in the Few-Cycle Regime. *Opt Express* (2013) 21:5536–49. doi:10.1364/oe.21.005536
65. Kerbstadt S, Timmer D, Englert L, Bayer T, and Wollenhaupt M. Ultrashort Polarization-Tailored Bichromatic fields from a CEP-Stable white Light Supercontinuum. *Opt Express* (2017) 25:12518. doi:10.1364/oe.25.012518
66. Patas A, Matthews M, Hermelin S, Gateau J, Kasparian J, Wolf JP, et al. Modifications of Filament Spectra by Shaped Octave-Spanning Laser Pulses. *Phys Rev A* (2018) 98:033804. doi:10.1103/physreva.98.033804
67. Long S, Becker W, and McIver JK. Model Calculations of Polarization-dependent Two-Color High-Harmonic Generation. *Phys Rev A* (1995) 52: 2262–78. doi:10.1103/physreva.52.2262
68. Zuo T, and Bandrauk AD. High-order Harmonic Generation in Intense Laser and Magnetic fields. *J Nonlinear Optic Phys Mat* (1995) 04:533–46. doi:10.1142/s0218863595000227
69. Milosevic DB, Becker W, and Kopold R. Generation of Circularly Polarized High-Order Harmonics by Two-Color Coplanar Field Mixing. *Phys Rev A* (2000) 61:063403. doi:10.1103/PhysRevA.61.063403
70. Fleischer A, Kfir O, Diskin T, Sidorenko P, and Cohen O. Spin Angular Momentum and Tunable Polarization in High-Harmonic Generation. *Nat Photon* (2014) 8:543–9. doi:10.1038/nphoton.2014.108
71. Ivanov M, and Pisanty E. Taking Control of Polarization. *Nat Photon* (2014) 8:501–3. doi:10.1038/nphoton.2014.141
72. Kfir O, Grychtol P, Turgut E, Knut R, Zusin D, Popmintchev D, et al. Generation of Bright Phase-Matched Circularly-Polarized Extreme Ultraviolet High Harmonics. *Nat Photon* (2015) 9:99–105. doi:10.1038/nphoton.2014.293
73. Kerbstadt S, Eickhoff K, Bayer T, and Wollenhaupt M. Odd Electron Wave Packets from Cycloidal Ultrashort Laser fields. *Nat Commun* (2019) 10:658. doi:10.1038/s41467-019-08601-7
74. Song X, Yang S, Zuo R, Meier T, and Yang W. Enhanced High-Order Harmonic Generation in Semiconductors by Excitation with Multicolor Pulses. *Phys Rev A* (2020) 101:033410. doi:10.1103/physreva.101.033410
75. Ansari IN, Hofmann C, Medišauskas L, Lewenstein M, Ciappina MF, and Dixit G. Controlling Polarization of Attosecond Pulses with Plasmonic-Enhanced Bichromatic Counter-rotating Circularly Polarized fields. *Phys Rev A* (2021) 103:013104. doi:10.1103/physreva.103.013104
76. Astapenko VA. Radiative Processes in a Bichromatic Laser Field with Multiple Frequencies. *Quan Electron.* (2006) 36:1131–47. doi:10.1070/qe2006v036n12abeh013231
77. Solanpää J, and Räsänen E. Control of Rydberg-State Population with Realistic Femtosecond Laser Pulses. *Phys Rev A* (2018) 98:053422. doi:10.1103/physreva.98.053422
78. Ohmura H, and Saito N. Quantum Control of a Molecular Ionization Process by Using Fourier-Synthesized Laser fields. *Phys Rev A* (2015) 92:053408. doi:10.1103/physreva.92.053408
79. Dienstbier P, Paschen T, and Hommelhoff P. Coherent Control at Gold Needle Tips Approaching the strong-field Regime. *Nanophotonics* (2021). doi:10.1515/nanoph-2021-0242
80. Mohammadzadeh A, and Miri M. Resonance Fluorescence of a Hybrid Semiconductor-Quantum-Dot-Metal-Nanoparticle System Driven by a Bichromatic Field. *Phys Rev B* (2019) 99:115440. doi:10.1103/physrevb.99.115440
81. Baumert T, Buehler B, Grosser M, Thalweiser R, Weiss V, Wiedenmann E, et al. Femtosecond Time-Resolved Wave Packet Motion in Molecular Multiphoton Ionization and Fragmentation. *J Phys Chem* (1991) 95: 8103–10. doi:10.1021/j100174a019
82. Meier C, and Engel V. Electron Kinetic Energy Distributions from Multiphoton Ionization of Na_2 with Femtosecond Laser Pulses. *Chem Phys Lett* (1993) 212:691–6. doi:10.1016/0009-2614(93)85506-j
83. Eppink ATJB, and Parker DH. Velocity Map Imaging of Ions and Electrons Using Electrostatic Lenses: Application in Photoelectron and Photofragment Ion Imaging of Molecular Oxygen. *Rev Scientific Instr* (1997) 68:3477–84. doi:10.1063/1.1148310
84. Whitaker B. *Imaging in Molecular Dynamics*. 1 edn.. Cambridge University Press (2003). p. 249.
85. Schomas D, Rendler N, Krull J, Richter R, and Mudrich M. A Compact Design for Velocity-Map Imaging of Energetic Electrons and Ions. *J Chem Phys* (2017) 147:013942. doi:10.1063/1.4984076
86. Ullrich J, Moshammer R, Dorn A, D rner R, Schmidt LPH, and Schmidt-B cking H. Recoil-ion and Electron Momentum Spectroscopy: Reaction-Microscopes. *Rep Prog Phys* (2003) 66:1463–545. doi:10.1088/0034-4885/66/9/203
87. Dörner R, Mergel V, Jagutzki O, Spielberger L, Ullrich J, Moshammer R, et al. Cold Target Recoil Ion Momentum Spectroscopy: a 'momentum Microscope' to View Atomic Collision Dynamics. *Phys Rep* (2000) 330:95–192. doi:10.1016/s0370-1573(99)00109-x
88. Garcia GA, Nahon L, and Powis I. Two-dimensional Charged Particle Image Inversion Using a Polar Basis Function Expansion. *Rev Scientific Instr* (2004) 75:4989–96. doi:10.1063/1.1807578
89. Wollenhaupt M, Krug M, Köhler J, Bayer T, Sarpe-Tudoran C, and Baumert T. Three-dimensional Tomographic Reconstruction of Ultrashort Free Electron Wave Packets. *Appl Phys B* (2009) 95:647–51. doi:10.1007/s00340-009-3513-0
90. Smeenk C, Arissian L, Staudte A, Villeneuve DM, and Corkum PB. Momentum Space Tomographic Imaging of Photoelectrons. *J Phys B: Mol Opt Phys* (2009) 42:185402. doi:10.1088/0953-4075/42/18/185402
91. Hockett P, Staniforth M, and Reid KL. Photoelectron Angular Distributions from Rotationally State-Selected NH3(B1E$''$): Dependence on Ion Rotational State and Polarization Geometry. *Mol Phys* (2010) 108:1045–54. doi:10.1080/00268971003639266
92. Maurer J, Dimitrovski D, Christensen L, Madsen LB, and Stapelfeldt H. Molecular-frame 3d Photoelectron Momentum Distributions by Tomographic Reconstruction. *Phys Rev Lett* (2012) 109:123001. doi:10.1103/physrevlett.109.123001
93. Chen C, Tao Z, Hernández-García C, Matyba P, Carr A, Knut R, et al. Tomographic Reconstruction of Circularly Polarized High-Harmonic fields: 3d Attosecond Metrology. *Sci Adv* (2016) 2:e1501333. doi:10.1126/sciadv.1501333
94. Eklund M, Hultgren H, Kiyan I, Helm H, and Hanstorp D. Tomography of Photoelectron Distributions Produced through strong-field Photodetachment of Ag^-. *Phys Rev A* (2020) 102:023114. doi:10.1103/physreva.102.023114

95. Wollenhaupt M, Lux C, Krug M, and Baumert T. Tomographic Reconstruction of Designer Free-Electron Wave Packets. *ChemPhysChem* (2013) 14:1341–9. doi:10.1002/cphc.201200968
96. Wollenhaupt M, Krug M, and Baumert T. Elektronenwellen nach maß. *Phys.Journ.* (2012) 11:37–43.
97. Lux C, Wollenhaupt M, Sarpe C, and Baumert T. Photoelectron Circular Dichroism of Bicyclic Ketones from Multiphoton Ionization with Femtosecond Laser Pulses. *Chemphyschem* (2015) 16:115–37. doi:10.1002/cphc.201402643
98. Hockett P, Wollenhaupt M, Lux C, and Baumert T. Complete Photoionization Experiments via Ultrafast Coherent Control with Polarization Multiplexing. *Phys Rev Lett* (2014) 112:223001. doi:10.1103/physrevlett.112.223001
99. Kerbstadt S, Pengel D, Johannmeyer D, Englert L, Bayer T, and Wollenhaupt M. Control of Photoelectron Momentum Distributions by Bichromatic Polarization-Shaped Laser fields. *New J Phys* (2017) 19:103017. doi:10.1088/1367-2630/aa83a4
100. Bayer T, Gräfing D, Kerbstadt S, Pengel D, Eickhoff K, Englert L, et al. Time-resolved 3d Imaging of Ultrafast Spin-Orbit Wave Packet Dynamics. *New J Phys* (2019) 21:033001. doi:10.1088/1367-2630/aafb87
101. Eickhoff K, Kerbstadt S, Bayer T, and Wollenhaupt M. Dynamic Quantum State Holography. *Phys Rev A* (2020) 101:013430. doi:10.1103/physreva.101.013430
102. Pengel D, Kerbstadt S, Johannmeyer D, Englert L, Bayer T, and Wollenhaupt M. Electron Vortices in Femtosecond Multiphoton Ionization. *Phys Rev Lett* (2017) 118:053003. doi:10.1103/PhysRevLett.118.053003
103. Pengel D, Kerbstadt S, Englert L, Bayer T, and Wollenhaupt M. Control of Three-Dimensional Electron Vortices from Femtosecond Multiphoton Ionization. *Phys Rev A* (2017) 96:043426. doi:10.1103/physreva.96.043426
104. Pengel D, Kerbstadt S, Bayer T, and Wollenhaupt M. Femtosekunden-Laserpulse Erzeugen Elektronenwirbel. *Phys Unserer Zeit* (2017) 48:162–3. doi:10.1002/piuz.201770404
105. Kerbstadt S, Eickhoff K, Bayer T, and Wollenhaupt M. Control of Free Electron Wave Packets by Polarization-Tailored Ultrashort Bichromatic Laser fields. *Adv Phys X* (2019) 4:1672583. doi:10.1080/23746149.2019.1672583
106. Kerbstadt S, Eickhoff K, Bayer T, and Wollenhaupt M. *Bichromatic Control of Free Electron Wave Packets*. Springer (2020). p. 43–76. doi:10.1007/978-3-030-47098-2_3
107. Chin SL, and Lambropoulos P. *Multiphoton Lonization of Atoms*. Elsevier (2012).
108. Berkowitz J. *Photoabsorption, Photoionization, and Photoelectron Spectroscopy*. Academic Press (2012).
109. Hockett P. *Quantum Metrology with Photoelectrons: Volume I: Foundations*. San Rafael, CA, United States: Morgan & Claypool Publishers (2018).
110. Hockett P. *Quantum Metrology with Photoelectrons: Volume II: Applications and Advances*. San Rafael, CA, United States: Morgan & Claypool Publishers (2018).
111. Faisal FHM. *Theory of Multiphoton Processes*. Springer Science & Business Media (1987).
112. Letokhov V. *Laser Photoionization Spectroscopy*. Elsevier (2012).
113. Wollenhaupt M, Assion A, and Baumert T. *Springer Handbook of Lasers and Optics, Vol. 2.* Springer (2012).
114. Bauer D. Computational strong-field Quantum Dynamics. In: *Intense Light-Matter Interactions*, 1. Berlin, Germany: De Gruyter (2017). doi:10.1515/9783110417265
115. Krug M, Bayer T, Wollenhaupt M, Sarpe-Tudoran C, Baumert T, Ivanov SS, et al. Coherent strong-field Control of Multiple States by a Single Chirped Femtosecond Laser Pulse. *New J Phys* (2009) 11:105051. doi:10.1088/1367-2630/11/10/105051
116. Wollenhaupt M, Bayer T, Vitanov NV, and Baumert T. Three-state Selective Population of Dressed States via Generalized Spectral Phase-step Modulation. *Phys Rev A* (2010) 81:053422. doi:10.1103/physreva.81.053422
117. Wollenhaupt M, Liese D, Präkelt A, Sarpe-Tudoran C, and Baumert T. Quantum Control by Ultrafast Dressed States Tailoring. *Chem Phys Lett* (2006) 419:184–90. doi:10.1016/j.cplett.2005.11.079
118. Wollenhaupt M, and Baumert T. Ultrafast strong Field Quantum Control on K_2 Dimers. *J Photochem Photobiol A: Chem* (2006) 180:248–55. doi:10.1016/j.jphotochem.2006.03.010
119. Bayer T, Wollenhaupt M, Braun H, and Baumert T. Ultrafast and Efficient Control of Coherent Electron Dynamics via Spods. *Adv Chem Phys* (2016) 159:235–82. doi:10.1002/9781119096276.ch6
120. Wollenhaupt M, Präkelt A, Sarpe-Tudoran C, Liese D, Bayer T, and Baumert T. Femtosecond strong-field Quantum Control with Sinusoidally Phase-Modulated Pulses. *Phys Rev A* (2006) 73:063409. doi:10.1103/physreva.73.063409
121. Bayer T, Philipp C, Eickhoff K, and Wollenhaupt M. Atomic Photoionization Dynamics in Ultrashort Cycloidal Laser fields. *Phy Rev A* (2020) 102:013104. doi:10.1103/physreva.102.013104
122. Meier C, and Engel V. Interference Structure in the Photoelectron Spectra Obtained from Multiphoton Ionization of Na_2 with a Strong Femtosecond Laser Pulse. *Phys Rev Lett* (1994) 73:3207–10. doi:10.1103/physrevlett.73.3207
123. Wollenhaupt M, Assion A, Bazhan O, Horn C, Liese D, Sarpe-Tudoran C, et al. Control of Interferences in an Autler-Townes Doublet: Symmetry of Control Parameters. *Phys Rev A* (2003) 68:015401. doi:10.1103/physreva.68.015401
124. Wollenhaupt M, Präkelt A, Sarpe-Tudoran C, Liese D, and Baumert T. Strong Field Quantum Control by Selective Population of Dressed States. *J Opt B: Quan Semiclass. Opt.* (2005) 7:S270–S276. doi:10.1088/1464-4266/7/10/010
125. Wollenhaupt M, Präkelt A, Sarpe-Tudoran C, Liese D, and Baumert T. Quantum Control by Selective Population of Dressed States Using Intense Chirped Femtosecond Laser Pulses. *Appl Phys B* (2006) 82:183–8. doi:10.1007/s00340-005-2066-0
126. Torosov BT, Shore BW, and Vitanov NV. Coherent Control Techniques for Two-State Quantum Systems: A Comparative Study. *Phys Rev A* (2021) 103: 033110. doi:10.1103/physreva.103.033110
127. Bayer T, Wollenhaupt M, Sarpe-Tudoran C, and Baumert T. Robust Photon Locking. *Phys Rev Lett* (2009) 102:023004. doi:10.1103/PhysRevLett.102.023004
128. Dudovich N, Polack T, Pe'er A, and Silberberg Y. Simple Route to strong-field Coherent Control. *Phys Rev Lett* (2005) 94:083002–4. doi:10.1103/PhysRevLett.94.083002
129. Wollenhaupt M, Präkelt A, Sarpe-Tudoran C, Liese D, and Baumert T. Quantum Control and Quantum Control Landscapes Using Intense Shaped Femtosecond Pulses. *J Mod Opt* (2005) 52:2187–95. doi:10.1080/09500340500275884
130. Bayer T, Wollenhaupt M, and Baumert T. Strong-field Control Landscapes of Coherent Electronic Excitation. *J Phys B: Mol Opt Phys* (2008) 41:074007–13. doi:10.1088/0953-4075/41/7/074007
131. Thallmair S, Siemering R, Kölle P, Kling M, Wollenhaupt M, Baumert T, et al. *The Interplay of Nuclear and Electronic Motion in the Control of Molecular Processes: A Theoretical Perspective*. Springer (2014). p. 213–48. doi:10.1007/978-3-642-45290-1_8
132. Braun H, Bayer T, Sarpe C, Siemering R, de Vivie-Riedle R, Baumert T, et al. Coupled Electron-Nuclear Wavepacket Dynamics in Potassium Dimers. *J Phys B: Mol Opt Phys* (2014) 47:124015. doi:10.1088/0953-4075/47/12/124015
133. Petersen J, and Mitrić R. Electronic Coherence within the Semiclassical Field-Induced Surface Hopping Method: strong Field Quantum Control in K_2. *Phys Chem Chem Phys* (2012) 14:8299–306. doi:10.1039/c2cp40747g
134. Feit MD, Fleck JA, and Steiger A. Solution of the Schrödinger Equation by a Spectral Method. *J Comput Phys* (1982) 47:412–33. doi:10.1016/0021-9991(82)90091-2
135. Mulliken RS. Role of Kinetic Energy in the Franck-condon Principle. *J Chem Phys* (1971) 55:309–14. doi:10.1063/1.1675522
136. Assion A, Geisler M, Helbing J, Seyfried V, and Baumert T. Femtosecond Pump-Probe Photoelectron Spectroscopy: Mapping of Vibrational Wave-Packet Motion. *Phys Rev A* (1996) 54:R4605–4608. doi:10.1103/physreva.54.r4605
137. Bayer T, Braun H, Sarpe C, Siemering R, von den Hoff P, de Vivie-Riedle R, et al. Charge Oscillation Controlled Molecular Excitation. *Phys Rev Lett* (2013) 110:123003. doi:10.1103/physrevlett.110.123003

138. Eickhoff K, Feld LC, Köhnke D, Englert L, Bayer T, and Wollenhaupt M. Coherent Control Mechanisms in Bichromatic Multiphoton Ionization. *J Phys B* (2021). doi:10.1088/1361-6455/ac11a0
139. Burger C, Frisch WF, Kardaś TM, Trubetskov M, Pervak V, Moshammer R, et al. Compact and Flexible Harmonic Generator and Three-Color Synthesizer for Femtosecond Coherent Control and Time-Resolved Studies. *Opt Express* (2017) 25:31130–9. doi:10.1364/oe.25.031130
140. Wirth A, Hassan MT, Grguras I, Gagnon J, Moulet A, Luu TT, et al. Synthesized Light Transients. *Science* (2011) 334:195–200. doi:10.1126/science.1210268
141. Liu J, and Kobayashi T. Generation of uJ-Level Multicolored Femtosecond Laser Pulses Using Cascaded Four-Wave Mixing. *Opt Express* (2009) 17:4984–90. doi:10.1364/oe.17.004984
142. Harris SE, and Sokolov AV. Subfemtosecond Pulse Generation by Molecular Modulation. *Phys Rev Lett* (1998) 81:2894–7. doi:10.1103/physrevlett.81.2894
143. Sokolov AV, Shverdin MY, Walker DR, Yavuz § DD, Burzo AM, Yin GY, et al. Generation and Control of Femtosecond Pulses by Molecular Modulation. *J Mod Opt* (2005) 52:285–304. doi:10.1080/09500340410001731020
144. Chan H-S, Hsieh Z-M, Liang W-H, Kung AH, Lee C-K, Lai C-J, et al. Synthesis and Measurement of Ultrafast Waveforms from Five Discrete Optical Harmonics. *Science* (2011) 331:1165–8. doi:10.1126/science.1198397
145. Weiner AM. Ultrafast Optical Pulse Shaping: A Tutorial Review. *Opt Commun* (2011) 284:3669–92. doi:10.1016/j.optcom.2011.03.084
146. Kerbstadt S, Englert L, Bayer T, and Wollenhaupt M. Ultrashort Polarization-Tailored Bichromatic fields. *J Mod Opt* (2017) 64:1010–25. doi:10.1080/09500340.2016.1271151
147. Kak AC, and Slaney M. *Principles of Computerized Tomographic Imaging*. New York: IEEE Press (1988). p. 1–339.
148. Itatani J, Levesque J, Zeidler D, Niikura H, Pépin H, Kieffer JC, et al. Tomographic Imaging of Molecular Orbitals. *Nature* (2004) 432:867–71. doi:10.1038/nature03183
149. Bergner K, Flamm D, Jenne M, Kumkar M, Tünnermann A, and Nolte S. Time-resolved Tomography of Ultrafast Laser-Matter Interaction. *Opt Express* (2018) 26:2873–83. doi:10.1364/oe.26.002873
150. Lux C, Wollenhaupt M, Bolze T, Liang Q, Köhler J, Sarpe C, et al. Circular Dichroism in the Photoelectron Angular Distributions of Camphor and Fenchone from Multiphoton Ionization with Femtosecond Laser Pulses. *Angew Chem Int Ed* (2012) 51:5001–5. doi:10.1002/anie.201109035
151. Zewail AH. Femtochemistry: Atomic-Scale Dynamics of the Chemical Bond. *J Phys Chem A* (2000) 104:5660–94. doi:10.1021/jp001460h
152. Paasch-Colberg T, Kruchinin SY, Sağlam Ö, Kapser S, Cabrini S, Muehlbrandt S, et al. Sub-cycle Optical Control of Current in a Semiconductor: from the Multiphoton to the Tunneling Regime. *Optica* (2016) 3:1358–61. doi:10.1364/optica.3.001358
153. Karras G, Ndong M, Hertz E, Sugny D, Billard F, Lavorel B, et al. Polarization Shaping for Unidirectional Rotational Motion of Molecules. *Phys Rev Lett* (2015) 114:103001. doi:10.1103/physrevlett.114.103001
154. Lin K, Tutunnikov I, Ma J, Qiang J, Zhou L, Faucher O, et al. Spatiotemporal Rotational Dynamics of Laser-Driven Molecules. *Adv Photon* (2020) 2:024002. doi:10.1117/1.ap.2.2.024002
155. Ngoko Djiokap JM, Hu SX, Madsen LB, Manakov NL, Meremianin AV, and Starace AF. Electron Vortices in Photoionization by Circularly Polarized Attosecond Pulses. *Phys Rev Lett* (2015) 115:113004. doi:10.1103/physrevlett.115.113004
156. Eickhoff K, Rathje C, Köhnke D, Kerbstadt S, Englert L, Bayer T, et al. Orbital Angular Momentum Superposition States in Transmission Electron Microscopy and Bichromatic Multiphoton Ionization. *New J Phys* (2020) 22:103045. doi:10.1088/1367-2630/abbe54
157. Ngoko Djiokap JM, Meremianin AV, Manakov NL, Hu SX, Madsen LB, and Starace AF. Multistart Spiral Electron Vortices in Ionization by Circularly Polarized Uv Pulses. *Phys Rev A* (2016) 94:013408. doi:10.1103/physreva.94.013408
158. Yuan KJ, Chelkowski S, and Bandrauk AD. Photoelectron Momentum Distributions of Molecules in Bichromatic Circularly Polarized Attosecond UV Laser fields. *Phys Rev A* (2016) 93:053425. doi:10.1103/physreva.93.053425
159. Ngoko Djiokap JM, Meremianin AV, Manakov NL, Hu SX, Madsen LB, and Starace AF. Kinematical Vortices in Double Photoionization of Helium by Attosecond Pulses. *Phys Rev A* (2017) 96:013405. doi:10.1103/physreva.96.013405
160. Yuan K-J, Lu H, and Bandrauk AD. Photoionization of Triatomic Molecular Ions H_3^{2+} by Intense Bichromatic Circularly Polarized Attosecond UV Laser Pulses . *J Phys B: Mol Opt Phys* (2017) 50:124004. doi:10.1088/1361-6455/aa72fa
161. Meng Li ML, Guizhong Zhang GZ, Tianqi Zhao TZ, Xin Ding XD, and Jianquan Yao JY. Electron Vortices in Photoionization by a Pair of Elliptically Polarized Attosecond Pulses. *Chin Opt Lett* (2017) 15:120202. doi:10.3788/col201715.120202
162. Djiokap JMN, and Starace AF. Doubly-excited State Effects on Two-Photon Double Ionization of Helium by Time-Delayed, Oppositely Circularly-Polarized Attosecond Pulses. *J Opt* (2017) 19:124003. doi:10.1088/2040-8986/aa8fc0
163. Li ZL, Li YJ, and Xie BS. Momentum Vortices on Pairs Production by Two Counter-rotating fields. *Phys Rev D* (2017) 96:076010. doi:10.1103/physrevd.96.076010
164. Li M, Zhang G, Kong X, Wang T, Ding X, and Yao J. Dynamic Stark Induced Vortex Momentum of Hydrogen in Circular fields. *Opt Express* (2018) 26:878–86. doi:10.1364/oe.26.000878
165. Li M, Zhang G, Ding X, and Yao J. Symmetric Electron Vortices of Hydrogen Ionized by Orthogonal Elliptical fields. *IEEE Photon J.* (2018) 10:1–9. doi:10.1109/jphot.2018.2854237
166. Li ZL, Xie BS, and Li YJ. Vortices in Multiphoton Pair Production by Two-Color Rotating Laser fields. *J Phys B: Mol Opt Phys* (2018) 52:025601. doi:10.1088/1361-6455/aaf3f9
167. Li M, Zhang G-z., Ding X, and Yao J-q.. Carrier Envelope Phase Description for an Isolated Attosecond Pulse by Momentum Vortices. *Chin Phys. Lett.* (2019) 36:063201. doi:10.1088/0256-307x/36/6/063201
168. Djiokap JMN, Meremianin AV, Manakov NL, Madsen LB, Hu SX, and Starace AF. Dynamical Electron Vortices in Attosecond Double Photoionization of H_2. *Phys Rev A* (2018) 98:063407. doi:10.1103/physreva.98.063407
169. Li M, Zhang G, Ding X, and Yao J. Ac Stark Effect on Vortex Spectra Generated by Circularly Polarized Pulses. *IEEE Photon J.* (2019) 11:1–11. doi:10.1109/jphot.2019.2916106
170. Armstrong GSJ, Clarke DDA, Benda J, Wragg J, Brown AC, and van der Hart HW. Modeling Tomographic Measurements of Photoelectron Vortices in Counter-rotating Circularly Polarized Laser Pulses. *Phys Rev A* (2019) 100:063416. doi:10.1103/physreva.100.063416
171. Chen Z, He PL, and He F. Spiral Nuclear Momentum Distribution for the Dissociation of H_2^+ in a Circularly Polarized Laser Pulse. *Phys Rev A* (2020) 101:033406. doi:10.1103/physreva.101.033406
172. Chen Z, and He F. Interference of Nuclear Wave Packets Carrying Different Angular Momenta in the Dissociation of $H_2{}^+$ in strong Circularly Polarized Laser Pulses. *Phys Rev A* (2020) 102:033107. doi:10.1103/physreva.102.033107
173. He Y, Zhang G, Tang J, Ding X, and Yao J. Optical-stark Induced Distortions in Vortex Momentum Distributions of P-Orbital Electrons of Neon Atoms. *IEEE Photon J.* (2020) 12:1–9. doi:10.1109/jphot.2020.3037714
174. Geng L, Cajiao VF, Kamiński JZ, Peng LY, and Krajewska K. Vortex Structures in Photodetachment by Few-Cycle Circularly Polarized Pulses. *Phys Rev A* (2020) 102:043117. doi:10.1103/physreva.102.043117
175. Varshalovich DA, Moskalev AN, and Khersonskii VK. *Quantum Theory of Angular Momentum*. Singapore: World Scientific Publishing Co. Pte. Ltd. (1988).
176. Zare RN. *Angular Momentum: Understanding Spatial Aspects in Chemistry and Physics*. Incorporated: Dover Publications (2007).
177. Kerbstadt S, Gabrisch L, Eickhoff K, Bayer T, and Wollenhaupt M. Imaging Multiple Rydberg Wave Packets from Shaper-Generated Two-Color Femtosecond Pump-Probe Sequences. *Phys Rev A* (2019) 99:013406. doi:10.1103/physreva.99.013406
178. Passig J, Zherebtsov S, Irsig R, Arbeiter M, Peltz C, Göde S, et al. Nanoplasmonic Electron Acceleration by Attosecond-Controlled Forward Rescattering in Silver Clusters. *Nat Commun* (2017) 8:1181. doi:10.1038/s41467-017-01286-w

179. Demekhin PV, Artemyev AN, Kastner A, and Baumert T. Photoelectron Circular Dichroism with Two Overlapping Laser Pulses of Carrier Frequencies ω and 2ω Linearly Polarized in Two Mutually Orthogonal Directions. *Phys Rev Lett* (2018) 121:253201. doi:10.1103/physrevlett.121.253201

180. Rozen S, Comby A, Bloch E, Beauvarlet S, Descamps D, Fabre B, et al. Controlling Subcycle Optical Chirality in the Photoionization of Chiral Molecules. *Phys Rev X* (2019) 9:031004. doi:10.1103/physrevx.9.031004

181. Eichmann H, Egbert A, Nolte S, Momma C, Wellegehausen B, Becker W, et al. Polarization-dependent High-Order Two-Color Mixing. *Phys Rev A* (1995) 51:R3414–R3417. doi:10.1103/physreva.51.r3414

182. Fan T, Grychtol P, Knut R, Hernández-García C, Hickstein DD, Zusin D, et al. Bright Circularly Polarized Soft X-ray High Harmonics for X-ray Magnetic Circular Dichroism. *Proc Natl Acad Sci USA* (2015) 112: 14206–11. doi:10.1073/pnas.1519666112

183. Eckart S, Richter M, Kunitski M, Hartung A, Rist J, Henrichs K, et al. Nonsequential Double Ionization by Counterrotating Circularly Polarized Two-Color Laser fields. *Phys Rev Lett* (2016) 117:133202. doi:10.1103/physrevlett.117.133202

184. Mancuso CA, Hickstein DD, Grychtol P, Knut R, Kfir O, Tong XM, et al. Strong-field Ionization with Two-Color Circularly Polarized Laser fields. *Phys Rev A* (2015) 91:031402R. doi:10.1103/physreva.91.031402

185. Mancuso CA, Hickstein DD, Dorney KM, Ellis JL, Hasovic E, Knut R, et al. Controlling Electron-Ion Rescattering in Two-Color Circularly Polarized Femtosecond Laser fields. *Phys Rev A* (2016) 93:053406. doi:10.1103/physreva.93.053406

186. Miloševic DB. Atomic and Molecular Processes in a strong Bicircular Laser Field. *Atoms* (2018) 6:61. doi:10.3390/atoms6040061

187. Baykusheva D, Zindel D, Svoboda V, Bommeli E, Ochsner M, Tehlar A, et al. Real-time Probing of Chirality during a Chemical Reaction. *Proc Natl Acad Sci USA* (2019) 116:23923–9. doi:10.1073/pnas.1907189116

188. Abel MJ, Pfeifer T, Jullien A, Nagel PM, Bell MJ, Neumark DM, et al. Carrier-envelope Phase-dependent Quantum Interferences in Multiphoton Ionization. *J Phys B: Mol Opt Phys* (2009) 42:075601. doi:10.1088/0953-4075/42/7/075601

189. Kerbstadt S, Pengel D, Englert L, Bayer T, and Wollenhaupt M. Carrier-envelope-phase Control of Asymmetries in the Multiphoton Ionization of Xenon Atoms by Ultrashort Bichromatic fields. *Phys Rev A* (2018) 97:063402. doi:10.1103/physreva.97.063402

190. Kerbstadt S, Pengel D, Bayer T, and Wollenhaupt M. CEP Control of Multiphoton Ionization Using Shaper-Generated Variable Frequency Ratio Bichromatic fields. *EPJ Web Conf* (2019) 205:07003. doi:10.1051/epjconf/201920507003

191. Paulus GG, Grasbon F, Walther H, Villoresi P, Nisoli M, Stagira S, et al. Absolute-phase Phenomena in Photoionization with Few-Cycle Laser Pulses. *Nature* (2001) 414:182–4. doi:10.1038/35102520

192. Kling MF, Rauschenberger J, Verhoef AJ, Hasović E, Uphues T, Milošević DB, et al. Imaging of Carrier-Envelope Phase Effects in Above-Threshold Ionization with Intense Few-Cycle Laser fields. *New J Phys* (2008) 10: 025024–17. doi:10.1088/1367-2630/10/2/025024

193. Kling MF, Siedschlag C, Verhoef AJ, Khan JI, Schultze M, Uphues T, et al. Control of Electron Localization in Molecular Dissociation. *Science* (2006) 312:246–8. doi:10.1126/science.1126259

194. Sansone G, Kelkensberg F, Pérez-Torres JF, Morales F, Kling MF, Siu W, et al. Electron Localization Following Attosecond Molecular Photoionization. *Nature* (2010) 465:763–6. doi:10.1038/nature09084

195. Alnaser AS, and Litvinyuk IV. Subfemtosecond Directional Control of Chemical Processes in Molecules. *J Phys B: Mol Opt Phys* (2017) 50: 032002. doi:10.1088/1361-6455/50/3/032002

196. Krüger M, Schenk M, and Hommelhoff P. Attosecond Control of Electrons Emitted from a Nanoscale Metal Tip. *Nature* (2011) 475:78–81. doi:10.1038/nature10196

197. Schiffrin A, Paasch-Colberg T, Karpowicz N, Apalkov V, Gerster D, Mühlbrandt S, et al. Optical-field-induced Current in Dielectrics. *Nature* (2013) 493:70–4. doi:10.1038/nature11567

198. Piglosiewicz B, Schmidt S, Park DJ, Vogelsang J, Gross P, Manzoni C, et al. Carrier-envelope Phase Effects on the strong-field Photoemission of Electrons from Metallic Nanostructures. *Nat Photon* (2014) 8:38–43. doi:10.1038/nphoton.2013.344

199. Süßmann F, Seiffert L, Zherebtsov S, Mondes V, Stierle J, Arbeiter M, et al. Field Propagation-Induced Directionality of Carrier-Envelope Phase-Controlled Photoemission from Nanospheres. *Nat Commun* (2015) 6: 7944. doi:10.1038/ncomms8944

200. Ciappina MF, Pérez-Hernández JA, Landsman AS, Okell WA, Zherebtsov S, Förg B, et al. Attosecond Physics at the Nanoscale. *Rep Prog Phys* (2017) 80: 054401. doi:10.1088/1361-6633/aa574e

201. Higuchi T, Heide C, Ullmann K, Weber HB, and Hommelhoff P. Light-field-driven Currents in Graphene. *Nature* (2017) 550:224–8. doi:10.1038/nature23900

202. Wollenhaupt M, Assion A, Graefe O, Liese D, Sarpe-Tudoran C, Winter M, and Baumert T. Changes of the Electronic Structure along the Internuclear Coordinate Studied by Ultrafast Photoelectron Spectroscopy: the $2^1\ \Sigma_u^+$ Na_2 Double Minimum State. *Chem Phys Lett* (2003) 376:457–64. doi:10.1016/s0009-2614(03)00994-1

203. Valance A, and Tuan QN. The Molecular Electronic Structure of the Lowest $^{1,3}\Sigma_{g,u}^+$ States of Na_2 and K_2. *J Phys B: Mol Phys* (1982) 15:17–33. doi:10.1088/0022-3700/15/1/009

204. Arasaki Y, Takatsuka K, Wang K, and McKoy V. Femtosecond Energy- and Angle-Resolved Photoelectron Spectra. *Chem Phys Lett* (1999) 302:363–74. doi:10.1016/s0009-2614(99)00153-0

205. Arasaki Y, Takatsuka K, Wang K, and McKoy V. Femtosecond Energy- and Angle-Resolved Photoelectron Spectroscopy. *J Chem Phys* (2000) 112: 8871–84. doi:10.1063/1.481534

206. Neufeld O, and Cohen O. Optical Chirality in Nonlinear Optics: Application to High Harmonic Generation. *Phys Rev Lett* (2018) 120:133206. doi:10.1103/physrevlett.120.133206

207. Beaulieu S, Comby A, Clergerie A, Caillat J, Descamps D, Dudovich N, et al. Attosecond-resolved Photoionization of Chiral Molecules. *Science* (2017) 358:1288–94. doi:10.1126/science.aao5624

208. Powis I. *Photoelectron Circular Dichroism*, Vol. 1. Wiley (2012). p. 407–31. doi:10.1002/9781118120187.ch15

209. Ordonez AF, and Smirnova O. Generalized Perspective on Chiral Measurements without Magnetic Interactions. *Phys Rev A* (2018) 98: 063428. doi:10.1103/physreva.98.063428

210. Ayuso D, Neufeld O, Ordonez AF, Decleva P, Lerner G, Cohen O, et al. Synthetic Chiral Light for Efficient Control of Chiral Light-Matter Interaction. *Nat Photon* (2019) 13:866–71. doi:10.1038/s41566-019-0531-2

211. Neufeld O, Ayuso D, Decleva P, Ivanov MY, Smirnova O, and Cohen O. Ultrasensitive Chiral Spectroscopy by Dynamical Symmetry Breaking in High Harmonic Generation. *Phys Rev X* (2019) 9:031002. doi:10.1103/physrevx.9.031002

212. Neufeld O, Tzur ME, and Cohen O. Degree of Chirality of Electromagnetic fields and Maximally Chiral Light. *Phys Rev A* (2020) 101:053831. doi:10.1103/physreva.101.053831

213. Tang Y, and Cohen AE. Enhanced Enantioselectivity in Excitation of Chiral Molecules by Superchiral Light. *Science* (2011) 332:333–6. doi:10.1126/science.1202817

214. Traum C, Henzler P, Lohner S, Becker H, Nabben D, Gumbsheimer P, et al. Multicolor Femtosecond Pump-Probe System with Single-Electron Sensitivity at Low Temperatures and High Magnetic fields. *Rev Scientific Instr* (2019) 90:123003. doi:10.1063/1.5126157

215. Luu TT, Garg M, Kruchinin SY, Moulet A, Hassan MT, and Goulielmakis E. Extreme Ultraviolet High-Harmonic Spectroscopy of Solids. *Nature* (2015) 521:498–502. doi:10.1038/nature14456

216. Ohmura H, and Saito N. Sub-optical-cycle Attosecond Control of Molecular Ionization by Using Fourier-Synthesized Laser fields. *Phys Rev A* (2020) 101: 043419. doi:10.1103/physreva.101.043419

217. Zhang L, Wang G-L, Zhao S-F, and Zhou X-X. Controlling of strong Tunable Thz Emission with Optimal Incommensurate Multi-Color Laser Field. *Phys Plasmas* (2017) 24:023116. doi:10.1063/1.4976549

218. Liu S, Fan Z, Lu C, Gui J, Luo C, Wang S, et al. Coherent Control of Boosted Terahertz Radiation from Air Plasma Pumped by a Femtosecond Three-Color Sawtooth Field. *Phys Rev A* (2020) 102:063522. doi:10.1103/physreva.102.063522

219. Yuan KJ, and Bandrauk AD. Controlling Circularly Polarized High-Order Harmonic Generation in Molecules by Intense Tricircular Laser Pulses. *Phys Rev A* (2019) 100:033420. doi:10.1103/physreva.100.033420
220. Pfeiffer AN, Cirelli C, Smolarski M, and Keller U. Recent Attoclock Measurements of strong Field Ionization. *Chem Phys* (2013) 414:84–91. doi:10.1016/j.chemphys.2012.02.005
221. Wituschek A, von Vangerow J, Grzesiak J, Stienkemeier F, and Mudrich M. A Simple Photoionization Scheme for Characterizing Electron and Ion Spectrometers. *Rev Scientific Instr* (2016) 87:083105. doi:10.1063/1.4960401
222. Bruss D, and Leuchs G. *Quantum Information, 2 Volume Set: From Foundations to Quantum Technology Applications*. John Wiley & Sons (2019).
223. Nawrocki W. *Introduction to Quantum Metrology: Quantum Standards and Instrumentation*. Heidelberg: Springer (2015).
224. Spektor G, Kilbane D, Mahro AK, Frank B, Ristok S, Gal L, et al. Revealing the Subfemtosecond Dynamics of Orbital Angular Momentum in Nanoplasmonic Vortices. *Science* (2017) 355:1187–91. doi:10.1126/science.aaj1699
225. Henzler P, Traum C, Holtkemper M, Nabben D, Erbe M, Reiter DE, et al. Femtosecond Transfer and Manipulation of Persistent Hot-trion Coherence in a Single Cdse/znse Quantum Dot. *Phys Rev Lett* (2021) 126:067402. doi:10.1103/PhysRevLett.126.067402
226. Hickstein DD, Dollar FJ, Grychtol P, Ellis JL, Knut R, Hernández-García C, et al. Non-collinear Generation of Angularly Isolated Circularly Polarized High Harmonics. *Nat Photon* (2015) 9:743–50. doi:10.1038/nphoton.2015.181

Conflict of Interest: The authors declare that the research was conducted in the absence of any commercial or financial relationships that could be construed as a potential conflict of interest.

frontiers | Frontiers in Physics

REVIEW
published: 21 June 2022
doi: 10.3389/fphy.2022.854039

The RVP Method—From Real Ab-Initio Calculations to Complex Energies and Transition Dipoles

Arie Landau[1,2]*, *Idan Haritan*[1]* *and Nimrod Moiseyev*[1,3]*

[1]Schulich Faculty of Chemistry, Technion-Israel Institute of Technology, Haifa, Israel, [2]Institute of Advanced Studies in Theoretical Chemistry, Technion-Israel Institute of Technology, Haifa, Israel, [3]Faculty of Physics, Technion-Israel Institute of Technology, Haifa, Israel

The purpose of this review is to describe the rationale behind the RVP (resonance *via* Padé) approach for calculating energies and widths of resonances, while emphasizing a solid mathematical ground. The method takes real input data from stabilization graphs, where quasi-discrete continuum energy levels are plotted as a function of a parameter, which gradually makes the employed basis functions more diffuse. Thus, input data is obtained from standard quantum chemistry packages, which are routinely used for calculating molecular bound electronic states. The method simultaneously provides the resonance positions (energies) and widths (decay rates) *via* analytical continuations of real input data into the complex plane (*via* the Padé approximant). RVP holds for isolated resonances (in which the energy-gap between resonance states is smaller than their decay rates). We focus also on the ability to use an open-source "black-box" code to calculate the resonance positions and widths as well as other complex electronic properties, such as transition dipoles.

Keywords: resonances, ab-initio, electronic structure, stabilization graph, analytical continuation, RVP

Edited by:
Tamar Seideman,
Northwestern University,
United States

Reviewed by:
Pierre Descouvemont,
Université Libre de Bruxelles, Belgium
Michael Falcetta,
Grove City College, United States

***Correspondence:**
Arie Landau
alandau@technion.ac.il
Idan Haritan
haritan@campus.technion.ac.il
Nimrod Moiseyev
nimrod@technion.ac.il

Specialty section:
This article was submitted to Physical Chemistry and Chemical Physics,
a section of the journal Frontiers in Physics

Received: *13 January 2022*
Accepted: *22 April 2022*
Published: *21 June 2022*

Citation:
Landau A, Haritan I and Moiseyev N (2022) The RVP Method—From Real Ab-Initio Calculations to Complex Energies and Transition Dipoles.
Front. Phys. 10:854039.
doi: 10.3389/fphy.2022.854039

1 INTRODUCTION AND MOTIVATION

1.1 Resonances in Chemistry

Resonances are perhaps one of the most striking phenomena in chemistry [1, 2]. Molecules in metastable states (so called resonances) have enough energy to ionize or dissociate but do not do it right away. They have finite lifetimes and decay to the products which can be electrons, ions and radicals. The decay rates can vary from case to case and can be different by many order of magnitudes and there may be several open decay channels.

Let's consider the following illustrative triatomic (ABC) molecular reaction that occurs on a ground electronic potential energy surface,

$$\begin{array}{lll} A + BC \rightarrow [ABC]^{\#} & \rightarrow AB + C & \\ \text{Or} & \rightarrow AC + B & \\ \text{Or} & \rightarrow A + BC^{*}. & \end{array} \tag{1}$$

Where $[ABC]^{\#}$ represents an activated complex that has enough energy to dissociate to several different products and, BC^{*} is the diatomic molecule BC in an excited ro-vibrational state. This reaction takes place for a specific collision energy (within a given uncertainty) at which the activated complex is created in a well defined metatsable state. This metastable state is known as a resonance state, as time passes it decays into the reaction products. The energy of the activated complex above the lowest energy threshold (i.e., above the minimal energy in which it can dissociates) is the resonance *position*, E_{res}. The *decay rate* or *width* of the activated complex, Γ_{res}, is inverse proportional to the *lifetime* of the activated complex, where $2\pi\hbar$ is the proportional parameter. The decay rate, Γ_{res}, is a sum over the partial decay rates into all the possible products. That is,

$$\Gamma_{res} = \Gamma_{AB+C} + \Gamma_{AC+B} + \Gamma_{A+BC^*}.$$

The difference between the energy of the activated complex in a resonance (metastable) state and the energies of the different bound-state energies of the reaction products provide the relative kinetic energies of the $AB + C$, $AC + B$ and $A + BC^*$ products. The energy and width of the activated complex and the partial decay rates can be calculated from a single eigenfunction of the time independent nuclear Schrödinger equation when outgoing boundary conditions are imposed [1–3]. Notice that by imposing outgoing boundary conditions on the non-equilibrium reaction presented in **Eq. 1** will turn the real physical molecular Hamiltonian into a non-Hermitian Hamiltonian, as will be explained in details below. The resonance *via* Padé (RVP) method, which is the focus of this review, enables the calculations of the energy and decay rate of such an activated complex. In principle, also the partial widths can be calculated by RVP, but the way to do it is out of the scope of this review.

A second illustration examines the autoionization process in the helium atom. Helium has an infinite number of discrete bound states. The bound states of helium are associated with the ground and singly excited electronic states. Contrary, the doubly-excited states must ionize after a finite period of time, i.e., these states are resonance states,

$$\mathrm{He}^{**} \rightarrow \mathrm{He}^{+} + e^{-}. \tag{2}$$

Let us prove it. The starting point in our proof is to neglect the electronic repulsion and approximate the energy of a doubly-excited helium (He**) as,

$$E_{n_1>1,n_2>1}(\mathrm{no-repulsion}) = -Z^2\left(\frac{1}{n_1^2}+\frac{1}{n_2^2}\right)13.6\,\mathrm{eV},$$

where $Z = 2$. This value must be lower than the *exact* energy of a doubly-excited helium state since the electronic repulsion was neglected. Therefore, whenever

$$-Z^2\left(\frac{1}{n_1^2}+\frac{1}{n_2^2}\right)13.6\,\mathrm{eV} > -Z^2\frac{1}{n_{ion}^2}13.6\,\mathrm{eV}$$

ionization takes place, where n_1, n_2 are the neutral He electronic levels and n_{ion} is the level of He⁺. This inequality can be reformulated as,

$$\frac{n_1^2 n_2^2}{n_1^2+n_2^2} > n_{ion}^2.$$

The lowest doubly-excited states occur when $n_1 = n_2 = 2$, for which $\frac{n_1^2 n_2^2}{n_1^2+n_2^2} = 2$, i.e., the energies of these He** states are higher than the ionization threshold (corresponding to $n_{ion} = 1$). As long as $\frac{n_1^2 n_2^2}{n_1^2+n_2^2} \leq 4$ (corresponding to $n_{ion} = 2$), there is only one open channel–autoionization decay into the helium cation in its ground electronic state. In case $\frac{n_1^2 n_2^2}{n_1^2+n_2^2} > 4$, there will be several open decay channels involving also excited helium-cation states. Note that the spontaneous-emission time of He** is longer by several order of magnitude than the resonance lifetime. The spontaneous-emission time can be estimated using the Einstein coefficient for spontaneous emission (A, which is proportional to the calculated transition dipoles and the energy differences between the relevant states) [4], where the emission time is $T = A^{-1}$. The resonance lifetimes are inverse proportional to the calculated widths. Therefore, auto-ionization would dominate the dynamics of He**.

These kind of resonances are referred to *Feshbach* type resonances [2] since their energies (for $n_1 = n_2 = 2$) are *below* their own ionization threshold, i.e., He^{*+}(2s or 2p), but *above* the He^{+}(1s) threshold. Thus, Feshbach resonances are associated with two-electron processes. Therefore, dynamical electronic correlation, in which one go beyond the mean field (Hartree Fock) approximation, must be considered. Imposing outgoing boundary conditions on the electronic solutions of the time-independent Scrödinger equation makes the electronic Hamiltonian non-Hermitian, as in the above molecular dissociation example. Thus, the resonance energy positions and decay rates of He**, and any chemical systems in autoionization states, can be immediately obtained from the eigenvalue spectrum of a non-Hermitian Hamiltonian (see the next section for more details). Moreover, below we show that RVP can be used to study the autoionization process in **Eq. 2** with great accuracy.

Another type of metastable electronic states are the *shape-type* resonances [2], which lay above their *own* ionization threshold, therefore they represent a one-electron transition and they can be obtained within the Hartree-Fock approximation. This is a one-electron process, in which an electron tunnels through a potential barrier that results from a mean repulsion potential that corresponds to all the other electrons. Of course, for accurate calculations of energies and widths (inverse lifetimes) one should go beyond the mean field approximation. The simplest examples for electronic shape-type resonances are the ground electronic states of the molecular Hydrogen, Nitrogen and CO anions [5, 6]. Notice that in such anionic-resonance cases the decay process is referred to as autodetachment.

Uracil anion is an example for a biochemical system in which ionization and dissociation may occur simultaneously. Attachment of an electron to uracil leads to two types of electronic resonance anion states. Shape resonances appear as an electron is attached to one of the unoccupied π^* orbitals of the neutral ground state of uracil. Alternatively, an electron can be attached to excited states of the neutral uracil, forming an electronica Feshbach resonances. In addition to the autoionization process associated electronic resonance states, also dissociative electron attachment (DEA) processes may follow upon the creation of a uracil anion. Uracil may undergo DEA into $C_3H_3N_2O^-$ by eliminating CO and H [7]. These autoionization and DEA process may result in damage to

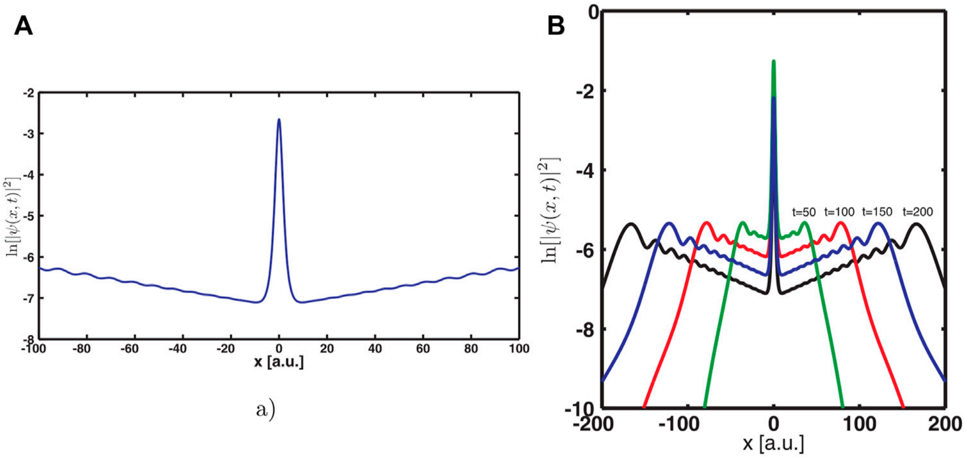

FIGURE 1 | (A) Illustration of the asymptotic divergence of the resonance state density for the model potential $V(x) = (1 - cosh^{-2}(x))^2 \exp(-0.05x^2)$ **(B)** The probability density of the wavepacket at different times on a logarithmic scale. Note that the region of exponential increase in the spatial domain is expanding with time. Reprinted from Ref. [3], Copyright (Year), with permission from Elsevier.

the RNA strand. Below we show that RVP can be used in studying such processes, by calculating the complex energies of the lowest three shape-type states of the uracil anion as well as the transition dipoles between them.

All in all, electronic resonances refer to autoionization (e.g., **Eq. 2**) and nuclear resonances refer to a situation in which a molecule pre-dissociates (e.g., **Eq. 1**). Notice that autoionization can become a more complicated and "rich" phenomenon, as in the case of: Auger [8–11], ICD (interatomic Coulombic decay) [12–20], ETMD (electron-transfer mediated decay) [15, 20–23], etc. Nuclear shape-type and Feshbach-type resonances are described in detail in Chapter 2 in Ref. 1 that is dedicated to Resonances Phenomena in Nature. Of course, often the decay of the electron and nuclear resonance states may happen simultaneously. As for example,

$$A + BC \rightarrow [ABC]^{\#} \rightarrow AB + C^{+} + e^{-}.$$

The RVP method, which is described below, is applicable to all these cases.

1.2 Wavepacket Time-Dependent Propagation vs. Time-Independent Stationary Solutions *via* Outgoing Boundary Conditions

Let us first briefly explain the motivation to look for such a comparison. In scattering theory resonances are associated with wavefunctions or eigenstates of the time-independent Schrödinger equation (TISE), which only consist of outgoing waves at the asymptote. The physical reason is clear. The system is prepared in a metastable state and as time passes it breaks apart into sub-systems as described above. Solving the TISE with such outgoing boundary conditions (OBCs) results in a discrete spectrum with real and complex eigenvalues, which are associated with bound states and resonances, respectively [1–3]. Notice that such a spectrum characterizes the non-Hermitian quantum mechanics (NHQM) formalism, i.e., by imposing OBCs we turn the QM problem into the NH regime. The bound state eigenvalues are real and the corresponding eigenfunctions are exactly as usual (i.e, decay asymptotically to zero). The resonance eigenvalues are complex, $E_{res} - \frac{i}{2}\Gamma_{res}$. The real part, E_{res}, corresponds to the resonance energy position, while the imaginary part, Γ_{res}, corresponds to the resonance decay rate (inversely proportional to the resonance lifetime) [1]. Alas, the asymptotes of the corresponding resonance eigenfunctions exponentially diverge. This asymptotic exponential divergent of the TISE is also obtained by wavepacket propagation calculations as illustrated in **Figure 1A**.

This seems to contradict the representation of resonances as the solutions of the time-dependent Schrödinger equation (TDSE) known as wavepackets. Since resonances are embedded in the continuous part of the spectrum they cannot be described using a single stationary eigenstate. Though, at any given time of the dynamics, the wavepackets are represented as superpositions of the (Hermitian) Hamiltonian eigenstates. Thus, wavepackets by definition are square integrable functions, i.e., their asymptotes decay exponentially and do not exponentially diverge.

The answer to this puzzle was given in Refs. [1, 3, 24]: before a wavepacket decays at the asymptote it actually diverges exponentially (at very large but finite distance from the interaction region). **Figure 1B** illustrates this point at different dynamic times. The conclusion is quite clear. It is appropriate to impose OBCs in order to describe a decaying system since the corresponding solution of the TISE with OBCs also display the same divergence as the wavepacket solution of the TDSE does.

So which method, out of the two, is recommended for calculating resonances? The answer is that neither of them can be recommended for realistic molecular systems. The reason is as follows: within Hermitian QM we cannot use the TISE and we are forced to solve the TDSE; this presents a major numerical difficulty when considering standard quantum chemistry

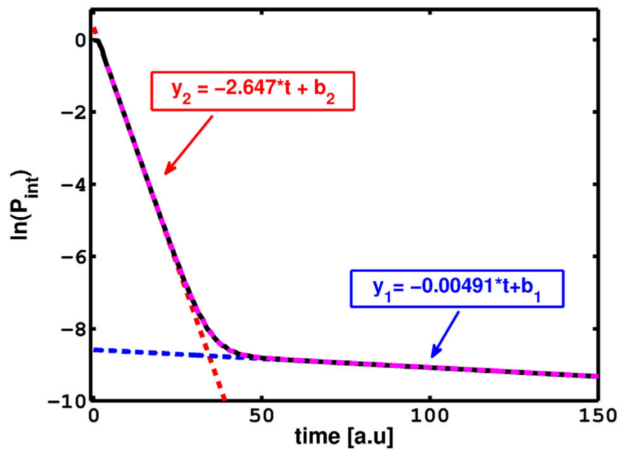

FIGURE 2 | The survival probability, $P_{\text{int}} = |\langle\Psi(0)|\Psi(t)\rangle|^2$, as a function of time. The initial Gaussian mainly populates the two narrowest resonances of the model potential $V(x) = (x^2/2 + 0.8)\exp(-0.2x^2)$. The slope of each line represents the decay rate of each resonance. The larger slope (of y_2) is the decay rate of the shorter resonance while the smaller slope (of y_1) is for the longer (i.e. narrower) resonance. Reprinted by permission of the publisher (Taylor & Francis Ltd, http://www.tandfonline.com).

packages for calculating resonance states. Within NHQM, solving the TISE with OBCs does not allow one to use square integrable basis sets, which transform the partial differential eigenvalue problem into a matrix eigenvalue problem, as in the Hermitian case. Therefore, a practical approach for describing resonances would be to transform the problem into the NH regime while retaining the square-integrability of the eigenstates. Such a procedure (the so-called complex scaling, which is described in the next section) can be used within many-body electronic structure formalism.

Let us briefly explain why the asymptote of the resonance wavefunction diverges exponentially in space but decays exponentially in time. The time-independent Schrödinger equation is given by,

$$\hat{H}|\Psi_E\rangle = E|\Psi_E\rangle, \tag{3}$$

where $E = E_{threshold} + |\hbar k|^2/(2m)$ and $E_{threshold}$ is the ionization/dissociation threshold energy. The asymptote of an eigenfunction associated with an above threshold energy and with only one open decay channel is given by,

$$\langle r|\Psi_E\rangle \xrightarrow{r\to\infty} A_{out}(E)\frac{e^{ikr}}{\sqrt{r}} + A_{in}(E)\frac{e^{-ikr}}{\sqrt{r}}. \tag{4}$$

The scattering matrix is the ratio between the amplitudes of the incoming $[A_{in}(E)]$ and the outgoing $[A_{out}(E)]$ waves. The poles of the scattering matrix are complex and the associated wavevectors take discrete values,

$$k_n = k_n^{Re} - ik_n^{Im} = |k_n|e^{-i\phi_n} \tag{5}$$

when $\phi_n \geq 0$, for which $A_{in}(E_n) = 0$ (see chapter 4 in Ref. [1]). Therefore, since

$$e^{ik_n r} = e^{i|k_n|r\exp(-i\phi_n)} \xrightarrow{r\to\infty} \infty, \tag{6}$$

the resonance function is not part of the Hilbert space. That is, it is not a square integrable function since it exponentially diverges in space. Due to this spatial behavior the resonance wavefuctions can not be expanded with a basis set of square integrable functions, as in the calculations of bound electronic states. Therefore we need to find out how we can transform the electronic coordinates such that the resonance wavefunction will remain square integrable and can be described as a finite linear combination of square integrable basis functions. As for example Gaussians which are used in standard electronic structure calculations.

Now, let's turn to the exponential decay of the resonance function in time. The time phase factor

$$e^{-iE_n t/\hbar} = e^{-i\mathrm{Re}E_n t/\hbar} e^{-\mathrm{Im}E_n t/\hbar} \xrightarrow{t\to\infty} 0, \tag{7}$$

where $E_n = \mathrm{Re}E_n + i\mathrm{Im}E_n$ (and for resonances $\mathrm{Im}E_n < 0$) and the number of particles is conserved only when $\hbar k_n^{Re} t = r$ (for explanation see Ref. [1] on the coupling of space and time even in the non-relativistic quantum mechanics framework). An interesting situation, which demonstrates the decay of the resonance function in time is presented in **Figure 2**. When the initial wavepacket mainly populates the two narrowest resonances of a model Hamiltonian, which is given in the caption of **Figure 2**. As one can see from **Figure 2** first the shorter resonance decays and only then the resonance with longer lifetime (smaller width) decays. The plot of the log of the survival probability as function of time gives two straight lines that their slopes provide the decay rates of the two resonances initially populated.

1.3 Complex Scaling Transformations in Order to Calculate Resonances by Methods Originally Developed for Bound States

It is straightforward to realize that **Eq. 6**, when $r \to re^{i\theta}$ and using **Eq. 5**, becomes,

$$e^{+ik_n r\exp(i\theta)} = e^{+i|k_n|r\exp[i(\theta-\phi_n)]} \xrightarrow{r\to\infty} 0, \tag{8}$$

when $\theta \geq \phi_n$. And since (**Eq. 5**)

$$k_n = |k_n|e^{-i\phi_n} = \sqrt{2m(E_n - E_{threshold})}/\hbar,$$

the condition $\theta \geq \phi_n$ yields,

$$\tan(2\theta) \geq \frac{2\Gamma_n}{Re[E_n] - E_{threshold}}. \tag{9}$$

Where $\{E_n\}$ are the complex resonances energies, $\Gamma_n = -2\mathrm{Im}[E_n]$, m is the mass of the emitted particle (e.g., an electron) and $E_{threshold}$ is the ionization/dissociation threshold energy. For additional details see Chapter 5.2 in Ref. [1]. In such a case, the resonance state can be represented as a square integrable function, thus, it can be expanded in terms of localized basis functions (such as Gaussians), similarly to a bound state. Upon such complex coordinate rotation, the Hamiltonian becomes non-Hermitian and the complex resonance energies are obtained regardless of the value of the rotation angle θ inside the interval $[\theta_c, \pi/4]$. (The upper limit on the θ interval is also explained in Chapter 5.2 in Ref. [1].)

This raises the question: is it possible to rotate the coordinate into the complex plane? If the physical potential is an analytical function, as in the case of atomic potentials, the coordinates of the system can be rotated into the complex half lower plane when $\theta_c < \theta < \pi/4$. However, the molecular electronic Hamiltonian within the Born-Oppenheimer approximation is singular at the nuclei positions and therefore a uniform analytical continuation into the complex plane by $r_e \rightarrow r_e e^{i\theta}$ is not allowed. This complication results in different methodologies for tackling this problem. The rigorous solution to this problem is to chose complex electronic coordinates that remain real inside an interaction volume, which include all the molecular nuclei. By that we avoid the singularities in the electron-nucleus attractive potential terms, and rotate the coordinate into the complex plane *only out* of the interaction volume by using θ. **Section 4** presents several methods, which introduce such complex electronic coordinates that avoid these singularities. By using one of these complex electronic coordinates, the non-Hermitian (NH) Hamiltonian, $\hat{H}(r_e^\theta)$, is obtained. This NH operator can be represented using a finite matrix that is spanned by finite number of Gaussian basis functions. The non-Hermitian Hamiltonian matrix elements are given by

$$H^\theta_{\zeta,\zeta'} = \langle G_\zeta | \hat{H}\left(r_e^\theta\right) | G_{\zeta'} \rangle, \tag{10}$$

where $\{G_\zeta(r_e)\}_{\zeta=1,2,\ldots N}$ represents a set of Gaussian basis functions.

Here we are coming to a delicate point which is important for the RVP method. Rather than computing the complex matrix elements for a non-Hermitian Hamiltonian operator $[\hat{H}(r_e^\theta)]$, we can calculate the complex matrix elements by keeping the molecular Hamiltonian operator real $[\hat{H}(r_e)]$, as usual, and use complex transformed Gaussian basis functions instead. Moreover, since we want to move into the complex plane outside the interaction volume, we can complex transform only the diffuse Gaussians of the employed basis set [25]. To a good approximation, these diffuse Gaussians span the space outside the interaction volume. Therefore, transforming only these diffuse Gaussians will transform only the electronic coordinates outside the interaction volume. In this case, the non-Hermitian Hamiltonian matrix elements become

$$H^\theta_{\zeta,\zeta'} = \langle \left[G_\zeta^{-\theta}\right]^* | \hat{H}(r_e) | G_{\zeta'}^{-\theta} \rangle,$$

where the complex diffuse Gaussians are given by [26],

$$\left\{G_\zeta\left(r_e^{-\theta}\right) = (x_e - x_N)^n (y_e - y_N)^m (z_e - z_N)^l \exp\left(-\zeta\eta^{-2}\left[(r_e - r_N)^2\right]\right)\right\}_{\zeta=1,2,\ldots N}, \tag{11}$$

and where $\eta = \alpha e^{i\theta}$ and the electronic vector position is $r_e = (x_e, y_e, z_e)$ centered on the nuclei $R_N = (x_N, y_N, z_N)$. Notice that one needs to avoid the complex conjugate in the matrix elements (the so called c-product, see Ref. [1]) and therefore we get,

$$H^\theta_{\zeta,\zeta'} = \langle G_\zeta^{+\theta} | \hat{H}(r_e) | G_{\zeta'}^{-\theta} \rangle. \tag{12}$$

Examining the NH Hamiltonian matrix elements, one can see that going into the complex plane can be made even simpler. From Ref. [27] we know that the Hamiltonian matrix elements, unlike the operator itself, can be analytically dilated. Therefore, one does not even have to use complex diffuse Gaussians to obtain these matrix elements. Instead, one can calculate these elements as a function of the parameter η but with $\theta = 0$, i.e., calculate the matrix elements as a function of α. Then, analytically dilate this parameter into the complex plane by substituting $\eta = \alpha e^{i\theta}$. In other words, to simplify things further and avoid the use of *complex* diffuse Gaussian basis functions, one can use *real* diffuse Gaussian basis functions, which depend on the real parameter, α, and then make this parameter complex by taking $\theta \neq 0$. Doing so, one can obtain the NH matrix elements by using real functions and the real Hamiltonian.

Needless to say that even this kind of simplification is not straightforward to apply and requires the modifications of the standard (Hermitian) quantum chemistry packages, which include variety of *ab-initio* methods (based on MP (Møller Plesset perturbation theory), CI (configuration interaction), CC (coupled cluster) and more.

Here we are coming to the new approach we developed, in which we take one step further in the analytic continuation direction and replace the analytic dilation of the Hamiltonian matrix elements with that of *a single eigenvalue*. A proof of this point is given in the next two sections. Obviously, there is a great numerical advantage to analytical continuation of a single eigenvalue over an $N \times N$ matrix elements, where N is the number of basis functions employed. Since the Padé approximant (see **Section 2.2**) is used for the analytical continuation the method is know as Resonance *via* Padé (RVP). There are additional numerical advantages to RVP. Standard NHQM methods commonly work directly in the complex plane in order to calculate the resonance eigenvalue [6, 25–40]. RVP belongs to a subgroup of methods, which move into the NHQM regime *via* analytical continuation [41–44] It is based on the stabilization technique [45–49], where the real energy levels are plotted as a function of a parameter (α as denoted above) that controls the diffuseness of the Gaussian basis functions (see details in **Section 2.1**). The stabilization calculation, which is computationally the most demanding step, is followed by a very "cheap" analytical continuation step [50] (see **Section 3**). Therefore, analytical-continuation methods that are based on the stabilization technique hold two distinct advantages: First, Matsika and co-workers showed that the computation time required by the stabilization technique is an order of magnitude lower than the time required by a NHQM approach that works literally in the complex plane [43]. Second, the versatility in generating the stabilization graph opens the door for various applications. That is, stabilization graphs can be calculated using any standard quantum chemistry packages, with any existing Hermitian electronic structure method, see for example Ref. [44].

1.4 Proof of Concept for the Resonance *via* Padé Method for Small Hamiltonian Matrices

In this section we explain the concept behind the RVP method and its connection to the analytical continuation of the real Hamiltonian matrix elements (HMEs); we stated above that in order to calculate resonances in the complex plane one can analytically dilate the real HMEs into the complex plane. This means that in order to calculate resonances one needs to obtain the matrix elements as a function of a real parameter, α. Therefore, the characteristic polynomial for this matrix will also depend on α, and in turn the solution of this polynomial will also depend on α. The solution of this polynomial is in fact the eigenvalue (energy level) that we are looking for. We conclude that if the real Hamiltonian matrix elements can be analytically dilated into the complex plane, also the eigenvalues can be dilated into the complex plane. Further details are given below.

Thus, one can avoid the numerical diagonalization of a non-Hermitian *complex* matrix and replace it with Hermitian electronic-structure calculations that yield *real* eigenvalues, which can be dilated into to complex plane. Similarly, one can carry out dilation into the complex plane and obtain complex properties other than the energy, such as complex dipole transitions and other properties that are calculated as expectation values. This is because the eigenvectors can be expressed as a linear combination of the HMEs, therefore we claim that they also depend on α, and can be analytically dilated into the complex plane. Thus, one can avoid the numerical calculations of the eigenvectors of the non-Hermitian complex matrix, and obtain complex energies and expectation values by analytical continuation.

Unfortunately, closed form expressions of the eigenvalues and eigenvectors as function of the HMEs are known only for small Hamiltonian matrices, i.e., less than 5 × 5. Namely, such closed form expressions are known only for Hamiltonian matrices constructed from two, three or four basis functions. Nevertheless, we can use the Padé approximant in order to get closed form expressions for the eigenvalues and expectation values for relatively large matrices, which are typically used in electronic structure calculations. However, before going into the procedure for large and finite analytical expressions (that are required for actual chemical problems) we want to establish the proof for the small dimensional matrices.

Let us show it for the simple 2 × 2 Hamiltonian matrix. The HMEs are function of a real scaling parameter η, where we chose $\eta = \alpha e^{i\theta}$ with $\theta = 0$. The eigenvalues are given by

$$E_{\pm}(\eta) = \frac{H_{11}(\eta) + H_{22}(\eta)}{2} \pm \frac{1}{2}\sqrt{\left(H_{11}(\eta) + H_{22}(\eta)\right)^2 + 4H_{12}(\eta)H_{21}(\eta)}.$$

It is clear that if the HMEs are known analytical functions of η, one can dilate them into the complex plane by substituting complex values for $\eta \rightarrow \alpha e^{i\theta}$ with $\theta \neq 0$. Then, analytically calculate the stationary points in the complex plane (to satisfy the complex variational principle as described in Ref. [1]). The stationary points are associated with the resonance complex eigenvalues, where $\mathrm{Re}[E_{\pm}]$ are the energy positions and $-2\mathrm{Im}[E_{\pm}] = \Gamma$ are the widths. Similarly, the real dipole transitions can be expressed as function of a real scaling parameter,

$$D_{+,-}(\eta) = \left[\Psi_{+}^{\dagger}(\eta)\right]^{T} d(\eta)\left[\Psi_{-}(\eta)\right].$$

For the 2 × 2 real Hamiltonian matrix case the vectors $[\Psi_{\pm}(\eta)]$ are analytically obtained as function of the real HMEs. The components of the eigenvectors $\begin{pmatrix} [\psi_{\pm}(\eta)]_1 \\ [\psi_{\pm}(\eta)]_2 \end{pmatrix}$ are given as usual by,

$$[\psi\pm(\eta)]_1 = \frac{H_{12}(\eta)}{E_{\pm} - H_{11}(\eta)}[\psi\pm(\eta)]_2$$

where

$$[\psi\pm(\eta)]_1^2 + [\psi\pm(\eta)]_2^2 = 1.$$

Thus the complex dipole transitions can be associated with stationary solutions in the complex plane obtained by analytic dilation of $D_{+,-}(\eta)$ into the complex plane.

Similar expressions can be derived for the 3 × 3 and 4 × 4 cases. However, for larger matrices we shell use the Padé approximant in order to get closed form expressions for the eigenvalues and dipole transitions as a function of (a real) η. And then, carry out the analytical continuation into the complex plane and look for stationary solutions, which are associated with the resonance positions and widths or the complex dipole transitions, as detailed in **Section 2** and **Section 3**.

1.5 Resonance *via* Padé for a Large and Finite Sized Hamiltonian Matrix

In the above section we saw that *complex* resonance eigenvalues and dipole transitions can be obtained by analytical continuation from *real* eigenvalues and dipole transitions, which are obtained from standard (Hermitian and real) calculations. However, this analysis is limited to small number of basis functions (<5) for which we have closed form analytical expressions. The extension of this approach to large matrices, i.e., to large number of basis functions, requires the use of a numerical scheme to describe either $\{E_j(\eta)\}_{j=1,2,..,N}$ or $\{D_{j,j'}(\eta)\}_{j,j'=1,2,..,N}$ by a closed form analytical expression. One such scheme is based on the Padé approximant, in which the energy and dipoles are expressed as a rational fraction of polynomials,

$$E_j(\eta) \approx \frac{\sum_{p=0}^{N_p} a_{j,p}\eta^p}{\sum_{q=0}^{N_q} b_{j,q}\eta^q} \tag{13}$$

and,

$$D_{j,j'}(\eta) \approx \frac{\sum_{p=0}^{M_p} c_{j,j',p}\eta^p}{\sum_{q=0}^{M_q} d_{j,j',q}\eta^q}. \tag{14}$$

The main question is from where do we get the data from which we will fit the coefficients in the above expression. The answer to this question is that we take it from *stabilization graphs*, see **Section 2.1** for more details.

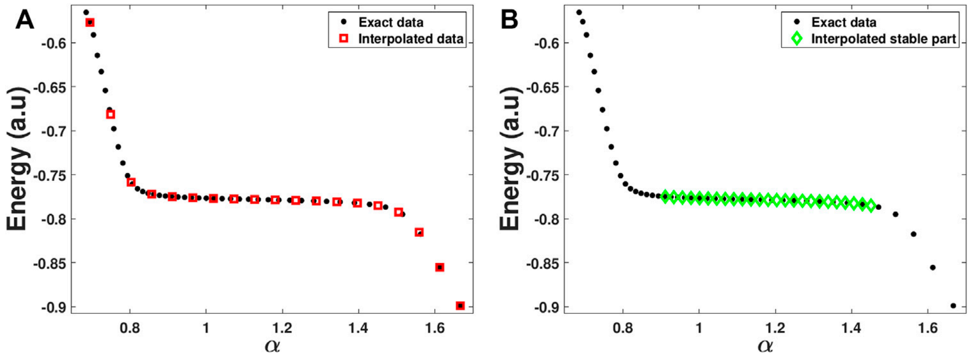

FIGURE 3 | The stabilization graph of the He**(2s^2) resonance state, where the real energy level is plotted as a function of a real parameter (α) that controls the diffuseness of the Gaussian basis functions. The plot illustrates the different steps within the automated RVP algorithm. **(A)** Calculated (black circles) and interpolated (red squares) data points. **(B)** The interpolated stable region produced by step 1 of the automated RVP algorithm (green diamonds) that serves as input for the Padé/Schlessinger point method.

Other questions we need to answer are:

(Q1) How to select the initial real data points from the stabilization graphs?
(Q2) How to select the N_p, N_q or M_p, M_q parameters of the polynomials?
(Q3) How to optimize the real approximated polynomial expansions, i.e., the $a_{j,p}$, $b_{j,q}$ or $c_{j,j',p}$, $d_{j,j',q}$ coefficients, to the ab-initio stabilization calculations?
(Q4) How to locate the stationary solutions in the complex plane, which are associated with the resonance positions and widths or with the complex transition dipoles?

These questions are answered in **Section 2** (specifically **Section 2.2**), which discusses the RVP formalism in details.

2 THE RESONANCE *VIA* PADÉ METHOD—RESONANCE *VIA* PADÉ IN PRACTICE FOR LARGE HAMILTONIAN MATRICES

2.1 Real Stabilization Graphs

As mentioned above, our new approach to introduce non-Hermiticity and obtain resonances is by analytic dilation of eigenvalues from the stable part of a stabilization graph into the complex plane. Since we use the Padé approximant as our analytical continuation method, we call our new approach Resonance *Via* Padé, RVP. This approach, unlike uniform complex scaling, uses standard, Hermitian, calculations to obtain the resonance position and width, and does not modify the Hamiltonian.

In the RVP method, as a first step, the energy spectrum is calculated using Hermitian codes as a function of a generalized box quantization parameter, $E(\alpha)$ where $\alpha = \eta$ (with $\theta = 0$ and $\eta = \alpha e^{i\theta}$). For example, the eigenvalues can be calculated as a function of the number of basis functions (BFs) [45] or when finite given BFs are scaled by a real factor [47, 48, 51]. In practice, to scale the BFs by a real factor, one can use Gaussian base functions and divide the exponents of the Gaussians by the real factor α (see **Eq. 11**). Calculating the energy spectrum with these BFs will produce $E(\alpha)$. Note that in this case, $\alpha < 1$ will cause the spatial distribution of the Gaussians to compress, and $\alpha > 1$ will cause it to expand. Therefore, we typically employ the range: $0.6 < \alpha < 2.0$.

In such calculations, when continuously increasing α, the discrete energy levels of the quasi-continuum spectra are highly affected (i.e., lowered). Resonance states, unlike the delocalized quasi-continuum states are much less affected by small variations of α [1, 52], since resonance states are typically much more localized in the interaction region, see Figures 3.5 and 3.6 in Ref. [1]. Therefore, while quasi-continuum states significantly change as α is varied, resonance states remain relatively stable. This is why a graph portraying $E(\alpha)$ as function of α around the resonance energy is named a stabilization graph, as illustrated in **Figure 3A**.

In such a graph, an energy level crossing is expected between the highly affected delocalized quasi-continuum states and the stable resonance energy. However, since states with the same symmetry cannot cross each other in the adiabatic representation, avoided crossings are obtained in the graph. In these avoided crossings, a transition from a localized state to a delocalized quasi-continuum state occurs. Therefore, the avoided crossings are associated with branch points (BPs) in the complex energy plane (see chapter 9 in Ref. [1]). Consequently, $E(\alpha)$ is not an analytic function of α.

Nevertheless, while the avoided crossings correspond to a mixing between two functions: a localized function and a delocalized quasi-continuum function, the stable part of the stabilization graph, in between two avoided crossings, corresponds to a single function, localized in the interaction region. Therefore, the stable part of the stabilization is expected to be locally analytic, while the avoided crossings are expected to be non-analytic. Thus, the stable regions contain all the relevant information for analytical continuation into the complex plane. A numerical proof for this point is given in Refs. [52, 53] and the figures within.

This is how the RVP approach avoids the non-analytic parts in the stabilization graph. In this approach, a single energy level, obtained from the stable part of the stabilization graph, is analytically dilated using the Padé approximant. Namely, the stable part of the stabilization graph, which has a smaller slope than the unbound energies [46], is fitted as a function of a real scaling parameter to a ratio between two polynomials (like **Eq. 13**):

$$E(\alpha) = \frac{P(\alpha)}{Q(\alpha)}. \tag{15}$$

where $P(\alpha)$ and $Q(\alpha)$ are polynomial functions of a real scaling parameter, α. As the focus of the analytic continuation scheme is not on the avoided crossing regions, but rather on the stable part of the stabilization graph, excellent results are obtained [50, 53].

2.2 Resonances by Analytical Continuation of the Padé-Schlessinger Method Into the Complex Energy Plane

As previously explained, the stable part of the stabilization graph is expected to be locally analytic. Yet this is not all, this stable region is also known to contain information on the resonance lifetime. It has already been shown by Hazi and Taylor. [46], that the slope of the stable region is related to the width of the resonance. That is, as the resonance width increases the slope of the stable part increases. Furthermore, as shown in Section 3.4 in Ref. [1] (and Figures 3.4–3.8 wherein), one can even estimate the resonance width by analysing the localized function that is associated with the stable region's eigenvalues. In this case, the width is proportional to the square of the ratio between the normalized amplitude of the function out of the interacting region and in the interaction region. So, the stable region in a stabilization graph contains enough information on the resonance lifetime and all the relevant information for analytic dilation into the complex plane.

Therefore, it is clear why this region should be used if one wants to carry analytical continuation to the complex plane and gain insight on the resonance lifetime. In other words, the answer to Q1 in **Section 1.5** is clear - the initial real data points from the stabilization graphs one needs to use is the data from the stable part of the stabilization graph.

Indeed, as a second step in the RVP method, data from the stable region is analytically dilated into the complex plane using the Padé approximant (**Eq. 15**) in order to locate stationary points (SPs), resonances. In Ref. [53], an analytical path from the stable region towards a complex stationary point is shown. This path goes between the BPs and bypass them. This is an additional proof that using Padé, one can always remain on an analytic path in the complex plane that goes towards a stationary point. Notice that the existence of such a path results from the use of a finite basis set, which are always used in any electronic-structure calculation [53].

In practice, within the RVP method, an analytic Padé function is fitted using the Schlessinger point method [54] to data from the stable region. The Schlessinger point method requires a set of M data points (α_i) and their corresponding eigenvalues (E_i), and then the Schlessinger truncated continued fraction assumes the following form:

$$C_M(\alpha) = \cfrac{E(\eta_1)}{1 + \cfrac{z_1(\alpha-\alpha_1)}{1+\cfrac{z_2(\alpha-\alpha_2)}{\vdots\, z_{M-1}(\alpha-\alpha_{M-1})}}}, \tag{16}$$

where the z_i coefficients need to be determined recursively such that

$$C_M(\alpha_i) = E(\alpha_i), \quad i = 1, 2, \ldots, M. \tag{17}$$

This truncated continued fraction can be transformed to a Padé like form (**Eq. 15**). Thus, by choosing to use the Schlessinger point method for the Padé approximant, one obtains automatically from the data points, all the information on the Padé function, namely the answers to Q2 and Q3 in **Section 1.5** above. Q2 deals with the degree of the polynomials in the Padé function, and Q3 deals with their coefficients. Clearly, both are determined by the data set itself satisfying **Eq. 17**.

Once the z_i coefficients are determined, and **Eq. 16** is completed, an analytic continuation into the complex plane is performed. This is done by substituting a complex η, instead of α, i.e. $\eta = \alpha e^{i\theta}$ with $\theta \neq 0$. Then, SPs, resonances, can be identified by generating α- and θ-trajectories and looking for cusps in the complex plane [52, 55]. Alternatively, SPs can be identified by solving the algebraic equation $\frac{dE}{d\eta} = 0$ [52]. While solving an algebraic equation is easier than looking for cusps in the complex plane, the SPs found by solving the algebraic equation are not necessarily associated with resonances [52]. This means that if we solve the algebraic equation some SPs are unphysical. Therefore, to identify the resonance energy and lifetime, we use a clusterization technique described in Ref. [50] as the final step of the RVP method. In practice, we generate **Eq. 16** for different input sets, where all sets are taken from the stable region. This way we get a large number of SPs by solving the algebraic equation for each set. The SPs depend on the input points chosen for the analytical dilation, where as mentioned, some SPs are also unphysical. The physical SPs should not depend strongly on the variation of the input data, unlike the unphysical ones. Therefore, we examined the SPs by statistical distribution and look for clusters of SPs obtained from different input data. The mean value of the cluster is reported as the resonance complex energy. In this way, we finally answer Q4 in **Section 1.5** above: We understand that we locate the stationary solution in the complex plane, by solving the algebraic equation $\frac{dE}{d\eta} = 0$ for many input sets, and by using a statistical clusterization technique.

To sum up, by using the RVP method, analytic continuation of a single eigenvalue level into the complex plane can be employed, provided that the input data is taken from the stable region of a stabilization graph since it is a local analytic region. Therefore, we can divide the RVP method to three steps. In the first step the stable region data is fitted into a Padé/Schlessinger function and dilated into the complex plane. An analytic path from the stable region to the complex SPs, which avoids any of the BPs, exist when a finite basis set is employed. In the second step, the SPs are located using the algebraic equation $\frac{dE}{d\eta} = 0$, for different input data sets. Then, as a final step, the clusterization technique locates the physical complex resonance values out of the total SPs.

3 AUTOMATIC CALCULATIONS OF RESONANCES BY THE RESONANCE *VIA* PADÉ METHOD: THE "PUSH OF A BUTTON APPROACH"

Based on all the knowledge we have reviewed in this body of work, and all the knowledge we have accumulated throughout the years on the RVP method, recently we were able to take the next step in implementing the RVP method, and produced an automated RVP package (https://pypi.org/project/automatic-rvp/). This package, given a stabilization graph from other Hermitian computations, is able, in the click of a button, of automatically calculating the resonance energy and width and presenting it with the relevant statistical data. Doing so, the package goes through three steps:

1. Recognizing the analytical part of the stabilization graph.
2. Constructing RVP approximation for different inputs.
3. Running statistics.

In the first step, the package is given a stabilization graph produced by other Hermitian computations, and its goal is to recognize the analytical, stable, part of the graph. Practically, the package gets as input the α values as the x variables, and the real energy values (E) as the y variables, $f(x)$, (black circles in **Figure 3A**).

At first, the package interpolates the data between min(α) to max(α) through the makima interpolation [56–58], and estimates the y values of equally distributed x values. The number of these x values is **40%** of the initial α values, and they are ranging from min(α) to max(α). In this point, we have two sets of data: the initial set of α and E values (black circles in **Figure 3A**), and the interpolated set of x and y values (red squares in **Figure 3A**). The interpolated set aim is to portray the structure of the function $f(x)$ in a general form, without any focus on small deviation in the original data.

Next, the package identifies the stable region of the stabilization graph. It does so by looking for two consecutive data points in the interpolated set, which have the smallest numerical slope between them. Afterwards, the slope between this couple and all the other data points in the interpolated set is calculated. Then the package looks for all the data points in the interpolated set that are adjacent to the couple and have a slope value between **70%** and **130%** of the original slope found. If the number of points that meet this criterion is more than or equal to **10**, the package proceed to the next stage and sets the range between the min(x) found and the max(x) found as the x range corresponding to the analytical, stable, part of the stabilization graph. If the number of points is less than **10**, the package looks for two other consecutive data points in the interpolated set, which have the second smallest numerical slope between them, and so on.

In the next stage, the package checks the number of α values it has in the x range it found. If the number is smaller than **25**, the package produces an error message. If not, the package estimates through the makima interpolation, the y values of equally distributed 25 x values in the range it found. These 25 x points and their y values are considered as the analytical, stable, part of the stabilization graph (see the green diamonds in **Figure 3B**). The aim of this stage is to avoid overfitting of data, therefore the data is interpolated over the range of x found in the previous stage.

In step 2 of the package, the data is divided into all possible subset containing between **8** and **25** consecutive data points. Each subset is fitted to a Padé approximant, which is stored as a symbolic function [59]. This symbolic function is later derived to find the SPs. Convergence of the SPs is checked with respect to the number of input points (M from **Eq. 16** and **17**), and the difference between $C_M(\eta)$ and $C_{M-1}(\eta)$ is reported as the error of the SP [53]. At the end of this step, all of the SPs, with their α, θ and error values, are collected.

In step 3 of the package, the collected SPs are first screened: SPs with more than 25% error in their imaginary energy part are thrown out. The number of SPs left is termed n. Later, the collection of SPs is normalized in the real and imaginary energy axes. This stage aims to an equal distribution of SPs for every problem, so the next stage in the package can be problem-independent.

In the next stage, the packages looks for clusters according to the DBSCAN algorithm [60]. This algorithm requires two parameters: ϵ which is the maximal distance between 2 core points of the cluster, and *minPT* which is the minimum number of points required to form a cluster. In our case, *minPT* is the minimum between 100 and 8% of n, and ϵ is varied in iterations between 0.001 and 5 in leaps of 0.001.

In every iteration, the clusters are screened, and all of the physical clusters are evaluated and graded between 1 and 3, based on their size and standard deviation. The higher the grade is, the better the cluster is: We are looking for a cluster as big as possible, with the smallest standard deviation possible. All the clusters, together with their grades are stored. In the next iteration, ϵ is raised, and the newly found physical clusters are graded. This time, the clusters are compared to the stored clusters. Any cluster that was upgraded, is deleted from the storage and is saved with the new data and grade. Any new clusters with a grade of 1 or 2 is also stored. All the other clusters are thrown away, and then ϵ is raised again in iterations, until it reaches a value of 5.

At the end of this stage, the package reports all the stored clusters with a grade 3 or 2. In addition to the cluster mean real energy and mean imaginary energy, the package presents the following statistical data: the cluster grade, the real energy standard deviation, the imaginary energy standard deviation, the imaginary energy coefficient of variance, the mean α value, the α standard deviation, the mean θ value, the θ standard deviation, the ϵ in which the cluster was found, the size of the cluster and the size of the cluster in percentage relative to n.

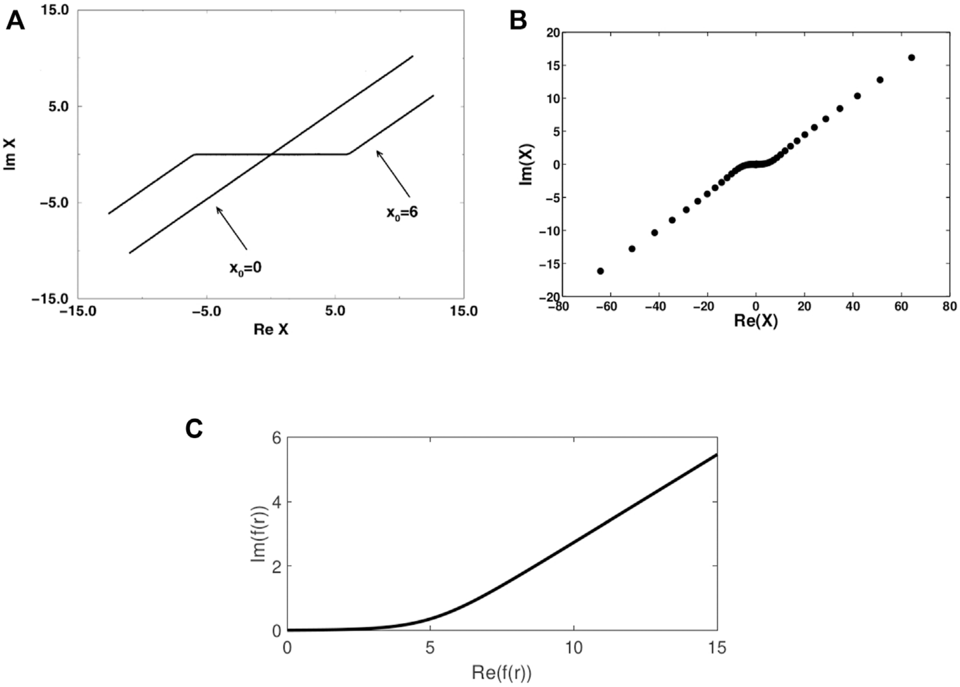

FIGURE 4 | (A) A schematic representation of a uniform ($x_0 = 0$) and exterior ($x_0 = 6$) complex contours of integration for calculating the non-Hermitian Hamiltonian matrix elements (Reprinted from Ref. [2], Copyright (1998), with permission from Elsevier). **(B)** and **(C)** presents smooth exterior complex contours from numerical calculations using **(B)** CBF (Reprinted (adapted) with permission Ref. [62]. Copyright (2016) American Chemical Society) and **(C)** RVP (Reprinted (adapted) with permission Ref. [63]. Copyright (2021) American Chemical Society), as described in the text.

Of course, all of these steps are transparent to the end user, and given the stabilization graph, one gets, at the push of a button, a list of clusters containing the resonance mean energy and width and the above statistical data. Additionally, the user is also presented with the stabilization graph, on which the chosen stable part is marked. Yet, it is important to note that the package is also modular, and the user can change every parameter marked in bold in the above description. Furthermore, the user can choose, if desired, to run all the steps together or to run only some step individually.

4 THE EQUIVALENCE BETWEEN RESONANCE *VIA* PADÉ AND OTHER NON-HERMITIAN METHODS IN CHEMISTRY

RVP belongs to the group of methods that operate within the non-Hermitian (NH) quantum mechanics (QM) formalism [6, 25–40]. Other NH methods that are considered herein are: complex scaling, complex basis function and reflection-free complex absorbing potential. The equivalence between the different methods is illustrated below by comparing the complex electronic coordinate, which are obtained by RVP and by the other NH methods. Notice that these complex electronic coordinate remain real inside the interaction region as discussed in **Section 1.3** above.

The most straightforward approach for studying resonances is complex scaling (CS) [1, 2]. In this approach the coordinates are rotated into the complex plane, i.e., the method is associated with a contour of integration that is rotated into the complex plane. The scaling can be uniform or partial. Uniform scaling is associated with a uniform complex contour (UCC), in which $\vec{r} \to \vec{r_\eta} = \eta\vec{r}$ for any value of $|\vec{r}|$, where $\vec{r}$ is the electron coordinate vector and $\eta = \alpha e^{i\theta}$ is the complex scaling parameter (θ and α are the rotation and stretching real parameters). Partial scaling is associated with a smooth exterior complex contour (SECC). In contrary to atomic calculations, for which it is suitable to use a UCC, in molecular calculations, the contour of integration should take into account the singularity in the Born-Oppenheimer Hamiltonian. A SECC avoids the singularity points in the Coulombic potential terms of the molecular Hamiltonian (see discussion in **Section 1.3**). In addition, using a SECC reduces the number of basis functions (BFs) required for describing the interaction region [26, 51]. The imaginary part of the SECC is as close as one wishes to zero in the interaction region and beyond some critical point in the coordinate space $\vec{r} \to \eta\vec{r}$. The SECC smoothly detaches from the real axis into the complex plane around $|\vec{r}| = r_0$; see for example Ref. [61] for an explicit expression. The SECC is the analytical (smooth) form of the *exterior complex contour of integration*. This contour can be represented in spherical coordinated as $\vec{r_\eta} = \vec{r}$ for $|\vec{r}| < r_0$ and $\vec{r_\eta} = \frac{\vec{r}}{|\vec{r}|}[r_0 + \eta(|\vec{r}| - r_0)]$ for $|\vec{r}| > r_0$ (regardless of the symmetrical properties of the molecular potential, as long as r_0

is sufficiently large). **Figure 4A** presents such a (one-dimension $r \rightarrow x$) complex contours of integration for the uniform ($x_0 = 0$) and exterior ($x_0 = 6$) cases.

Another approach for studying resonances is to augment the physical Hamiltonian with a complex absorbing potential (CAP) in order to guarantee that the asymptotes of the resonance eigenfunctions decay to zero. However, the CAP must be a reflection-free CAP (RF-CAP) in order to perfectly absorb and avoid generation of reflections, which temper with the description of the resonance wavefunction in the interior region [61]. If the CAP is not a RF-CAP one should remove the artificial effect of the CAP on the solutions of the time-independent Schrödeinger equation. Note that it is challenging to remove this effect within the framework of finite basis set calculations, however, schemes for such a removal can be found in Refs. [6, 64, 65]. The RF-CAP, on the contrary, is a perfectly absorbing potential, which avoids the reflection problem by definition. Importantly, the absorbing potential introduced within the RF-CAP method, is *derived* from a complex contour of integration, specifically, using a SECC. Therefore, the equivalence between CS and RF-CAP emerges directly from the construction of the absorbing potential [61].

Alternatively, it is possible to use complex basis functions (CBFs), i.e., complex Gaussian functions [25, 26, 38, 39]. Within the CBF approach one can carry out analytical continuation of the Hamiltonian matrix elements (as discussed in **Section 1.4**), in which the Gaussian exponential parameters are scaled by $e^{-2i\theta}$ (and fixing the stretching parameter $\alpha = 1$). CBF can be used uniformly, if all the Gaussian basis functions are scaled by the complex factor, or partially, if only the diffuse basis functions are scaled. Importantly, the CBF method is also associated with a complex contour of integration [62, 63]. Such a complex CBF contour can be obtained by diagonalizing the matrix of the one-particle coordinate operator $\vec{x}$ that is represented by the employed basis set in the electronic-structure calculations (whose matrix elements were continued into the complex plane). It was shown that there is a correlation between uniform CBF and UCC and between partial CBF and SECC [62, 63], **Figure 4B** presents a partial CBF contour of integration (i.e., a SECC). It is calculated using an even-tempered Gaussian basis set, where the diffused functions are analytically dilated into the complex plane. The even-tempered Gaussians basis set is given as, $\{x^n e^{-\zeta_k x^2}\}_{n=0,1,\ k=0,1,\ldots,k_{max}}$ with $\zeta_k = \zeta_0 \epsilon_0^{k-1}$ meaning, $\zeta_0 > \zeta_1 > \zeta_2 \ldots$. And for $\zeta_k < \zeta_{th}$, $\zeta_k \rightarrow \zeta_k e^{-2i\theta}$, where ζ_{th} is a threshold parameter. Diagonalizing the $\vec{x}$ matrix yields the eigenvalues of the coordinate operator, $\{x_k\}_{k=1,2,..}$, which represent the grid points that corresponds to the complex contour of integration. The CBF complex coordinate contour in **Figure 4B** is obtained using $\zeta_{th} = 0.1$, $k_{\max} = 41$, $\zeta_0 = 1000$ $\epsilon_0 = 1.4125$ and $\theta = 0.25$. Moreover, **Eqs 10**, **12** demonstrate a mathematical equivalence between the uniform-CBF and uniform-CS methods for one-center Gaussian functions.

RVP is conceptually equivalent to CBF, however here the basis functions are scaled by a real parameter $\eta = \alpha e^{i\theta}$ with $\theta = 0$. Again, the scaling can be done uniformly, such that all the basis functions are scaled, or partially, in which only the diffuse basis functions are scaled. Calculating the RVP complex contour is done in two steps. First, the contour is obtained in a similar fashion to CBF, but here the contour lay on the real axis. Next, by dilating it into the complex plane we obtain the complex RVP contour. We do it in a similar manner to the analytical continuation employed in RVP for the energies (see details in **Section 2.2**), but unlike the energy case here we substitute into the fitted Padé function the scaling parameters that yield the resonance energy, i.e., $\eta_{res} = \alpha_{res} e^{i\theta_{res}}$. In Ref. [63] it was shown that partial scaling within RVP is associated with a SECC, whereas uniform scaling is associated with a UCC. **Figure 4C** presents a partial scaling RVP radial contour of integration (i.e., a SECC). This contour is associated with the electronic $1s^2 2p3s\,^1P$ resonance state of beryllium. The cutoff parameter used for the partial scaling of the employed 14s14p5d basis set is $\alpha_{th} = 0.15$. The $\alpha_{res} = 0.873$ and $\theta_{res} = 0.579$ values that corresponds to the resonance energy, are also used in generating the contours.

The ability to associate a complex coordinate contours for CS, RF-CAP, CBF and RVP suggests similarities between these NHQM methods. The rationale behind this is that all these NHQM methods introduce, indirectly, outgoing boundary conditions to the many-electron problem, which manifests in a complex contour of integration.

5 RESONANCE *VIA* PADÉ: CALCULATIONS OF RESONANCE POSITIONS, WIDTHS AND COMPLEX DIPOLE TRANSITIONS FROM STANDARD-HERMITIAN QUANTUM CHEMISTRY PACKAGES

Below we present several illustrative applications of RVP for atomic and molecular systems. Atomic helium, the triplet Van-der Walls ^{3}He*–H$_2$ supermolecule, and the RNA base uracil anion. Helium was chosen as a benchmark due to the availability of extremely accurate reference complex energies and transition dipoles. ^{3}He*–H$_2$ was chosen since it illustrates the remarkable agreement of the theoretical RVP calculations with the cold-collision experimental results. Moreover, while the excited helium is in the ^{3}S state (in the He(^{3}S,1s2s) + H$_2$ collision) the agreement between the calculated and measured reaction rates where not so sensitive to the accuracy of the calculated resonance width. However, for the He(^{3}P,1s2p) + H$_2$ case the agreement between theory and experiment were obtained only for accurate calculations of the width. The agreement between the quantum RVP calculations and the cold-chemistry measurements illustrates the capabilities of our method. The uracil anion example illustrates the ability of RVP in carrying out NHQM ab-initio calculations for many-electron many-atom molecules with biological interest.

5.1 Benchmarking of the Resonance *via* Padé Approach for Complex Energies as Well as for Complex Dipole Transitions

5.1.1 Complex Energies–Positions and Widths

In previous studies RVP was benchmark by examining several small-to medium-size chemical systems for which there exist

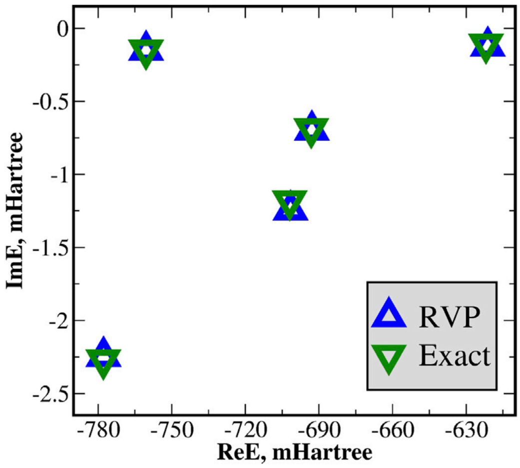

FIGURE 5 | The RVP complex energies (Re*E*+*i*Im*E*) of the doubly excited Feshbach He** states contrasted with the exact values, in mHartree. These energies are also presented in **Table 1**. The RVP energies are in remarkable agreement with the exact ones. Reprinted (adapted) with permission Ref. [50]. Copyright (2019) American Chemical Society.

TABLE 1 | Multiple complex energies of the doubly-excited He** Feshbach states; RVP vs. exact values. These values are also represented graphically in **Figure 5**. Reprinted (adapted) with permission Ref. [50]. Copyright (2019) American Chemical Society.

State	ReE, mHartree		ImE, mHartree	
	RVP	Exact	RVP	Exact
$^12s^2$	−777.7858	−777.8676^a	−2.246	−2.271^a
^32s2p	−760.4625	−760.4906^b	−0.151	−0.1495^b
$^12p^2$	−701.5648	−701.946^c	−1.244	−1.181^c
^12s2p	−692.8821	−693.1349^d	−0.698	−0.687^d
$^12p^2$	−621.1877	−621.9273^a	−0.120	−0.108^a

[a] *Ref. [70].*
[b] *Ref. [72].*
[c] *Ref. [69].*
[d] *Ref. [71].*

reliable and accurate experimental data or theoretical values. These systems include the doubly-excited Feshbach states of: helium (multiple states) [50, 53], H^- ($2s^2$) [53], beryllium ($1s^22p3s^1P$) [63] and H_2 ($^1\Sigma_g^+(1\sigma_u^2)$ at 1.4 and 2.0 Bohr) [50]. In addition the shape-type $^2\Pi$ resonance state of N_2^- at the equilibrium distance of the neutral system, R_{NN} = 1.0975 Å [50]. And the energy positions and decay rates of the three lowest π^* shape-type resonances of the uracil anion [66]. Finally, the reaction rates of the [He(^{3}S,1s2s) + H_2] and [He(^{3}P,1s2p) + H_2] collisions [67, 68]. Comparison of these RVP calculated results to available values from literature was successful. Some of these benchmarking are presented below.

One of the best system for studying autoionization is the doubly-excited He** atom (**Eq. 2**) since exact calculations (i.e., converged non-relativistic energies) are available [69–72]. In addition, very accurate complex transition dipole values that can be used as a reference have been reported [73]. Helium is a two electron system, hence it is possible to calculate its resonance positions and widths using full configuration interaction (FCI) and complex scaling (CS) with a very large and highly optimized one-electron basis set (ExTG5G), these CS/FCI/ExTG5G [36, 73] energies are in perfect agreement with the exact ones [69–72]. From the electronic structure point of view FCI involve no approximation, therefore comparing our FCI/RVP with the reference FCI/CS allows for a pure comparison between the two non-Hermitian methodologies. Furthermore, there are several doubly-excited He** resonance states, which allows examining

TABLE 2 | Complex transition dipoles of helium in milli-atomic units. The state labels in the first column corresponds to the labels in **Figure 6**. The reference values refer to a very accurate results obtained by complex scaling (CS) and full configuration interaction (FCI) with a very large (ExTG5G) basis set [36, 75]. The RVP transition dipoles are calculated using two type of truncated ExTG5G basis sets, where Basis-I is larger than Basis-II. Reprinted (adapted) with permission Ref. [74]. Copyright (2020) American Chemical Society.

Transition	Reference		Basis-I		Basis-II	
	Reμ	Imμ	Reμ	Imμ	Reμ	Imμ
1↔6	35.4	+12.11	34.88	+12.44	35.99	+12.99
2↔6	313.0	−3.598	313.0	−3.021	313.1	−4.136
3↔4	−123.1	−2.554	−122.8	−2.403	−125.5	−2.367
3↔5	328.8	+0.193	326.8	+0.140	321.4	+0.119
3↔7	−192.5	+0.3475	−192.4	+0.3571	−192.4	+0.2619
4↔6	1522.7	−9.73	1528.9	−10.24	1529.3	−10.79
5↔6	1705.45	−3.767	1704.42	−4.030	1693.6	−4.499
6↔7	−2161.4	−1.007	−2163.4	−1.164	−2167.5	−2.570

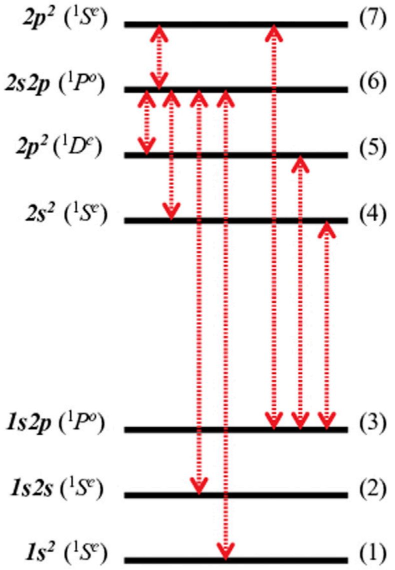

FIGURE 6 | A schematic representation of the atomic helium energy levels. The singly and doubly excited states correspond to bound and resonance states, respectively. There are three bound states (at the bottom of the figure) and four resonance states (at the top). The left-hand side shows the spectroscopic atomic term symbols, which are associated with the index lables (shown on the right-hand side). The red double arrows represent the dipole allowed transitions, these eight complex dipoles are presented in **Table 2**. Reprinted (adapted) with permission Ref. [74]. Copyright (2020) American Chemical Society.

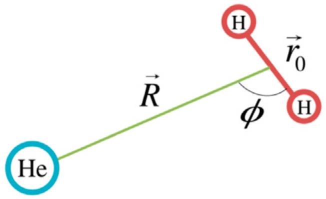

FIGURE 7 | Schematic representation of the He*–H_2 supermolecule. Reprinted (adapted) with permission Ref. [67]. Copyright (2017) American Chemical Society.

the performance of RVP in case of multiple resonances; that is, we tested the reliability of the computed energy difference between resonance states. Therefore, it is also suitable for examining the quality of the RVP transition dipoles between resonance states.

The five lowest doubly-excited resonance states of He** are calculated and compared with the exact values [69–72]. Clearly, from **Figure 5** and **Table 1** the RVP energies are in remarkable agreement with the exact ones. Notice that this agreement is further improved by increasing the size of the basis set used within the RVP calculations, as presented in Ref. [74].

5.1.2 Complex Transitions Dipole

Table 2 presents the complex dipole transitions between different electronic states of helium. The transitions shown on the left column correspond to the labeling presented in **Figure 6**. Since these dipoles involve transitions from bound or resonance states always into a resonance state they become complex in accordance with the non-Hermitian theory. The *reference* values in **Table 2** corresponds to very accurate theoretical values obtained by a CS/FCI with a very large ExTG5G basis set, see Refs. [36, 75] for details. These values can be regarded as exact since ExTG5G is highly-extended and optimised even for treating highly excited helium Rydberg states. In order to calculate the RVP transition dipoles we use two different basis sets, Basis-I and Basis-II. They are obtained by truncating the ExTG5G basis set, i.e., by omitting the most diffuse basis functions (which are essential for studying highly excited Rydberg states). Basis-I is a more extended basis set than Basis-II. Both basis sets yield good agreement with the reference CS values. For the real part of the transition dipoles, Reμ, RVP is converged since the difference between Basis-I and Basis-II is very small, nevertheless the agreement of Basis-I with the reference values is better than that of Basis-II. For the imaginary part of the transition dipoles, Imμ, Basis-I clearly works better than Basis-II. Seven out of the total eight transitions calculated with Basis-I are in better agreement with the reference values than the Basis-II results. For the eighth transition, from the 2nd to the 6th states, both Basis-I and Basis-II give the same error with respect to the reference value. Since the RVP complex transition dipoles are in agreement with the very accurate FCI/CS/ExTG5G dipoles and since the trend of the results with respect to the size of the basis set behave as expected, we conclude that the RVP approach is suitable for calculating electronic properties other than energies.

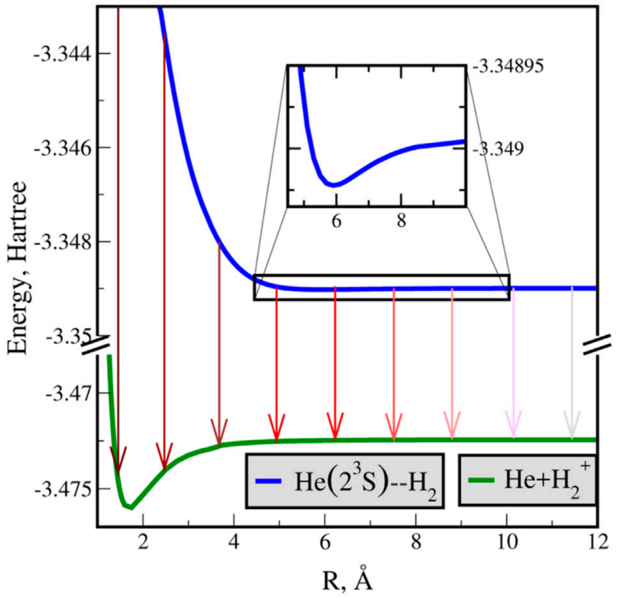

FIGURE 8 | Potential energy curves of the neutral-excited (He(^{3}S,1s2s) + H_2, in blue) and cation (He(^{1}S,1s^2) + H_2^+, in green) systems at $\phi = \pi/2$. Energies are in Hartrees and the intermolecular separation in angstroms. The excited (blue) state is approximated as bound state in the continuum, i.e., using standard Hermitian formalism. In addition, decay rates are presented schematically by red arrows (according to the RVP results presented below). The intensity of the red color reflects the decay rate from the neutral-excited state to the cation state, where stronger intensities indicate higher decay rates. Enlarging the region around 6 Å, see inset, reveals a shallow well. The experimental observation of the autoionization process is associated with this region [81]. Reprinted (adapted) with permission Ref. [67]. Copyright (2017) American Chemical Society.

5.2 Complex Potential Energy Surfaces for ^{3}*He*–*H*$_2$ Penning Ionization Reaction

The calculated RVP complex potential energy surfaces (CPESs) that are presented below play a crucial role in the interpretation and analysis of the reaction rates (RRs) measured in cold molecular collision.

5.2.1 He(^{3}S,1s2s) + H_2

Herein, we present investigation of the following molecular reaction:

$$\mathrm{He}(^3\mathrm{S},1s2s) + \mathrm{H}_2 \rightarrow [\mathrm{He}^*\text{–}\mathrm{H}_2] \rightarrow \mathrm{He}(^1\mathrm{S},1s^2) + \mathrm{H}_2^+ + e^-,$$

which allows direct comparison with the experimental results. Thus, it can be considered as an additional benchmarking of RVP. This particular Penning ionization process was studied experimentally at very low temperatures [76]. That is, experimental cold-chemistry RRs are available. RR calculations require the CPES of the He*–H_2 supermolecule, which is obtained from the RVP complex eigenvalues as a function of the geometrical configuration of this system. The sensitivity of

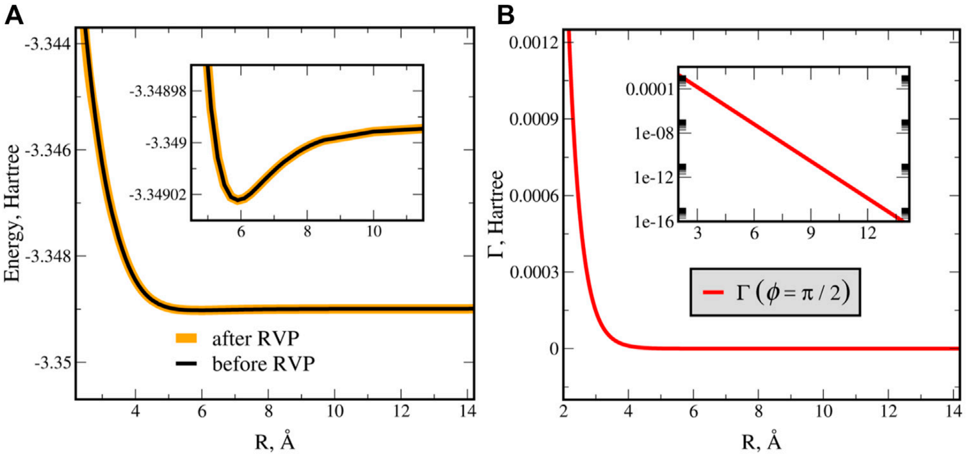

FIGURE 9 | The RVP complex potential energy surface in T-shape ($\phi = \pi/2$) geometry of He(^3S,1s2s) + H_2. The real part is presented in panel **(A)**, where the inset zooms into the shallow well. The orange curve (the real part (Re$E(R)$) of the complex RVP curve) and the black curve (the approximated Hermitian calculations) are in agreement. The imaginary part, i.e., the decay rate ($\Gamma(R) = -2\mathrm{Im}E(R)$), is presented in panel **(B)**. The decay rate fits into a single exponential curve (see inset in logarithmic scale), which confirms that this autoionization is a Penning ionization [79]. Reprinted (adapted) with permission Ref. [67]. Copyright (2017) American Chemical Society.

such a quantum process to the CPES structure poses a challenge to any state-of-the-art ab-initio calculations since autoionization becomes more pronounced as the temperature decline.

The computational details are: the real PES and the stabilization graphs are calculated with the equation-of-motion coupled cluster (EOM-CC) method with singles, doubles, and perturbative triples corrections [EOM-CCSD(dT)] [77]. The ^1S ground state of He–H_2 is the reference configuration used to calculate the target ^3S resonance state. For the basis set we use the primitive 5ZP set [78]. The hydrogen molecule is treated as a rigid rotor with a fixed distance, $r_0 = 0.74085$ Å. The distance R varied over a wide range, while the angle is restricted to $\phi = 0$ and $\phi = \pi/2$. See **Figure 7** for the definition of these parameters. Using these two angles we can expressed the CPES, $E(R, \phi)$, as a power series (in $\cos\phi$). See Ref. [67] for additional details.

Figure 8 displays the real potential curve (blue) for the He* – H_2 supermolecule at $\phi = \pi/2$ (T-shape). In addition, it shows a schematic representation of the RVP decay rates using red arrows (the actual RVP calculations are presented below), where a darker shade corresponds to a faster decay, and a lighter shade to a slower decay. The autoionization state decays into the potential energy curve of the cation ground state of the supermolecule (green). The cation surface represents the ionization threshold for this autoionization process. The area of interest, in which the autoionization was observed experimentally [76], is shown as inset in **Figure 8**. A shallow potential well is exposed, which could be overlooked on larger scale, see the black rectangle on the blue curve in **Figure 8**. The depth of the well for the T-shape and linear (not shown here) geometries is around 2.87×10^{-5} and 5.012×10^{-5} Hartree (6.3 and 11 cm^{-1}), respectively, which emphasizes the need for a highly accurate CPES.

The CPES is obtained by recalculating the RVP complex energies at each molecular configuration. That is, calculating at different distances, R at for both T-shape and linear geometries. The position [Re$E(R, \phi)$] and decay rate [$\Gamma(R, \phi) = -2\mathrm{Im}E(R, \phi)$], for the T-shape geometry of He*–H_2 are presented in **Figures 9A,B**, respectively. From **Figure 9A** it is clearly seen that the depth of the potential well remains unchanged after analytic continuation. Thus, the approximation of the resonance as bound state in the continuum is justified, however this approximation does not provide the decay rate of the resonance state. The calculated RVP decay rate, **Figure 9B**, is fitted into a single exponential curve (or linear in logarithmic scale, see inset). The Penning ionization decay rate is associated with a single exponential function [79]. Therefore, we conclude that the autoionization process under study corresponds to a Penning ionization. A similar behavior was also observed for the complex potential of the linear geometry (not shown).

Next, the *ab-initio* RVP CPES was used to compute the RRs for the above collision with ortho- and para-hydrogen molecules. The CPES is represented as a truncated interaction potential [$E(R, \phi) \rightarrow V(R, \phi)$], which is expressed as a power series (in $\cos\phi$) [67]. Then, we solve the nuclear time-independent Schrödeinger equation with $V(R, \phi)$ for the metastable and cationic product. The nuclear eigenvalues and eigenfunctions of the metastable state and product state were integrated into the scattering theory to compute the RRs. The computing of the RRs were done by using the non-Hermitian time independent scattering theory (see derivation given in Chapter 8 of Ref. [1] and references therein) within the framework of the adiabatic approximation first derived for cold molecular collisions in Ref. [80].

Figure 10 presents the RRs calculated with the RVP CPES and measured by the cold-chemistry experiment. The experimental curves is in blue and our theoretical findings in red, we observe excellent agreement for both the para-H_2 and ortho-H_2 cases. Notice that our results are within the experimental uncertainty, see Ref. [67] for details. In addition, the theoretical RRs are

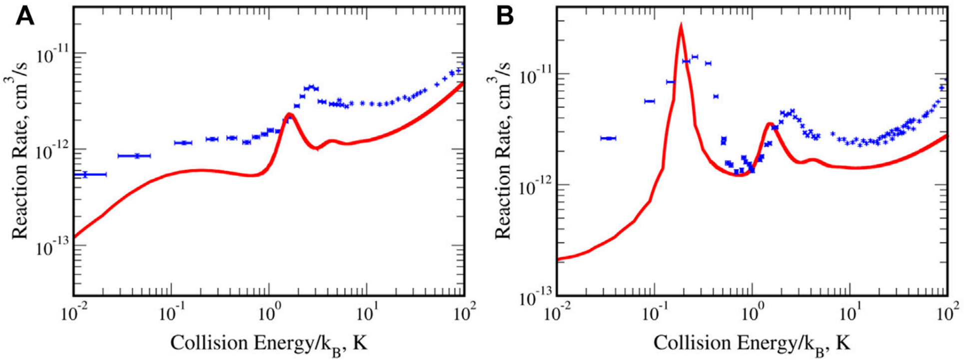

FIGURE 10 | The reaction rates for the He(^{3}S,1s2s) + H_2 collision. Panel **(A)** for H_2 in its rotational ground state (para) and **(B)** in its first excited state (ortho). The peaks are associated with nuclear resonances of the He*−H_2 supermolecule. Reprinted (adapted) with permission Ref. [67]. Copyright (2017) American Chemical Society.

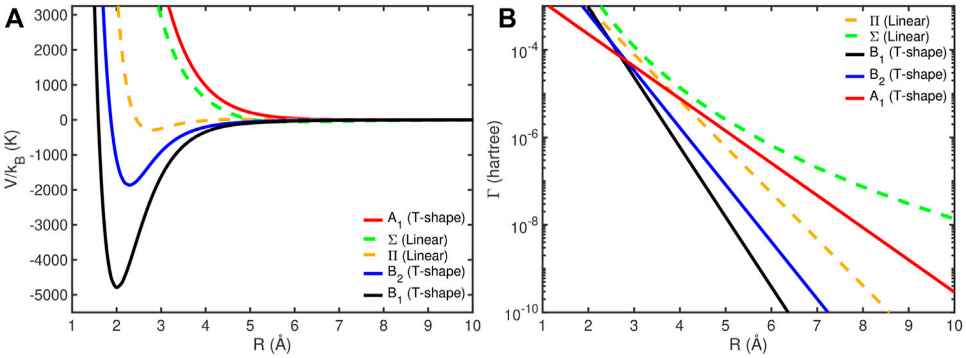

FIGURE 11 | The RVP complex potential energy surface of He(^{3}P,1s2p) + H_2 in T-shape and linear geometries. The real part (Re$E(R)$) is presented in panel **(A)**. The decay rate ($\Gamma(R) = -2\mathrm{Im}E(R)$) is presented in panel **(B)** in logarithmic scale. Reprinted (adapted) with permission Ref. [68]. Copyright (2019) American Chemical Society.

calculated in an *ab-initio* fashion without any fitting parameters, where only the Planck's constant, charges, and masses of the electrons and nuclei were used as input parameters. It demonstrate the accuracy of the calculated CPES, which allows interpretation of the observed resonance phenomena. Finally, it illustrates the universality of the RVP approach in calculating CPESs and reaction rates for any many-atom system in any decay process.

The RVP reaction rate [67], in red, is in excellent agreement with the experimental one [81], in blue. The theoretical results are computed using the RVP *ab-initio* complex potential energy surface, without using any fitting parameter. Adopted from Ref. [67].

5.2.2 He(^{3}P,1s2p) + H_2

In an additional cold chemistry experiment, structures in the measured RRs, associated with resonances, were reported in a collision between the ground-state hydrogen isotopologues (H_2/HD) with helium atoms, but now, in an excited triplet P-state [82]. That is:

$$\mathrm{He}(^3\mathrm{P},1s2p) + \mathrm{H}_2 \rightarrow [\mathrm{He}^{*}\text{–}\mathrm{H}_2] \rightarrow \mathrm{He}(^1\mathrm{S},1s^2) + \mathrm{H}_2^+ + e^-.$$

A theoretical explanation of the appearance of these structures was not given. However, in Ref. [68] we presented a quantum *ab-initio* calculation that interpreted this experiment. This emphasis the need for proper CPESs, in which the real and imaginary parts are computed at the same level of theory.

The RVP CPESs were calculated using the two of the most symmetric orientations of the supermolecule, $\phi = 0$ and $\phi = \pi/2$, i.e., with H_2 perpendicular and parallel to the collision trajectory. The computational details are similar to the ones given in the ^{3}S case. The linear configuration give rise to one Σ and one Π states since He is in a P state. Whereas, the T-shape configuration display the C_{2v} point group symmetry and give rise to three potentials with A_1, B_1, and B_2 symmetries. Therefore, *five* different potential curves are obtained. **Figure 11** present these complex potentials, where the real parts (Re$E(R)$) are presented in **Figure 11A**, showing three attractive and two repulsive curves. The imaginary part is shown in **Figure 11B**, where each decay rate curve fits into a single exponential curve (or liner in logarithmic scale). This suggests that this autoionizations are Penning ionizations [79]. B_1, which has the most attractive potential (with about 4800 K depth at 2Å) and also has the

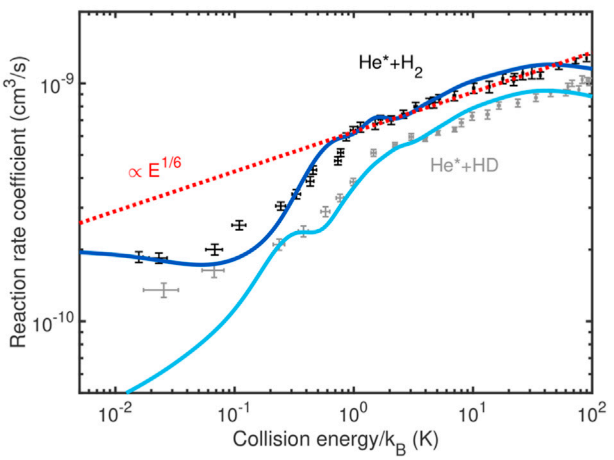

FIGURE 12 | The reaction rates for the He(^{3}P,1s2p) + H_2 collision. The theoretical reaction rate is shown in blue and the experimental one in black dots with error bars over a temperature range of 0.01 K till 100 K (For the isotopic collision we use cyan and gray for the theoretical and experimental rates, respectively.) The *ab-initio* theoretical results (based on the RVP complex surfaces) are in agreement with the experimental reaction rates also in the low temperature region (< 1 K). The red dashed line is the theoretical Langevin power law ($E^{1/6}$). The power law matches well with the reaction rate till 0.8K, below this temperature it fails and cannot explain the observed drop. Reprinted (adapted) with permission Ref. [68]. Copyright (2019) American Chemical Society.

highest decay rate (in black), is the dominated potential in the reaction rate calculations, as discussed below.

Next we identify these CPESs as the interaction potentials in the nuclear Hamiltonian $[E(R, \phi) \rightarrow V(R, \phi)]$, again, expressed as a power series (in cosϕ), see Ref. [68] for details. The RRs were calculated using the solutions of the nuclear time-independent Schrödeinger equation. The experimentally measured RRs found that the Penning ionization product weight is 90% at all collision energies [82]. Therefore, we assumed that Penning ionization dominated the whole process. The theoretical Penning-ionization RR obtained for the He(2^3P) + H_2 system is shown in **Figure 12**. Notice that H_2 is in the ground ($J = 0$) para state of the rotational levels. It is possible to recover pure para-hydrogen in a cold-collision experiment, which makes the para-H_2 an exciting molecular species to study. The figure compares the theoretical RR (in blue) with the experimental one (in black) for the temperature range of 0.01–100 K. In addition, we also report the RR for the He(2^3P) + HD(J = 0) case, it is behavior is nearly identical to the He(2^3P) + H_2(J = 0) case. Finally, the Langevin power law is shown (in red dashed line), which scales as $E^{1/6}$. The Langevin power law was calculated with a coefficient value of 122a.u. [82]. Notice that the RVP calculations do not include any external scaling or fitting parameter. Our results are in good agreement with the experimental RRs over the entire temperature range. The theoretical reaction rate reproduces the experimental structure also below 1 K. At this temperature a transition from the classical to the quantum domain occurs.

In the experimental work [82], the authors had related their theoretical reaction rate on the long range Van der-Waal's interaction, where the potential scales as $1/R^6$. Moreover, they claimed that the entire reaction rate would be controlled by the classical Langevin power law. However, based on our *ab-initio* quantum calculations, a clear transition from this "classical" regime to the quantum region is observed. Specifically, the RR of He(2^3P) + para-H_2 behaves as the power law at the asymptote for relatively high temperatures. However quantum effects become dominant below 1 K. This can be seen very clearly in **Figure 12** as a sharp drop in the RR coefficient. Above 1 K (i.e., above this drop) the classical power law can be used in order to predict the RR. But below 1 K, the classical explanation completely fails and the RR coefficients are governed by quantum laws.

Notice that the RR can be reproduce using *only* the T-shape B_1 potential but to achieve a quantitative agreement with experimental date the entire CPESs need to be considered. The asymptote ($R \rightarrow \infty$) of the collision coordinate is the entry channel of the reactants. At the asymptote all the five potential are degenerate, therefore we expect that all states will contribute. However, the B_1 state alone dominated the collision process. The B_1 potential is the most symmetric, it has the deepest well, i.e., lowest in energy, and it has the fastest decay rate, see **Figure 11**. Thus, the majority of the reactants will populate B_1 and the collision is along this particular adiabatic surface, see Ref. [68] for additional details.

5.3 Resonances of Uracil Anion

5.3.1 Complex Energies–Position and Width

Resonance (metastable) states can be generated, for example, by an absorption of slow electrons by neutral nucleobases in their ground state. It was suggested that such resonance states play a key-role in DNA or RNA damage [83]. In this section, we present an *ab-initio* investigation, using RVP, of the uracil anion. We present, for its three low lying shape-type resonance states the positions and decay rates. We also present the calculation of the complex transition dipoles between these metastable states. These electronic properties are a prerequisite for a future *ab-initio* light-matter interaction study. Notice that this is the first application of RVP to a medium-size system.

The presented results are converged with respect to the size of the one-electron basis set. Since polarized basis functions appear to be essential we consider the Dunning's basis sets. We find that it is necessary to employ the triple-ζ basis set, cc-pVTZ. However, additional diffuse functions are mandatory, by systematically adding these on top of the cc-pVTZ basis set we conclude that cc-pVTZ+2s2p2d is the optimal basis set. Where two diffuse functions with s, p and d angular momentum are added to the cc-pVTZ set of each atom, while for the hydrogens we use aug-cc-pVTZ. The stabilization graphs of the three uracil anion shape-type resonance states, at the EOM-EA-CCSD/cc-pvTZ+2s2p2d level, are presented in **Figure 13**.

Table 3 presents the converged RVP results compared with the most recent theoretical results. These studies include the Generalized Padé Approximation (GPA) approach that is also based on the stabilization technique [42, 43], and complex absorbing potential (CAP) added to the symmetry-adapted cluster-configuration interaction (SAC-CI) approach [84]. We observe the same trend for all the recent theoretical results (presented in **Table 3**). This is encouraging since earlier studies [85–88] presented a wide range of values for the positions and widths.

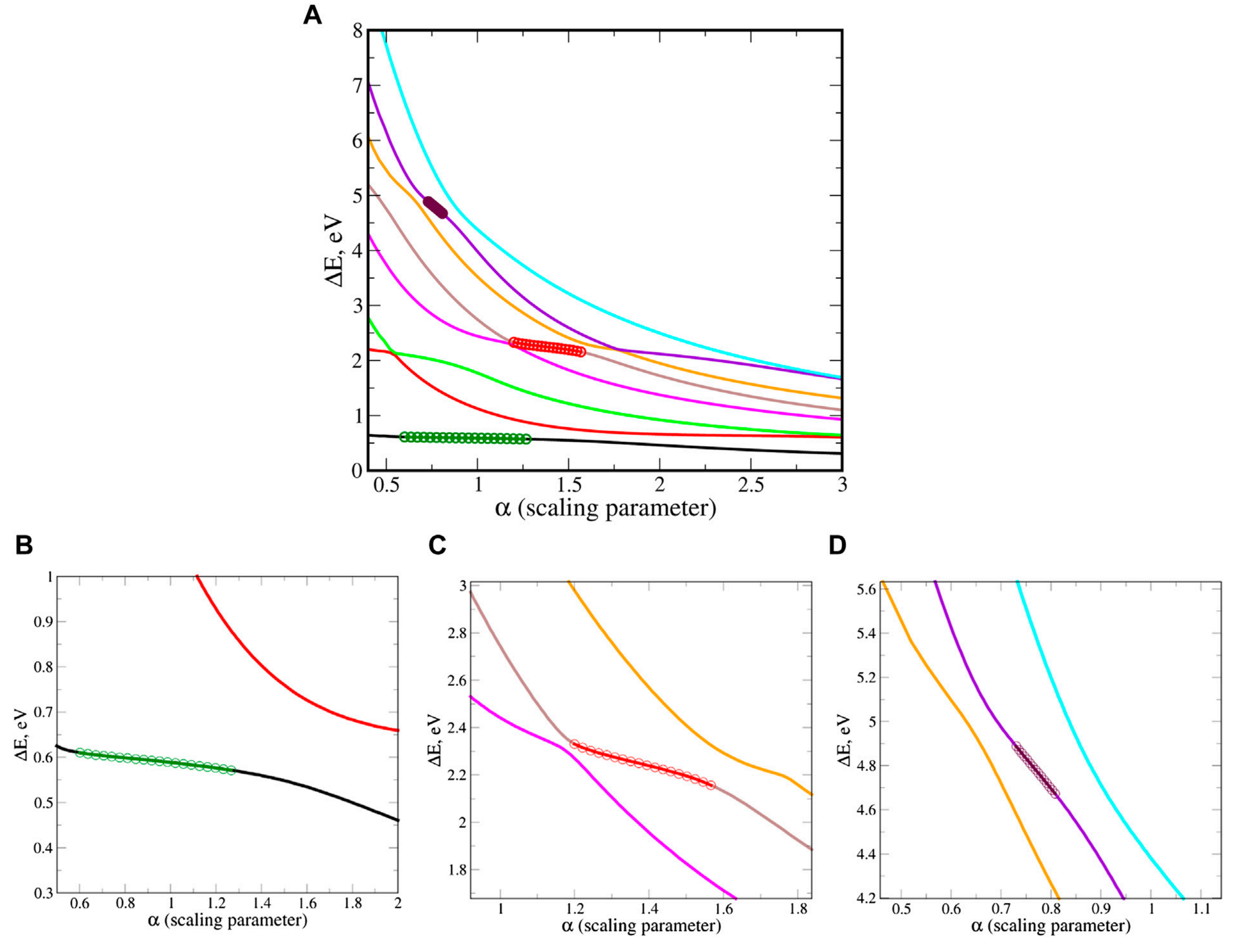

FIGURE 13 | (A) Stabilization (energy) graphs for the uracil anion. This is an EOM-EA-CCSD/cc-pVTZ+2s2p2d calculation. Circles represent the input data for the RVP method, which is taken from the stable region. **(B–D)** zoom into the stable part that corresponds to the $1\pi^*$, $2\pi^*$ and $3\pi^*$ states, respectively. Reprinted from Ref. [66], with the permission of AIP Publishing.

5.3.2 Complex Transition Dipoles Between the Uracil Anion Resonances

Complex dipole transitions between the lowest shape-type metastable states are computed using the energy-converged, cc-pVTZ+2s2p2d, basis set. The RVP procedure for calculating complex dipole transitions is illustrated in **Figure 14** for the $1\pi^* \leftrightarrow 2\pi^*$ case, i.e., between the 1st and 2nd shape-type states. The energy stabilization graph for these states is presented in **Figure 14A**. We highlight (in black) an area for which there is an overlap between the two stable regions. This overlap region in parameter space corresponds to a "macroscopic stability" in the dipole transition graph, **Figure 14B**. It is an analytic region, in which the change in the values is relatively small, in the current case less than 10% of the dipole value itself. The "macroscopic stability" idea was defined for situations in which the variational principle does not hold [92]. In such cases and, unlike the case of energy stabilization graphs, the behaviour of the continuum states that are scaled by a parameter is not well defined. In the energy stabilization graphs case, the energy of a continuum state will always decrease as α (the real scaling parameter) increases, i.e., as the space spanned by the basis set is increased. Contrary, in transition dipole calculations the dipole can either decrease or increase. Therefore, in the dipole transition case one obtains different shapes of stabilization graphs, as in **Figure 14B**, additional dipole stabilization plots can be found in the supporting information in Refs. [66, 74].

TABLE 3 | Energy positions (E_r) and widths (Γ, in parenthesis) of the lowest three shape-type resonances of uracil anion calculated using RVP and compared with other theoretical works. Adopted from Ref. [66].

	$E_r(\Gamma)$, eV		
	$1\pi^a$	**$2\pi^a$**	**$3\pi^a$**
RVP[b]	0.597 (0.014)	2.183 (0.140)	4.858 (0.657)
GPA[a]	0.61 (0.02)	2.28 (0.07)	4.98 (0.34)
CAP[c]	0.57 (0.05)	2.21 (0.10)	4.82 (0.58)

this work, EOM-EA-CCSD/cc-pVTZ+2s2p2d.
[a] *EOM-EA-CCSD/aug-cc-pVDZ+1s1p1d [89, 90].*
[b] *this work, EOM-EA-CCSD/cc-pVTZ+2s2p2d.*
[c] *SAC-CI/cc-pVDZ+2s5p2d [91].*

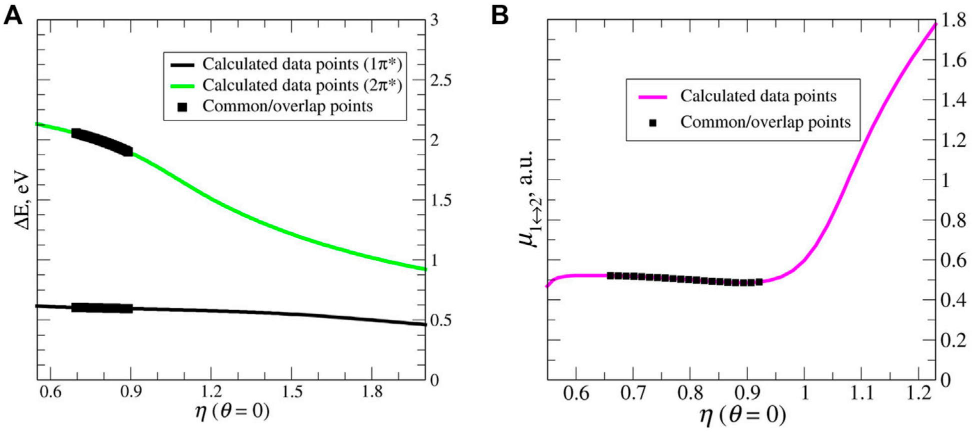

FIGURE 14 | (A) Stabilization (energy) graphs for the $1\pi^*$ and $2\pi^*$ resonance states of the uracil anion. The black squares represent the overlap region (in the energy) between the two electronic resonance states. **(B)** Stabilization (dipole transitions) graphs for $1\pi^* \leftrightarrow 2\pi^*$. The black points corresponds to a stable part on the graph, which has the same α-range as the overlap (energy) region. These points are used as input within RVP. This is n EOM-EA-CCSD/cc-pVTZ+2s2p2d calculation. Reprinted from Ref. [66], with the permission of AIP Publishing.

TABLE 4 | Complex dipole transitions (in a.u.) between the three lowest shape-type resonances of the uracil anion calculated with RVP. Electronic-structure method: EOM-EA-CCSD. Basis set: cc-pVTZ+2s2p2d. Reprinted from Ref. [66], with the permission of AIP Publishing.

Reμ	**Imμ**	**Reμ**	**Imμ**	**Reμ**	**Imμ**
$1\pi^* \leftrightarrow 2\pi^*$		**$1\pi^* \leftrightarrow 3\pi^*$**		**$2\pi^* \leftrightarrow 3\pi^*$**	
5.089e-01	−3.599e-03	8.782e-01	−6.017e-03	8.204e-01	−1.628e-02

Technically, the complex dipole transitions are calculated in a similar manner to the procedure for calculating the complex resonance energies [74]. Input data for fitting a Padé polynomial function are taken as the points marked in black in **Figure 14B**. Once in possession of a Padé function, analytical dilation into the complex plane is allowed. Next, one search for SPs clusters, i.e., complex dipoles are identified using the clusterization technique [50]. The results, i.e., the complex dipole transitions between the three low-laying resonance states, are given in **Table 4**. Notice that the real part dominant the three dipole transitions, where the imaginary part corresponds to about 1% of it or less.

6 SUMMARY

The RVP (Resonance *via* Padé) method and its applications have been described. The method enables the calculations of complex eigenvalues and energy surfaces associated with resonance states with finite lifetimes, also know as metastable states. Moreover, RVP allows calculations of other complex electronic properties, such as complex dipole transitions and moments. As illustrative numerical applications we present the calculations of: multiple doubly excited helium resonance states and the transitions between them, the ^{3}He*–H_2 cold collision, and uracil anion (an RNA nuclear base).

Since RVP is based on the stabilization technique, the complex properties are computed from real eigenvalues and real dipole transitions obtained from standard (Hermitian) quantum chemistry packages. The transition from the real axis into the complex plane is done by analytical continuation, specifically using the Padé approximant. The rational, mathematical logic and the methodology of RVP are presented here.

The ability to calculate *ab-initio* energies and lifetimes for small to medium-size systems (even with biological relevant) opens the door for investigating reactions of such molecules in which autoionization takes place. While the ability to also compute their complex dipole transitions enables investigating photo induced dynamics of such biological molecules.

Moreover, we describe an open-source code, which can be used as a "black box" to calculate complex physical properties from real input data with the RVP method. For the automatic code see (https://pypi.org/project/automatic-rvp/).

AUTHOR CONTRIBUTIONS

AL—writing and calculations. IH—writing and calculations. NM—writing and ideas.

FUNDING

We acknowledge the Israel Science Foundation (Grant No. 1661/19) for a partial support.

REFERENCES

1. Moiseyev N. *Non-Hermitian Quantum Mechanics*. Cambridge: Cambridge University Press (2011).
2. Moiseyev N. Quantum Theory of Resonances: Calculating Energies, Widths and Cross-Sections by Complex Scaling. *Phys Rep* (1998) 302:212–93. doi:10.1016/s0370-1573(98)00002-7
3. Klaiman S, Gilary I. On Resonance: A First Glance into the Behavior of Unstable States. *Adv Quan Chem* (2012) 63:1–31. doi:10.1016/b978-0-12-397009-1.00001-1
4. Hilborn RC. Einstein Coefficients, Cross Sections, F Values, Dipole Moments, and All That. *Am J Phys* (1982) 50:982–6. doi:10.1119/1.12937
5. Zuev D, Jagau T-C, Bravaya KB, Epifanovsky E, Shao Y, Sundstrom E, et al. Complex Absorbing Potentials within EOM-CC Family of Methods: Theory, Implementation, and Benchmarks. *J Chem Phys* (2014) 141:024102. doi:10.1063/1.4885056
6. Landau A, Moiseyev N. Molecular Resonances by Removing Complex Absorbing Potentials via Padé; Application to CO− and N2−. *J Chem Phys* (2016) 145:164111. doi:10.1063/1.4965887
7. Fennimore MA, Karsili TNV, Matsika S. Mechanisms of H and CO Loss from the Uracil Nucleobase Following Low Energy Electron Irradiation. *Phys Chem Chem Phys* (2017) 19:17233–41. doi:10.1039/c7cp01345k
8. Trinter F, Schöffler MS, Kim H-K, Sturm FP, Cole K, Neumann N, et al. Resonant Auger Decay Driving Intermolecular Coulombic Decay in Molecular Dimers. *Nature* (2014) 505:664–6. doi:10.1038/nature12927
9. Murphy BF, Osipov T, Jurek Z, Fang L, Son S-K, Mucke M, et al. Femtosecond X-Ray-Induced Explosion of C_{60} at Extreme Intensity. *Nat Commun* (2014) 5:4281. doi:10.1038/ncomms5281
10. Galli L, Son S-K, White TA, Santra R, Chapman HN, Nanao MH. Towards Rip Using Free-Electron Laser Sfx Data. *J Synchrotron Radiat* (2015) 22:249–55. doi:10.1107/s1600577514027854
11. Li Z, Vendrell O, Santra R. Ultrafast Charge Transfer of a Valence Double Hole in Glycine Driven Exclusively by Nuclear Motion. *Phys Rev Lett* (2015) 115:143002. doi:10.1103/physrevlett.115.143002
12. Cederbaum LS, Zobeley J, Tarantelli F. Giant Intermolecular Decay and Fragmentation of Clusters. *Phys Rev Lett* (1997) 79:4778–81. doi:10.1103/physrevlett.79.4778
13. Scheit S, Averbukh V, Meyer H-D, Moiseyev N, Santra R, Sommerfeld T, et al. On the Interatomic Coulombic Decay in the Ne Dimer. *J Chem Phys* (2004) 121:8393–8. doi:10.1063/1.1794654
14. Sisourat N, Kryzhevoi NV, Kolorenč P, Scheit S, Jahnke T, Cederbaum LS. Ultralong-Range Energy Transfer by Interatomic Coulombic Decay in an Extreme Quantum System. *Nat Phys* (2010) 6:508–11. doi:10.1038/nphys1685
15. Gokhberg K, Kolorenč P, Kuleff AI, Cederbaum LS. Site- and Energy-Selective Slow-Electron Production Through Intermolecular Coulombic Decay. *Nature* (2014) 505:661–3. doi:10.1038/nature12936
16. Iablonskyi D, Nagaya K, Fukuzawa H, Motomura K, Kumagai Y, Mondal S, et al. Slow Interatomic Coulombic Decay of Multiply Excited Neon Clusters. *Phys Rev Lett* (2016) 117:276806. doi:10.1103/physrevlett.117.276806
17. Ren X, Jabbour Al Maalouf E, Dorn A, Denifl S. Direct Evidence of Two Interatomic Relaxation Mechanisms in Argon Dimers Ionized by Electron Impact. *Nat Commun* (2016) 7:11093. doi:10.1038/ncomms11093
18. Landau A, Ben-Asher A, Gokhberg K, Cederbaum LS, Moiseyev N. Ab Initio Complex Potential Energy Curves of the He*(1s2p^{1}P)–Li Dimer. *J Chem Phys* (2020) 152:184303. doi:10.1063/5.0008337
19. Ben-Asher A, Landau A, Cederbaum LS, Moiseyev N. Quantum Effects Dominating the Interatomic Coulombic Decay of an Extreme System. *J Phys Chem Lett* (2020) 11:6600–5. doi:10.1021/acs.jpclett.0c01974
20. Jabbari G, Gokhberg K, Cederbaum LS. Competition Between Interatomic Coulombic Decay and Autoionization of Doubly-Excited Atoms. *Chem Phys Lett* (2020) 754:137571. doi:10.1016/j.cplett.2020.137571
21. Sakai K, Stoychev S, Ouchi T, Higuchi I, Schöffler M, Mazza T, et al. Electron-Transfer-Mediated Decay and Interatomic Coulombic Decay from the Triply Ionized States in Argon Dimers. *Phys Rev Lett* (2011) 106:033401. doi:10.1103/PhysRevLett.106.033401
22. LaForge AC, Stumpf V, Gokhberg K, von Vangerow J, Stienkemeier F, Kryzhevoi NV, et al. Enhanced Ionization of Embedded Clusters by Electron-Transfer-Mediated Decay in Helium Nanodroplets. *Phys Rev Lett* (2016) 116:203001. doi:10.1103/physrevlett.116.203001
23. Unger I, Seidel R, Thürmer S, Pohl MN, Aziz EF, Cederbaum LS, et al. Observation of Electron-Transfer-Mediated Decay in Aqueous Solution. *Nat Chem* (2017) 9:708–14. doi:10.1038/nchem.2727
24. Goldzak T, Gilary I, Moiseyev N. Resonance Energies, Lifetimes and Complex Energy Potential Curves from Standard Wave-Packet Calculations. *Mol Phys* (2012) 110:537–46. doi:10.1080/00268976.2012.662599
25. McCurdy CW, Jr, Rescigno TN. Extension of the Method of Complex Basis Functions to Molecular Resonances. *Phys Rev Lett* (1978) 41:1364–8. doi:10.1103/physrevlett.41.1364
26. White AF, Head-Gordon M, McCurdy CW. Complex Basis Functions Revisited: Implementation with Applications to Carbon Tetrafluoride and Aromatic N-Containing Heterocycles within the Static-Exchange Approximation. *J Chem Phys* (2015) 142:054103. doi:10.1063/1.4906940
27. Moiseyev N, Corcoran C. Autoionizing States of H_2 and H^{-2} Using the Complex-Scaling Method. *Phys Rev A* (1979) 20:814–7. doi:10.1103/physreva.20.814
28. Rescigno TN, McCurdy CW, Jr, Orel AE. Extensions of the Complex-Coordinate Method to the Study of Resonances in Many-Electron Systems. *Phys Rev A* (1978) 17:1931–8. doi:10.1103/physreva.17.1931
29. Sajeev Y, Moiseyev N. Reflection-Free Complex Absorbing Potential for Electronic Structure Calculations: Feshbach-Type Autoionization Resonances of Molecules. *J Chem Phys* (2007) 127:034105. doi:10.1063/1.2753485
30. Ghosh A, Karne A, Pal S, Vaval N. CAP/EOM-CCSD Method for the Study of Potential Curves of Resonant States. *Phys Chem Chem Phys* (2013) 15:17915–21. doi:10.1039/c3cp52552j
31. Sommerfeld T, Santra R. Efficient Method to Perform CAP/CI Calculations for Temporary Anions. *Int J Quan Chem.* (2001) 82:218–26. doi:10.1002/qua.1042
32. Feuerbacher S, Sommerfeld T, Santra R, Cederbaum LS. Complex Absorbing Potentials in the Framework of Electron Propagator Theory. Ii. Application to Temporary Anions. *J Chem Phys* (2003) 118:6188–99. doi:10.1063/1.1557452
33. Bravaya KB, Zuev D, Epifanovsky E, Krylov AI. Complex-Scaled Equation-Of-Motion Coupled-Cluster Method with Single and Double Substitutions for Autoionizing Excited States: Theory, Implementation, and Examples. *J Chem Phys* (2013) 138:124106. doi:10.1063/1.4795750
34. Jagau T-C, Zuev D, Bravaya KB, Epifanovsky E, Krylov AI. Correction to "A Fresh Look at Resonances and Complex Absorbing Potentials: Density Matrix-Based Approach". *J Phys Chem Lett* (2015) 6:3866. doi:10.1021/acs.jpclett.5b02017
35. Kunitsa AA, Granovsky AA, Bravaya KB. CAP-XMCQDPT2 Method for Molecular Electronic Resonances. *J Chem Phys* (2017) 146:184107. doi:10.1063/1.4982950
36. Kaprálová-Žďánská PR, Šmydke J. Gaussian Basis Sets for Highly Excited and Resonance States of Helium. *J Chem Phys* (2013) 138:024105. doi:10.1063/1.4772468
37. Benda Z, Jagau T-C. Communication: Analytic Gradients for the Complex Absorbing Potential Equation-Of-Motion Coupled-Cluster Method. *J Chem Phys* (2017) 146:031101. doi:10.1063/1.4974094
38. White AF, Epifanovsky E, McCurdy CW, Head-Gordon M. Second Order Møller-Plesset and Coupled Cluster Singles and Doubles Methods with Complex Basis Functions for Resonances in Electron-Molecule Scattering. *J Chem Phys* (2017) 146:234107. doi:10.1063/1.4986950
39. Hernández Vera M, Jagau T-C. Resolution-of-the-Identity Second-Order Møller-Plesset Perturbation Theory with Complex Basis Functions: Benchmark Calculations and Applications to Strong-Field Ionization of Polyacenes. *J Chem Phys* (2020) 152:174103. doi:10.1063/5.0004843
40. Parravicini V, Jagau T-C. Embedded Equation-Of-Motion Coupled-Cluster Theory for Electronic Excitation, Ionisation, Electron Attachment, and Electronic Resonances. *Mol Phys* (2021) 119:e1943029. doi:10.1080/00268976.2021.1943029
41. McCurdy CW, McNutt JF. On the Possibility of Analytically Continuing Stabilization Graphs to Determine Resonance Positions and Widths Accurately. *Chem Phys Lett* (1983) 94:306–10. doi:10.1016/0009-2614(83)87093-6

42. Chao JSY, Falcetta MF, Jordan KD. Application of the Stabilization Method to the $H^{-2}(1^2g)$ and $Mg^{-}(1^2p)$ Temporary Anion States. *J Chem Phys* (1990) 93:1125–35. doi:10.1063/1.459176
43. Thodika M, Fennimore M, Karsili TNV, Matsika S. Comparative Study of Methodologies for Calculating Metastable States of Small to Medium-Sized Molecules. *J Chem Phys* (2019) 151:244104. doi:10.1063/1.5134700
44. Thodika M, Mackouse N, Matsika S. Description of Two-Particle One-Hole Electronic Resonances Using Orbital Stabilization Methods. *J Phys Chem A* (2020) 124:9011–20. doi:10.1021/acs.jpca.0c07904
45. Holøien E, Midtdal J. New Investigation of the 1se Autoionizing States of He and H^{-}. *J Chem Phys* (1966) 45:2209–16.
46. Hazi AU, Taylor HS. Stabilization Method of Calculating Resonance Energies: Model Problem. *Phys Rev A* (1970) 1:1109–20. doi:10.1103/physreva.1.1109
47. Taylor HS. Models, Interpretations, and Calculations Concerning Resonant Electron Scattering Processes in Atoms and Molecules. *Adv Chem Phys* (1971) 18:91–147.
48. Taylor HS, Hazi AU. Comment on the Stabilization Method: Variational Calculation of the Resonance Width. *Phys Rev A* (1976) 14:2071–4. doi:10.1103/physreva.14.2071
49. Landau A. Shaping and Controlling Stabilisation Graphs for Calculating Stable Complex Resonance Energies. *Mol Phys* (2019) 117:2029–42. doi:10.1080/00268976.2019.1575993
50. Landau A, Haritan I. The Clusterization Technique: A Systematic Search for the Resonance Energies Obtained via Padé. *J Phys Chem A* (2019) 123:5091–105. doi:10.1021/acs.jpca.8b12573
51. Landau A, Haritan I, Kaprálová-Žďánská PR, Moiseyev N. Advantages of Complex Scaling Only the Most Diffuse Basis Functions in Simultaneous Description of Both Resonances and Bound States. *Mol Phys* (2015) 113:3141–6. doi:10.1080/00268976.2015.1080872
52. Haritan I, Moiseyev N. On the Calculation of Resonances by Analytic Continuation of Eigenvalues from the Stabilization Graph. *J Chem Phys* (2017) 147:014101. doi:10.1063/1.4989867
53. Landau A, Haritan I, Kaprálová-Žd’ánská PR, Moiseyev N. Atomic and Molecular Complex Resonances from Real Eigenvalues Using Standard (Hermitian) Electronic Structure Calculations. *J Phys Chem A* (2016) 120:3098–108. doi:10.1021/acs.jpca.5b10685
54. Schlessinger L. Use of Analyticity in the Calculation of Nonrelativistic Scattering Amplitudes. *Phys Rev* (1968) 167:1411–23. doi:10.1103/physrev.167.1411
55. Moiseyev N, Friedland S, Certain PR. Cusps, θ Trajectories, and the Complex Virial Theorem. *J Chem Phys* (1981) 74:4739–40. doi:10.1063/1.441624
56. Cleve M. *Makima Piecewise Cubic Interpolation* (2019). Available from: https://blogs.mathworks.com/cleve/2019/04/29/makima-piecewise-cubic-interpolation/.
57. Akima H. A New Method of Interpolation and Smooth Curve Fitting Based on Local Procedures. *J ACM* (1970) 17:589–602. doi:10.1145/321607.321609
58. Akima H. A Method of Bivariate Interpolation and Smooth Surface Fitting Based on Local Procedures. *Commun ACM* (1974) 17:18–20. doi:10.1145/360767.360779
59. Meurer A, Smith CP, Paprocki M, Čertík O, Kirpichev SB, Rocklin M, et al. SymPy: Symbolic Computing in Python. *PeerJ Comput Sci* (2017) 3:e103. doi:10.7717/peerj-cs.103
60. Ester M, Kriegel H-P, Sander J, Xu X. A Density-Based Algorithm for Discovering Clusters in Large Spatial Databases with Noise. *Kdd* (1996) 96:226–31.
61. Moiseyev N. Derivations of Universal Exact Complex Absorption Potentials by the Generalized Complex Coordinate Method. *J Phys B: Mol Opt Phys* (1998) 31:1431–41. doi:10.1088/0953-4075/31/7/009
62. Ben-Asher A, Moiseyev N. On the Equivalence of Different Methods for Calculating Resonances: From Complex Gaussian Basis Set to Reflection-Free Complex Absorbing Potentials via the Smooth Exterior Scaling Transformation. *J Chem Theor Comput.* (2016) 12:2542–52. doi:10.1021/acs.jctc.6b00059
63. Ben-Asher A, Landau A, Moiseyev N. Uniform vs Partial Scaling within Resonances via Pade Based on the Similarities to Other Non-Hermitian Methods: Illustration for the Beryllium $1s^22p3s$ State. *J Chem Theor Comput.* (2021) 17:3435–44. doi:10.1021/acs.jctc.1c00223
64. Riss UV, Meyer H-D. Calculation of Resonance Energies and Widths Using the Complex Absorbing Potential Method. *J Phys B: Mol Opt Phys* (1993) 26:4503–35. doi:10.1088/0953-4075/26/23/021
65. Lefebvre R, Sindelka M, Moiseyev N. Resonance Positions and Lifetimes for Flexible Complex Absorbing Potentials. *Phys Rev A* (2005) 72:052704. doi:10.1103/physreva.72.052704
66. Buskila G, Landau A, Haritan I, Moiseyev N, Bhattacharya D. Complex Energies and Transition-Dipoles for the Uracil Anion Shape-Type Resonances from Stabilization Curves via Padé. *J Chem Phys* (2022) 156:194101. doi:10.1063/5.0086887
67. Bhattacharya D, Ben-Asher A, Haritan I, Pawlak M, Landau A, Moiseyev N. Polyatomic AB Initio Complex Potential Energy Surfaces: Illustration of Ultracold Collisions. *J Chem Theor Comput.* (2017) 13:1682–90. doi:10.1021/acs.jctc.7b00083
68. Bhattacharya D, Pawlak M, Ben-Asher A, Landau A, Haritan I, Narevicius E, et al. Quantum Effects in Cold Molecular Collisions from Spatial Polarization of Electronic Wave Function. *J Phys Chem Lett* (2019) 10:855–63. doi:10.1021/acs.jpclett.8b03807
69. Lindroth E. Calculation of Doubly Excited States of Helium with a Finite Discrete Spectrum. *Phys Rev A* (1994) 49:4473–80. doi:10.1103/physreva.49.4473
70. Burgers A, Wintgen D, Rest J-M. Highly Doubly Excited *S* States of the Helium Atom. *J Phys B: Mol Opt Phys* (1995) 28:3163–83. doi:10.1088/0953-4075/28/15/010
71. Rost JM, Schulz K, Domke M, Kaindl G. Resonance Parameters of Photo Doubly Excited Helium. *J Phys B: Mol Opt Phys* (1997) 30:4663–94. doi:10.1088/0953-4075/30/21/010
72. Argenti L. Rydberg and Autoionizing Triplet States in Helium up to the N=5 Threshold. *At Data Nucl Data Tables* (2008) 94:903–80. doi:10.1016/j.adt.2008.03.003
73. Kaprálová-Žďánská PR, Moiseyev N. Helium in Chirped Laser Fields as a Time-Asymmetric Atomic Switch. *J Chem Phys* (2014) 141:014307. doi:10.1063/1.4885136
74. Bhattacharya D, Landau A, Moiseyev N. Ab Initio Complex Transition Dipoles Between Autoionizing Resonance States from Real Stabilization Graphs. *J Phys Chem Lett* (2020) 11:5601–9. doi:10.1021/acs.jpclett.0c01519
75. Pick A, Kaprálová-Žďánská PR, Moiseyev N. AB-Initio Theory of Photoionization via Resonances. *J Chem Phys* (2019) 150:204111. doi:10.1063/1.5098063
76. Henson AB, Gersten S, Shagam Y, Narevicius J, Narevicius E. Observation of Resonances in Penning Ionization Reactions at Sub-Kelvin Temperatures in Merged Beams. *Science* (2012) 338:234–8. doi:10.1126/science.1229141
77. Manohar PU, Krylov AI. A Noniterative Perturbative Triples Correction for the Spin-Flipping and Spin-Conserving Equation-Of-Motion Coupled-Cluster Methods with Single and Double Substitutions. *J Chem Phys* (2008) 129:194105. doi:10.1063/1.3013087
78. Jorge FE, Sagrillo PS, de Oliveira AR. Gaussian Basis Sets of 5 Zeta Valence Quality for Correlated Wave Functions. *Chem Phys Lett* (2006) 432:558–63. doi:10.1016/j.cplett.2006.10.026
79. Miller WH, Morgner H. A Unified Treatment of Penning Ionization and Excitation Transfer. *J Chem Phys* (1977) 67:4923–30. doi:10.1063/1.434674
80. Pawlak M, Shagam Y, Narevicius E, Moiseyev N. Adiabatic Theory for Anisotropic Cold Molecule Collisions. *J Chem Phys* (2015) 143:074114. doi:10.1063/1.4928690
81. Klein A, Shagam Y, Skomorowski W, Żuchowski PS, Pawlak M, Janssen LMC, et al. Directly Probing Anisotropy in Atom-Molecule Collisions Through Quantum Scattering Resonances. *Nat Phys* (2017) 13:35–8. doi:10.1038/nphys3904
82. Shagam Y, Klein A, Skomorowski W, Yun R, Averbukh V, Koch CP, et al. Molecular Hydrogen Interacts More Strongly when Rotationally Excited at Low Temperatures Leading to Faster Reactions. *Nat Chem* (2015) 7:921–6. doi:10.1038/nchem.2359
83. Lipton MS, Fuciarelli AF, Springer DL, Edmonds CG. The Study of Radiation Induced Dna-Protein Crosslinks by Electrospray Ionization Mass

Spectrometry. In: *Radiation Damage in DNA: Structure/Function Relationships at Early Times*. Columbus, OH: Battelle Press (1995).

84. Kanazawa Y, Ehara M, Sommerfeld T. Low-Lying π* Resonances of Standard and Rare DNA and RNA Bases Studied by the Projected CAP/SAC-CI Method. *The J Phys Chem A* (2016) 120:1545–53. doi:10.1021/acs.jpca.5b12190
85. Cheng H-Y, Chen C-W. Energy and Lifetime of Temporary Anion States of Uracil by Stabilization Method. *J Phys Chem A* (2011) 115:10113–21. doi:10.1021/jp205986z
86. Dora A, Tennyson J, Bryjko L, van Mourik T. R-Matrix Calculation of Low-Energy Electron Collisions with Uracil. *J Chem Phys* (2009) 130:164307. doi:10.1063/1.3119667
87. Gianturco FA, Lucchese RR. Radiation Damage of Biosystems Mediated by Secondary Electrons: Resonant Precursors for Uracil Molecules. *J Chem Phys* (2004) 120:7446–55. doi:10.1063/1.1688320
88. Kossoski F, Bettega MHF, Varella MTDN. Shape Resonance Spectra of Uracil, 5-Fluorouracil, and 5-Chlorouracil. *J Chem Phys* (2014) 140:024317. doi:10.1063/1.4861589
89. Fennimore MA, Matsika S. Core-Excited and Shape Resonances of Uracil. *Phys Chem Chem Phys* (2016) 18:30536–45. doi:10.1039/c6cp05342d
90. Fennimore MA, Matsika S. Correction: Core-Excited and Shape Resonances of Uracil. *Phys Chem Chem Phys* (2017) 19:29005–6. doi:10.1039/c7cp90241g
91. Ehara M, Kanazawa Y, Sommerfeld T. Low-Lying π Resonances Associated with Cyano Groups: A CAP/SAC-CI Study. *Chem Phys* (2017) 482:169–77. doi:10.1016/j.chemphys.2016.09.033
92. Moiseyev N, Weinhold F. Criteria of Accuracy of Resonance Eigenvalues. *Int J Quan Chem* (1980) 17:1201–11. doi:10.1002/qua.560170614

Conflict of Interest: The authors declare that the research was conducted in the absence of any commercial or financial relationships that could be construed as a potential conflict of interest.

Advantages of publishing in Frontiers

OPEN ACCESS
Articles are free to read
for greatest visibility
and readership

FAST PUBLICATION
Around 90 days
from submission
to decision

HIGH QUALITY PEER-REVIEW
Rigorous, collaborative,
and constructive
peer-review

TRANSPARENT PEER-REVIEW
Editors and reviewers
acknowledged by name
on published articles

Frontiers
Avenue du Tribunal-Fédéral 34
1005 Lausanne | Switzerland

Visit us: www.frontiersin.org
Contact us: frontiersin.org/about/contact

REPRODUCIBILITY OF RESEARCH
Support open data
and methods to enhance
research reproducibility

DIGITAL PUBLISHING
Articles designed
for optimal readership
across devices

FOLLOW US
@frontiersin

IMPACT METRICS
Advanced article metrics
track visibility across
digital media

EXTENSIVE PROMOTION
Marketing
and promotion
of impactful research

LOOP RESEARCH NETWORK
Our network
increases your
article's readership